2019

Integrated computational and full-scale physical simulation of dynamic soil-pile group interaction

Zhiyan Jiang
Iowa State University

Integrated computational and full-scale physical simulation of dynamic soil-pile group interaction

by

Zhiyan Jiang

A dissertation submitted to the graduate faculty

in partial fulfillment of the requirements for the degree of

DOCTOR OF PHILOSOPHY

Major: Civil Engineering (Geotechnical Engineering)

Program of Study Committee:
Jeramy C. Ashlock, Major Professor
Vernon Schaefer
Bora Cetin
Sri Sritharan
Wei Hong

The student author, whose presentation of the scholarship herein was approved by the program of study committee, is solely responsible for the content of this dissertation. The Graduate College will ensure this dissertation is globally accessible and will not permit alterations after a degree is conferred.

Iowa State University

Ames, Iowa

2019

DEDICATION

To my beloved parents, Tao Jiang and Xiaoxian Chen.

TABLE OF CONTENTS

Page

LIST OF FIGURES

Page

LIST OF TABLES

Page

ACKNOWLEDGMENTS

I would like to thank my adviser, Dr. Jeramy Ashlock, for his mentoring on my studies. He showed me the characteristics a qualified researcher should have – rigor, persistence, tolerance, and patience. I am grateful to have this opportunity studying in the United States, which reshaped my attitude towards myself and this world.

I am honored to have Drs. Vernon Schaefer, Sri Sritharan, Bora Cetin, and Wei Hong serving on my program of study committee.

Many thanks to my friends Liangyu and Liang for their help in my life. In addition, I would also like to appreciate assistance on my research from my colleagues Kanika, Cheng, and Zhao, among others.

I am grateful to my parents and uncle. It is their encouragement and support that helped me overcome many challenges to complete my Ph.D. study.

This material is based upon work supported by the National Science Foundation under Grant No. 1351828 entitled “CAREER: A Framework for Integrated Computational and Physical Simulation of Dynamic Soil-Pile Group Interaction”. This support is gratefully acknowledged.

ABSTRACT

Three dimensional dynamic soil-pile group interaction has been a subject of significant research interest over the past several decades, and remains an active and challenging topic in geotechnical engineering. A variety of dynamic excitation sources may potentially induce instabilities or even failures of pile groups. Employing modern experimental and numerical techniques, the dynamics of pile groups is examined in this study by integrated physical and computational simulations. In the physical phase, full-scale in-situ elastodynamic vibration tests were conducted on a single pile and a 2×2 pile group. Comprehensive site investigations were conducted for obtaining critical soil parameters for use in dynamic analyses. Broadband random excitation was applied to the pile cap and the response of the pile and soil were measured, with the results presented in multiple forms to reveal the dynamic characteristics of the pile-soil system. In the computational phase, the BEM code BEASSI was extended and modified to enable analysis of 3D dynamic pile group problems, and the new code was validated and verified by comparison to reference cases from the literature. A new theoretical formulation for analysis of multi-modal vibration of pile groups by accelerance functions is established using the method of sub-structuring. Various methods for interpreting the numerical results are presented and discussed. Case studies and further calibration of the BEM soil profiles are conducted to optimize the match between the theoretical and experimental accelerance functions. Parametric studies are performed to quantify the influence of the primary factors in the soil-pile system. It is shown that the new 3D disturbed zone continuum models can help improve the accuracy of dynamic soil-pile interaction analysis for pile groups in layered soils. This study therefore helps to advance the fundamental knowledge on

dynamic soil-pile interaction by improving the accuracy of current computational models, and contributes additional physical tests to the experimental database in the literature. The specific impedance functions generated herein can be immediately used in practice, and the underlying general 3D disturbed-zone computational framework can readily be applied to other pile group problems of interest to researchers and practitioners.

CHAPTER 1. INTRODUCTION, BACKGROUND, AND METHODOLOGY

1.1 Introduction to Soil-Pile Group Interaction Problems

1.1.1 Research Background

Dynamic soil-pile interaction is a complex subject involving the mechanics of soils and piles interacting due to seismic soil motions or transmission of structural vibrations through a substructure. As structural elements that are driven into the ground to transfer superstructure loads to the soil strata, piles are often installed in groups rather than as isolated single piles to increase overall strength, stiffness, and redundancy. For example, piles for most highway structures are installed in groups to support massive foundation loads (Hannigan et al. 2006). Due to their wide application in civil engineering, the safety of pile groups under dynamic excitations has been a concern and major research focus among scholars for several decades. Potential sources of dynamic excitations include earthquakes, blast loadings, machine vibrations, traffic vibrations, pile driving, and wind and wave loadings, among others (Clough and Penzien 1995). Each of these dynamic excitation sources may induce potential instabilities, excessive motion, or even failures of pile groups.

Dynamic soil-pile group interaction became the subject of much research interest in the late 1970's due to increasing demands of the nuclear power industry and developments in off-shore engineering, and it has remained an active and challenging area in geotechnical engineering to the present day. Higher demands on safety of buildings against earthquakes (Mylonakis and Gazetas 2000) lead to more stringent design requirements for pile foundations (e.g., CEN: Euro code-8-5), which are presently the most common type of deep foundation for large structures. Dynamic soil-pile group interaction is also an important consideration in design of machine foundations for vibrations to avoid resonance (Gazetas 1983). Additionally,

the pile vibration problem, known as the radiation problem in continuum wave mechanics, or the impedance problem in soil dynamics, is a fundamental component of sub-structuring approaches to seismic problems.

Several aspects make dynamic interaction between deep foundations such as drilled shafts and driven piles, and the surrounding soils complicated. These include the three-dimensional nature of the underlying wave propagation phenomena, sensitivity of the foundation response to the in-situ and load-transfer induced spatial variation of the soil's shear modulus and damping profiles, influence of the relative pile and soil material properties, interfacial pile-soil contact conditions, and disturbance of the soil as a result of installation of either driven piles (e.g., Hannigan et al. 2006) or drilled shafts (Brown et al. 2010).

Past studies suggest that the dynamic response of pile groups strongly contrasts that of the more widely studied and thus well-known case of single pile response, therefore field tests on single piles may not be able to predict the behavior of pile groups (Kaynia and Kausel 1982). Previous studies on dynamics of pile groups also reveal that interaction effects are frequency-dependent and controlled by various factors, such as pile parameters including embedded and unembedded lengths, radius, shear modulus, spacing, pile group layout, and more complicated soil parameters such as the profiles of soil shear modulus and damping, the three-dimensional stress field caused by soil self-weight (Chandrasekaran et al. 2010a) as well as static or dynamic foundation loads, and the mechanical soil response within disturbed zones around the pile group. The effects of these parameters have not yet been completely understood, and several are further examined in this study using computational and experimental methods.

1.1.2 Literature Review

1. Methods for dynamic pile group problems

Novak (1974) proposed an approximate method for predicting the dynamic response of single piles embedded in linear elastic soils. The method is based on Winkler's model or so-called 'p-y and t-z curves' (Poulos 1968; Matlock 1970), in which the pile is simplified as a beam-column that is supported by the soil through predefined independent nonlinear springs whose stiffnesses (p or t) in the horizontal (y) and vertical (z) directions are typically empirically back-calculated from full-scale load tests (e.g., Broms 1964; API 1987). Pile displacements and the soil resistance per unit length acting on the pile are obtained by solving the governing equations based on Euler-Bernoulli beam theory with fixed or pinned head conditions. It is known that the pile response is affected by the soil-to-pile mass ratio, ratio of soil shear wave velocity to soil longitudinal wave velocity, pile slenderness ratio, ratio of static load to Euler's buckling load, and dimensionless frequency. Among these parameters, the wave velocity ratio and slenderness ratios are the most critical factors. Compared with more rigorous solutions, Novak's approximate method yields lower stiffness and damping, which may be due to an imperfect bond between pile and soil. Application of the approximate method was extended to the more general case of a layered medium by Novak and Aboul-Ella (1978a, 1978b). In comparison with more rigorous solutions, the approximate method can provide satisfactory results for the single pile case when the dimensionless frequency ($a_o = \omega r_o / \mathrm{v}_s$) is greater than 0.3. Results at lower dimensionless frequencies can be approximated as constant and equal to those calculated at $a_o = 0.3$.

Group interaction factors for static analysis of vertical and horizontal deformations of pile groups have typically been derived by superposition of interaction factors from a two-pile

arrangement consisting of a reference pile and a single adjacent pile (EI Sharnouby and Novak 1986; EI Sharnouby and Novak 1990). However, by considering only two piles, this approach neglects the influence of the remaining piles in a group. The static interaction factors were also applied to dynamic cases for study of the response of offshore towers under wave excitations (El Sharnouby and Novak 1984; Novak and Mitwally 1990). For the special case when the pile cap is rigid, such an interaction factor is typically referred to as a group efficiency ratio (GER).

Nogami (1983) and Nogami and Chen (1984) introduced a simplified method to account for all piles of a group, based on the vertical displacement and force responses derived for single piles by Nogami and Novak (1976), with the added assumption of plane strain conditions. The displacement and vertical force acting on a given pile in a group were obtained by superposition of the influence of all other piles in the group. The equations of motion for pile segments interacting with soil were assembled by treating the piles as Winkler models with uncoupled springs acting along their length. The results revealed that dynamic group effects can be strongly frequency dependent, and are also related to the ratio of pile spacing to shear wavelength in the soil media.

Kagawa (1983) conducted a parametric study on factors influencing the dynamic behavior of a 2×1 pile group by modeling the soil-pile system as a beam-on-Winkler foundation as described by Kagawa and Kraft (1981a, 1981b). The results suggest that dimensionless frequency, pile spacing ratio, directional angle between two piles, and local pile flexibility/compressibility are primary factors, while the slenderness ratio, pile-head fixity condition, and soil Poisson's ratio have minor influences. When the spacing between two piles is less than 30 pile diameters for the lateral mode or 20 pile diameters for the vertical mode, the effects on stiffness and damping resulting from pile-to-pile interaction are pronounced.

When the interaction effects become dominant, the frequency-dependent stiffness (or "spring coefficient") of a pile group can either become negative due to inertia effects increasing with frequency, or exceed the summation of single pile stiffnesses. Pile-group effects are strongly frequency dependent, thus simply using the theory from static cases is not appropriate in dynamic cases. Under seismic loading conditions, piles deform due to both free-field soil deformation and inertial loads from the superstructure. Kagawa (1983) indicated that the pile-group effects are independent of loading conditions. In other words, the stiffness and damping of a pile group subjected to seismic motion can also be obtained by analyzing the pile group under pile-head loading conditions.

A simple method was developed by Dobry and Gazetas (1988) for computing dynamic impedances of floating rigidly-capped pile groups with consideration of pile-soil-pile interaction. Their parametric studies show that groups with close pile spacing behave as if being isolated, and the group factor exhibits a smooth variation with frequency. Specifically, when the shear wavelength (λ) in the soil is greater than the pile spacing (s), the soil region within the piles tends to vibrate in phase with the piles, making the pile-soil system respond like a block. For groups with ample spacing at low frequency with sufficiently long relevant wavelengths, the group stiffness decreases with frequency. Beyond a limiting frequency, wave interference phenomena begin to dominate the group response.

For axial vibration, Gazetas and Makris (1991) derived the displacement of a given pile in a group with soil modeled as a series of springs and dashpots (i.e., a Winkler model). The radiation condition was determined based on the amplitude of pile-head displacement as well as wave attenuation. For the lateral seismic response, Makris and Gazetas (1992) similarly

accounted for pile-soil interaction through a dynamic Winkler model with frequency-dependent springs and dashpots.

A three-dimensional continuum-based numerical approach developed by Kaynia and colleagues for dynamic pile problems (Kaynia 1982; Kaynia and Kausel 1982; Kaynia 1988; Kaynia and Kausel 1991; Kaynia and Mahzooni 1994) is based on Green's functions for buried dynamic barrel loads and disk loads (see Andersen 2006; Kausel 2006). Analyses of the dynamic response of a 4×4 pile group with various spacing ratios (Kaynia and Kausel 1982) suggested that for close spacing, inertia effects and interaction effects dominate group response when frequency is beyond a certain limit. The analyses also demonstrated that significant interaction effects are essentially due to out-of-phase interactions for the horizontal and vertical vibration modes, but are due to in-phase vibration in the rocking and torsional modes. In order to describe dynamic interaction, a new dynamic interaction factor similar to Poulos' static one was defined. The numerical results demonstrated that while the response of a single pile is mainly affected by the near-surface soil profiles, the response of a pile group is influenced greatly by characteristics of deeper layers.

Methods developed to compute the dynamic response of pile groups with consideration of pile-soil-pile interaction can be categorized mainly into two widely-used types: 1) dynamic Winkler-foundation type models; and 2) 3D elastic continuum models, including the Finite Element Method (FEM) and Boundary Element Method (BEM). Due to the nature of the Winkler-foundation, the focus in the pile-soil system is the 2-dimensional pile response while the Poisson's effect in the soil as well as coupling between soil layers are typically neglected. Analytical solutions for stiffness of 'soil springs' for a half-space soil medium (e.g., Bycroft 1956; Baranov 1967; Novak and Beredugo 1972; Veletsos and Verbic 1973; Luco 1974) as

employed in Novak's method cannot account for coupling along soil-pile interfaces. For instance, Baranov's solution (1967) regards the lateral resistance of each soil layer as vertically isolated without considering the coupled shear deformation of adjacent soil layers. Furthermore, the stiffness at the pile toe in the aforementioned studies is typically treated as that of a ring or disk on the surface of an elastic half-space, or taken as rigidly supported by rock, ignoring the effect of the pile toe's embedment and flexibility within the soil profile. Additionally, the piles in the aforementioned studies are commonly simplified as prismatic bars, and information about the actual cross-sectional geometry is consequently ignored. This could result in erroneous identical surface tractions on piles having different cross-sections.

Dobry and Gazetas (1988) suggested that use of Winkler model methods for computing the dynamic vertical response of pile groups is only valid for relatively short and/or stiff piles that behave as 'rigid' piles, and provided only a rough estimation for long and flexible piles. Specifically, the displacement at the pile toe is required to be at least 80% of that at top for a pile to be classified as rigid. An additional shortcoming of such methods is that inhomogeneity is only considered in the vertical direction, whereas the soil around piles is horizontally heterogeneous due to effects of pile installation and local increases in stress and strain due to load transfer from the piles. Ultimately, it is recognized that spring stiffnesses and dashpot coefficients are evaluated in an approximate rather than rigorous way. In analyzing lateral response, the method only applies to horizontally homogeneous soil since waves are assumed to spread out horizontally. In addition, the rocking deformation mode of each individual pile is assumed to cause no deformation of other piles, which may not be the actual case.

Three-dimensional continuum models can provide relatively more rigorous solutions, and are thus often used as benchmarks. For example, impedance functions and dynamic

interaction factors derived by Kaynia and Kausel (1982, 1991) using continuum-based analytical and numerical approaches have been widely used as benchmark solutions (e.g., Novak and Mitwally 1990; Makris and Gazetas 1992; Klar and Frydman 2002; Ghasemzadeh and Alibeikloo 2011). They are also generally capable of providing a complete study on pile groups under all vibration modes in a vertically inhomogeneous soil medium. More importantly, continuum models can account for coupled compatibility conditions between soil and piles as well as shear transfer between soil layers, and enable an accurate estimation of stress and strain fields in the soil region surrounding the piles. This capability creates the potential for incorporating nonlinear material behavior, which for soils is strongly dependent on both the stress and strain fields. On the other hand, continuum models require significantly greater computational capability and time than the commonly used simplified methods, especially when the number of piles increases and closed-form theoretical fundamental solutions are not applicable to the problem at hand.

For pile groups with more than two piles, superposition of interaction factors is commonly used (Gazetas et al. 1991; Gazetas et al. 1993). This is based on the assumption that the presence of the second free-head pile does not affect the displacements of the first loaded pile (Kaynia and Kausel 1982). However, the interaction factor is mathematically accurate only when it is calculated with an account of all piles present in the system (Novak 1991). A benchmark studied by Dobry and Gazetas (1988) suggests the simplified method provides good predictions of group interaction factors for small pile groups (such as 2×1, 2×2, 3×3) at low frequencies for which the relevant wavelength in the soil is greater than six times the pile diameter, but overestimates the resonant peaks of larger groups (e.g., 4×4). This is because interaction between two piles is reduced due to scattering of waves and shadow-forming among

other piles. Kaynia (1988) performed a study on dynamic response of pile groups embedded in homogeneous and nonhomogeneous soil media, concluding that for very close pile spacings (e.g., S=2.5d, where d is pile diameter) the superposition of interaction factors may not provide accurate solutions. El-Marsafawi et al. (1992) suggested that the superposition method works well in general, except for the cases of vertical response of stiff end-bearing piles, or at high frequencies for nonhomogeneous soils.

2. Disturbed-zone models

To simplify analyses, soils are often idealized as consisting of horizontally uniform layers. But soil properties can vary with distance from a pile or pile group due to 1) perturbation caused by forcing a pile into the soil during driving (O'Neil et al. 1982; Tomlinson 1994), 2) the dependence of soil properties on the state of stress at a point (Seed and Idriss 1970; Duncan and Chang 1970), and 3) the nonlinear dependence of shear modulus and damping on shear strain (e.g., Hardin and Drnevich 1972a 1972b; Kokusho et al. 1982; Vucetic and Dobry 1991; Borden et al. 1996; Stokoe et al. 1999). For instance, soils in the vicinity of a pile subjected lateral loads can have a lower shear modulus and higher damping ratio than soils farther away, due to the larger shear strains imposed in the soil near the pile. To account for such effects in their approximate methods, Novak and Sheta (1980) proposed a simple 2D disturbed boundary zone surrounding a pile, in which the soil has a lower shear modulus and larger material damping than that in the outer region. In their plane strain solution, the mass of the boundary zone was neglected to prevent wave reflections from the interface of the two zones. Otherwise, such reflections would cause false undulations in impedances, making them impractical in application.

However, Veletsos and Dotson (1986, 1988) demonstrated that the effects of inertia in the boundary zone cannot be ignored, and therefore presented new analyses, limited to vertical and torsional modes, of a similar radially inhomogeneous model consisting of two concentric zones – a thin, annular inner zone of disturbed material and an outer zone of undisturbed materials – with the same mass density in both zones. Continuous and discontinuous radial variations in shear modulus were examined and compared to the homogeneous case. The results for zero material damping showed that undulations appear in the vertical and torsional impedances and increase as the size of the boundary zone increases, due to the discontinuous shear modulus at the interface. A higher ratio of shear modulus in the outer zone relative to the inner zone leads to higher stiffness and radiation-damping factors for small boundary zones, but at higher frequencies this behavior can reverse and undulate as the boundary zone grows larger. For torsional excitation, the damping factor usually decreases with increasing modulus ratio unless the boundary zone is very large, because torsionally excited layers are less affected by the outer zone. After adding material damping to both zones, the torsional mode is affected more due to its lower radiation damping than the vertical mode. When shear modulus is assumed to continuously increase with radial distance in the form of a power function, the corresponding stiffness and damping curves vary monotonically and are no longer oscillatory, as expected.

El Naggar and Novak (1994) applied the disturbed-zone model to account for gapping and nonlinear behavior of soil in the inner zone and elastic behavior in the outer (far field) zone for axial pile vibration. A Winkler model was developed for both zones by employing springs using Kelvin's viscoelastic model, with additional frictional sliders in the nonlinear, disturbed inner zone. In addition, plastic sliders were used between the pile surface and the inner zone

so that slippage could be modeled once the soil stress exceeded its ultimate strength. Displacement and stress in the inner zone were analyzed as a plane-strain problem and the soil was assumed to follow a hyperbolic constitutive law (Kondner 1963a 1963b) when loaded and behave elastically when unloaded. Upon analyzing the pile driving process, Statnamic loading tests, and harmonic vibrations, the proposed model predicted the responses of single piles and pile groups satisfactorily.

Han (1997) proposed a model for vertical vibration of single piles in which the soil shear modulus varied parabolically from the pile surface to the boundary zone's outer surface. The shear modulus also varied smoothly across the boundary interface, so no artificially reflected waves were induced. Han's study suggested that when excitation intensities increase, the stiffness and damping factors as well as resonant frequencies decrease, while resonant amplitudes increase. Solutions from a model without the inner boundary zone overestimated the stiffness and damping of the soil-pile system, leading to a higher resonant frequency and a lower resonant amplitude.

Yang et al. (2009) established a multiple concentric disturbed-zone model for vertical vibration of a single pile. In their 3D axisymmetric model, it was assumed that soil in each annular disturbed zone was a homogeneous, isotropic linear viscoelastic medium, and the pile had a circular cross-section. The support at the bottom of the pile and soil zones was simplified as elastic springs. In addition, only vertical displacement of the soil was considered while the radial displacement was ignored. Theoretical solutions in the frequency domain and semi-analytical solutions in the time domain revealed that when the soil strength increased from the outer zone to the inner zone (i.e., soil strengthening around the pile), both real and imaginary parts of the impedance functions were smooth. When the soil around the pile was weakened in

the radial direction from the outer to the inner zone, significant oscillations appeared in both the impedance functions and the velocity admittance curves (which are frequency response functions of displacement per unit force), as the reflected waves decayed less rapidly. As the thickness (or "step size") of the annular disturbed zones increased, the reflected waves decayed more rapidly if soil near the pile was strengthened and more slowly if soil near the pile was weakened. Wu et al. (2013) applied a similar concentric disturbed-zone model to a tapered pile in layered soils to study effects of soil compaction around jacked piles. The support at bottom of the pile and the disturbed zones were modeled by viscoelastic springs, and it was determined that the compaction had a beneficial effect on tapered piles at low frequencies, but a detrimental effect at high frequencies.

The disturbed-zone models proposed in the existing literature have been applied for calibration of theoretical predictions using results of physical tests. For example, Kim et al. (1987) established a weak zone which had an outside radius of 1.5 times the pile radius and 0.78 times the pile length. The soil shear modulus within the weak zone was 80% of that for the undisturbed soil. Vaziri and Han (1991) established a cylindrical weakened zone around the pile to approximately account for effects of soil nonlinearity due to frozen soil layers, slippage, and lack of bonding between the pile and soil. The experimental case of unfrozen soil was analyzed with the boundary zone, and close agreement was observed between the theoretical and experimental results at all excitation magnitudes. The boundary zone parameters included shear modulus, damping ratio, and thickness, and had appreciable impacts on the overall response of pile-soil system.

Biswas et al. (2013) conducted a series of small-scale vibration tests on a 2×2 pile group in clay soils. The pile cap was excited by a harmonic horizontal force using a mechanical Lazan

(eccentric mass type) oscillator which induced coupled horizontal and rocking motions. The effects of nonlinearity and slippage were accounted for by an inner boundary zone containing soils with reduced shear modulus and increased damping relative to the semi-infinite outer region, using the methods of Novak and Sheta (1980) and Han (1997). Test results showed that by an appropriate estimation of nonlinear parameters such as the modulus reduction factor, damping in the weak zone, and separation length, Novak and Sheta's method provided satisfactory predictions in terms of the horizontal and rocking stiffnesses of the pile group, while Han's method did not. Both stiffness and damping of the pile group were found to decrease with increasing excitation intensity for the coupled horizontal-rocking vibration mode studied. This was reasoned to result from development of a weak boundary zone around the piles under high intensity force, in addition to separation from the soil.

Manna et al. (2013) conducted dynamic model-scale tests on a single pile and a 2×2 pile group. The experimental results were compared to two analytical approaches; a linear analysis using Novak's plane strain theory with static interaction factors, and nonlinear analysis using Novak's model with dynamic interaction factors. To approximately account for effects of slippage and nonlinearity, the piles were modeled as being surrounded by two concentric cylindrical zones; an outer infinite region and an inner weak zone. The gapping was accounted for by specifying zero soil shear modulus in the topmost layer within the inner zone. Nonlinearity was incorporated by increasing the damping ratio and thickness of the inner zone with excitation frequency, while shear modulus was decreased. After incorporation of the weak cylindrical zone, the predicted resonant frequencies decreased greatly and became very close to the observed values for both horizontal and rocking motions. It was also pointed out that the

accuracy of nonlinear dynamic responses depend on the boundary zone parameters and soil-pile separation, which require more theoretical and experimental research.

Similar analytical approaches were applied by Elkasabgy and Naggar (2013) for analyzing the vertical dynamic responses of a helical pile and a steel driven pipe pile. The boundary zone had a thickness of 1.2 times radius of the pile. The theoretical solution from the linear analysis highly overestimated both the stiffness and damping of the piles due to the assumed perfect bonding, which resulted in much higher resonant frequencies and lower vibration amplitudes. On the other hand, with soil parameters in the boundary obtained by trial-and-error, the nonlinear approach provided reasonable estimations for both impedance functions and response curves. The improved agreement verified that soil disturbance generated during installation and driving of helical and pipe piles can significantly affect their dynamic response.

A fully three-dimensional viscoelastic disturbed-zone concept in layered soils has also been established by Ashlock (2006) based on boundary element models calibrated to results of scaled-model centrifuge vibration tests of single piles. With the aid of the centrifuge data and the BEM program BEASSI, Ashlock demonstrated that even for the ideal case of laboratory-prepared uniform clean, dry sands, both the homogeneous and the theoretically more appropriate pure square-root half-space model provide poor agreement with multi-modal experimental results. He therefore proposed a continuum model with consideration of pile installation and load-transfer effects, as well as the in-situ inhomogeneous soil profile. After calibrating the model against centrifuge test data of solid piles, the model was shown to predict the observed behavior of hollow piles at various centrifugal g-levels with high accuracy. The study thus demonstrated that incorporation of mechanics-based local perturbations of the soil's

far-field shear modulus and damping within a 3D disturbed zone around the piles can improve accuracy of prediction for the boundary element models. The disturbed-zone model was also applied to full-scale vibration tests on a single pile in significantly more complicated natural soil conditions by Fotouhi (2014), as well as surface footings at various centrifuge scales (Ashlock and Pak 2009), and reduced field scale (Ashlock and Phipps 2011). A selection of disturbed-zone models from the previous studies are illustrated in Figure1.1.

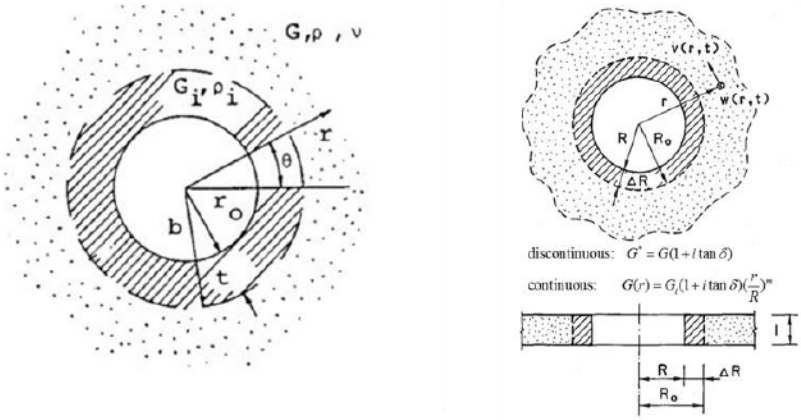

(a) Novak and Sheta (1980) (b) after Veletsos and Dotson (1986)

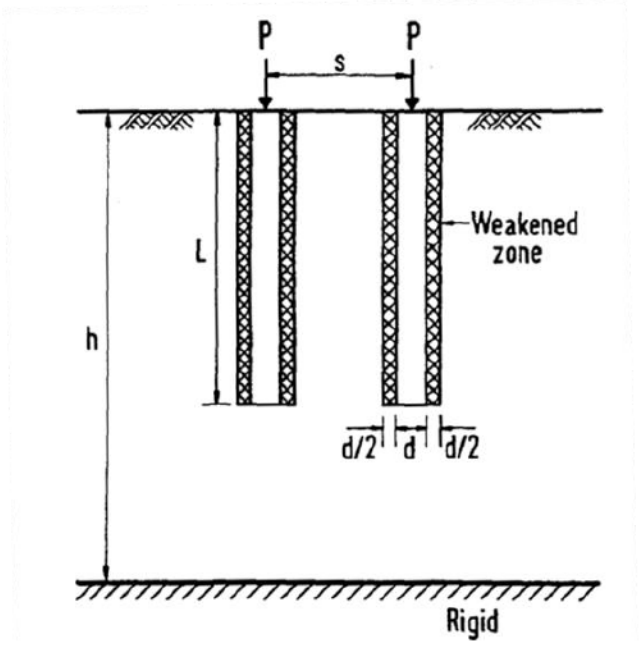

(c) Chow (1991)

Figure 1.1 *Previous disturbed zone models proposed for piles.*

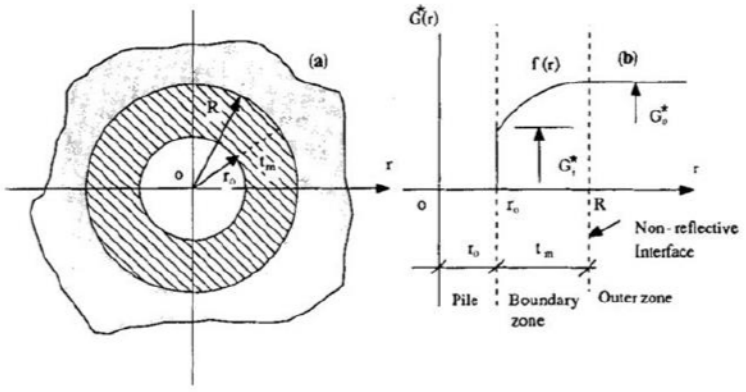

(d) Han (1997)

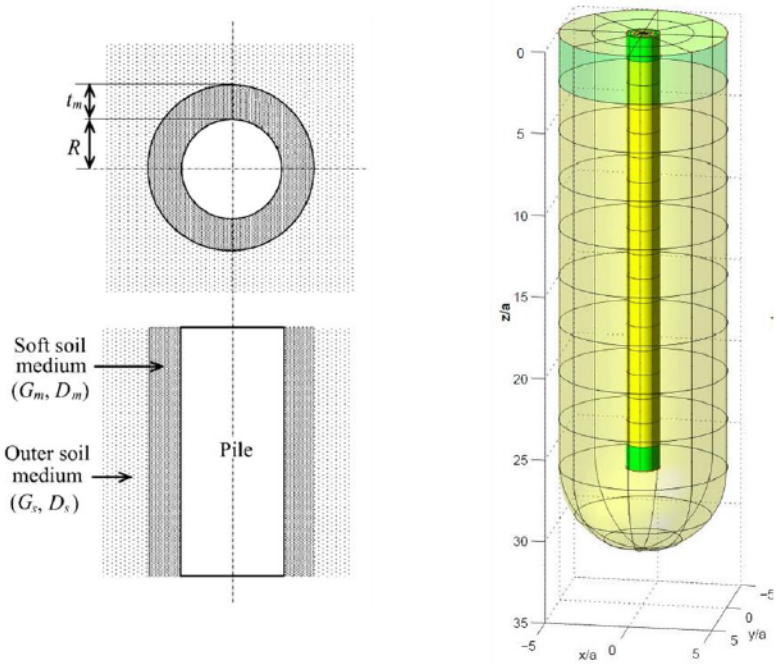

(e) Manna et al. (2013) (d) Ashlock (2006)

Figure1.1 *(continued)*

Disturbed-zone models have thus been proven capable of improving accuracy for various analytical and computational methods, and are being applied on more complex dynamic SSI problems. As detailed above, the disturbed-zone model was originally developed based on axisymmetric plane-strain assumptions, but there are several shortcomings of such

models that can be improved. First, the plane-strain assumption limits application of the models to only single long, circular piles. For short piles, errors caused by the plane-strain assumption at the pile toe can be significant, and the disturbed zone should be extended below the pile toe as a semi-circular region in 2D or a hemispherical cap in 3D. Otherwise the perturbed soils below the pile toe would not be considered in the vertical vibration mode. Second, the soil in each of the two zones was assumed to be homogeneous or radially inhomogeneous in some studies, but not typically layered. In other words, horizontal inhomogeneity was considered but not vertical inhomogeneity. Additionally, the excitation force was typically limited to vertical and torsional cases, for which the plane-strain assumption is valid. For the coupled horizontal-rocking mode of vibration, the theoretical solutions could not be derived. The above limitations can be overcome with the help of more general 3D numerical models, as developed in this study.

Finally, disturbed-zone models have yet to be rigorously studied in dynamic pile group cases. The infinite number of possible combinations of layout and number of piles in a group, vibration amplitudes, loading directions and their combinations, and layered in-situ soil profiles make it difficult to establish an appropriate disturbed zone that will work well in all cases. A rigorous study of 3D disturbed-zone continuum models for pile groups is proposed herein, with layered soil profiles inside and outside the disturbed zone, and parametric variations in modulus, damping, and shape and size of the disturbed zone.

3. Full-scale and small-scale experimental studies

Novak and Grigg (1976) conducted small-scale tests on a single pile and a 2×2 pile group in fine silty sand and began investigating group effects experimentally. In the pile group tests, each pile had a diameter of 2.4 in. and a length of 82 in., with a slenderness ratio (length

over radius) of 69.1. Shear wave velocities at different depths were measured by the steady state vibration technique (Richart et al. 1970). Group parameters, such as group stiffness, group damping, natural frequency, and first resonant amplitude were calculated by superposition of interaction factors. The results suggested that further effort was needed to improve the accuracy of theoretical group interaction factors.

El Sharnouby and Novak (1984) performed a more detailed small-scale experimental study on a massive group of 102 steel pipes having 26.7 mm diameter and 1.06 m length, with a rigid pile cap 6 cm above the ground. Shear wave velocities were measured by cross-hole and steady-state vibration techniques. Forced vibration experiments were conducted under various excitation amplitudes controlled by adjusting the number of masses on an eccentric mass oscillator. The measured responses were validated to be linear at low amplitudes and even at large displacement amplitudes of 0.2 mm. In a companion paper (Novak and El Sharnouby 1984), three main methods were compared with the experimental results - the static interaction approach, dynamic interaction factor approach, and direct dynamic analysis approach. In order to fit the static interaction approach to the test data for vertical and horizontal vibration modes, the static interaction factor needed to be adjusted and an arbitrary damping interaction factor included. The equivalent pier concept was employed, which regards the pile and adjacent soils as a composite body, and can match the peak of response curves at low frequencies but not at high frequencies. The dynamic interaction factors from Kaynia and Kausel (1982) tended to overestimate damping for the vertical mode, but gave reasonable agreement for the horizontal response. It was reported that including an ad-hoc apparent mass as well as an arbitrary damping interaction factor or a weak zone around the piles can improve the fit by dynamic pile group analyses, which by themselves tended to overestimate damping.

Vaziri and Han performed full-scale field studies of dynamic response of piles under lateral excitations in frozen and unfrozen soils. In the single pile tests (Vaziri and Han 1991), dynamic soil properties were measured by the in-situ cross-hole technique and laboratory tests such as the triaxial test. The reinforced concrete pile had a diameter of 0.32 m and a length of 7.5 m, and was cast in silty clays with lenses of a sandy clay mixture. A 0.3m-thick concrete pile cap was cast with a minimum clearance of 0.02 m from the ground surface. An exciter was placed on top of the pile cap to apply harmonic force, and two horizontal displacement transducers measured the horizontal vibration while another two measured the rotational motion. Theoretical solutions were calculated using Novak's DYNA model. The tests showed that the frozen top layer had a profound influence on the pile response by providing a substantial increase in the horizontal stiffness. The vibration in unfrozen soils showed strong nonlinearity due to soil yielding and possible pile separation. In subsequent tests at the same site (Han and Vaziri 1992), a 2×3 group of piles having the same properties as the single pile was used. The reinforced concrete pile cap had dimensions of 2.5 m × 1.6 m × 0.5 m, and a clearance of 0.25 m above the ground. Excitation and measurement were similar to the single pile case. The test results were interpreted in forms of displacement magnitude, pile group impedance, and group efficiency ratio. It was concluded that the pile-soil-pile interaction resulted in a reduction in stiffness and increase in damping for the soil. As frequency increased, the group efficiency ratio for stiffness decreased while that for damping increased. The presence of a frozen soil layer resulted in a reduction in displacement magnitude and increase in resonant frequency.

El-Marsafawi et al. (1992) conducted model tests on a group of six steel pipe piles. The soil consisted of silty fine sand with a gravel seam, resting on dense silty till. The soil shear

wave velocity profile was measured using the cross-hole and steady state vibration techniques. The pipe piles had an outer diameter of 101.6 mm, thickness of 6.35 mm and were driven to a depth of 2.75 m with closed ends. A hexagonal reinforced concrete cap of 0.2 m thickness was seated on the piles, 0.15 m above the ground. The system was excited harmonically by a mechanical oscillator in vertical and horizontal directions. For vertical vibration, four velocity transducers were mounted vertically on top of pile cap at equidistant locations from the foundation center on two axes of symmetry, and the measurements were averaged to eliminate rocking components. For horizontal and rocking vibration, two velocity transducers were installed on either side of the foundation at the centroid level and another two velocity transducers were mounted vertically on top. A dual-beam oscilloscope was used to monitor the phase shift between different velocity measurements. The vibration of the pile group exhibited moderate nonlinearity. Theoretical results were calculated by Novak's method and compared to the experimental data for both the pile group and single pile. The results suggested that stiffnesses for small displacements were well estimated but damping values were over-estimated. Two weak-zone models were established to account for separation and pile installation effects.

Chandrasekaran et al. (2010b, 2013) studied the dynamic and cyclic lateral and bending behavior of small-scale pile groups in clay. The experimental soil was classified as CH with shear wave velocity measured by the cross-hole technique. Small aluminum tubes having an outer diameter of 25.6 mm and inner diameter of 18.6 mm were used, with the length to diameter ratio varied from 15 to 40 and spacing to diameter ratio varied from 3 to 9. The pile cap was an aluminum plate 150 mm above the ground surface. Cyclic loads were applied by an electrodynamic exciter with a power amplifier. For the lateral response, test results of a 2×2

pile group exhibited larger hysteresis loops at higher frequencies and pore water pressures reached maximum values at the resonant frequency. The resonant frequency decreased as loading amplitude increased, which was due to the decrease in modulus and increase in hysteretic damping when shear strain increases. Normalized pile-head displacement curves under different loading amplitudes did not overlap, and exhibited nonlinear behavior such that the resonant peak frequency reduced with increasing load amplitude, while the resonant peak leaned towards the left due to the well-known snap-through effect. Compared to the static case, the peak dynamic displacement was amplified by a factor greater than 2. The resonant frequency decreased and peak amplitude increased as the pile spacing decreased or the number of piles increased, because of interaction effects and nonlinearity of the soil-pile system. An equivalent damping ratio and stiffness constant were calculated by modeling the system as a single degree of freedom (SDOF) system. The bending response was shown to be strongly frequency-dependent. In a 3×3 pile group, the corner piles had much higher bending moments at the pile cap than the central pile. The group interaction effects also resulted in higher forces acting on a pile in a group than when isolated.

Elkasabgy and El Naggar (2011, 2013) conducted full-scale tests on a single helical pile and a driven steel pipe pile. Subsurface conditions were obtained by CPT and SPT tests and soil behavior types included silt, clay, silty clay, silty sand and, sandy silt. Both piles had outer diameters of 0.324 m, inner diameters of 0.305 m, and lengths of 9 m, and were driven closed-ended. A superstructure was simulated by a rectangular steel plate 0.6 m off the ground with test body plates stacked above. The excitation force was generated by a Lazan mechanical oscillator and the magnitude of excitation was adjusted by degree of eccentricity of the rotating masses. Two uniaxial accelerometers were mounted on top of the test body equidistant from

the central axis, and a triaxial accelerometer was mounted on one side of the test body at the centroid elevation. The helical pile and the driven pile were tested two weeks after installation and the helical pile was tested again 9 months after installation. Vertical displacement amplitude was calculated from the acceleration measurement, and showed slight to moderate nonlinearity for the helical pile, with significant recovery in shear modulus between the two tests. The driven pile showed similar performance characteristic to the helical pile. Experimental bending moments measured by strain gauges suggested an insignificant influence on the load transfer mechanism for the helical pile.

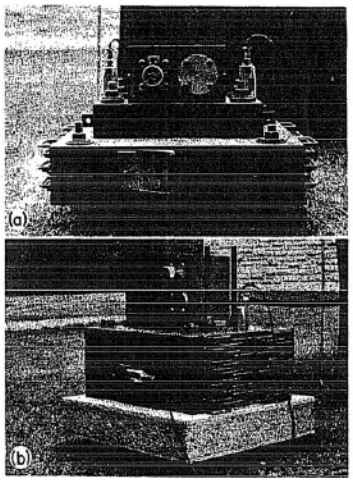

(a) Novak and Grigg (1976)

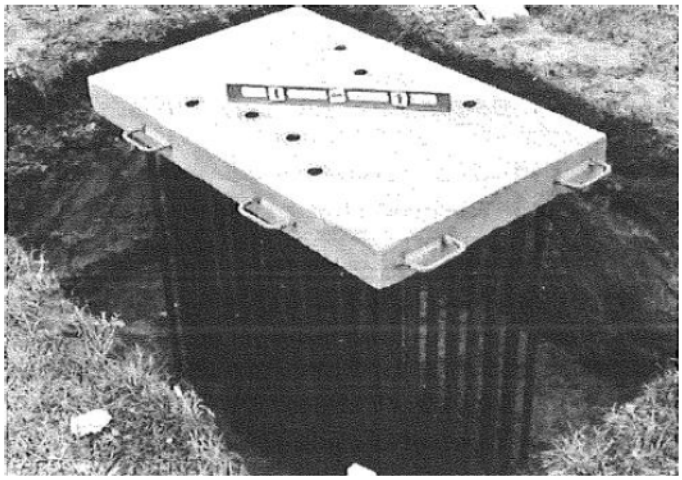

(b) EI Sharnouby and Novak (1984)

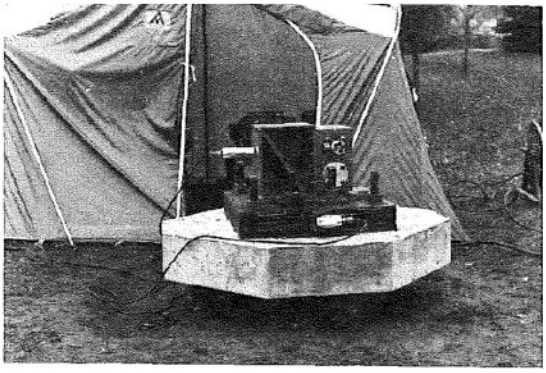

(c) El-Marsafawi et al. (1992)

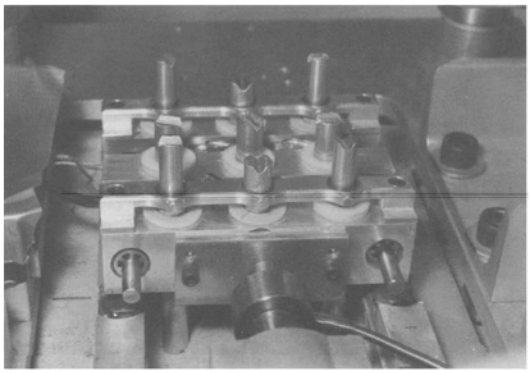

(d) McVay et al. (1994)

Figure 1.2 *Selected previous experimental pile studies.*

(e) Rollins et al. (2003b)

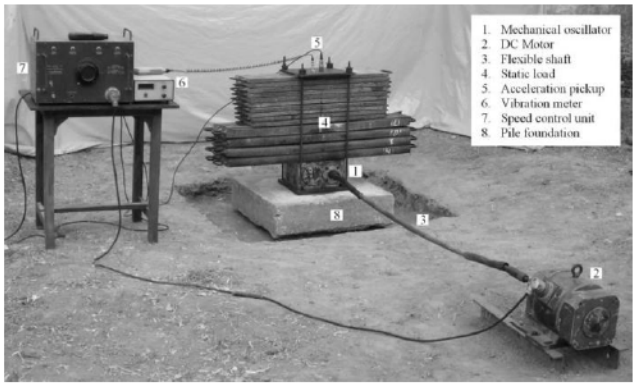

(f) Manna and Baidya (2010)

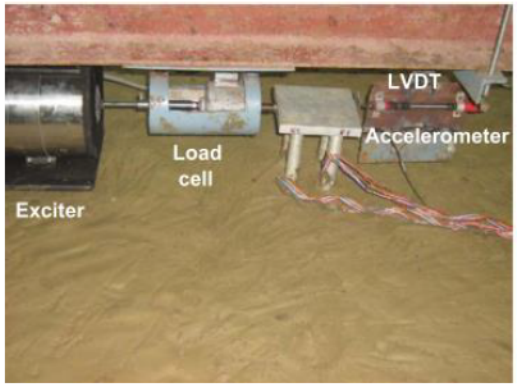

(g) Chandrasekaran et al. (2013)

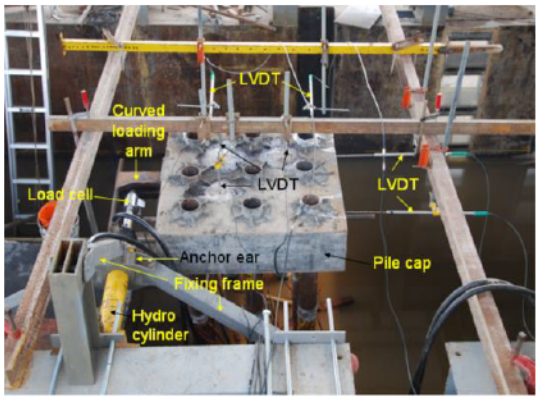

(h) Kong et al. (2015)

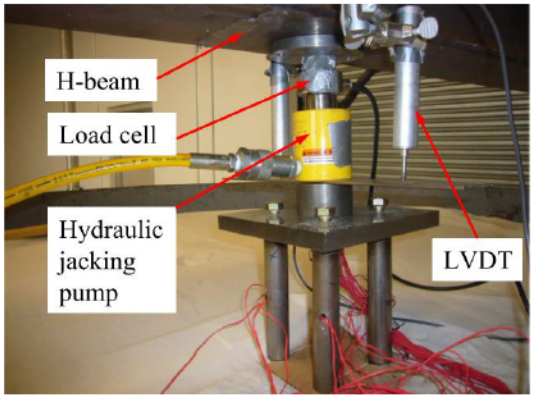

(i) Choi et al. (2017)

Figure 1.2 *(continued)*

Table 1.1 summarizes previous experimental studies on the dynamic response of single piles and tests on pile groups. Due to the relatively limited number of studies on the dynamics of pile groups, static pile-group tests were also included for reference. Small-scale and even full-scale experiments have become a main methodology in dynamic soil-pile interaction since the 1980s, however the volume of full-scale experimental studies in the literature has remained much smaller than theoretical and numerical ones. Although challenging to carry out, physical simulations make it possible to observe how a pile group actually responds under dynamic excitation by measuring the natural frequencies and pile cap accelerations and displacement amplitudes. From the literature review, it is clear that the available data on in-situ full-scale tests is still insufficient in terms of the range of force and excitation frequency, and the spacing and layout of pile groups. The limited collection of full-scale vibration tests makes it worthwhile to contribute further to such a database, to help build a foundation for further studies. In addition, when apparent discrepancies are found between the observed and predicted responses, opportunities are presented to improve both the experimental methods as well as the analytical or computational models. To this end, the proposed study will involve performance of new full-scale vibration and cyclic tests on a single pile and a 2×2 pile group, and development of new computational models for dynamic soil pile-group interaction analyses.

Table 1.1 *Summary of previous experimental studies on dynamic response of single piles and pile groups.*

Author (year)	Scale[a]	# of piles	Pile type	Outer diameter/ width (m)	Driven depth/length (m)	S/d ratio	Soil type	Loading type – direction[b]	Loading device
Novak and Grigg (1976)	S	2×2, single	steel pipe	0.061, 0.089	2.08~2.35	7.5, 11.25	silty sand, gravel, till	D - H V	Lazan oscillator
Scott et al. (1982)	F	single	open-ended steel pipe	0.61	9.8	N.A.	saturated medium dense silty sand	D - H	vibration generator
El Sharnouby and Novak (1984)	S	102	steel pipe	0.0267	1.06	3	artificial mixture	D - H V T	Lazan oscillator
Blaney and O'Neil (1986)	F	single	closed-ended steel pipe	0.273	13.4	N.A.	OC clay	D – H	linear inertia mass vibrator
Hassini and Woods (1989)	S	2×2, 2×1	steel pipe	0.06	1.98	2~10	SP	D – H V	electro-magnetic exciter; rotating-mass shaker
Blaney et al. (1987)	F	3×3	closed-ended steel pipe	0.273	13.1	3	OC clay	D – V	linear inertia mass vibrator
Crouse and Cheang (1987)	F	4×4, 3×2	concrete-encases steel pile	0.32, 0.324	12.2	4.1, 2.8; 5, 4.7	sand, silty sand, gravelly sand	D - H	quick-release
Finn and Gohl (1987)	S	2×1, single	steel tube	0.00952	0.2095	2,4,6	dense and loose sand	D - H	centrifuge
Kim et al. (1987)	S	single	cast-in-place RC pile	0.15	1.5,2.3,3	N.A.	SP	D – V	electro-magnetic vibrator

Table 1.1 *(continued)*

Blaney and O'Neil. (1989)	F	3×3	closed-ended steel pipe	0.273	13.7	N.A.	OC clay	D – H	linear inertia mass vibrator
Vaziri and Han (1991)	F	3×2, single	cast RC pile	0.32	7.5	2.81	silty clay w/ lenses of sandy clay	D – H	Lazan oscillator
El-Marsafawi et al (1992)	S	6	steel pipe	0.102	3.05	3,4	silty sand, silty till	D – H V	mechanical oscillator
Finn and Gohl (1992)	S	2×2, 2×1, single	aluminum tube	0.00635	0.61	N.A.	dense and loose sand	D - H	shaking table
Sy and Siu (1992)	F	single	cast-in-place RC pile	0.51	8.5	N.A.	sand/gravel fill, silt, sand	D – H V	electro-magnetic shaker
Yao and Kobayashi (1992)	S	4	aluminum rectangular hollow pile	0.025	1.75	21	saturated siliceous sand No.6	D – H	shaking table
Zhu et al. (1992)	F	40, single	RC pile	0.5	18, 22, 28	N.A.	silty clay, clay, silty sand, hard sand	D – H V	vibrator
McVay et al. (1995)	S	3×3, single	aluminum tube	0.0077	0.235	3,5	SP	S – H	centrifuge
Burr et al. (1997)	S	2×2	steel tube	0.0254,0.0381,0.051	N.A.	2.25~15.0	stiff cohesive volcanic-ash; soft saturated clay	D - H	vibrator
Wilson et al. (1997)	S	2×2, 3×3, single	aluminum model pile	0.022	0.559	4	Nevada sand	D – H	centrifuge

Table 1.1 *(continued)*

Rollins et al. (1998)	F	3×3, single	closed-ended steel pipe	0.324	9.1	3	ML,CL,SP, CH,SM	S – H	hydraulic jack
Brown et al. (2001)	F	3×3, 3×4	steel pipe	0.273	12	3,4	organic clay, alluvial sand; CL,ML,SM	S,D - H	hydraulic jack; Statnamic device
Rollins et al. (2003b)	F	3×3	closed-ended steel pipe	0.324	9.1	2.8, 5.65	ML,CL,SP, CH,SM	D – H	Statnamic device
Rollins et al. (2006)	F	3×3, 3×4, 3×5, single	closed-ended steel pipe	0.324	11.9	3.3,4. 4,5.65	CH,SM,CL, SM	S – H	hydraulic jack
Stewart et al. (2007)	F	3×3, single	cast-in-place RC pile	0.61	7.62	3	silty clay, silty sand, sandy silt	S - H	actuator
Ashlock and Pak (2009)	S	single	tubular and solid aluminum pile	0.00914,0.0 094	0.122,0.127	N.A.	silica F-75 Ottawa sand	D – H V	centrifuge
Manna and Baidya (2009)	F	single	cast-in-place RC pile	0.45	22	N.A.	SM,CH,CL, ML,SM	S,D - V	hydraulic jack, Lazan oscillator
Manna and Baidya (2010)	S	2×2, single	cast-in-place RC pile	0.1	1,1.5,2	2,3,4	CL,CI,CH	D – V	Lazan oscillator
Chandrasekaran et al. (2010a)	S	1×2, 2×2, 1×4,3×3	aluminum tube	0.026	0.39~1.04	3,5,7, 9	fat clay	S - H	slotted weights

Table 1.1 *(continued)*

Chandrasekaran et al. (2010b, 2013)	S	1×2, 2×2, 3×3	aluminum tube	0.026	0.39~1.04	3,5,7	fat clay	D - H	pneumatic power cylinders
Dai et al. (2012)	F	1×2, 2×2, 3×3, single	cast-in-place RC pile	0.4	20,24	2.5,3	clay, silt, silt mixed with silty sand, soft clay	S - V	hydraulic jack
Fotouhi and Ashlock (2012)	F	single	steel H pile	0.256	6	N.A.	lean clay with gravel, silt-clay, sandy gravel	D – H V	servo-hydraulic inertial shaker
Elkasabgy and El Naggar (2013)	F	single	helical and pipe piles	0.324	9	N.A.	silt, silty clay, silty sand, sandy silt, clay	D - V	Lazan oscillator
Kong et al. (2015)	S	3×3	steel tube	0.114	5.95	6,11	saturated silt	S - H	hydraulic actuator
Taghavi et al. (2016)	S	2×2, single	steel tube	(0.29 m in prototype)	(16 m in prototype)	3,7	OC clay, dense sand	S - H	centrifuge
Choi et al. (2017)	L	2×2	closed-ended steel pipe	0.03	1.2	3	silica F-55 sand (SP)	S – H V	hydraulic jack
Pender et al. (2018)	F	single	closed-ended steel pipe	0.220	7.75	N.A.	stiff silty clay	D - H	sledge hammer; pull-release

Scale[a]: F – full-scale; S – small-scale; L – large-scale.

Loading type – direction[b]: S – static loading; D – dynamic loading; H – horizontal; V – vertical; T – torsional.

N.A. = not applicable.

1.2 Statement of Problem and Methodology

The problem studied in the thesis is the dynamic response of a single floating pipe pile and a 2×2 pile group, as part of a research project supported by the National Science Foundation (Grant No. 1351828). The problem is studied in integrated computational and experimental phases.

For the experimental phase, pipe piles with an outer diameter of 0.219 m (8.625 in.) and length of 7.62 m (25 ft) were driven open-ended at the former Spangler Geotechnical Laboratory site at Iowa State University. Small strain elastodynamic vibration tests on the single pile and 2×2 pile group were performed using a servo-hydraulic inertial shaker developed in a previous NSF Network for Earthquake Engineering Simulation (NEES) project. First, the vertical vibration mode was tested using vertical centric (VC) excitation, and then the coupled horizontal-rocking mode was tested using horizontal centric (HC) excitation. More realistic multi-modal (vertical plus horizontal-rocking) tests were then performed by applying vertical eccentric (VE) excitation. By comparing test results, the hypothesis that a single multi-modal VE test on a pile group can more efficiently replace sequential VC and HC tests was examined, thereby eliminating the problem of differing soil stress histories and contact conditions when the modes are measured in separate sequential tests as in most experimental studies. Similar to the previous NEES study on single piles (Fotouhi and Ashlock 2012), the vibration tests were performed with successively increasing excitation levels for each of three broadband excitation types: random (R), swept-sine (S), and chaotic impulse (C). Following the vibration tests, the piles will be tested under quasi-static cyclic horizontal forcing using a large hydraulic actuator to apply progressively larger displacements until failure for a separate study.

In the computational phase of this study, the 3D BEM disturbed-zone models were used to calculate impedance functions at the ground-surface elevation for the single pile and pile group in the frequency domain. The impedances are complex-valued force/displacement and moment/rotation ratios. The theoretical accelerance functions (frequency-dependent ratios of linear or angular acceleration to force) at the pile cap centroid are formulated and calculated in Section 3.5.2, using the method of sub-structuring with the BEM impedance functions as inputs. For the calibration process, the soil property profiles inside and outside the disturbed zone were varied parametrically based on mechanics considerations, to minimize the misfit between the theoretical and measured experimental accelerance functions. Parametric studies were also conducted to study effects of the discretization of soil layers, pile group gapping, pile spacing, disturbed zone dimensions and shape, and superstructure properties.

This study aims to advance fundamental knowledge on dynamic pile-soil interaction, to ultimately improve the accuracy with which current computational models can simulate and predict the true multi-modal viscoelastic vibration responses. It also contributes an additional experimental database on full-scale single and pile group tests, enabling further studies on viscoelastic and nonlinear pile group responses.

CHAPTER 2. FULL-SCALE IN-SITU DYNAMIC VIBRATION TESTS

2.1 Site Investigation

Site investigation is the process whereby all relevant information concerning the site of a proposed civil engineering or building development and its surrounding area is gathered. Techniques used in some previous in-situ pile experiments are summarized in Table 2.1. The cone penetration test (CPT) appears to be the most frequently used technique, followed by the standard penetration test (SPT) and the cross-hole seismic test.

Table 2.1 *Site investigation techniques applied in previous in-situ pile experiments.*

Author (year)	Site investigation technique
Novak and Grigg (1976)	Rubber balloon method, steady-state vibration
Scott et al. (1982)	CPT
El Sharnouby and Novak (1984)	cross-hole, steady-state vibration
Blaney et al. (1986)	CPT, cross-hole
Crouse and Cheang (1987)	CPT, downhole
Kim et al. (1987)	cross-hole
Vaziri and Han (1991)	cross-hole
El-Marsafawi et al (1992)	cross-hole, steady-state vibration
Sy and Siu (1992)	SCPT, CPT, SPT
Rollins et al. (1998)	SPT, CPT, DMT, PMT, VST
Stewart et al. (2007)	SCPT, CPT, PMT, downhole
Manna and Baidya (2009)	SPT
Manna and Baidya (2010)	SPT, cross-hole
Dai et al. (2012)	CPT
Fotouhi and Ashlock (2012)	CPT
Elkasabgy and El Naggar (2013)	CPT, SCPT, SPT
Kong et al. (2015)	CPT
Pender et al. (2018)	CPT
Bharathi (2019)	CPT, SPT

To acquire accurate soil profiles for the present study, comprehensive site investigation was conducted by in-situ tests and laboratory tests. In-situ tests were conducted on March 28th, 2017, including standard penetration tests (SPT), cone penetration tests (CPT), and seismic

cone penetration tests (SCPT). In addition to the disturbed soil samples obtained from SPT tests, several thin-walled tube samples were retrieved for laboratory testing. Soil classification tests were performed on the SPT samples, and cyclic triaxial tests are currently being performed for use in the related study on cyclic lateral pile tests and FEM analysis.

2.1.1 SPT Tests

The SPT test was introduced by the Raymond Pile Company in 1902 and remains one of the most common in-situ tests worldwide. It is conducted during the advancement of a soil boring to obtain an approximate measure of the dynamic soil resistance and to collect disturbed soil samples (ASTM D1586). In this study, SPT tests (Figure 2.1(a)) were conducted in boreholes at two locations: 1.524 m from the center of the pile group (labeled as SPT-1) and 1.524 m away from the center of the single pile (labeled SPT-2). Soil samples retrieved by the SPT split-barrel sampler (Figure 2.1(b)) were preliminarily classified as glacial till clays with some small sand lenses, and further confirmed to have USCS classifications of lean clay (CL) up to a depth of 15.24 m, with clayey sand (SC) from 8.69 m to 9.144 m depth. Energy-corrected SPT blowcounts (N_{60}) were calculated based on the formula

$$N_{60} = \frac{N\eta_H\eta_B\eta_S\eta_R}{60} \tag{2.1}$$

where N is the uncorrected blow count, η_H is the hammer efficiency (%), η_B is a correction for borehole diameter, η_S is a sampler correction, and η_R is a correction for rod length (Das 2014). Raw N-values, along with the applied correction factors and energy-corrected N_{60} values are summarized in Table 2.2. Refusal was reached at depths of 16.5 m and 18 m in Boreholes SPT-1 and SPT-2, respectively.

(a) boring and logging (b) split-barrel sampler

Figure 2.1 *Standard penetration tests performed at the test site.*

Table 2.2 *Summary of SPT results.*

	Average depth (m)	N	η_H	η_B	η_S	η_R	N_{60}
SPT-1	1.30	11	80	1	1	0.75	11
	2.82	12	80	1	1	0.75	12
	4.34	15	80	1	1	0.85	17
	5.87	13	80	1	1	0.95	16
	7.39	21	80	1	1	0.95	27
	8.92	15	80	1	1	0.95	19
	10.44	48	80	1	1	1	64
	11.96	34	80	1	1	1	45
	13.49	24	80	1	1	1	32
	15.01	26	80	1	1	1	35
	16.54	97	/	/	/	/	/
	18.06	100	/	/	/	/	/
SPT-2	1.30	8	80	1	1	0.75	8
	2.82	10	80	1	1	0.75	10
	4.34	13	80	1	1	0.85	15

Table 2.2 *(continued)*

	5.87	**10**	**80**	**1**	**1**	**0.95**	**13**
	7.39	19	80	1	1	0.95	24
	8.92	19	80	1	1	0.95	24
	10.44	27	80	1	1	1	36
	11.96	28	80	1	1	1	37
	13.49	21	80	1	1	1	28
	15.01	25	80	1	1	1	33
	16.54	48	80	1	1	1	64
	18.06	99	/	/	/	/	/

2.1.2 CPT Tests

Cone penetration testing is a modern and expedient approach for site investigation that involves pushing an instrumented electronic penetrometer into the soil and recording measurements of tip resistance, sleeve friction, and optionally pore water pressure every few centimeters of depth. In this study, CPT soundings were conducted at three locations: the center of the pile group (denoted CPT-1), 1.53 m west of the single pile (denoted CPT-2) and 4.42 m south from the approximate center of the single pile and the pile group (denoted CPT-3c), with data recorded every 5 cm. The resulting measured tip resistance q_t, sleeve friction f_s, and pore pressure u_2 are shown in Figure 2.2. CPT-1 indicated a stiff layer at depth of 11 m. CPT-2 and CPT-3c showed a hard layer at depth about 9 m. All three tests show general consistency, especially for the top 8 m depth, suggesting a favorable horizontal homogeneity. The depths to the water table at the time of site investigation were 5.21 m, 3.66 m, and 2.26 m for the three CPT soundings. Ground water table within piles was also measured immediately after the experiments had been completed. The results suggest an average water table at 3.53 m for the pile group and 3.61 m for the single pile.

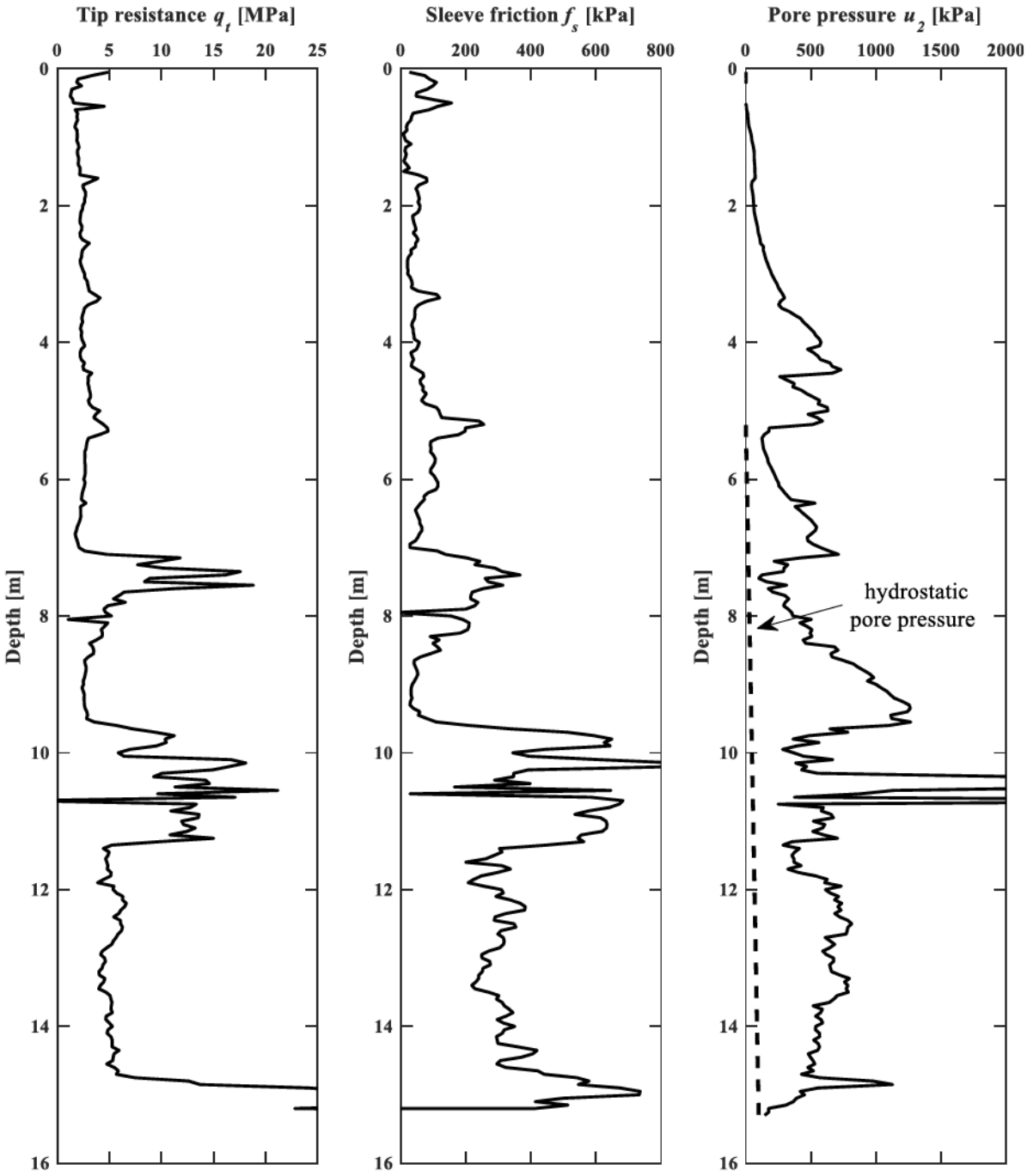

(a) CPT-1

Figure 2.2 *CPT test data from the project site.*

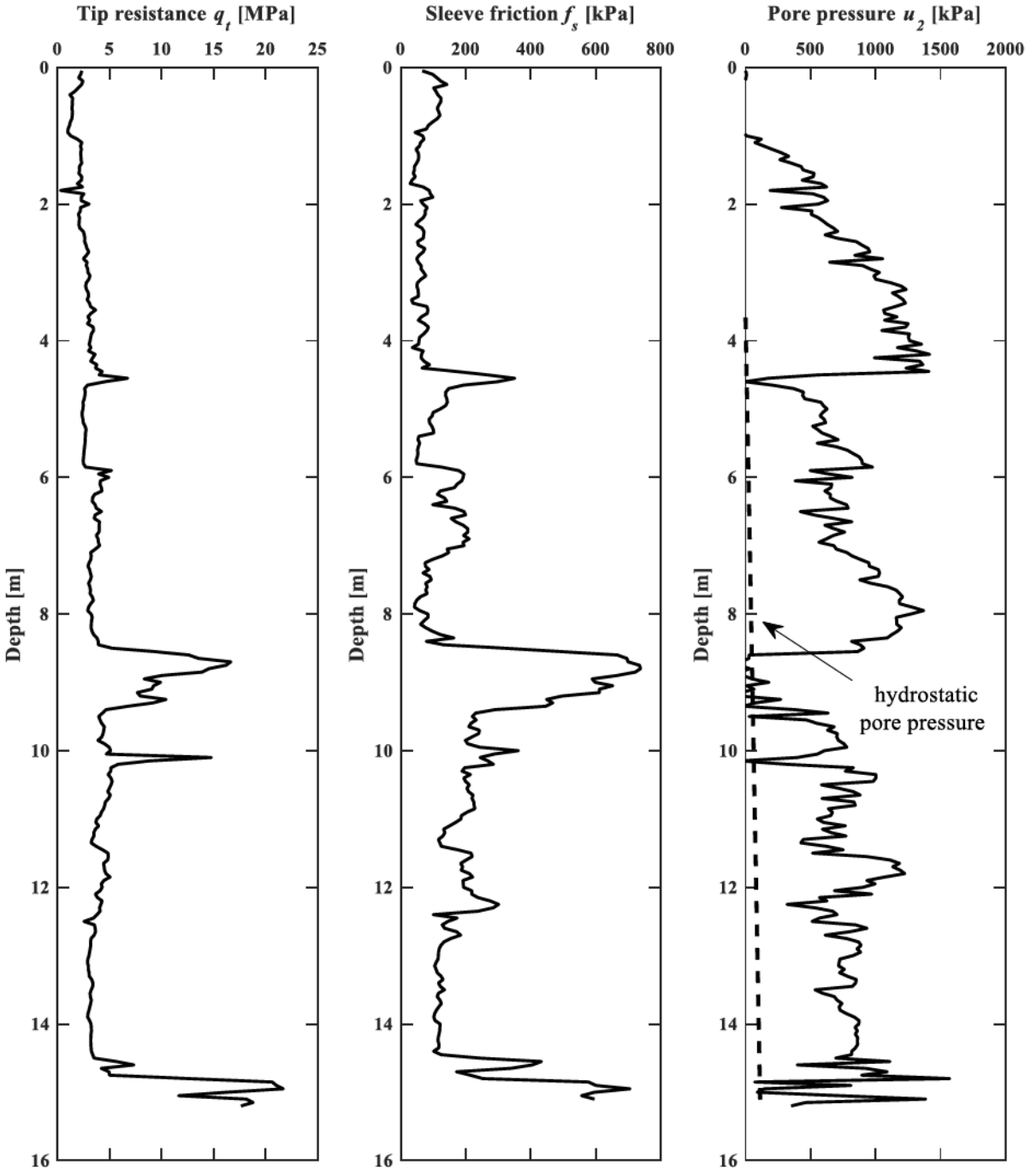

(b) CPT-2

Figure 2.2 *(continued)*

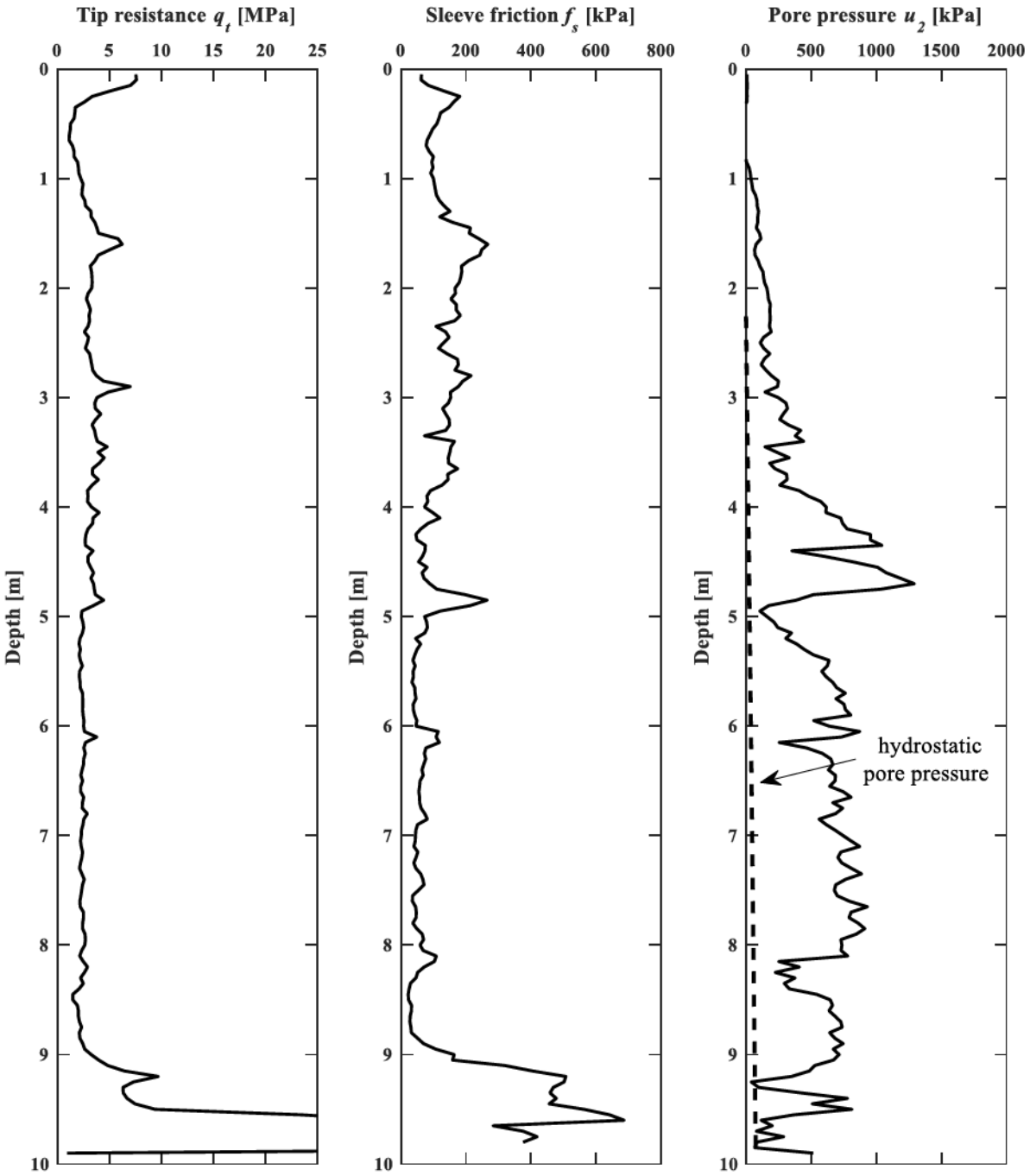

(c) CPT-3c

Figure 2.2 *(continued)*

2.1.3 SCPT Tests

Although the CPT is regarded as an appropriate test for determining the stratigraphy and shear strength of soil, its prediction for soil modulus can be poor, especially for overconsolidated soils (Robertson et al. 1986). The use of geophones incorporated into the cone penetrometer enables the shear wave velocity to be measured in seismic CPT tests (SCPT), from which the small-strain shear modulus can be more accurately obtained. For the current study, SCPT tests were performed at the three sounding locations, termed SCPT-1, SCPT-2, and SCPT-3c. Seismic primary (P, or compressional) and secondary (S, or shear) waves were recorded at approximately 1 m depth intervals using a sampling frequency of 25,625 Hz and recording period of 100 ms (Figure 2.3). A spring-loaded mechanical impactor was placed under one of the CPT rig's footplates to provide a repeatable impact source for S waves, and a sledgehammer with trigger was used to impact a steel plate bolted to three plywood layers to generate P waves. Since only a single seismic receiver was used each time, such measurements are referred as pseudo-interval measurements. Previous studies have shown that the standard deviation of such measurements is less than 1.5% of the mean value for both pseudo- and true time-interval measurements, with the latter obtained simultaneously using a pair of accelerometers (Rice 1984). This suggests low deviations in multiple pseudo-interval measurements. To increase the signal to noise ratio of the data, several impacts were applied at each measurement depth and the resulting signals were stacked.

The seismic wave signals are susceptible to environmental vibrations and high-frequency electrical noise especially at great depths, as well as low-frequency noise below 1 Hz due to DC drift. Campanella and Stewart (1992) suggested that the bulk of the signal energy occurs below 200 Hz. Transforming the signals into the frequency domain confirmed that the

energy in the current study is mainly below 210 Hz. Therefore, the data was band-pass filtered between 1 and 210 Hz.

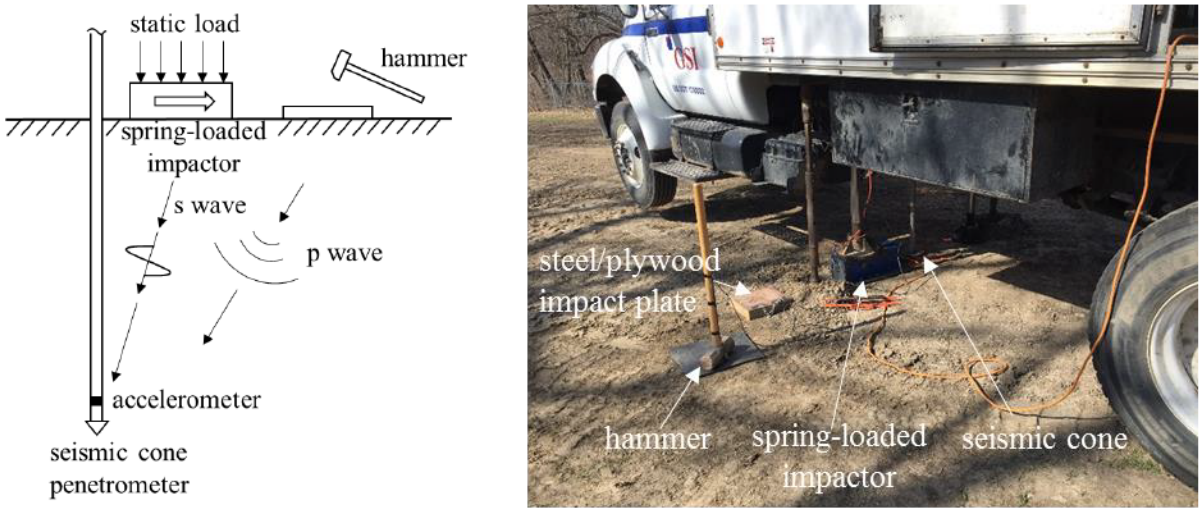

(a) SCPT setup (b) SCPT equipment used

Figure 2.3 *Schematic and photo of seismic CPT test.*

2.2 Interpretation of Site Investigation Data

Among all the parameters characterizing soil properties, four of them are crucial in soil dynamics – shear modulus, material damping ratio, Poisson's ratio, and density (Kramer 1996). The soil small-strain shear modulus, minimum material damping ratio, and Poisson's ratio are determined from the SCPT test data in this section.

2.2.1 In-Situ Small-Strain Shear Modulus Profiles of Soil

In general, using measured in-situ shear wave velocities is the most reliable means to evaluate the in-situ shear modulus profile of a particular soil deposit (Kramer 1996). Small-strain shear modulus of soil G_s can be calculated as:

$$G_s = \rho_s v_s^2 \tag{2.2}$$

where ρ_s is soil density and v_s is soil shear wave velocity. Three common methods for analyzing shear wave velocity profiles in SCPT tests are the arrival time method, cross-over method, and cross-correlation method (Robertson et al. 1986; Campanella and Stewart 1992). In the arrival time method, the shear wave velocity is calculated as

$$v_s = \frac{L_2 - L_1}{t_2 - t_1} \tag{2.3}$$

where L_1, L_2 and t_1, t_2 are travel distances and corresponding travel times from the excitation location to two neighboring observation points. However, determination of the arrival times requires subjective judgement between different potential instances of the wave arrival, such as the first significant increase in acceleration amplitude. Also, the accuracy of the arrival time is affected by reading errors, especially as the signal-to-noise ratio decreases as the depth of observation points increases.

To overcome these shortcomings, the cross-over method was proposed. It assumes that a signal with identical amplitude and shape but opposite vibration direction will be obtained if the initial excitation direction is reversed. When two signals intersect after their first peaks, the time is recorded as the cross-over time and differences in such times between adjacent observation points result in an average shear wave velocity. An example of applying the cross-over method on SCPT-2 test data and the resulting cross-over times are shown in Figure 2.4. The cross-over time, however, may be shifted if the signal is perturbed near the cross-over point (e.g., at depth of 12.45 m and 14.45 m in the data shown), which can occur due to interference by the arrivals of direct and reflected primary and shear waves in layered soils.

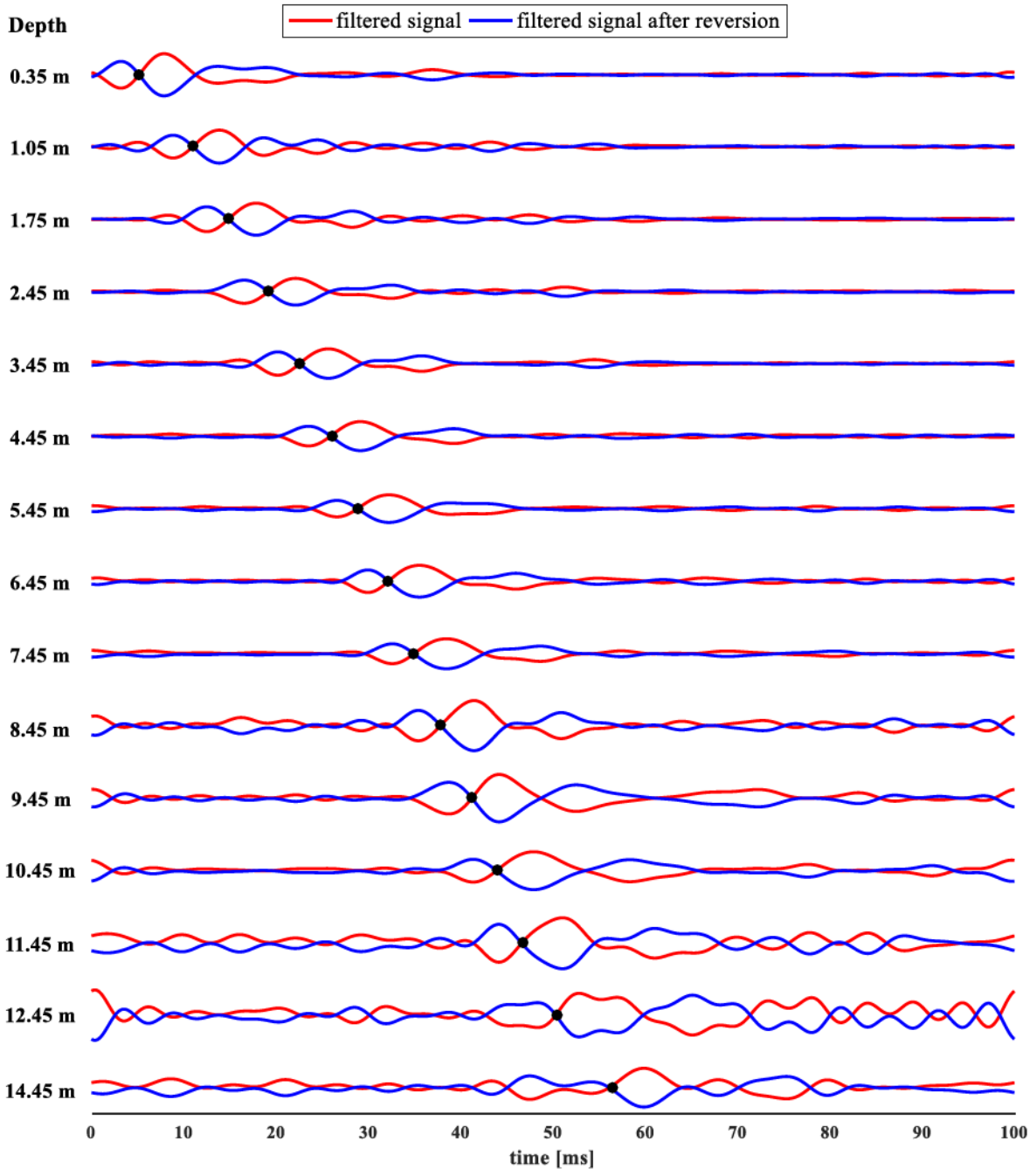

Figure 2.4 *Application of the cross-over method on SCPT-2 data with marked cross-over points.*

The cross-correlation method, which utilizes the entire records of the velocity or acceleration signals, was employed by Campanella and Stewart (1992). Its physical meaning is the determination of a time shift by which two signals have the best overall agreement. The method can be implemented in either the frequency domain or the time domain. When implemented in the time domain, the correlation coefficient decreases as the time shift approaches ±1 recording period. When implemented in the frequency domain, use of the fast Fourier transform (FFT) procedure inherently assumes the finite sample record to be periodic. As a result, an unreasonable negative time shift instead of a normal positive time shift can sometimes be identified. To avoid this problem, the original signals can be processed by zero padding, i.e., adding a long series of zeros at the beginning and the end of the signals. Then the cross-correlation in the frequency-domain approach has a period longer than the recording period, and yields almost the same results as the time-domain approach. Additionally, a windowing function is required to avoid discontinuities at the beginning and end of the record. Both the time- and frequency-domain approaches were used with the SCPT data, and the resulting differences in peak time shifts were found to be negligible. Therefore, the frequency domain cross-correlation approach is adopted herein. An example of applying the cross-correlation method to the SCPT-2 data in both the time and frequency domains is shown in Figure 2.5. For each pair of receiver depths, the actual time shift is identified as the one having the peak cross-correlation coefficient.

Shear wave velocity profiles determined by the arrival time, cross-over, and cross-correlation methods are compared in Figure 2.6(a), demonstrating a reasonable agreement for depths up to a few meters. At greater depths, the results by the arrival time method deviate from the other two methods and exhibit greater variations. This can be attributed to the

previously discussed errors in estimating the pseudo-interval arrival time, which at any observation point would affect both the upper and lower neighboring layers, underestimating the velocity of one layer while overestimating the velocity of the other. All three methods show divergence with increasing depth. The increasing perturbation of the signals due to dispersion, as well as decreasing signal-to-noise ratios with depth affects not only the arrival times and cross-over times, but also leads to very low normalized cross-correlation coefficients as shown in Figure 2.5. It should be noted that the shear wave velocity for the soil layer between ground level and the first observation points cannot be determined by either the cross-correlation method or cross-over method, and thus the shear wave velocity was linearly extrapolated for this layer. The arrival time method led to a much higher shear wave velocity value for this layer because the sensitivity to reading errors is high when the travelling time is short.

In the absence of SCPT data, empirical correlations to corrected CPT tip resistance and sleeve friction measurements are alternative options used to obtain shear wave velocities, although the data points from which these correlations were determined exhibit significant scatter. For comparison with the SCPT results, correlations by Hegazy and Mayne (1995) for all soil types and Mayne and Rix (1995) for clay soils are shown in Figure 2.6(b), which reveal that both correlations conform fairly well to the SCPT results in general, although that of Mayne and Rix (1995) appears to overestimate the influence of tip resistance. Empirical correlations by Wair et al. (2012) employing SPT blow counts were also studied to estimate shear wave velocity for all soil types and for clays and silts. The results shown in Figure 2.6(b) suggest that both of the correlations follow the overall increasing trend with depth, but underestimate the velocities for the soils in this study.

Hegazy and Mayne (1995),

$$\text{All soils: } V_s = [10.1 \cdot \log q_t - 11.4]^{1.67} [f_s / q_t \cdot 100]^{0.3} \quad (2.4)$$

Mayne and Rix (1995),

$$\text{Clays: } V_s = 1.75(q_t)^{0.627} \quad (2.5)$$

Wair et al. (2012),

$$\text{Quaternary soils: } V_s = 30 N_{60}{}^{0.215} \sigma_v{}'^{0.275} \quad (2.6)$$

$$\text{Quaternary clays and silts: } V_s = 26 N_{60}{}^{0.17} \sigma_v{}'^{0.32} \quad (2.7)$$

In summary, the empirical correlations between shear wave velocity and CPT tip resistance and sleeve friction fit the SCPT results well and are able to capture sharp variations. The SPT correlations to effective stress and corrected N_{60} underestimated the velocities and provided limited resolution, because SPT tests are typically performed at 5 ft intervals. The soil density was assumed to be 1936.8 kg/cm^3 (120 lb/ft^3) for all soil layers. Using this soil density with the SCPT shear wave velocity profiles determined by the cross-correlation method gives the in-situ small-strain shear modulus profiles for the location of the pile group (SCPT-1) and the single pile (SCPT-2) presented in Figure 2.7.

2.2.2 In-Situ Minimum Material Damping Profiles of Soil

Although no hysteretic dissipation of energy occurs at small strain levels in the ideal case, experiments have suggested a minimum damping ratio at small strains (e.g., Stokoe et al. 1999; Drnevich 2017). Efforts have been made to obtain soil damping ratios from SCPT tests (e.g. Stewart 1992; Karl et al. 2006). Due to the very small vibration amplitudes in SCPT tests,

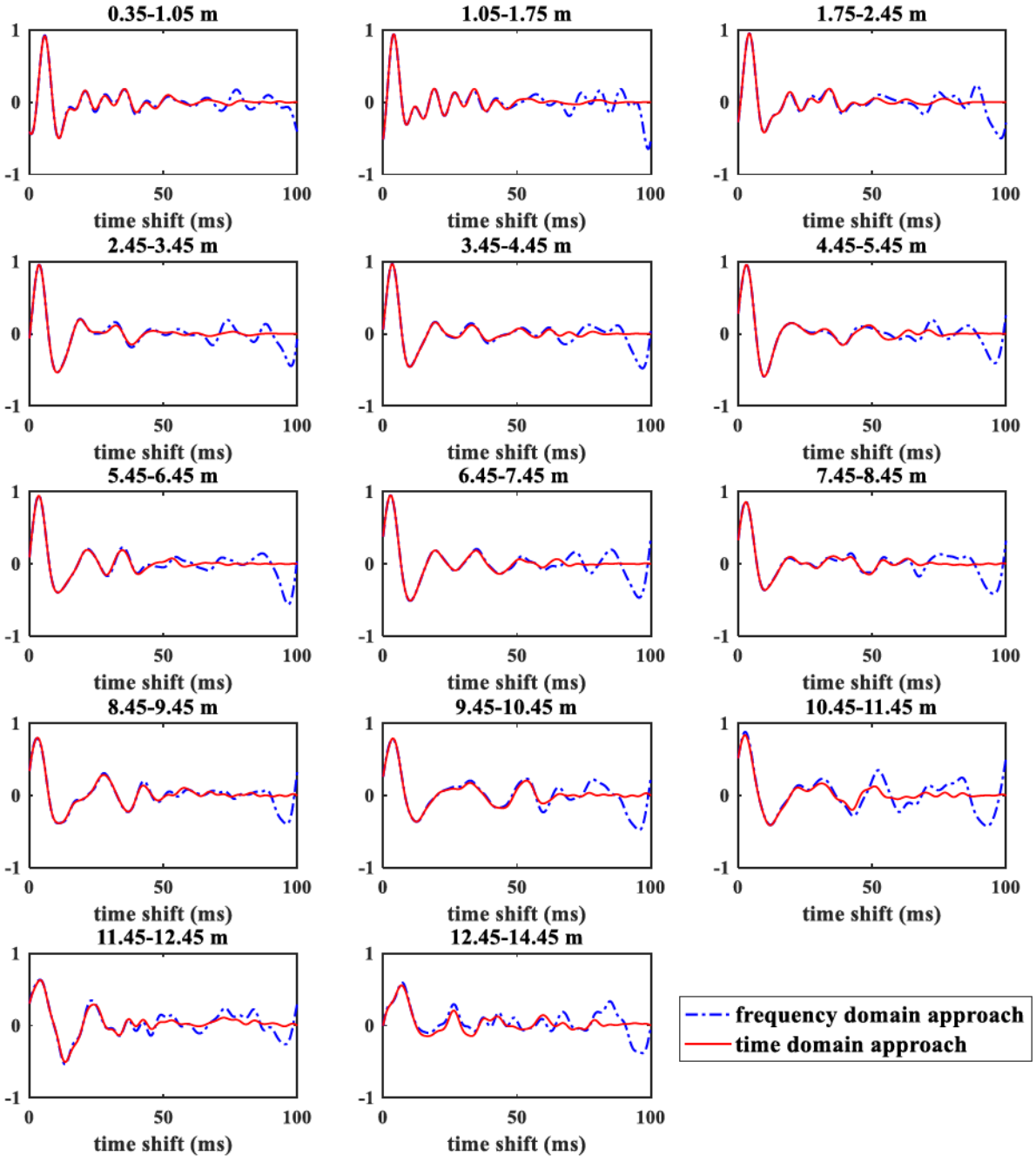

Figure 2.5 *Cross-correlation coefficients for data from SCPT-2, used to determine time shifts between the pairs of receiver depths indicated in graph titles.*

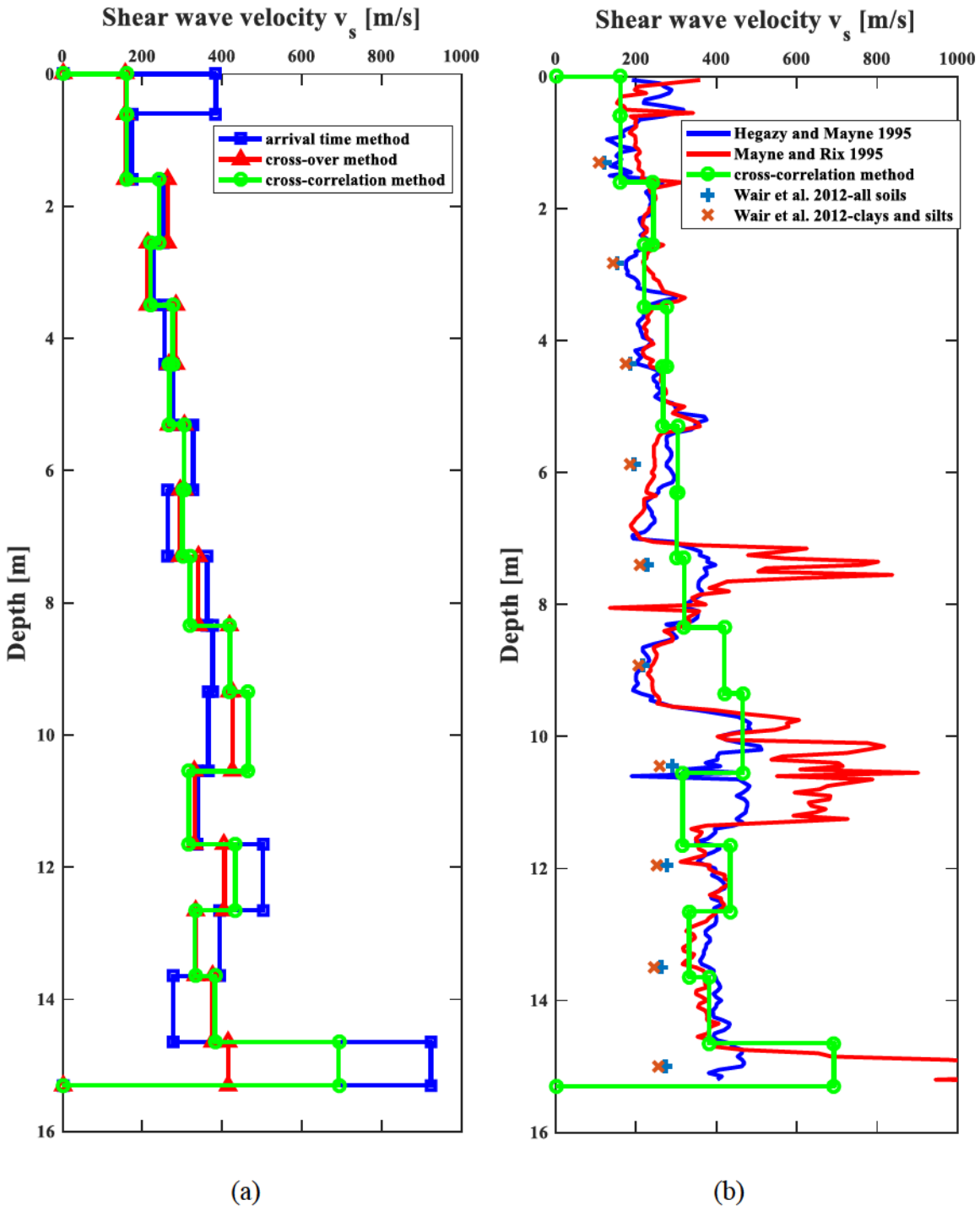

Figure 2.6 *Shear wave velocity profiles for data from SCPT-1; (a) comparison of three methods for estimating velocities , (b) comparison of cross-correlation method to empirical CPT and SPT correlations.*

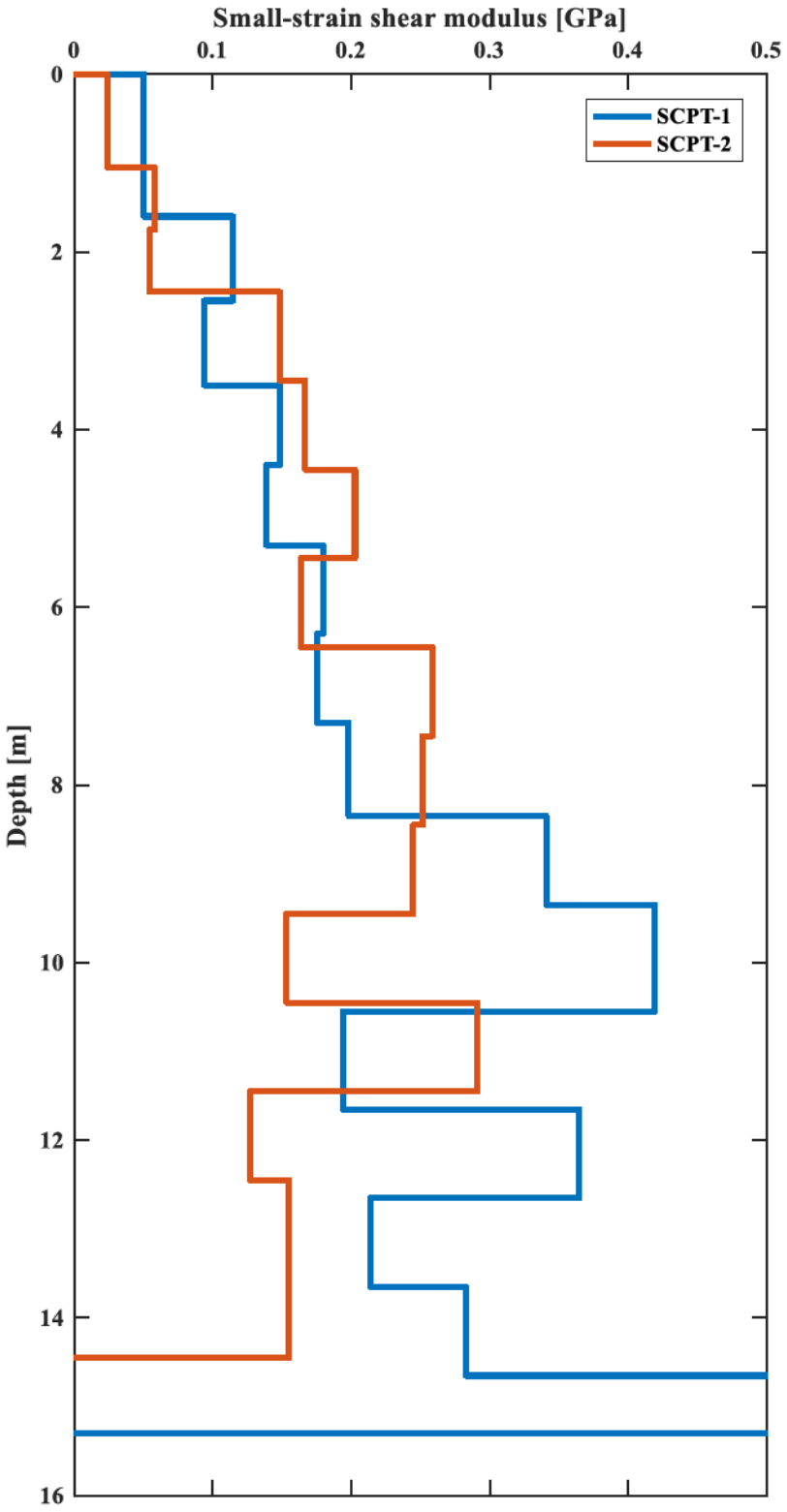

Figure 2.7 *In-situ small-strain shear modulus profiles of soil at the test pile locations.*

for which shear strain is assumed to be less than 10^{-3}%, such material damping values are considered to be the small-strain minimum damping.

Stewart (1992) studied six methods and concluded that the spectral ratio slope (SRS) method is capable of avoiding effects of radiation damping and is believed to be a reliable method for estimating material damping from SCPT data. For simplicity, the calculation can be summarized by the two equations below:

$$k = \frac{\partial^2(-\ln\frac{A_R}{A_0})}{(\partial f \partial R)} \tag{2.8}$$

$$D_s = \frac{kV_s}{2\pi} \tag{2.9}$$

where A_R is the FFT amplitude (m) of the sensor's signal at depth R (m), A_0 is the FFT amplitude (m) of a reference signal at a typical depth of 3-5 m or within a shallow surficial layer, f is frequency (Hz), V_s (m/s) is shear wave velocity of the corresponding layer, k is the slope of the spectral ratio (s/m), and D_s is the material damping ratio. Shear wave signals must first be windowed with a length of one cycle to obtain smooth spectral curves.

In the present study, the signal at a depth of 0.6 m was selected as the reference, and peak FFT frequencies were around 80 Hz for all measurement depths. After performing trials on several potential frequency ranges, the optimum frequency range for analysis was considered to be 60–100 Hz (Figure 2.8), which covers most of the frequencies over which the peaks have relatively flat logarithmic ratios. The CPT tip resistance and sleeve friction suggest that there is a stiff layer between 7.05 and 8.1 m, but it is too thin to be captured by the 1-m sampling interval of the seismic tests. Points denoting $\partial(-\ln A_R / A_0)/\partial f$ from depths of 0.6 m to 9.55 m appear to be fitted by a straight line and thus the soils are idealized as a single layer.

Averaging the piecewise material damping ratios leads to an average value of 3.4% and 2.6% for SCPT-1 and SCPT-2, respectively (Jiang and Ashlock 2018).

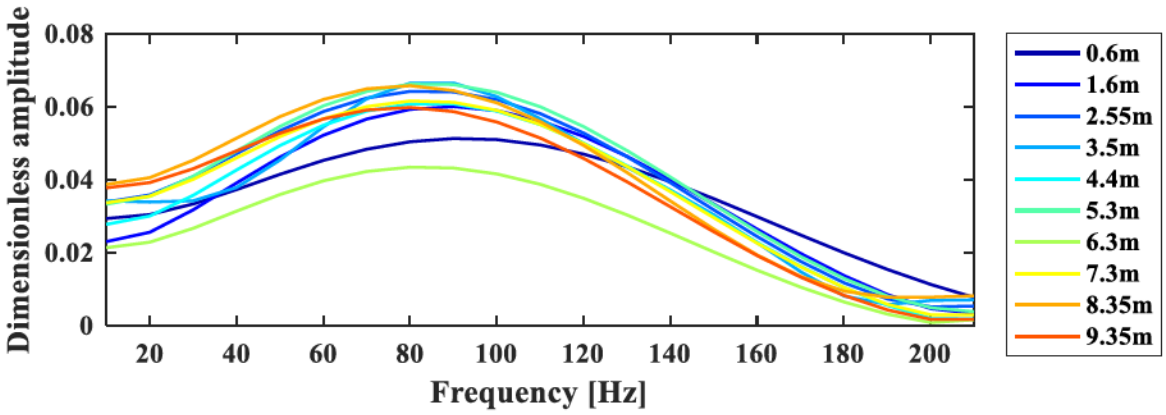

(a) SCPT-1

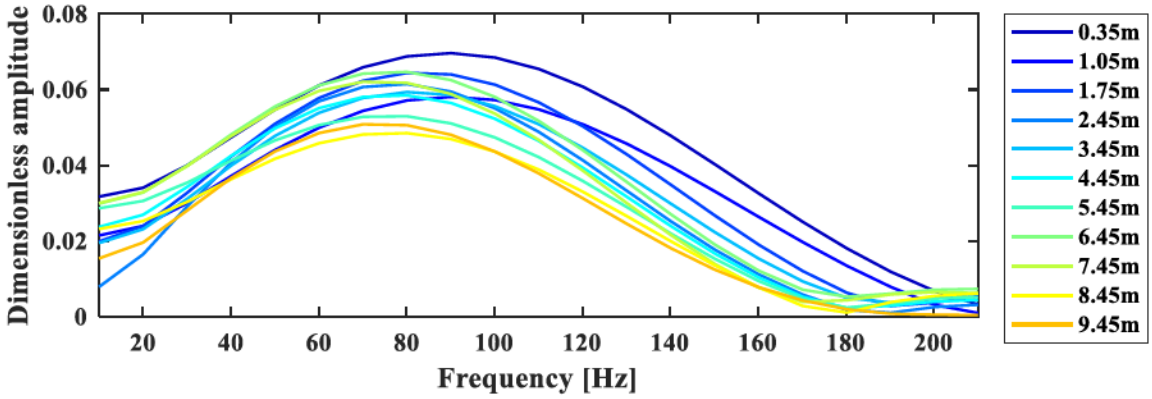

(b) SCPT-2

Figure 2.8. *FFT spectra of shear wave responses from SCPT-1 and SCPT-2 data.*

2.2.3 Poisson's Ratio Profiles of Soil

The soil Poisson's ratio can be back-calculated from three-dimensional S- and P-wave velocities measured in in-situ tests, using to the following relations from elasticity theory:

$$v_s = \sqrt{\mu / \rho} \tag{2.10}$$

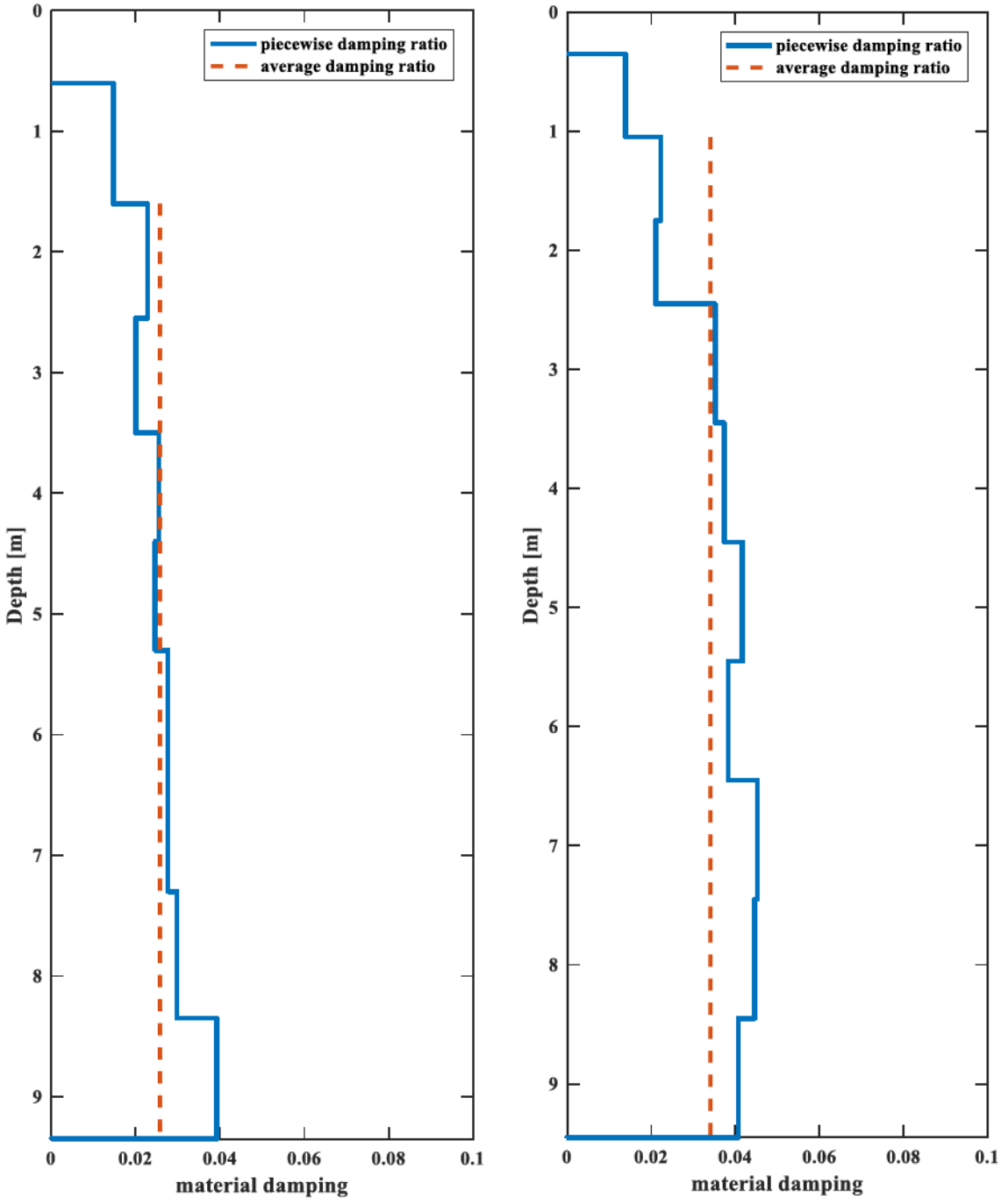

(c) SCPT-1 (d) SCPT-2

Figure 2.9. *Soil minimum material damping ratio profiles by SRS method using SCPT data.*

$$v_p = \sqrt{(\lambda + 2\mu)/\rho} \tag{2.11}$$

where v_s and v_p are secondary (shear) wave and primary (compressional) wave velocities in soil, ρ is soil density, and λ and μ are Lamé constants. The Poisson's ratio ν can thus be determined as:

$$\nu = \frac{0.5(v_p^2 - 2v_s^2)}{v_p^2 - v_s^2} \tag{2.12}$$

Due to insufficient P-wave velocity data in sounding SCPT-1, shear and primary wave profiles measured in SCPT-2 were used to estimate the Poisson's ratio profile of the clayey soil (Table 2.3). The resulting Poisson's ratio profile was relatively constant with depth and had an average value of 0.42 for the depth range 0 to 10.45 m, and did not vary sharply across the groundwater table.

Table 2.3 *Determination of Poisson's ratio.*

Depth range (m)	S-wave velocity (m/s)	P-wave velocity (m/s)	Poisson's ratio
1.05-1.75	173.1	438.0	0.41
1.75-2.45	167.3	340.2	0.34
2.45-3.45	276.7	896.0	0.45
3.45-4.45	293.4	826.6	0.43
4.45-5.45	323.4	1243.6	0.46
5.45-6.45	290.6	830.4	0.43
6.45-7.45	365.4	1246.8	0.45
7.45-8.45	360.4	998.0	0.43
8.45-9.45	355.4	768.0	0.36
9.45-10.45	281.2	907.9	0.45

2.3 Piles and Pile Caps: Design, Construction and Installation

Both the 2×2 pile group and the single pile consisted of steel pipe piles having the properties shown in Table 2.4.

All five piles were driven open-ended by a DELMAG D12 diesel hammer to a depth of 7.62 m, and the pile segments above ground were trimmed after construction of the pile caps. The embedded pile segments were sufficiently long to capture horizontal characteristics of the

Table 2.4 *Summary of pile properties.*

Outer diameter (m)	0.219
Thickness (cm)	0.818
Embedded length (m)	7.62
Unembedded length (m)	0.965
Young's modulus (GPa)	200
Poisson's ratio	0.26
Ultimate compressive strength (MPa)	374
Ultimate tensile strength (MPa)	498

pile-soil interaction, and ensure a "long-pile" failure in the planned cyclic lateral tests. The Canadian Foundation Engineering Manual (2006) categorizes driven piles into displacement piles, small displacement piles, and non-displacement piles. Steel pipe piles driven with closed end are displacement piles, in which case the soils are completely displaced by the driven piles. Piles driven with open ends are small displacement piles, which allows a partial plug of soil into the pipes.

To quantify the degree of soil disturbance, the soil plug length was measured during pile driving in this study. A small hole was created on each pile before driving at a location 10.668 m from the pile toe, where the hole would not affect either driving or integrity of piles in vibration tests, as it was above the pile cutoff elevation. A tape measure with weight attached at its end was used to measure the total distance from the surface of the plugged soil inside the pile, through the hole and back to the ground level. The actual soil plugging distance can be calculated as:

$$L_p = c - [M - (c - D)] = 2c - M - D \tag{2.13}$$

where L_p is the soil plug length (m), c is the distance from the hole to the pile toe (10.668 m), M is the tape measure reading (m), and D is the penetration depth of the pile (m) (see Figure 2.10).

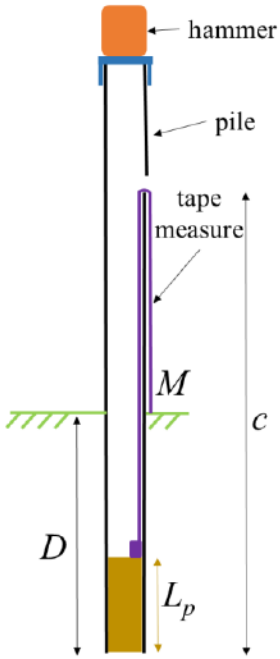

Figure 2.10 *Measurement of instantaneous soil plug length during pile driving.*

The relation of the measured L_p and D data is plotted in (Figure 2.11a). Despite a few irregular data points likely resulting from measurement error, both the pile group and single pile show fair consistency in their soil plug length, which suggests that the presence of nearby piles or driving sequence has negligible effects on soil plugging for this soil profile and pile type. Soil plugging is commonly quantified by the plug length ratio (PLR) and the incremental filling ratio (IFR). The PLR is defined as ratio of soil plug length to pile penetration depth at the end of pile installation:

$$\text{PLR} = \frac{L_i}{D_p} \tag{2.14}$$

A PLR of zero or one indicates a displacement or non-displacement pile, respectively. In this study, the average plugging length is approximately 3.0 m, giving a PLR of 40% which corresponds to small-displacement piles. However, PLR only represents soil plugging in an average sense, and does not reveal the trend of soil plugging during pile installation. To this end, the IFR was also calculated, which is defined as the ratio of incremental plug length to incremental pile penetration depth:

$$\text{IFR} = \frac{\Delta L_i}{\Delta D_p} \times 100\% \tag{2.15}$$

It is difficult to calculate IFR directly based on discrete measurements of soil plug length. One reason is that piles were driven continuously by the diesel hammer and it is impractical to take readings at an interval smaller than 0.305 m (1 ft). In addition, the plug length measurement is sensitive to uneven soil plugging and reading errors, which may result in sharp variations and even negative values for IFR at some points.

As a solution, the soil plug length vs. depth data was first fitted by a monotonically increasing function. Among the common curve fitting functions, a power function was observed to give the best agreement with the highest R^2 values. In addition, the power function has an intercept of zero, conforming to the fact that soil plug length must be zero before piles are driven. The curve fitting results are shown in Table 2.5.

Table 2.5 *Parameters for fitting measured soil plug lengths with power function.*

Pile	Power function $L = a\,D^b$ (L and D are in meters)		
	a	b	R^2
Group-NE	1.0729	0.6779	0.9867
Group-SE	0.8195	0.7904	0.9812
Group-SW	1.1976	0.6579	0.9615
Group-NW	2.3140	0.4450	0.8023
Single pile	1.4908	0.5667	0.9878

Once coefficients of the curve fitting function are determined, it is easy to calculate IFR by taking the 1st order derivative of the function. The resulting IFR is shown in Figure 2.11(b), indicating a quickly decreasing trend at depths above 1.52 m and a gradual reduction below this depth.

Blow counts per 0.3048 m (1 ft) of pile penetration were recorded and are shown in . The blows counts increase steadily with penetration depth and reach a maximum value of 29 blows at a depth of 5.5 m, and a general consistency is observed among all the piles. The southeast (SE) group pile exhibits a deviation from the others due to a malfunction of the diesel hammer, which resulted in uneven hammer energy delivered per blow. Blow counts were also compared to pile drivability analyses to ensure pile integrity during installation.

Pile caps are often included in dynamic pile testing to incorporate inertial effects of the superstructure reality so that the physical behavior of actual structures can be well simulated in the vibration tests. In previous studies involving pile tests, the pile caps were typically assembled using steel or wooden weights (e.g., Manna and Baidya 2010; Elkasabgy and El Naggar 2013; Pender 2018), or cast as concrete blocks (e.g., Blaney and O'Neil 1989; Sy and Siu 1992; Fotouhi 2014). For the present study, two reinforced concrete pile caps (Figure 2.13) were constructed and their properties are listed in . Due to limitations on construction at the test site, the pile caps were precast in the laboratory with corrugated oversized steel pipes blocking out the pile locations, then the pile caps were grouted to the piles in the field. The quality of grouting is important, since the grout is susceptible to the water-grout ratio, temperature, and the mixing procedure. Therefore the 28-day compressive strength of nine grout cubes (5.08 cm on a side) was measured, and the values varied from 39 to 59 MPa with

a mean value of 49 MPa. To create flat contact surfaces at the shaker mounting locations on top of the pile caps, a 1.25 cm (0.5 in.) thick hydrostone layer was formed on the two pile caps.

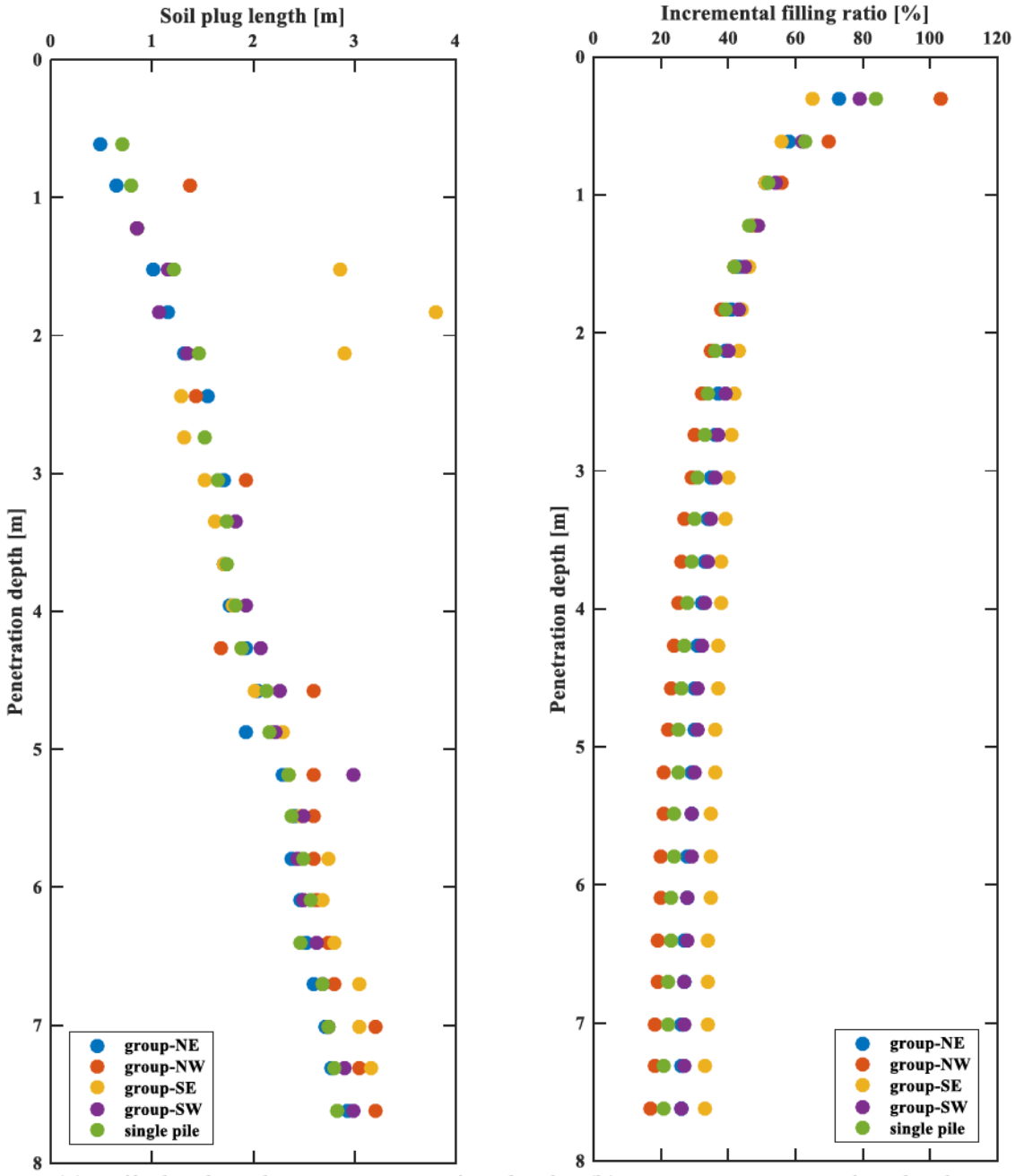

(a) Soil plug length versus penetration depth (b) IFR versus penetration depth

Figure 2.11 *Results of soil plugging measurements during pile driving.*

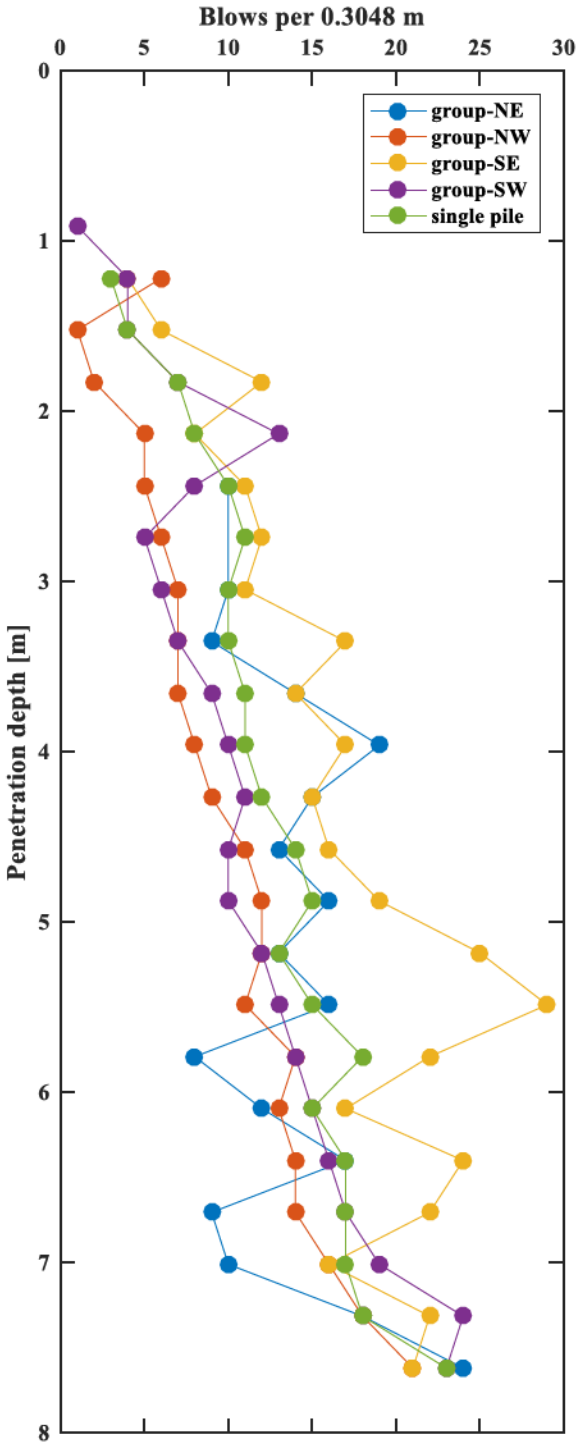

Figure 2.12 *Pile blow count per 0.3048 m (1 ft) of penetration versus total penetration depth.*

(a) For single pile (b) For pile group

Figure 2.13 *Construction of the pile caps.*

Table 2.6 *Properties of the concrete pile caps.*

	Pile cap for single pile	**Pile cap for pile group**
Length (m)	0.914	1.600
Width (m)	0.914	1.600
Height (m)	0.762	0.762
Mass (kg)	1,474.0	4,272.8

2.4 Loading System and Load Cases

Full-scale tests require using versatile excitation devices such as hydraulic actuators, mechanical oscillators, Statnamic devices, and cables for pull-and-release tests. In this study the pile caps were loaded by a servo-hydraulic inertial shaker. It consisted of a static frame that was bolted to the pile cap, and a moving part that was driven by a hydraulic actuator to provide uniaxial dynamic force. The moving part was made up of a carriage to which up to 14 steel plates could be fastened to increase the inertial force. When fully loaded, the shaker could deliver a maximum dynamic force of 8,900 N. Depending on the mounting location of the shaker, tests were categorized as vertical-centric (VC), vertical- eccentric (VE), or horizontal-centric (HC) tests. In the VC tests, the shaker was mounted on the top of the pile cap at the

center position, inducing only the vertical mode of vibration. In the HC tests, the shaker was mounted on the side of the pile cap at the mid-height to induce the coupled lateral-rocking modes. In the VE tests, the shaker was mounted on the top of the pile cap but offset towards either the east or west side, inducing a combination of the vertical and coupled lateral-rocking modes simultaneously.

Compared to hydraulic actuators, an inertial shaker can more easily provide either horizontal or vertical force simply by being mounted on different faces of the pile cap. No reaction frames or walls are required, which reduces test space and saves cost and time. Lazan mechanical oscillators (a type of compact eccentric mass shaker with adjustable eccentricity) have proven to be useful in past tests of single piles with excitation frequencies typically below 60 Hz. However, they are limited to harmonic motion and thus cannot deliver excitation over a wide frequency range simultaneously, which would enable faster transfer function based testing approaches. Pile group testing may also require a wider excitation range to capture higher resonant frequencies due to much higher vertical and rocking stiffnesses compared to single piles. For instance, Novak and Grigg (1976) stated that the vertical resonant peak for a group of four piles was beyond the working frequency of the oscillator and could not be observed. Blaney et al. (1987) captured a resonant peak at 70 Hz for a 3×3 pile group.

Compared to both hydraulic actuators and Lazan oscillators, the inertial shaker covers a wider range of excitation frequencies, and can deliver arbitrary broadband excitation types such as random (white noise) and swept sine forcing. The frequency response curves plotted based on data provided by the manufacturer (Figure 2.14) show that the maximum force can be generally achieved at 8 Hz or 16 Hz, depending on the load condition, and maintain at a constant magnitude up to a frequency of 256 Hz. Below a frequency of 8 Hz down to the

minimum operational frequency of 1 Hz, the maximum dynamic force gradually decreases due to the actuator's maximum displacement of +/−12.7 mm (0.5 in.). The inertial shaker can be controlled in real time by either force or displacement feedback, although displacement control is more robust as it is the industry standard. The shaker system includes a servo-controller unit with internal PID feedback control, which accepts a user-generated voltage (±5 V for displacement control or ±10 V for force control) as the input control signal.

Based on its merits, the broadband random excitation technique was implemented in the tests. Specifically, the inertial shaker was used in displacement-control mode using three types of control signals; random noise (R), swept-sine signal (S), and chaotic impulse (C). The random noise signal was uniform white noise with a user-specified amplitude. Statistically, it had a uniform distribution of amplitude in the time domain and a constant amplitude in the frequency domain. The swept-sine signal was a sinusoidal signal with its instantaneous frequency varying linearly with time. Within a short period, the signal swept through a broad frequency range instead of focusing at a single frequency as in the harmonic vibration tests. The chaotic impulse signal was a combination of repetitive short impulses and rest times, which resulted in a mix of forced vibration and free vibration responses. The rest times between two adjacent impulses was controlled so that the free vibration would remain active until a new impulse was applied. Several different methods of implementing the chaotic impulse signals were examined, as will be discussed in a later section. Each of the three excitation types were applied to the pile cap using at least four sequentially increasing excitation levels in different tests. The naming convention for the tests is as follows:

"single pile (**S**)/pile group (**G**) – test type (**VC/HC/VE**) – (direction for VE offset (**W/E**)) - excitation type (**R/C/S**) and excitation level (**1-4**)"

For example, **S-VC-R1** refers to a vertical centric test on the single pile with random forcing at excitation level 1. Similarly, **G-VE-W-C4** refers to a vertical eccentric test on the pile group with the shaker on the west side of the pile cap, with chaotic impulse forcing at excitation level 4. After trying several different sampling frequencies, a value of 512 Hz was chosen for a tradeoff between resolution and efficiency, corresponding to a sampling period of 4 s using 2,048 samples per window in the time domain. To reduce effects of random noise on the data, 30 spectral averages were used in each test. Fotouhi and Ashlock (2012) validated that the inertial shaker system used in this study could successfully be employed for vibration tests of single piles using broadband excitation. The same question will be explored for pile groups in this study.

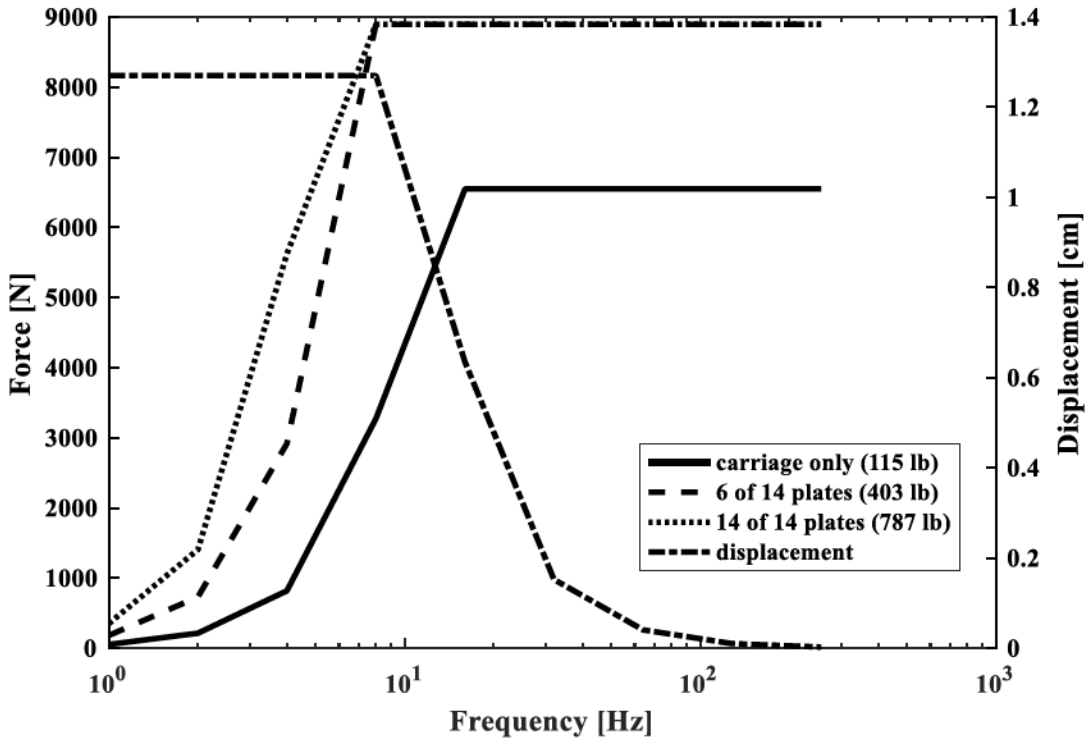

Figure 2.14 *Spectral performance curves of the hydraulic inertial shaker.*

2.5 Measurement and Data Acquisition

The primary measurements in the vibration tests were the directional accelerations at several points on the surfaces of the pile caps. Two accelerometers were mounted on the moving mass of the shaker to measure its instantaneous acceleration in the shaking direction and the perpendicular direction. On each pile cap, four accelerometers were mounted in the central plane of motion, 2.54 cm away from the edges on the top and two side surfaces. For the single pile, eight strain gauges were adhered to the pile at two elevations (5.1 cm and 88.9 cm from the bottom of the pile cap). For each pile in the pile group, one or two strain gauges were also installed at these same elevations. The output of typical accelerometers exhibits a decrease in magnitude and increase in phase as frequency approaches zero. To properly capture the low-frequency responses including the lateral mode's peak, string potentiometers (stringpots) were therefore used to measure lateral displacements of the pile caps and unembedded pile segments. Additionally, it is useful to measure the soil motion and wave attenuation at the ground level, and calculate transfer functions relating the pile cap motion to that of the soil. Such measurements will allow additional constraints for calibration of the computational models in future studies. For this purpose, six accelerometers were embedded 5.1 to 10.2 cm within the soil in two horizontal directions to measure vertical accelerations. Detailed instrumentation plans tests are shown in Figure 2.15 and Figure 2.16, respectively, with the shaker position corresponding to S-HC and G-HC tests. Actual instrumentations are showed in Figure 2.17 and Figure 2.18.

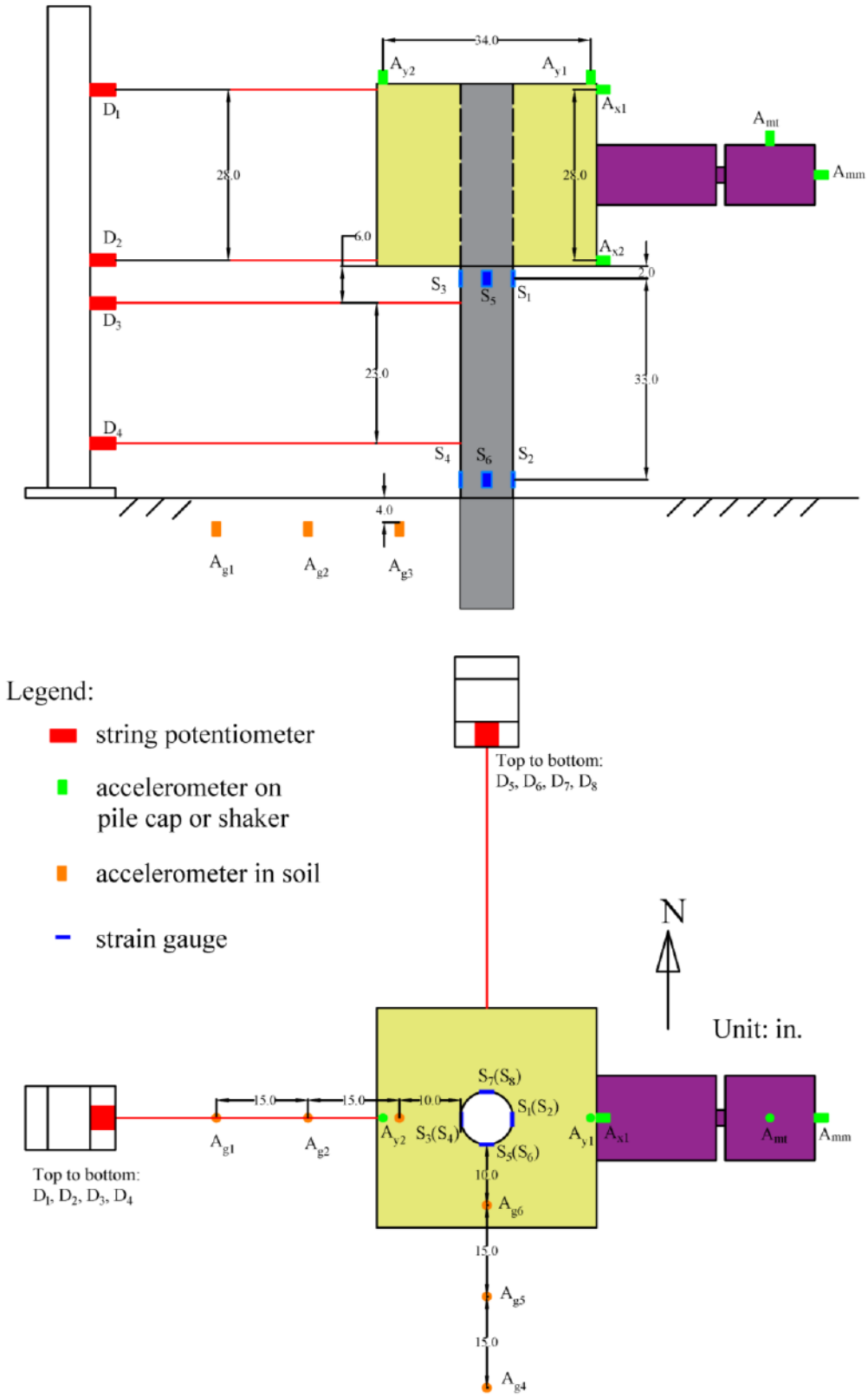

Figure 2.15 *Instrumentation schematic for single pile tests (S-HC test shown).*

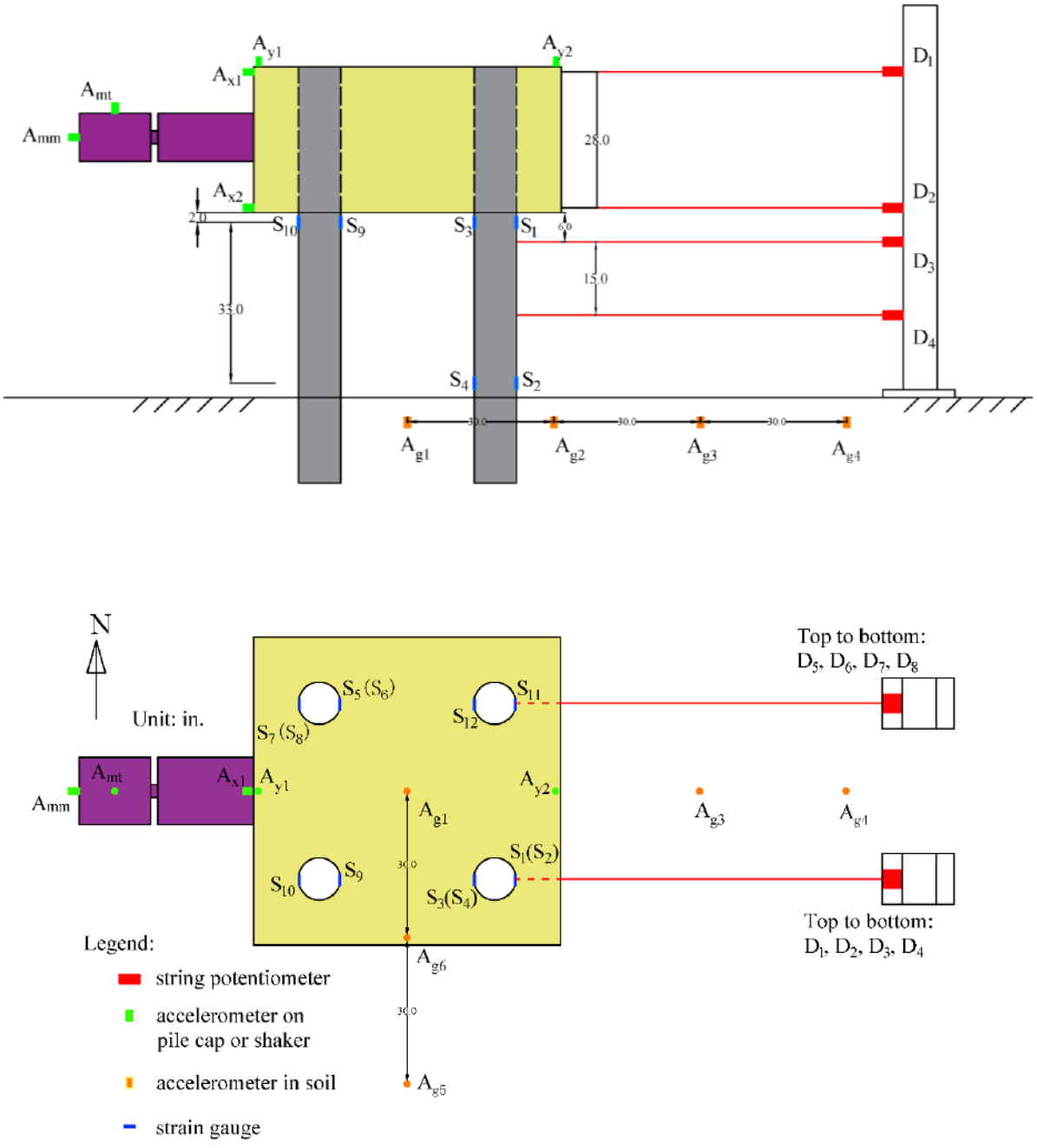

Figure 2.16 *Instrumentation schematic for pile group tests (G-HC test shown).*

Figure 2.17 *Actual instrumentation for S-HC tests.*

Figure 2.18 *Actual instrumentation for G-HC tests.*

A multi-channel dynamic signal analyzer (Figure 2.19) was developed by expanding and improving a previous LabVIEW program. The analyzer was designed for the following purposes: 1) configuring and generating the excitation signal for input to the shaker servo-controller; 2) recording, analyzing, and displaying the near real-time response in time and frequency domains; and 3) storing the test data. Accordingly, a hardware system was developed consisting of one National Instruments (NI) 9263 analog voltage output module, six 9234 sound and vibration input modules, two 9237 strain/bridge input modules, and two cDAQ-9172 compact data acquisition chassis (Figure 2.20). All input modules were put on the same chassis to ensure rigorous synchronization of sampling and the other chassis was used for the only output module.

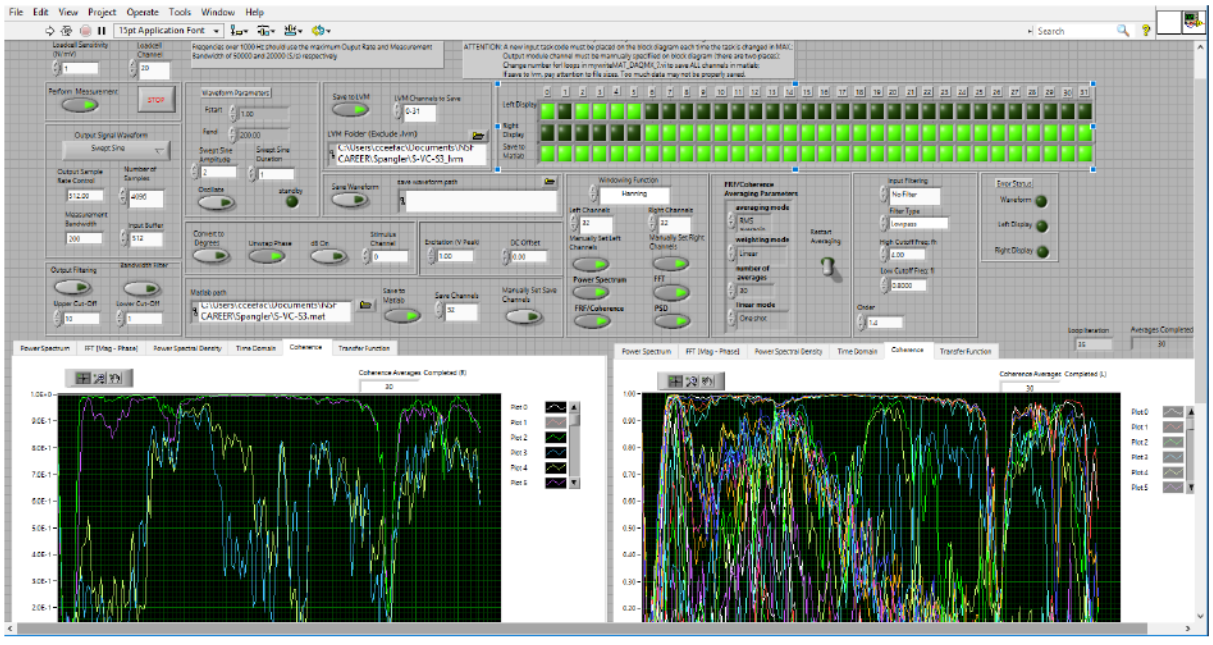

Figure 2.19 *User interface of the portable NI dynamic signal analyzer.*

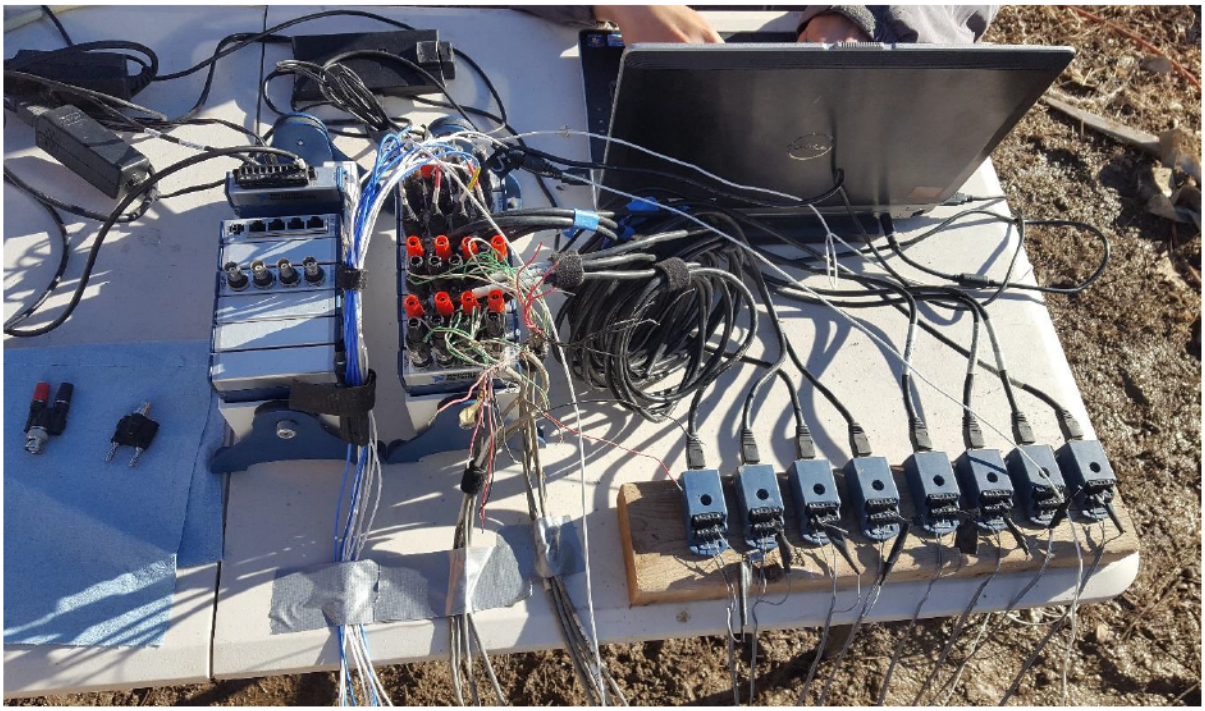

Figure 2.20 *Hardware system consisting of NI modules and chassis.*

The acceleration time-domain data was processed and interpreted as five frequency domain functions – the fast Fourier transform (FFT) spectrum, power spectrum (PS), power spectral density (PSD), coherence function (COH), and acceleration transfer functions. The FFT spectrum presents the complex-valued magnitude and phase angle of a single dynamic signal in the frequency domain. Similarly, the real-valued power spectral density describes the energy distribution of a single signal over the frequency spectrum. For the coherence and transfer functions, the acceleration of the shaker's moving mass was taken as the reference signal. Thus the coherence function indicates the correlation between the output acceleration responses and the input excitation (which is the acceleration of the moving inertial mass). A perfect linear system with zero noise, time-invariant properties, zero measurement error, and all output energy caused only by the measured input energy leads to a coherence value of unity at all frequencies. Deviations from any of these conditions, such as nonlinearities, time-

dependent material properties, or external noise in the output signals decreases the coherence towards zero. Thus coherence values closer to unity suggest better data quality for elastodynamic vibration measurements.

The accelerance function is the frequency-domain transfer function of directional acceleration at any desired point on the pile cap to the force applied to the pile cap. To enable comparison with the theoretical transfer functions (acceleration/force ratios), the experimental transfer functions (acceleration/acceleration ratios) are divided by the value of the shaker's moving mass. In other words, the applied force is taken as the value of the inertial mass times its measured acceleration. Compared to normalization of dynamic response by force in the time domain, the accelerance describes not only the amplitude of the acceleration/force ratio in the frequency domain, but also the phase shift due to radiation damping and material damping.

To minimize effects of experimental noise, the dynamic signal analyzer programmed in LabVIEW makes use of averaging of all spectral quantities by measuring over a selected number of sequential time windows. The statistically averaged versions of the spectral quantities described above are calculated as follows for the one-sided auto-spectral density:

$$\overline{G}_{yy}(f_k) = \frac{2}{n_d N \Delta t} \sum_{i=1}^{n_d} Y_i^*(f_k) Y_i(f_k), \quad k = 0,1,...N-1 \tag{2.16}$$

the one-sided cross-spectral density:

$$\overline{G}_{xy}(f_k) = \frac{2}{n_d N \Delta t} \sum_{n=1}^{n_d} X_i^*(f_k) Y_i(f_k), \quad k = 0,1,...N-1 \tag{2.17}$$

the one-sided auto-power spectrum:

$$\overline{P}_{yy}(f_k) = \overline{G}_{yy}(f_k) \times \frac{F_s}{N}, \quad k = 0,1,...N-1 \tag{2.18}$$

the coherence function:

$$\gamma_{xy}^2(f_k) = \frac{\left|\overline{G}_{xy}(f_k)\right|^2}{\overline{G}_{xx}(f_k)\overline{G}_{yy}(f_k)}, \quad k = 0,1,\ldots N-1 \tag{2.19}$$

and finally the transfer function:

$$A_i(f_k) = \frac{\overline{G}_{xy}(f_k)}{\overline{G}_{xx}(f_k)} \tag{2.20}$$

where subscripts x and y denote the acceleration of the moving mass and observation point, respectively; X and Y denote corresponding fast Fourier transforms; superscript * denotes the complex conjugate; N denotes the number of discrete sample points; Δt denotes the sampling time interval; F_s is sampling frequency; and n_d is the number of spectral averages.

The sampling frequency for output excitation signals was 512 Hz. The measurement frequency range of the input signals was set to 1-200 Hz. The corresponding sampling frequency for input was roughly 512 Hz, making the Nyquist frequency higher than 200 Hz and the resulting signals alias-free. A common issue in digital signal processing is spectral leakage when the captured signals are not exactly periodic. Thus Hanning windowing was used to minimize the influence of spectral leakage. Another issue for dynamic testing is random ambient noise, which can be reduced by increasing the number of spectral averages (Bendat and Piersol 1986). To minimize the influence of random noise, the sampling processes were continuously repeated over sequential time windows as mentioned previously, and the frequency response functions were averaged using the root-mean-square (RMS) method. Practice suggested that the spectral measurements converged quickly with n_d =30 averages.

2.6 Test Results and Discussion

2.6.1 Excitation of the Moving Mass

To further elaborate upon the broadband random excitation technique, actual acceleration records and FFTs for the moving mass recorded during the tests are presented. The instantaneous force applied to the pile cap (and stationary part of the shaker) is the product of the moving mass and its instantaneous acceleration. In this section, representative data from G-VE-W tests are presented. Examples of time histories and RMS-averaged FFT spectra of acceleration for the moving mass at various excitation levels for random, swept-sine, and, chaotic impulse signals are shown in Figure 2.21 to Figure 2.23. As expected, higher excitation levels result in higher instantaneous amplitudes of acceleration and FFT magnitudes. For random and swept-sine signals, the maximum acceleration exceeds 20 m/s^2, indicating an excitation force of at least 7.1 kN. As the excitation intensity is increased, the FFT spectra suggest that peak frequencies decrease from 18 Hz to 12 Hz for the random signals, from 16 Hz to 13 Hz for the swept-sine signals, and from 16 Hz to 15 Hz for the chaotic impulses. The chaotic impulse excitation type induced relatively lower forces, and exhibited less change in frequency for different amplitudes.

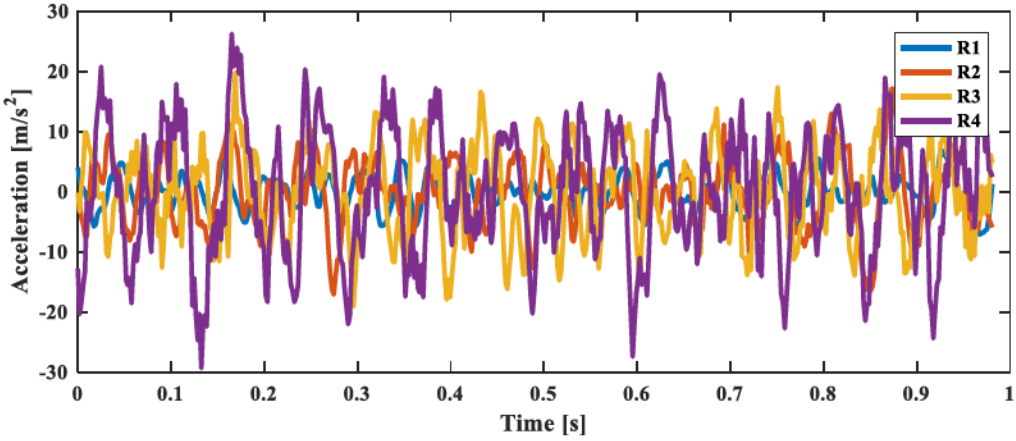

(a) Acceleration records

Figure 2.21 *Acceleration records and FFTs of the moving mass due to random excitation (R) in G-VE-W tests.*

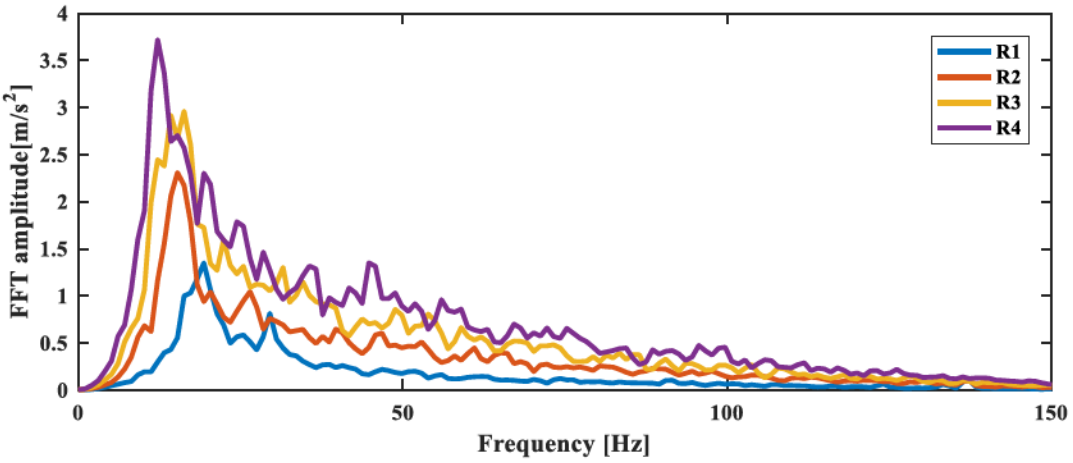

(b) FFT transforms

Figure 2.21 *(continued)*

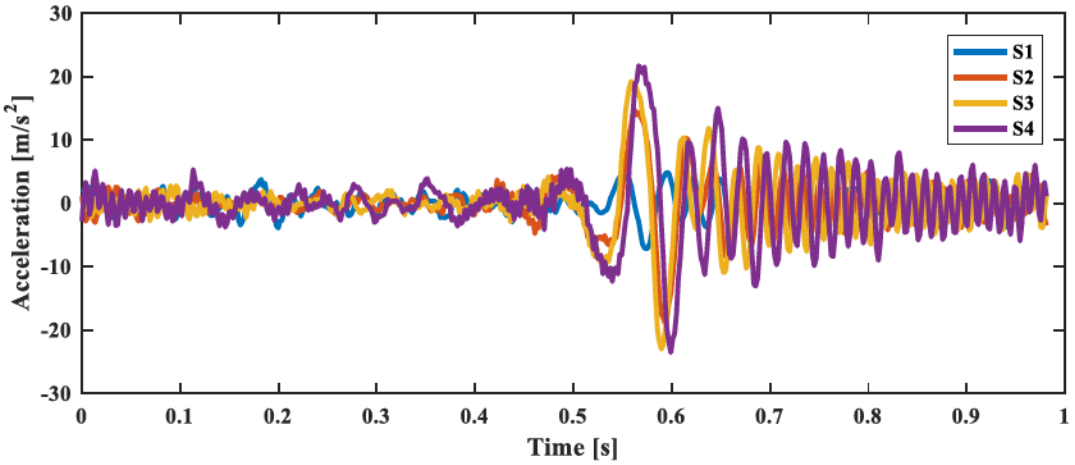

(a) Acceleration records

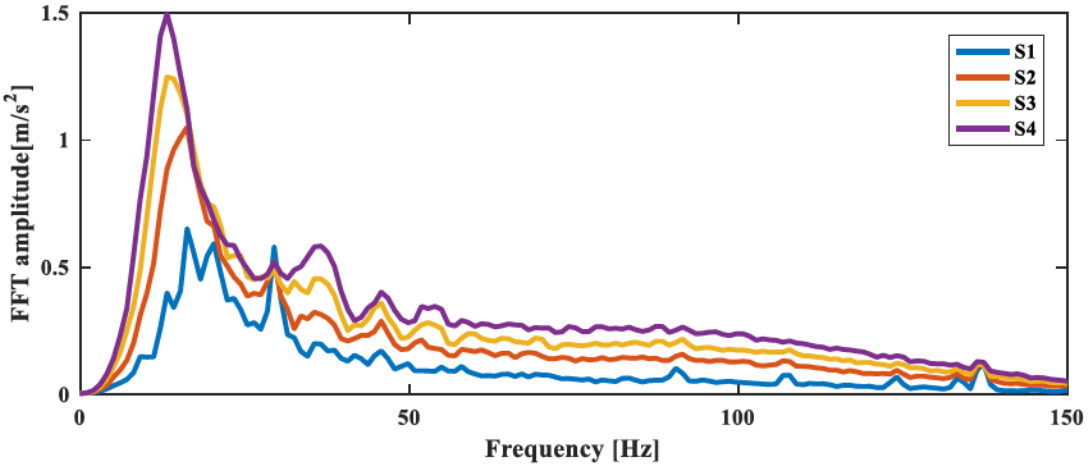

(b) FFT transforms

Figure 2.22 *Acceleration records and FFTs of the moving mass due to swept-sine excitation (S) in G-VE-W tests.*

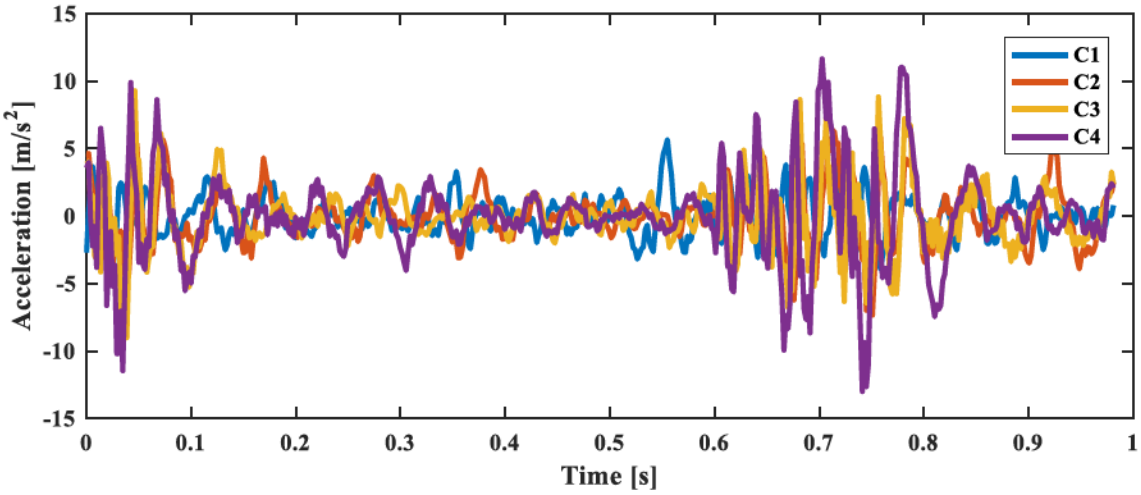

(a) Acceleration records

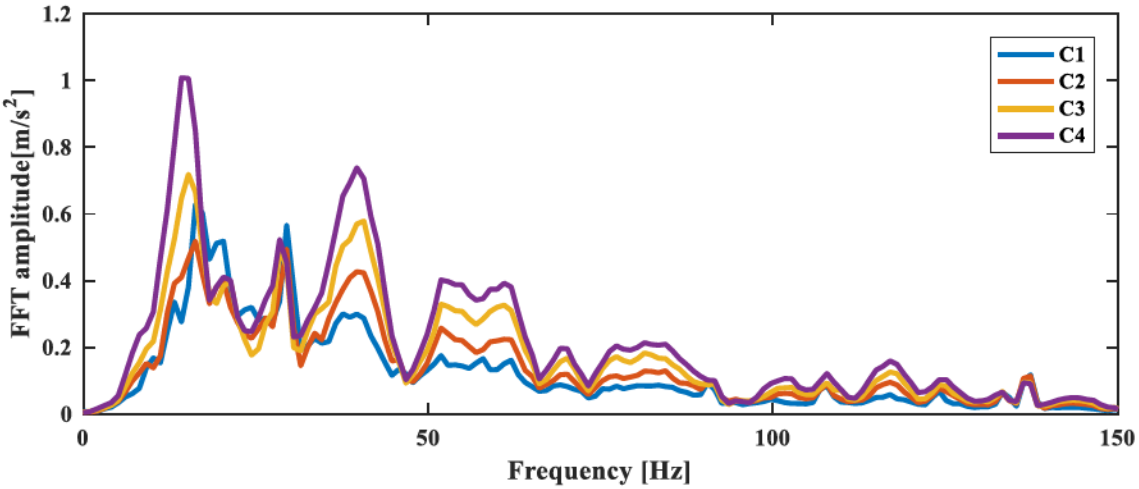

(b) FFT transforms

Figure 2.23 *Acceleration records and FFTs of the moving mass due to chaotic excitation (C) in G-VE-W tests.*

2.6.2 Power Spectral Density

Since multiple accelerometers were used in the tests, for simplicity, power spectral density is reported herein only for accelerometers A_{z1} and A_{x1} in S-VC, S-VE-W, S-HC, G-VC, G-VE-W, and G-HC tests (Figure 2.24 and Figure 2.25). For these two accelerometers attached to the pile caps, the PSD amplitude generally increased with excitation intensity as expected. The random excitation signals induced the strongest energy, followed by swept-sine and finally chaotic impulse signals. For a given excitation type, the PSD curves follow similar trends at the different excitation levels, except for the lowest excitation intensity in a few cases. For example in S-HC tests, the ambient noise was more predominant than the applied excitation. Another interesting finding is that when the input buffer (number of sample points for each measurement) was set to 512 samples in the first few S-VC tests, the PSD curves appear to be smooth with a frequency domain resolution of 0.983 data points per Hz. In order to better capture potential sharp peaks in the subsequent tests, the input buffer was increased to 2,048 samples with a resolution of 3.93 points per Hz. However, when this was done all PSD curves became noisy, regardless of excitation type and intensity. Generally, the pile cap responses to random forcing were least influenced and those for chaotic impulse forcing appeared to be most susceptible. As the excitation level increases, the PSD curves become even nosier. This phenomenon will require further study, and may be related to the digital sampling parameters.

2.6.3 Coherence Functions

To be consistent with the previous section, coherence functions are presented only for accelerometers A_{z1} and A_{x1} in Figure 2.26 and Figure 2.27. For a given excitation type, the coherence is typically far below unity over a wide frequency range at the lowest excitation

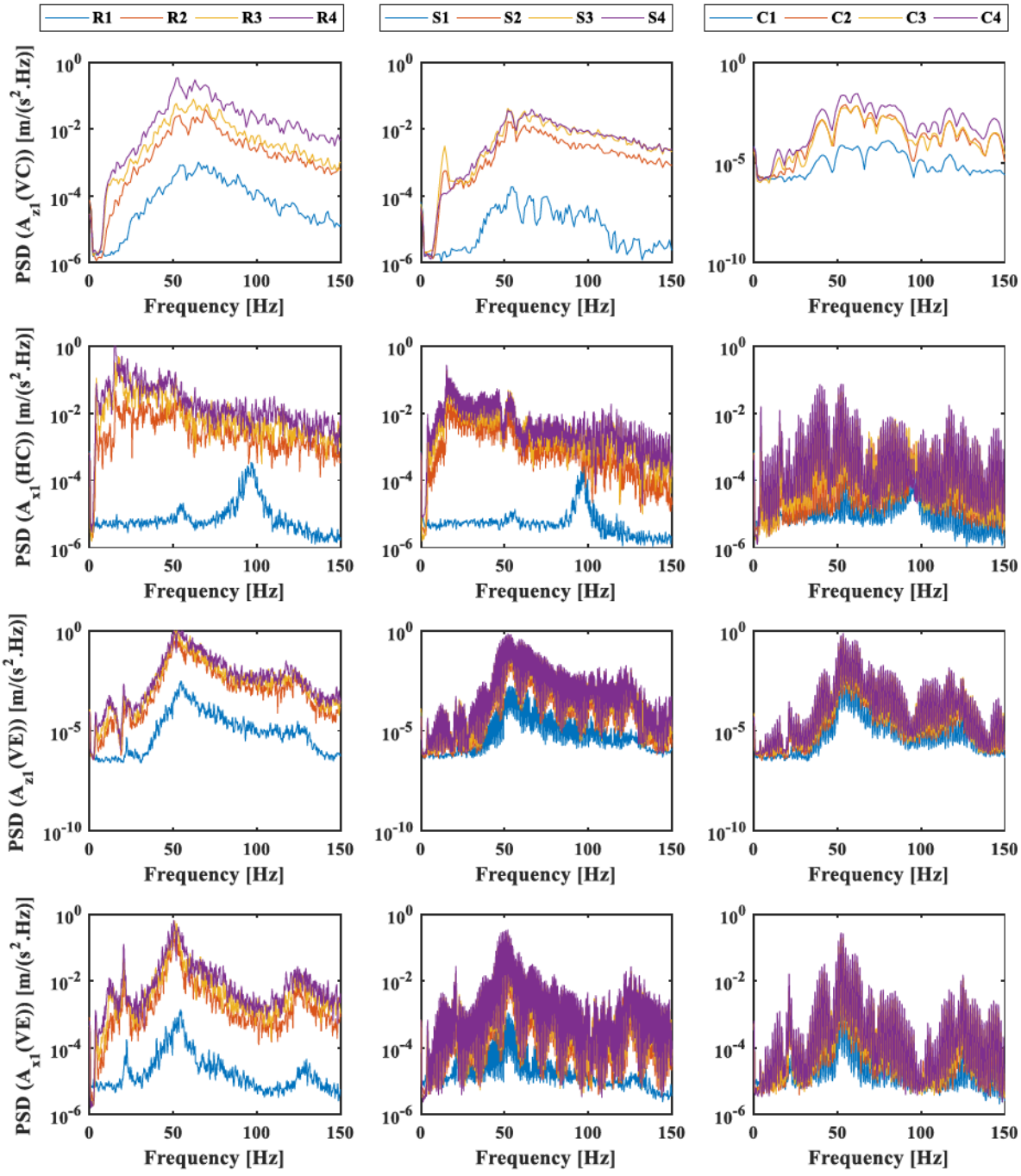

Figure 2.24 *PSD for single pile in VC, VE, and HC tests with various excitation types and intensities.*

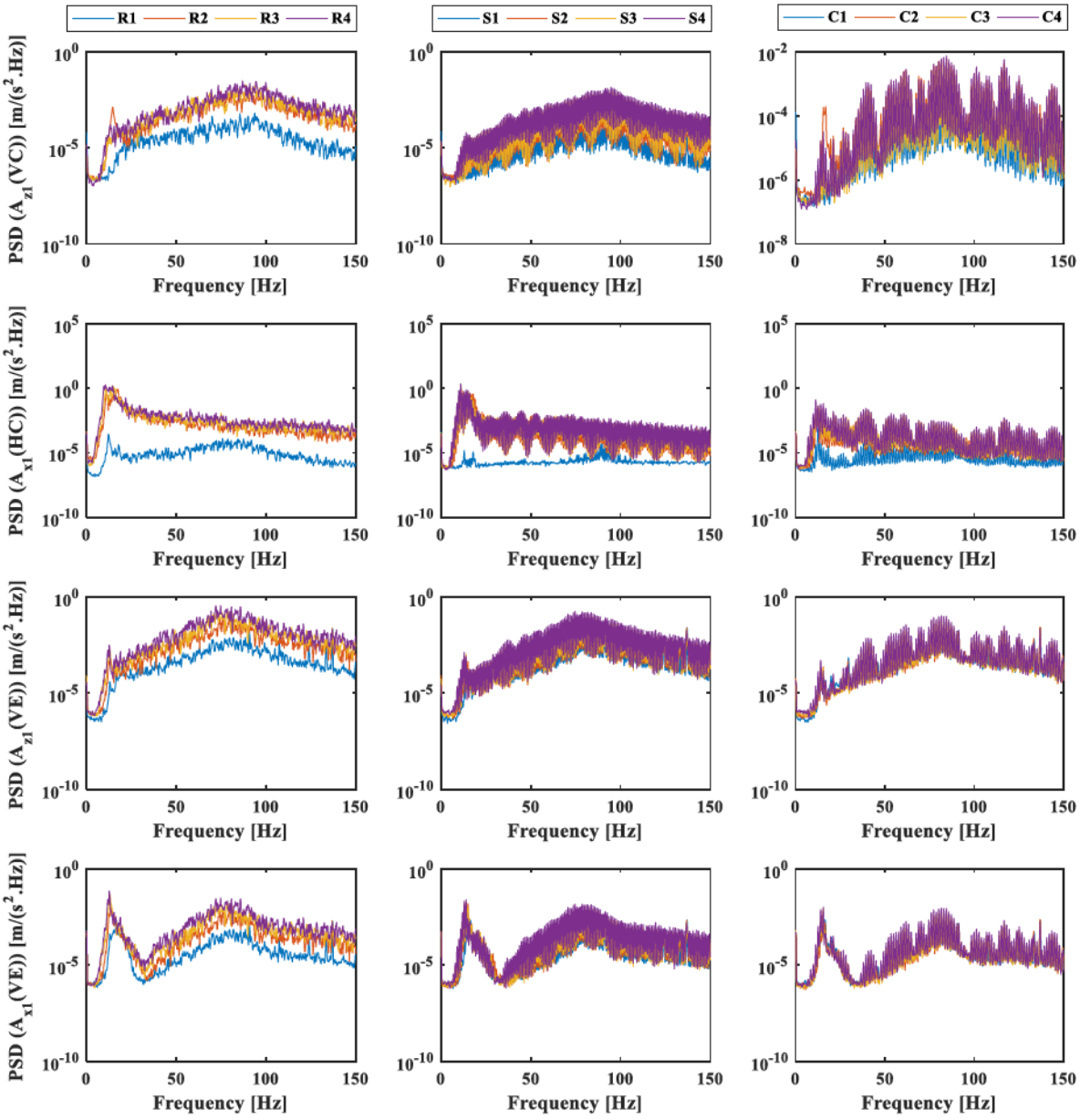

Figure 2.25 *PSD for pile group in VC, VE, and HC tests with various excitation types and intensities.*

levels. As excitation level increases, the coherence functions quickly approach unity, especially at low and high frequencies. At the highest excitation level 4, most excitation types generally resulted in reasonable quality coherences near unity over the entire frequency range in VC tests. As shown by the spectral performance of the inertial shaker in Figure 2.14, the excitation force degrades quickly below 8 Hz, which is also confirmed by the coherence functions quickly dropping to zero below 9 Hz. Additionally, reduced coherence can be also observed at other frequencies for a few of the VE and HC tests. For instance, the coherence for accelerometer A_{x1} in VE tests for the pile group all present substantial drops around 33 Hz. A strong excitation level may induce large deformations of the soil, exhibiting a nonlinear response from the pile-soil system and consequently decreasing the coherence. This phenomenon can be seen in the S-HC-R tests, for which coherence decreases between 40 and 120 Hz as excitation intensity increases from R2 to R4. This same phenomenon is not observed in the G-HC-R tests, likely due to a much higher lateral stiffness. Overall, the data quality are satisfactory in terms of coherence and most of the tests remained in the linear range for all excitation levels.

2.6.4 Accelerance Functions

For dynamic tests of the pile-soil system, it is desirable to present the experimental accelerance functions in a concise way at representative points. In this study, the experimental accelerance functions are translated to the centroid of the pile cap, under the assumption that the pile cap behaves as a rigid body over the frequency range of interest. As will be discussed in Section 3.5.2, displacement at the centroid of the pile cap $\mathbf{U}(C)$ can be expressed as

$$\mathbf{U}(C) = \mathbf{T}_{CP}\mathbf{U}(P) \tag{2.21}$$

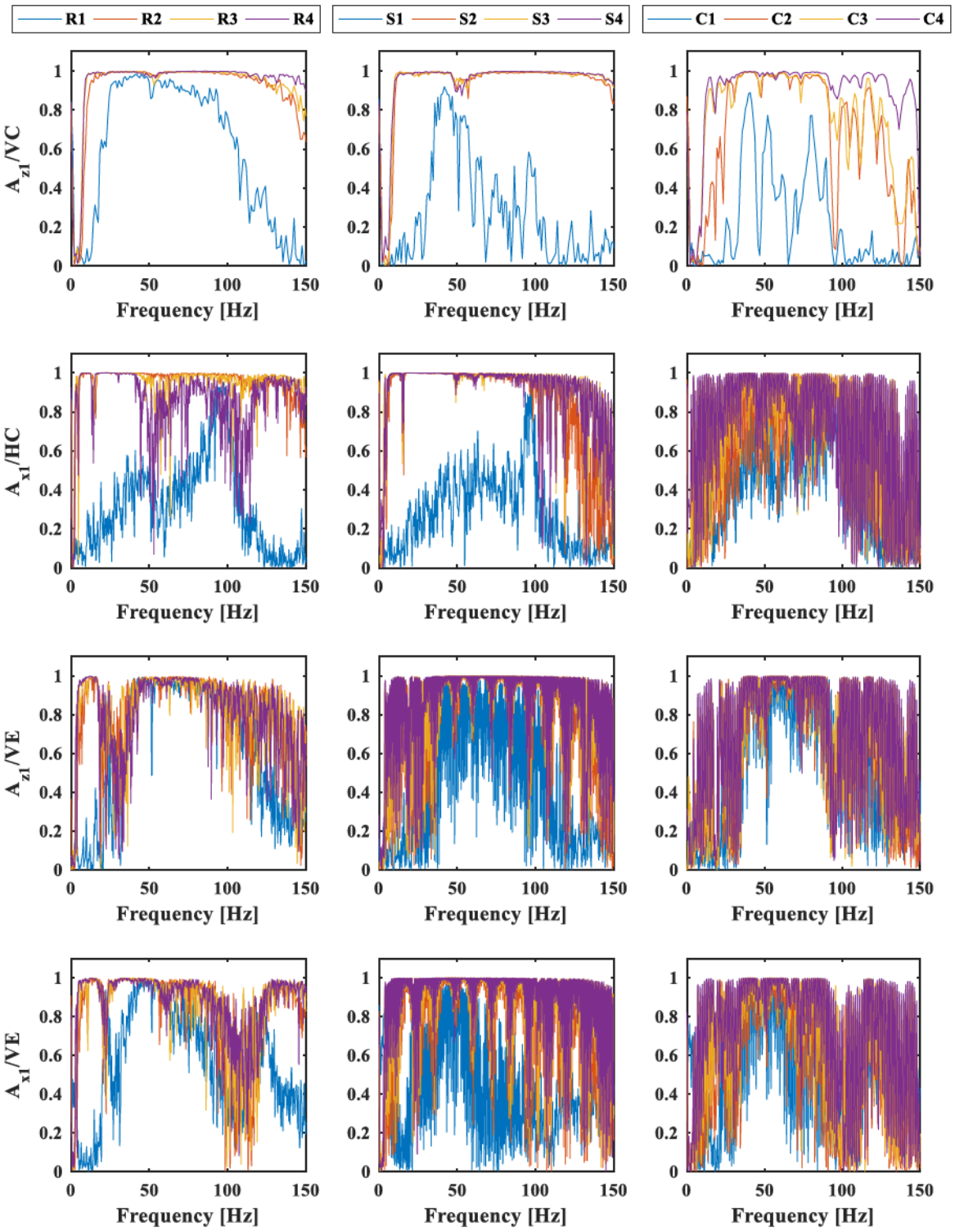

Figure 2.26 *Coherence functions for single pile in VC, VE, and HC tests with various excitation types and intensities.*

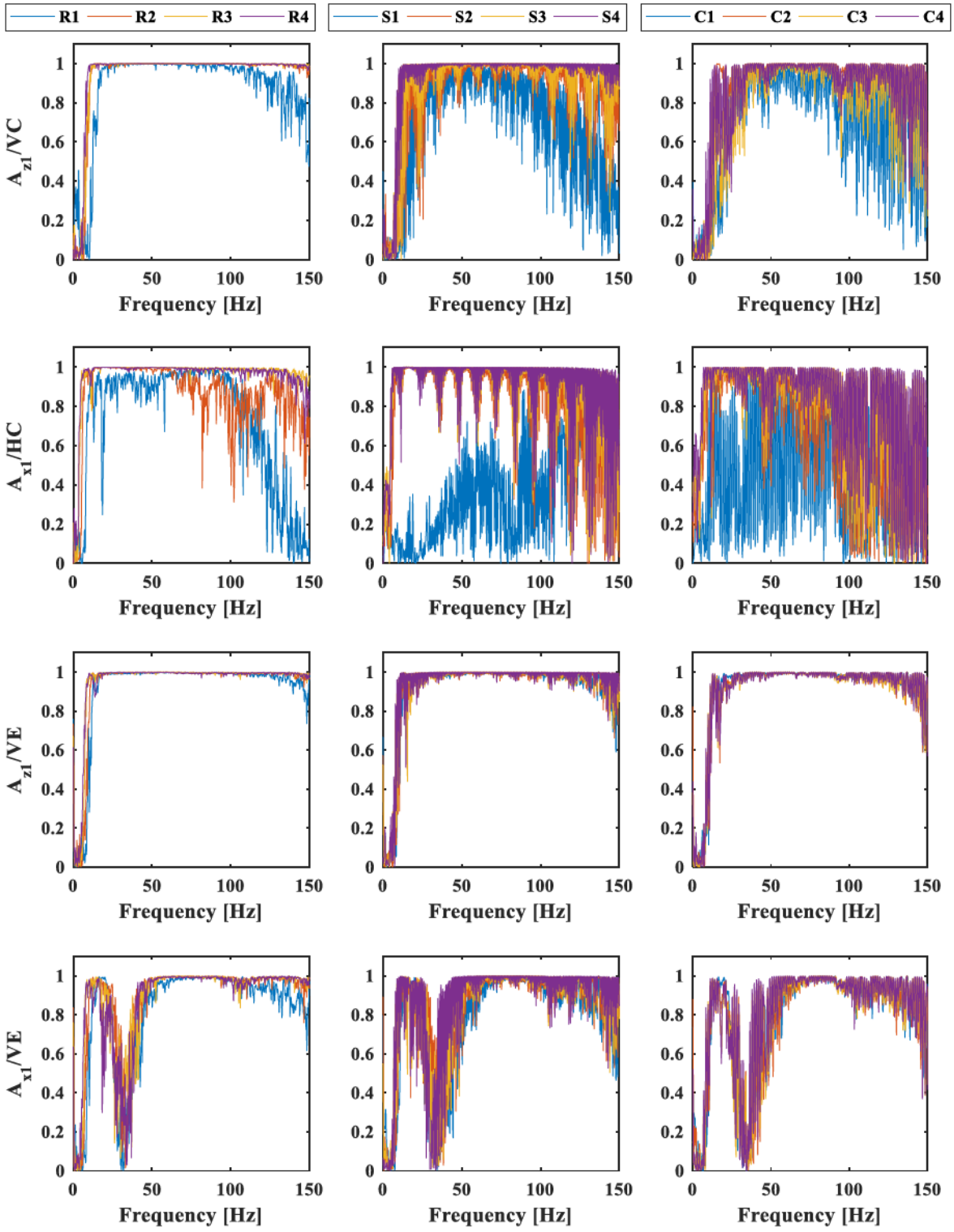

Figure 2.27 *Coherence functions for pile group in VC, VE, and HC tests with various excitation types and intensities.*

where $\mathbf{T}_{CP}$ is the kinematic transformation matrix,

$$\mathbf{T}_{CP} = \begin{bmatrix} 1 & 0 & -e_p \\ 0 & 1 & h_p \\ 0 & 0 & 1 \end{bmatrix} \tag{2.22}$$

and $\mathbf{U}(P) = [U_y(x_p,y_p)\ U_x(x_p,y_p)\ \Theta_z(x_p,y_p)]^T$ is the Fourier-transformed displacement vector at any point P on the pile cap. Converting the Fourier-transformed displacement vectors to acceleration by multiplying $(i\omega)^2$ on both sides, and dividing by the applied force gives the relation

$$\mathbf{A}(C) = \mathbf{T}_{CP}\mathbf{A}(P) \tag{2.23}$$

where $\mathbf{A}(C)$ is the accelerance vector at the centroid, and $\mathbf{A}(P)$ is the accelerance at any point on the pile cap (defined in Eq. 3.69). For simplicity, the notation

$$\mathbf{A}(C) = \begin{bmatrix} A_{yc} \\ A_{xc} \\ A_{rc} \end{bmatrix} \tag{2.24}$$

will be used to denote the vertical, horizontal, and rotational components of centroidal accelerance. Considering the VC, VE, and HC excitation force types described previously, a total of nine unique centroidal accelerances exist for planar motion of the pile cap (Table 2.7).

Table 2.7 Summary of centroidal accelerance functions for the three test types

Directional acceleration at centroid	**Excitation force type**		
	VC	**VE**	**HC**
A_{yc}	A_{yc} / VC	A_{yc} / VE	A_{yc} / HC
A_{xc}	A_{xc} / VC	A_{xc} / VE	A_{xc} / HC
A_{rc}	A_{rc} / VC	A_{rc} / VE	A_{rc} / HC

Example calculations for determining centroidal A_{yc}/VC and A_{xc}/HC accelerances from those measured on the pile-cap surface in S-VC tests are presented below. The vertical centroidal accelerance can be determined using accelerations A_{y1}, A_{y2}, or their average. Using either A_{y1} or A_{y2} gives

$$A_{yc} = A_{y1} - e_{y1}A_r(y1) \tag{2.25}$$

or

$$A_{yc} = A_{y2} - e_{y2}A_r(y2) \tag{2.26}$$

Due to symmetry of the locations of A_{y1} and A_{y2},

$$e_{y1} + e_{y2} = 0 \tag{2.27}$$

and assuming the pile cap is rigid,

$$A_r(y1) = A_r(y2) \tag{2.28}$$

Therefore adding equation ((2.25) and (2.26) provides the averaged vertical accelerance as simply

$$A_{yc} = \frac{A_{y1} + A_{y2}}{2} \tag{2.29}$$

Similarly, in S-HC tests, assume P is at accelerometers A_{x1} and A_{x2}, respectively. By symmetry,

$$h_{x1} + h_{x2} = 0 \tag{2.30}$$

Then the horizontal centroidal accelerance can be calculated as

$$A_{xc} = \frac{A_{x1} + A_{x2}}{2} \tag{2.31}$$

As for rocking acceleration, it can be determined from the vertical accelerances as

$$A_{rc} = \frac{A_{y1} - A_{y2}}{e_o} \tag{2.32}$$

or from the horizontal accelerances as

$$A_{rc} = \frac{A_{x2} - A_{x1}}{h_o} \tag{2.33}$$

where $e_o = 0.8636$ m is the horizontal distance between accelerometers A_{y1} and A_{y2}, and $h_o = 0.7112$ m is the vertical distance between accelerometers A_{x1} and A_{x2}. It can be shown that (2.32) and (2.33) provide consistent results (Figure 2.28) and thus A_{rc} is averaged as:

$$A_{rc} = \frac{1}{2}\left(\frac{A_{z1} - A_{z2}}{e_o} + \frac{A_{x2} - A_{x1}}{h_o}\right) \tag{2.34}$$

In the general case for which the centroid of the pile cap and shaker's stationary mass are not at the geometric center of the pile cap, as is the case for VE tests, Eqns. (2.27) and (2.30) no longer hold. The vertical centroidal accelerance can be determined more generally for such cases by substituting Eqn. (2.33) into the average of Eqns. (2.25) and (2.26), to give

$$A_{yc} = A_{y2}\frac{e_{y1}}{e_o} - A_{y1}\frac{e_{y2}}{e_o} \tag{2.35}$$

which simplifies to Eqn. (2.29) when the centroid is at the geometric center, as $e_{y1} = -e_{y2} = e_o / 2$. Similarly, the horizontal centroidal accelerance for such cases can be expressed as

$$A_{xc} = A_{x2}\frac{h_{x1}}{h_o} - A_{x1}\frac{h_{x2}}{h_o} \tag{2.36}$$

Similar equations can be derived for the pile group with attention to the sign convention. For example, due to the new layout for accelerometers, rocking acceleration can be taken as:

$$A_{rc} / VE = \frac{1}{2Q_V}\left(\frac{A_{y2} - A_{y1}}{e_o} + \frac{A_{x1} - A_{x2}}{h_o}\right) \tag{2.37}$$

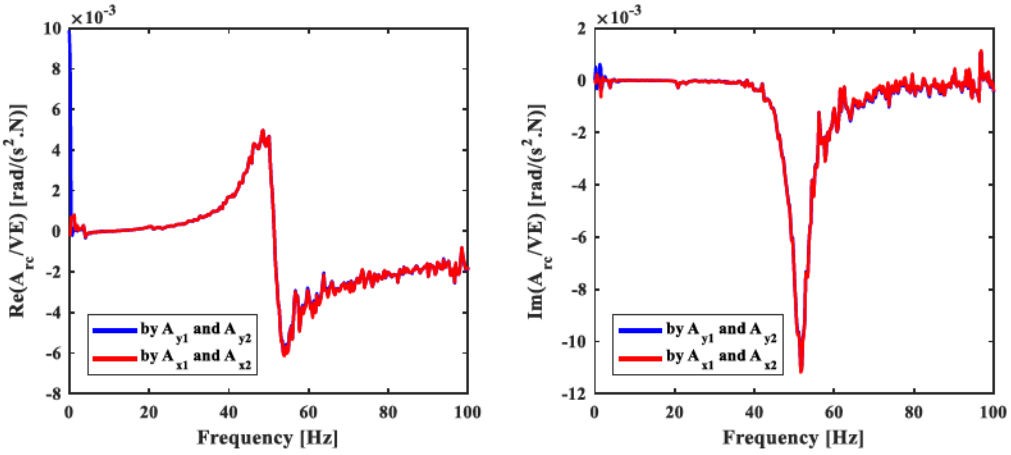

Figure 2.28 *Agreement of rocking accelerance calculated using pairs of vertical or horizontal accelerometers for test S-VE-R2.*

Among the nine accelerances in Table 2.7, six of them are regarded as primary, as they are necessary for characterizing the vertical and lateral-rocking modes; A_{yc}/VC, A_{xc}/HC and A_{rc}/HC if combining separate VC and HC tests, or A_{yc}/VE, A_{xc}/VE and A_{rc}/VE if using a single VE test. The remaining four accelerances are either minor or theoretically zero, and not presented herein.

1. Single pile tests

The A_{yc} / VC accelerances are highly consistent for all excitation types (Figure 2.29). A unique resonant peak for the imaginary part is found at 72 Hz. For random excitation, accelerance at level R1 slightly deviates from higher level excitations at frequencies below 20 Hz and above 70 Hz. This is due to the low signal-to-noise ratio, which was already illustrated by the coherence function. Accelerances for S1 and C1 differ even more from higher excitation levels and no unique peaks can be observed. With an increasing excitation force, the resonant peaks by random and chaotic signals show slight shifts towards the left, indicting minor degrees of nonlinearity. The resonant peaks are more consistent for swept-sine excitation.

Theoretically, the lateral stiffness of a single pile is significantly lower than the vertical stiffness. Thus the horizontal accelerations for horizontal excitation were expected to be larger than for the vertical mode. For HC tests (Figure 2.30), none of the lowest excitation levels R1, S1, and C1 were large enough to induce the intended resonance. This phenomenon is attributed to the friction of the rails of the shaker's moving mass, and the lower excitation levels being not much stronger than the ambient vibration sources. At the higher excitation levels, the resonant peaks were captured as expected. The strongest resonant A_{xc}/HC peaks occurred at around 4.5 Hz and 15.5 Hz, respectively. In addition, a weak third peak can be observed near 51 Hz. The first peak is attributed to the horizontal resonance of the pile-cap-soil system, which typically occurs at a frequency below 10 Hz. The third peak is due to coupled lateral and rocking motion. The second resonant peak, however, is unintended. Its resonant peak at 15 Hz is obviously beyond the range of the horizontal mode and far below the resonant peak for the rocking mode. Possible explanations are (1) that the moving masses, though seated on a pair of guide rails, had a degree of freedom not only in the excitation direction, but also in the vertical direction due to the rotation of the pile cap. Including this effect in the equation of motion for the isolated free body diagram of the moving masses renders the governing system of differential equations nonlinear and significantly more complicated, and this secondary effect was neglected for simplicity, (2) the legs of the shaker's base were not truly rigid and therefore introduced an additional cantilever-type vibration mode of the shaker itself, or (3) a slight rotational degree of freedom (independent of the pile cap's rotation) that was observed for the shaker's moving masses as they accelerated along the loading direction. These hypothesis all relate to additional unintended motion of the moving masses, and are supported by the transfer function of A_{mt}, which suggests a substantial amplification effect transverse to

the direction of shaking at around 15 Hz. Another noticeable finding is that the resonant amplitude for the horizontal mode varies significantly for all excitation types and levels. One reason is that the amplitude is sensitive to soil damping near the ground level, which depends on the dynamic strain level. The low horizontal stiffness allows for relatively large soil deformations, and thus a larger variation in damping ratio with excitation intensity. Another possible reason for the variation in resonant amplitude is the sampling resolution. The buffer size of 4,096 samples and approximate sampling frequency of 512 Hz resulted in a resolution of 0.254 Hz in the frequency domain. This may not have been sufficient to fully capture the sharp horizontal resonant peak.

The A_{yc} / VE accelerance functions exhibit consistent trends regardless of excitation signal type (Figure 2.32), and are very similar to the A_{yc} / VC ones. Excluding the lowest excitation levels, the imaginary part exhibits a peak at 62 Hz. The different locations of the external force and centroid compared to VC tests results in an additional influence from the rocking mode, which decreases the amplitudes of the curves at around 50 Hz.

The A_{xc} / VE accelerance functions (Figure 2.33) also show the three resonant peaks observed in A_{xc} / HC accelerances, but with much lower amplitudes for the horizontal mode. The fundamental frequency also shows a minor decrease from 4.58 Hz to 4.07 Hz, likely due to the higher moment of inertia resulting from moving the shaker to the HC position. The second resonant peak due to resonance of the moving mass exhibits the opposite trend; with the excitation force offset from the centroid of the pile cap, this unintended rocking mode becomes more significant.

A single sharp resonant peak is found for the A_{rc} / VE accelerance (Figure 2.34). Higher excitation levels leads to slightly lower resonant peak frequencies.

2. Pile group tests

Results for the G-VC, G-VE-W, and G-HC tests are shown in Figure 2.35 - Figure 2.40. For A_{yc} / VC, the single resonant frequency is found near 90 Hz, which is higher than for the single pile tests. The maximum amplitude for the imaginary part also greatly drops from 2.9×10^{-3} m/(s^2.N) to 1.3×10^{-3} m/(s^2.N). This is due to the substantial increase in vertical stiffness for the pile group. Random excitations provided the cleanest responses, especially at frequencies beyond 100 Hz.

The A_{xc} / HC accelerance for the pile group presents a strong resonant peak at 12 Hz, which is approximately four times higher than the frequency for the single pile. A very small peak also appears near 18 Hz. The resonant amplitude is less susceptible to the excitation type due to the greater pile cap mass and resulting smaller strains in the soil. The increasing random excitation levels only slightly decrease the resonant peak amplitude. Compared to the single pile case, the second unintended resonant peaks almost disappear, except for the lowest excitation level, while the coupled rocking mode is completely eliminated. These differences are attributed to the massive pile cap, and the axial resistance of the piles against rotation. With the same excitation as in the S-HC tests, less rocking motion and coupled horizontal motion were induced. The resonance due to the moving mass then became less significant.

The A_{yc} / VE accelerance shows not only a resonant peak for the vertical mode around 95 Hz, but also a small additional 'hump' at around 75 Hz caused by interaction with the rocking mode. As the excitation increases, the amplitude of the vertical mode decreases while that of the rocking mode becomes more dominant.

For A_{xc} / VE, both the horizontal mode and the rocking mode were well captured. Similar to A_{xc} / HC, the additional unintended resonance due to the moving mass becomes almost negligible.

The rocking mode A_{rc} / VE is also well characterized with a peak at 80 Hz, which is higher than the corresponding value of 50 Hz in the single pile case. The horizontal mode at 14 Hz is also captured with a very small peak. Slight nonlinearity induced by the increasing excitation force can be clearly seen for all excitation types.

Accelerance functions for soil accelerometers in S-VC tests are analyzed herein. According to the instrumentation plan, A_{g1} and A_{g4}, as well as A_{g2} and A_{g5} had the same distance to the pile. If the soil profile is assumed to be axisymmetric, wave propagation induced by a single pile in VC tests is supposed to be axisymmetric as well. This assumption is verified by comparing magnitude of transfer functions of A_{g1} to A_{g4}, and A_{g2} to A_{g5}. Accelerometer A_{g4} malfunctioned during the test and thus is not reported herein. Accelerance functions for the remaining five accelerometers due to all excitation types at intensity level 2 to 4 are shown in Figure 2.41(a). For a radiation problem as in this study, the closest observation point should have the highest vibration magnitude due to energy dissipation when waves propagate in soil, and the farthest observation point should have the lowest magnitude. This is verified by the distinguishable resonant peaks that are differentiated by the distance from accelerometers to the pile. In addition, excitation type and intensity didn't result in significant difference in either resonant frequency or amplitude. The peak magnitude versus distance for all excitations is plotted in Figure 2.41(b) to examine wave attenuation at the ground level. A drastic decrease in the peak magnitude with increasing distance is observed. Wave attenuation is well demonstrated by fitting the data using power function.

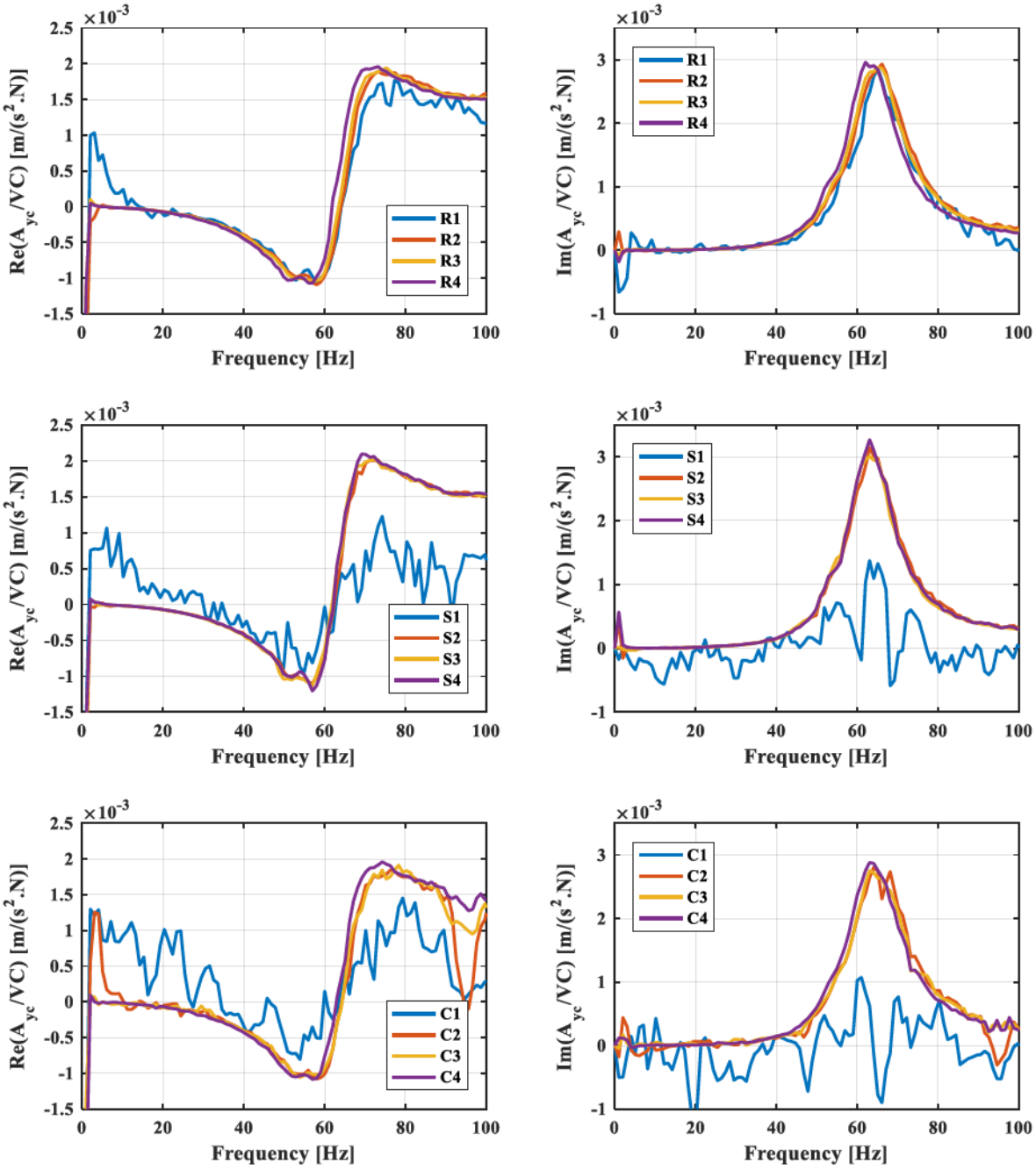

Figure 2.29 A_{yc} / VC *accelerance functions for single pile in S-VC tests with various excitation types and intensities.*

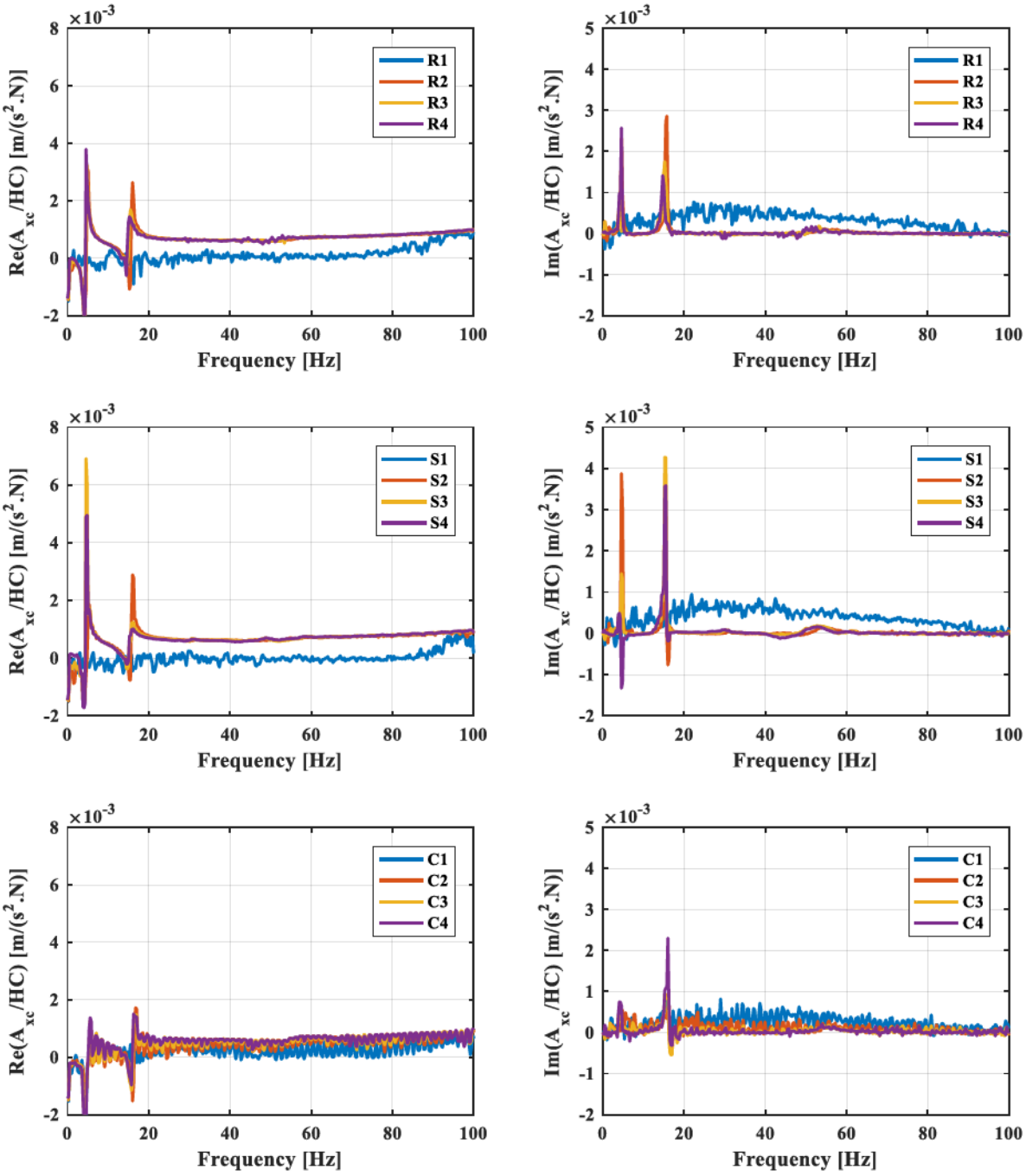

Figure 2.30 A_{xc} / HC *accelerance functions for single pile in S-HC tests with various excitation types and intensities.*

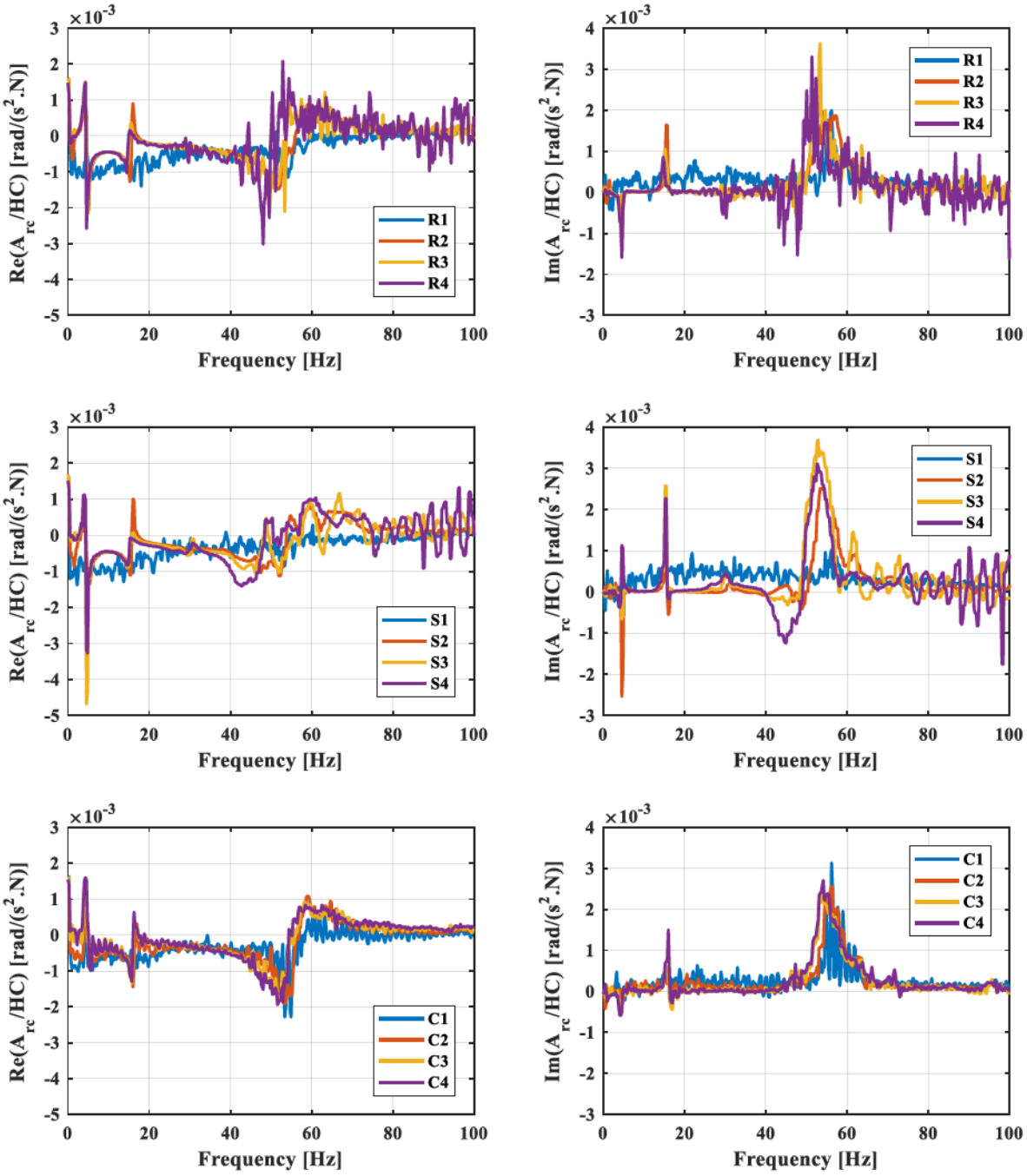

Figure 2.31 A_{rc} / HC *accelerance functions for single pile in S-HC tests with various excitation types and intensities.*

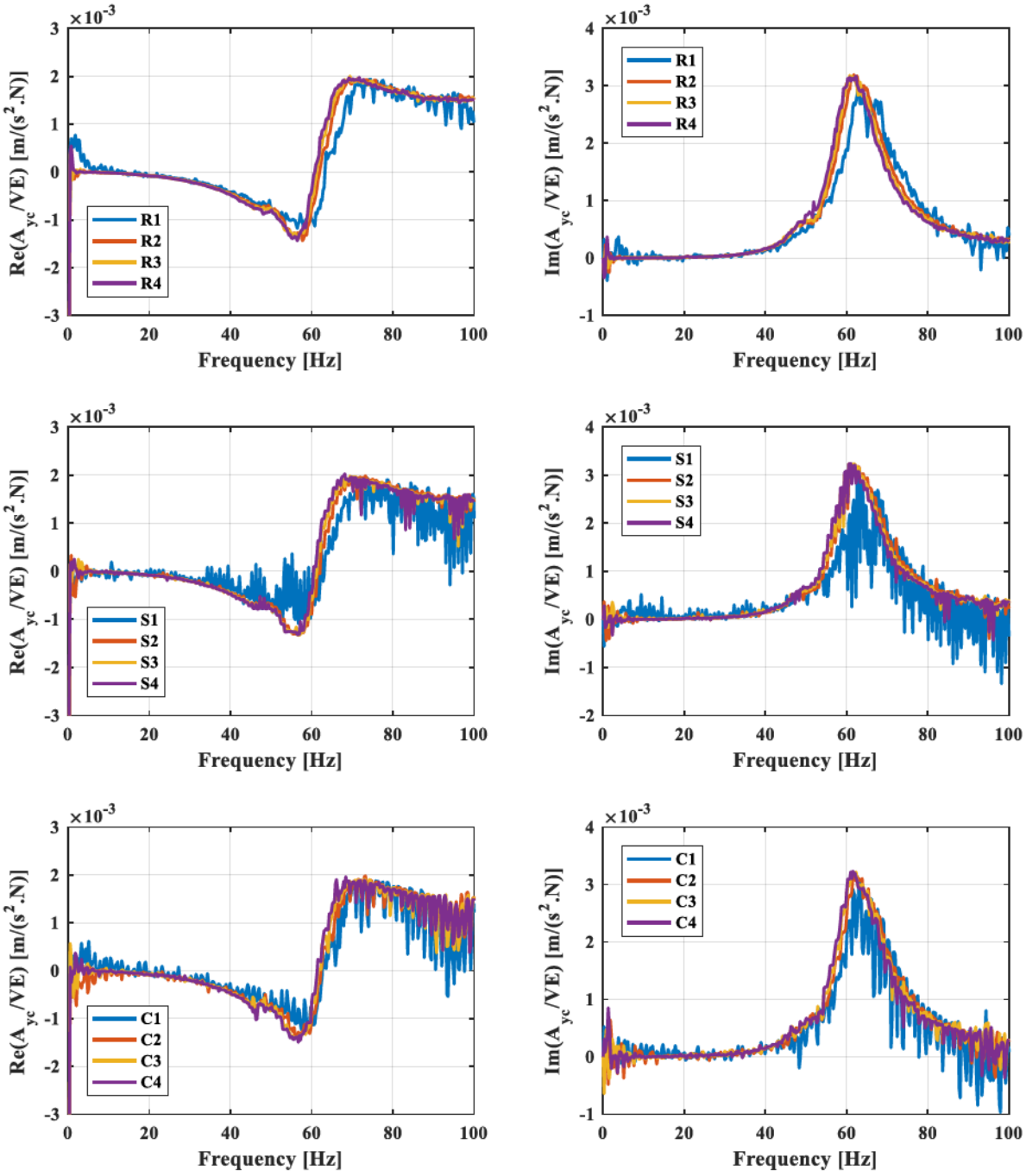

Figure 2.32 A_{yc} / VE *accelerance functions for single pile in S-VE-W tests with various excitation types and intensities.*

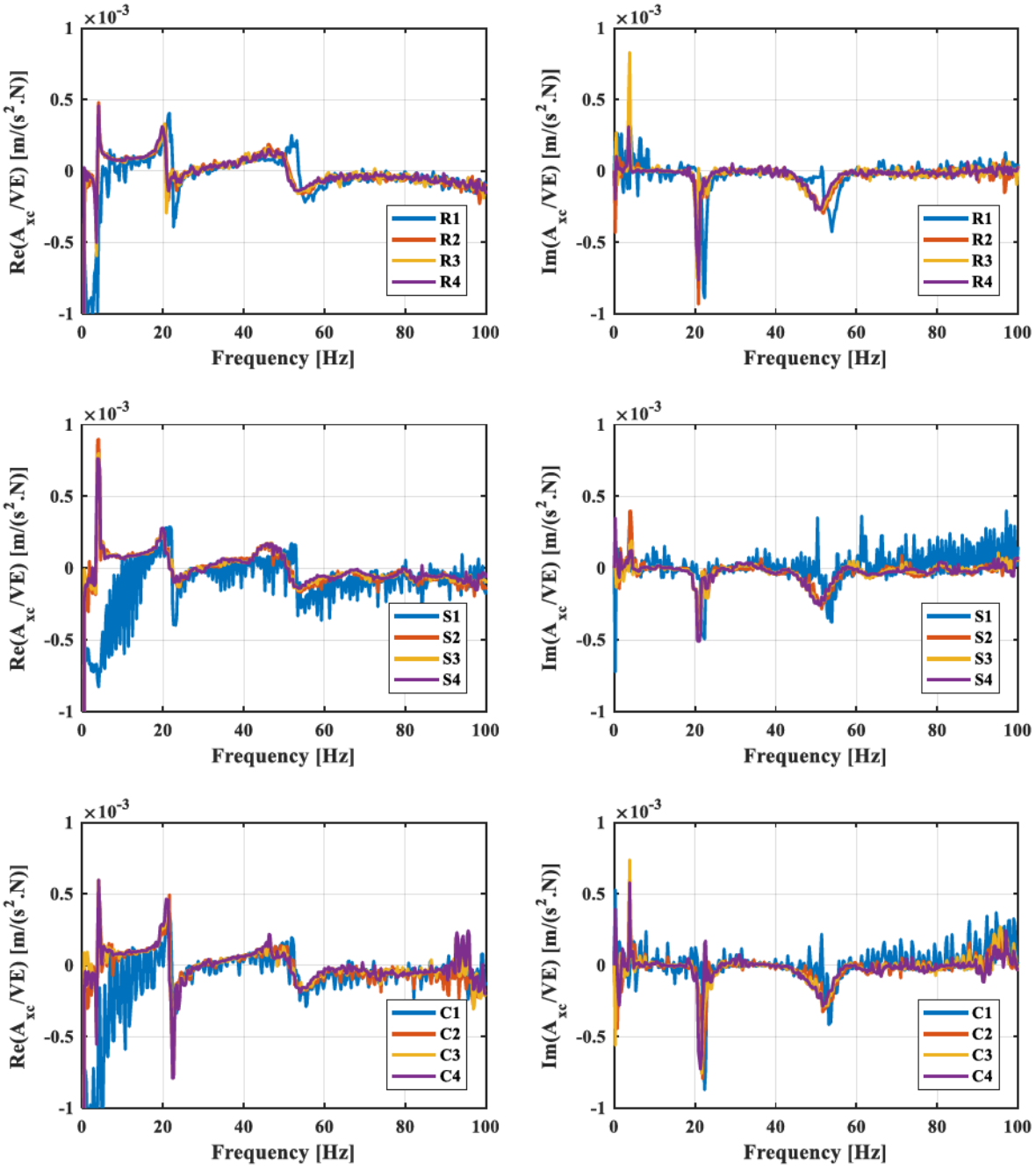

Figure 2.33 A_{xc} / VE *accelerance functions for single pile in S-VE-W tests with various excitation types and intensities.*

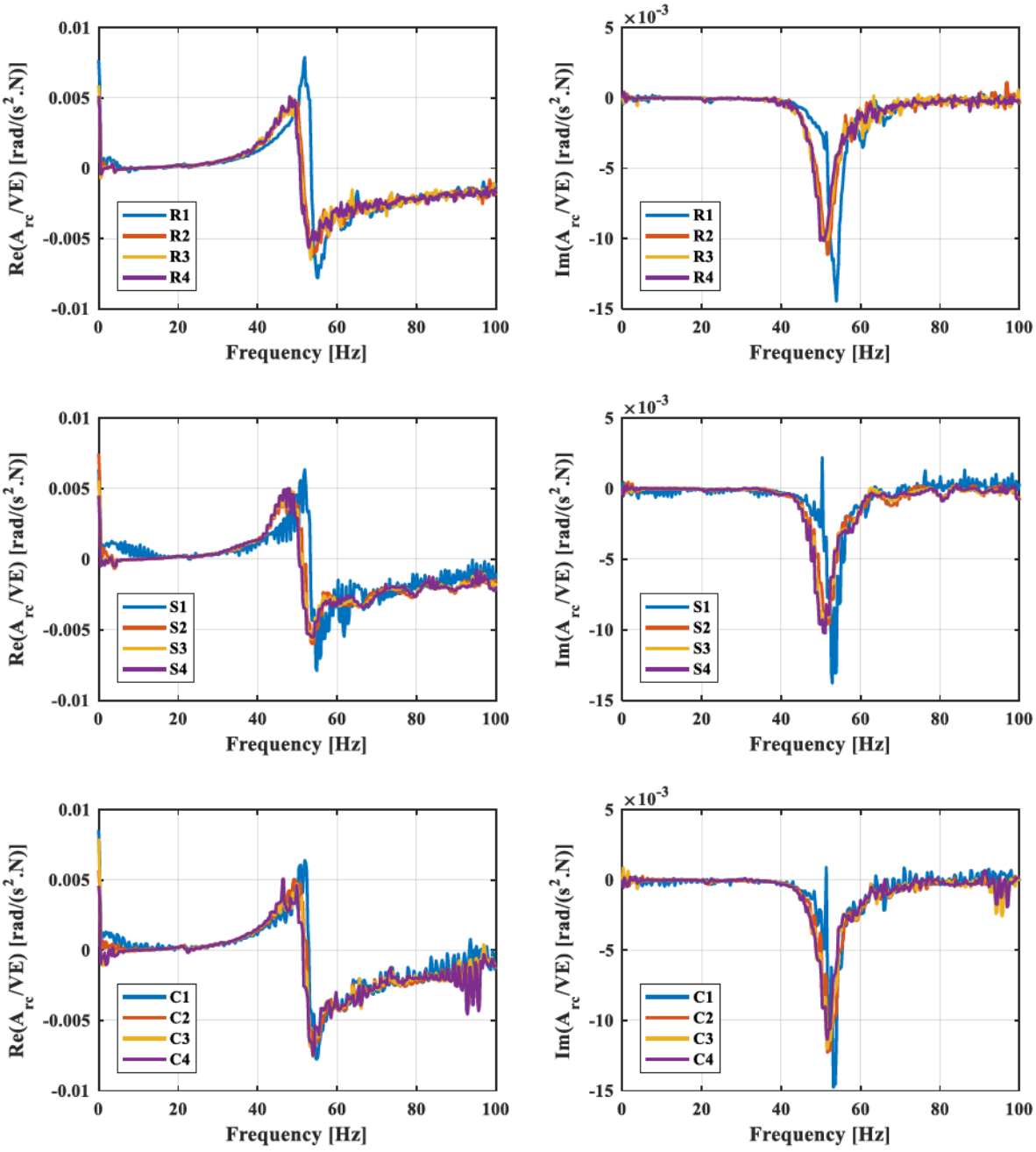

Figure 2.34 A_{rc} / VE *accelerance functions for single pile in S-VE-W tests with various excitation types and intensities.*

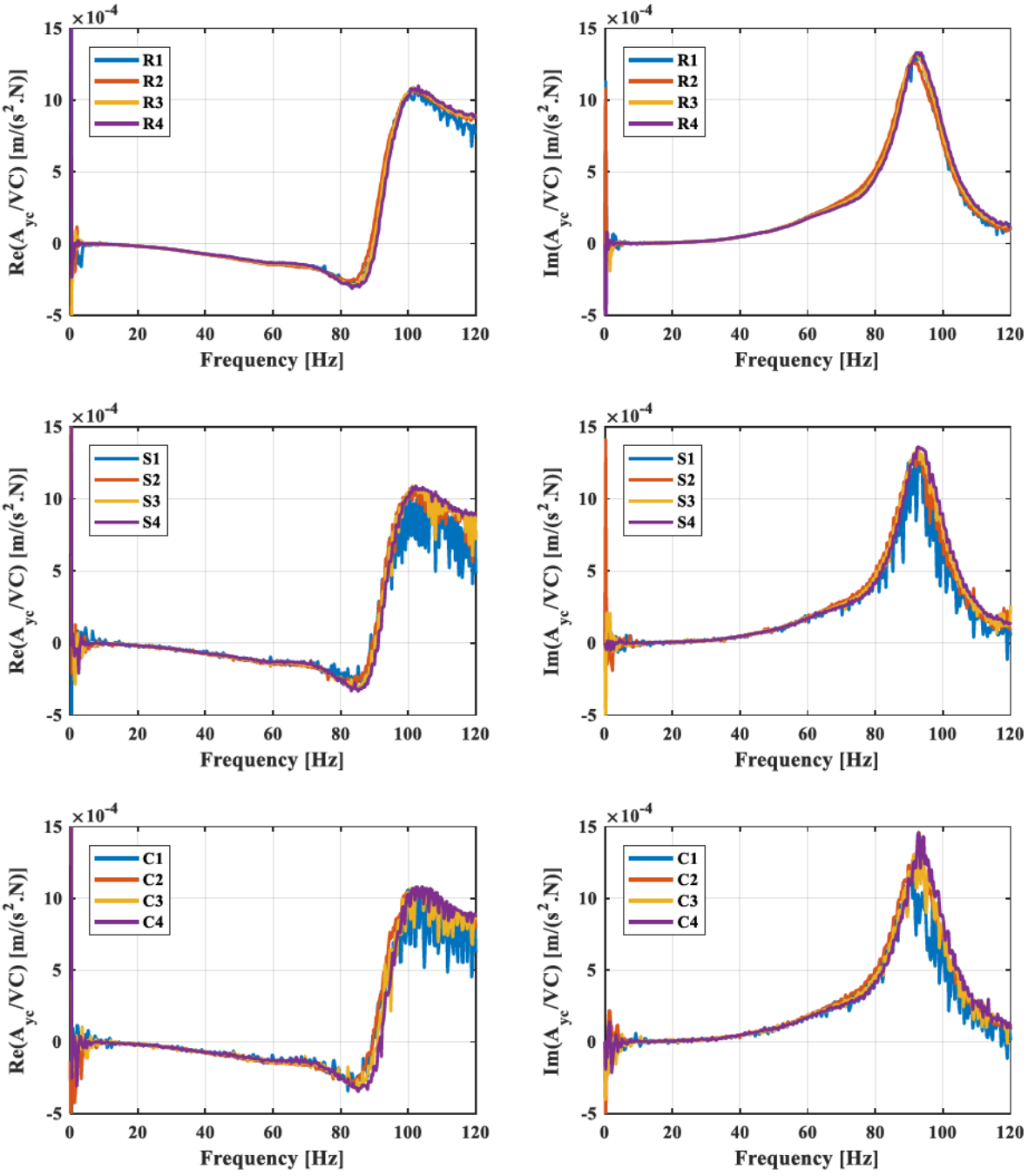

Figure 2.35 A_{yc} / VC *accelerance functions for pile group in G-VC tests with various excitation types and intensities.*

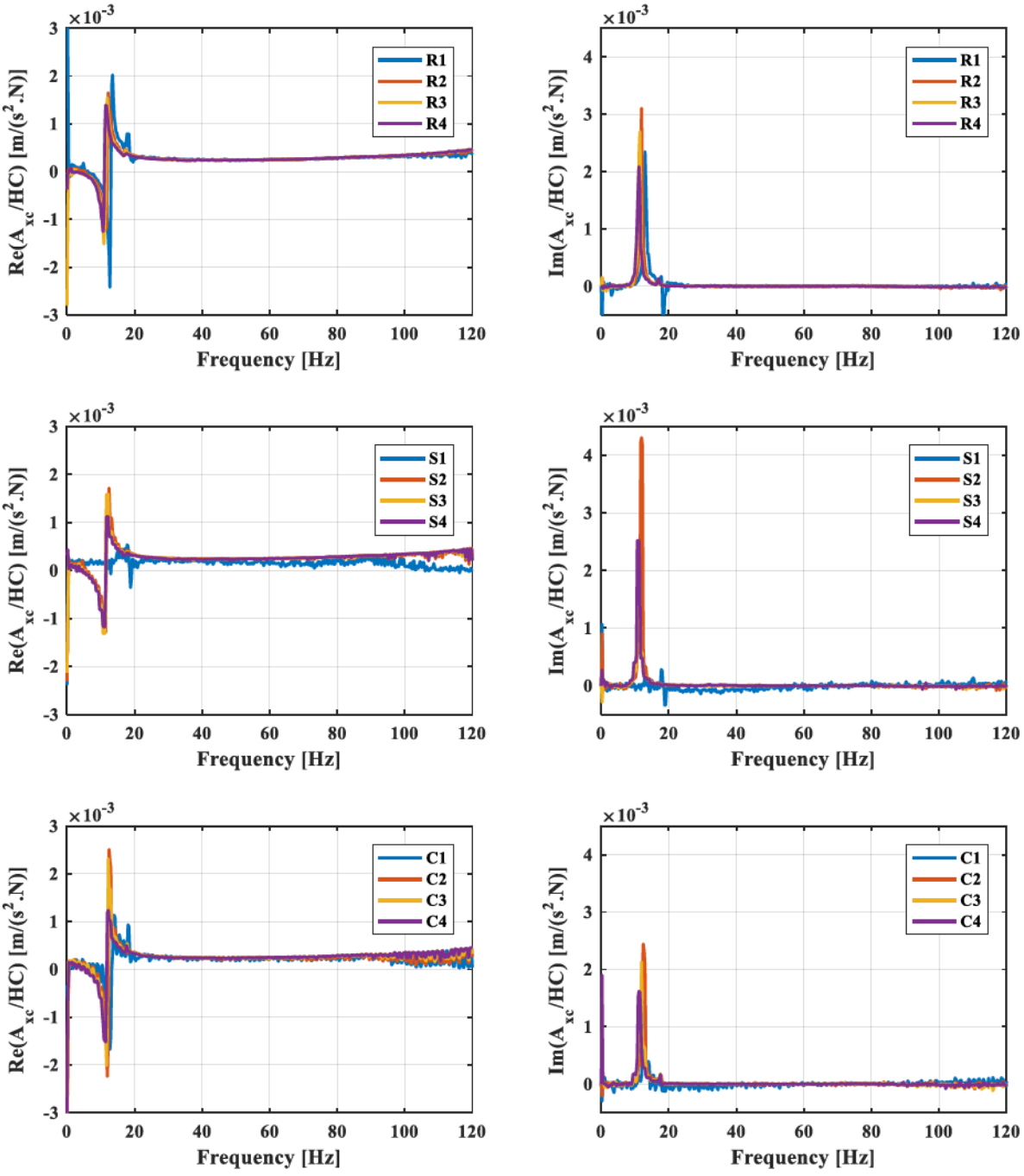

Figure 2.36 A_{xc} / HC *accelerance functions for pile group in G-HC tests with various excitation types and intensities.*

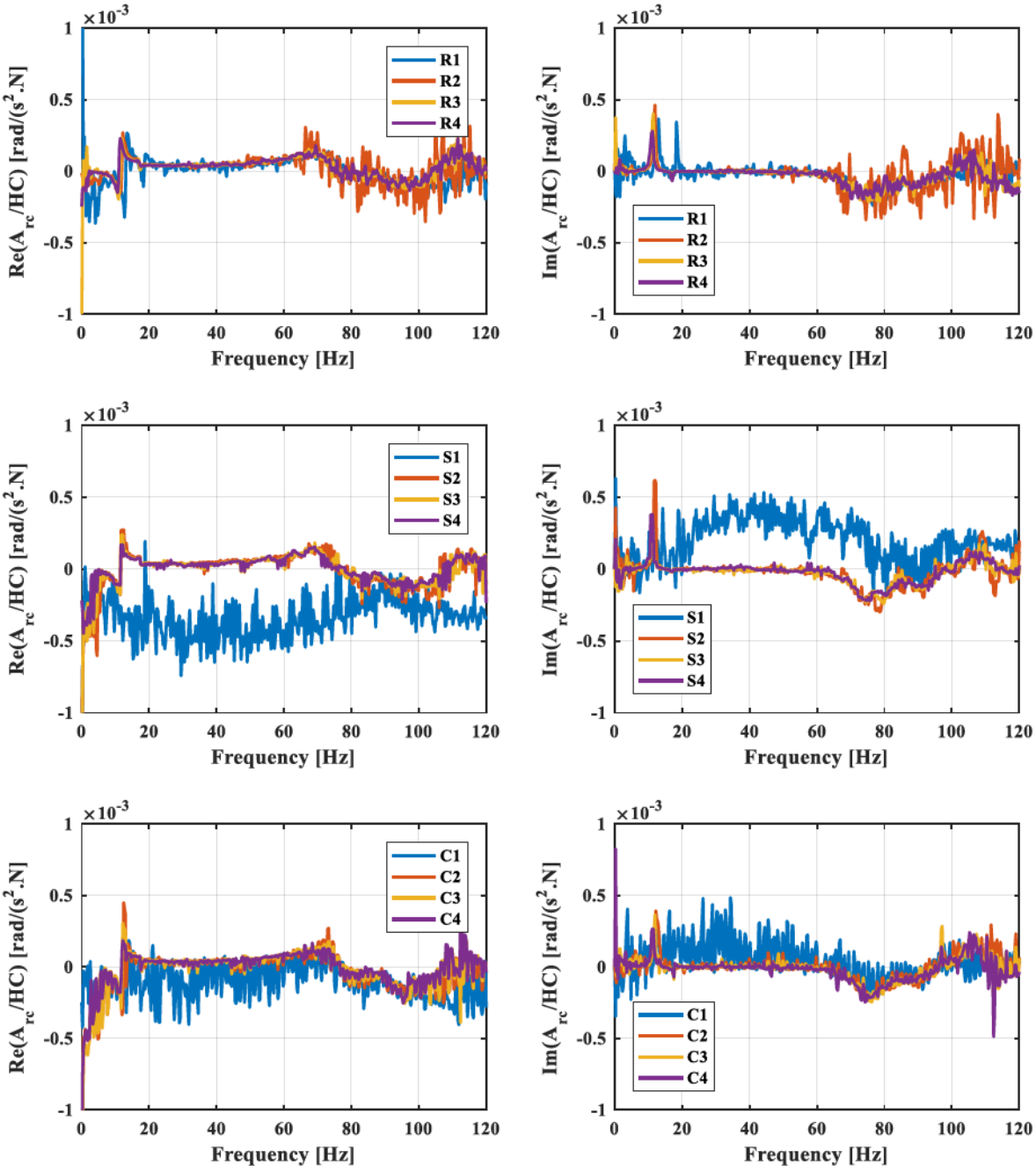

Figure 2.37 A_{rc} / HC *accelerance functions for pile group in G-HC tests with various excitation types and intensities.*

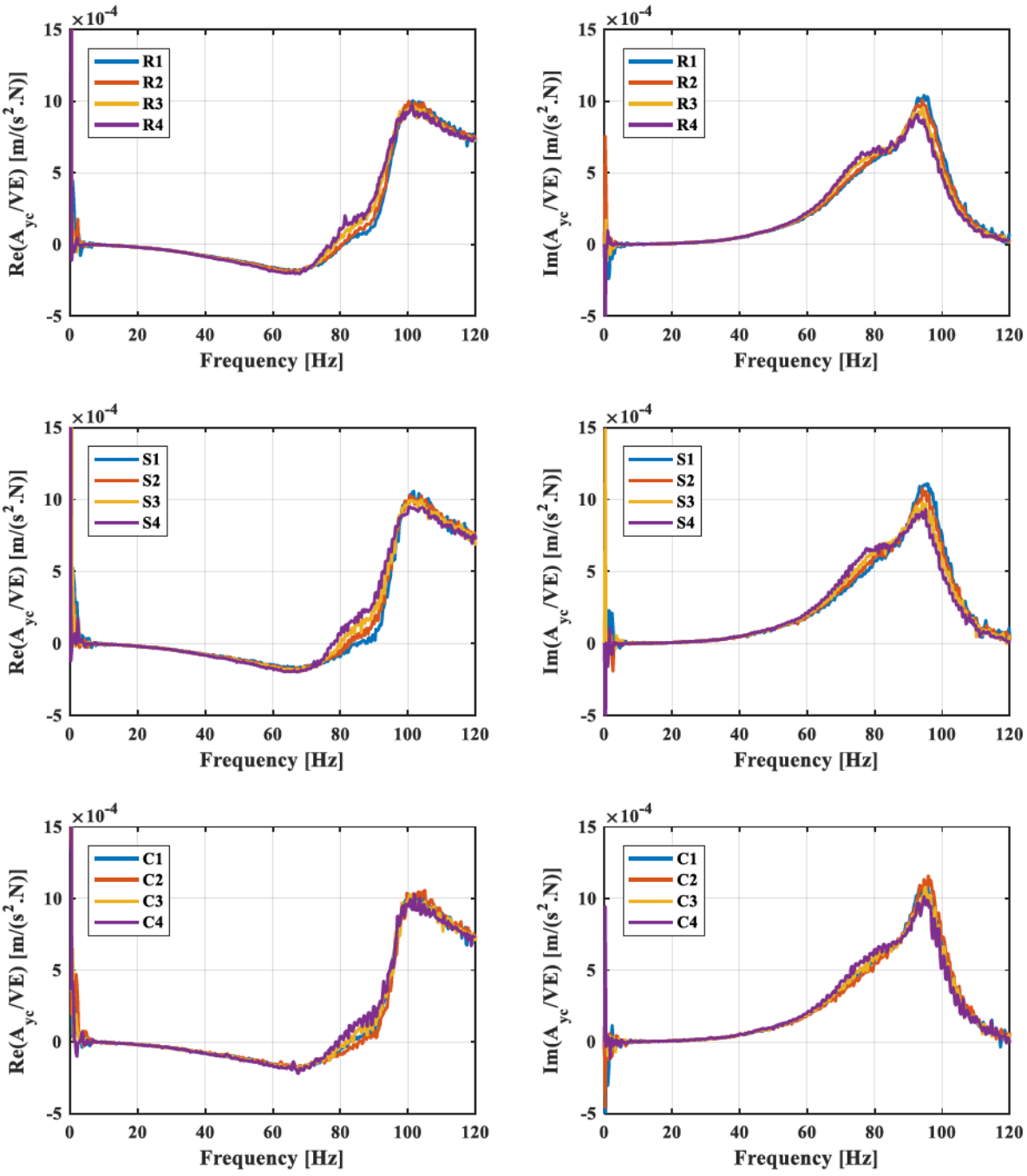

Figure 2.38 A_{yc} / VE *accelerance functions for pile group in G-VE-W tests with various excitation types and intensities.*

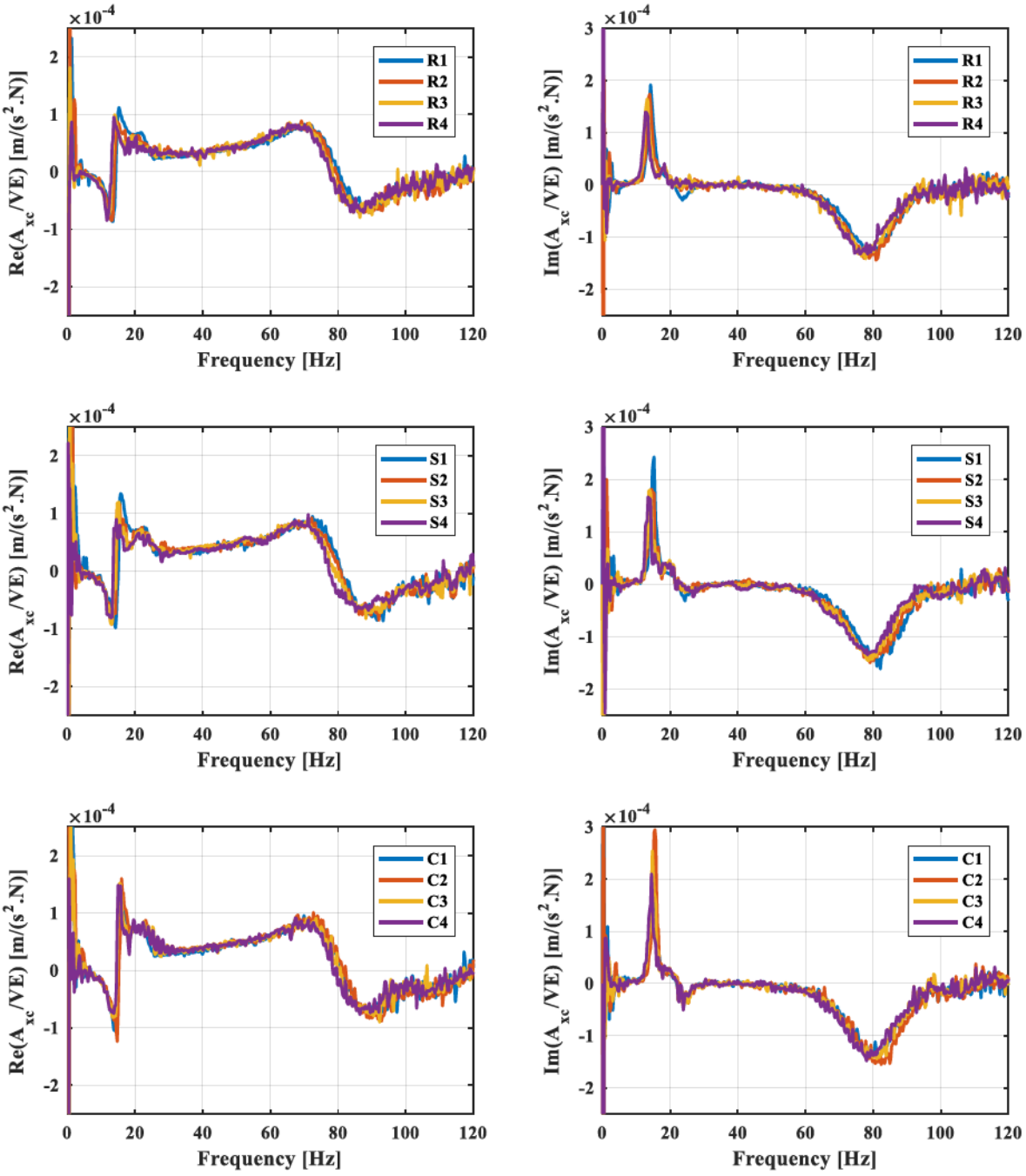

Figure 2.39 A_{xc} / VE *accelerance functions for pile group in G-VE-W tests with various excitation types and intensities.*

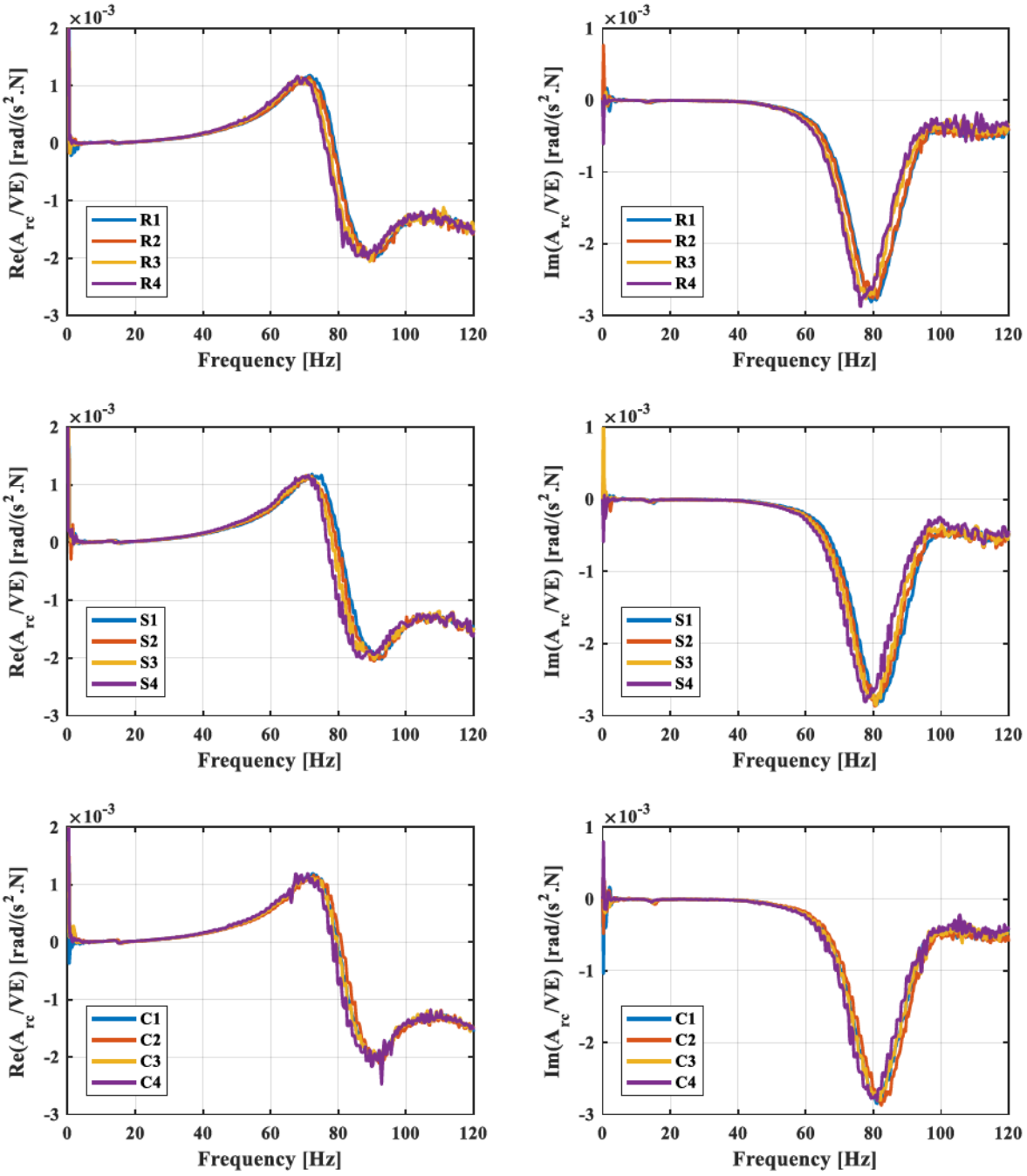

Figure 2.40 A_{rc} / VE *accelerance functions for pile group in G-VE-W tests with various excitation types and intensities.*

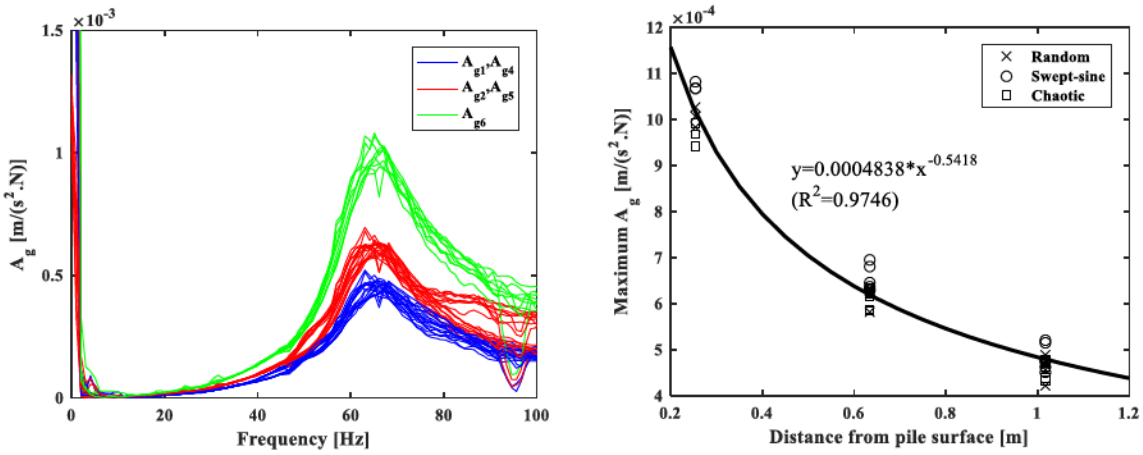

(a) Magnitude of accelerances (b) attenuation of accelerances on the ground level

Figure 2.41 Dynamic responses for soil accelerometers.

2.6.5 Transfer Functions for Pile Strain Gauges

The resonance of the pile cap-shaker system can also be demonstrated by the axial deformation of the unembedded pile segment, which was measured by strain gauges in this study. Theoretically, for S-VC tests the pile should only show compression-tension behavior. Transfer function for strain gauges is defined as

$$S/VC = \frac{S}{Q_V} \tag{2.38}$$

where S is the strain gauge reading. The results suggest general consistency for the four strain gauges at each of the two elevations. However, the transfer functions for strain gauges near the pile cap show more deviations than those at low elevation. A possible reason is the perturbations on the pile cap, which had greater impact on the closer strain gauges. Magnitude of transfer functions for the bottom four strain gauges due to excitations R4, S4, and C4 are shown in Figure 2.42. A unique resonant peak is identified at round 63 Hz, which is consistent with the resonant peaks in accelerance functions for pile ans soil accelerometers. All four strain

gauges exhibit similar trends, although strain gauges S_2 and S_6 present relatively greater undulations and lower peak amplitudes. Among the three excitation types, the random signals elicited the smoothest responses, followed by the swept-sine signals. The chaotic signals induced greatest deviated signals. In general, transfer functions for strain gauges present similar outcome for all random, swept-sine and chaotic signals and validate the effectiveness of the broadband excitation technique.

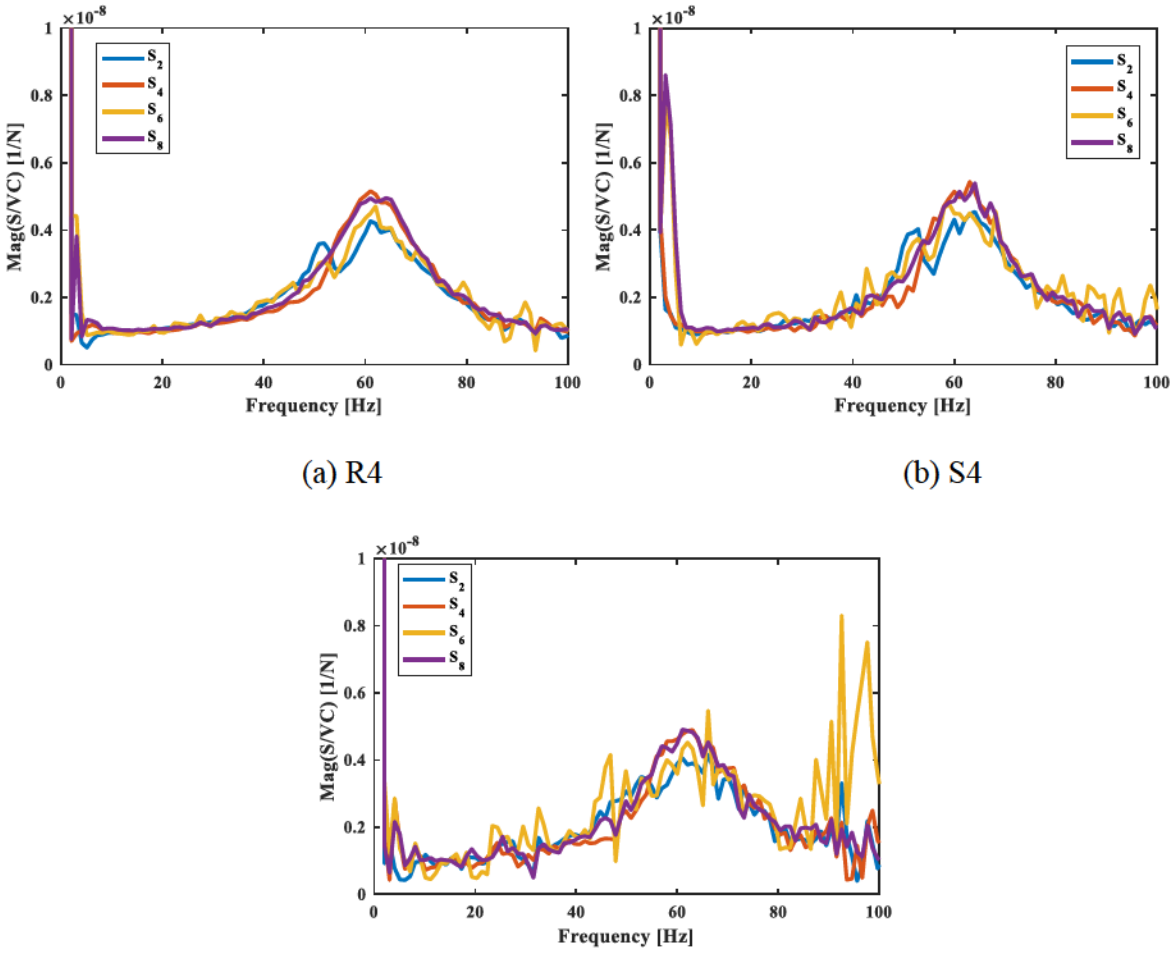

(a) R4

(b) S4

(C) C4

Figure 2.42 Magnitude of accelerance functions for strain gauges by excitation level 4.

2.7 Appendix

2.7.1 Calculation of Mass and Moment of Inertia of the Pile Caps

1. Theoretical derivations for pile cap of the single pile

a. Mass

The concrete and the embedded pile segments constitute total mass. The grout is assumed to be part of the concrete block.

$$M_c = (V_{block} - V_{hole})\rho_c = (2.5\times 3\times 3 - \frac{\pi}{4}0.7188^2\times 2.5)\,ft^3 \times 143.96 lb/ft^3 = 3093.0 lb = 1404.2 kg$$

$$M_{tube} = \frac{\pi}{4}(0.7188^2 - 0.665^2)\times 2.5\,ft^3 \times 490 lb/ft^3 = 71.6 lb = 32.5 kg$$

$$M_{cap} = M_c + M_{tube} = 1404.2 + 32.5 = 1436.7 kg$$

b. Position of the centroid

Due to geometric symmetry and homogeneity, the centroid of the pile cap is at its geometric center. With the origin for the superstructure at the ground level,

$$centroid\ height = 3.17\,ft + 2.5/2\,ft = 4.42\,ft = 1.347 m$$

c. Polar moment of inertia with respect to rocking axis (z'-z')

Similar to calculation of mass, the polar moment of inertia can be calculated by superposition of the concrete block and the embedded pile segment.

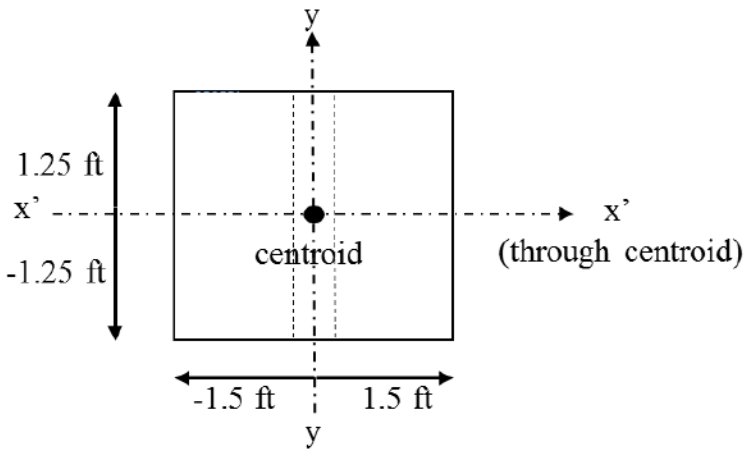

Figure 2.43 *Front view of the pile cap for the single pile.*

For the concrete block,

$$I_{z'z'}^{concrete} = (I_{x'x'}^{block} - I_{x'x'}^{cylinder}) + (I_{yy}^{block} - I_{yy}^{cylinder})$$

where,

$$I_{x'x'}^{block} = \int_{-1.25}^{1.25} 3 \times 3y^2 dy = 11.719\, ft^5$$

$$I_{x'x'}^{cylinder} = \int_{-1.25}^{1.25} y^2 \times (\frac{\pi}{4} \times 0.7188^2) dy = 0.528\, ft^5$$

$$I_{yy}^{block} = \int_{-1.5}^{1.5} x^2 \times 2.5 \times 3 dx = 16.875\, ft^5$$

$$I_{yy}^{cylinder} = \int x^2 \times (2R\sin\theta \times 2.5) dx \qquad \text{(see Figure 2.44)}$$

note that $x = R\cos\theta$, $R = 0.7188\, ft / 2 = 0.3594\, ft$ and $\theta \in [0, \pi]$. Then,

$$I_{yy}^{cylinder} = \int_{\pi}^{0} (R\cos\theta)^2 \times 2R\sin\theta \times 2.5 \times (-R\sin\theta) d\theta = 0.03276\, ft^5$$

Thus, $I_{z'z'}^{concrete} = (11.719 - 0.528) + (16.875 - 0.03276) = 28.03324\, ft^5$

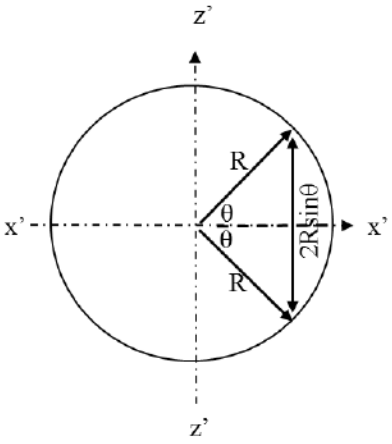

Figure 2.44 *Top view of the pile cap for the single pile.*

For the embedded pile segment,

$$I_{x'x'}^{hole} = \int_{-1.25}^{1.25} y^2 \times (\frac{\pi}{4} \times 0.665^2) dy = 0.45228\, ft^5$$

$$I_{yy}^{hole} = \int x^2 \times (2R\sin\theta \times 2.5)dx$$

note that $x = R\cos\theta$, $R = 0.665/2 = 0.3325\,ft$ and $\theta \in [0, \pi]$. Thus,

$$I_{yy}^{hole} = \int_0^{\pi} (R\cos\theta)^2 \times 2R\sin\theta \times 2.5 \times R\sin\theta d\theta = 0.02400\,ft^5$$

Then

$$I^{pipe} = (I_{x'x'}^{cylinder} - I_{x'x'}^{hole}) + (I_{yy}^{cylinder} - I_{yy}^{hole}) = (0.528 - 0.45228) + (0.03276 - 0.02400) = 0.08448\,ft^5$$

Incorporating densities of concrete and steel pipe piles,

$$I_{all} = I^{concrete} \times \rho_c + I^{pipe} \times \rho_p = 28.03324 \times 143.96 + 0.08448 \times 490$$
$$= 4077.06 lb.ft^2 = 171.81 \text{kg.m}^2$$

2. Theoretical derivation for pile cap of the pile group

a. Mass

$$M_c = (V_{block} - 4V_{hole})\rho_c =$$
$$(2.5 \times 5.25 \times 5.25 - 4 \times \frac{\pi}{4} 0.7188^2 \times 2.5)\,ft^3 \times 143.96 lb/ft^3 = 9335.6 lb = 4238.3\,kg$$

$$M_{tube} = 4 \times \frac{\pi}{4}(0.7188^2 - 0.6650^2) \times 2.5\,ft^3 \times 490 lb/ft^3 = 286.51 lb = 130.0 kg$$

$$M_{cap} = M_c + M_{tube} = 4238.3 + 130.0 = 4368.3 kg$$

b. Position of centroid

$$centroid\ height = 3.17\,ft + 2.5/2\,ft = 4.42\,ft = 1.347 m$$

c. Polar moment of inertia (see Figure 2.45)

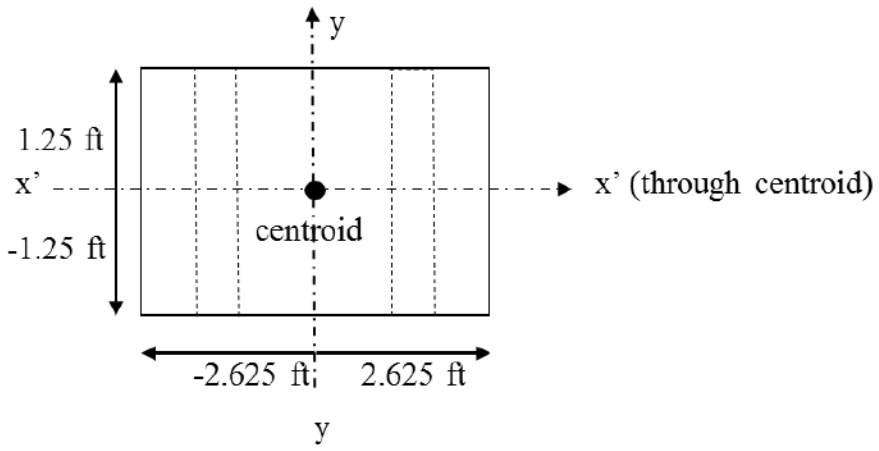

Figure 2.45 *Front view of the pile cap for the pile group.*

$$I_{z'z'}^{concrete} = (I_{x'x'}^{block} - I_{x'x'}^{cylinder}) + (I_{yy}^{block} - I_{yy}^{cylinder})$$

where,

$$I_{x'x'}^{block} = \int_{-1.25}^{1.25} 5.25 \times 5.25 y^2 dy = 35.889\, ft^5$$

$$I_{x'x'}^{cylinder} = 4 \times \int_{-1.25}^{1.25} y^2 \times (\frac{\pi}{4} \times 0.7188^2) dy = 2.113\, ft^5$$

$$I_{yy}^{block} = \int_{-2.625}^{2.625} x^2 \times 2.5 \times 5.25 dx = 158.26\, ft^5$$

$$I_{yy}^{cylinder} = 4 \times \int x^2 \times (2R \sin\theta \times 2.5) dx \qquad \text{(see Figure 2.46)}$$

note that $x = 1.5 - R\cos\theta$, $R = 0.7188/2 = 0.3594\, ft$ and $\theta \in [0, \pi]$.

Thus $I_{y'y'}^{cylinder} = 4 \times \int_0^{\pi} (1.5 - R\cos\theta)^2 \times 2R \sin\theta \times 2.5 \times R \sin\theta d\theta = 9.256\, ft^5$

Then,

$$I_{z'z'}^{concrete} = (I_{x'x'}^{block} - I_{x'x'}^{cylinder}) + (I_{yy}^{block} - I_{yy}^{cylinder}) = (35.889 - 2.113) + (158.26 - 9.256) = 182.78\, ft^5$$

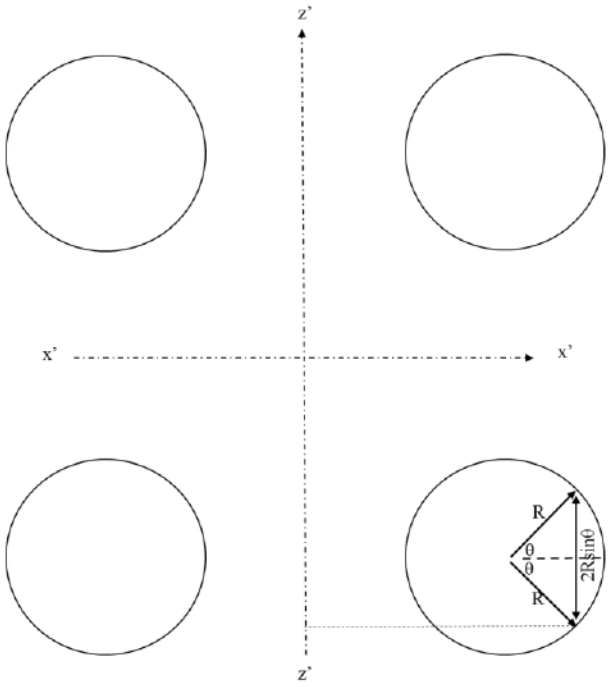

Figure 2.46 *Top view of the pile cap for the pile group.*

For embedded pile segments,

$$I_{x'x'}^{hole} = 4 \times \int_{-1.25}^{1.25} y^2 \times (\frac{\pi}{4} \times 0.665^2) dy = 1.809\, ft^5$$

$$I_{yy}^{hole} = 4 \times \int x^2 \times (2R \sin\theta \times 2.5) dx$$

where $x = 1.5 - R\cos\theta$, $R = 0.665\, ft / 2 = 0.3325\, ft$ and $\theta \in [0, \pi]$. Thus

$$I_{yy}^{hole} = 4 \times \int_{0}^{\pi} (1.5 - R\cos\theta)^2 \times 2R\sin\theta \times 2.5 \times R\sin\theta d\theta = 7.9108\, ft^5$$

Then

$$I_{z'z'}^{pipe} = (I_{x'x'}^{cylinder} - I_{x'x'}^{hole}) + (I_{yy}^{cylinder} - I_{yy}^{hole}) = (2.113 - 1.809) + (9.256 - 7.9108) = 1.6492\, ft^5$$

Incorporating densities of concrete and piles,

$$I_{all} = I_{z'z'}^{concrete} \times \rho_c + I_{z'z'}^{pipe} \times \rho_p = 182.78 \times 143.96 + 1.6492 \times 490 = 27121.117 lb.ft^2 = 1142.887\, \mathrm{kg.m^2}$$

3. Comparison with numerical results

The pile cap inertial properties were also analyzed using computer-aided design (CAD) software (Figure 2.47) and the results are compared to the theoretical calculations in Table 2.8. The theoretical results conform fairly well to the numerical ones with a maximum relative error of 4.1%. Since the CAD models are more precise by including rebars, differentiating grout from concrete, and excluding PVC corridors, the numerical results are adopted in this study.

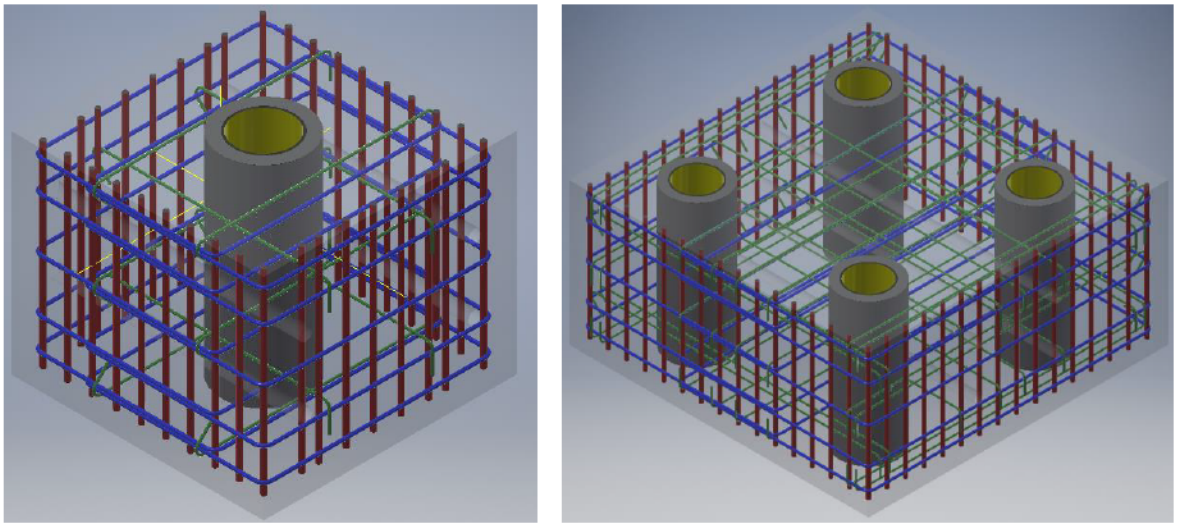

(a) Single pile (b) Pile group

Figure 2.47 CAD models for the pile caps.

Table 2.8 Comparison of analytical and numerical results of geometric properties

	Parameter	Theoretical calculation	CAD model	Relative error
Cap of single pile	mass	1436.7 kg	1482.0 kg	-3.1 %
	centroid x	0	2.54×10^{-5} m	/
	centroid y	0	7.62×10^{-5} m	/
	centroid z	1.347 m	$(1.347+2.54 \times 10^{-5})$ m	/
	$I_{z'z'}$	171.81 kg.m^2	179.24 kg.m^2	-4.1 %
Cap of pile group	mass	4368.3 kg	4303.7 kg	1.5 %
	centroid x	0	5.08×10^{-5} m	/
	centroid y	0	4.83×10^{-4} m	/
	centroid z	1.347 m	$(1.347+2.54 \times 10^{-5})$ m	/
	$I_{z'z'}$	1142.89 kg.m^2	1125.08 kg.m^2	1.6 %

2.7.2 Approach of the Cross-correlation Method in the Frequency Domain (Campanella and Stewart 1992)

1. Transforming from time domain to frequency domain

F1 = FFT of signal $f_1(t)$ at observation point 1;

F2 = FFT of signal $f_2(t)$ at observation point 2;

C1 = complex conjugate of F1;

C2 = complex conjugate of F2;

2. cross-correlation

C1F2 = C1 × F2;

corr = inverse FFT of C1F2;

3. Normalization

F1C1 = F1×C1; F2C2 = F2×C2;

i_F1C1 = inverse FFT of F1C1; i_F2C2 = inverse FFT of F2C2;

A_1 = maximum value of i_F1C1; A_2 = maximum value of i_F2C2;

$$normalized\ corr = \frac{corr}{\sqrt{A_1.A_2}} \tag{2.39}$$

2.7.3 Approach of the Cross-Correlation Method in the Time Domain

1. Calculating cross-correlation value in time domain

$$corr(\tau) = \int_0^T f_1(t) f_2(t+\tau) dt \tag{2.40}$$

where $\tau \in (-T, T)$ is time shift of by signal $f_2(t)$ and T is total sampling period.

2. Normalization

$$normalized\ corr = \frac{corr}{\sqrt{A_1.A_2}}$$

2.7.4 Raw and Filtered SCPT Signals

The raw and filtered SCPT signals at each observation point are presented in Figure 2.48. Grey lines denote raw signals and black lines denote filter signals, which was band-pass filtered between 1 and 210 Hz.

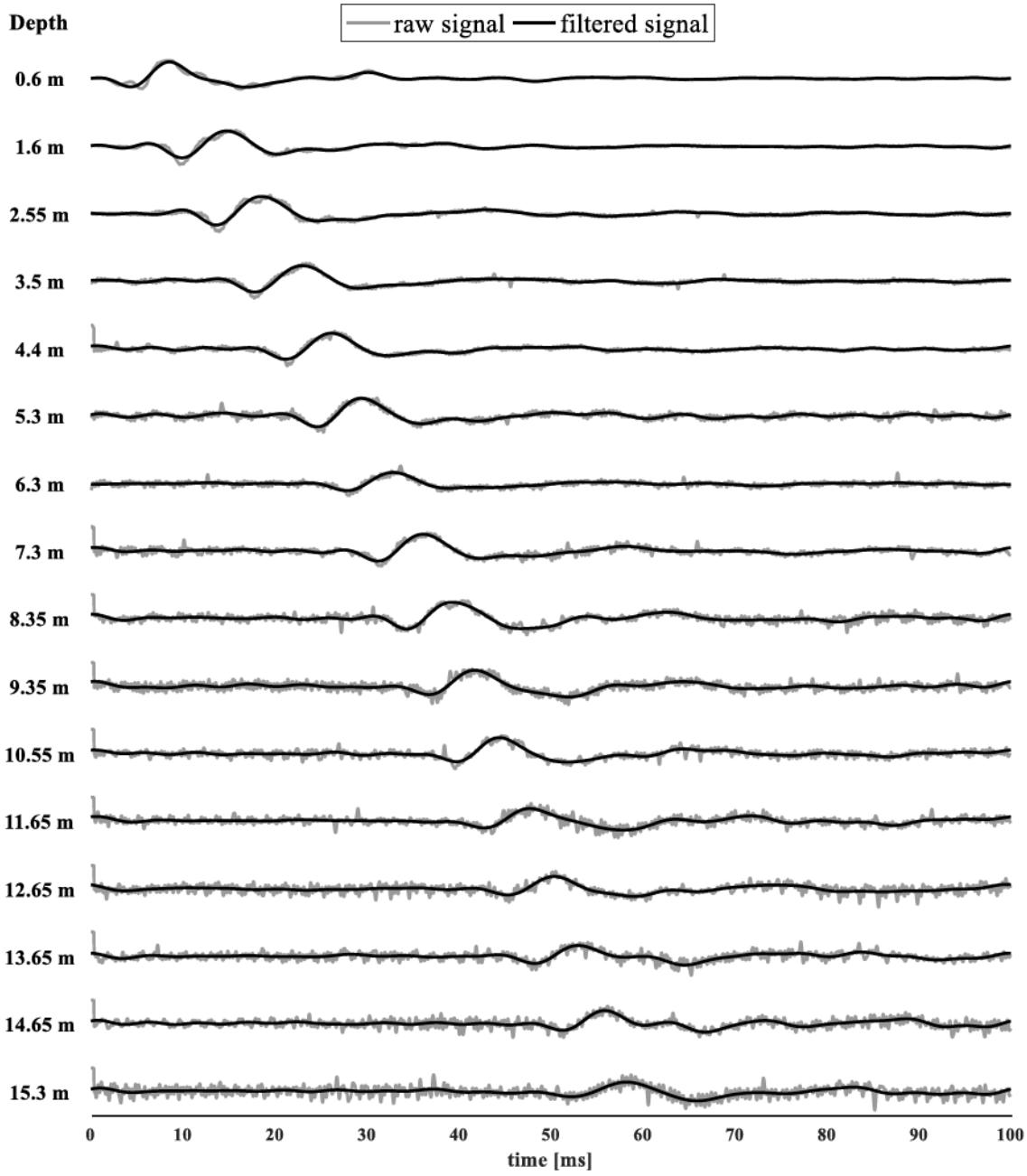

(a) SCPT-1 S-wave response

Figure 2.48 *SCPT S-wave response.*

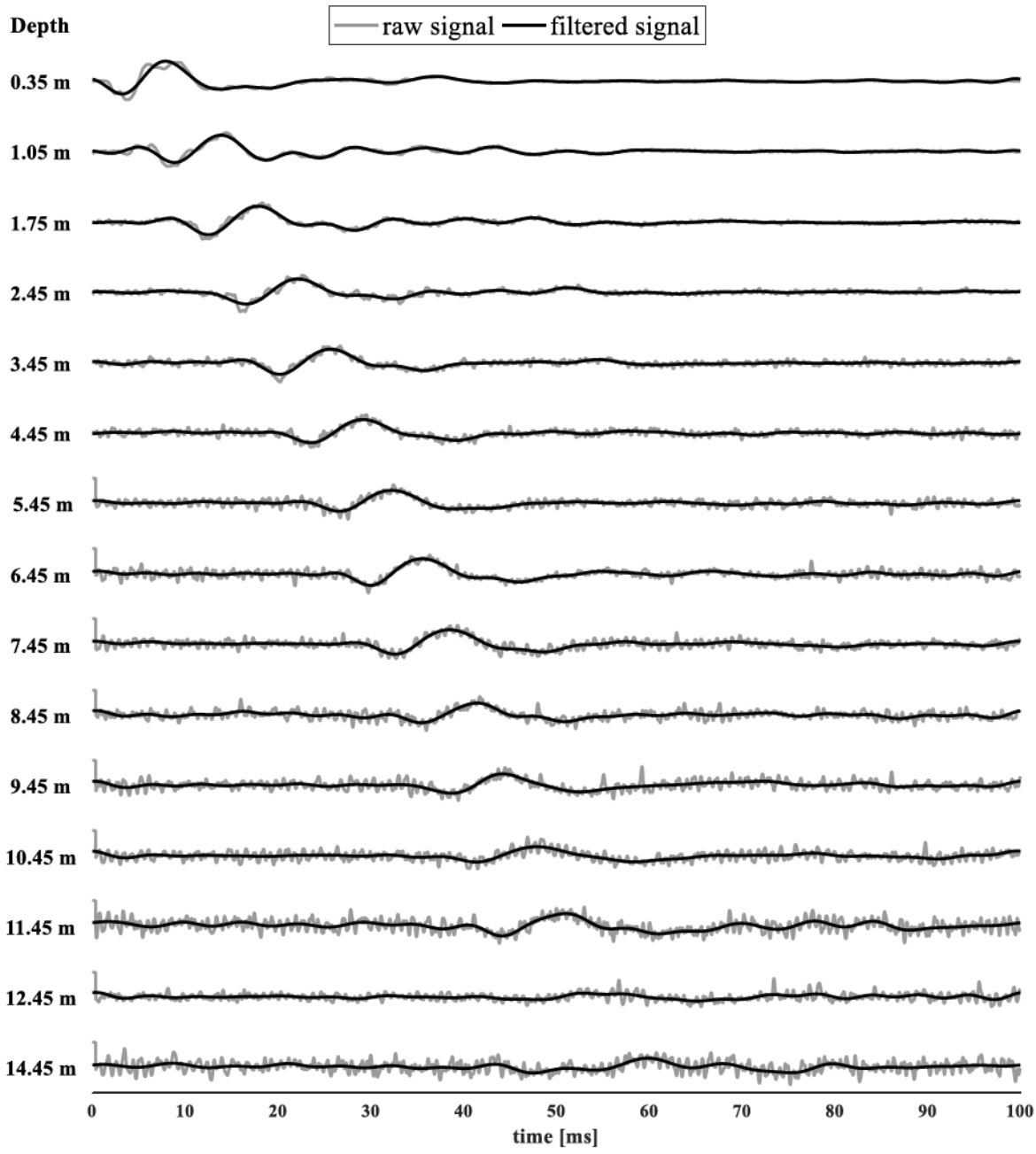

(b) SCPT-2 S-wave response

Figure 2.48 *(continued)*

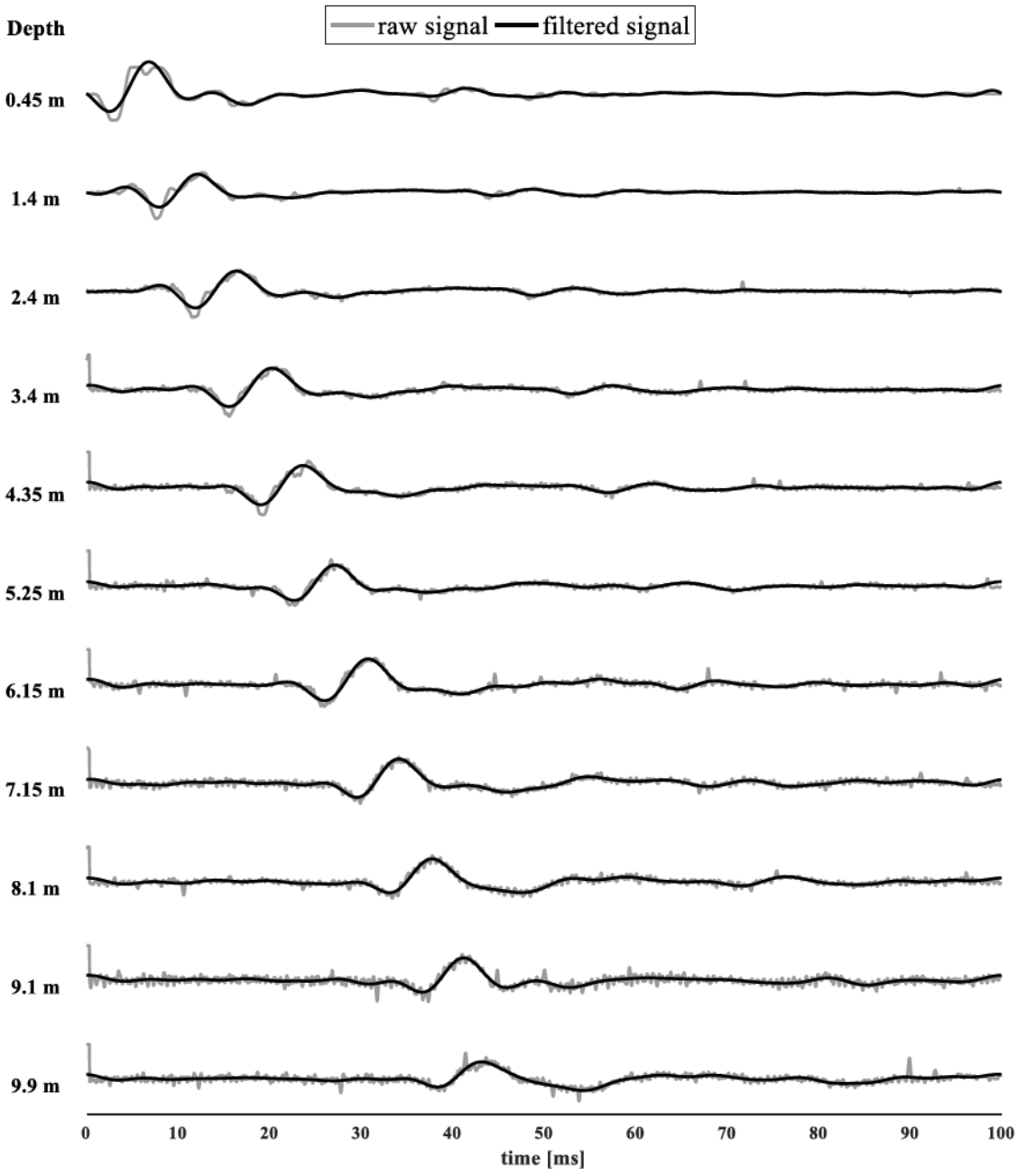

(c) SCPT-3c S-wave response

Figure 2.48 *(continued)*

CHAPTER 3. COMPUTATIONAL SIMULATION OF SOIL-PILE GROUP INTERACTION

3.1 Fundamentals of BEM

The finite difference method (FDM), finite element method (FEM), and boundary element method (BEM) are three numerical techniques for solving complex engineering mechanics problems that cannot be solved in closed form. Compared to the other two methods, BEM is particularly useful for solving geotechnical problems involving wave propagation in a half-space. The most important feature of BEM is that the dimensions of the problem are reduced by one, either from three dimensions to two or from two dimensions to one. Correspondingly, for 3D problems only 2D surfaces of boundaries rather than entire volume are discretized. Another advantage of BEM is its high accuracy in stress concentration problems (such as re-entrant corners), using relatively fewer elements. For pile-soil interaction problems, stress concentrations can occur at the pile head and pile toe, and need to be properly handled. Additionally, BEM is able to rigorously handle infinite or semi-infinite domains in wave-propagation problems, without suffering from undesirable boundary effects like wave reflection from artificially truncated boundaries (Brebbia et al. 1984; Brebbia and Domínguez 1989). As a pioneer in the application of BEM, Domínguez (1978a, 1978b) was the first to apply the method to foundation mechanics problems to obtain impedances of rectangular foundations embedded in an elastic half-space, as noted by Kausel (2010). Around the same time, Banerjee (1978) developed boundary element approaches for axially loaded single piles. Since that time, significant advances have been made in the application of BEM to dynamic problems for shallow and deep foundations. The fundamentals of BEM are elaborated in this section.

Consider a 3D steady-state linear elastodynamic problem within an isotropic and homogeneous medium. The dynamic response in the time domain at any point with Cartesian coordinates $\boldsymbol{\xi} = (\xi_1, \xi_2, \xi_3)$ in an elastic domain $\boldsymbol{\Omega}$ is governed by the following equations:

$$\text{equations of motion: } \sigma_{ij,j} + f_i - \rho \frac{\partial^2 u_i}{\partial t^2} = 0 \tag{3.1}$$

$$\text{strain-displacement equations: } \varepsilon_{ij} = \frac{1}{2}(u_{i,j} + u_{j,i}) \tag{3.2}$$

$$\text{material constitutive model: } \sigma_{ij} = C_{ijkl} u_{k,l} \tag{3.3}$$

where $\sigma_{ij}(\boldsymbol{\xi}, t)$ is the Cauchy stress tensor; $f_i(\boldsymbol{\xi}, t)$ is the body force per unit volume in the i-direction; ρ is mass density; $u_i(\boldsymbol{\xi}, t)$ is the displacement field in the i-direction; C_{ijkl} is the 4th rank elasticity tensor. The above equations can also be applied to linear viscoelastic dynamic problems by means of the correspondence principle (Christensen 1971) by introducing the complex-valued shear modulus:

$$G^* \equiv G(1 + 2iD) \tag{3.4}$$

where G is the elastic shear modulus and D is the material damping ratio.

Combining Equations (3.1) to (3.3) leads to the Navier equations of motion:

$$(\lambda + \mu) \frac{\partial^2 u_j(\boldsymbol{\xi}, t)}{\partial x_i \partial x_j} + \mu \frac{\partial^2 u_i(\boldsymbol{\xi}, t)}{\partial x_j \partial x_j} + f_i = \frac{\partial^2 u_i(\boldsymbol{\xi}, t)}{\partial t^2} \tag{3.5}$$

where $u(\boldsymbol{\xi}, t)$ is the unknown displacement field.

Equation (3.5) can be converted to boundary integral equations, either through reciprocal theorems (e.g., Green's third identity, Betti's theorem, or the principle of virtual work) or weighted residual techniques. Reciprocal theorems have physical interpretations, whereas the weighted residual technique is a general mathematics approach for more complex

equations. The dynamic Betti reciprocal theorem approach, also known as the Betti-Rayleigh theorem (Achenbach 1973), is adopted herein:

$$\begin{aligned}&\int_{\Gamma} t_i^{(2)}(\xi,t_2)u_i^{(1)}(\xi,t_1)d\Gamma + \int_{\Omega}\left[f_i^{(2)}(\xi,t_2) - \rho\ddot{u}_i^{(2)}(\xi,t_2)\right]u_i^{(1)}(\xi,t_1)d\Omega = \\ &\int_{\Gamma} t_i^{(1)}(\xi,t_1)u_i^{(2)}(\xi,t_2)d\Gamma + \int_{\Omega}\left[f_i^{(1)}(\xi,t_1) - \rho\ddot{u}_i^{(1)}(\xi,t_1)\right]u_i^{(2)}(\xi,t_2)d\Omega\end{aligned} \tag{3.6}$$

where $t_i(\xi,t) = \sigma_{ij}(\xi,t)\eta_j(\xi)$ is defined as the surface traction in the i-direction; $\eta_j(\xi)$ is the outward normal vector of the boundary; superscripts (1) and (2) refer to states at times $t = t_1$ and $t = t_2$, respectively; and Γ is the boundary of domain Ω.

A fundamental-solution state is defined such that it corresponds to the domain response due to a unit magnitude load acting at the source point $\boldsymbol{\xi} = \boldsymbol{x}$ and emission time τ. Typically the load is a concentrated force represented by $\delta(\boldsymbol{\xi} - \boldsymbol{x})\delta(t - \tau)$, where δ is the Dirac delta function. The resulting traction and displacement at observation point ξ are denoted as the fundamental solutions $\hat{\boldsymbol{t}}(\boldsymbol{\xi},\tau,\boldsymbol{x})$ and $\hat{\boldsymbol{u}}(\boldsymbol{\xi},\tau,\boldsymbol{x})$. Fundamental solutions that satisfy a given set of boundary conditions are called Green's functions. For convenience, State (1) is taken to be the fundamental-solution state for a point source, and State (2) is regarded as the unknown physical state for which a solution is sought. While the fundamental solutions for a full-space in the time-space domain are relatively easy to derive, those for layered half-space media, as typically assumed for soil profiles, can only be derived in the frequency domain (Andersen 2006). For this reason, (3.6) is converted from the time-space domain to the time-frequency domain by taking Fourier transforms of both sides;

$$\int_{\Gamma} T_i\hat{U}_i d\Gamma + \int_{\Omega} F_i\hat{U}_i d\Omega = \int_{\Gamma} \hat{T}_i U_i d\Gamma + \int_{\Omega} \hat{F}_i U_i d\Omega \tag{3.7}$$

where it can be shown that the inertia terms cancel each other in the frequency domain. The point source $\hat{F}_i = \hat{F}_i^k$ ($k = 1,2,3$) denotes a body force at $\boldsymbol{x} \in \Omega$ in the k-direction in the frequency domain, which has the following properties:

$$\begin{cases} \hat{F}_i^k(\boldsymbol{\xi}, \omega, \boldsymbol{x}) = \delta_{ik}\delta(\boldsymbol{x} - \boldsymbol{\xi}) \\ \int_\Omega \hat{F}_i^k(\boldsymbol{\xi}, \omega, \boldsymbol{x}) d\Omega = 1 \end{cases} \tag{3.8}$$

where δ_{ik} is the Kronecker delta function. Equation (3.7) can be simplified to the following fundamental integral statement (Guzina 1996):

$$D(\boldsymbol{x})U_k(\boldsymbol{x}, \omega) = \int_\Gamma T_i(\boldsymbol{\xi}, \omega)\hat{U}_i^k(\boldsymbol{\xi}, \omega, \boldsymbol{x}) d\Gamma - \int_\Gamma \hat{T}_i^k(\boldsymbol{\xi}, \omega, \boldsymbol{x})U_i(\boldsymbol{\xi}, \omega) d\Gamma + \int_\Omega F_i(\boldsymbol{\xi}, \omega)\hat{U}_i^k(\boldsymbol{\xi}, \omega, \boldsymbol{x}) d\Omega \qquad D(\boldsymbol{x}) = \begin{cases} 1, \boldsymbol{x} \in \Omega \\ 0, \boldsymbol{x} \notin \Omega \end{cases} \tag{3.9}$$

The above formulation is derived for interior problems (Figure 3.1(a)), in which a finite domain without any cavity Ω is enclosed by a boundary surface Γ. To derive the formulation for exterior problems (Figure 3.1(b)), in which a multiply-connected domain extends to infinity and encloses a cavity defined by the boundary Γ, the domain can be treated as a special case of an interior domain, in the sense that the domain is enclosed by two separate boundaries, Γ and Γ_γ. The additional boundary Γ_γ can be treated as a surface having center at x and an infinite radius $\gamma \to \infty$. Applying these changes, Equation (3.9) becomes

$$\begin{aligned} D(\boldsymbol{x})U_k(\boldsymbol{x}, \omega) = & \int_\Gamma T_i(\boldsymbol{\xi}, \omega)\hat{U}_i^k(\boldsymbol{\xi}, \omega, \boldsymbol{x}) d\Gamma - \int_\Gamma \hat{T}_i^k(\boldsymbol{\xi}, \omega, \boldsymbol{x})U_i(\boldsymbol{\xi}, \omega) d\Gamma \\ & + \int_{\Gamma_\gamma} \left[T_i(\boldsymbol{\xi}, \omega)\hat{U}_i^k(\boldsymbol{\xi}, \omega, \boldsymbol{x}) - \hat{T}_i^k(\boldsymbol{\xi}, \omega, \boldsymbol{x})U_i(\boldsymbol{\xi}, \omega) \right] d\Gamma \\ & + \int_\Omega F_i(\boldsymbol{\xi}, \omega)\hat{U}_i^k(\boldsymbol{\xi}, \omega, \boldsymbol{x}) d\Omega \qquad D(\boldsymbol{x}) = \begin{cases} 1, \boldsymbol{x} \in \Omega \\ 0, \boldsymbol{x} \notin \Omega \end{cases} \end{aligned} \tag{3.10}$$

The Sommerfeld radiation condition is applied at Γ_γ, i.e.,

$$\lim_{\gamma \to \infty} \int_{\Gamma_\gamma} \left[T_i(\boldsymbol{\xi}, \omega)\hat{U}_i^k(\boldsymbol{\xi}, \omega, \boldsymbol{x}) - \hat{T}_i^k(\boldsymbol{\xi}, \omega, \boldsymbol{x})U_i(\boldsymbol{\xi}, \omega) \right] d\Gamma = 0 \tag{3.11}$$

Its physical meaning is that the response of divergent waves decays to zero as $(\boldsymbol{\xi}-\boldsymbol{x})$ approaches infinity. Then Equation (3.10) reduces to (3.9).

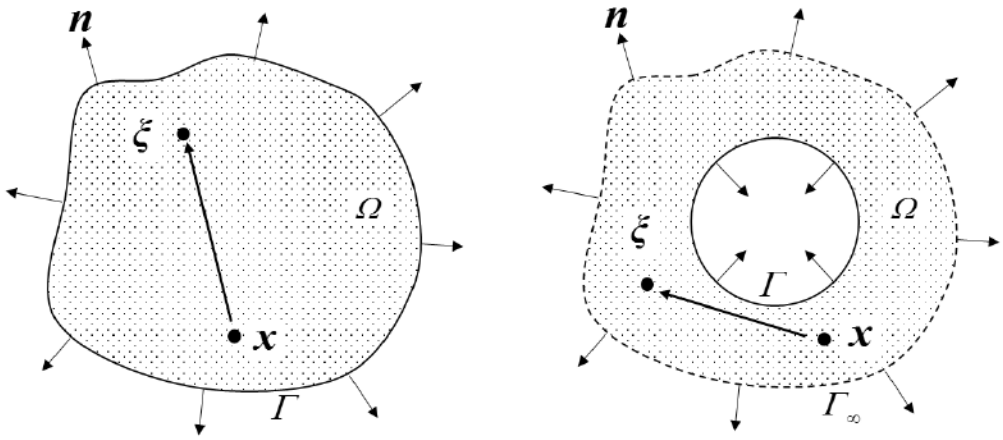

(a) Interior problem (b) Exterior problem

Figure 3.1 *Two basic boundary value problem types.*

To derive the boundary integral equation, assume the observation point $\boldsymbol{y}$ is on Γ and take the limit as the source point $\boldsymbol{x}$ goes to the boundary. When $\boldsymbol{x}$ approaches y on the boundary (Figure 3.2), the displacement fundamental solution $\hat{U}_i^k$ is weakly singular and the traction fundamental solution $\hat{T}_i^k$ is strongly singular. Thus the second term on the right hand side of Equation (3.9) is not integrable.

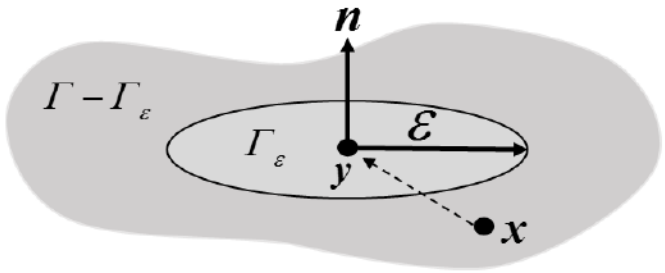

Figure 3.2 *Source point* $\boldsymbol{x}$ *approaches point* $\boldsymbol{y}$ *on boundary.*

The traditional method for addressing the strongly singular traction is to assume that point $\boldsymbol{y}$ is surrounded by a circular infinitesimal area Γ_ε and consider the limit as the radius ε approaches zero. Equation (3.10) is therefore decomposed as

$$\begin{aligned} U_k(\boldsymbol{x},\omega) = &\int_\Gamma T_i(\boldsymbol{\xi},\omega)\hat{U}_i^k(\boldsymbol{\xi},\omega,\boldsymbol{x})d\Gamma - \int_{\Gamma-\Gamma_\varepsilon} \hat{T}_i^k(\boldsymbol{\xi},\omega,\boldsymbol{x})U_i(\boldsymbol{\xi},\omega)d\Gamma \\ &- \int_{\Gamma_\varepsilon} \hat{T}_i^k(\boldsymbol{\xi},\omega,\boldsymbol{x})U_i(\boldsymbol{\xi},\omega)d\Gamma + \int_\Omega F_i(\boldsymbol{\xi},\omega)\hat{U}_k(\boldsymbol{\xi},\omega,\boldsymbol{x})d\Omega \end{aligned} \tag{3.12}$$

As the source point $\boldsymbol{x}$ approaches point $\boldsymbol{y}$,

$$\begin{aligned} \lim_{\boldsymbol{x}\to\boldsymbol{y}} U_k(\boldsymbol{x},\omega) = &\lim_{\boldsymbol{x}\to\boldsymbol{y}} \int_\Gamma T_i(\boldsymbol{\xi},\omega)\hat{U}_i^k(\boldsymbol{\xi},\omega,\boldsymbol{x})d\Gamma - \lim_{\boldsymbol{x}\to\boldsymbol{y}} \int_{\Gamma-\Gamma_\varepsilon} \hat{T}_i^k(\boldsymbol{\xi},\omega,\boldsymbol{x})U_i(\boldsymbol{\xi},\omega)d\Gamma \\ &- \lim_{\boldsymbol{x}\to\boldsymbol{y}} \int_{\Gamma_\varepsilon} \hat{T}_i^k(\boldsymbol{\xi},\omega,\boldsymbol{x})U_i(\boldsymbol{\xi},\omega)d\Gamma + \lim_{\boldsymbol{x}\to\boldsymbol{y}} \int_\Omega F_i(\boldsymbol{\xi},\omega)\hat{U}_k(\boldsymbol{\xi},\omega,\boldsymbol{x})d\Omega \end{aligned} \tag{3.13}$$

Note that over the surface $\Gamma-\Gamma_\varepsilon$, the integral involving $\hat{T}_i^k$ is nonsingular. It is reasonable to assume that the displacement fields $\hat{U}_i^k$ and U_k satisfy the Hölder continuity condition:

$$U_i(\boldsymbol{\xi},\omega) = U_i(\boldsymbol{y},\omega) + O(|\boldsymbol{\xi}-\boldsymbol{y}|^\alpha), \quad 0<\alpha\le 1 \tag{3.14}$$

which indicates that the displacement field is C^1 continuous. Taking the limit of Equation (3.13) as $\varepsilon\to 0$, the second integral on the right hand side exists in the sense of the Cauchy principle value, i.e.,

$$-\int_{\Gamma-\Gamma_\varepsilon} \hat{T}_i^k(\boldsymbol{\xi},\omega,\boldsymbol{y})U_i(\boldsymbol{\xi},\omega)d\Gamma = -\lim_{\varepsilon\to 0}\lim_{\boldsymbol{x}\to\boldsymbol{y}} \int_{\Gamma-\Gamma_\varepsilon} \hat{T}_i^k(\boldsymbol{\xi},\omega,\boldsymbol{x})U_i(\boldsymbol{\xi},\omega)d\Gamma \tag{3.15}$$

and the third term on right hand side can be rewritten as

$$-\lim_{\varepsilon\to 0}\int_{\Gamma_\varepsilon} \hat{T}_i^k(\boldsymbol{\xi},\omega,\boldsymbol{y})\left[U_i(\boldsymbol{\xi},\omega)-U_i(\boldsymbol{y},\omega)\right]d\Gamma - U_i(\boldsymbol{y},\omega)\lim_{\boldsymbol{x}\to\boldsymbol{y}}\lim_{\varepsilon\to 0}\int_{\Gamma_\varepsilon} \hat{T}_i^k(\boldsymbol{\xi},\omega,\boldsymbol{x})d\Gamma \tag{3.16}$$

where the first term is $-\lim_{\varepsilon\to 0}\int_{\Gamma_\varepsilon} O(\frac{1}{|\boldsymbol{\xi}-\boldsymbol{y}|^2})O(|\boldsymbol{\xi}-\boldsymbol{y}|^\alpha)d\Gamma$, which is weakly singular and thus integrable. In the limit $\varepsilon\to 0$, this term vanishes. Substitution of Equations (3.15) and (3.16) into Equation (3.13) leads to boundary integral equation:

$$c_{ik}(\boldsymbol{y})U_i(\boldsymbol{y},\omega) = \int_\Gamma T_i(\boldsymbol{\xi},\omega)\hat{U}_i^k(\boldsymbol{\xi},\omega,\boldsymbol{y})d\Gamma - \lim_{\varepsilon\to 0}\lim_{\boldsymbol{x}\to\boldsymbol{y}}\int_{\Gamma-\Gamma_\varepsilon}\hat{T}_i^k(\boldsymbol{\xi},\omega,\boldsymbol{x})U_i(\boldsymbol{\xi},\omega)d\Gamma + \int_\Omega F_i(\boldsymbol{\xi},\omega)\hat{U}_k(\boldsymbol{\xi},\omega,\boldsymbol{y})d\Omega \tag{3.17}$$

where the geometry constant $c_{ik}(\boldsymbol{y}) = \delta_{ik} + \lim_{\varepsilon\to 0}\lim_{\boldsymbol{x}\to\boldsymbol{y}}\int_{\Gamma_\varepsilon}\hat{T}_i^k(\boldsymbol{\xi},\omega,\boldsymbol{x})d\Gamma$. For a smooth surface, it can be shown that $c_{ik}(\boldsymbol{y}) = 1/2$.

However, using Equation (3.17) directly presents two difficulties: 1) evaluation of the Cauchy principle values; and 2) calculation of the geometry constants. To avoid such difficulties, an alternative regularization technique was applied by Guzina (1996), resulting in the regularized direct boundary integral equation (BIE) for both interior and exterior domain problems;

$$U_k(\boldsymbol{y},\omega)\begin{pmatrix}0\text{ (interior problem)}\\ 1\text{ (exterior problem)}\end{pmatrix} = \int_\Gamma T_i(\boldsymbol{\xi},\omega)\hat{U}_i^k(\boldsymbol{\xi},\omega,\boldsymbol{y})d\Gamma - \int_\Gamma\left[\hat{T}_i^k(\boldsymbol{\xi},\omega,\boldsymbol{y})\right]_1\left[U_i(\boldsymbol{\xi},\omega)-U_i(\boldsymbol{y},\omega)\right]d\Gamma - \int_\Gamma\left[\hat{T}_i^k(\boldsymbol{\xi},\omega,\boldsymbol{y})\right]_2 U_i(\boldsymbol{\xi},\omega)d\Gamma + \int_\Omega F_i(\boldsymbol{\xi},\omega)\hat{U}_i^k(\boldsymbol{\xi},\omega,\boldsymbol{y})d\Omega \tag{3.18}$$

where $\left[\hat{T}_i^k(\boldsymbol{\xi},\omega,\boldsymbol{y})\right]_1$ and $\left[\hat{T}_i^k(\boldsymbol{\xi},\omega,\boldsymbol{y})\right]_2$ are the singular and regular parts, respectively, of the traction fundamental solutions.

To solve (3.18) numerically for the unknown tractions and displacements, the actual boundaries of the pile and soil domains are discretized into elements over which the geometry, displacement, and traction are interpolated by assumed shape functions. The integration over each element's 3D surface is performed numerically by Gauss quadrature in an auxiliary 2D local domain such that global coordinates $\boldsymbol{\xi} = (\xi_1,\xi_2,\xi_3)$ are mapped to local coordinates $\boldsymbol{\eta} = (\eta_1,\eta_2)$. The method of collocation is then applied, in which the point load in the fundamental solution is assumed to act in each of the three coordinate directions at one node

of the mesh, and the entire regularized BIE (3.18) is evaluated numerically to give three equations (one for each direction of the point load) in terms of all nodal tractions and displacements. Similarly, the collocation node is then taken to act at the second node of the mesh giving three more equations, and so on. Assuming a total of N nodes for collocation on the boundary mesh, looping over all collocation nodes in each direction generates $3N$ equations. The equations are then rearranged by separating the coefficients of the nodal displacements and tractions (the coefficients are integrals of the product of fundamental solutions and shape functions), providing a system of equations in the form

$$\mathbf{HU} = \mathbf{GT} \tag{3.19}$$

where **U** is the nodal displacement vector; **T** is the nodal traction vector; and **H** and **G** are coefficient matrices. For a well-posed problem, either displacement or traction at each node must be given as boundary conditions,

$$\begin{cases} U(\boldsymbol{y},\omega) = \overline{U} & (\boldsymbol{y} \in \Gamma_U) \\ T(\boldsymbol{y},\omega) = \overline{T} & (\boldsymbol{y} \in \Gamma_T) \end{cases} \quad (\Gamma_U \cup \Gamma_T = \Gamma) \tag{3.20}$$

where $\overline{U}$ and $\overline{T}$ are known displacements and tractions, or else compatibility conditions of equal displacement and equal and opposite tractions are applied over elements at the interface of two domains (i.e., all embedded surfaces of piles and disturbed zones herein). Equation (3.19) is then rearranged into a system of equations,

$$\mathbf{Ax} = \mathbf{b} \tag{3.21}$$

where **A** is a dense complex matrix and **x** is a matrix containing all unknown tractions and displacements.

The computational simulations in this study are implemented using the 3D boundary element code BEASSI (Pak and Guzina 1999, 2002). BEASSI is able to handle soil layering,

multiple pile and soil domains, and singular contact tractions inherent to mixed boundary value problems by employing multi-layered Green's functions, a multi-domain formulation, and singular elements (Pak and Guzina 1999) or adaptive-gradient elements (Pak and Ashlock 2007). BEASSI was demonstrated to be accurate in solving dynamic soil-foundation interaction problems for single piles (Ashlock 2006; Fotouhi 2014) and surface footings (Pak and Ashlock 2011), and is further programmed and extended herein to enable the case of dynamic soil-foundation interaction problems for pile groups.

3.2 Framework of Computational Simulation

Computational simulation comprises three parts – preprocessing, computation, and postprocessing (Figure 3.3). Preprocessing aims at preparing all input files that contain information about the problem type, meshing, boundary conditions, and material properties. In this study, the presence of a 2×2 pile group and the surrounding soils are modeled such that the piles are solid cylinders and the soil is a layered linearly viscoelastic medium. For pipe piles and H piles, they can be idealized using equivalent axial and bending stiffness of the actual piles and handled by so-called structural Green's functions in BEASSI, which are mechanics-of-materials solutions for an Euler-Bernoulli beam-column converted to a BEM compatible format. A new mesh generator was also created to discretize the boundaries of the pile group and soil domain. Previous mesh generators for single pile problems were programmed in FORTRAN and MATLAB using structured meshing algorithms. For pile group problems, however, it is difficult to handle the wide variety of possible shapes, dimensions, number and spacings of the piles using a structured meshing algorithm for the traction-free soil surface around the piles. Therefore, the commercial pre/post-processing program GiD (www.gidhome.com) was adopted. Nodal coordinates, element connectivities,

boundary conditions, and general input information such as the boundary value problem type, domain numbers, and domain types were generated and assigned in GiD and collected in the input file *inp.dat* by creating a customized template. Pile properties are specified in the input file *rod.dat*, including the cross-sectional area, moment of inertia about the x and y axes, polar moment of inertia with respect to z axis, perimeter to area ratio, perimeter to moment of inertia ratio, and pile length. Soil profiles for each layered soil domain are specified in the input files *layerscoordN.dat*, where N is the domain number. These files contain the complex valued shear modulus, Poisson's ratio, density, and depth of the layer's bottom surface. The thickness of each soil layer was determined using MATLAB code such that it was compatible with the pile and disturbed-zone meshes.

In the input files, the actual dimensions and material parameters are specified as normalized dimensionless numbers for more efficient computation of the Green's functions in BEASSI;

$$\text{dimension}_{\text{normalized}} = \frac{\text{dimension}_{\text{actual}}}{a_{ref}} \tag{3.22}$$

$$G_{normalized} = \frac{G_{actual}}{G_{ref}} \tag{3.23}$$

$$\rho_{normalized} = \frac{\rho_{actual}}{\rho_{ref}} \tag{3.24}$$

$$\overline{\omega} = \frac{\omega a_{ref}}{\sqrt{G_{ref} / \rho_{ref}}} \tag{3.25}$$

where a_{ref} is a reference length, G_{actual} is the complex shear modulus defined by Equation (3.4); ρ_{actual} is the actual density; and ω denotes the actual circular frequency. The units of the reference parameters (and therefore all other parameters) can be chosen by the user, as long as

they produce a dimensionless result in Equation (3.25). The reference length is arbitrary, but is normally taken to be the pile radius. The reference shear modulus G_{ref} and density ρ_{ref} are typically chosen to be the shear modulus and density of the soil at a reference point. The normalized numerical output of BEASSI, including the impedances ($\bar{k}_{zz}$, $\bar{k}_{m_y x}$, $\bar{k}_{m_y r_y}$, $\bar{k}_{m_z r_z}$), nodal displacements ($\bar{u}_x$) and nodal tractions ($\bar{t}_x$), can be converted to actual dimensional values in the postprocessing as follows,

$$k_{zz} = a_{ref} G_{ref} \bar{k}_{zz} \tag{3.26}$$

$$k_{xx} = a_{ref} G_{ref} \bar{k}_{xx} \tag{3.27}$$

$$k_{m_y x} = a_{ref}^2 G_{ref} \bar{k}_{m_y x} \tag{3.28}$$

$$k_{m_y r_y} = a_{ref}^3 G_{ref} \bar{k}_{m_y r_y} \tag{3.29}$$

$$k_{m_z r_z} = a_{ref}^3 G_{ref} \bar{k}_{m_z r_z} \tag{3.30}$$

$$u_x = a_{ref} \bar{u}_x \tag{3.31}$$

$$t_x = a_{ref}^2 G_{ref} \bar{t}_x \tag{3.32}$$

In the computational phase of this study, the BEM analyses were performed on high performance supercomputing clusters at Iowa State University due to their speed and capability to handle parallel computations. The coefficient matrices **H** and **G** were written to files *DomN.dat* (where *N* is the domain number) to save time in later reanalyses in which the properties of the other domains were altered. Log files, including *log.dat*, *Qgphist.dat*, *Tgphist.dat,* were also saved during computation for troubleshooting purposes. The first of these files displays the completion percentage and final relative solution error, while the other two contain the converged Gauss integration rules from the adaptive integration scheme for

quadrilateral and triangular elements, respectively.The nodal displacements, as well as displacements at optional internal points are stored in the output files *ux.dat, uy.dat,* and *uz.dat*. Results of nodal tractions are stored in the output files *tx.dat, ty.dat,* and *tz.dat*. General information such as the resultant forces obtained by integrating the tractions over the pile head free surfaces, as well as the completion time and other problem parameters are stored in the file *out.dat*. The majority of the analyses were performed on the CyEnce supercomputing cluster. Detailed specifications of the CyEnce cluster are listed in Table 3.1.

Table 3.1 *Configuration of CyEnce cluster (http://www.hpc.iastate.edu/guides/cyence).*

Number of Nodes	Processors per Node	Cores per Node	Memory per Node	Interconnect	Local STMPDIR Disk	Accelerator Card
240	2 Intel E5 2650	16	128 GB	40 Gb IB	2.5 TB	N/A
24	2 Intel E5 2650	16	128 GB	40 Gb IB	2.5 TB	Two Nvidia K20
24	2 Intel E5 2650	16	128 GB	40 Gb IB	2.5 TB	Two 60 core Intel Phi 511OP
1	2 Intel E5 2650	32	1 TB	40 Gb IB	2.5 TB	N/A

GB=Gigabyte, TB=Terabyte, Gb=Gigabit, IB=Infiniband

In the postprocessing phase of the BEASSI analyses, the results of the nodal displacement and traction solutions are thoroughly interpreted. Nodal displacements on the boundaries and displacements at internal points of the domains are analyzed by the MATLAB code *fieldp4.m*, which was written in this study to numerically approximate strains from the internal displacement fields of the soil domains. The nodal displacements on pile boundaries were also used for analyzing pile deformations and internal force resultants. The resultant forces at the free surfaces of the pile heads, which are equal to the impedances due to the various prescribed unit displacements and rotations, are recorded in the file *out.dat* and

extracted by the post-processing Fortran 90 codes *cpostr.f90* and *cpostr4.f90* to create files of impedance functions. The impedance functions are plotted by the new MATLAB code *impedancep.m*. An overview of the computational simulation framework is shown in Figure 3.3, including the aforementioned pre- and post-processing routines as well as a few others. Incorporating the impedance functions into the substructuring formulation leads to theoretical multi-directional accelerance functions, as discussed in Section 3.5.

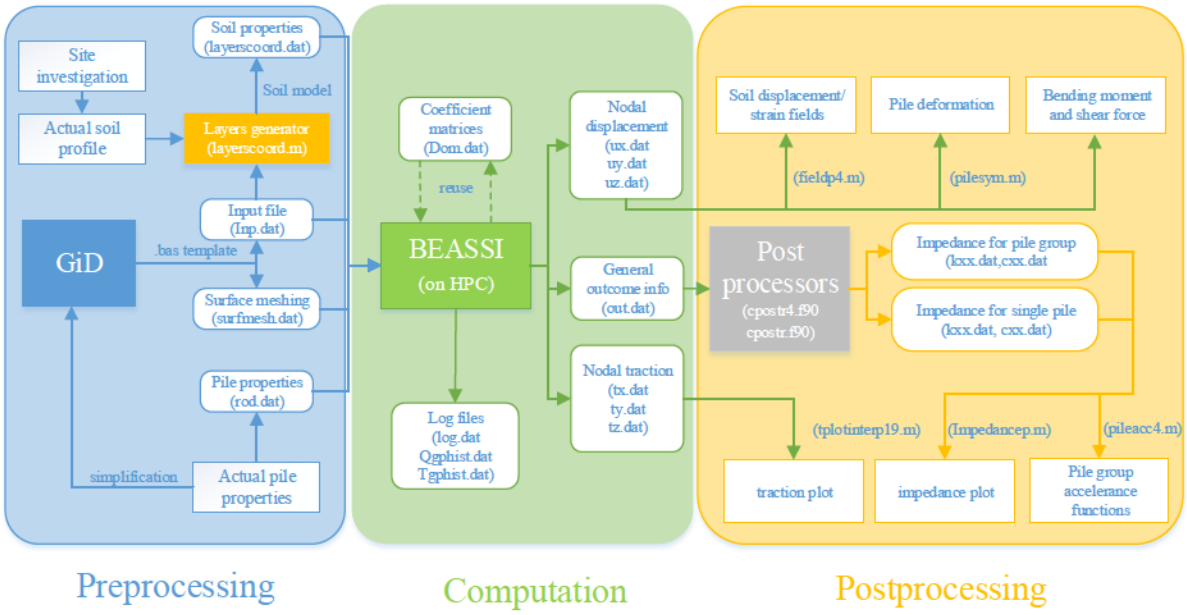

Figure 3.3 Framework of computational simulation.

3.3 Modification of BEASSI

At the beginning of the project, the BEASSI code was capable of handling surface and embedded footings and single pile problems. The program was therefore modified to allow additional piles treated as new domains, provided that a new mesh generator was created to properly handle the domain connectivity of the interface elements and specify element node numbering sequences to coordinate the outward normal vectors of each domain. Additionally,

the following major modifications were made to the code in order to expand BEASSI to handle pile group problems:

3.3.1 Definition of a New Boundary Value Problem Type

The predefined boundary conditions for 3D foundation radiation problems in the previous version of BEASSI applied the unit displacements or tractions to the top of every pile in the group simultaneously. Applying such boundary conditions to a pile group would physically correspond to unit displacements or rotations (with respect to the origin) of a rigid pile cap that is connected to the piles at ground level. However, for the field tests in this study, the pile cap is elevated above ground level to eliminate its interaction with the soil surface. The present analysis approach for pile groups requires a load or displacement to be prescribed to the head of one pile (which is at ground level in the BEASSI impedance analysis) while the rest of the pile heads remain fixed. The above ground lengths of the piles are then treated analytically as beam-columns. Therefore, a new predefined 'pile group' boundary value problem type was defined and programmed into BEASSI. In the new problem type, moments and rotations are applied with respect to the center of the individual loaded pile rather than the origin.

3.3.2 Separation of Forces and Moments in Output

For the formulation of the dynamic pile group accelerance problem used herein, it is necessary to differentiate between the forces and moments acting on each pile individually rather than just the resultant of the whole group. A new post-processing code *cpostr4.f90* was therefore written to extract this information from the output file *out.dat*.

3.3.3 Increasing the Upper Limit of Parallel Processes for Computation

The existing parallelized version of BEASSI (version P25r) was modified in 2007 to make it capable of using a maximum of 100 processors/cores (i.e., rank numbers 0 to 99) for

problems involving single piles. With an increase in the problem size required by pile groups, and the accessibility to more powerful computing clusters at present, it was essential to expand the maximum number of processors/cores to at least 1,000. The parallel computation was organized in a reliable way by formalizing log files and temporary output files for each core.

3.3.4 Integration of a Load Balancing Algorithm

An essential part of BEM analysis is the method of collocation to numerically evaluate the boundary integral equation. Collocation is the process of calculating the rows of the **H** and **G** coefficient matrices in the global system of equations **HU**=**GT** for a point load applied in the x, y, and z directions at a given node. In general, each node corresponds to three rows of **H** and **G**, one row for each direction of point load, and the columns correspond to numerical surface integrals of the product of a Green's function times a shape function over the element areas. For parallel computation, the previous BEASSI version P25r distributed all collocation nodes evenly across the available number of processors (*nprocs*). A total of n collocation nodes were therefore distributed across all CPU processors with each processor getting the integer part of the quotient $n/nprocs$. Then the remaining nodes were distributed to processors starting from the rank 0 until all the remaining nodes were distributed. This is the most common method for data distribution in application of the MPI (MPI Standard 2009) for parallel computation.

A critical issue in parallel computing is load balancing. For the aforementioned method for data distribution, however, assigning the same amount of collocation nodes for each processor does not guarantee the same completion time on each processor. After solving several problems of pile groups in layered disturbed zones, it was observed that a great variation in completion time existed among the different processors. In assembling **H** and **G** matrices for the disturbed zone, the variation of completion time among processors can exceed 24 hours, causing low computational efficiency as well as a waste of computational resources

when some processors complete their assigned collocation tasks early and remain unused while the other processors continue working on their tasks.

For example, Figure 3.4 contains a screenshot from the CyEnce cluster taken during an analysis. The log file Qgphist04.dat, which corresponds to the rank 4 processor, was last updated at 17:40, April 18th when this processor's collocation tasks had been completed and the processor became idle. Processors 3, 6, 7, 8, and 9 also stopped being updated by noon, April 19th, while processors 0, 1, 2, and 5, were still working. It can be seen that the collocation nodes assigned to processor 4 happened to result in the shortest workloads, and those assigned to processors 0, 1, 2, and 5 resulted in the longest workloads. Upon closer analysis, it was found that when the multi-layered Green's functions were applied to weak layers of interior domains such as the disturbed zones at high frequencies (e.g., $\overline{\omega} = 1$), collocation nodes on the traction-free surface created slow convergence in numerical integration on adaptive-gradient elements. With an increasing problem size and number of collocation nodes, the overall computational performance would further deteriorate.

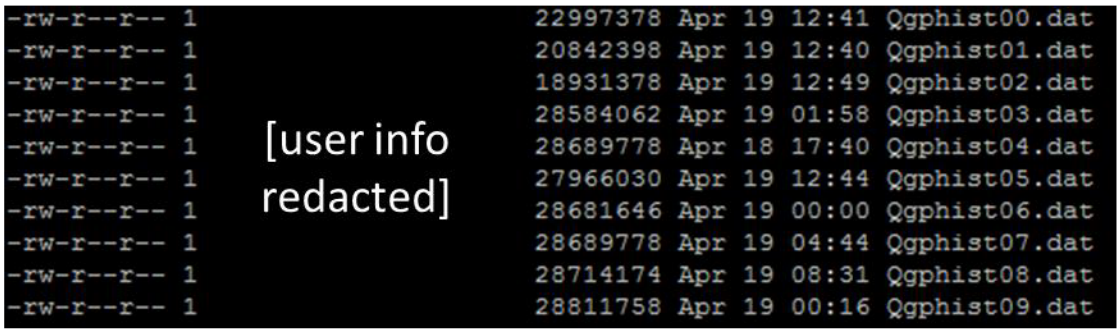

Figure 3.4 *A screenshot taken on the CyEnce cluster for log files during a running analysis.*

To solve this problem, a new parallel version of BEASSI (P29rl) featuring parallel load balancing was created (Figure 3.5). The principle was to create a way to distribute tasks dynamically at least twice, based on the runtime progress on each processor. If a processor

completes working on its initial collocation task ahead of others, it is given additional collocation nodes to work on in the second round. In this manner, all processors are kept occupied until all collocation nodes are distributed, thus reducing idle time and total runtime. The processor with rank 0 acts as the root processor. In version P29rl, the root processor is only responsible for distributing and collecting local H and G matrices to and from all other non-root processors, and no longer performs collocation computations as in previous versions.

Two new parameters *LB* and *init_nlocal* were introduced for load balancing. The parameter *LB* is a load-balancing parameter for specifying the fraction of collocation nodes for which load balancing will not be performed, and its value is a real number between 0 and 1. A value of *LB*=0 means load balancing is applied for all collocation nodes, while *LB*=1.0 means load balancing is turned off completely and nodes are distributed evenly as in previous versions of the program. In the first round of data distribution, $LB \times 100\%$ of the collocation nodes are evenly distributed across *nprocs*−1 processors. This leaves the remaining $(1-LB)\times 100\%$ of the collocation nodes available for distribution with load balancing in the second round.

After a job assigned in the first round is completed by any process, it sends a message along with the assembled local **H** and **G** matrices back to the root process, requesting a new job. The new job in the second (load balancing) round of data distribution will contain another *init_nlocal* collocation nodes to work on. If the number of remaining collocation nodes is less than *init_nlocal*, indicating that collocation is nearly complete, then the remaining collocation nodes are distributed in small batches , such as 1 or 2, for each new request from that point on. When all collocation nodes have been distributed and the corresponding locally assembled **H** and **G** matrices are collected by the root processor, BEASSI finishes collocation for the current material domain and enters into a new loop for the next domain until **H** and **G** matrices for all

domains are assembled. The total computation time and corresponding speedup depend on several problem-specific parameters including the number of collocation nodes and their geometry (i.e., the boundary mesh), the normalized frequency, soil layer thicknesses and profiles, and the relative speeds of collocation calculations vs. additional time required for each new data transfer as well as the associated overhead communication time for initiating the data transfers. To diminish potential bottlenecks caused by "problematic" collocation nodes which require much longer computation time, it is beneficial to handle them in the first round and deal with the others in the second round if possible. The new BEASSI version P29rl was verified to have satisfactory agreement with previous versions for both single piles and pile group problems. A few example cases are listed in Table 3.2.

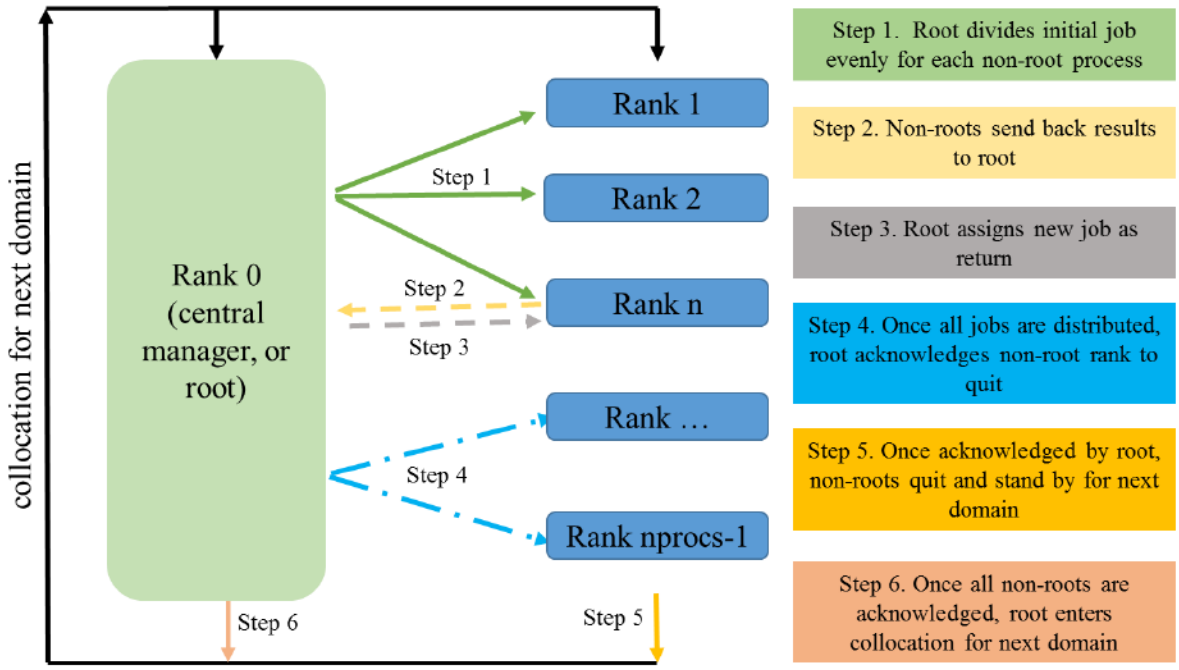

Figure 3.5 *Load balancing algorithm implemented in BEASSI Versions P29rl through P31rl.*

Table 3.2 *Accuracy verification of version P29rl vs. P25r.*

Case	Number of domains	Dimensionless frequency	Soil homogeneity	Parameter to compare	Absolute error
surface footing	1	0.05	homogeneous	tractions	$<10^{-8}$
				impedances	$<10^{-14}$
single pile	2	0.05	homogeneous	tractions	$<10^{-11}$
				impedances	$<10^{-14}$
single pile	3	1.00	layered	traction	$<10^{-13}$
				impedances	$<10^{-14}$
2×2 pile group	5	0.05	homogeneous	traction	$<10^{-14}$
				impedances	$<10^{-14}$
2×2 pile group	6	0.05	layered	traction	$<10^{-14}$
				impedances	$<10^{-14}$
2×2 pile group	6	0.25	layered	traction	$<10^{-14}$
				impedances	$<10^{-14}$

After modifying the code, a simple performance test (Table 3.3) was conducted on the CyStorm cluster using 16 MPI processes to analyze a single pile with disturbed zone at a relatively high frequency of $\bar{\omega} = 1.00$. The pile, disturbed zone, and soil domain had 626, 353, and 289 collocation nodes, respectively. A range of values of *LB* and *init_nlocal* were tested and the variation in collocation completion time among processors was found to be significant. The best performance was achieved with *LB* = 0 (i.e., load balancing for all nodes), and *init_nlocal* = 1. With a given *LB*, as *init_nlocal* increased from 1 to 10, performance deteriorated at an increasing rate even though communication time was reduced. This is because differentiation of completion time among processors at the end of the second round was magnified by an increasing granularity of data distribution. For example, at the time that the last 10 collocation nodes were all distributed to the same processor, a majority of the other processors had almost finished their tasks and could not help with these 10 nodes. This indicates that the negative effect of reducing granularity predominated over the positive effect of reducing communication overhead. Compared to the case of $LB = 0$, when *LB* was increased

to 0.6 the performance was slightly worse for *init_nlocal* = 1, 2, or 5 but commensurate for *init_nlocal* = 10. This may be explained by an inequality in performance among the processors. Part of the processors with slightly better performance handled more collocation nodes. Overall, version P29rl delivered a significant improvement in the total run time.

Table 3.3 *Total run times (hrs:mins) for load balancing performance test of BEASSI P29rl for a 3-domain problem*

LB	*init_nlocal*				previous version (*LB*=1)
	1	2	5	10	
0	2:33	2:35	2:59	4:15	7:58
0.6	2:48	2:48	2:49	4:14	

3.3.5 Parallelization of Linear Equation Solver and Displacement Calculations for Internal Points

In the previous BEASSI version P25rl, the serial equation solver zgesvx from the Linear Algebra PACKage (LAPACK) was employed on the root node for solving the complex system of equations **Ax**=**b** for surface footing and single pile problems. Solving this system of equations for such problems typically took no more than ten minutes, as the majority of the run time was required for calculation of the **H** and **G** matrices due to the numerically evaluated layered Green's functions. For 2×2 pile group problems, however, solution of **Ax**=**b** took nearly three hours when **b** had a size of 25,000×4 complex numbers (for 4 right hand sides). Additionally, the maximum problem size that could be analyzed was limited to that which could fit in the memory of the root node. To reduce the equation solving time and greatly expand the maximum problem size by fully utilizing the distributed computational resources, the serial equation solver was replaced by a parallel one. Two data distribution approaches for employing a parallel solver were examined:

1. Distributing matrix **b** to four processors

For **A**x=**b** assembled in BEASSI, matrix **b** comprises four columns as $\mathbf{b}=[\mathbf{b}_1,\mathbf{b}_2,\mathbf{b}_3,\mathbf{b}_4]$ denoting the four types of predefined boundary conditions. As a preliminary attempt, the four columns were distributed to four processors so that each of these processors only needed to solve for one RHS independently using the original serial solver zgesvx (Figure 3.6). When computation on each processor is completed, result vectors $\mathbf{x}_1$, $\mathbf{x}_2$, $\mathbf{x}_3$ and $\mathbf{x}_4$ are collected back to the root to form complete solution x. The performance of this approach was expected to increase by four times.

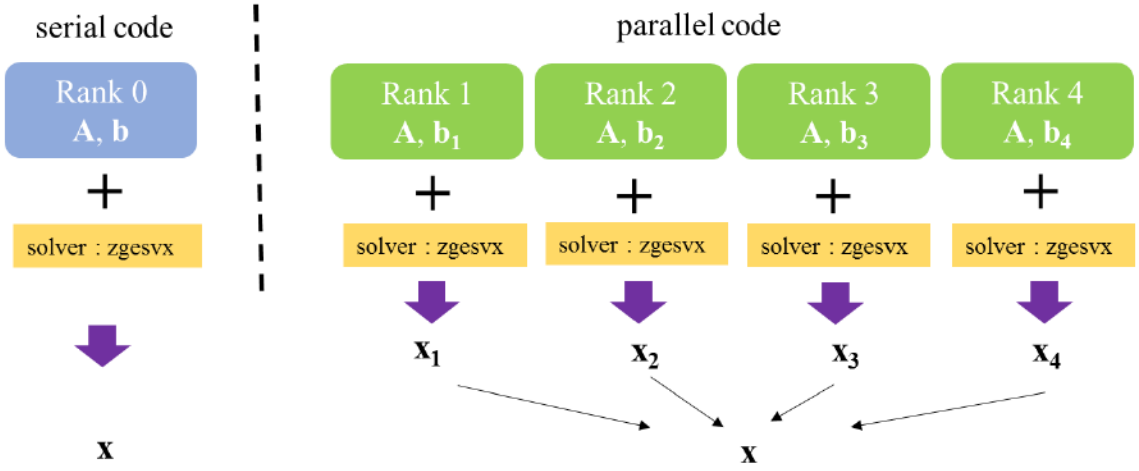

Figure 3.6 *Data distribution of matrix* ***b***.

Performance tests were conducted for a single pile and a 2×2 pile problems, when four processors either resided on the same compute node or spread across four computation nodes. The results are shown in Table 3.4. When four processors were all on a single compute node, improvement in performance was negligible, regardless of problem size. When four processors were distributed across four different compute nodes, there was about 18% improvement. The explanation is provided as follows.

Table 3.4 *Results of performance test with approach 1.*

Case	Serial code	Parallel code	
		4 processors on 1 node	4 processors on 4 nodes
small (single pile problem)	0.60 mins	0.57 mins (-5%)	0.49 mins (-18%)
large (pile group problem)	35.55 mins	35.39 mins (-0.45%)	29.53 mins (-17%)

Solver zgesvx employs LU decomposition, including three steps:

Step 1: Decomposition/factorization, $\mathbf{A} = \mathbf{LU}$. This is to transform $\mathbf{A}$ into a multiplication of a lower unit triangle matrix and an upper triangle matrix. Then the original system of equations becomes $\mathbf{LUx_i} = \mathbf{b_i}$. This step is identical on all four processors.

Step 2: Forward substitution, $\mathbf{Ly_i} = \mathbf{b_i}$. This is to solve intermediate variable $\mathbf{y_i}$, where $\mathbf{y_i} = \mathbf{Ux_i}$. This step is unique on each processor due to the unique right-hand-side $\mathbf{b_i}$.

Step 3: Back substitution, $\mathbf{Ux_i} = \mathbf{y_i}$. This is to solve the unknown $\mathbf{x_i}$ on each processor. Subsequent to Step 2, Step 3 is also unique on each processor.

Assume dimension of $\mathbf{A}$ is $n \times n$ and take only one RHS as an example. In Step 1, the number of operations is about $\frac{2}{3}n^3$. In Steps 2 and Step 3, the total number of operations is $n^2 + n^2 = 2n^2$. The comparison is provided in . It is indicated that Step 1 dominates computation complexity and number of columns in RHS hardly affects time. An increase in row number of matrices $\mathbf{y_i}$ and $\mathbf{x_i}$ would not magnify such variation in performance.

When n is 3753 for the pile group problem in the performance test, the ratio of $(\frac{2}{3}n^3 + 2 \times n^2)$ to $(\frac{2}{3}n^3 + 8 \times n^2)$ is nearly unity. A problem with greater size would result in even

less difference in the number of operations (Figure 3.7). This helps to explain that the problem size had negligible influence on performance.

Table 3.5. *Computation complexity by LU decomposition.*

	Number of operations on each processor			
	Step 1	Step 2	Step 3	Total
Serial code	$\frac{2}{3}n^3$	$4\times n^2$	$4\times n^2$	$\frac{2}{3}n^3+8\times n^2$
Parallel code by approach 1	$\frac{2}{3}n^3$	n^2	n^2	$\frac{2}{3}n^3+2\times n^2$

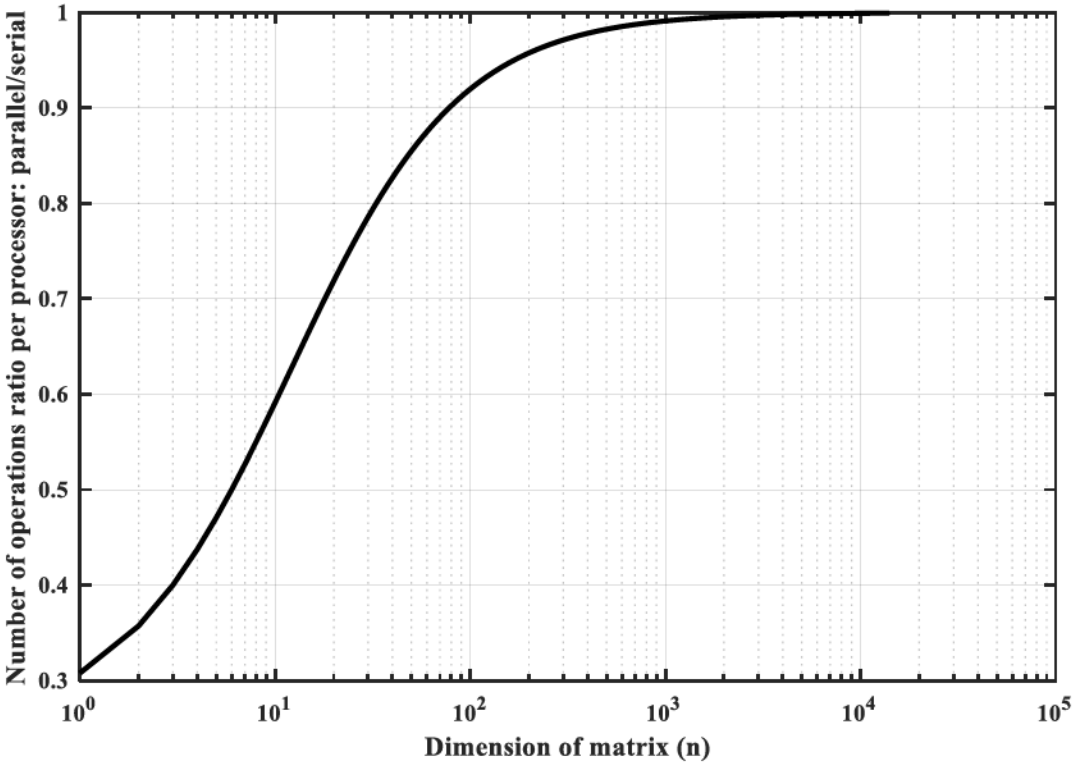

Figure 3.7 *Ratio of average number of operations per processor: parallel/serial.*

When four processors resided on four different compute nodes, L3 caches on all the 4 CPU chips could be used instead of just one for the serial version. Each Intel Xenon E5 2650 CPU was equipped with 20MB L3 cache. When 4 processes were dispersed to four compute

nodes, ideally a total of 80 MB L3 caches were available. This explains why the corresponding performance was improved by around 18%.

2. Distributing both matrices **A** and **b**

Another approach is replacing the serial equation solver by its parallel counterpart pzgesv in the Scalable Linear Algebra PACKage (ScaLAPACK). Expert solver routine pzgesv was called as:

call subroutine PZGESV (N, NRHS, A, IA, JA, DESCA, IPIV, B, IB, JB, DESCB, INFO)

The meaning of each argument is listed in Table 3.6. Among the 12 dummy arguments required, only four vary across processors and need to be individually specified. The remaining input arguments are identical on each processor.

Table 3.6 *Parameter description of parallel solver pzgesv.*

Argument	**Description**	**Vary among processors? (Y/N)**
N	number of rows/columns of matrix **A**	N
NRHS	number of RHS, i.e., number of columns in matrix **b**	N
A	blocked local submatrix on each processor	Y
IA, JA	the row and column indices indicating the first row and column of matrix **A**	N
DESCA	array descriptor for submatrix A, indicating how **A** is blocked	Y
ipiv	output indicating pivoting information	N
B	blocked local submatrix **b** on each processor	Y
IB, JB	the row and column indices indicating the first row and column of matrix **b**	N
DESCB	array descriptor for matrix **b**, indicating how **b** is blocked	Y
INFO	output containing error message	N

To apply the parallel solver, **A** and **b** need to be cyclically blocked for data distribution. Cyclic blocking can be either one-dimensional (i.e., column or row blocking), or two-dimensional. An example of 2D blocking is demonstrated in Figure 3.8(a). A block size of 2×2 (highlightened by the same color) and a processor grid size of 2×3 (partitioned by thick solid lines in Figure 3.8(b)) are specified for matrix **A**. In the 1st dimension (row), the block on the

1st, 2nd rows and 1st, 2nd columns is mapped to processor (0,0). The block on the 3rd, 4th columns and 1st, 2nd rows is mapped to processor (0,1). And the block on the 1st, 2nd rows and the 5th, 6th columns is mapped to processor (0,2). Similar procedure is implemented for the 2nd dimension (column). This process is repeated until all blocks are mapped. Eventually, all entries marked by the same color are mapped to the same processor as in Figure 3.8(b).

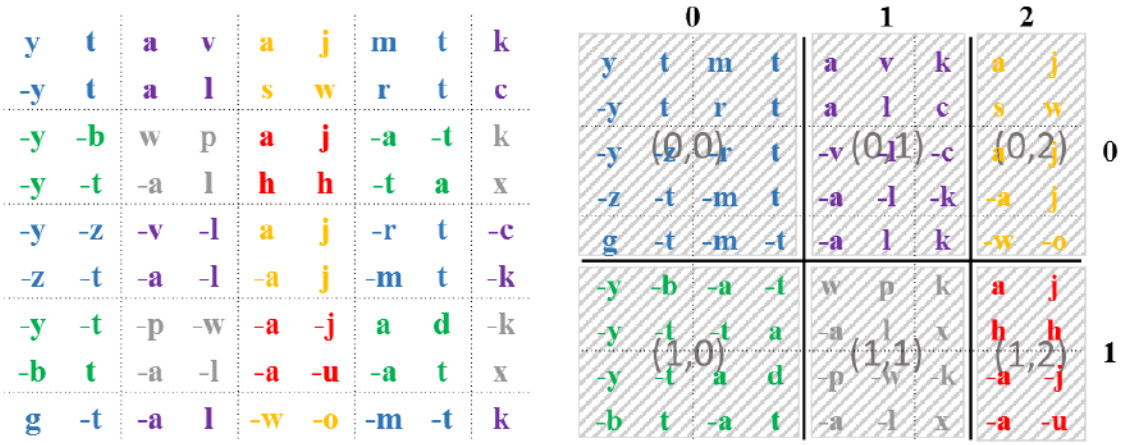

(a) 2×2 blocking of matrix A **(b) mapping of matrix A to processor grid**

Figure 3.8 *Demonstration of 2-D Cyclic blocking.*

For BEASSI, column blocking is the simplest way because of the simplicity in data distribution because of the limited columns in matrix **b**. In 3D problems, each collation point is always assocated with 3 rows and 3 columns in **H** and **G**, which means the dimension of the matrix **A** is always a multiple of 3. Thus block size is set to be 3×3 permanently to avoid inducing any minor submatrices during mapping as the last row and column in Figure 3.8(a). The approach of using the parallel solver is shown in Figure 3.9. MPI non-blocking routines, such as mpi_isend and mpi_ibcast were used for data distribution. The performance of the parallel solver in solving a 25,000 ×25,000 complex system of equations is shown in Figure 3.10(a), which indicates a favorable performance.

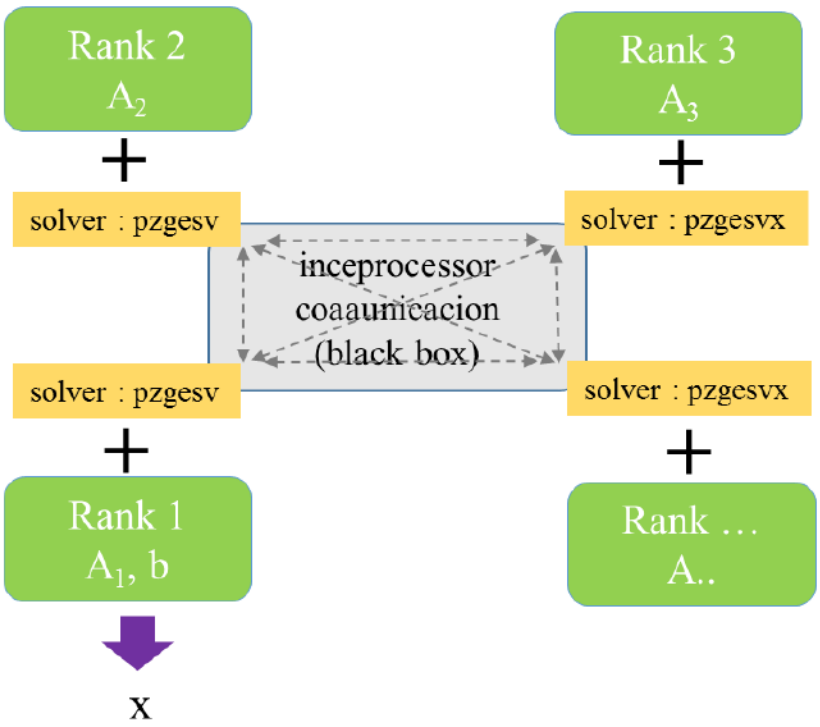

Figure 3.9 *Principle of using parallel solver.*

For solving a given system of linear equations, the accuracy is related to condition number of the left-hand-side matrix **A**. A higher condition number means that the solutions are more sensitive to perturbations such as round-off errors. Since BEASSI uses normalized shear moduli, densities, and dimensions, it is always possible to keep the condition number in a proper range by choosing appropriate reference numbers. Computational error is quantified herein by relative solution error $\left|(A\bar{x}-b)/b\right|$, where $\bar{x}$ is numerical solution. The accuracy of the parallel solver was verified by a sample calculation for a surface footing problem at $\bar{\omega}=0.05$. Tractions and impedances by the serial and parallel solvers are compared in Table 3.7 and Table 3.8. In terms of traction, absolute difference between the two solvers is at magnitude of 10^{-10}. As for impedance, absolute error is confined within 10^{-5}. The accuracy of the parallel solver is validated.

After incorporating of the load balancing algorithm and the parallel solver, BEM analyses for the 2×2 pile group in a layered disturbed zone surrounded by a layered half-space required 8 - 10 hours with 96 processors. Actual scalability can be quantified by speedup $R(p)$ and serial fraction s. Theoretical speedup and serial fraction can be estimated by Amdahl's law. Assume a program employing p processors take serial execution time T_s and parallel execution time T_p, respectively. By definition,

$$R(p) = \frac{T_s + T_p}{T_s + T_p / p} \tag{3.33}$$

$$s = \frac{T_s}{T_s + T_p} \tag{3.34}$$

Eliminating T_s and T_p leads to

$$R(p) = \frac{p}{ps - s + 1} \tag{3.35}$$

$$\text{or } s = \frac{p - R}{Rp - R} \tag{3.36}$$

A single pile in layered soil was analyzed at a normalized excitation frequency of $\bar{\omega} = 0.05$ and the performance is shown in Figure 3.10(b). With the parallelized code and 96 processors, the computation took less than 10 minutes with a speedup of 72.3, a significant improvement from 715 minutes by the serial code. In practice, the speedup is not strictly commensurate with the number of processors. This is due to the increasing latency, communication overhead, contention of the multiple cores for shared cache and system memories with increasing number of processors. Additionally, the root does not participate in collocation. In this test, serial fraction of the code decreased from 11.4% to 0.3% as number of processor decreased from 4 to 96. These drastic improvements in efficiency validated the

scalability of the parallelized BEASSI code. Further performance improvement may be expected using 2D cyclic blocking, optimized block size, highly-optimized mathematical libraries, and iterative solvers.

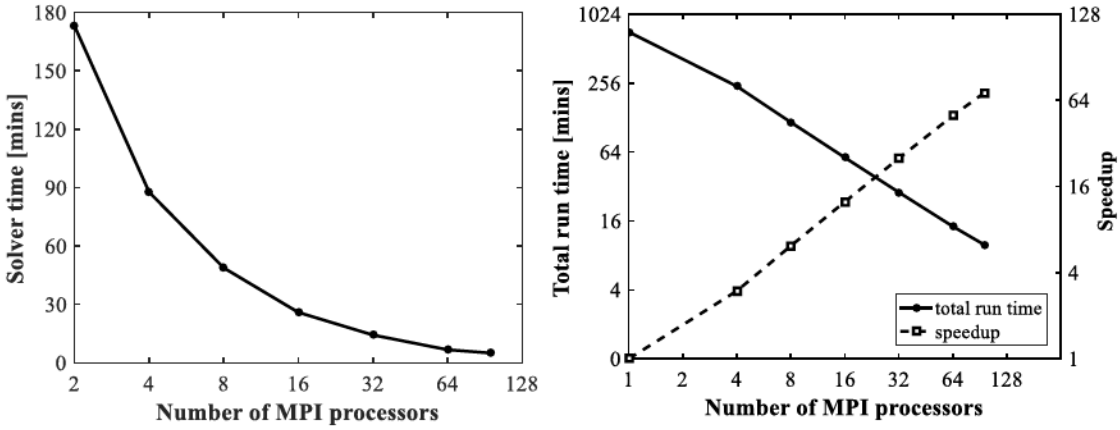

(a) performance of the parallel solver (b) overall performance and scalability

Figure 3.10 *Improvement of performance of BEASSI with parallelization.*

Table 3.7 *Comparison on traction between parallel and serial solvers.*

Collocation node number	**Parallel solver (pzgesv)**		**Serial solver (zgesvx)**	
	real part	imaginary part	real part	imaginary part
1	-1.444378×10^{3}	-6.646648×10^{1}	-1.444378×10^{3}	-6.646648×10^{1}
2	-2.679455×10^{2}	-1.201007×10^{1}	-2.679455×10^{2}	-1.201007×10^{1}
3	-3.134729×10^{1}	-1.004866×10^{0}	-3.134729×10^{1}	-1.004866×10^{0}
4	-2.704894×10^{1}	-9.343959×10^{-1}	-2.704894×10^{1}	-9.343959×10^{-1}
5	-2.376813×10^{1}	-9.115086×10^{-1}	-2.376813×10^{1}	-9.115086×10^{-1}
6	-1.183689×10^{1}	-4.536136×10^{-1}	-1.183689×10^{1}	-4.536136×10^{-1}
7	-1.931943×10^{-7}	-8.859091×10^{-9}	-1.931782×10^{-7}	-8.858053×10^{-9}

Table 3.8 *Comparison on impedances between parallel and serial solvers.*

Normalized impedance	Parallel solver (pzgesv)		Serial solver (zgesvx)	
	real part	imaginary part	real part	imaginary part
$\bar{k}_{vv}$	6.38321	0.30050	6.38321	0.30050
$\bar{k}_{hh}$	5.35903	0.18750	5.35903	0.18750
$\bar{k}_{mm}$	5.91598	0.00223	5.91598	0.00223
$\bar{k}_{mh}$	0.69066	0.02105	0.69066	0.02105
$\bar{k}_{hm}$	0.67559	0.02026	0.67559	0.02026
$\bar{k}_{tt}$	8.51830	-0.00018	8.51830	-0.00018

3.3.6 Optimization of Memory Management

For a typical 6-domain problem, dimensions of matrix **A** can be as great as 25,000 × 25,000 (i.e., a total of 0.63 billion double precision complex numbers). For existing versions of BEASSI, matrices **A** and matrix **b** were allocated on every processor, which resulted in a considerable repetition when **A** only needed to be stored on one processor. A simple test was performed on a 6-domain problem with results shown in Table 3.9. For the serial solver, its performance should ideally be independent of number of processors when memory is sufficient and this is validated by the similar performance in cases s1 and s2. On CyEnce cluster, each computation node is configured with two CPU sockets and two physical memory modules. Though both memory modules are shared by the two CPUs, it is faster for a CPU to access the memory module that is physically located closer. When number of processors increase to 8 in case s3, node memory usage exceed 50%. This indicates the root processor had to access the farther memory module, and explains why performance is slightly poorer than cases s1 and s2. Duplication of matrices **A** and **b** on one more processor resulting in about 7% more memory usage. When a total of 16 processors were employed in case s4, the actual node memory must have exceeded 100%. Even so, no error message showed up due to the memory paging.

Table 3.9 *Test on memory usage for serial and parallel solvers.*

BEASSI version	Case	Number of MPI processors	Solver time (mins)	Max. node memory usage (%)
P30rl with serial solver	s1	2	197.25	17.4
	s2	4	196.75	29.6
	s3	8	218.63	59.8
	s4	16	231.73	86.0
P31rl with parallel solver	p1	2	173.00	17.3
	p2	4	87.70	19.7
	p3	8	48.77	21.4
	p4	16	25.90	25.0
	p5	32	14.27	16.9
	p6	64	6.70	13.0

A computer is capable of addressing memory beyond the amount physical installation on the system (e.g., 128 GB each node on CyEnce cluster) by nonphysical memory. The nonphysical memory, also called virtual memory, is a section of secondary storage (usually hard disk) used to emulate the real memory. When memory become insufficient on a computer, the operating system automatically backs pages of memory up on the hard disk and frees up the corresponding RAM. This mechanism prevents operating system from running out of memory and explains why only 86% of memory was used in case s4. However, too much reliance on memory paging would jeopardize performance because assessing hard disk is substantially slower than assessing memory.

As a solution, matrix **A** was only allocated on root processor in version P31rl. As indicated in Table 3.9, when number of processors increases from 2 to 16, maximum memory usage remained below 25%. More importantly, with more than 16 processors employed, the maximum memory usage for each node decreased to only 13%, ensuring the computing capability in handling pile group problems.

3.4 Validation and Verification of BEASSI

The updated BEASSI code is compiled and run on a new cluster and on a new problem type, and it is crucial to verify its accuracy on pile group problems. A series of tests were implemented to progressively verify the program's capabilities.

3.4.1 Validation of New Hardware and Software

Since BEASSI has never been run before on the high performance CyEnce cluster, it is important to verify the new hardware and software as the first step, using solutions obtained from previous versions of BEASSI on a different cluster. The software on CyEnce includes new versions of the operating system, MPI compiler, static libraries, and mesh generator GiD. A case of a single pile with an embedment ratio of $L/a = 26.586$ in a square-root half-space without a disturbed zone obtained using the parallel BEASSI version P25r (Ashlock 2006) was used as a benchmark and reanalyzed. Using the original input files, the output of the new BEASSI P29rl was almost identical to the previous version P25r results (Figure 3.11), which demonstrates that the many changes to the code as well as the new operating system, MPI compiler version, and static libraries on the CyEnce cluster are reliable. The same case was analyzed after creating new input files using the preprocessor GiD to define and mesh the geometry, resulting in negligible differences from the original input files (Figure 3.12). The minor differences mainly result from slightly different discretization of the meshes producing different round-off errors. Thus, the capability of the new version of GiD is also verified.

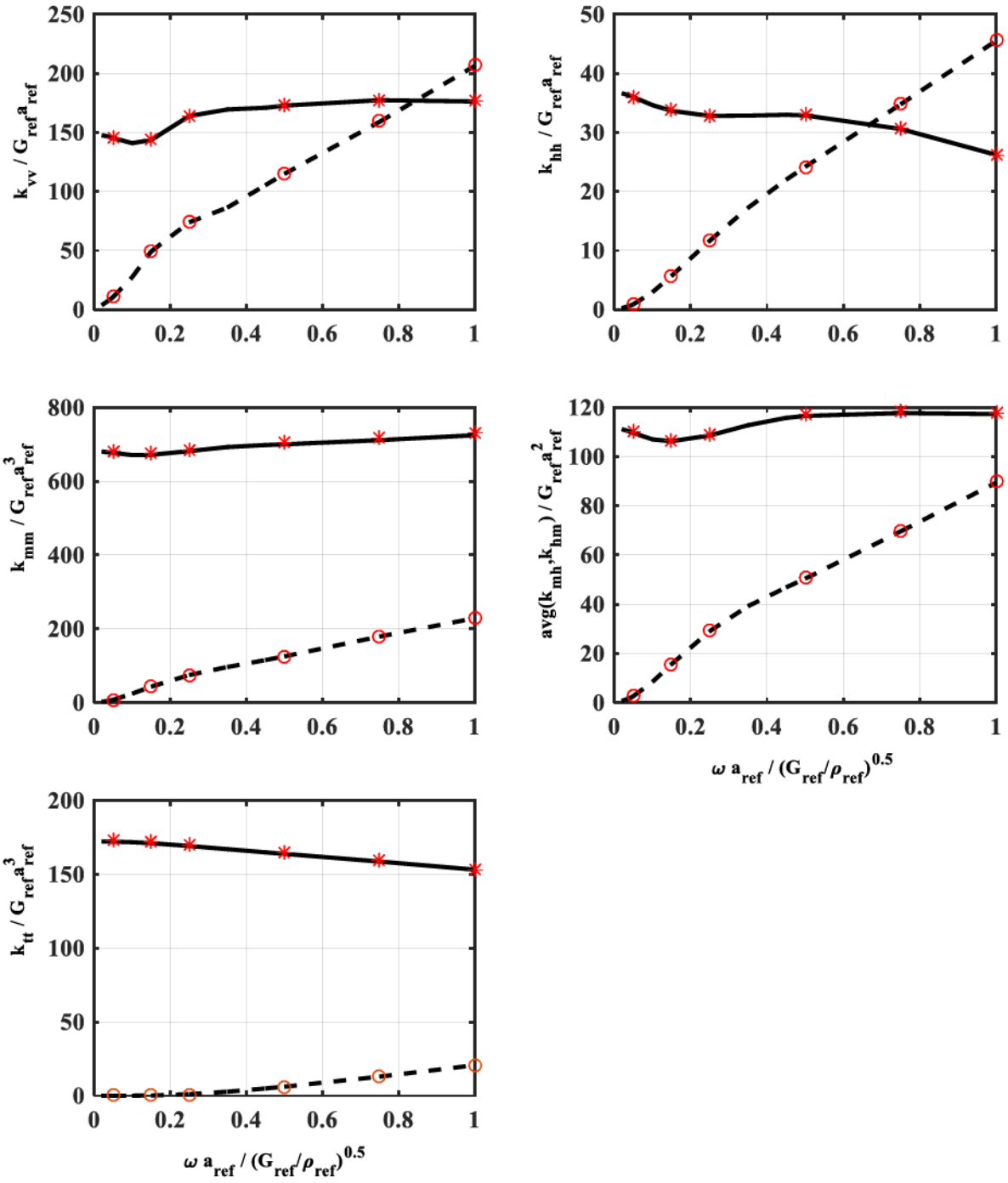

Figure 3.11 *Impedance functions for single pile benchmark study using BEASSI (Black lines: benchmark results of Ashlock (2006); red markers: results using the same input files on CyEnce cluster using BEASSI P29rl).*

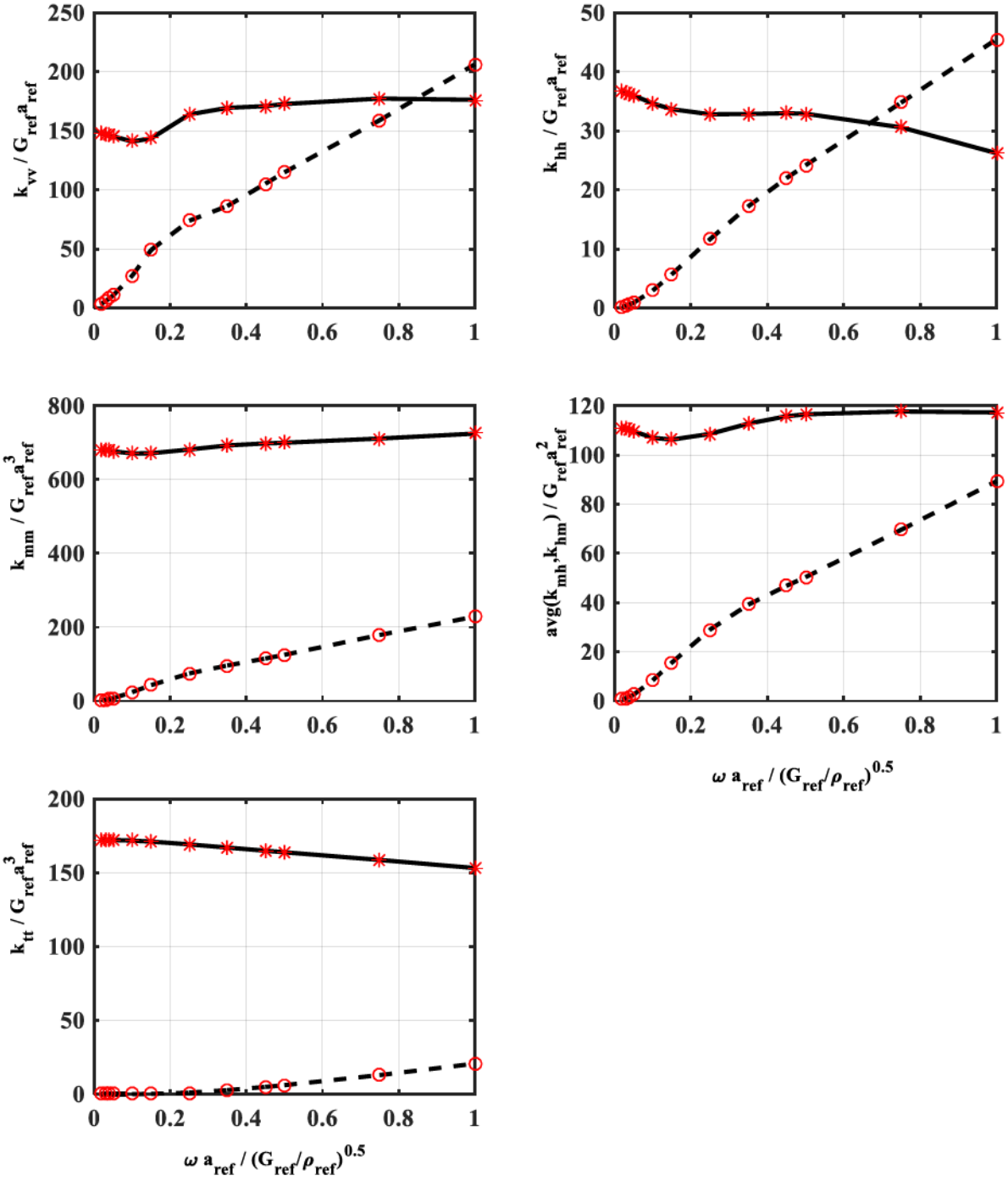

Figure 3.12 *Impedance functions for single pile benchmark study using benchmark case's input files vs. new input files created with GiD (black lines: benchmark inputs; red markers: new inputs using GiD).*

3.4.2 Validation on Multi-Domain Problems

The feature of regularized multi-domain formulation in BEASSI can be verified by comparing a 6-domain model to a 5-domain model. When the two models have the same soil properties within the disturbed zone and in the half-space, and identical pile properties, the 5-domain model reduces to a special case of the 6-domain model. Ideally, identically impedance functions should be expected from both models. A reference study was conducted for the two models with homogeneous soil profiles (Figure 3.13). Dimensionless soil and pile properties are listed in Table 3.10. The resulting impedances presented in Figure 3.14 show favorable agreement. The relative error slightly increases with frequency and is less than 1%.

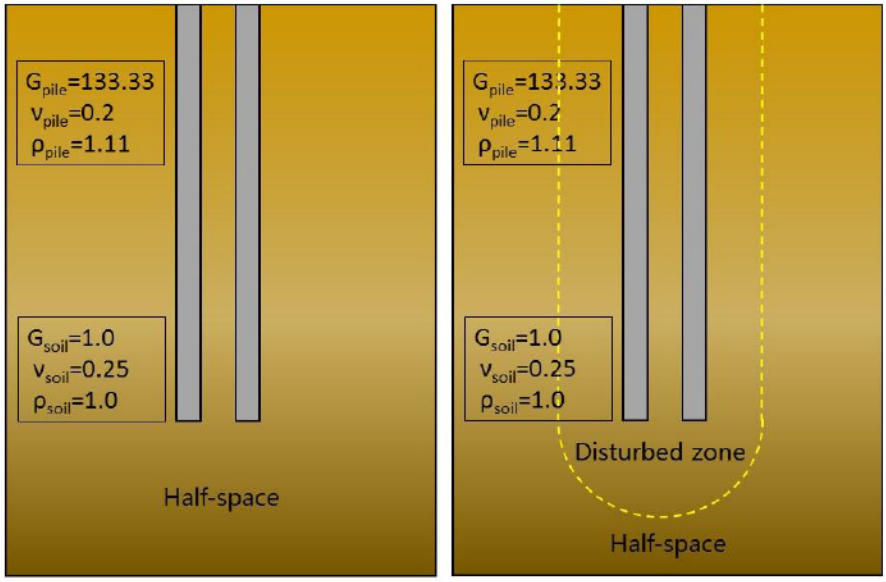

(a) 5-domain model (b) 6-domain model

Figure 3.13 *Comparison of models of pile group with and without disturbed zone in homogeneous soil.*

Table 3.10 *Dimensionless parameters of the 5-domain and the 6-domain models with homogeneous soil profiles.*

Pile	Radius	1
	Length	25
	Spacing	4
	Shear modulus	(133.33 , 0)
	Poisson's ratio	0.2
	Density	1.11
Soil	Shear modulus	(1.0, 0)
	Poisson's ratio	0.25
	Density	1.0

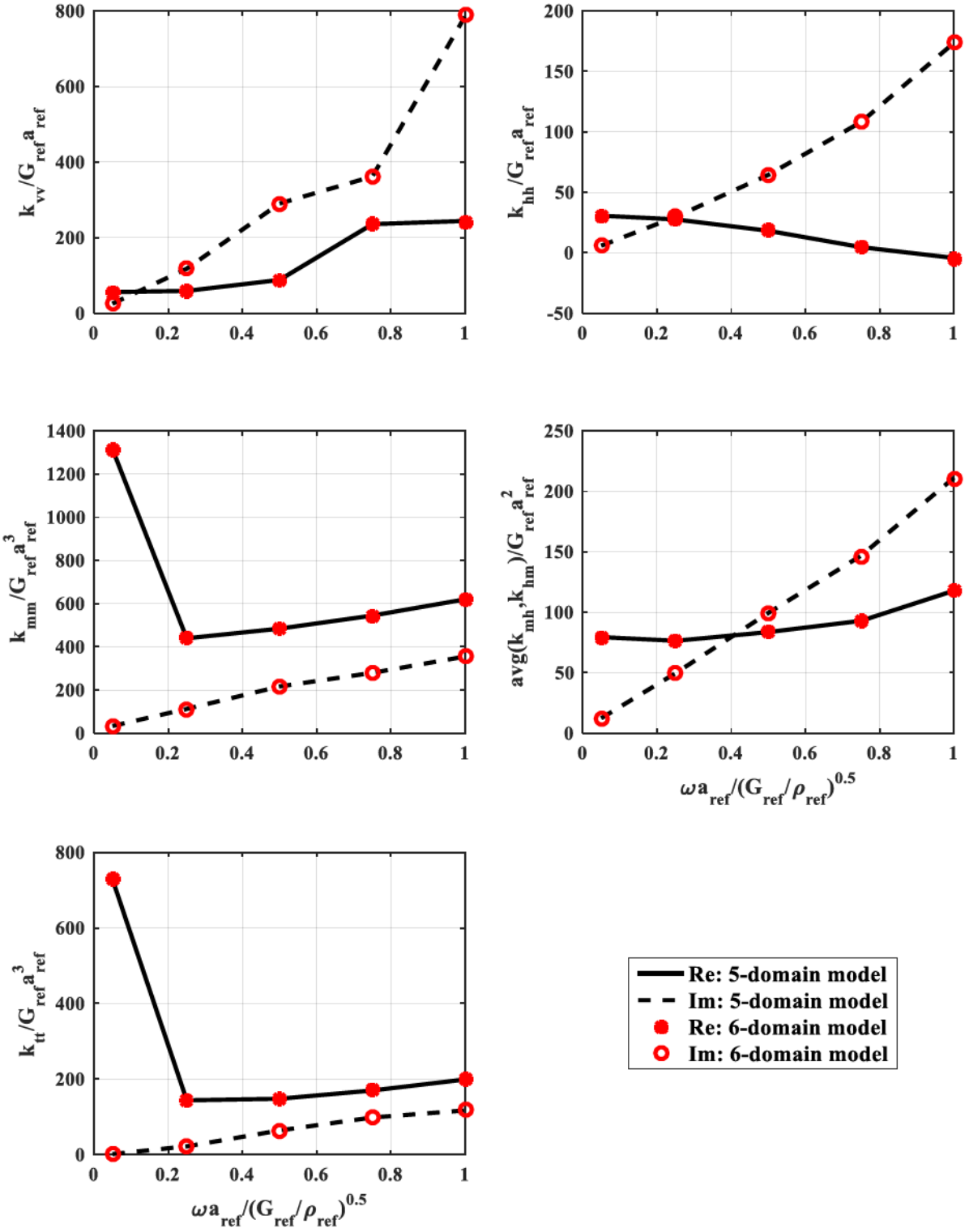

Figure 3.14 *Comparison on impedances of a 5-domain model and a 6-domain model with the same homogeneous soil profiles.*

In addition to the case of homogeneous soil profiles, comparison was also made for layered soil profiles. A 5-domain model and a 6-domain model were established based on the preliminary design of the full-scale tests. Pile and soil parameters are summarized in Table 3.11. Soil shear modulus profile was based the reported results at the same site by Shelman et al. (2010) and are presented in Figure 3.15. The resulting impedance functions are presented in Figure 3.16. For frequencies lower than 0.25, the impedances of the two confirm fairly well with each other. At higher frequencies, impedance functions begin to deviate. This can be attributed to the wave reflections at the artificial boundaries of the inclusion, and numerical error in integration. At higher frequencies, the wave reflections have more significant impact on piles. In general, the impedance functions for the 6-domain model match well with those for the 5-domain model. BEASSI featuring multi-domain regularized formulation is validated.

Table 3.11 *Dimensionless parameters of the 5-domain and the 6-domain models with layered soil profiles.*

Pile	Outer radius	1
	Thickness	0.058
	Length	66.78
	Spacing	8.348
	Shear modulus	(407.3, 0)
	Poisson's ratio	0.2
	Density	3.64
Soil	Shear modulus and damping	see Figure 3.15
	Poisson's ratio	0.25
	Density	1.0

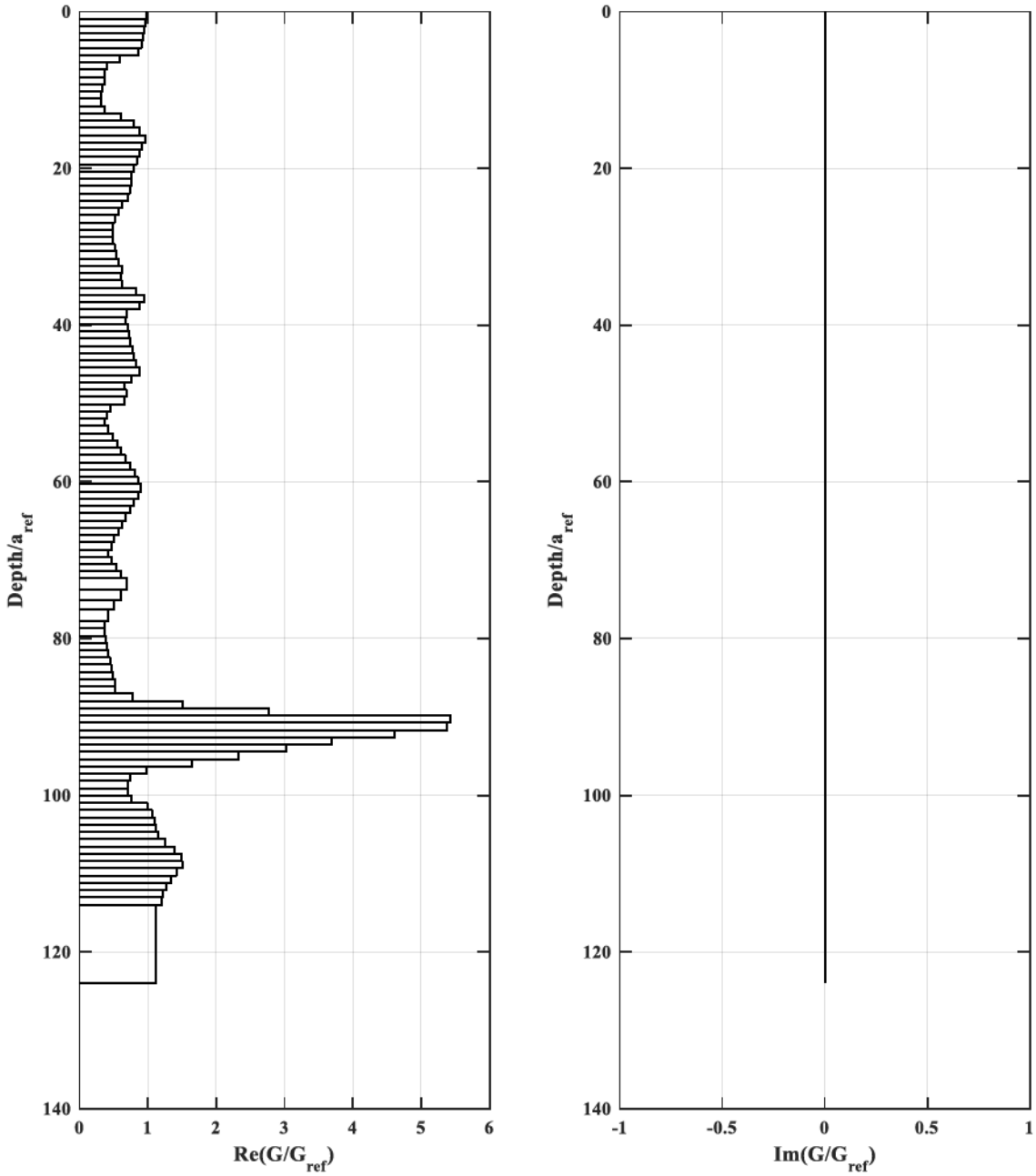

Figure 3.15 *Layered soil profile for comparison of a 5-domain and a 6-domain models.*

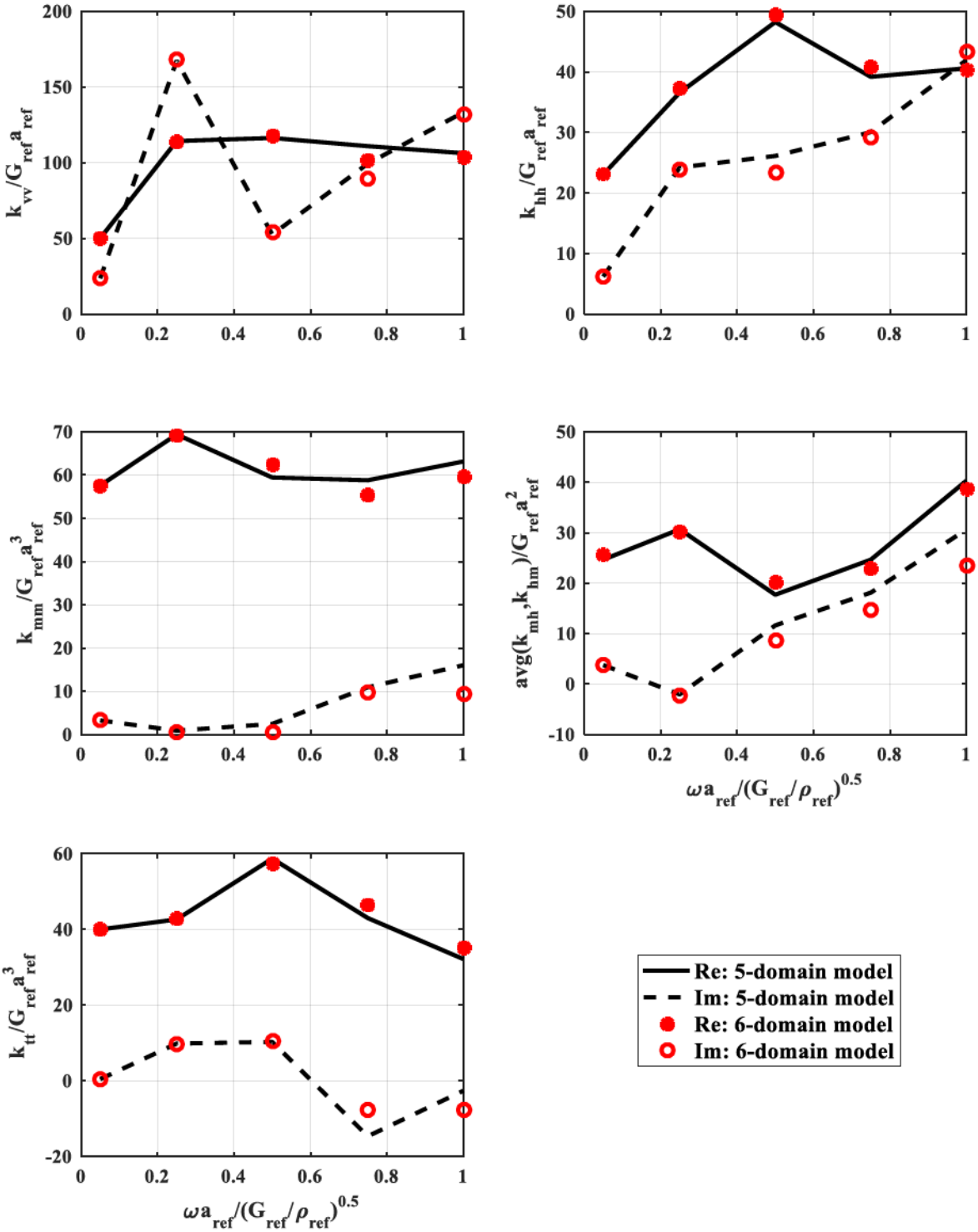

Figure 3.16 *Comparison on impedances of a 5-domain model and a 6-domain model in layered soils.*

3.4.3 Validation of Structural Green's Functions on Pile Group

In the boundary element formulation, structural Green's functions, which are based on Euler-Bernoulli beam theory, are applied for the pile domains. To validate its application on pile group problems, a comparison was made between models using the structural Green's functions (Abedzadeh 1993) and 3D dynamic point-load Green's functions for the viscoelastic full-space (Domínguez and Abascal 1984).

Dimensionless pile and soil properties are listed in Table 3.12 and corresponding impedance functions are compared in Figure 3.17. The differences in $\bar{k}_{vv}$ and $\bar{k}_{mm}$ are found to be negligible. For $\bar{k}_{hh}$, deviation becomes noticeable when dimensionless frequency is beyond 0.5. For $\bar{k}_{tt}$ and average of $\bar{k}_{mh}$ and $\bar{k}_{hm}$, structural Green's functions resulted in a slight higher stiffness at frequencies lower than 0.6 and lower stiffness at higher frequencies. Overall consistency is observed for all impedance functions. The difference is attributed to the assumption of plane cross-section in the Euler-Bernoulli beam theory such that cross-section remains as plane during deformation. Such difference is expected to diminish with a higher shear modulus ratio of pile to soil. Therefore, using structural Green's functions to model piles is proved to be valid.

Table 3.12 *Pile and soil properties in comparison of the structural and 3D dynamic point-load Green's functions.*

Pile	Radius	1
	Length	25
	Complex shear modulus	(133.33, 0)
	Poisson's ratio	0.2
	Density	1.11
Soil	Complex shear modulus	(1.0, 0)
	Poisson's ratio	0.25
	Density	1.00
Pile spacing		4

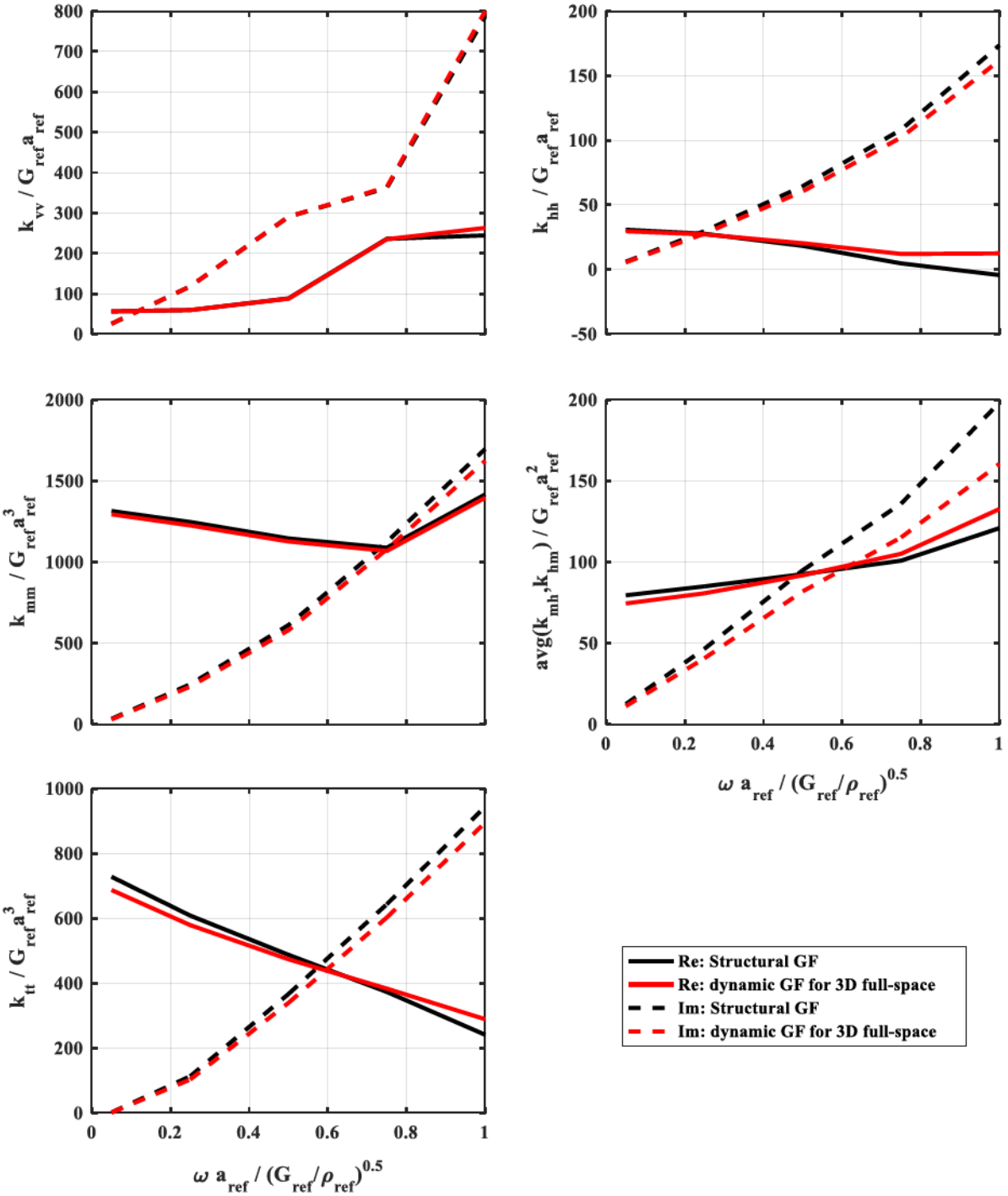

Figure 3.17 *Comparison of structural Green's functions and 3D dynamic point-load Green's functions.*

3.4.4 Verification of BEASSI's Capability on Static Pile Group Problems

El Sharnouby and Novak (1990) calculated the static settlement of vertically loaded piles by treating the piles and soil as a composite continuum and specifying conditions of equilibrium for discrete nodes. The Poisson's ratio of the soil was 0.5 and that of the pile was not specified. The results were presented in the form of interaction factors as introduced by Poulos (1968), defined as:

$$\alpha = \frac{\text{settlement of one pile owing to adjacent pile load}}{\text{pile settlement under its own load}} \tag{3.37}$$

A corresponding case of two floating piles in a homogenous half-space was analyzed by BEASSI for various spacing and elastic modulus ratios. The length-to-diameter ratio of the piles was $L/d = 25$ and the soil Poisson's ratio was set to $\nu_s = 0.49$ to avoid numerical instabilities. Pile Poisson's ratios of $\nu_p = 0.2$ and $\nu_p = 0.49$ were analyzed, which had little effect on the results. The results from the rigorous three-dimensional BEASSI analysis follow similar trends as El Sharnouby and Novak (1990), with interaction factors decreasing with increasing pile spacing (s), as shown in Figure 3.18. For the lowest modulus ratio, the two analyses match very well, with a maximum interaction difference of 0.036 which diminishes with increasing spacing. For higher modulus ratios, the differences are slightly greater but similar trends are observed. For the case E_p/E_s=10,000 at a spacing of S/d=2 for example, the interaction factors from BEASSI and the reference study are 0.638 and 0.706, respectively. In the reference study, piles were discretized into a limited number of elements with identical vertical shear stresses assumed. Additionally, surface loads as well as axial loads were reduced to point loads. These simplifications, which were not applied in BEASSI, increase the stiffness of the soil-pile system and lead to the slightly higher interaction factors.

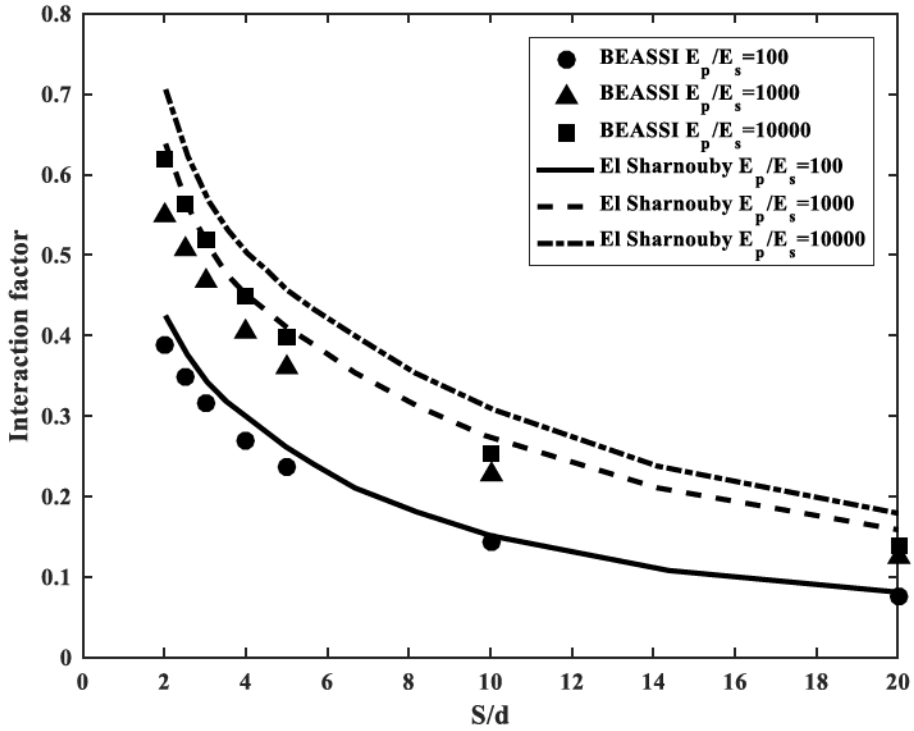

Figure 3.18 *Comparison of interaction factors from BEASSI and El Sharnouby and Novak (1990) for floating pile with Poisson's ratio of 0.2 in homogeneous soil (Ashlock and Jiang 2017).*

3.4.5 Verification on Dynamic Pile Group Problems

To verify the program's capabilities for dynamic problems, the impedance functions of a 2×2 pile group in a homogeneous half-space were calculated and compared to those of Kaynia and Kausel (1982). The pile and soil parameters for this case were $E_p / E_s = 10^2$, $\nu_s = 0.40$, $\nu_p = 0.25$, $L/d = 15$, and $S/d = 5$, with a mass density ratio of $\rho_s / \rho_p = 0.70$, where subscript p refers to the pile and subscript s to the soil, E is Young's modulus, ν is Poisson's ratio, ρ is mass density, and L, d and S are the pile embedded length, diameter, and spacing, respectively. In BEASSI, the vertical, horizontal, rocking, coupling (horizontal-rocking), and torsional impedances at the specified frequency were obtained using BEASSI by

prescribing unit displacements or rotations at the pile head in the corresponding directions and appropriately integrating the resulting tractions to obtain the resultant forces and/or moments.

The real and imaginary parts of the impedances for the 2×2 pile group are presented in Figure 3.19. The equivalent dashpot coefficients reported in the reference solutions were converted to corresponding imaginary parts of the impedance functions for comparison with BEASSI. For consistency with the reference case, the vertical impedance $k_{vv}(a_0)$ and rocking impedance $k_{mm}(a_0)$ were also normalized by the static values $Nk_{vv}^{S}(0)$ and $\sum x_i^2 k_{vv}^{S}(0)$, respectively, while the horizontal impedance $k_{hh}(a_0)$ and torsional impedance $k_{tt}(a_0)$ were normalized by $Nk_{hh}^{S}(0)$ and $\sum r_i^2 k_{hh}^{S}(0)$, where $N=4$ refers to the number of piles, x_i is the distance between the pile center and the rocking axis, r_i is the distance between the pile center and the center of rotation for torsion, and superscript *S* refers to the single pile's stiffness. The dimensionless frequency is defined as $a_o = \omega d / C_s$ where C_s is the shear wave velocity of the soil and $\omega = 2\pi f$ is the circular frequency of excitation. The results from BEASSI match the reference solution well, especially at low frequencies. As the normalized frequency approaches zero, both methods tend towards a similar value of static stiffness. When a_o exceeds 0.6, the stiffness (real part of impedance) obtained by BEASSI is generally slightly lower than the reference solutions and the damping (imaginary part of impedance) diverges slightly from the reference solutions. From these benchmark comparisons, the modified BEASSI program are considered to be verified for solving pile group problems.

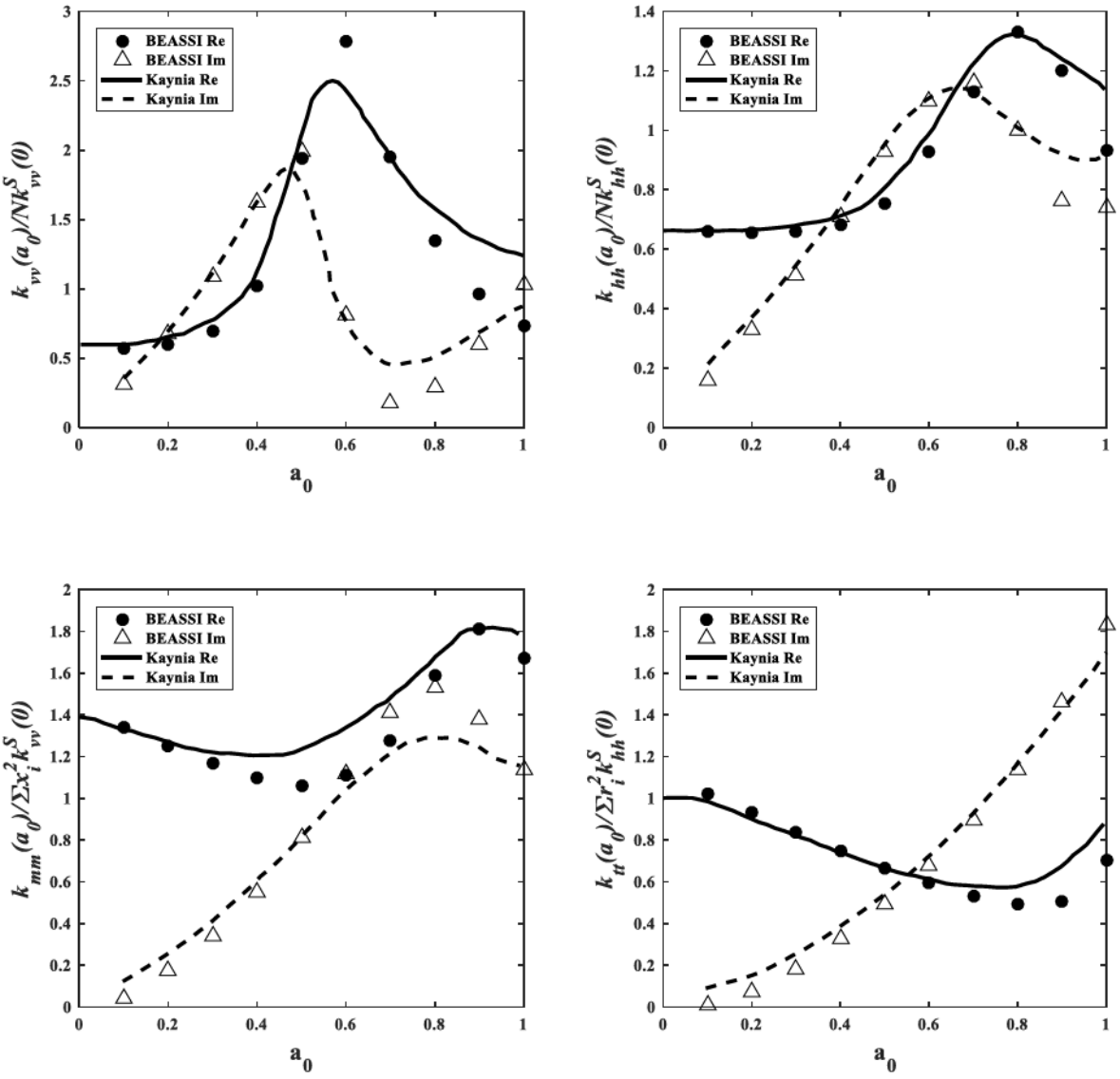

Figure 3.19 *Comparison of normalized impedances for 2×2 pile group in homogeneous half space to results of Kaynia and Kausel (1982).*

3.4.6 Validation of 3D Disturbed-Zone Model

Impedance functions for the case of a pile group within a single disturbed zone are very limited in the existing literature. Instead, pile group analyses with disturbed zones are typically based on superposition of single pile analyses and dynamic soil-pile interaction factors, with the assumption that the presence of a second (free-headed) pile does not affect the displacements of the first (loaded) pile. For example, a dynamic vibration case study of a single floating pile and a single rigidly supported pile in horizontally inhomogeneous soils was reported by Veletsos and Dotson (1988). The relative pile and soil parameters used were $G_p / G_s^i = 1{,}094$, $\nu_s = 1/3$, $\nu_p = 1/6$, and $L/d = 20$, with the ratio of G_s^o to G_s^i varied from 1 to 4, in which G denotes shear modulus, ν is Poisson's ratio, and L/d is the pile's length to diameter ratio. Subscripts p and s refer to the pile and soil, and i and o refer to the inner and outer soil zones, respectively. The case corresponding to zero material damping for both pile and soil domains is considered herein, and the thickness of the cylindrical disturbed zone was $0.25d$.

A 3D BEM model was established with BEASSI to reanalyze the case study using a disturbed zone consisting of a cylindrical part with a hemispherical cap beneath, consistent with the proposed pile group model shown in Figure 3.20. By setting the soil properties within the hemispherical cap to be identical to those in the surrounding half-space, the established BEM model becomes a 3D equivalent to the 2D model in the literature. The rigidly supported 3D pile case can then be approximated by simply increasing the soil shear modulus below the pile tip until the impedances show negligible changes with further increases in modulus.

The impedance results in Veletsos and Dotson (1988) are expressed in the form:

$$\tilde{K}_w = (\tilde{K}_{st})_w(\tilde{\alpha}_w + ia_i\tilde{\beta}_w) \tag{3.38}$$

where $\tilde{K}_w$ is vertical impedance, $(\tilde{K}_{st})_w$ is the static vertical stiffness of a floating pile in a homogeneous half space, $\tilde{\alpha}_w$ and $\tilde{\beta}_w$ are dimensionless factors that depend on the relative pile and soil properties, and $(\tilde{K}_{st})_w$ is taken from Poulos and Davis (1980) as

$$(\tilde{K}_{st})_w = 30.1G_i d \tag{3.39}$$

Because the dynamic multilayered Green's functions in BEASSI are undefined at a zero frequency, the static stiffnesses were evaluated asymptotically by setting the dimensionless frequency to a suitably small value of 0.03. The resulting error in $(\tilde{K}_{st})_w$ from BEASSI relative to the value in Eqn. (3.39) was only 4%. The impedances from the 3D BEASSI analysis are compared to the 2D results of Veletsos and Dotson (1988) in Figure 3.21, in which a_i denotes dimensionless frequency. A nearly perfect agreement can be seen over the range of modulus ratios analyzed, with the only exception being the values of $\tilde{\beta}_w$ at low frequency for the rigidly supported pile case. This is due to the cut-off frequency effect (Gazetas and Makris 1991), which is captured in BEASSI. The results of this case study thus provide a validation of BEASSI's capabilities for handling horizontal inhomogeneity with the proposed 3D disturbed zone models.

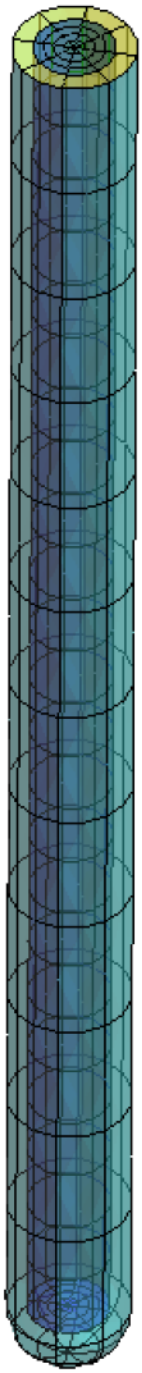

Figure 3.20 *The BEM model for reanalyzing case study by Veletsos and Dotson (1988).*

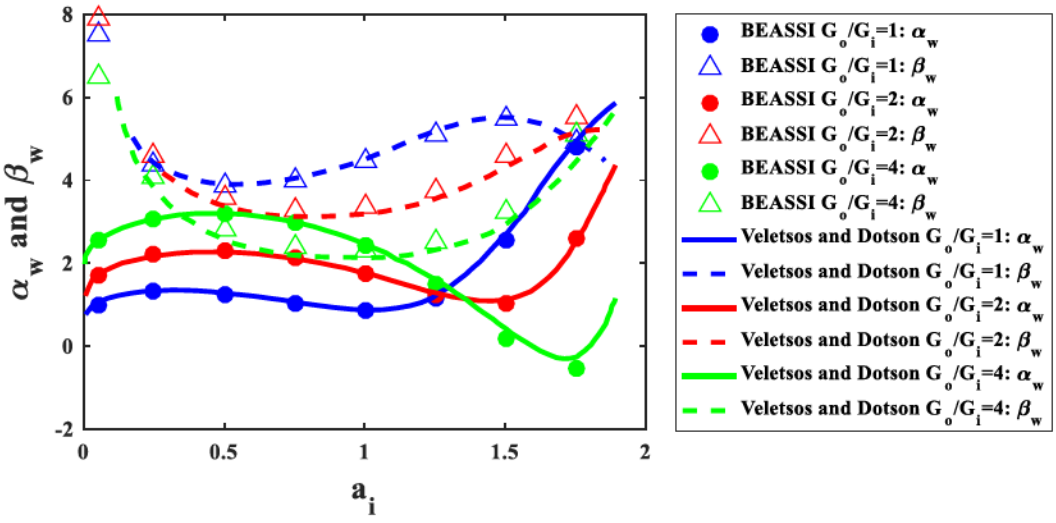

(a) Floating pile

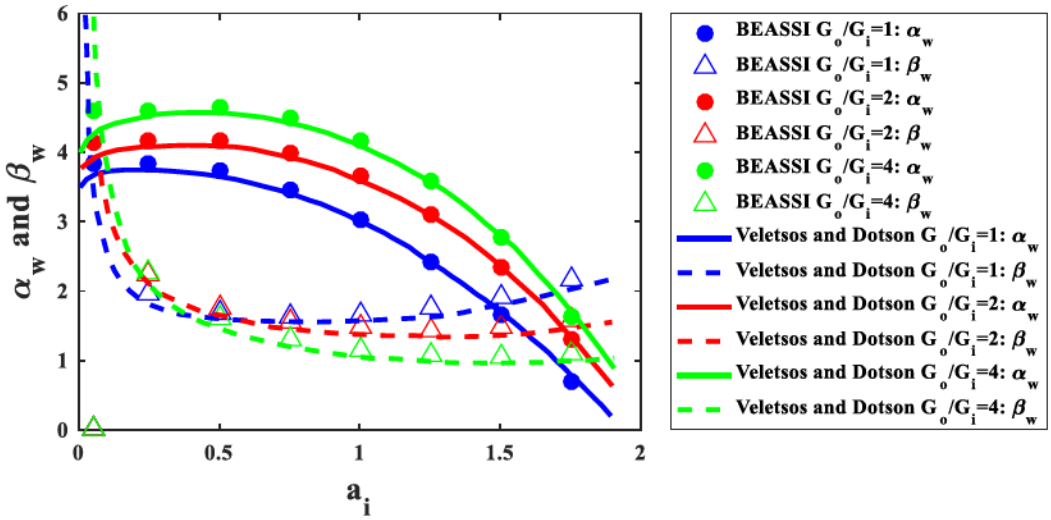

(b) Rigidly-supported pile

Figure 3.21 *Comparison of results by BEASSI and Veletsos and Dotson (1988).*

3.5 Sub-structuring Formulation for Dynamic Pile Group Problems

To analyze the full-scale tests in Chapter 2, theoretical accelerance functions must be derived. A general formulation for the dynamic response of a pile group in terms of transfer functions of directional pile-cap acceleration per unit applied force was developed by the method of sub-structuring (Ashlock and Jiang 2017). In the current study, the embedded pile segments and surrounding layered soil domains are modeled as substructure components and BEASSI is used to determine their impedance functions, while the superstructure components consist of unembedded pile segments which are analyzed as Euler-Bernoulli beam-column, and the pile cap-shaker system which is analyzed as a rigid body (the moving mass of the shaker is treated as a separate rigid body) (Figure 3.22). Once the pile impedance functions at the soil surface elevation are obtained from BEASSI, they are input to the mathematical formulation to determine the theoretical acceleration-over-force transfer functions of the soil-pile-cap system. Numerical analyses of substructure are time-consuming while analytical analyses of superstructure are fast. Therefore, instead of modeling the entire system numerically, application of method of sub-structuring can reduce scale of numerical models, and adapt impedance functions for diverse superstructures.

3.5.1 Substructure Formulation

In the frequency domain, a general elementary submatrix relating the force and moment resultants at the elevation of the ground-surface at a fixed Pile i due to 3D displacements and rotations of Pile j can be expressed as:

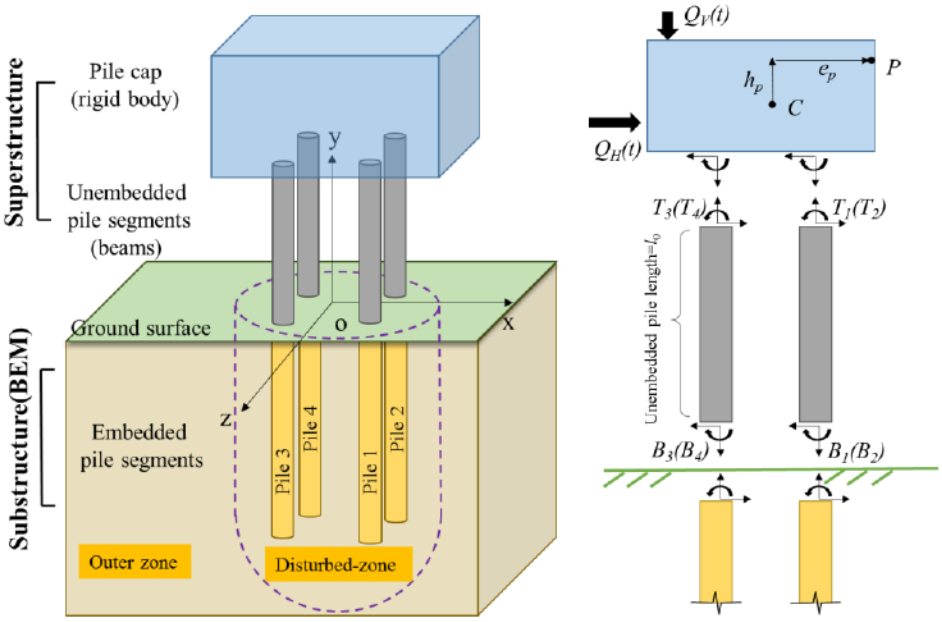

Figure 3.22 *Sub-structuring method and notation for analysis of pile group.*

$$\begin{bmatrix} F_x^{i-j} \\ F_y^{i-j} \\ F_z^{i-j} \\ M_x^{i-j} \\ M_y^{i-j} \\ M_z^{i-j} \end{bmatrix}(\omega) = \begin{bmatrix} k_{xx}^{i-j} & k_{xy}^{i-j} & k_{xz}^{i-j} & k_{xr_x}^{i-j} & k_{xr_y}^{i-j} & k_{xr_z}^{i-j} \\ k_{yx}^{i-j} & k_{yy}^{i-j} & k_{yz}^{i-j} & k_{yr_x}^{i-j} & k_{yr_y}^{i-j} & k_{yr_z}^{i-j} \\ k_{zx}^{i-j} & k_{zy}^{i-j} & k_{zz}^{i-j} & k_{zr_x}^{i-j} & k_{zr_y}^{i-j} & k_{zr_z}^{i-j} \\ k_{m_xx}^{i-j} & k_{m_xy}^{i-j} & k_{m_xz}^{i-j} & k_{m_xr_x}^{i-j} & k_{m_xr_y}^{i-j} & k_{m_xr_z}^{i-j} \\ k_{m_yx}^{i-j} & k_{m_yy}^{i-j} & k_{m_yz}^{i-j} & k_{m_yr_x}^{i-j} & k_{m_yr_y}^{i-j} & k_{m_yr_z}^{i-j} \\ k_{m_zx}^{i-j} & k_{m_zy}^{i-j} & k_{m_zz}^{i-j} & k_{m_zr_x}^{i-j} & k_{m_zr_y}^{i-j} & k_{m_zr_z}^{i-j} \end{bmatrix}(\omega) \begin{bmatrix} U_x^j \\ U_y^j \\ U_z^j \\ \Theta_x^j \\ \Theta_y^j \\ \Theta_z^j \end{bmatrix}(\omega) \qquad (3.40)$$

where the first subscript refers to force or moment with respect to x, y, or z axes of the observed Pile i, and the second subscript refers to translation or rotation with respect to the x, y, or z axes of the loaded Pile j. In this equation, all values are considered to be frequency-dependent Fourier transforms of their corresponding time-domain variables, and four local Cartesian coordinate system are considered at the top center of each individual pile. The entries of the stiffness matrix are the complex-valued impedance functions related to the particular combination of observed and loaded piles. For linear viscoelastic analysis of the soil-pile system, the pile group impedance may be obtained by linear superposition of the contributions

of the individual piles, by assembling the individual pile impedance submatrices into a global stiffness matrix as follows:

$$\begin{bmatrix} \mathbf{F}^1 \\ \mathbf{F}^2 \\ \mathbf{F}^3 \\ \mathbf{F}^4 \end{bmatrix} = \begin{bmatrix} \mathbf{K}^{1-1} & \mathbf{K}^{1-2} & \mathbf{K}^{1-3} & \mathbf{K}^{1-4} \\ \mathbf{K}^{2-1} & \mathbf{K}^{2-2} & \mathbf{K}^{2-3} & \mathbf{K}^{2-4} \\ \mathbf{K}^{3-1} & \mathbf{K}^{3-2} & \mathbf{K}^{3-3} & \mathbf{K}^{3-4} \\ \mathbf{K}^{4-1} & \mathbf{K}^{4-2} & \mathbf{K}^{4-3} & \mathbf{K}^{4-4} \end{bmatrix} \begin{bmatrix} \mathbf{U}^1 \\ \mathbf{U}^2 \\ \mathbf{U}^3 \\ \mathbf{U}^4 \end{bmatrix} \text{ or } \mathbf{F}^i = \mathbf{K}^{i-j}\mathbf{U}^j \tag{3.41}$$

where each of the 6×1 $\mathbf{F}^i$ vectors contains the forces and moments at the ground surface elevation for Pile i, and $\mathbf{U}^j$ contains the corresponding displacements and rotations for Pile j. The global stiffness matrix comprises 16 of the 6×6 elementary stiffness matrices $\mathbf{K}^{i-j}$ relating force and moment resultants at Pile i to the displacements and rotations of Pile j, which accounts for effects of pile-soil-pile interaction. The inverse of the global stiffness matrix is the global compliance matrix, which can be used to calculate displacements and rotations of each pile head for given applied forces and moments.

The global matrix in Equation (3.41) has 24×24 entries, making it massive for practical analyses. However, by taking advantage of the pile group symmetries, BEM mesh, and Green's functions for the soil and piles, the global matrix can be condensed such that displacements need to be specified at only one of the piles in the BEM analysis. In this study, all piles have identical properties, and the soil profile is axisymmetric in the half-space and has two planes of symmetry in the disturbed zone. By Betti's reciprocal theorem, the global stiffness matrix is symmetric for a linear system. Thus the elementary stiffness matrices above the main diagonal of the global matrix can be determined from their counterparts in the lower triangular part. Derivation of submatrices in lower triangle is discussed below in details. Additionally, the elementary matrices $\mathbf{K}^{2-2}$, $\mathbf{K}^{3-3}$, and $\mathbf{K}^{4-4}$ on the main diagonal can be inferred from $\mathbf{K}^{1-1}$

with proper sign changes to account for the relative positions of the local Cartesian coordinate systems at each pile head.

$$\mathbf{K}^{1\text{-}1} = \begin{bmatrix} k_{xx}^{1-1} & & & & & \\ k_{yx}^{1-1} & k_{xx}^{1-1} & & & sym. & \\ k_{zx}^{1-1} & k_{zx}^{1-1} & k_{zz}^{1-1} & & & \\ k_{m_x x}^{1-1} & -k_{m_y x}^{1-1} & k_{m_x z}^{1-1} & k_{m_y r_y}^{1-1} & & \\ k_{m_y x}^{1-1} & -k_{m_x x}^{1-1} & k_{m_y z}^{1-1} & k_{m_x r_y}^{1-1} & k_{m_y r_y}^{1-1} & \\ k_{m_z x}^{1-1} & -k_{m_z x}^{1-1} & k_{m_z z}^{1-1} & k_{m_z r_y}^{1-1} & k_{m_z r_y}^{1-1} & k_{m_z r_z}^{1-1} \end{bmatrix} \tag{3.42}$$

$$\mathbf{K}^{2\text{-}2} = \begin{bmatrix} k_{xx}^{1-1} & & & & & \\ -k_{yx}^{1-1} & k_{xx}^{1-1} & & & sym. & \\ k_{zx}^{1-1} & -k_{zx}^{1-1} & k_{zz}^{1-1} & & & \\ -k_{m_x x}^{1-1} & -k_{m_y x}^{1-1} & -k_{m_x z}^{1-1} & k_{m_y r_y}^{1-1} & & \\ k_{m_y x}^{1-1} & k_{m_x x}^{1-1} & k_{m_y z}^{1-1} & -k_{m_x r_y}^{1-1} & k_{m_y r_y}^{1-1} & \\ -k_{m_z x}^{1-1} & -k_{m_z x}^{1-1} & -k_{m_z z}^{1-1} & k_{m_z r_y}^{1-1} & -k_{m_z r_y}^{1-1} & k_{m_z r_z}^{1-1} \end{bmatrix} \tag{3.43}$$

$$\mathbf{K}^{3\text{-}3} = \begin{bmatrix} k_{xx}^{1-1} & & & & & \\ -k_{yx}^{1-1} & k_{xx}^{1-1} & & & sym. & \\ -k_{zx}^{1-1} & k_{zx}^{1-1} & k_{zz}^{1-1} & & & \\ -k_{m_x x}^{1-1} & -k_{m_y x}^{1-1} & k_{m_x z}^{1-1} & k_{m_y r_y}^{1-1} & & \\ k_{m_y x}^{1-1} & k_{m_x x}^{1-1} & -k_{m_y z}^{1-1} & -k_{m_x r_y}^{1-1} & k_{m_y r_y}^{1-1} & \\ k_{m_z x}^{1-1} & k_{m_z x}^{1-1} & -k_{m_z z}^{1-1} & -k_{m_z r_y}^{1-1} & k_{m_z r_y}^{1-1} & k_{m_z r_z}^{1-1} \end{bmatrix} \tag{3.44}$$

$$\mathbf{K}^{4\text{-}4} = \begin{bmatrix} k_{xx}^{1-1} & & & & & \\ k_{yx}^{1-1} & k_{xx}^{1-1} & & & sym. & \\ -k_{zx}^{1-1} & -k_{zx}^{1-1} & k_{zz}^{1-1} & & & \\ k_{m_x x}^{1-1} & -k_{m_y x}^{1-1} & -k_{m_x z}^{1-1} & k_{m_y r_y}^{1-1} & & \\ k_{m_y x}^{1-1} & -k_{m_x x}^{1-1} & k_{m_x z}^{1-1} & k_{m_x r_y}^{1-1} & k_{m_y r_y}^{1-1} & \\ -k_{m_z x}^{1-1} & k_{m_z x}^{1-1} & k_{m_z z}^{1-1} & -k_{m_z r_y}^{1-1} & -k_{m_z r_y}^{1-1} & k_{m_z r_z}^{1-1} \end{bmatrix} \tag{3.45}$$

Within each elementary matrix, number of independent entries can be further reduced by considering the symmetry of the pile group. For example, with uniform spacing in the

horizontal directions, the influence of Pile 3 on Pile 1 is symmetric to that of Pile 2 on Pile 1. Thus $\mathbf{K}^{3-1}$ can be inferred from $\mathbf{K}^{2-1}$ by applying an appropriate coordinate transformation matrix. Similarly, $\mathbf{K}^{3-2}$ is associated with $\mathbf{K}^{4-1}$ by mirroring with respect to the vertical x-z plane of the substructure coordinate system. Finally, $\mathbf{K}^{4-2}$ is equivalent to $\mathbf{K}^{3-1}$ and $\mathbf{K}^{4-3}$ is equivalent to $\mathbf{K}^{2-1}$ by mirroring with respect to the x-z and y-z, respectively. In theory, the entries of four columns in the global matrix (a total of 96 elements) are sufficient to derive the remaining entries. However, the actual numerical results may not strictly satisfy such symmetry due to discretization and interpolation errors and accumulation of round-off errors in the BEM, which are amplified by increasing frequency. 6-domain models show greater deviations than 5-domain models.

$$\mathbf{K}^{2\text{-}1} = \begin{bmatrix} k_{xx}^{2-1} & k_{yx}^{3-1} & k_{xz}^{2-1} & -k_{yr_y}^{3-1} & k_{xr_y}^{2-1} & k_{xr_z}^{2-1} \\ k_{yx}^{2-1} & k_{xx}^{3-1} & k_{yz}^{2-1} & -k_{xr_y}^{3-1} & k_{yr_y}^{2-1} & k_{yr_z}^{2-1} \\ k_{zx}^{2-1} & k_{zx}^{3-1} & k_{zz}^{2-1} & -k_{zr_y}^{3-1} & k_{zr_y}^{2-1} & k_{zr_z}^{2-1} \\ k_{m_x x}^{2-1} & -k_{m_y x}^{3-1} & k_{m_x z}^{2-1} & k_{m_y r_y}^{3-1} & k_{m_x r_y}^{2-1} & k_{m_x r_z}^{2-1} \\ k_{m_y x}^{2-1} & -k_{m_x x}^{3-1} & k_{m_y z}^{2-1} & k_{m_x r_y}^{3-1} & k_{m_y r_y}^{2-1} & k_{m_y r_z}^{2-1} \\ k_{m_z x}^{2-1} & -k_{m_z x}^{3-1} & k_{m_z z}^{2-1} & k_{m_z r_y}^{3-1} & k_{m_z r_y}^{2-1} & k_{m_z r_z}^{2-1} \end{bmatrix} \tag{3.46}$$

$$\mathbf{K}^{3\text{-}1} = \begin{bmatrix} k_{xx}^{3-1} & k_{yx}^{2-1} & k_{xz}^{3-1} & -k_{yr_y}^{2-1} & k_{xr_y}^{3-1} & k_{xr_z}^{3-1} \\ k_{yx}^{3-1} & k_{xx}^{2-1} & k_{yz}^{3-1} & -k_{xr_y}^{2-1} & k_{yr_y}^{3-1} & k_{yr_z}^{3-1} \\ k_{zx}^{3-1} & k_{zx}^{2-1} & k_{zz}^{3-1} & -k_{zr_y}^{2-1} & k_{zr_y}^{3-1} & k_{zr_z}^{3-1} \\ k_{m_x x}^{3-1} & -k_{m_y x}^{2-1} & k_{m_x z}^{3-1} & k_{m_y r_y}^{2-1} & k_{m_x r_y}^{3-1} & k_{m_x r_z}^{3-1} \\ k_{m_y x}^{3-1} & -k_{m_x x}^{2-1} & k_{m_y z}^{3-1} & k_{m_x r_y}^{2-1} & k_{m_y r_y}^{3-1} & k_{m_y r_z}^{3-1} \\ k_{m_z x}^{3-1} & -k_{m_z x}^{2-1} & k_{m_z z}^{3-1} & k_{m_z r_y}^{2-1} & k_{m_z r_y}^{3-1} & k_{m_z r_z}^{3-1} \end{bmatrix} \tag{3.47}$$

$$\mathbf{K}^{4\text{-}1} = \begin{bmatrix} k_{xx}^{4-1} & k_{yx}^{4-1} & k_{xz}^{4-1} & -k_{yr_y}^{4-1} & k_{xr_y}^{4-1} & k_{xr_z}^{4-1} \\ k_{yx}^{4-1} & k_{xx}^{4-1} & k_{yz}^{4-1} & -k_{xr_y}^{4-1} & k_{yr_y}^{4-1} & k_{yr_z}^{4-1} \\ k_{zx}^{4-1} & k_{zx}^{4-1} & k_{zz}^{4-1} & -k_{zr_y}^{4-1} & k_{zr_y}^{4-1} & k_{zr_z}^{4-1} \\ k_{m_xx}^{4-1} & -k_{m_yx}^{4-1} & k_{m_xz}^{4-1} & k_{m_yr_y}^{4-1} & k_{m_xr_y}^{4-1} & k_{m_xr_z}^{4-1} \\ k_{m_yx}^{4-1} & -k_{m_xx}^{4-1} & k_{m_yz}^{4-1} & k_{m_xr_y}^{4-1} & k_{m_yr_y}^{4-1} & k_{m_yr_z}^{4-1} \\ k_{m_zx}^{4-1} & -k_{m_zx}^{4-1} & k_{m_zz}^{4-1} & k_{m_zr_y}^{4-1} & k_{m_zr_y}^{4-1} & k_{m_zr_z}^{4-1} \end{bmatrix} \tag{3.48}$$

$$\mathbf{K}^{3\text{-}2} = \begin{bmatrix} k_{xx}^{4-1} & -k_{yx}^{4-1} & k_{xz}^{4-1} & k_{yr_y}^{4-1} & k_{xr_y}^{4-1} & -k_{xr_z}^{4-1} \\ -k_{yx}^{4-1} & k_{xx}^{4-1} & -k_{yz}^{4-1} & -k_{xr_y}^{4-1} & -k_{yr_y}^{4-1} & k_{yr_z}^{4-1} \\ k_{zx}^{4-1} & -k_{zx}^{4-1} & k_{zz}^{4-1} & k_{zr_y}^{4-1} & k_{zr_y}^{4-1} & -k_{zr_z}^{4-1} \\ -k_{m_xx}^{4-1} & -k_{m_yx}^{4-1} & -k_{m_xz}^{4-1} & k_{m_yr_y}^{4-1} & -k_{m_xr_y}^{4-1} & k_{m_xr_z}^{4-1} \\ k_{m_yx}^{4-1} & k_{m_xx}^{4-1} & k_{m_yz}^{4-1} & -k_{m_xr_y}^{4-1} & k_{m_yr_y}^{4-1} & -k_{m_yr_z}^{4-1} \\ -k_{m_zx}^{4-1} & -k_{m_zx}^{4-1} & -k_{m_zz}^{4-1} & k_{m_zr_y}^{4-1} & -k_{m_zr_y}^{4-1} & k_{m_zr_z}^{4-1} \end{bmatrix} \tag{3.49}$$

$$\mathbf{K}^{4\text{-}2} = \begin{bmatrix} k_{xx}^{3-1} & -k_{yx}^{2-1} & k_{xz}^{3-1} & k_{yr_y}^{2-1} & k_{xr_y}^{3-1} & -k_{xr_z}^{3-1} \\ -k_{yx}^{3-1} & k_{xx}^{2-1} & -k_{yz}^{3-1} & -k_{xr_y}^{2-1} & -k_{yr_y}^{3-1} & k_{yr_z}^{3-1} \\ k_{zx}^{3-1} & -k_{zx}^{2-1} & k_{zz}^{3-1} & k_{zr_y}^{2-1} & k_{zr_y}^{3-1} & -k_{zr_z}^{3-1} \\ -k_{m_xx}^{3-1} & -k_{m_yx}^{2-1} & -k_{m_xz}^{3-1} & k_{m_yr_y}^{2-1} & -k_{m_xr_y}^{3-1} & k_{m_xr_z}^{3-1} \\ k_{m_yx}^{3-1} & k_{m_xx}^{2-1} & k_{m_yz}^{3-1} & -k_{m_xr_y}^{2-1} & k_{m_yr_y}^{3-1} & -k_{m_yr_z}^{3-1} \\ -k_{m_zx}^{3-1} & -k_{m_zx}^{2-1} & -k_{m_zz}^{3-1} & k_{m_zr_y}^{2-1} & -k_{m_zr_y}^{3-1} & k_{m_zr_z}^{3-1} \end{bmatrix} \tag{3.50}$$

$$\mathbf{K}^{4\text{-}3} = \begin{bmatrix} k_{xx}^{2-1} & -k_{yx}^{3-1} & -k_{xz}^{2-1} & k_{yr_y}^{3-1} & k_{xr_y}^{2-1} & k_{xr_z}^{2-1} \\ -k_{yx}^{2-1} & k_{xx}^{3-1} & k_{yz}^{2-1} & -k_{xr_y}^{3-1} & -k_{yr_y}^{2-1} & -k_{yr_z}^{2-1} \\ -k_{zx}^{2-1} & k_{zx}^{3-1} & k_{zz}^{2-1} & -k_{zr_y}^{3-1} & -k_{zr_y}^{2-1} & -k_{zr_z}^{2-1} \\ -k_{m_xx}^{2-1} & -k_{m_yx}^{3-1} & k_{m_xz}^{2-1} & k_{m_yr_y}^{3-1} & -k_{m_xr_y}^{2-1} & -k_{m_xr_z}^{2-1} \\ k_{m_yx}^{2-1} & k_{m_xx}^{3-1} & -k_{m_yz}^{2-1} & -k_{m_xr_y}^{3-1} & k_{m_yr_y}^{2-1} & k_{m_yr_z}^{2-1} \\ k_{m_zx}^{2-1} & k_{m_zx}^{3-1} & -k_{m_zz}^{2-1} & -k_{m_zr_y}^{3-1} & k_{m_zr_y}^{2-1} & k_{m_zr_z}^{2-1} \end{bmatrix} \tag{3.51}$$

To validate the above derivations, a global stiffness matrix for a 5-domain model was assembled by displacing each individual pile. Pile and soil properties listed in Table 3.10 and

$\bar{\omega} = 0.05$ were used. The numerical results conform to the above theoretical derivation in good sense (Figure 3.23)

As an alternative, the validation was implemented by comparing the impedance of a 2×2 pile group with a fictitious rigid pile cap at ground level by the derivations and direct analysis. The assembled global impedance matrix was multiplied by a displacement vector to obtain resultant forces at each pile head. For horizontal vibration of the pile cap, the displacement vectors for each pile are:

$$\mathbf{U}^1 = \mathbf{U}^2 = \mathbf{U}^3 = \mathbf{U}^4 = \begin{bmatrix} 1 & 0 & 0 & 0 & 0 & 0 \end{bmatrix}^T \tag{3.52}$$

Adding up horizontal resultant forces at head of all piles - F_x^1, F_x^2, F_x^3 and F_x^4, is the horizontal impedance of the pile group. Similar displacement vectors were applied for vertical, rocking, and torsional vibration of the pile cap,

vertical:

$$\mathbf{U}^1 = \mathbf{U}^2 = \mathbf{U}^3 = \mathbf{U}^4 = \begin{bmatrix} 0 & 0 & 1 & 0 & 0 & 0 \end{bmatrix}^T$$

rocking:

$$\mathbf{U}^1 = \mathbf{U}^2 = \begin{bmatrix} 0 & 0 & -S_x/2 & 0 & 1 & 0 \end{bmatrix}^T$$
$$\mathbf{U}^3 = \mathbf{U}^4 = \begin{bmatrix} 0 & 0 & S_x/2 & 0 & 1 & 0 \end{bmatrix}^T$$

torsional:

$$\mathbf{U}^1 = \begin{bmatrix} -S_x/2 & S_y/2 & 0 & 0 & 0 & 1 \end{bmatrix}^T$$
$$\mathbf{U}^2 = \begin{bmatrix} S_x/2 & S_y/2 & 0 & 0 & 0 & 1 \end{bmatrix}^T$$
$$\mathbf{U}^3 = \begin{bmatrix} -S_x/2 & -S_y/2 & 0 & 0 & 0 & 1 \end{bmatrix}^T$$
$$\mathbf{U}^4 = \begin{bmatrix} S_x/2 & -S_y/2 & 0 & 0 & 0 & 1 \end{bmatrix}^T$$

where S_x and S_y are pile spacings in x and y directions, respectively.

F_{x1}^{1}		22.349	0.583	-0.217	-0.779	35.934	0.698	-4.048	-0.340	-0.181	0.308	-5.633	2.101	-8.191	0.340	1.400	-0.383	-10.749	0.530	-2.419	-1.110	0.287	1.381	-3.851	0.247		u_{x1}^{1}
F_{y1}^{1}		0.583	22.348	-0.229	-35.900	0.779	-0.711	0.340	-8.190	1.396	10.738	0.383	-0.528	-0.340	-4.049	-0.179	5.629	-0.308	-2.102	-1.110	-2.419	0.286	3.847	-1.382	-0.247		u_{y1}^{1}
F_{z1}^{1}		-0.216	-0.229	50.535	-0.816	0.873	0.000	-0.182	-1.396	-15.112	-0.280	0.484	-0.109	-1.400	-0.179	-15.113	-0.489	0.276	0.111	-0.286	-0.285	-6.292	-0.095	0.094	0.000		u_{z1}^{1}
M_{x1}^{1}		-0.780	-35.956	-0.813	142.019	-1.102	0.957	-0.310	10.763	0.270	-16.819	-0.493	0.756	0.384	5.635	-0.487	-10.158	0.493	2.618	1.385	3.853	0.094	-7.061	1.994	0.405		θ_{x1}^{1}
M_{y1}^{1}		35.990	0.781	0.870	-1.102	142.287	0.953	-5.640	-0.385	0.482	0.493	-10.176	2.620	-10.774	0.310	-0.266	-0.494	-16.852	0.760	-3.857	-1.386	-0.092	1.994	-7.074	0.405		θ_{y1}^{1}
M_{z1}^{1}		0.698	-0.710	0.000	0.955	0.952	52.812	-2.101	-0.528	0.109	0.755	-2.615	0.448	0.530	2.101	-0.111	-2.613	0.758	0.447	-0.247	0.247	0.000	-0.405	-0.405	0.072		θ_{z1}^{1}
F_{x2}^{2}		-4.048	0.340	-0.181	-0.308	-5.633	-2.101	22.349	-0.583	-0.217	0.779	35.934	-0.698	-2.419	1.110	0.287	-1.381	-3.851	-0.247	-8.191	-0.340	1.400	0.383	-10.749	-0.530		u_{x2}^{2}
F_{y2}^{2}		-0.340	-8.1902	-1.396	10.738	-0.383	-0.528	-0.583	22.348	0.229	-35.900	-0.779	-0.711	1.110	-2.419	-0.286	3.847	1.382	-0.247	0.340	-4.049	0.179	5.629	0.308	-2.102		u_{y2}^{2}
F_{z2}^{2}		-0.182	1.3965	-15.112	0.280	0.484	0.109	-0.216	0.229	50.535	0.816	0.873	0.000	-0.286	0.285	-6.292	0.095	0.094	0.000	-1.400	0.179	-15.113	0.489	0.276	-0.111		u_{z2}^{2}
M_{x2}^{2}		0.310	10.763	-0.270	-16.819	0.493	0.756	0.780	-35.956	0.813	142.019	1.102	0.957	-1.385	3.853	-0.094	-7.061	-1.994	0.405	-0.384	5.635	0.487	-10.158	-0.493	2.618		θ_{x2}^{2}
M_{y2}^{2}		-5.640	0.3847	0.482	-0.493	-10.176	-2.620	35.990	-0.781	0.870	1.102	142.287	-0.953	-3.857	1.386	-0.092	-1.994	-7.074	-0.405	-10.774	-0.310	-0.266	0.494	-16.852	-0.760		θ_{y2}^{2}
M_{z2}^{2}	=	2.101	-0.5281	-0.109	0.755	2.615	0.448	-0.698	-0.710	0.000	0.955	-0.952	52.812	0.247	0.247	0.000	-0.405	0.405	0.072	-0.530	2.101	0.111	-2.613	-0.758	0.447	×	θ_{z2}^{2}
F_{x3}^{3}		-8.191	-0.340	-1.400	0.383	-10.749	0.530	-2.419	1.110	-0.287	-1.381	-3.851	0.247	22.349	-0.583	0.217	0.779	35.934	0.698	-4.048	0.340	0.181	-0.308	-5.633	2.101		u_{x3}^{3}
F_{y3}^{3}		0.340	-4.049	-0.179	5.629	0.308	2.102	1.110	-2.419	0.286	3.847	1.382	0.247	-0.583	22.348	-0.229	-35.900	-0.779	0.711	-0.340	-8.190	1.396	10.738	-0.383	0.528		u_{y3}^{3}
F_{z3}^{3}		1.400	-0.179	-15.113	-0.489	-0.276	-0.111	0.286	-0.285	-6.292	-0.095	-0.094	0.000	0.216	-0.229	50.535	-0.816	-0.873	0.000	0.182	-1.396	-15.112	-0.280	-0.484	0.109		u_{z3}^{3}
M_{x3}^{3}		-0.384	5.635	-0.487	-10.158	-0.493	-2.618	-1.385	3.853	0.094	-7.061	-1.994	-0.405	0.780	-35.956	-0.813	142.019	1.102	-0.957	0.310	10.763	0.270	-16.819	0.493	-0.756		θ_{x3}^{3}
M_{y3}^{3}		-10.774	-0.310	0.266	0.494	-16.852	0.760	-3.857	1.386	0.092	-1.994	-7.074	0.405	35.990	-0.781	-0.870	1.102	142.287	0.953	-5.640	0.385	-0.482	-0.493	-10.176	2.620		θ_{y3}^{3}
M_{z3}^{3}		0.530	-2.101	0.111	2.613	0.758	0.447	-0.247	-0.247	0.000	0.405	-0.405	0.072	0.698	0.710	0.000	-0.955	0.952	52.812	-2.101	0.528	-0.109	-0.755	-2.615	0.448		θ_{z3}^{3}
F_{x4}^{4}		-2.419	-1.110	-0.287	1.381	-3.851	-0.247	-8.191	0.340	-1.400	-0.383	-10.749	-0.530	-4.048	-0.340	0.181	0.308	-5.633	-2.101	22.349	0.583	0.217	-0.779	35.934	-0.698		u_{x4}^{4}
F_{y4}^{4}		-1.110	-2.419	-0.286	3.847	-1.382	0.247	-0.340	-4.049	0.179	5.629	-0.308	2.102	0.340	-8.190	-1.396	10.738	0.383	0.528	0.583	22.348	0.229	-35.900	0.779	0.711		u_{y4}^{4}
F_{z4}^{4}		0.286	0.285	-6.292	0.095	-0.094	0.000	1.400	0.179	-15.113	0.489	-0.276	0.111	0.182	1.396	-15.112	0.280	-0.484	-0.109	0.216	0.229	50.535	0.816	-0.873	0.000		u_{z4}^{4}
M_{x4}^{4}		1.385	3.853	-0.094	-7.061	1.994	-0.405	0.384	5.635	0.487	-10.158	0.493	-2.618	-0.310	10.763	-0.270	-16.819	-0.493	-0.756	-0.780	-35.956	0.813	142.019	-1.102	-0.957		θ_{x4}^{4}
M_{y4}^{4}		-3.857	-1.386	0.092	1.994	-7.074	-0.405	-10.774	0.310	0.266	-0.494	-16.852	-0.760	-5.640	-0.385	-0.482	0.493	-10.176	-2.620	35.990	0.781	-0.870	-1.102	142.287	-0.953		θ_{y4}^{4}
M_{z4}^{4}		0.247	-0.247	0.000	0.405	0.405	0.072	-0.530	-2.101	-0.111	2.613	-0.758	0.447	2.101	0.528	0.109	-0.755	2.615	0.448	-0.698	0.710	0.000	-0.955	-0.952	52.812		θ_{z4}^{4}

Figure 3.23 *Derived global stiffness matrix by direct analysis.*

As a comparison, reference solutions of vertical and horizontal impedances of the pile group can be directly analyzed by BEASSI, prescribing simultaneous unit displacements or rotation to the rigid pile cap. Then the stiffness and damping of pile group is the resultant force or moment integrated over all pile heads. To this end, both 5-domain and 6-domain models were analyzed, which suggests favorable agreement (Figure 3.24 and Figure 3.25). It can be concluded that the assembly of global impedance matrix by symmetry for substructure is reliable.

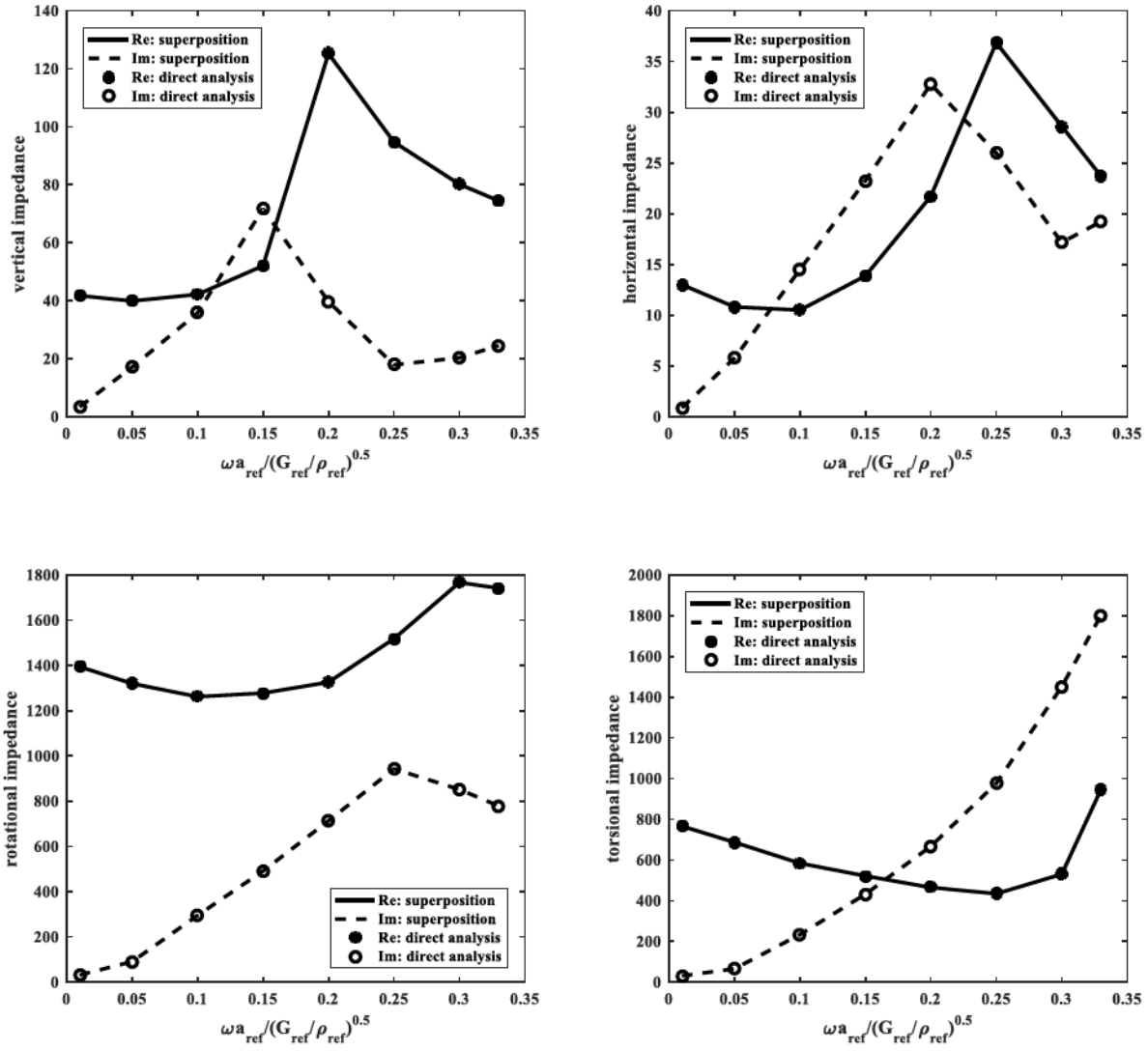

Figure 3.24 *Group impedances in vertical, horizontal, rocking, and torsional directions for 5-domain model by superposition and direct analysis.*

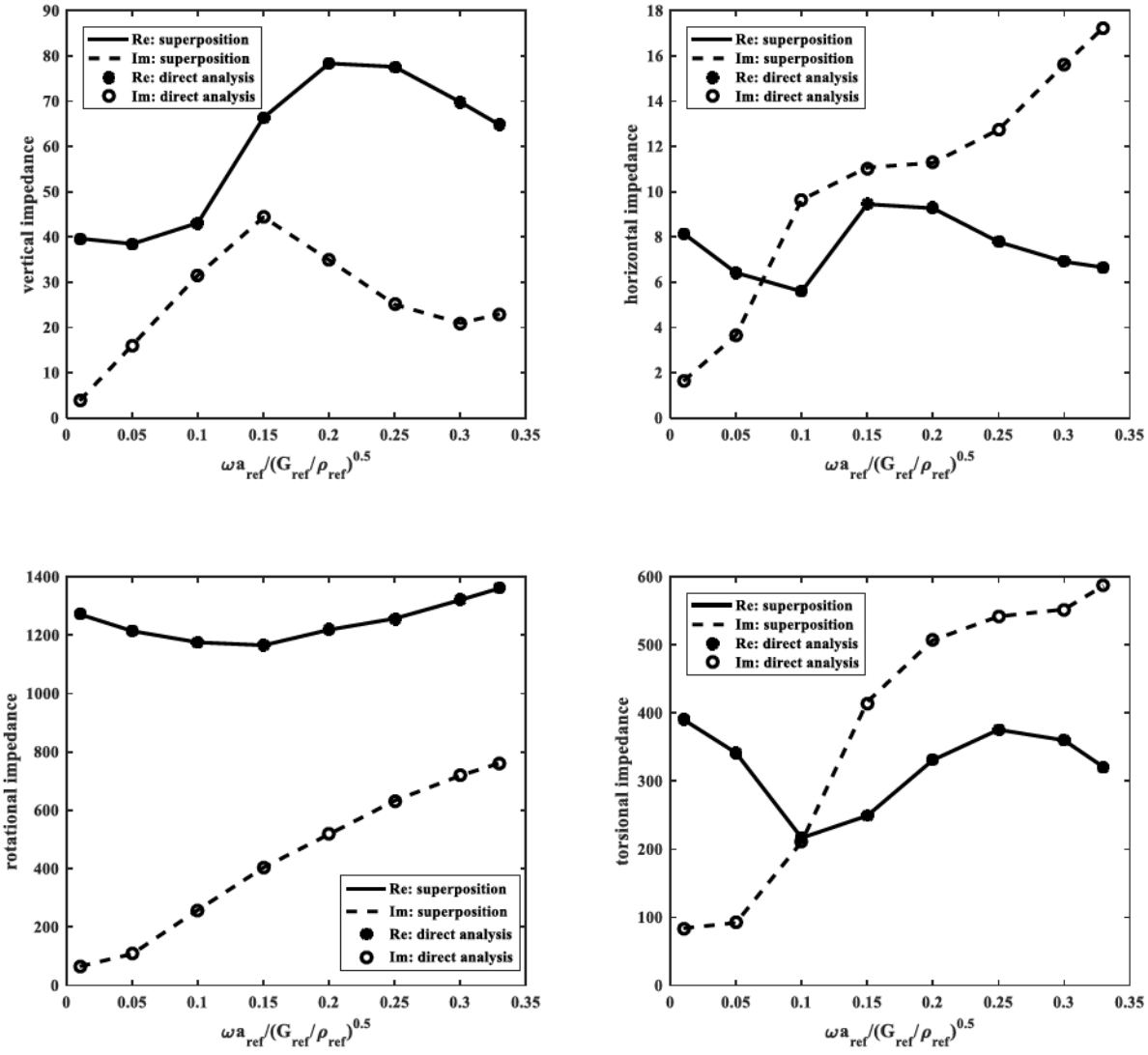

Figure 3.25 *Group impedances in vertical, horizontal, rocking, and torsional directions for 6-domain model by superposition and direct analysis.*

El-Marsafawi et al. (1992) applied superposition through dynamic interaction factor, which was derived on two-pile cases. Numerical tests on a 3×3 pile group indicated discrepancies at high frequencies between the superposition and the direct methods. In this study, all elementary submatrices are derived with presence of all piles.

3.5.2 Superstructure Formulation

In the present analysis, the acceleration response is desired at an arbitrary point P (x_p, y_p, z_p) on the pile cap. For planar motion, the displacement and force vectors at P can be simplified to:

$$\mathbf{U}(P)=\begin{bmatrix} U_y(x_p,y_p) \\ U_x(x_p,y_p) \\ \Theta_z(x_p,y_p) \end{bmatrix} \quad \text{and} \quad \mathbf{F}(P)=\begin{bmatrix} F_y(x_p,y_p) \\ F_x(x_p,y_p) \\ M_z(x_p,y_p) \end{bmatrix}$$

where the superstructure coordinate system of Figure 3.22 is adopted for simplicity. For rigid body motion of the pile cap, the displacement of point P can be related to that of the centroid point C through

$$\mathbf{U}(P)=\mathbf{T}_{PC}\mathbf{U}(\mathrm{C}), \text{ where } \mathbf{T}_{PC}=\mathbf{T}_{CP}^{-1}=\begin{bmatrix} 1 & 0 & e_p \\ 0 & 1 & -h_p \\ 0 & 0 & 1 \end{bmatrix} \tag{3.53}$$

In Equation (3.54), $\mathbf{T}_{PC}$ is a 3×3 kinematic transformation matrix containing the horizontal eccentricity $e_P=x_P-x_C$ and height $h_P=y_P-y_C$ of point P with respect to the centroid of the cap-shaker system. Eliminating $\mathbf{U}(C)$ by setting P equal to points T_1 and T_3 gives the displacement compatibility condition for rigid body motion of the pile cap as:

$$\mathbf{T}_{T_1C}^{-1}\mathbf{U}(T_1)-\mathbf{T}_{T_3C}^{-1}\mathbf{U}(T_3)=0 \tag{3.54}$$

Dynamic force and moment equilibrium for planar motion of the pile cap then give the three equations of motion:

$$-Q_V-F_y(T_1)-F_y(T_2)-F_y(T_3)-F_y(T_4)=-m\omega^2U_y(C) \tag{3.55}$$

$$Q_H-F_x(T_1)-F_x(T_2)-F_x(T_3)-F_x(T_4)=-m\omega^2U_x(C) \tag{3.56}$$

$$
\begin{aligned}
&-Q_V e_v - Q_H h_H - [F_y(T_1) + F_y(T_2)]e_{T_1} - [F_y(T_3) + F_y(T_4)]e_{T_3} \\
&-[F_x(T_1) + F_x(T_2)](-h_{T_1}) - [F_x(T_3) + F_x(T_4)](-h_{T_3}) \\
&-M_z(T_1) - M_z(T_2) - M_z(T_3) - M_z(T_4) = -J\omega^2\Theta_z(C)
\end{aligned} \tag{3.57}
$$

where m and J are the mass and centroidal polar mass moment of inertia of the pile cap; ω is circular frequency; and U, Θ, F and M denote Fourier transforms of the centroidal displacement and rotation, and forces and moments displacement, and rotation quantities at the pile heads. The three equations of motion can above be expressed in matrix-vector form as

$$
\mathbf{Q} - \mathbf{T}_{T_1C}^T[\mathbf{F}(T_1) + \mathbf{F}(T_2)] - \mathbf{T}_{T_3C}^T[\mathbf{F}(T_3) + \mathbf{F}(T_4)] = -\omega^2\mathbf{M}\mathbf{U}(C) \tag{3.58}
$$

where $\mathbf{Q} = \begin{bmatrix} -Q_V \\ Q_H \\ (-Q_V e_V - Q_H e_H) \end{bmatrix}$ is the external forcing vector, $\mathbf{F} = \begin{bmatrix} F_y \\ F_x \\ M_z \end{bmatrix}$ is the vector of forces and moments at the pile head, and $\mathbf{M} = \begin{bmatrix} m & 0 & 0 \\ 0 & m & 0 \\ 0 & 0 & J \end{bmatrix}$. By symmetry, $\mathbf{F}(T_1) = \mathbf{F}(T_2)$ and $\mathbf{F}(T_3) = \mathbf{F}(T_4)$ and the equations of motion can therefore be simplified to

$$
-\omega^2\mathbf{M}\mathbf{T}_{CT_1}\mathbf{U}(T_1) + 2\mathbf{T}_{T_1C}^T\mathbf{F}(T_1) + 2\mathbf{T}_{T_3C}^T\mathbf{F}(T_3) = \mathbf{Q} \tag{3.59}
$$

The governing differential equations of motion for the axial and bending deformation of the unembedded pile segments can be expressed in the frequency domain as:

$$
\frac{d^2U_y(y,\omega)}{dy^2} + \left(\frac{\omega}{C_p}\right)^2 U_y(y,\omega) = 0, \text{ where } F_y(y,\omega) = E_P A_P \frac{dU_y(y,\omega)}{dy} \tag{3.60}
$$

$$F_y(y,\omega) = E_P A_P \frac{dU_y(y,\omega)}{dy} \tag{3.61}$$

and

$$\frac{d^4 U_x(y,\omega)}{dy^4} - \beta^4 U_x(y,\omega) = 0 \tag{3.62}$$

where $C_P = \sqrt{E_P / \rho_p}$ is one-dimensional primary wave velocity of the pile and

$$\beta^4 \equiv \omega^2 \frac{\rho_p A_p}{E_p I_p} \tag{3.63}$$

The general solutions to the wave equations (3.62) and (3.62) can be obtained in terms of six undetermined coefficients $\mathbf{C} = [\mathrm{C}_1, ..., C_6]^T$ as in Ashlock (2006)

$$\begin{cases} U_y(y,w) = c_1 \sin(\alpha y) + c_2 \cos(\alpha y) \\ F_y(y,w) = E_P A_p \alpha [c_1 \cos(\alpha y) - c_2 \sin(\alpha y)] \end{cases} \tag{3.64}$$

$$\begin{cases} U_x(y,w) = c_3 \sin(\beta y) + c_4 \cos(\beta y) + c_5 e^{-\beta y} + c_6 e^{\beta(y-l_0)} \\ \Theta(y,w) = -\beta c_3 \cos(\beta y) + \beta c_4 \sin(\beta y) + \beta c_5 e^{-\beta y} - \beta c_6 e^{\beta(y-l_o)} \\ M(y,w) = E_P I_P \beta^2 c_3 \sin(\beta y) + E_P I_P \beta^2 c_4 \cos(\beta y) - E_P I_P \beta^2 c_5 e^{-\beta y} - E_P I_P \beta^2 c_6 e^{\beta(y-l_o)} \\ F_x(y,w) = E_P I_P \beta^3 c_3 \cos(\beta y) - E_P I_P \beta^3 c_4 \sin(\beta y) + E_P I_P \beta^3 c_5 e^{-\beta y} - E_P I_P \beta^3 c_6 e^{\beta(y-l_o)} \end{cases}$$

(3.65)

and expressed for any point $P = (x_p, 0 \le y_p \le l_0)$ along one of the unembedded pile segments as

$$\mathbf{S}(P)\mathbf{C} = \begin{bmatrix} \mathbf{U}^T(P) \\ \mathbf{F}^T(P) \end{bmatrix} \tag{3.66}$$

where

$$\mathbf{S}(P)=\begin{bmatrix} \sin(\alpha\, y_p) & \cos(\alpha\, y_p) & 0 \\ 0 & 0 & \sin(\beta\, y_p) \\ 0 & 0 & -\beta\cos(\beta\, y_p) \\ E_pA_p\alpha\cos(\alpha\, y_p) & -E_pA_p\alpha\sin(\alpha\, y_p) & 0 \\ 0 & 0 & E_pI_p\beta^3\cos(\beta\, y_p) \\ 0 & 0 & E_pI_p\beta^2\sin(\beta\, y_p) \end{bmatrix} \begin{bmatrix} 0 & 0 & 0 \\ \cos(\beta\, y_p) & e^{-\beta y_p} & e^{\beta(y_p-l_o)} \\ \beta\sin(\beta\, y_p) & \beta e^{-\beta y_p} & -\beta e^{\beta(y_p-l_o)} \\ 0 & 0 & 0 \\ -E_pI_p\beta^3\sin(\beta\, y_p) & E_pI_p\beta^3 e^{-\beta y_p} & -E_pI_p\beta^3 e^{\beta(y_p-l_o)} \\ E_pI_p\beta^2\cos(\beta\, y_p) & -E_pI_p\beta^2 e^{-\beta y_p} & -E_pI_p\beta^2 e^{\beta(y_p-l_o)} \end{bmatrix} \tag{3.67}$$

and $\alpha \equiv \omega / C_P$. The coefficients $\mathbf{C}$ can be eliminated by relating the beam-column wave equation solutions in Equation (3.66) at the top and bottom of the un-embedded pile segments. For Pile 1 and Pile 2, this can be written as

$$\mathbf{S}^{-1}(T_1)\begin{bmatrix}\mathbf{U}(T_1)\\ \mathbf{F}(T_1)\end{bmatrix}=\mathbf{S}^{-1}(B_1)\begin{bmatrix}\mathbf{U}(B_1)\\ \mathbf{F}(B_1)\end{bmatrix} \tag{3.68}$$

Similarly, for Piles 3 and 4:

$$\mathbf{S}^{-1}(T_3)\begin{bmatrix}\mathbf{U}(T_3)\\ \mathbf{F}(T_3)\end{bmatrix}=\mathbf{S}^{-1}(B_3)\begin{bmatrix}\mathbf{U}(B_3)\\ \mathbf{F}(B_3)\end{bmatrix} \tag{3.69}$$

For the planar motion under consideration, the forces and moments vectors at the ground level can be expressed in terms of the impedance functions obtained from the BEM substructure analysis as:

$$\begin{cases}\mathbf{F}(B_1)=\left[\mathbf{K}^{1-1}(\omega)+\mathbf{K}^{1-2}(\omega)\right]\mathbf{U}(B_1)+\left[\mathbf{K}^{1-3}(\omega)+\mathbf{K}^{1-4}(\omega)\right]\mathbf{U}(B_3)\\ \mathbf{F}(B_3)=\left[\mathbf{K}^{3-1}(\omega)+\mathbf{K}^{3-2}(\omega)\right]\mathbf{U}(B_1)+\left[\mathbf{K}^{3-3}(\omega)+\mathbf{K}^{3-4}(\omega)\right]\mathbf{U}(B_3)\end{cases} \tag{3.70}$$

where $\mathbf{U}(B_1)=\mathbf{U}(B_2)$ and $\mathbf{U}(B_3)=\mathbf{U}(B_4)$ by symmetry, and only the impedances relevant to motion in the superstructure's *x*-*y* plane are included in the 3×3 $\mathbf{K}^{i-j}$ matrices. For the case of a 2×2 pile group, the off-diagonal submatrices $\mathbf{K}^{1\text{-}2}, \mathbf{K}^{1\text{-}3}, \mathbf{K}^{1\text{-}4}, \mathbf{K}^{3\text{-}1}, \mathbf{K}^{3\text{-}2}$, and $\mathbf{K}^{3\text{-}4}$ account for pile-soil-pile interaction. In the present study, the diagonal matrices such as $\mathbf{K}^{1\text{-}1}$ and $\mathbf{K}^{3\text{-}3}$ also include the influence of the other piles on the loaded pile, which was neglected in the dynamic interaction factor analysis of Kaynia and Kausel (1982). The effect of neglecting pile-soil-pile interaction can be examined by replacing all off-diagonal submatrices of the global stiffness in Equation (3.41) with zeros.

Retaining the effects of pile-soil-pile interaction, Equations (3.54), (3.59), and (3.68) - (3.70) can be combined into a 24×24 system of simultaneous equations:

$$\begin{bmatrix}
\mathbf{S}(B_1)\mathbf{S}^{-1}(T_1) & \mathbf{0}_{6x6} & -\mathbf{I}_{6x6} & \mathbf{0}_{6x6} \\
\mathbf{0}_{6x6} & \mathbf{S}(B_3)\mathbf{S}^{-1}(T_3) & \mathbf{0}_{6x6} & \mathbf{0}_{6x6} \\
\begin{bmatrix} -\omega^2\mathbf{M}\mathbf{T}_{CT_1} & 2\mathbf{T}_{T_1C}^{T} \\ \mathbf{T}_{T_1C}^{-1} & \mathbf{0}_{3x3} \end{bmatrix} & \begin{bmatrix} \mathbf{0}_{3x3} & 2\mathbf{T}_{T_3C}^{T} \\ -\mathbf{T}_{T_3C}^{-1} & \mathbf{0}_{3x3} \end{bmatrix} & \begin{bmatrix} \mathbf{K}^{1-1}(\omega)+\mathbf{K}^{1-2}(\omega) & -\mathbf{I}_{3x3} \\ \mathbf{K}^{3-1}(\omega)+\mathbf{K}^{3-2}(\omega) & \mathbf{0}_{3x3} \end{bmatrix} & \mathbf{0}_{6x6} \\
\mathbf{0}_{6x6} & \mathbf{0}_{6x6} & \begin{bmatrix} \mathbf{K}^{1-3}(\omega)+\mathbf{K}^{1-4}(\omega) & \mathbf{0}_{3x3} \\ \mathbf{K}^{3-3}(\omega)+\mathbf{K}^{3-4}(\omega) & -\mathbf{I}_{3x3} \end{bmatrix} & \mathbf{0}_{6x6} \\
\mathbf{0}_{6x6} & & & -\mathbf{I}_{6x6} \\
 & & & \mathbf{0}_{6x6}
\end{bmatrix}
\begin{bmatrix} \mathbf{U}(T_1) \\ \mathbf{F}(T_1) \\ \mathbf{U}(T_3) \\ \mathbf{F}(T_3) \\ \mathbf{U}(B_1) \\ \mathbf{F}(B_1) \\ \mathbf{U}(B_3) \\ \mathbf{F}(B_3) \end{bmatrix}
=
\begin{bmatrix} \mathbf{0} \\ \mathbf{0} \\ \mathbf{0} \\ \mathbf{0} \\ \mathbf{Q} \\ \mathbf{0} \\ \mathbf{0} \\ \mathbf{0} \end{bmatrix} \tag{3.71}$$

where the S sub-matrices are also functions of ω and each entry of the right hand side is a 3x1 vector. This system of equations can be solved numerically for the ratios of unknown displacements and forces to the applied force (e.g., $\mathbf{U}(T_1)/Q$, etc.), by first dividing both sides

by $Q = Q_V$ with $Q_H = 0$ for vertical forcing or $Q = Q_H$ with $Q_V = 0$ for horizontal forcing. The theoretical accelerance functions for any point P on the surface of the pile cap can then be calculated using one of the displacement vector solutions, e.g.

$$\mathbf{A}(P) = -\omega^2 \frac{\mathbf{U}(P)}{Q} = -\omega^2 \mathbf{T}_{PT_1} \frac{\mathbf{U}(T_1)}{Q}$$

where

$$\mathbf{T}_{PT_1} = \mathbf{T}_{PC}\mathbf{T}_{T_1C}^{-1} = \begin{bmatrix} 1 & 0 & (x_P - x_{T_1}) \\ 0 & 1 & -(y_P - y_{T_1}) \\ 0 & 0 & 1 \end{bmatrix}. \tag{3.72}$$

3.6 Three-dimensional BEM Disturbed-zone Model

3.6.1 BEM Model for a 2×2 Pile Groups

Simplified disturbed-zone models have been shown effective for adequate prediction of dynamic response of single piles (e.g., Vaziri and Han 1991; Manna and Baidya 2010). However, research on 3*D* disturbed-zone models for pile groups in layered soils remains limited. If the pile spacing s is sufficiently large such that the motion of each pile negligibly affects the others, disturbed zones may be used around each individual pile. For typical smaller values of pile spacing, a single disturbed zone surrounding all piles may be more efficient. For either scenario, the size and shape of the disturbed zone must first be defined. For example, Blaney and O'Neil (1986, 1989) performed full-scale dynamic lateral tests on a closed-ended single pile and pile group in stiff overconsolidated clay. They postulated inelastic soil deformations within a horizontal distance of 1.2 m (4.4 times the pile diameter D) from the center of the single pile, and within 1.0 m of the perimeter of the 3×3 pile group (for which

S=3D and D=0.273 m), outside of which the soil deformation attenuated rapidly. The soil motion beyond this zone appeared to be dominated by the propagation of elastic body and surface waves. Because of the relatively small pile spacing of 4.17D in this study, a single disturbed zone is adopted around the pile group.

Disturbed zones in previous studies were originally developed based on axisymmetric plane-strain assumptions and simply surrounded the pile by a thin cylindrical body without modeling the perturbed soils below the pile toe (e.g., Veletsos and Dotson 1986; Han and Sabin 1995), which can greatly affect the vertical vibration mode. A general disturbed-zone model is expected to be able to capture the observed behavior of multiple vibration modes of pile groups, including horizontal, vertical, rocking and torsional modes. To this end, a disturbed zone having a cylindrical shape with a hemispherical cap was adopted for single piles by Ashlock (2006), and is developed for pile groups herein. The inner and outer zones enable an approximate account of horizontal heterogeneity, and the multilayered viscoelastic fundamental solutions in BEASSI (Pak and Guzina 2002) enable piecewise vertical heterogeneities of the soil's density, Poisson's ratio, shear modulus and damping ratio. The length of the cylindrical disturbed zone is taken to be the same as that of the piles, and the radius is set to $(\sqrt{2}/2)S+2.5d$ (Figure 3.26). Parametric studies were also performed, revealing that the pile group impedances have a relatively lower sensitivity to the radius of the disturbed zone than to the modulus and damping profiles within the zone.

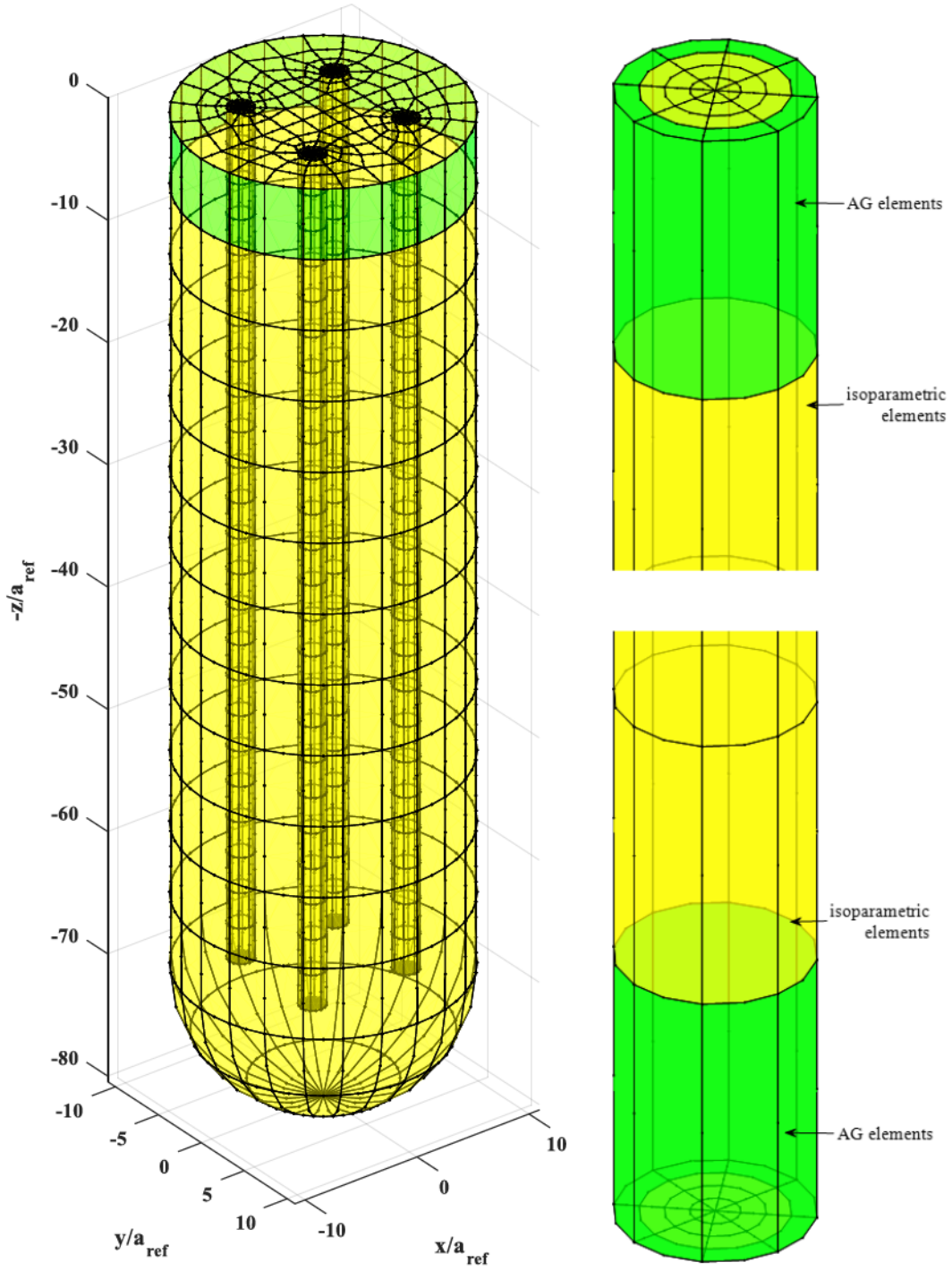

Figure 3.26 *Three-dimensional disturbed-zone BEM model for a 2×2 pile group.*

3.6.2 Boundary Discretization

As mentioned previously, the surfaces of the pile and soil domains were discretized using quadratic and adaptive gradient elements. Through parametric studies, the authors determined that the horizontal traction-free surface on the upper boundary of the disturbed zone in Figure 3.26 does not benefit from mesh refinement, and needs only to provide a compatible transition between the pile meshes and that of the outer embedded surface of the disturbed zone at the ground level. Convergence studies were also performed on the meshes of the pile and disturbed zone, with particular attention to the number of elements in the vertical direction, as this was the most influential parameter. Convergence for dynamic problems is related not only to the mesh itself, but also to the excitation frequency and material properties. For example, a higher frequency or lower shear modulus lead to shorter shear wavelengths and sharper variations in tractions and displacements, requiring a finer mesh to capture their details. In the present study, the range of interest for the normalized circular frequency $\bar{\omega}$ is from 0.01 to 0.33, which corresponds to actual linear frequencies up to 156 Hz. This range is sufficient to cover typical frequencies of interest in seismic problems, as well as higher-frequency applications such as machine vibration problems, and is also sufficient to capture the resonant accelerance peaks from the field-scale pile vibration tests. A convergence study on the mesh size is presented in the following, using a soil profile determined from three seismic cone penetration soundings performed at the field test site.

1. Effect of mesh refinement along pile length

From mesh refinement studies, it was first determined that the impedances were most sensitive to the number of pile elements in the vertical direction, and use of 4 elements in the radial direction with 8 in the circumferential direction was adequate for convergence. Four pile meshes termed A, B, C, and D were then examined with 12, 24, 36, and 72 vertical elements, respectively. BEASSI is able to handle multiple thin soil layers per element by dividing vertical elements into corresponding sub-regions for integration, which captures the discontinuities in the Green's functions thus enabling convergence of the adaptive integration scheme. To keep the soil profile fixed while varying only the number of vertical pile elements, the soil profiles were uniformly discretized into a total of 72 layers along the pile length (with additional layers below the piles). Therefore Meshes A, B, C, and D had 6, 3, 2, and 1 layers, respectively, per vertical pile element within the disturbed zone.

Most of the resulting impedances in the elementary matrix $\mathbf{K}^{1-1}$ exhibited good consistency, except for $\bar{k}_{xx}^{1-1}$ and $\bar{k}_{m_y x}^{1-1}$, which deviate at high frequency for the coarsest Mesh A. These results also indicate that the horizontal impedances are the most sensitive ones to discretization along the pile length, followed by the horizontal-rocking coupling impedances. Similar convergence trends, although with nearly negligible impedance deviations, were also observed in the off-diagonal elementary matrices $\mathbf{K}^{2-1}$, $\mathbf{K}^{3-1}$, and $\mathbf{K}^{4-1}$. Impedances from these matrices also quantify the forces transferred to the other piles through pile-soil-pile interaction which, as expected, are much smaller than those on the loaded pile. Based on the above results, pile Mesh B is deemed to give the optimum balance of accuracy and efficiency.

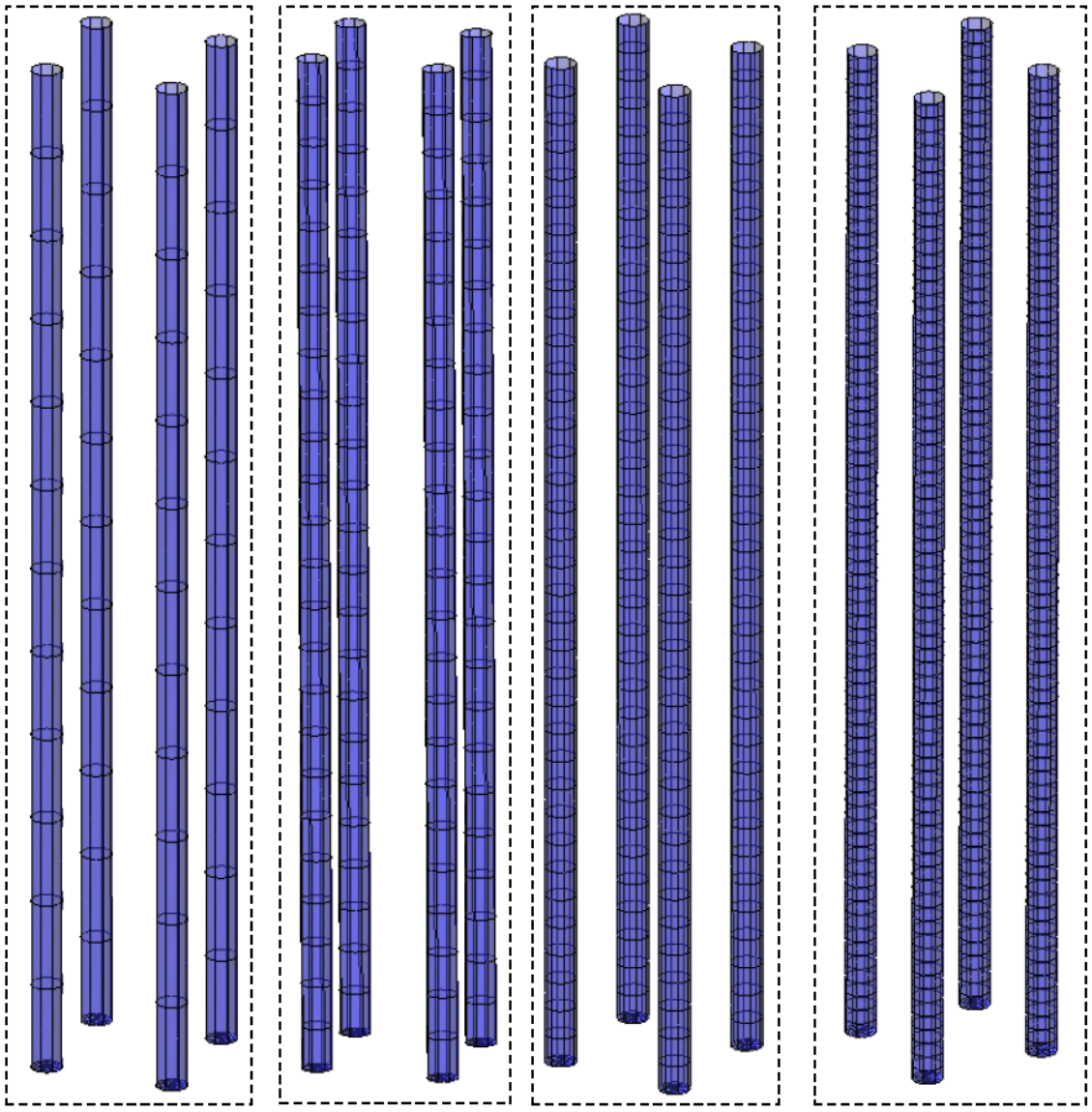

(a) Mesh A (b) Mesh B (c) Mesh C (d) Mesh D

Figure 3.27 *Mesh refinement along pile length.*

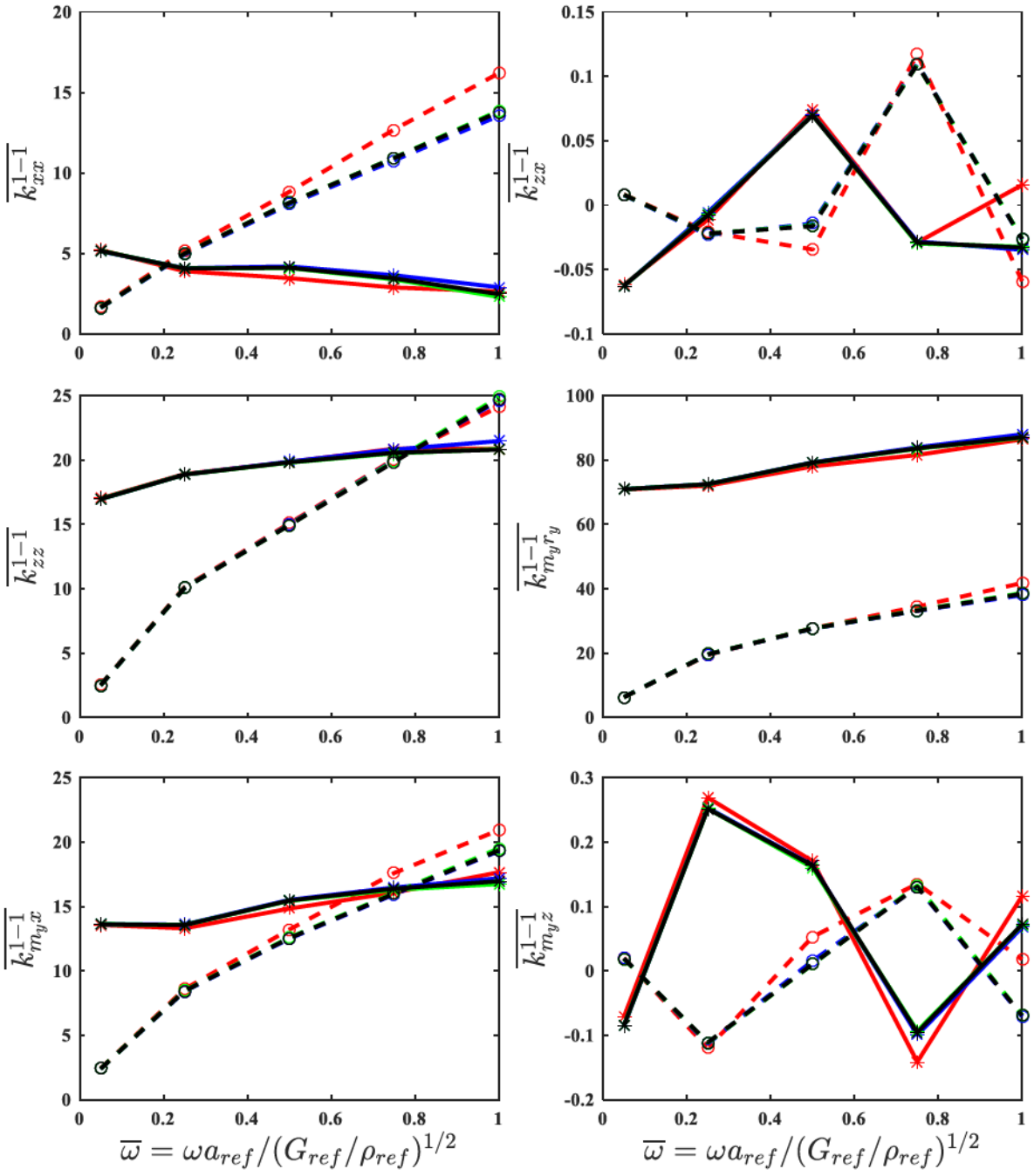

(a) Primary impedance functions in $\mathbf{K}^{1\text{-}1}$

Figure 3.28 *Convergence study on mesh along piles using CPT-correlation soil profile and a 6-domain model (red lines - Mesh A; blue lines – Mesh B; green lines – Mesh C; black lines – Mesh D).*

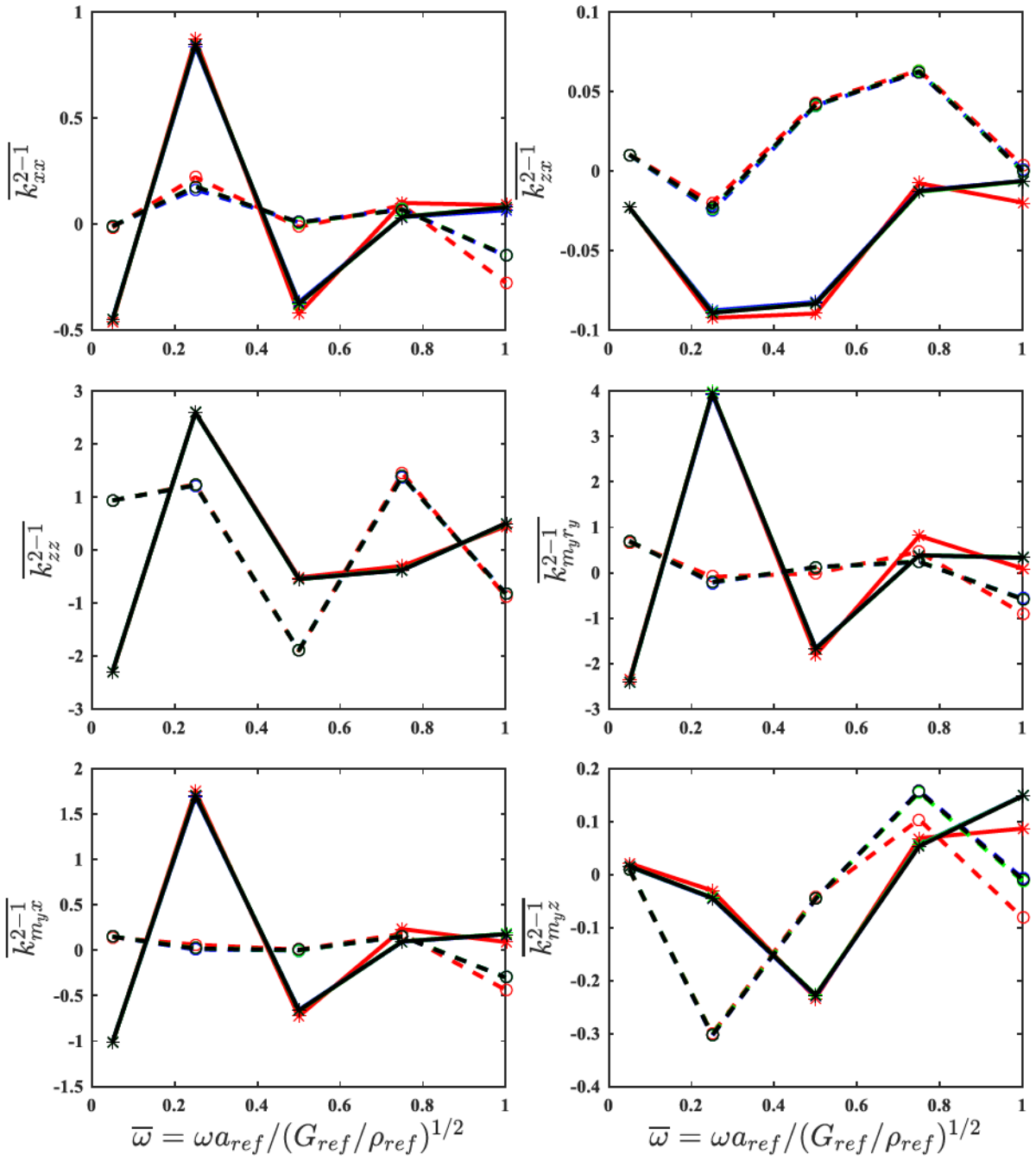

(b) Primary impedance functions in $\mathbf{K}^{2\text{-}1}$

Figure 3.28 *(continued)*

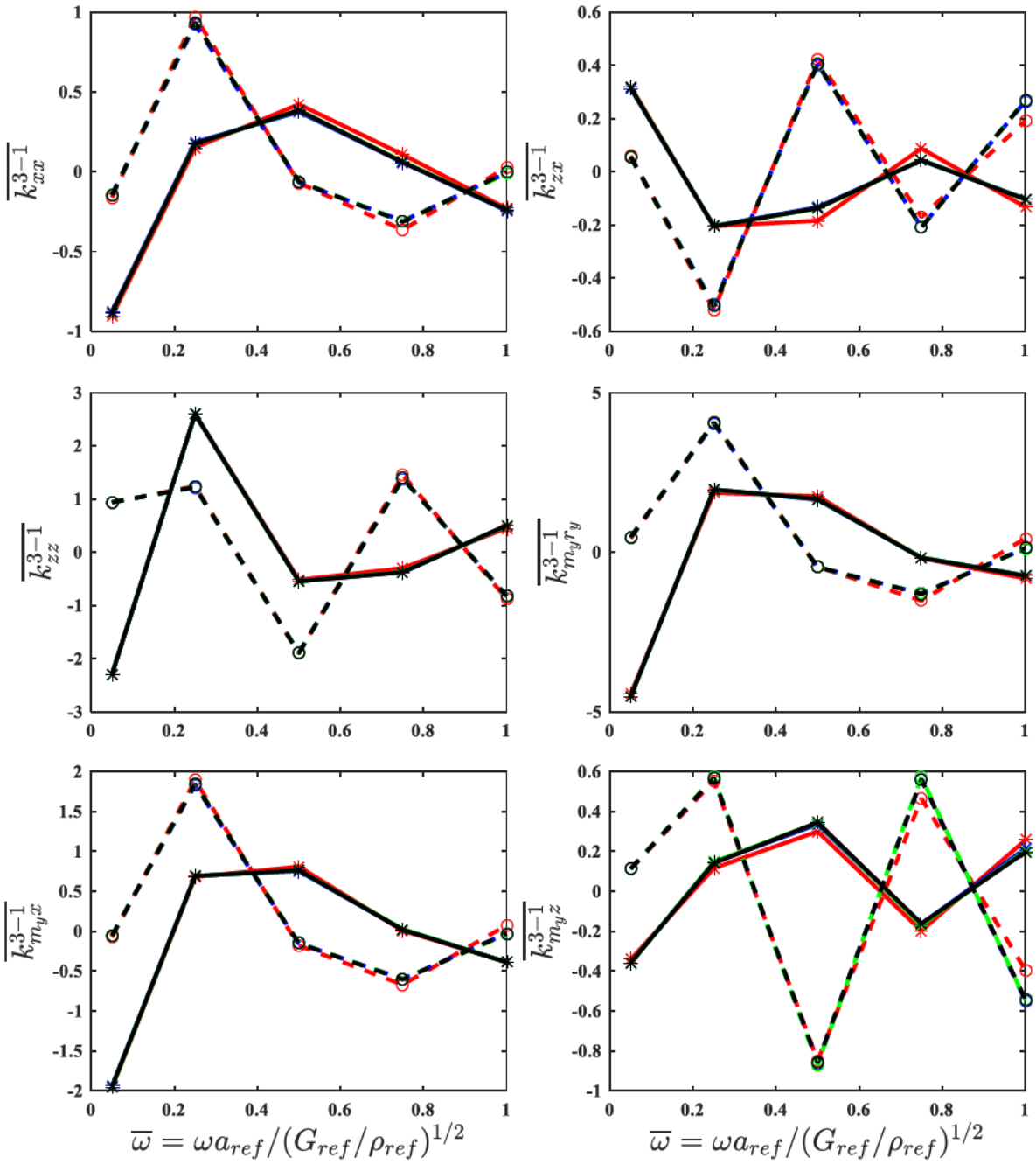

(c) Primary impedance functions in $\mathbf{K}^{3\text{-}1}$

Figure 3.28 *(continued)*

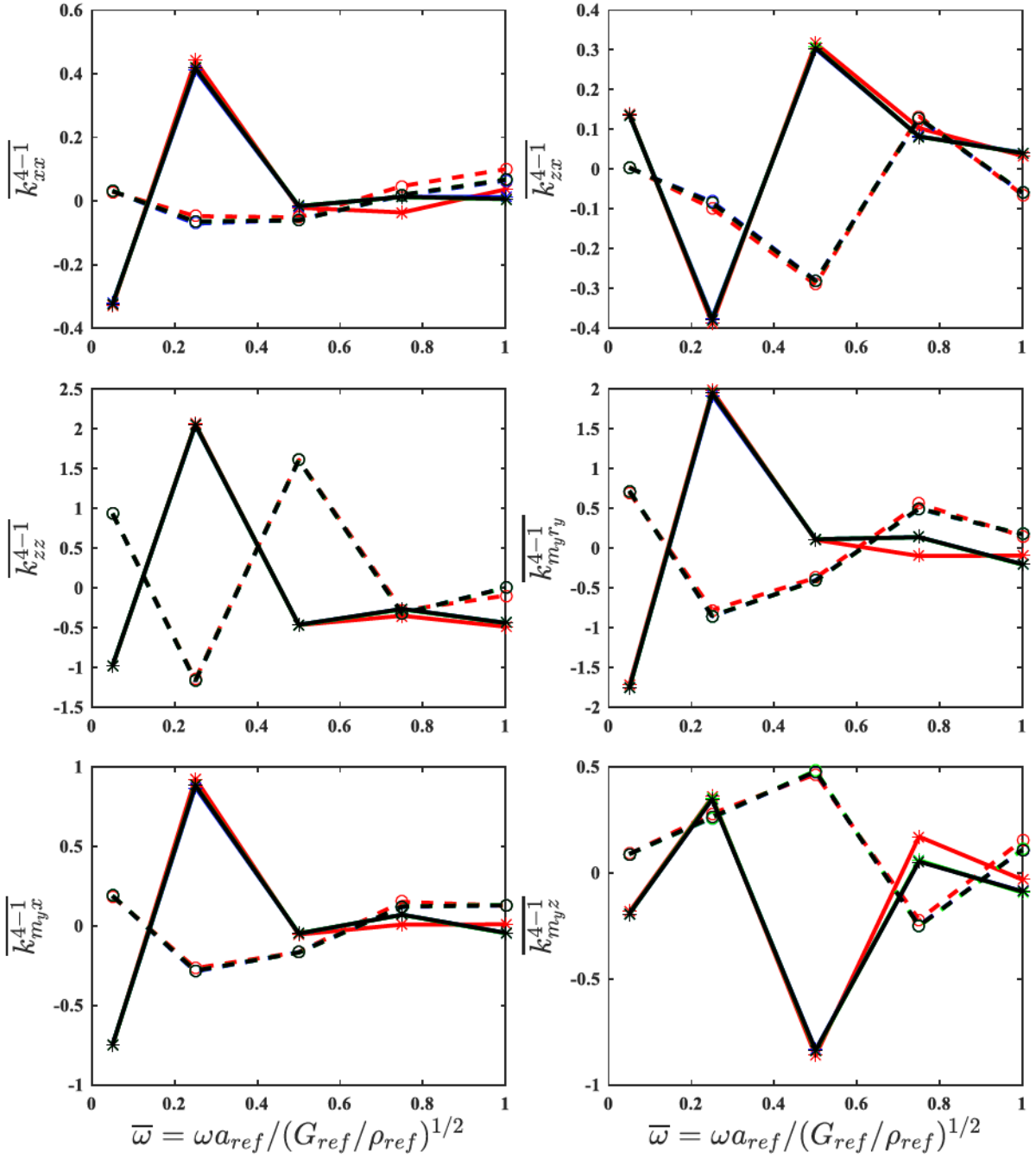

(d) Primary impedance functions in $\mathbf{K}^{4\text{-}1}$

Figure 3.28 *(continued)*

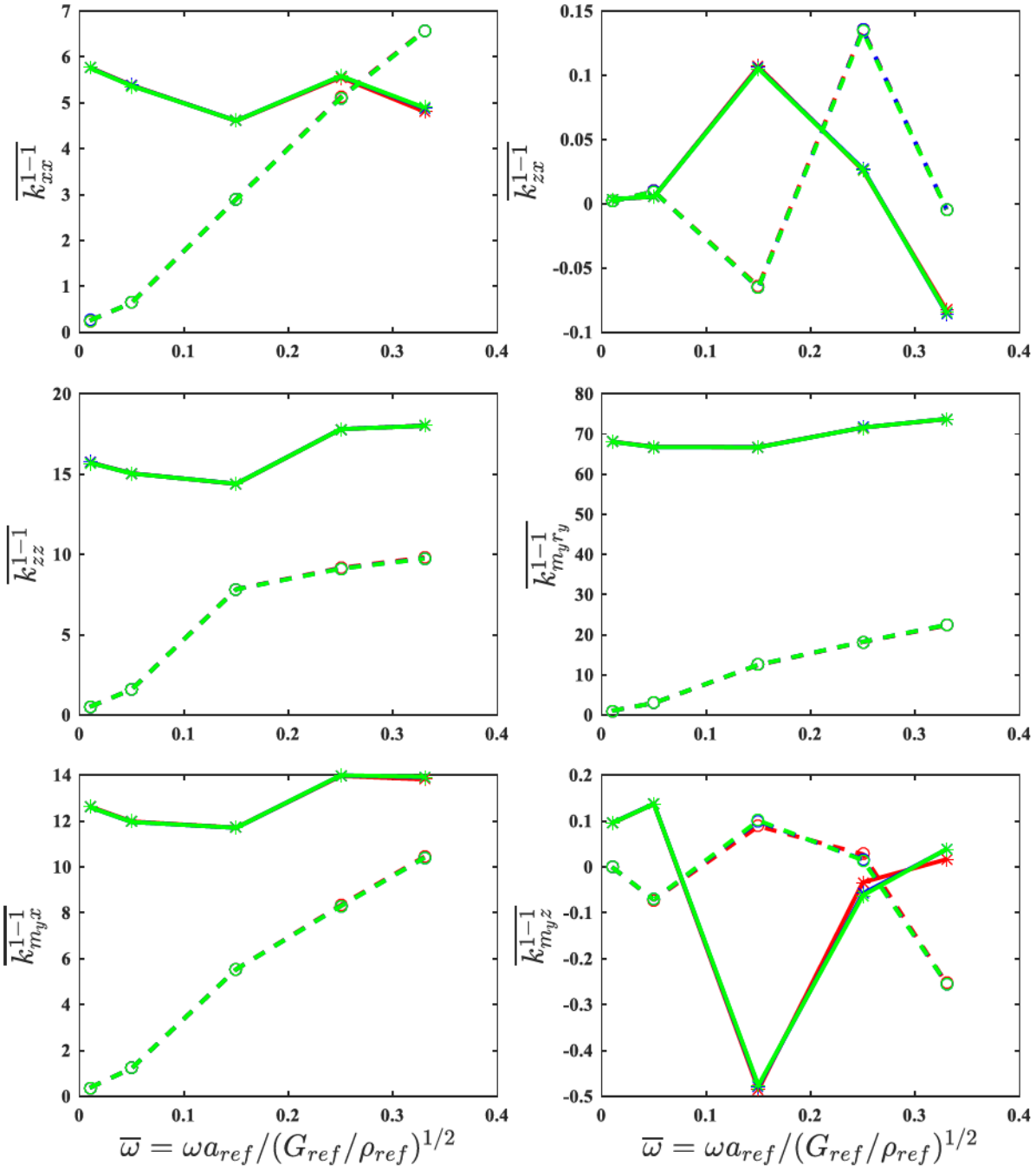

(a) Primary impedance functions in $\mathbf{K}^{1\text{-}1}$

Figure 3.29 *Convergence study on mesh along piles using SCPT soil profile and a 5-domain model (red lines - Mesh A; blue lines – Mesh B; green lines – Mesh C).*

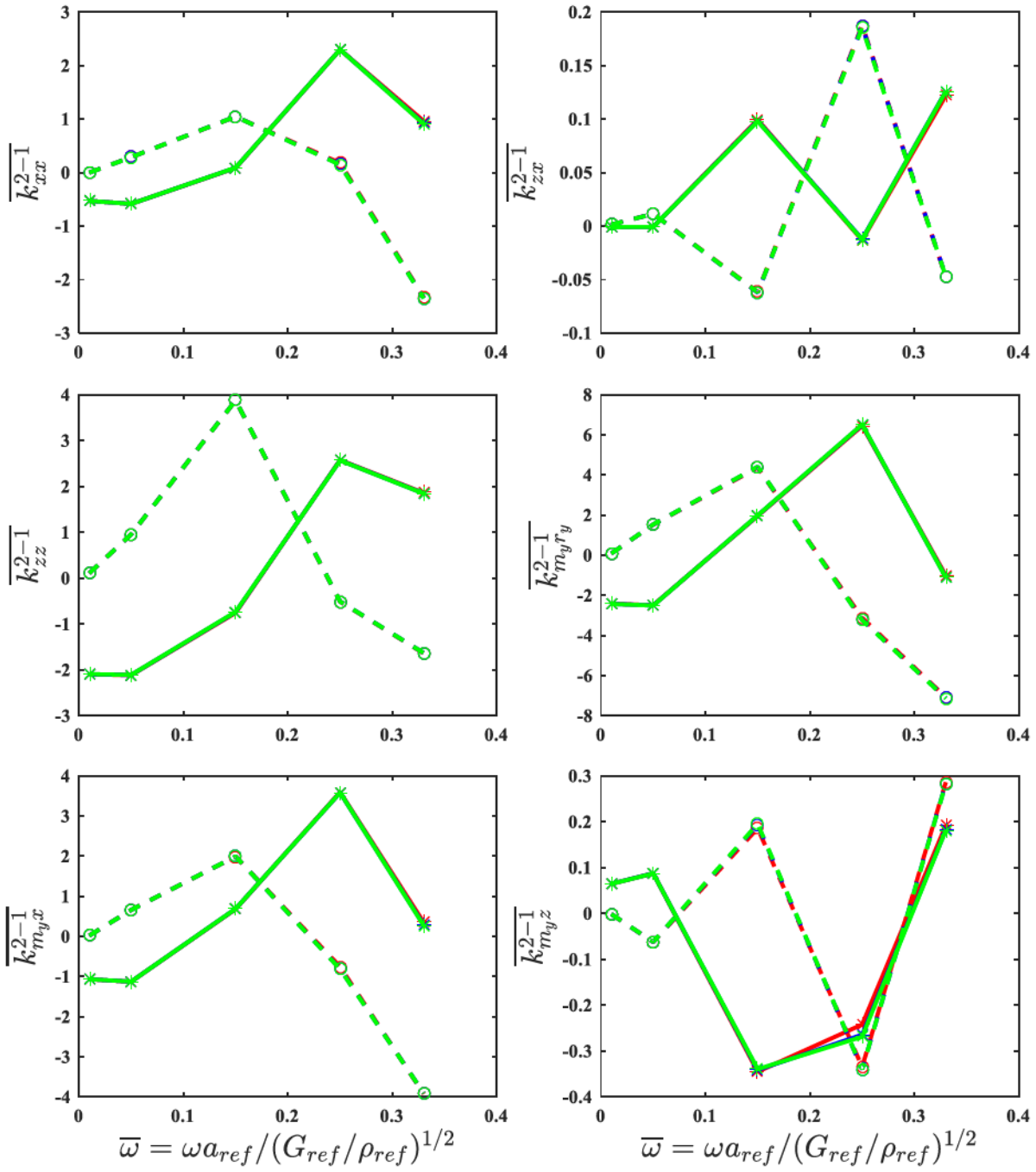

(b) Primary impedance functions in $\mathbf{K}^{2\text{-}1}$

Figure 3.29 *(continued)*

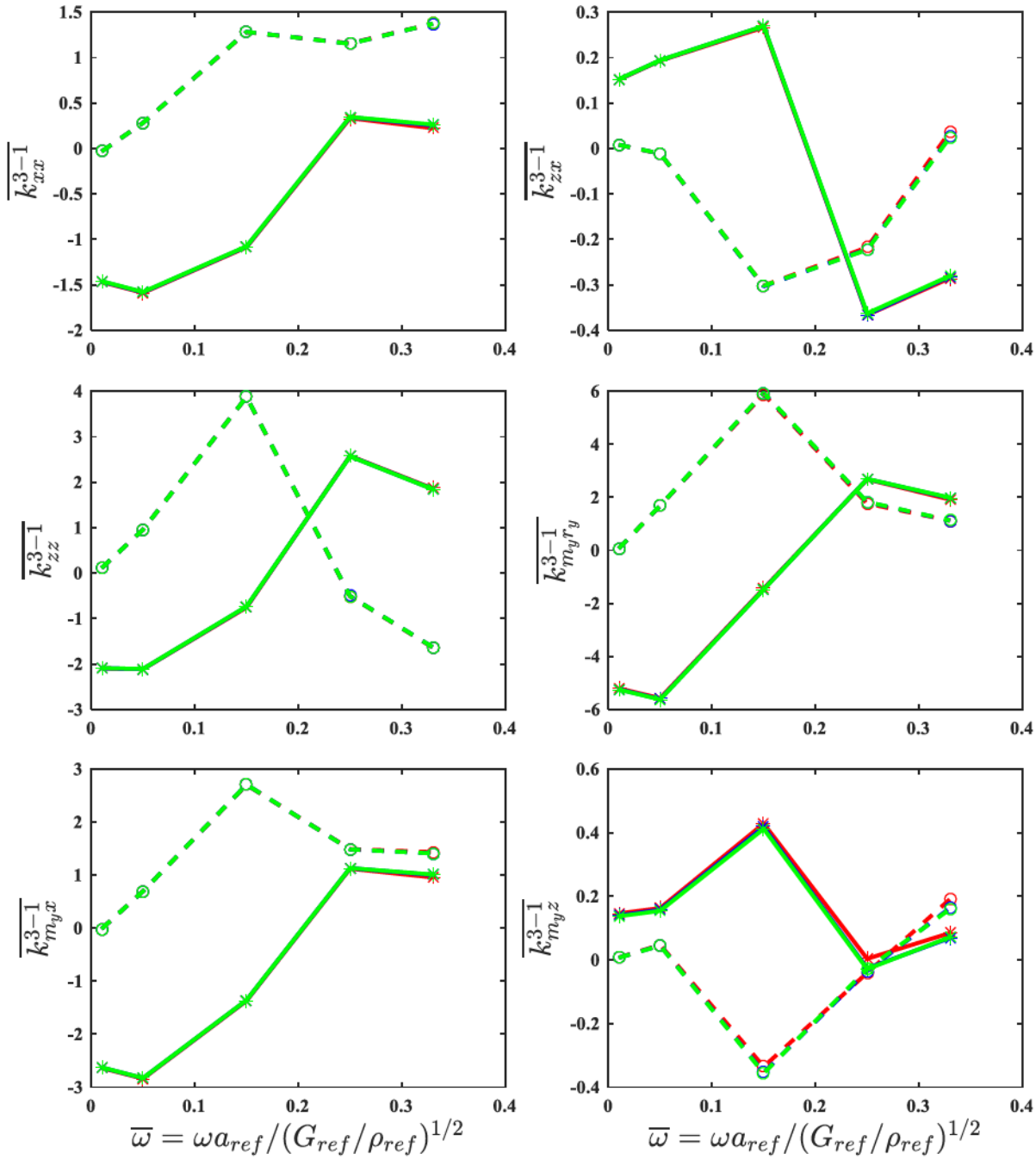

(c) Primary impedance functions in $\mathbf{K}^{3\text{-}1}$

Figure 3.29 *(continued)*

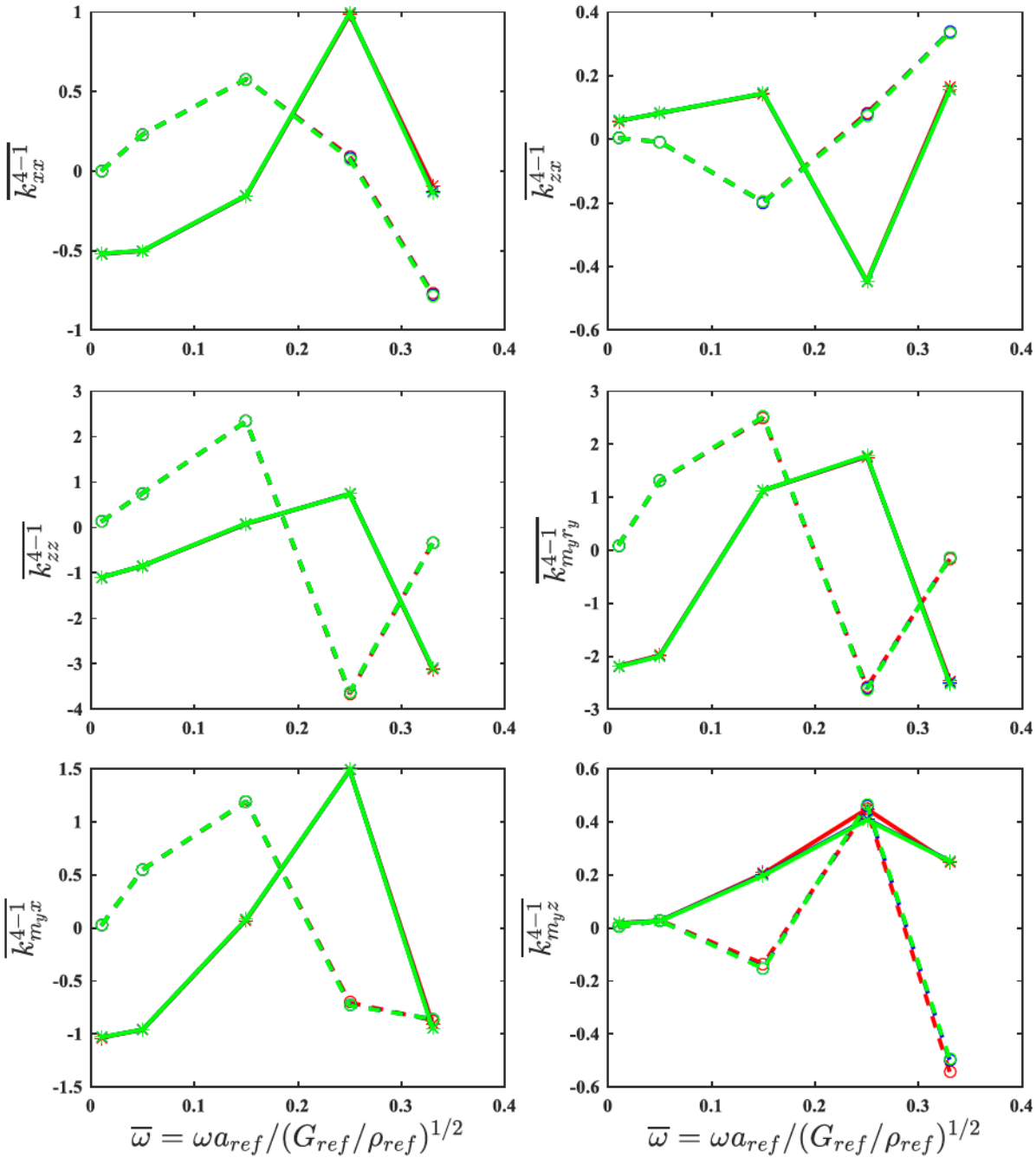

(d) Primary impedance functions in $\mathbf{K}^{4\text{-}1}$

Figure 3.29 *(continued)*

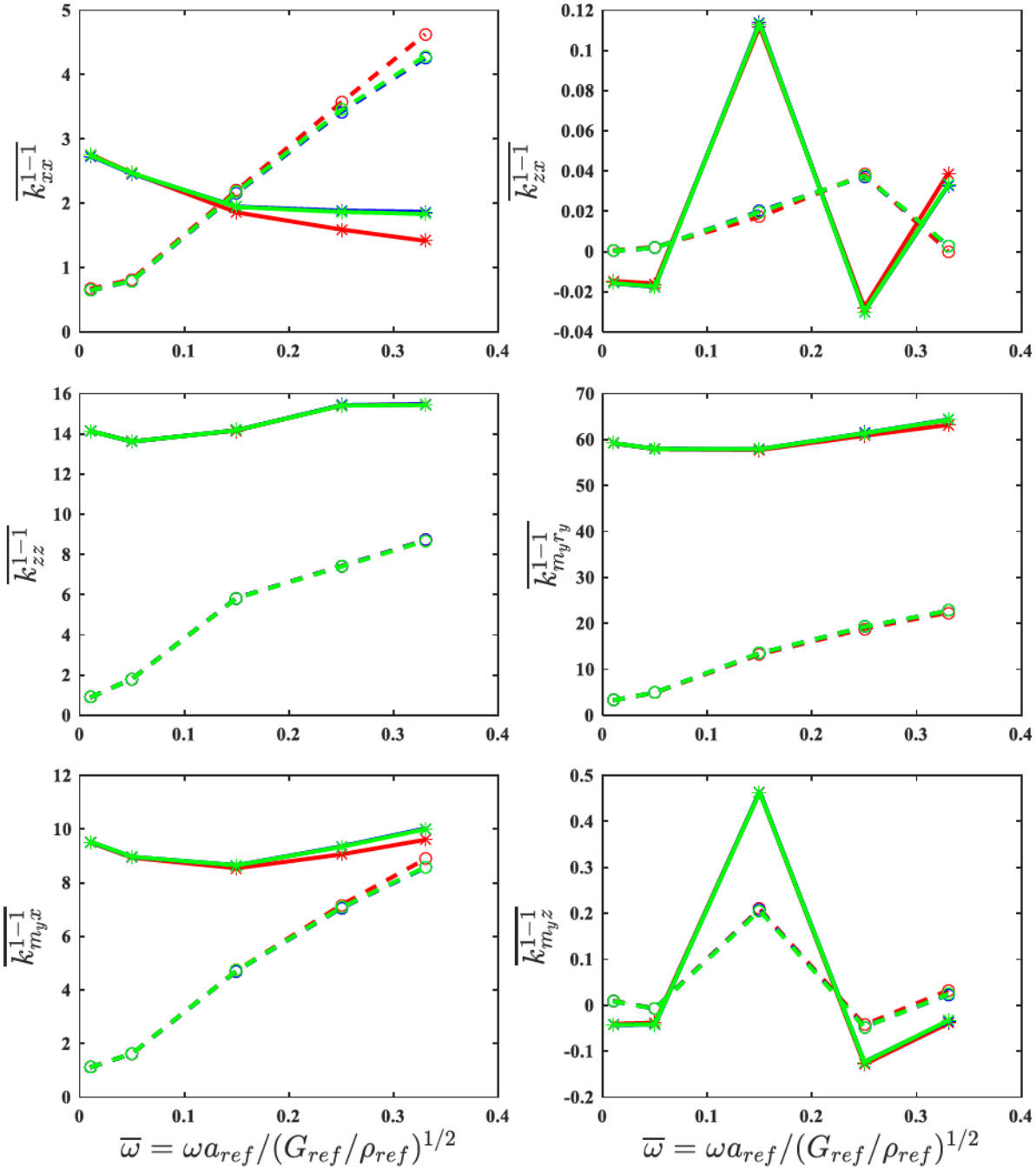

(a) Primary impedance functions in $\mathbf{K}^{1\text{-}1}$

Figure 3.30 *Convergence study on mesh along piles using SCPT soil profile and a 6-domain model (red lines - Mesh A; blue lines – Mesh B; green lines – Mesh C).*

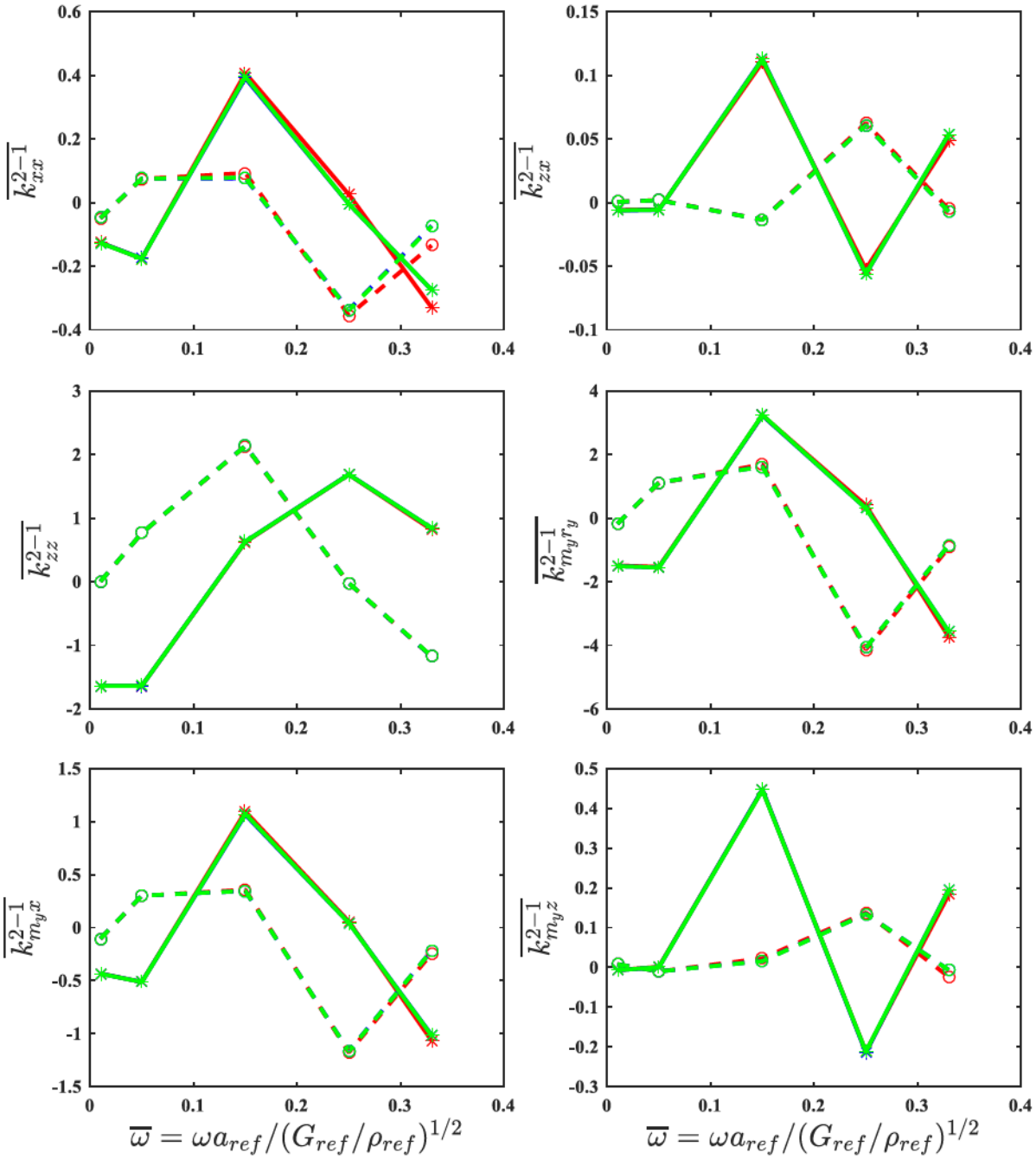

(b) Primary impedance functions in $\mathbf{K}^{2\text{-}1}$

Figure 3.30 *(continued)*

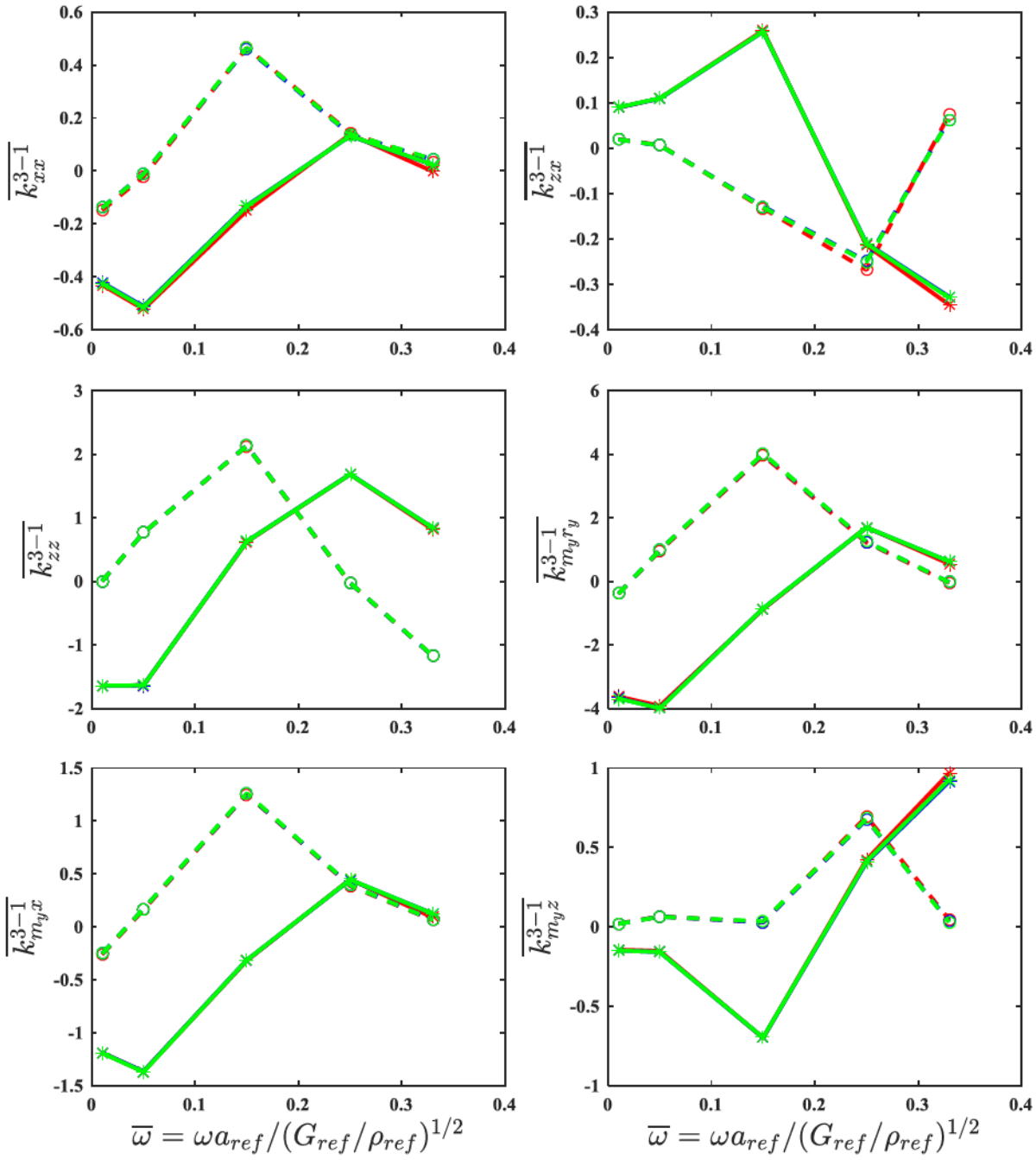

(c) Primary impedance functions in $\mathbf{K}^{3\text{-}1}$

Figure 3.30 *(continued)*

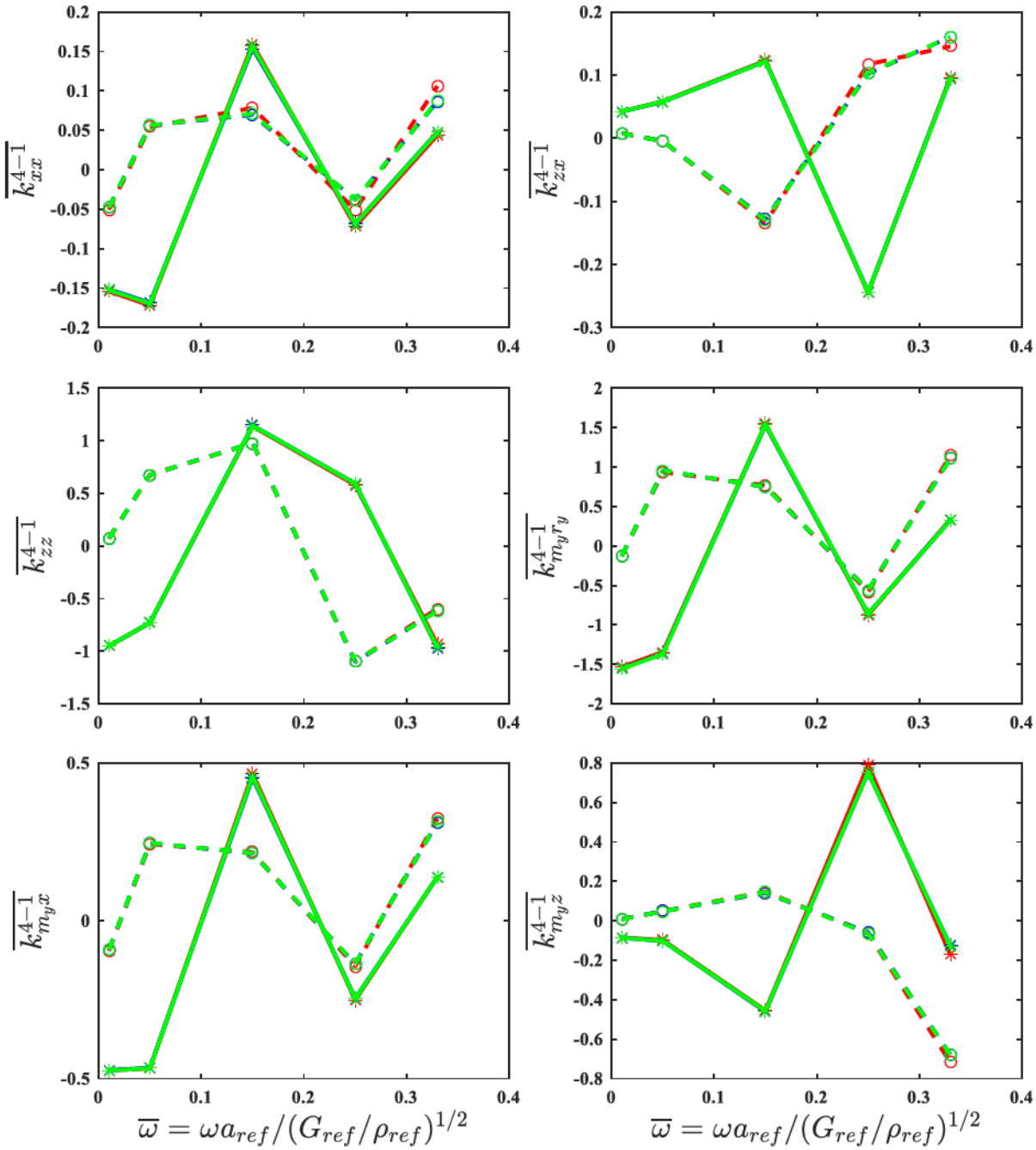

(d) Primary impedance functions in $\mathbf{K}^{4\text{-}1}$

Figure 3.30 *(continued)*

2. Mesh along cylindrical part of the disturbed zone

The impedances were less sensitive to the number of inclusion elements in the vertical direction. Three pile meshed termed E, F, and G were examined with 6, 12, and 24 vertical elements for the cylindrical part of inclusion, respectively. Therefore Meshes E, F, G had 12, 6, and 3 layers, respectively, per vertical inclusion element for the cylindrical part. For a 6-domain model with continuous CPT-correlated soil profiles, all three types of meshes suggest favorable agreement on impedance matrices in $\mathbf{K}^{1-1}$ (Figure 3.32), except for $\overline{k}_{zx}^{1-1}$ and $\overline{k}_{m_y z}^{1-1}$,which show deviations even at low frequencies for the coarsest Mesh D. Similar trends were also observed in the off-diagonal elementary matrices $\mathbf{K}^{2-1}$, $\mathbf{K}^{3-1}$, and $\mathbf{K}^{4-1}$, such that impedance functions begin to deviation when frequency is higher than 0.25. For the 6-domain model with piecewise SCPT soil profile, Mesh F and Mesh G lead to very close results while Mesh E still diverge when frequency is beyond 0.25 (Figure 3.33). Based on the above results, Mesh F mesh provides the best balance between accuracy and efficiency.

In conclusion, convergence is observed by mesh refinement of pile mesh and inlcusion mesh. As expected, converged results for impedance functions are commonly observed at low frequencies below 0.25. When excitation frequency is higher than 0.5, impedance functions begin to diverge, and the degree is associated with the loading direction and the force or moment observed. For the frequency range of interest in this study, Mesh B for pile mesh and Mesh F for inclusion mesh are adopted to balance accuracy of numerical results and time efficiency.

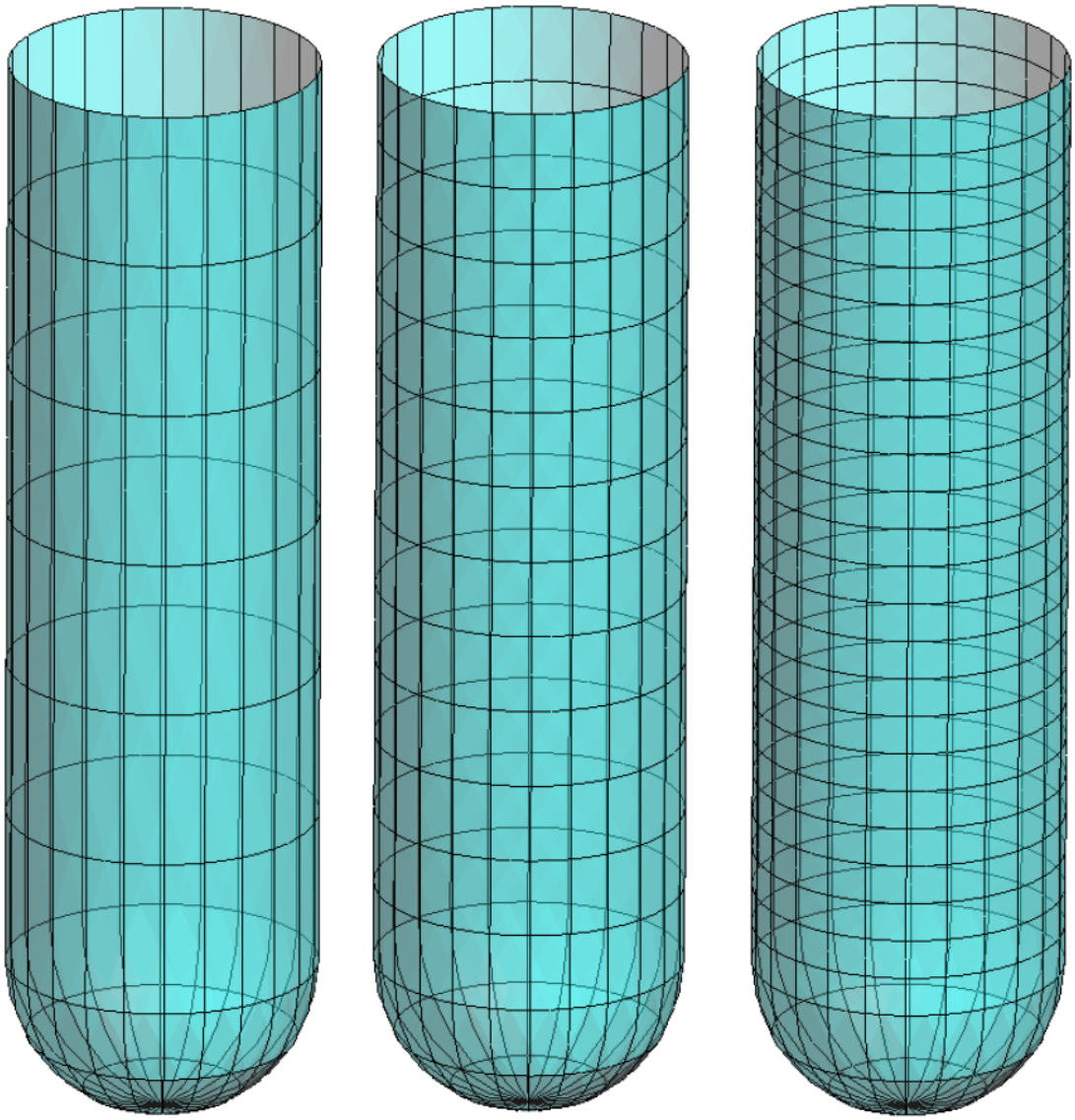

(a) Mesh E (b) Mesh F (c) Mesh G

Figure 3.31 *Mesh refinement along disturbed-zone depth.*

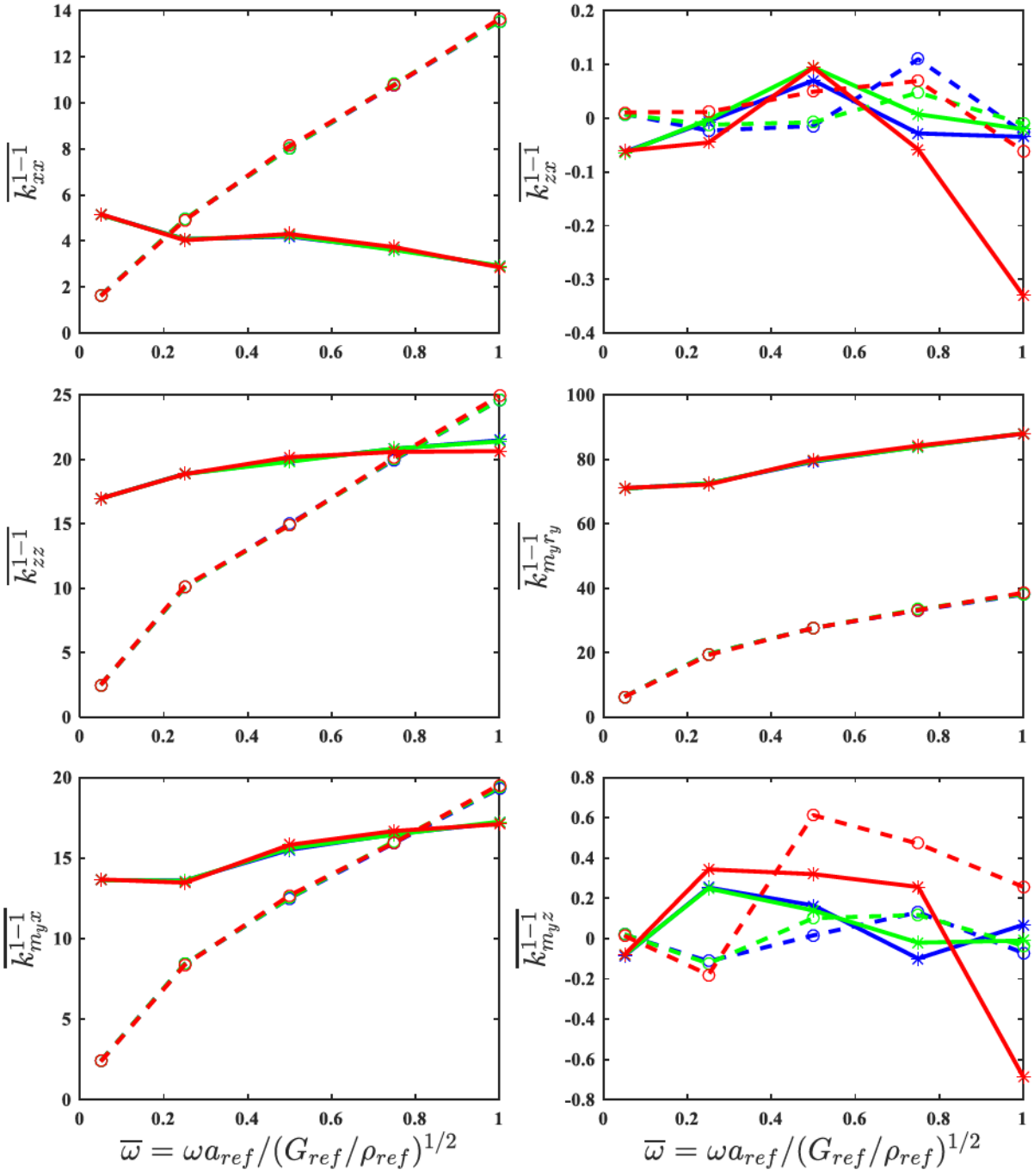

(a) Primary impedance functions in $\mathbf{K}^{1\text{-}1}$

Figure 3.32 *Convergence study on mesh along disturbed zone using CPT-correlated soil profile with a 6-domain model (red lines - Mesh E; blue lines – Mesh F; green lines – Mesh G).*

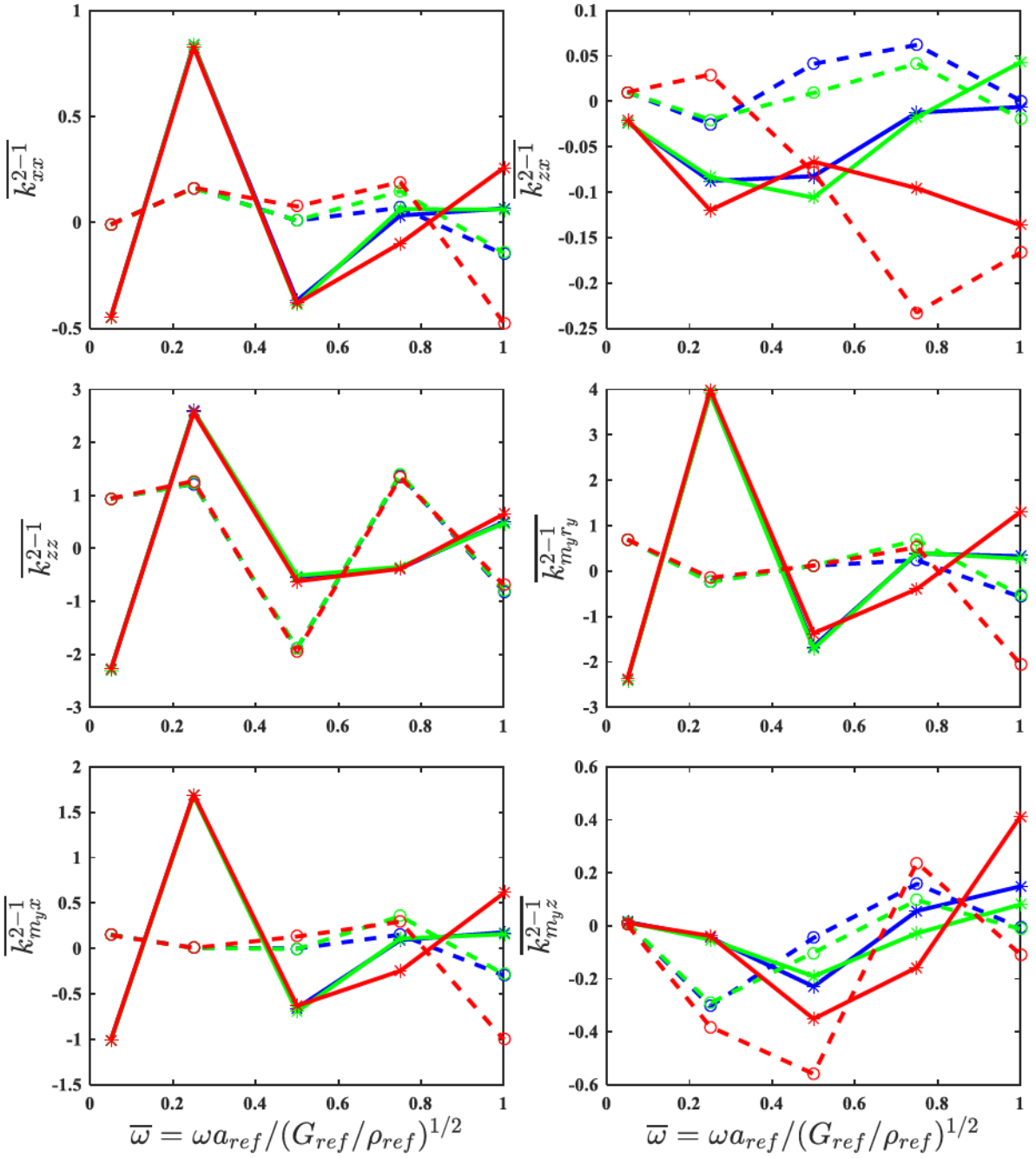

(b) Primary impedance functions in $\mathbf{K}^{2\text{-}1}$

Figure 3.32 *(continued)*

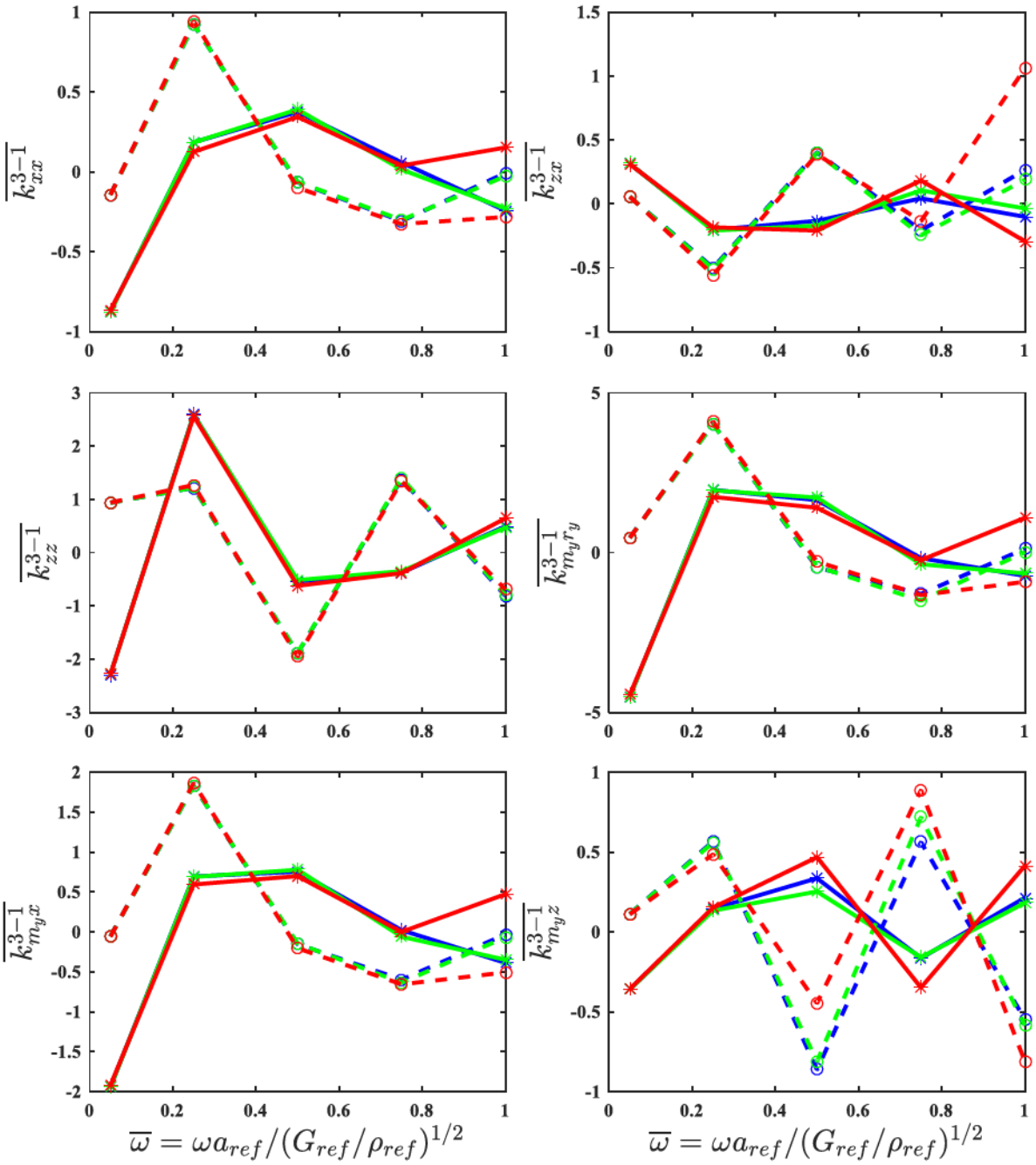

(c) Primary impedance functions in $\mathbf{K}^{3\text{-}1}$

Figure 3.32 *(continued)*

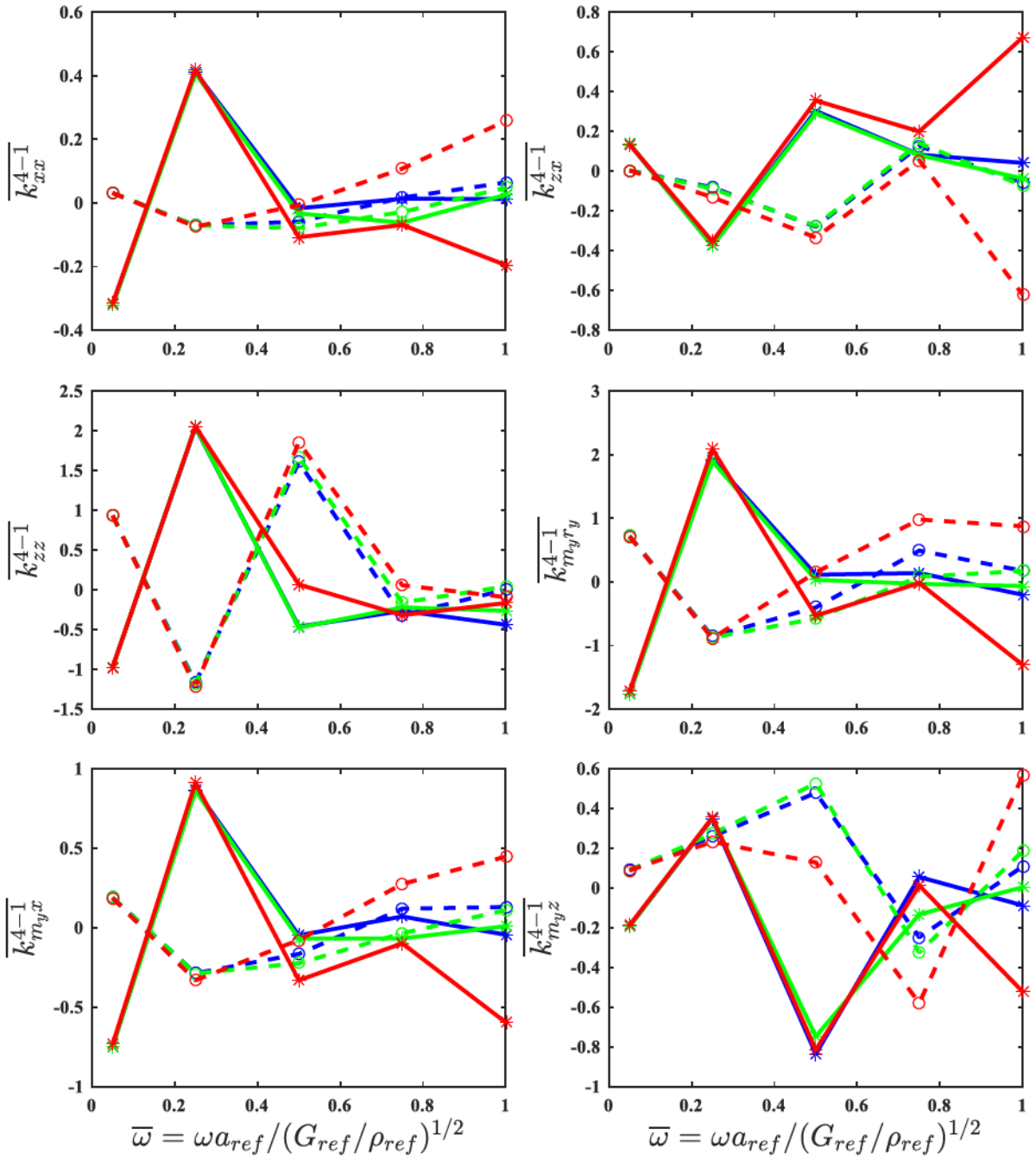

(d) Primary impedance functions in $\mathbf{K}^{4\text{-}1}$

Figure 3.32 *(continued)*

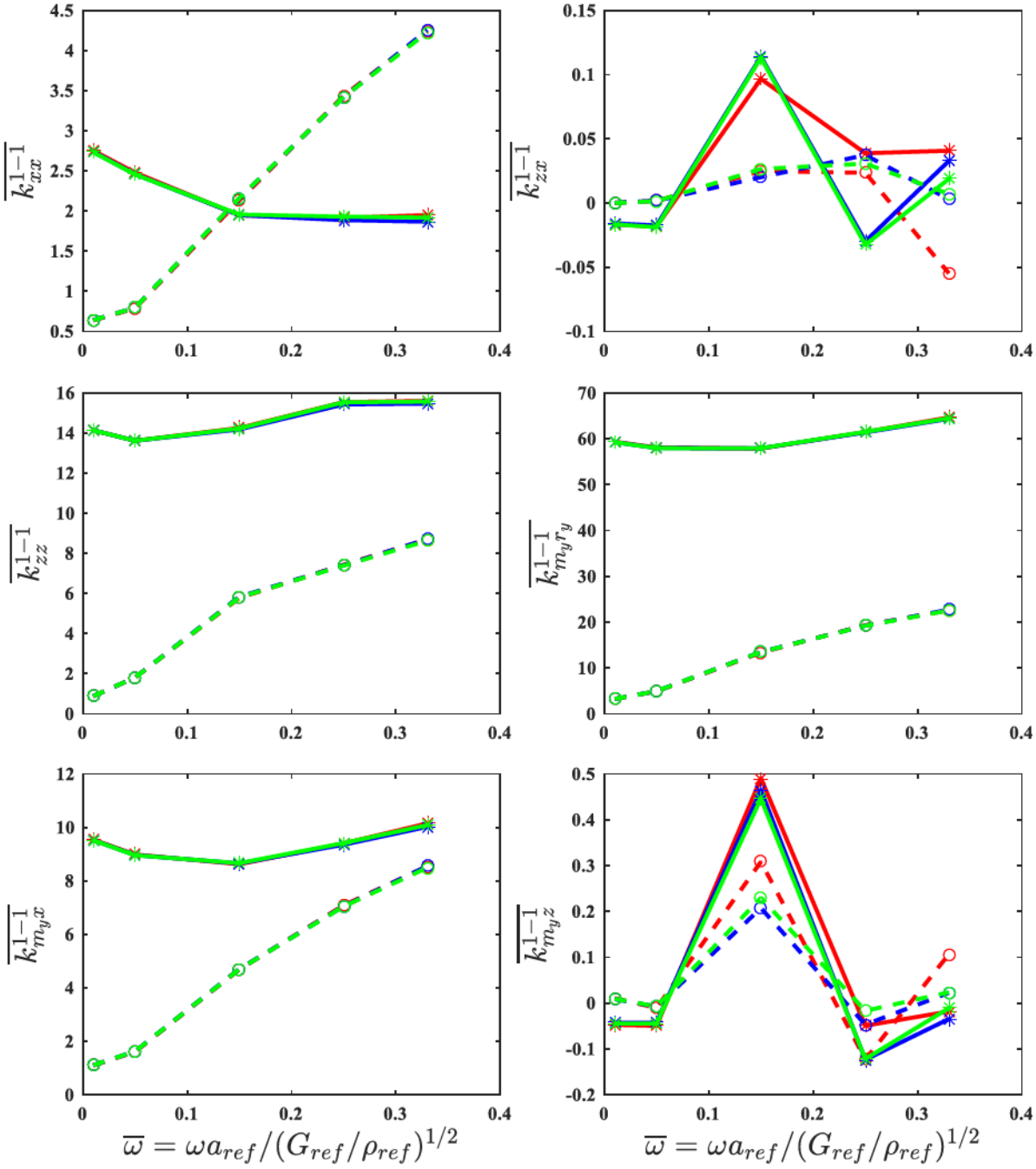

(a) Primary impedance functions in $\mathbf{K}^{1\text{-}1}$

Figure 3.33 *Results of convergence study on mesh along disturbed zone using SCPT soil profile and a 6-domain model (red lines - Mesh E; blue lines – Mesh F; green lines – Mesh G).*

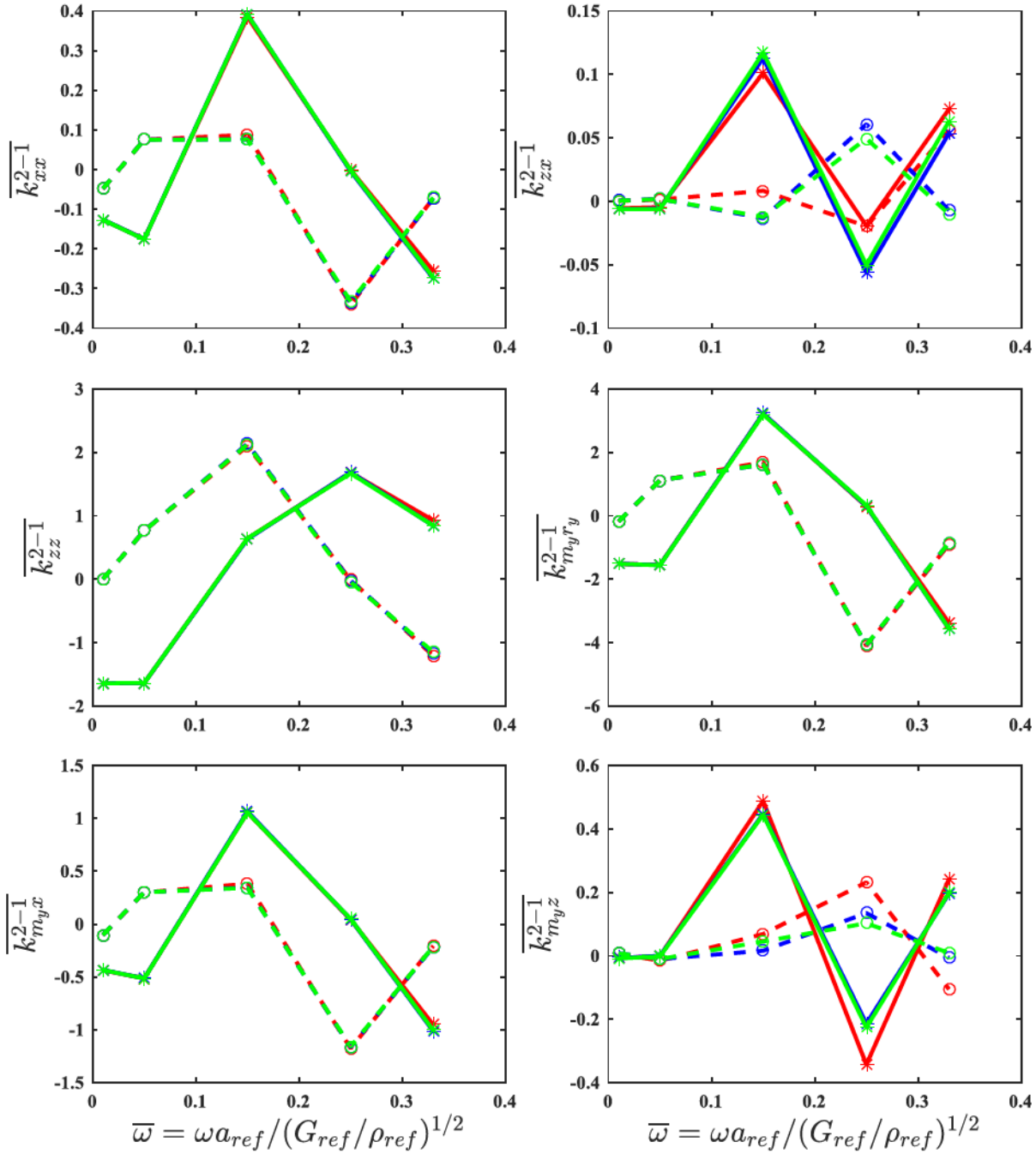

(b) Primary impedance functions in $\mathbf{K}^{2\text{-}1}$

Figure 3.33 *(continued)*

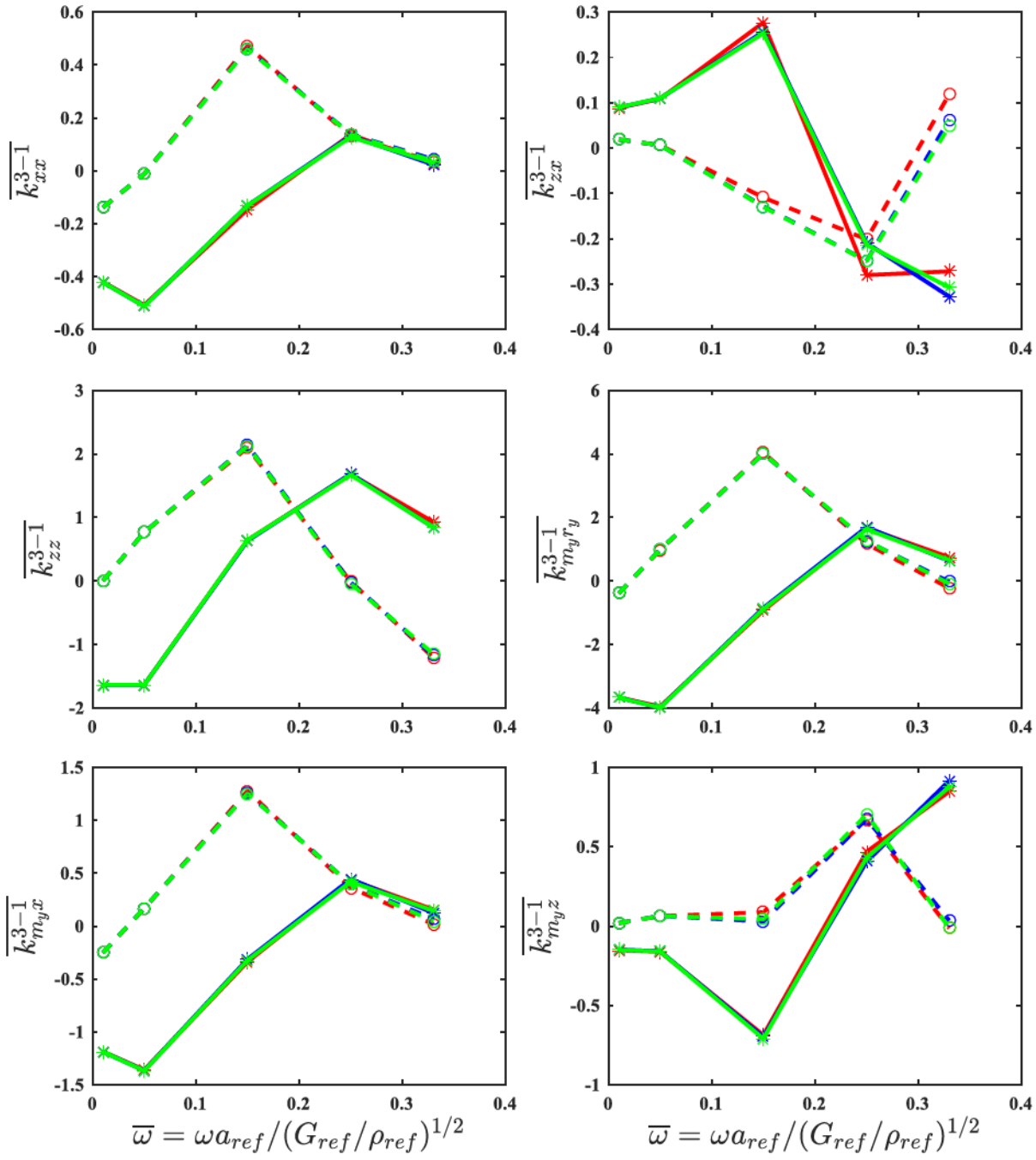

(c) Primary impedance functions in $\mathbf{K}^{3\text{-}1}$

Figure 3.33 *(continued)*

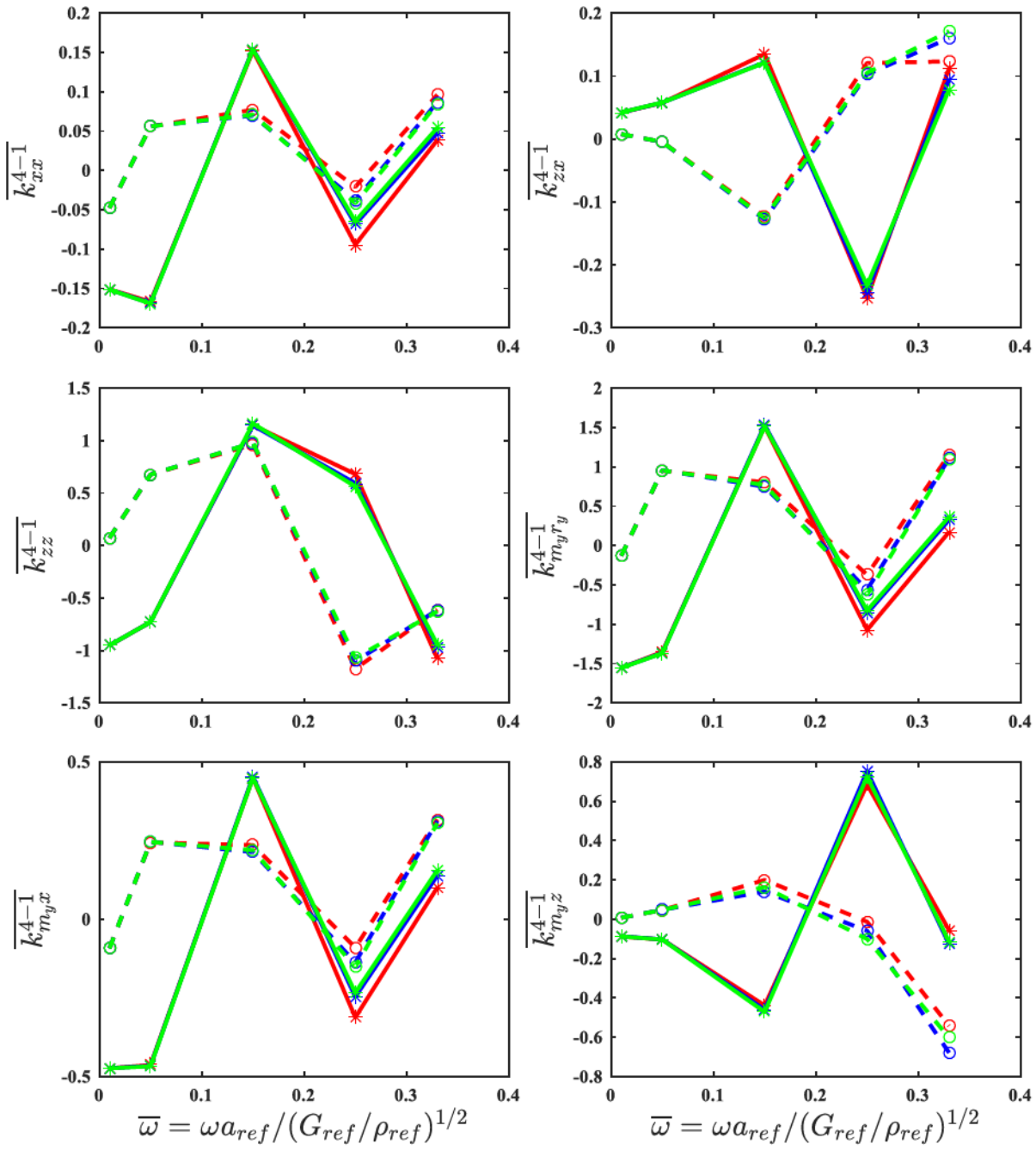

(d) Primary impedance functions in $\mathbf{K}^{4\text{-}1}$

Figure 3.33 *(continued)*

3.7 Interpretation of Numerical Results

BEM analyses provide direct results of nodal displacements, nodal tractions, and optional internal displacements. In addition to impedance functions at pile head, the results can be interpreted for other terms to characterize pile-soil-pile interaction. These include group efficiency ratio, pile group deformation, displacement, strain and stress fields of soil, and pile internal forces.

3.7.1 Group Efficiency Ratio

Group efficiency ratio is a term widely used to quantify the overall performance of pile group. However, the exact definition appear to vary in previous studies. Gazetas and Makris (1991) defined 'dynamic stiffness group factor' $k^{(n)}$ and 'damping group factor' $D^{(n)}$ as the ratio of dynamic pile group stiffness $\overline{K}^{(n)}$ or damping $\overline{C}^{(n)}$ to the sum of static stiffnesses by single pile $K^{(1)}$:

$$\begin{cases} k^{(n)} = \dfrac{\overline{K}^{(n)}}{nK^{(1)}} \\ D^{(n)} = \dfrac{\overline{C}^{(n)}}{nK^{(1)}} \end{cases} \tag{3.73}$$

where n is number of piles. In static and nonlinear pile problems, the efficiency ratios are commonly defined in terms of force instead of impedance. For example, McVay et al. (1995), Chandrasekaran et al. (2010b), and Salgado et al. (2014) referred group efficiency as the ratio of resistance for a pile group to resistance for a single pile at the same displacement level (e.g., 1~3 in.) multiplied by pile number. Becker and Moore (2006) and Tomlinson and Woodward (2008) defined similar concepts as ratio of ultimate load capacity of pile group to ultimate load capacity of single pile multiplied by the pile number. For clarity, notation by Novak and Mitwally (1990), Han and Vaziri (1992), Manna and Baidya (2010) is adopted in this study:

$$\text{GER}=\frac{\text{stiffness or damping of pile group}}{\text{N}\times\text{stiffness or damping of single pile}} \tag{3.74}$$

where N is the number of piles in the group. This notation is more useful for elastodynamics as in this study. In addition, it associates impedances (stiffnesses and dampings) of pile group and single pile at the same frequency, which is more practical in engineering designs. A GER equal to unity indicates either no pile-soil-pile interaction or such effect being counteracted as if the piles were isolated. A GER different from unity indicates overall behavior of pile group are either enhanced or reduced by pile-soil-pile interaction. The direct analysis method discussed in Section 3.5.2 for is applied here for calculating group impedances of a 5-domain model and a 6-domain model. The impedances of single pile as reference are obtained from a 2-domain model and a 3-domain model, which have the same soil profiles as the pile group. The vertical and horizontal group efficiency ratios are shown in Figure 3.34 and Figure 3.35, respectively. The two models suggest similar trends of GER for either vertical or horizontal direction. For the 5-domain model, the vertical stiffness ratio is below unity at frequencies below 0.15 and starts to increase quickly towards a peak before a final decrease starting at frequency of 0.2. Damping ratio increases quickly to the highest point at frequency around 0.15, which is followed by a drastic reduction. The stiffness ratio can be as high 1.8 for vertical vibration and 1.7 for lateral vibration. For the 6-domain model, the calculated GERs for vertical and horizontal stiffnesses exhibit similar trends, as both are below unity at normalized frequencies below 0.15 and increase towards a peak around a normalized frequency of 0.2. The GERs for damping both increase quickly to a peak at an intermediate frequency between 0.15 and 0.2, followed by a sharp reduction. In general, these GER values demonstrate how the soil-pile interaction varies with frequency and provide sights into design of pile groups for achieving highest stiffness or lowest damping.

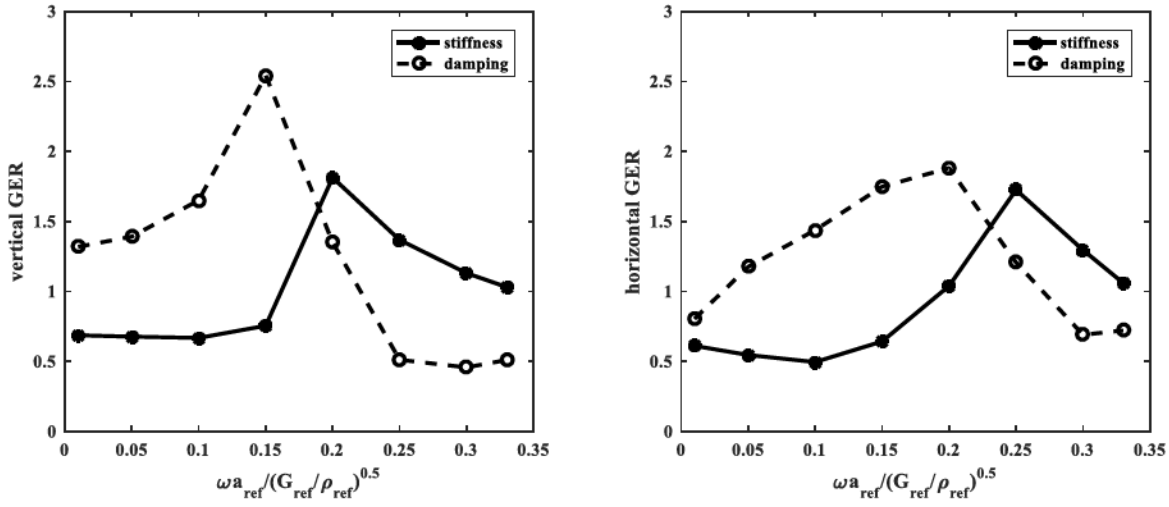

Figure 3.34 *Vertical and horizontal GER for a 2×2 pile group without disturbed zone.*

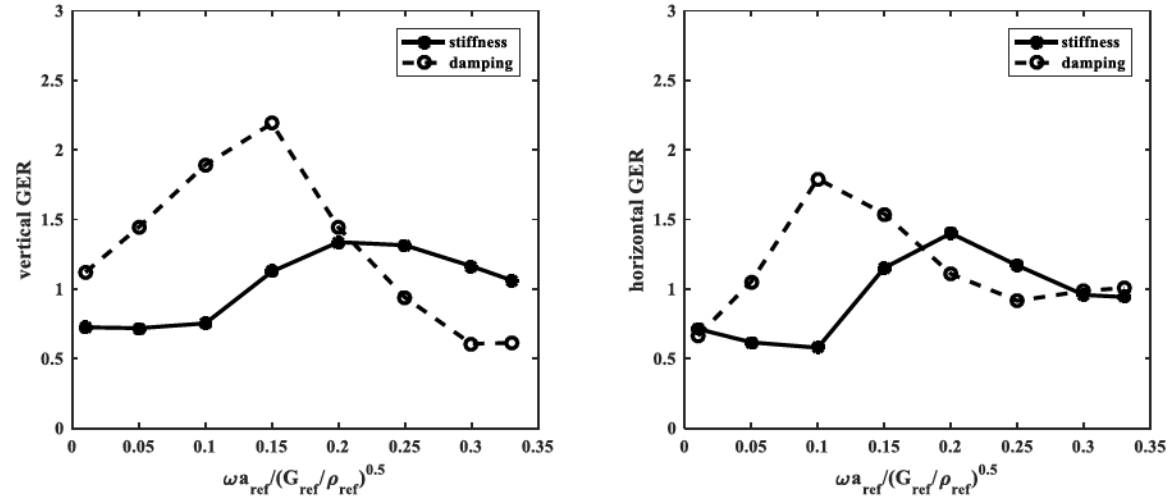

Figure 3.35 *Vertical and horizontal GER for a 2×2 pile group with disturbed zone.*

3.7.2 Pile Group Deformation

Pile deformation is a common interpretation for pile problems. For simplicity, three-dimensional deformation of piles are presented using displacements along piles' central axes herein. Based on the plane cross-section assumption in the structural Green's functions, displacements along the pile central axis can be calculated by averaging nodal displacements at the same depths in BEM models.

Once a pile is loaded at head, adjacent piles deform correspondingly due to pile-soil-pile interaction. As introduced in Section 3.3.1, the new predefined complex boundary condition at head of Pile 1 is the translation and rotation by complex value 1+0i. In Equation (3.71), if the external force matrix Q is substituted with real numbers, then the initial phase angle of excitation force is assumed to be zero. However the actual complex displacements at head of each pile commonly have non-zero imaginary part. This means the nodal displacements on piles by BEASSI need to be scaled for actual pile deformation.

The physical meaning of scaling is illustrated by an example of a single pile in Figure 3.36. Assume vector x_a denoting the predefined B.C. at point a, which has zero phase angle and magnitude of unity. Vector x_c denotes the corresponding displacement vector at point c on pile at the same time. Vector x_a' refers to the actual displacement of pile at ground level that is obtained from the sub-structuring formulation, and the actual displacement at point c is represented by vector x_c'

.

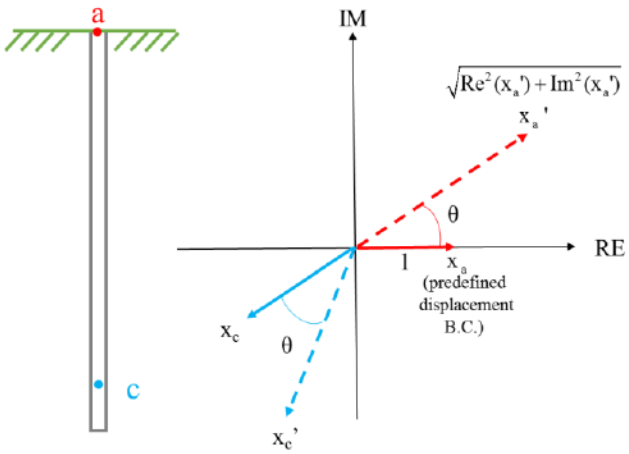

Figure 3.36 *Displacements on pile in complex coordinate system.*

Displacement vector x_c' is derived in two steps. In the first step, consider x_a rotating θ with constant magnitude. For steady-state forced vibrations at a given frequency, difference in phase angle for displacement vectors at two given points remains constant. Otherwise, the two displacement vectors would have different circular frequencies, which is unrealistic. If x_a has a rotation of θ, then vector x_c must follow the same way. Through transformation matrix, the new coordinates of vector x_c become:

$$\begin{cases} \mathrm{RE}(\mathbf{x_c'}) = \mathrm{RE}(\mathbf{x_c})\cos\theta - \mathrm{IM}(\mathbf{x_c})\sin\theta \\ \mathrm{IM}(\mathbf{x_c'}) = \mathrm{RE}(\mathbf{x_c})\sin\theta + \mathrm{IM}(\mathbf{x_c})\cos\theta \end{cases} \tag{3.75}$$

where $\cos\theta = \mathrm{IM}(\mathbf{x_a'})/\mathrm{RE}(\mathbf{x_a'})$. In the second step, consider scaling magnitude of x_a'. For linear viscoelastic vibration problems, relative magnitude of displacements at two points remain constantly proportional regardless of amplitude of excitation and phase angle. This denotes that both real and imaginary parts of vector at point C must be simultaneously scaled by $\sqrt{\mathrm{RE}^2(\mathbf{x_a'}) + \mathrm{IM}^2(\mathbf{x_a'})}$ just as $\mathbf{x_a'}$. Disproportionate scaling in real part and imaginary part would induce change of the relative phase angle. The final displacement vector at point c can be expressed as:

$$\begin{cases} \mathrm{RE}(\mathbf{x_c'}) = \sqrt{\mathrm{RE}^2(\mathbf{x_a'}) + \mathrm{IM}^2(\mathbf{x_a'})}\left[\mathrm{RE}(\mathbf{x_c})\cos\theta - \mathrm{IM}(\mathbf{x_c})\sin\theta\right] \\ \mathrm{IM}(\mathbf{x_c'}) = \sqrt{\mathrm{RE}^2(\mathbf{x_a'}) + \mathrm{IM}^2(\mathbf{x_a'})}\left[\mathrm{RE}(\mathbf{x_c})\sin\theta + \mathrm{IM}(\mathbf{x_c})\cos\theta\right] \end{cases} \tag{3.76}$$

A more concise way is multiplying displacement vector $\mathbf{x_c}$ from BEM analysis by actual complex displacement vector $\mathbf{x_a'}$:

$$\mathbf{x_c'} = \left[\mathrm{RE}(\mathbf{x_c}) + \mathrm{IM}(\mathbf{x_c})\mathrm{i}\right] \bullet \left[\mathrm{RE}(\mathbf{x_a'}) + \mathrm{IM}(\mathbf{x_a'})\mathrm{i}\right] \tag{3.77}$$

As for the physical meaning, the real part of $\mathbf{x}_c'$ denotes the actual displacement at point c when the instantaneous phase shift of external force Q is zero. The imaginary part refers to actual displacement when phase angle of Q is $-\pi/2$.

Superposition can be applied not only for group impedance, but also for displacements of pile group. Displacement vectors at a given point along central axis of four piles can be expressed as:

$$\begin{cases} \mathbf{u}^1 = \mathbf{u}^{1-1} + \mathbf{u}^{1-2} + \mathbf{u}^{1-3} + \mathbf{u}^{1-4} \\ \mathbf{u}^2 = \mathbf{u}^{2-1} + \mathbf{u}^{2-2} + \mathbf{u}^{2-3} + \mathbf{u}^{2-4} \\ \mathbf{u}^3 = \mathbf{u}^{3-1} + \mathbf{u}^{3-2} + \mathbf{u}^{3-3} + \mathbf{u}^{3-4} \\ \mathbf{u}^4 = \mathbf{u}^{4-1} + \mathbf{u}^{4-2} + \mathbf{u}^{4-3} + \mathbf{u}^{4-4} \end{cases} \tag{3.78}$$

Each displacement vector comprises three directional components:

$$\mathbf{u}^{i-j} = \begin{bmatrix} u_x^{i-j} \\ u_y^{i-j} \\ u_z^{i-j} \end{bmatrix} \tag{3.79}$$

In Equation (3.79), the first superscript denotes the observed pile and the second denotes the loaded pile. And each directional component can be derived by superposition of four types of vibrations predefined in BEASSI – vertical (z), horizontal (x), rotational (r_y), and torsional (r_z), i.e.,

$$\mathbf{u}^{i-j} = \begin{bmatrix} u_x^{i-j} \\ u_y^{i-j} \\ u_z^{i-j} \end{bmatrix} = \begin{bmatrix} \text{scaler}_z^j \cdot u_{xz}^{i-j} + \text{scaler}_x^j \cdot u_{xx}^{i-j} + \text{scaler}_{r_y}^j \cdot u_{xr_y}^{i-j} + \text{scaler}_{r_z}^j \cdot u_{xr_z}^{i-j} \\ \text{scaler}_z^j \cdot u_{yz}^{i-j} + \text{scaler}_x^j \cdot u_{yx}^{i-j} + \text{scaler}_{r_y}^j \cdot u_{yr_y}^{i-j} + \text{scaler}_{r_z}^j \cdot u_{yr_z}^{i-j} \\ \text{scaler}_z^j \cdot u_{zz}^{i-j} + \text{scaler}_x^j \cdot u_{zx}^{i-j} + \text{scaler}_{r_y}^j \cdot u_{zr_y}^{i-j} + \text{scaler}_{r_z}^j \cdot u_{zr_z}^{i-j} \end{bmatrix} \tag{3.80}$$

where the first subscripts denote direction of displacement for the observed Pile i and the second subscripts denote directional vibration of Pile j. scaler_z^j, scaler_x^j, $\text{scaler}_{r_y}^j$ and $\text{scaler}_{r_z}^j$ are actual directional displacements at head of Pile j. $\mathbf{u}^{i-j}$ is recorded as:

$$\mathbf{u}^{i-j}=\begin{bmatrix} u_{xz}^{i-j} & u_{xx}^{i-j} & u_{xr_y}^{i-j} & u_{xr_z}^{i-j} \\ u_{yz}^{i-j} & u_{yx}^{i-j} & u_{yr_y}^{i-j} & u_{yr_z}^{i-j} \\ u_{zz}^{i-j} & u_{zx}^{i-j} & u_{zr_y}^{i-j} & u_{zr_z}^{i-j} \end{bmatrix}\begin{bmatrix} \text{scaler}_z^j \\ \text{scaler}_x^j \\ \text{scaler}_{r_y}^j \\ \text{scaler}_{r_z}^j \end{bmatrix}=\begin{bmatrix} u_{xz}^{i-j} & u_{xx}^{i-j} & u_{xr_y}^{i-j} & u_{xr_z}^{i-j} \\ u_{yz}^{i-j} & u_{yx}^{i-j} & u_{yr_y}^{i-j} & u_{yr_z}^{i-j} \\ u_{zz}^{i-j} & u_{zx}^{i-j} & u_{zr_y}^{i-j} & u_{zr_z}^{i-j} \end{bmatrix}\text{scaler}^j \quad (3.81)$$

For planar motion of the pile group,

$$\begin{cases} \text{scaler}^1 \equiv \text{scaler}^2 \\ \text{scaler}^3 \equiv \text{scaler}^4 \end{cases} \quad (3.82)$$

In BEM analyses only Pile 1 is loaded at head and the rest piles are fixed at head. Thus displacement components u^{1-1}, u^{1-2}, u^{1-3}, and u^{1-4} are considered as known, and the remaining unknown displacement vectors can be derived by symmetry. Detailed derivations for each pile subjected to directional vibration are given below.

- Pile 1
  For vertical vibration,

$$u_{xz}^{1-1}=u_{xz}^{1-1},\quad u_{xz}^{1-2}=u_{xz}^{2-1},\quad u_{xz}^{1-3}=-u_{xz}^{3-1},\quad u_{xz}^{1-4}=-u_{xz}^{4-1}$$

$$u_{yz}^{1-1}=u_{yz}^{1-1},\quad u_{yz}^{1-2}=-u_{yz}^{2-1},\quad u_{yz}^{1-3}=u_{yz}^{3-1},\quad u_{yz}^{1-4}=-u_{yz}^{4-1}$$

$$u_{zz}^{1-1}=u_{zz}^{1-1},\quad u_{zz}^{1-2}=u_{zz}^{2-1},\quad u_{zz}^{1-3}=u_{zz}^{3-1},\quad u_{zz}^{1-4}=u_{zz}^{4-1}$$

  For horizontal vibration,

$$u_{xx}^{1-1}=u_{xx}^{1-1},\quad u_{xx}^{1-2}=u_{xx}^{2-1},\quad u_{xx}^{1-3}=u_{xx}^{3-1},\quad u_{xx}^{1-4}=u_{xx}^{4-1}$$

$$u_{yx}^{1-1}=u_{yx}^{1-1},\quad u_{yx}^{1-2}=-u_{yx}^{2-1},\quad u_{yx}^{1-3}=-u_{yx}^{3-1},\quad u_{yx}^{1-4}=u_{yx}^{4-1}$$

$$u_{zx}^{1-1}=u_{zx}^{1-1},\quad u_{zx}^{1-2}=u_{zx}^{2-1},\quad u_{zx}^{1-3}=-u_{zx}^{3-1},\quad u_{zx}^{1-4}=-u_{zx}^{4-1}$$

  For rocking vibration,

$$u_{xr_y}^{1-1}=u_{xr_y}^{1-1},\quad u_{xr_y}^{1-2}=u_{xr_y}^{2-1},\quad u_{xr_y}^{1-3}=u_{xr_y}^{3-1},\quad u_{xr_y}^{1-4}=u_{xr_y}^{4-1}$$

$$u_{yr_y}^{1-1}=u_{yr_y}^{1-1},\quad u_{yr_y}^{1-2}=-u_{yr_y}^{2-1},\quad u_{yr_y}^{1-3}=-u_{yr_y}^{3-1},\quad u_{yr_y}^{1-4}=u_{yr_y}^{4-1}$$

$$u_{zr_y}^{1-1}=u_{zr_y}^{1-1},\quad u_{zr_y}^{1-2}=u_{zr_y}^{2-1},\quad u_{zr_y}^{1-3}=-u_{zr_y}^{3-1},\quad u_{zr_y}^{1-4}=-u_{zr_y}^{4-1}$$

For torsional vibration,

$$u_{xr_z}^{1-1}=u_{xr_z}^{1-1},\quad u_{xr_z}^{1-2}=-u_{xr_z}^{2-1},\quad u_{xr_z}^{1-3}=u_{xr_z}^{3-1},\quad u_{xr_z}^{1-4}=-u_{xr_z}^{4-1}$$

$$u_{yr_z}^{1-1}=u_{yr_z}^{1-1},\quad u_{yr_z}^{1-2}=u_{yr_z}^{2-1},\quad u_{yr_z}^{1-3}=-u_{yr_z}^{3-1},\quad u_{yr_z}^{1-4}=-u_{yr_z}^{4-1}$$

$$u_{zr_z}^{1-1}=u_{zr_z}^{1-1},\quad u_{zr_z}^{1-2}=-u_{zr_z}^{2-1},\quad u_{zr_z}^{1-3}=-u_{zr_z}^{3-1},\quad u_{zr_z}^{1-4}=u_{zr_z}^{4-1}$$

- Pile 2

For vertical vibration,

$$u_{xz}^{2-1}=u_{xz}^{2-1},\quad u_{xz}^{2-2}=u_{xz}^{1-1},\quad u_{xz}^{2-3}=-u_{xz}^{4-1},\quad u_{xz}^{2-4}=-u_{xz}^{3-1}$$

$$u_{yz}^{2-1}=u_{yz}^{2-1},\quad u_{yz}^{2-2}=-u_{yz}^{1-1},\quad u_{yz}^{2-3}=u_{yz}^{4-1},\quad u_{yz}^{2-4}=-u_{yz}^{3-1}$$

$$u_{zz}^{2-1}=u_{zz}^{2-1},\quad u_{zz}^{2-2}=u_{zz}^{1-1},\quad u_{zz}^{2-3}=u_{zz}^{4-1},\quad u_{zz}^{2-4}=u_{zz}^{3-1}$$

For horizontal vibration,

$$u_{xx}^{2-1}=u_{xx}^{2-1},\quad u_{xx}^{2-2}=u_{xx}^{1-1},\quad u_{xx}^{2-3}=u_{xx}^{4-1},\quad u_{xx}^{2-4}=u_{xx}^{3-1}$$

$$u_{yx}^{2-1}=u_{yx}^{2-1},\quad u_{yx}^{2-2}=-u_{yx}^{1-1},\quad u_{yx}^{2-3}=-u_{yx}^{4-1},\quad u_{yx}^{2-4}=u_{yx}^{3-1}$$

$$u_{zx}^{2-1}=u_{zx}^{2-1},\quad u_{zx}^{2-2}=u_{zx}^{1-1},\quad u_{zx}^{2-3}=-u_{zx}^{4-1},\quad u_{zx}^{2-4}=-u_{zx}^{3-1}$$

For rocking vibration,

$$u_{xr_y}^{2-1}=u_{xr_y}^{2-1},\quad u_{xr_y}^{2-2}=u_{xr_y}^{1-1},\quad u_{xr_y}^{2-3}=u_{xr_y}^{4-1},\quad u_{xr_y}^{2-4}=u_{xr_y}^{3-1}$$

$$u_{yr_y}^{2-1}=u_{yr_y}^{2-1},\quad u_{yr_y}^{2-2}=-u_{yr_y}^{1-1},\quad u_{yr_y}^{2-3}=-u_{yr_y}^{4-1},\quad u_{yr_y}^{2-4}=u_{yr_y}^{3-1}$$

$$u_{zr_y}^{2-1}=u_{zr_y}^{2-1},\quad u_{zr_y}^{2-2}=u_{zr_y}^{1-1},\quad u_{zr_y}^{2-3}=-u_{zr_y}^{4-1},\quad u_{zr_y}^{2-4}=-u_{zr_y}^{3-1}$$

For torsional vibration,

$$u_{xr_z}^{2-1}=u_{xr_z}^{2-1},\quad u_{xr_z}^{2-2}=-u_{xr_z}^{1-1},\quad u_{xr_z}^{2-3}=u_{xr_z}^{4-1},\quad u_{xr_z}^{2-4}=-u_{xr_z}^{3-1}$$

$$u_{yr_z}^{2-1}=u_{yr_z}^{2-1},\quad u_{yr_z}^{2-2}=u_{yr_z}^{1-1},\quad u_{yr_z}^{2-3}=-u_{yr_z}^{4-1},\quad u_{yr_z}^{2-4}=-u_{yr_z}^{3-1}$$

$$u_{zr_z}^{2-1}=u_{zr_z}^{2-1},\quad u_{zr_z}^{2-2}=-u_{zr_z}^{1-1},\quad u_{zr_z}^{2-3}=-u_{zr_z}^{4-1},\quad u_{zr_z}^{2-4}=u_{zr_z}^{3-1}$$

- Pile 3

For vertical vibration,

$$u_{xz}^{3-1}=u_{xz}^{3-1},\quad u_{xz}^{3-2}=u_{xz}^{4-1},\quad u_{xz}^{3-3}=-u_{xz}^{1-1},\quad u_{xz}^{3-4}=-u_{xz}^{2-1}$$

$$u_{yz}^{3-1}=u_{yz}^{3-1},\quad u_{yz}^{3-2}=-u_{yz}^{4-1},\quad u_{yz}^{3-3}=u_{yz}^{1-1},\quad u_{yz}^{3-4}=-u_{yz}^{2-1}$$

$$u_{zz}^{3-1}=u_{zz}^{3-1},\quad u_{zz}^{3-2}=u_{zz}^{4-1},\quad u_{zz}^{3-3}=u_{zz}^{1-1},\quad u_{zz}^{3-4}=u_{zz}^{2-1}$$

For horizontal vibration,

$$u_{xx}^{3-1}=u_{xx}^{3-1},\quad u_{xx}^{3-2}=u_{xx}^{4-1},\quad u_{xx}^{3-3}=u_{xx}^{1-1},\quad u_{xx}^{3-4}=u_{xx}^{2-1}$$

$$u_{yx}^{3-1}=u_{yx}^{3-1},\quad u_{yx}^{3-2}=-u_{yx}^{4-1},\quad u_{yx}^{3-3}=-u_{yx}^{1-1},\quad u_{yx}^{3-4}=u_{yx}^{2-1}$$

$$u_{zx}^{3-1}=u_{zx}^{3-1},\quad u_{zx}^{3-2}=u_{zx}^{4-1},\quad u_{zx}^{3-3}=-u_{zx}^{1-1},\quad u_{zx}^{3-4}=-u_{zx}^{2-1}$$

For rocking vibration,

$$u_{xr_y}^{3-1}=u_{xr_y}^{3-1},\quad u_{xr_y}^{3-2}=u_{xr_y}^{4-1},\quad u_{xr_y}^{3-3}=u_{xr_y}^{1-1},\quad u_{xr_y}^{3-4}=u_{xr_y}^{2-1}$$

$$u_{yr_y}^{3-1}=u_{yr_y}^{3-1},\quad u_{yr_y}^{3-2}=-u_{yr_y}^{4-1},\quad u_{yr_y}^{3-3}=-u_{yr_y}^{1-1},\quad u_{yr_y}^{3-4}=u_{yr_y}^{2-1}$$

$$u_{zr_y}^{3-1}=u_{zr_y}^{3-1},\quad u_{zr_y}^{3-2}=u_{zr_y}^{4-1},\quad u_{zr_y}^{3-3}=-u_{zr_y}^{1-1},\quad u_{zr_y}^{3-4}=-u_{zr_y}^{2-1}$$

For torsional vibration,

$$u_{xr_z}^{3-1}=u_{xr_z}^{3-1},\quad u_{xr_z}^{3-2}=-u_{xr_z}^{4-1},\quad u_{xr_z}^{3-3}=u_{xr_z}^{1-1},\quad u_{xr_z}^{3-4}=-u_{xr_z}^{2-1}$$

$$u_{yr_z}^{3-1}=u_{yr_z}^{3-1},\quad u_{yr_z}^{3-2}=u_{yr_z}^{4-1},\quad u_{yr_z}^{3-3}=-u_{yr_z}^{1-1},\quad u_{yr_z}^{3-4}=-u_{yr_z}^{2-1}$$

$$u_{zr_z}^{3-1}=u_{zr_z}^{3-1},\quad u_{zr_z}^{3-2}=-u_{zr_z}^{4-1},\quad u_{zr_z}^{3-3}=-u_{zr_z}^{1-1},\quad u_{zr_z}^{3-4}=u_{zr_z}^{2-1}$$

- Pile 4

For vertical vibration,

$$u_{xz}^{4-1}=u_{xz}^{4-1},\quad u_{xz}^{4-2}=u_{xz}^{3-1},\quad u_{xz}^{4-3}=-u_{xz}^{2-1},\quad u_{xz}^{4-4}=-u_{xz}^{1-1}$$

$$u_{yz}^{4-1}=u_{yz}^{4-1},\quad u_{yz}^{4-2}=-u_{yz}^{3-1},\quad u_{yz}^{4-3}=u_{yz}^{2-1},\quad u_{yz}^{4-4}=-u_{yz}^{1-1}$$

$$u_{zz}^{4-1}=u_{zz}^{4-1},\quad u_{zz}^{4-2}=u_{zz}^{3-1},\quad u_{zz}^{4-3}=u_{zz}^{2-1},\quad u_{zz}^{4-4}=u_{zz}^{1-1}$$

For horizontal vibration,

$$u_{xx}^{4-1}=u_{xx}^{4-1},\quad u_{xx}^{4-2}=u_{xx}^{3-1},\quad u_{xx}^{4-3}=u_{xx}^{2-1},\quad u_{xx}^{4-4}=u_{xx}^{1-1}$$

$$u_{yx}^{4-1}=u_{yx}^{4-1},\quad u_{yx}^{4-2}=-u_{yx}^{3-1},\quad u_{yx}^{4-3}=-u_{yx}^{2-1},\quad u_{yx}^{4-4}=u_{yx}^{1-1}$$

$$u_{zx}^{4-1}=u_{zx}^{4-1},\quad u_{zx}^{4-2}=u_{zx}^{3-1},\quad u_{zx}^{4-3}=-u_{zx}^{2-1},\quad u_{zx}^{4-4}=-u_{zx}^{1-1}$$

For rocking vibration,

$$u_{xr_y}^{4-1}=u_{xr_y}^{4-1},\quad u_{xr_y}^{4-2}=u_{xr_y}^{3-1},\quad u_{xr_y}^{4-3}=u_{xr_y}^{2-1},\quad u_{xr_y}^{4-4}=u_{xr_y}^{1-1}$$

$$u_{yr_y}^{4-1}=u_{yr_y}^{4-1},\quad u_{yr_y}^{4-2}=-u_{yr_y}^{3-1},\quad u_{yr_y}^{4-3}=-u_{yr_y}^{2-1},\quad u_{yr_y}^{4-4}=u_{yr_y}^{1-1}$$

$$u_{zr_y}^{4-1}=u_{zr_y}^{4-1},\quad u_{zr_y}^{4-2}=u_{zr_y}^{3-1},\quad u_{zr_y}^{4-3}=-u_{zr_y}^{2-1},\quad u_{zr_y}^{4-4}=-u_{zr_y}^{1-1}$$

For torsional vibration,

$$u_{xr_z}^{4-1}=u_{xr_z}^{4-1},\quad u_{xr_z}^{4-2}=-u_{xr_z}^{3-1},\quad u_{xr_z}^{4-3}=u_{xr_z}^{2-1},\quad u_{xr_z}^{4-4}=-u_{xr_z}^{1-1}$$

$$u_{yr_z}^{4-1}=u_{yr_z}^{4-1},\quad u_{yr_z}^{4-2}=u_{yr_z}^{3-1},\quad u_{yr_z}^{4-3}=-u_{yr_z}^{2-1},\quad u_{yr_z}^{4-4}=-u_{yr_z}^{1-1}$$

$$u_{zr_z}^{4-1}=u_{zr_z}^{4-1},\quad u_{zr_z}^{4-2}=-u_{zr_z}^{3-1},\quad u_{zr_z}^{4-3}=-u_{zr_z}^{2-1},\quad u_{zr_z}^{4-4}=u_{zr_z}^{1-1}$$

Displacement at any point on a pile is calculated as below:

$$\mathbf{u}^1 = \begin{bmatrix} u_{xz}^{1-1} & u_{xx}^{1-1} & u_{xr_y}^{1-1} & u_{xr_z}^{1-1} \\ u_{yz}^{1-1} & u_{yx}^{1-1} & u_{yr_y}^{1-1} & u_{yr_z}^{1-1} \\ u_{zz}^{1-1} & u_{zx}^{1-1} & u_{zr_y}^{1-1} & u_{zr_z}^{1-1} \end{bmatrix} \begin{bmatrix} \text{scaler}_z^1 \\ \text{scaler}_x^1 \\ \text{scaler}_{r_y}^1 \\ \text{scaler}_{r_z}^1 \end{bmatrix} + \begin{bmatrix} u_{xz}^{2-1} & u_{xx}^{2-1} & u_{xr_y}^{2-1} & -u_{xr_z}^{1-2} \\ -u_{yz}^{2-1} & -u_{yx}^{2-1} & -u_{yr_y}^{2-1} & u_{yr_z}^{2-1} \\ u_{zz}^{2-1} & u_{zx}^{2-1} & u_{zr_y}^{2-1} & -u_{zr_z}^{2-1} \end{bmatrix} \begin{bmatrix} \text{scaler}_z^1 \\ \text{scaler}_x^1 \\ \text{scaler}_{r_y}^1 \\ \text{scaler}_{r_z}^1 \end{bmatrix}$$
$$+ \begin{bmatrix} -u_{xz}^{3-1} & u_{xx}^{3-1} & u_{xr_y}^{3-1} & u_{xr_z}^{3-1} \\ u_{yz}^{3-1} & -u_{yx}^{3-1} & -u_{yr_y}^{3-1} & -u_{yr_z}^{3-1} \\ u_{zz}^{3-1} & -u_{zx}^{3-1} & -u_{zr_y}^{3-1} & -u_{zr_z}^{3-1} \end{bmatrix} \begin{bmatrix} \text{scaler}_z^3 \\ \text{scaler}_x^3 \\ \text{scaler}_{r_y}^3 \\ \text{scaler}_{r_z}^4 \end{bmatrix} + \begin{bmatrix} -u_{xz}^{4-1} & u_{xx}^{4-1} & u_{xr_y}^{4-1} & -u_{xr_z}^{4-1} \\ -u_{yz}^{4-1} & u_{yx}^{4-1} & u_{yr_y}^{4-1} & -u_{yr_z}^{4-1} \\ u_{zz}^{4-1} & -u_{zx}^{4-1} & -u_{zr_y}^{4-1} & u_{zr_z}^{4-1} \end{bmatrix} \begin{bmatrix} \text{scaler}_z^3 \\ \text{scaler}_x^3 \\ \text{scaler}_{r_y}^3 \\ \text{scaler}_{r_z}^3 \end{bmatrix} \tag{3.83}$$

$$\mathbf{u}^2 = \begin{bmatrix} u_{xz}^{2-1} & u_{xx}^{2-1} & u_{xr_y}^{2-1} & u_{xr_z}^{2-1} \\ u_{yz}^{2-1} & u_{yx}^{2-1} & u_{yr_y}^{2-1} & u_{yr_z}^{2-1} \\ u_{zz}^{2-1} & u_{zx}^{2-1} & u_{zr_y}^{2-1} & u_{zr_z}^{2-1} \end{bmatrix} \begin{bmatrix} \text{scaler}_z^1 \\ \text{scaler}_x^1 \\ \text{scaler}_{r_y}^1 \\ \text{scaler}_{r_z}^1 \end{bmatrix} + \begin{bmatrix} u_{xz}^{1-1} & u_{xx}^{1-1} & u_{xr_y}^{1-1} & -u_{xr_z}^{1-1} \\ -u_{yz}^{1-1} & -u_{yx}^{1-1} & -u_{yr_y}^{1-1} & u_{yr_z}^{1-1} \\ u_{zz}^{1-1} & u_{zx}^{1-1} & u_{zr_y}^{1-1} & -u_{zr_z}^{1-1} \end{bmatrix} \begin{bmatrix} \text{scaler}_z^1 \\ \text{scaler}_x^1 \\ \text{scaler}_{r_y}^1 \\ \text{scaler}_{r_z}^1 \end{bmatrix}$$
$$+ \begin{bmatrix} -u_{xz}^{4-1} & u_{xx}^{4-1} & u_{xr_y}^{4-1} & u_{xr_z}^{4-1} \\ u_{yz}^{4-1} & -u_{yx}^{4-1} & -u_{yr_y}^{4-1} & -u_{yr_z}^{4-1} \\ u_{zz}^{4-1} & -u_{zx}^{4-1} & -u_{zr_y}^{4-1} & -u_{zr_z}^{4-1} \end{bmatrix} \begin{bmatrix} \text{scaler}_z^3 \\ \text{scaler}_x^3 \\ \text{scaler}_{r_y}^3 \\ \text{scaler}_{r_z}^4 \end{bmatrix} + \begin{bmatrix} -u_{xz}^{3-1} & u_{xx}^{3-1} & u_{xr_y}^{3-1} & -u_{xr_z}^{3-1} \\ -u_{yz}^{3-1} & u_{yx}^{3-1} & u_{yr_y}^{3-1} & -u_{yr_z}^{3-1} \\ u_{zz}^{3-1} & -u_{zx}^{3-1} & -u_{zr_y}^{3-1} & u_{zr_z}^{3-1} \end{bmatrix} \begin{bmatrix} \text{scaler}_z^3 \\ \text{scaler}_x^3 \\ \text{scaler}_{r_y}^3 \\ \text{scaler}_{r_z}^3 \end{bmatrix} \tag{3.84}$$

$$\mathbf{u}^3 = \begin{bmatrix} u_{xz}^{3-1} & u_{xx}^{3-1} & u_{xr_y}^{3-1} & u_{xr_z}^{3-1} \\ u_{yz}^{3-1} & u_{yx}^{3-1} & u_{yr_y}^{3-1} & u_{yr_z}^{3-1} \\ u_{zz}^{3-1} & u_{zx}^{3-1} & u_{zr_y}^{3-1} & u_{zr_z}^{3-1} \end{bmatrix} \begin{bmatrix} \text{scaler}_z^1 \\ \text{scaler}_x^1 \\ \text{scaler}_{r_y}^1 \\ \text{scaler}_{r_z}^1 \end{bmatrix} + \begin{bmatrix} u_{xz}^{4-1} & u_{xx}^{4-1} & u_{xr_y}^{4-1} & -u_{xr_z}^{4-1} \\ -u_{yz}^{4-1} & -u_{yx}^{4-1} & -u_{yr_y}^{4-1} & u_{yr_z}^{4-1} \\ u_{zz}^{4-1} & u_{zx}^{4-1} & u_{zr_y}^{4-1} & -u_{zr_z}^{4-1} \end{bmatrix} \begin{bmatrix} \text{scaler}_z^1 \\ \text{scaler}_x^1 \\ \text{scaler}_{r_y}^1 \\ \text{scaler}_{r_z}^1 \end{bmatrix}$$
$$+ \begin{bmatrix} -u_{xz}^{1-1} & u_{xx}^{1-1} & u_{xr_y}^{1-1} & u_{xr_z}^{1-1} \\ u_{yz}^{1-1} & -u_{yx}^{1-1} & -u_{yr_y}^{1-1} & -u_{yr_z}^{1-1} \\ u_{zz}^{1-1} & -u_{zx}^{1-1} & -u_{zr_y}^{1-1} & -u_{zr_z}^{1-1} \end{bmatrix} \begin{bmatrix} \text{scaler}_z^3 \\ \text{scaler}_x^3 \\ \text{scaler}_{r_y}^3 \\ \text{scaler}_{r_z}^4 \end{bmatrix} + \begin{bmatrix} -u_{xz}^{2-1} & u_{xx}^{2-1} & u_{xr_y}^{2-1} & -u_{xr_z}^{2-1} \\ -u_{yz}^{2-1} & u_{yx}^{2-1} & u_{yr_y}^{2-1} & -u_{yr_z}^{2-1} \\ u_{zz}^{2-1} & -u_{zx}^{2-1} & -u_{zr_y}^{2-1} & u_{zr_z}^{2-1} \end{bmatrix} \begin{bmatrix} \text{scaler}_z^3 \\ \text{scaler}_x^3 \\ \text{scaler}_{r_y}^3 \\ \text{scaler}_{r_z}^3 \end{bmatrix} \tag{3.85}$$

$$\mathbf{u}^4 = \begin{bmatrix} u_{xz}^{4-1} & u_{xx}^{4-1} & u_{xr_y}^{4-1} & u_{xr_z}^{4-1} \\ u_{yz}^{4-1} & u_{yx}^{4-1} & u_{yr_y}^{4-1} & u_{yr_z}^{4-1} \\ u_{zz}^{4-1} & u_{zx}^{4-1} & u_{zr_y}^{4-1} & u_{zr_z}^{4-1} \end{bmatrix} \begin{bmatrix} \text{scaler}_z^1 \\ \text{scaler}_x^1 \\ \text{scaler}_{r_y}^1 \\ \text{scaler}_{r_z}^1 \end{bmatrix} + \begin{bmatrix} u_{xz}^{3-1} & u_{xx}^{3-1} & u_{xr_y}^{3-1} & -u_{xr_z}^{3-1} \\ -u_{yz}^{3-1} & -u_{yx}^{3-1} & -u_{yr_y}^{3-1} & u_{yr_z}^{3-1} \\ u_{zz}^{3-1} & u_{zx}^{3-1} & u_{zr_y}^{3-1} & -u_{zr_z}^{3-1} \end{bmatrix} \begin{bmatrix} \text{scaler}_z^1 \\ \text{scaler}_x^1 \\ \text{scaler}_{r_y}^1 \\ \text{scaler}_{r_z}^1 \end{bmatrix}$$
$$+ \begin{bmatrix} -u_{xz}^{2-1} & u_{xx}^{2-1} & u_{xr_y}^{2-1} & u_{xr_z}^{2-1} \\ u_{yz}^{2-1} & -u_{yx}^{2-1} & -u_{yr_y}^{2-1} & -u_{yr_z}^{2-1} \\ u_{zz}^{2-1} & -u_{zx}^{2-1} & -u_{zr_y}^{2-1} & -u_{zr_z}^{2-1} \end{bmatrix} \begin{bmatrix} \text{scaler}_z^3 \\ \text{scaler}_x^3 \\ \text{scaler}_{r_y}^3 \\ \text{scaler}_{r_z}^4 \end{bmatrix} + \begin{bmatrix} -u_{xz}^{1-1} & u_{xx}^{1-1} & u_{xr_y}^{1-1} & -u_{xr_z}^{1-1} \\ -u_{yz}^{1-1} & u_{yx}^{1-1} & u_{yr_y}^{1-1} & -u_{yr_z}^{1-1} \\ u_{zz}^{1-1} & -u_{zx}^{1-1} & -u_{zr_y}^{1-1} & u_{zr_z}^{1-1} \end{bmatrix} \begin{bmatrix} \text{scaler}_z^3 \\ \text{scaler}_x^3 \\ \text{scaler}_{r_y}^3 \\ \text{scaler}_{r_z}^3 \end{bmatrix} \tag{3.86}$$

3.7.3 Analysis of Displacement, Strain, and Stress Fields within Soil

The previously cited BEM studies primarily utilized stresses and displacements on the boundary surfaces of the piles and disturbed zones. Though such analyses indicate how the piles behave, they don't provide details on behavior within the soil regions. Analyzing the stress and strain fields within the soil domains may provide further useful insights not only on contact conditions at the pile-soil interface, but also on the soil response within the disturbed zone. Furthermore, this information could enable more rigorous analyses for determining an appropriate size, shape, and soil profile for the disturbed zone. This section is about implementing a finite difference scheme into BEASSI to calculate displacement, stress, and strain fields within the material domains, as well as insights from applying such analyses to disturbed soil zones around pile groups. The overall framework for analysis of the displacement, stress, and strain fields is shown in Figure 3.37.

1. Obtaining displacement at internal points

Once nodal displacements and nodal tractions are solved for, they are substituted back into the governing boundary integral equation to evaluate the displacements at internal points. To derive stress and strain fields with reasonable resolution from a finite collection of internal

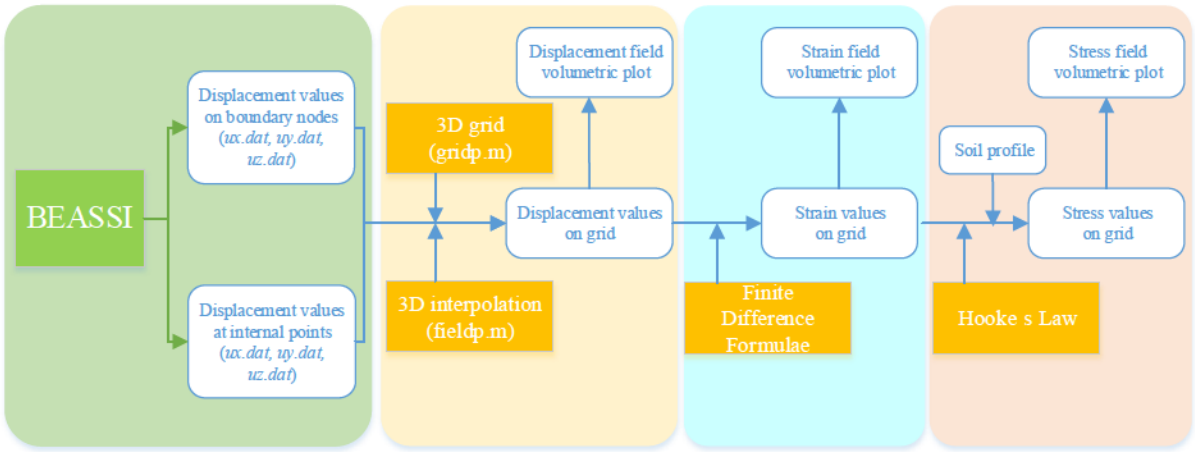

Figure 3.37 *Framework for analysis of displacement, stress and strain fields within soil domains.*

points, the density of the internal points must be sufficiently high so that the space in between the points can be well approximated. The ideal solution is creating a dense grid on which displacement at every point is computed directly by BEASSI. However, this solution requires tremendous computational time. As an alternative, a less number of representative internal points can be specified within the soil domain. With combination of the displacements at the boundary nodes and those at the internal points, displacements on a fine 3D grid can be approximated by interpolation. Figure 3.38(a) shows an example for a disturbed zone that comprises 4634 boundary nodes and 356 internal points. With the displacements interpolated at each point on a 3D orthogonal grid, it is easy to plot volumetric displacement field (Figure 3.38(b)). This solution makes balance among accuracy, completion time, and computational capability.

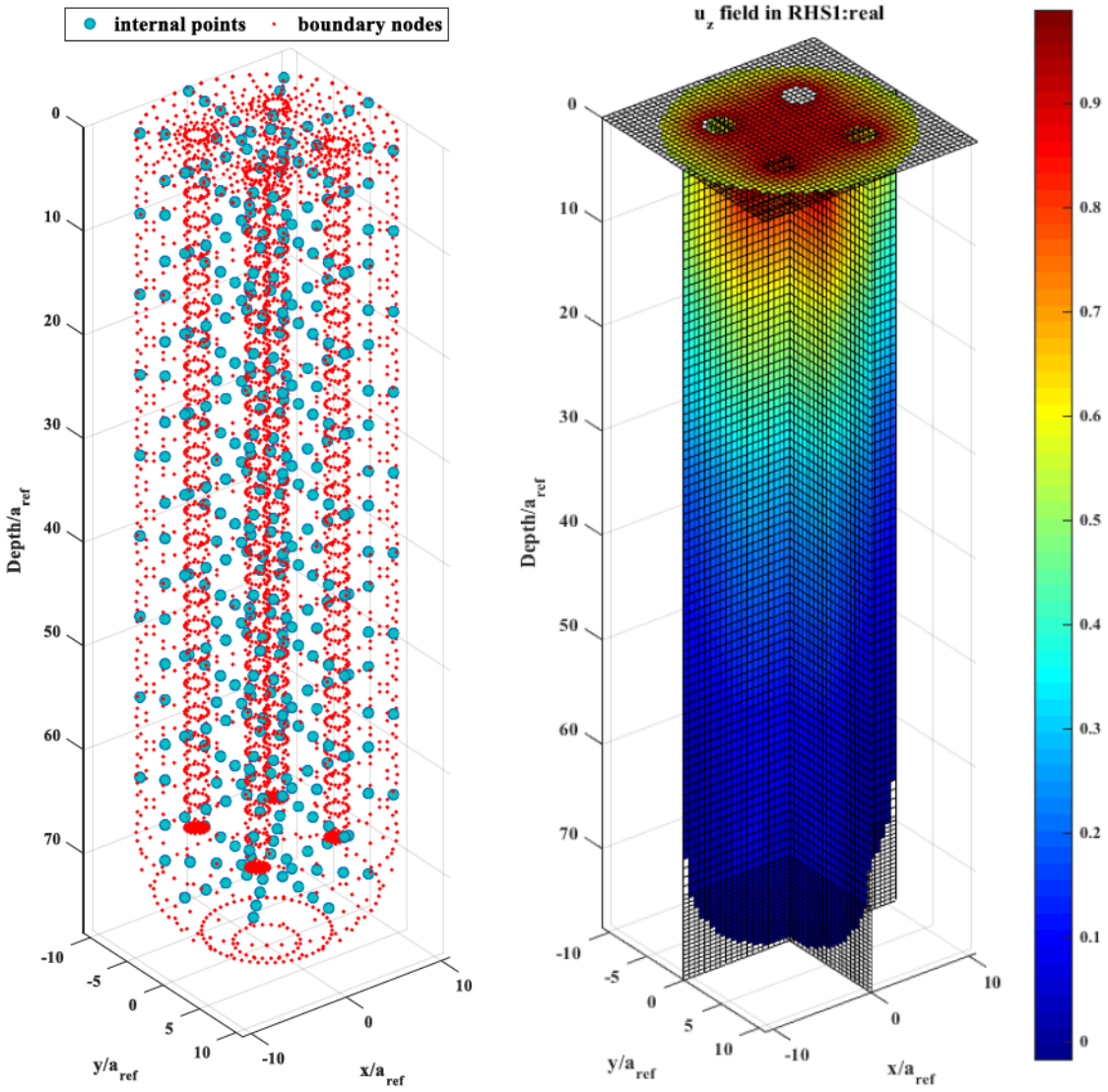

(a) boundary nodes and internal points (b) real part of displacement field u_z for vertical vibration

Figure 3.38 *Example of deriving displacement field in soil.*

The displacement field by 3D interpolation is the foundation for analyses of strain and stress fields, thus it is crucial to verify its accuracy. Ntotsios et al. (2015) modeled dynamic responses of a single pile and interaction between two piles with various spacings in multi-layered soils using commercial code ElastoDyanmics Toolbox (EDT), which is an extensive

set of MATLAB functions to model wave propagation in layered media based on direct stiffness method and the thin layer method (https://bwk.kuleuven.be/bwm/edt). In the example analysis, all piles have radii of 0.5m, lengths of 10m, elastic moduli of 50 GPa, damping loss factor of 0.01, Poisson's ratios of 0.3, and densities of 2,500 kg/m^3. The damping loss factor is defined for measuring intrinsic damping for viscoelastic materials as:

$$\eta = \frac{E''}{E'} \tag{3.87}$$

where E' and E'' are real (storage) and imaginary (loss) parts of a complex modulus, respectively (see Carfagni et al. 1998). Relation between damping loss factor η and the user-prescribed damping ratio ζ in BEASSI is,

$$\eta = 2\zeta \tag{3.88}$$

The spacings in the pile group cases are 2 m and 4 m, respectively. Depths of top three layers are 2m, 4m and 6m, respectively, and the last layer represents the half-space. Shear wave velocities from top to bottom are 185 m/s, 228 m/s, 260 m/s, and 309 m/s, respectively. The corresponding compressive wave velocities are 277 m/s, 373 m/s 485 m/s, and 944 m/s. For all soil layers, densities are 2,000 kg/m^3 and damping loss factors are 0.06. A harmonic force with frequency of 50 Hz and amplitude of unity is applied on the top of a pile, either vertically or horizontally. The second pile for the pile group cases is free at head. The resulting displacement fields on the free surface reported in the literature are presented in Figure 3.39. In single pile case (a), vertical excitation induces concentric circular wavefronts on x-y plane due to axisymmetry. When the second pile is located 2 m away from the loaded pile (c), diffraction is observed and becomes more apparent when the pile spacing increases to 4m (e). As for horizontal excitation, wavefronts on the x-y plane appear to be elliptical instead of

circular. With the presence of a second pile in the near region as in cases (d) and (f), no significant diffraction is observed even with an increasing pile spacing.

The three cases were reanalyzed by BEASSI and the results are plotted in Figure 3.39. The BEM results are in good agreement with the reference results, especially for vertical vibration of single pile and pile group. A small difference for horizontal vibration is observed such that the wavefronts by BEASSI are enclosed in y direction rather than open as in the reference solutions, which may be due to different numbers of point for interpolation. In general, the proposed solution for calculating displacement fields is validated.

Capturing curved boundaries of a 3D BEM domain using straight lines inevitably results in dentation. A simple technique for increasing resolution is decreasing length of the straight lines. As a trade-off, however, doubling the resolutions in all three directions leads to a surge in size of the 3D matrices that are used to store the displacements, strains, and stresses by a factor of 8. In this study, the x-y plane for the disturbed zone is discretized as 40×40. The x-z plane for the cylindrical region is discretized by 40×80 and for the hemispherical region is discretized by 40×20.

Components of the displacement field u_x, u_y, u_z on the traction-free surface for a 2×2 pile group embedded in a half-space due to vertical vibrations of the rigid pile cap at the dimensionless frequencies $\overline{w}=0.05$, $\overline{w}=0.50$ and $\overline{w}=1.00$ are shown in Figure 3.41 as an example. The deformation amplitudes can help identify size and shape of the disturbed zone regarding specific stresses and strains.

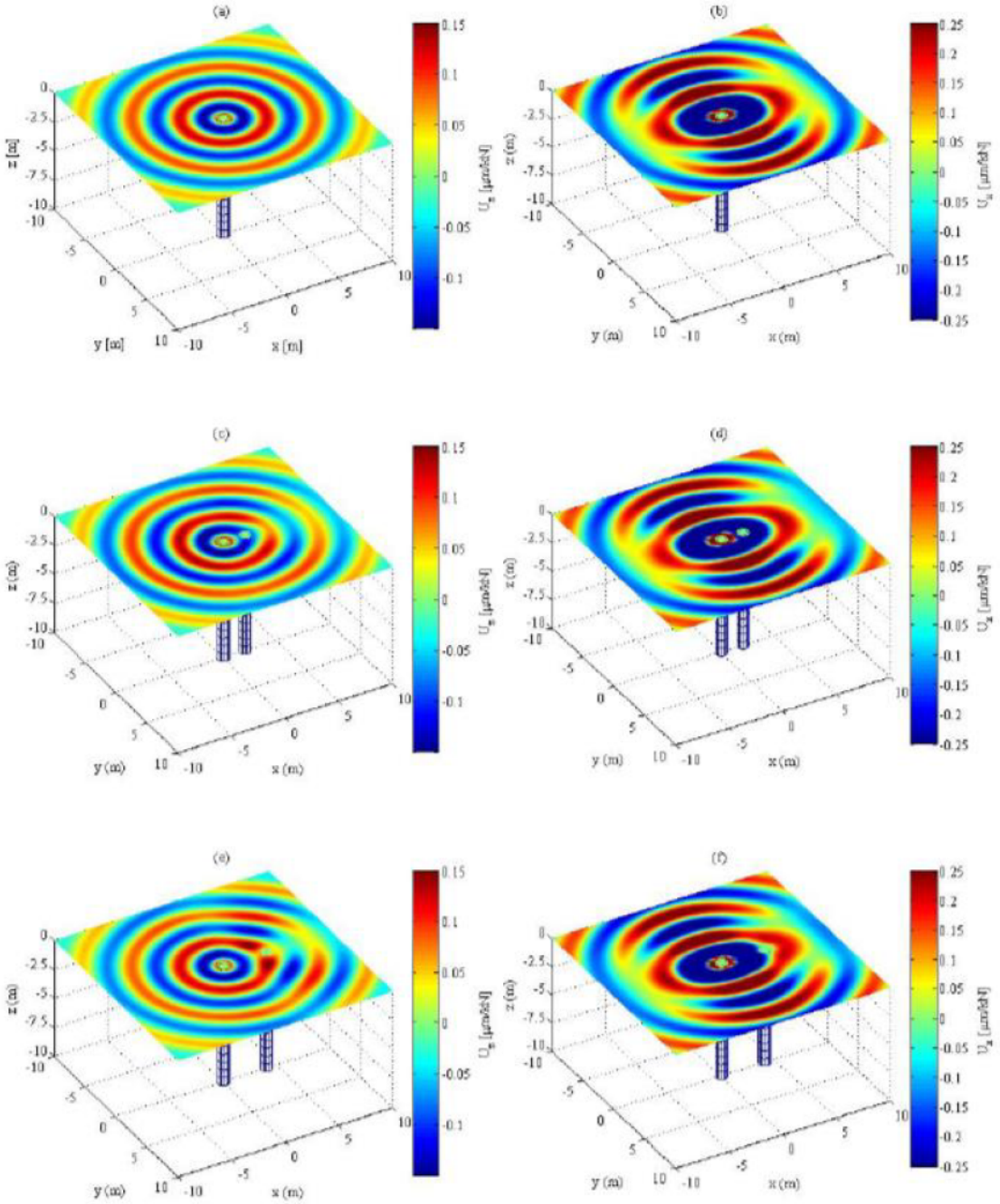

Figure 3.39 *Displacement fields in soil by Ntotsios et al. (2015).*
(a), (c), (e): u_z due to vertical loading; (b), (d), (f): u_x due to horizontal loading. (a),(b): single pile case; (c),(d): two-pile case with spacing of 2m; (e), (f): two-pile case with spacing of 4m.

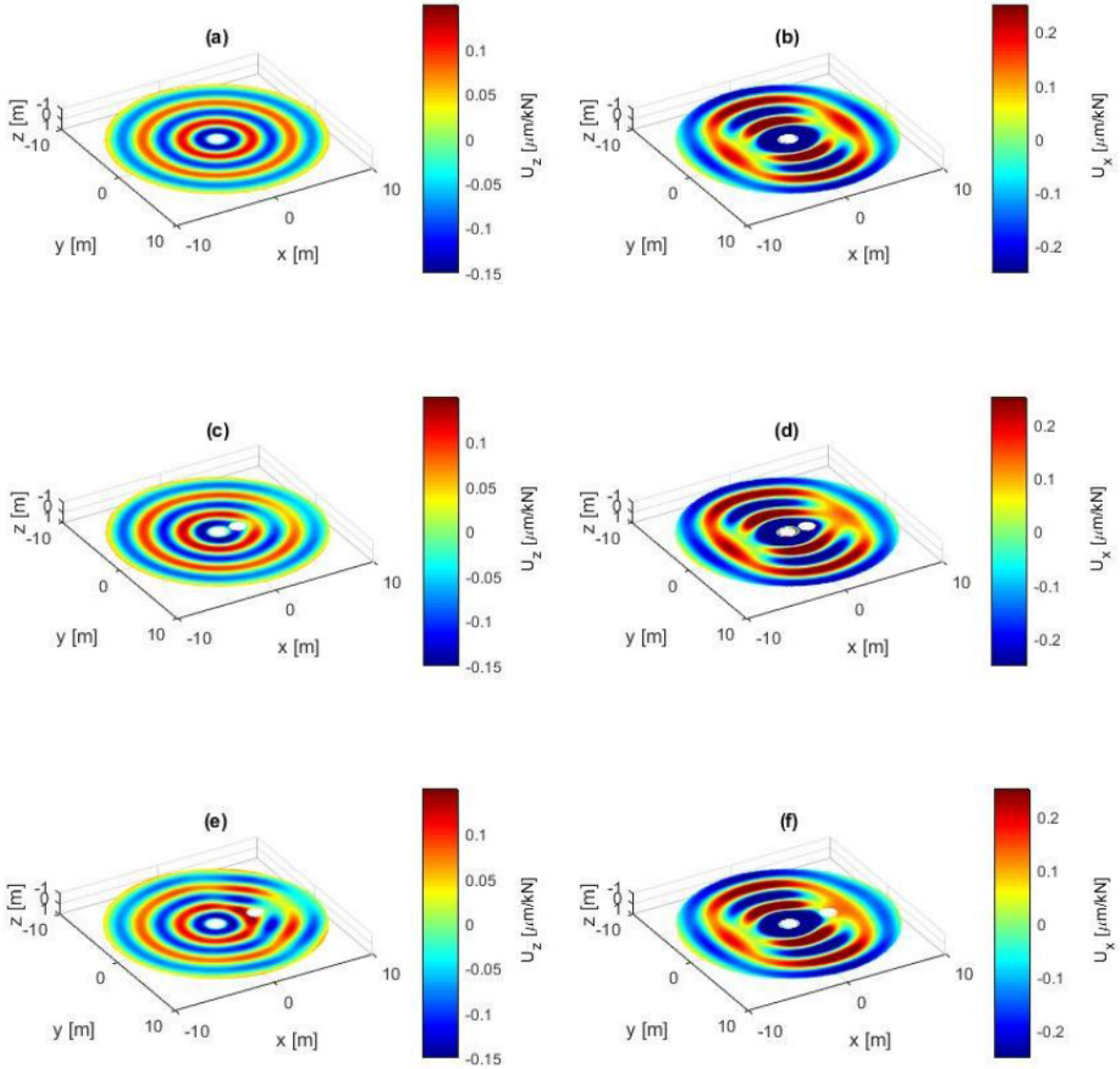

Figure 3.40 *Displacement fields by BEASSI.*
(a), (c), (e): u_z due to vertical loading ; (b), (d), (f): u_x due to horizontal loading. (a),(b): single pile case; (c),(d): two-pile case with spacing of 2m; (e), (f): two-pile case with spacing of 4m.

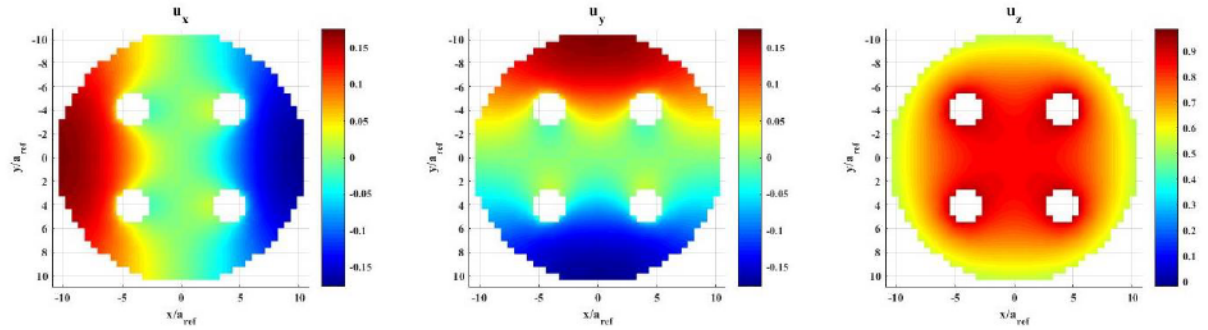

(a) x, y, and z components of displacement field at $\overline{\omega}=0.05$

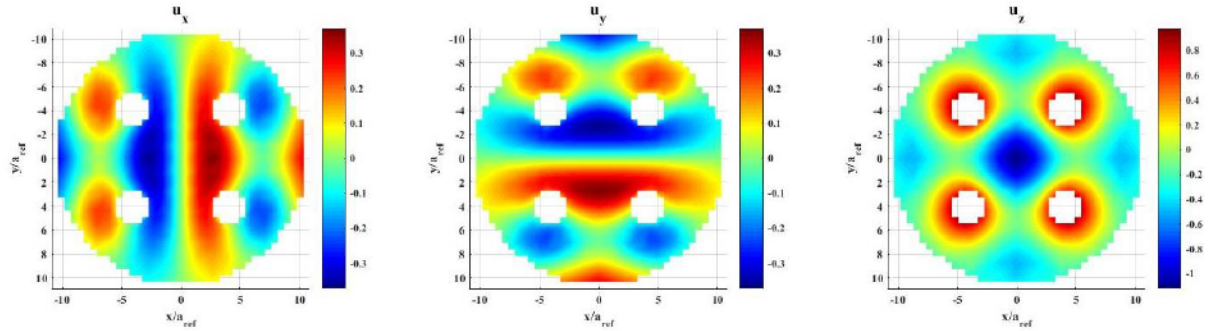

(b) x, y, and z components of displacement field at $\overline{\omega}=0.50$

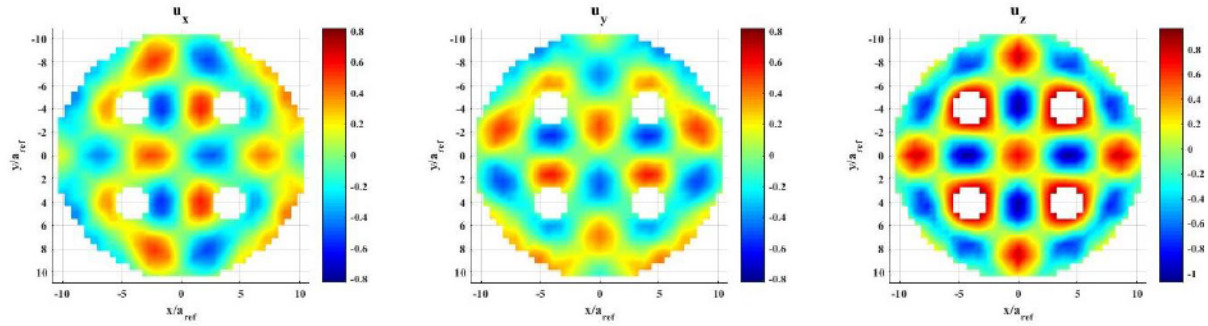

(c) x, y, and z components of displacement field at $\overline{\omega}=1.00$

Figure 3.41 *Deformation field on traction-free soil surface surrounding a 2×2 pile group resulting from vertical vibration of pile cap.*

For better visualization of soil deformation, the deformation at ground level can be calculated as:

$$\begin{cases} x_{new}(x,y,z) = x_{original}(x,y,z) + u_x(x,y,z) \\ y_{new}(x,y,z) = y_{original}(x,y,z) + u_y(x,y,z) \\ z_{new}(x,y,z) = z_{original}(x,y,z) + u_z(x,y,z) \end{cases} \tag{3.89}$$

where $x_{original}(x,y,z)$, $y_{original}(x,y,z)$, and $z_{original}(x,y,z)$ are the original coordinates at (x,y,z) on the 3D grid; $x_{new}(x,y,z)$, $y_{new}(x,y,z)$, $z_{new}(x,y,z)$ are new coordinates due to vibration.; $u_x(x,y,z)$, $u_y(x,y,z)$, and $u_z(x,y,z)$ are normalized displacements at (x,y,z);

The deformations of soil at various frequencies are shown in Figure 3.42. The deformation of soils around piles are highly frequency-dependent. At low frequency of 0.05, the deformation is as predictable as the static case such that soils close to the piles have greater downward deformation than the soils in the far region. At intermediate frequency of 0.50, soils surrounding piles generally have very small downward deformation while soils at the center of the pile group heave rather than being dragged down. At high frequency of 1.00, soil deformation become even more complex. Soils at the center of the pile group have downward movement.

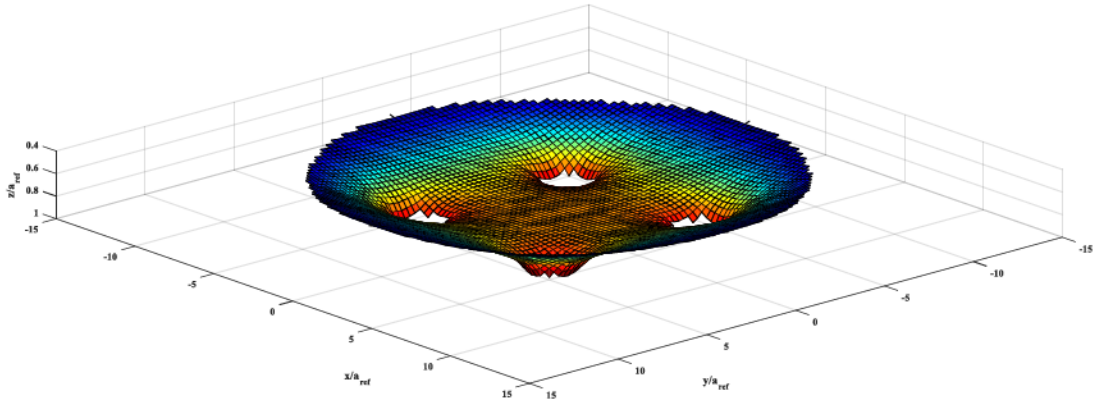

(a) Normalized deformation (real part) of soil at ground level at $\overline{w}=0.05$

Figure 3.42 *Visualization of normalized soil deformation at ground level for a 6-domain pile group model due to vertical rigid pile cap motion.*

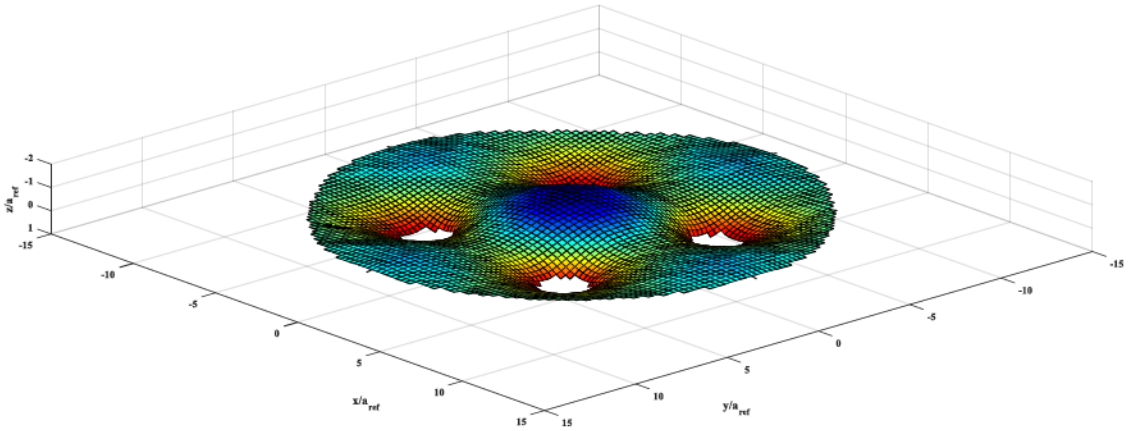

(b) Normalized deformation (real part) of soil at ground level at $\overline{w} = 0.50$

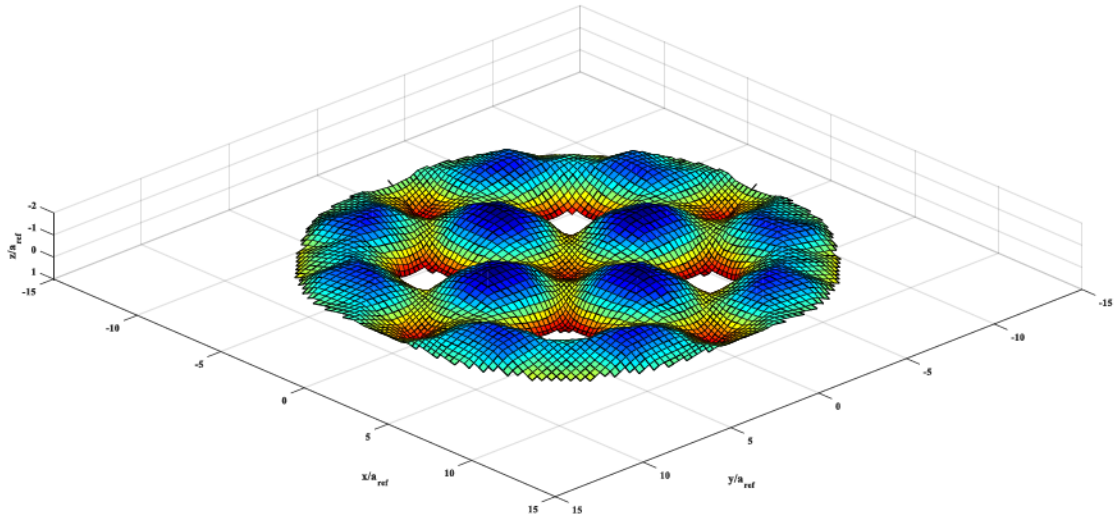

(c) Normalized deformation (real part) of soil at ground level at $\overline{w} = 1.00$

Figure 3.42 *(continued)*

2. Superposition of displacement field in soil

For rigid pile-cap motion, the actual displacement field in soil can be easily obtained by multiplying the normalized displacement field from BEASSI with the actual displacement or rotation of the rigid pile cap. However, if only one pile is loaded at head, the actual displacement field which associates with vibrations of all piles cannot be obtained directly. As

a solution, this displacement field in soil can be derived by symmetry as the global impedance matrix and the deformation of pile group.

- Pile 2
  For vertical excitation at head of Pile 2, displacement field in soil can be expressed as:

$$\begin{cases} u_x^{(2V)}(x,y,z) = (+1)u_x^{(1V)}(x,-y,z) \\ u_y^{(2V)}(x,y,z) = (+1)u_y^{(1V)}(x,-y,z)\cos(\pi) \\ u_z^{(2V)}(x,y,z) = (+1)u_z^{(1V)}(x,-y,z) \end{cases} \tag{3.90}$$

where subscripts of u denote directional components of soil displacements. Superscripts in parenthesis refer to the displacement fields due to the vibration of the corresponding piles. For example, $u_x^{(2V)}(x,y,z)$ means x component of displacement at point (x,y,z) when pile 2 is vertically loaded at its head. (+1) and (-1) signs on the right side of the equations denote if the loading directions need to be reversed for the derivation. Negative signs for coordinates refer to the point at a symmetric location with respect to (x,y,z) in the soil. $\cos(\pi)$ means that the component of displacement at point (x,y,z) derived for Pile 1 needs to be rotated by 180 degrees. Displacement fields due to horizontal, rotational, and torsional excitation at head of each individual pile are derived as follows:

For horizontal excitation:

$$\begin{cases} u_x^{(2H)}(x,y,z) = (+1)u_x^{(1H)}(x,-y,z) \\ u_y^{(2H)}(x,y,z) = (+1)u_y^{(1H)}(x,-y,z)\cos(\pi) \\ u_z^{(2H)}(x,y,z) = (+1)u_z^{(1H)}(x,-y,z) \end{cases} \tag{3.91}$$

rotational excitation:

$$\begin{cases} u_x^{(2R)}(x,y,z) = (+1)u_x^{(1R)}(x,-y,z) \\ u_y^{(2R)}(x,y,z) = (+1)u_y^{(1R)}(x,-y,z)\cos(\pi) \\ u_z^{(2R)}(x,y,z) = (+1)u_z^{(1R)}(x,-y,z) \end{cases} \tag{3.92}$$

torsional excitation:

$$\begin{cases} u_x^{(2T)}(x,y,z) = (-1)u_x^{(1T)}(x,-y,z) \\ u_y^{(2T)}(x,y,z) = (-1)u_y^{(1T)}(x,-y,z)\cos(\pi) \\ u_z^{(2T)}(x,y,z) = (-1)u_z^{(1T)}(x,-y,z) \end{cases} \tag{3.93}$$

- Pile 3

vertical excitation:

$$\begin{cases} u_x^{(3V)}(x,y,z) = (+1)u_x^{(1V)}(-x,y,z)\cos(\pi) \\ u_y^{(3V)}(x,y,z) = (+1)u_y^{(1V)}(-x,y,z) \\ u_z^{(3V)}(x,y,z) = (+1)u_z^{(1V)}(-x,y,z) \end{cases} \tag{3.94}$$

horizontal excitation:

$$\begin{cases} u_x^{(3H)}(x,y,z) = (-1)u_x^{(1H)}(-x,y,z)\cos(\pi) \\ u_y^{(3H)}(x,y,z) = (-1)u_y^{(1H)}(-x,y,z) \\ u_z^{(3H)}(x,y,z) = (-1)u_z^{(1H)}(-x,y,z) \end{cases} \tag{3.95}$$

rotational excitation:

$$\begin{cases} u_x^{(3R)}(x,y,z) = (-1)u_x^{(1R)}(-x,y,z)\cos(\pi) \\ u_y^{(3R)}(x,y,z) = (-1)u_y^{(1R)}(-x,y,z) \\ u_z^{(3R)}(x,y,z) = (-1)u_z^{(1R)}(-x,y,z) \end{cases} \tag{3.96}$$

torsional excitation:

$$\begin{cases} u_x^{(3R)}(x,y,z) = (-1)u_x^{(1R)}(-x,y,z)\cos(\pi) \\ u_y^{(3R)}(x,y,z) = (-1)u_y^{(1R)}(-x,y,z) \\ u_z^{(3R)}(x,y,z) = (-1)u_z^{(1R)}(-x,y,z) \end{cases} \tag{3.97}$$

- Pile 4

vertical excitation:

$$\begin{cases} u_x^{(4V)}(x,y,z) = (+1)u_x^{(1V)}(-x,-y,z)\cos(\pi) \\ u_y^{(4V)}(x,y,z) = (+1)u_y^{(1V)}(-x,-y,z)\cos(\pi) \\ u_z^{(4V)}(x,y,z) = (+1)u_z^{(1V)}(-x,-y,z) \end{cases} \tag{3.98}$$

horizontal excitation:

$$\begin{cases} u_x^{(4H)}(x,y,z) = (-1)u_x^{(1H)}(-x,-y,z)\cos(\pi) \\ u_y^{(4H)}(x,y,z) = (-1)u_y^{(1H)}(-x,-y,z)\cos(\pi) \\ u_z^{(4H)}(x,y,z) = (-1)u_z^{(1H)}(-x,-y,z) \end{cases} \tag{3.99}$$

rotational excitation:

$$\begin{cases} u_x^{(4R)}(x,y,z) = (-1)u_x^{(1R)}(-x,-y,z)\cos(\pi) \\ u_y^{(4R)}(x,y,z) = (-1)u_y^{(1R)}(-x,-y,z)\cos(\pi) \\ u_z^{(4R)}(x,y,z) = (-1)u_z^{(1R)}(-x,-y,z) \end{cases} \tag{3.100}$$

torsional excitation:

$$\begin{cases} u_x^{(4T)}(x,y,z) = (+1)u_x^{(1T)}(-x,-y,z)\cos(\pi) \\ u_y^{(4T)}(x,y,z) = (+1)u_y^{(1T)}(-x,-y,z)\cos(\pi) \\ u_z^{(4T)}(x,y,z) = (+1)u_z^{(1T)}(-x,-y,z) \end{cases} \tag{3.101}$$

The above displacement fields derived by application of symmetry without performing actual computation by BEASSI can be referred as “basic fields” and visualized by volumetric plot for better understanding. Figure 3.43 shows displacement field by direct BEM analysis with Pile 1 subjected to vertical loading. The corresponding displacement fields when Pile 2, Pile 3, and Pile 4 subjected to vertical loading are shown in Figure 3.44, Figure 3.45, and Figure 3.46, respectively.

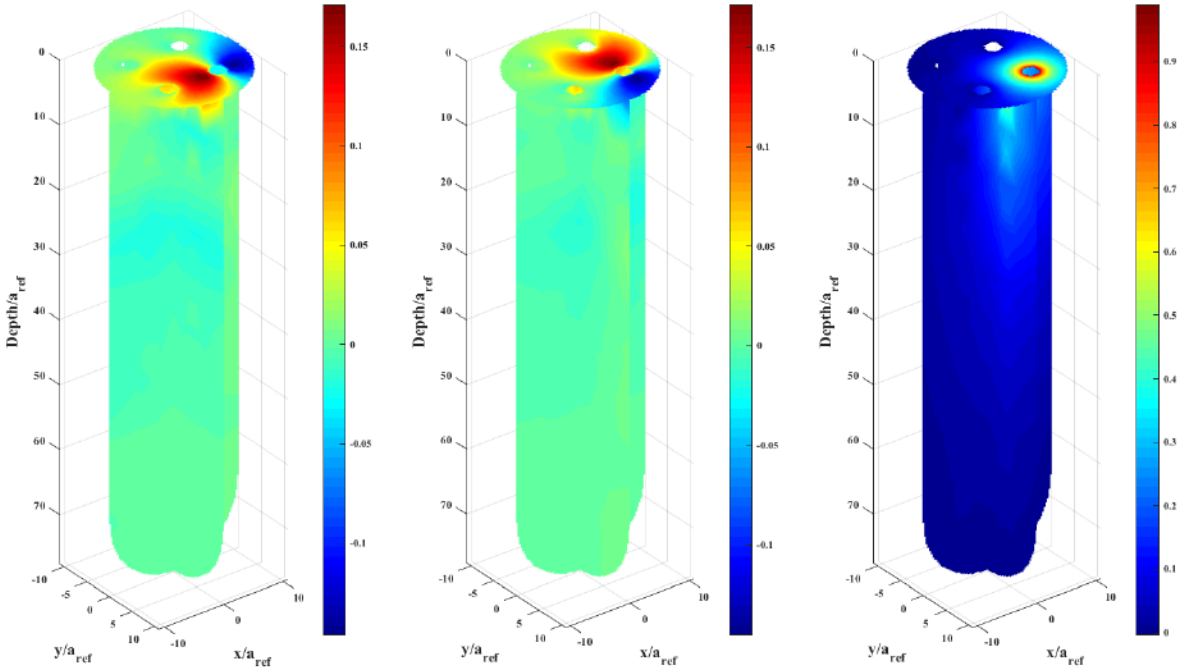

(a) u_x (b) u_y (c) u_z

Figure 3.43 *Displacement field (real part) determined directly by BEASSI due to Pile 1 subjected to vertical loading.*

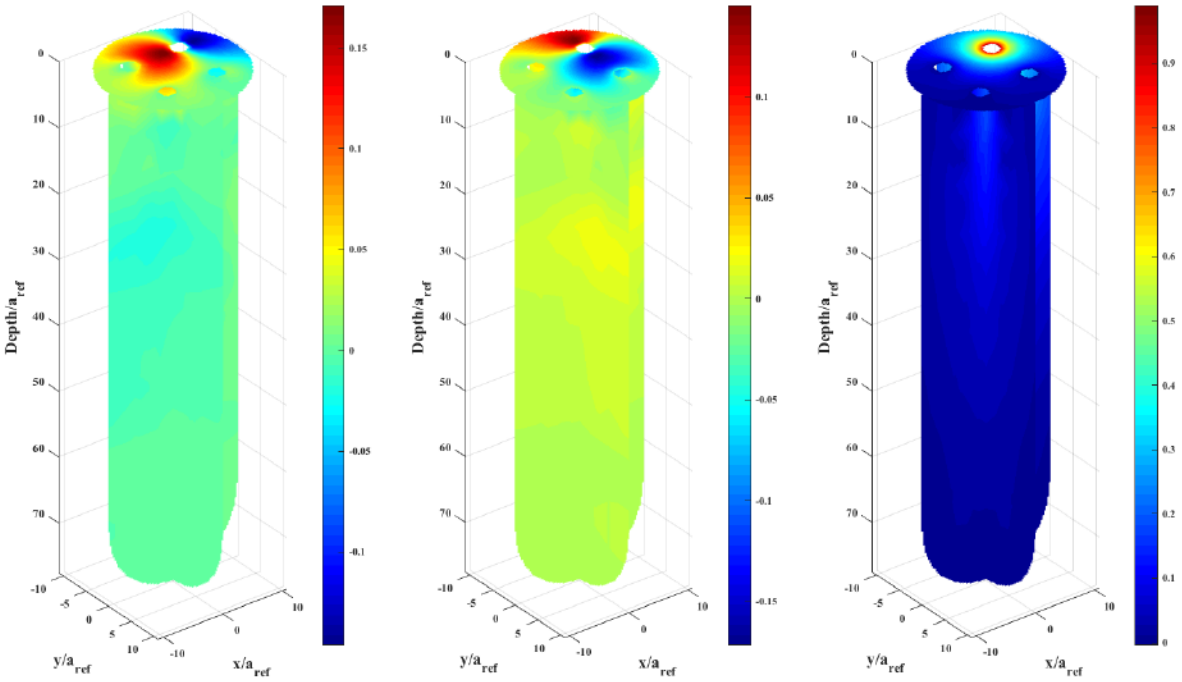

(a) u_x (b) u_y (c) u_z

Figure 3.44 *Derived displacement field (real part) due to Pile 2 subjected to vertical loading.*

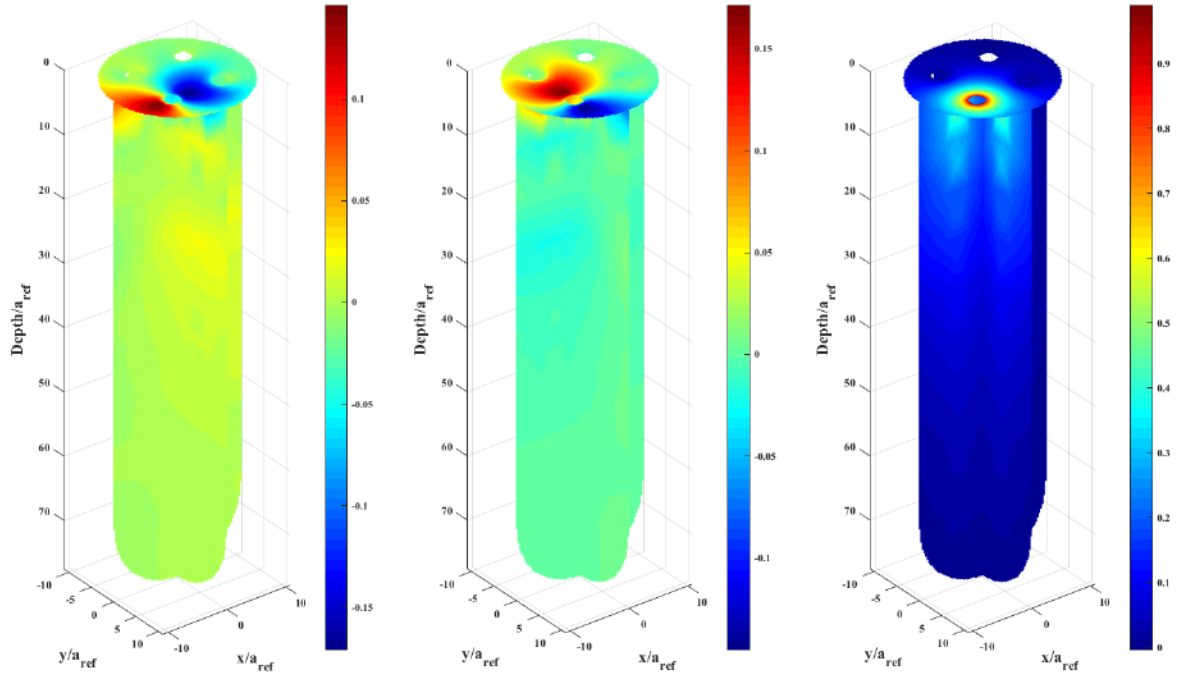

(a) u_x (b) u_y (c) u_z

Figure 3.45 *Derived displacement field (real part) due to Pile 3 subjected to vertical loading.*

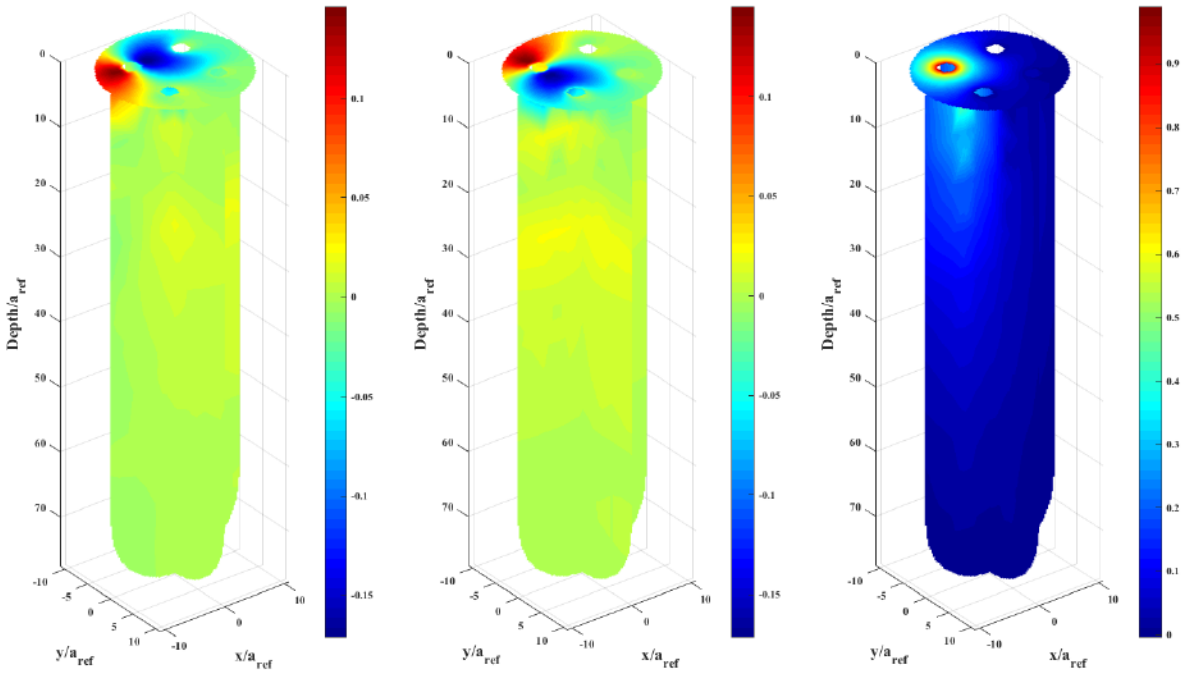

(a) u_x (b) u_y (c) u_z

Figure 3.46 *Derived displacement field (real part) due to pile 4 vertical vibration.*

To verify the above derivations, direct analysis was conducted in BEASSI by displacing Pile 2. The resulting displacement fields u_x, u_y, and u_z are shown in Figure 3.47. In comparison to the direct analysis, the derived displacement field appears to be reasonable. For rigorous comparison, relative error by two approaches is defined as

$$\text{relative error} = \frac{u_{\text{derived}} - u_{\text{BEASSI}}}{u_{\text{BEASSI}}} \tag{3.102}$$

where u_{derived} and u_{BEASSI} denote displacement by derivation and direct analysis at point (x, y, z), respectively. The relative errors for real and imaginary parts are plotted in Figure 3.48 and Figure 3.49, respectively.

Displacement field derived by symmetry is in favorable agreement with that by BEASSI directly. This is suggested by nearly zero relative error in most space of the soil domain. However, it is also noticeable that in the central region of disturbed zone relative

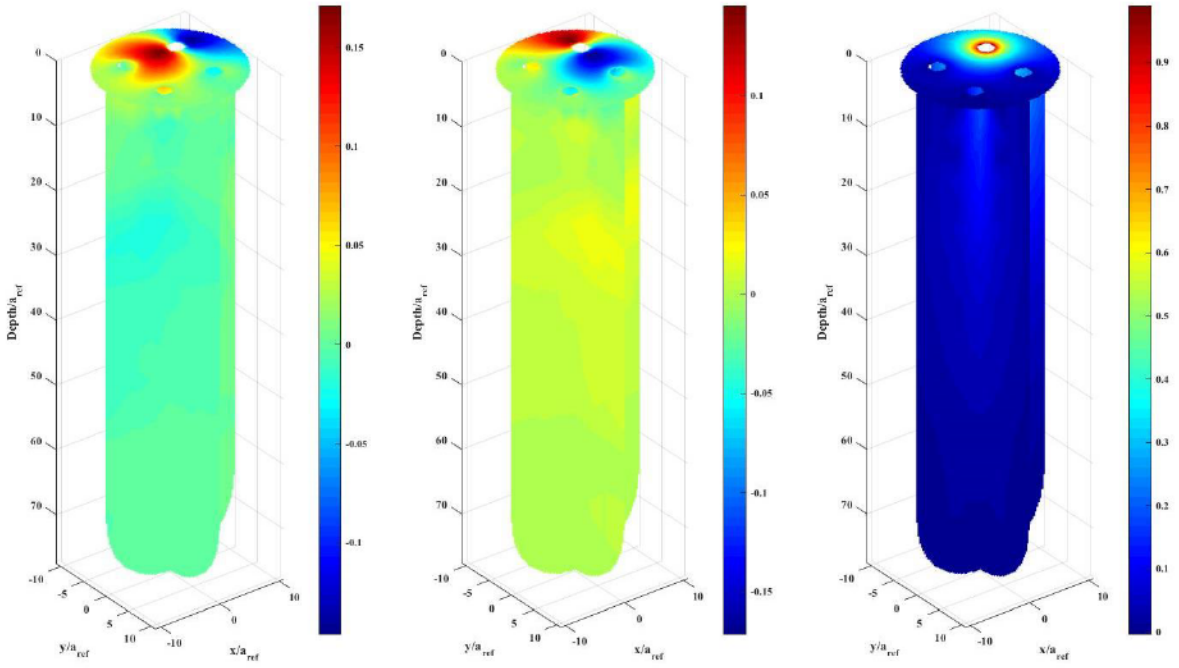

(a) u_x (b) u_y (c) u_z

Figure 3.47 *Displacement field (real part) determined by BEASSI due to pile 2 vertical vibration.*

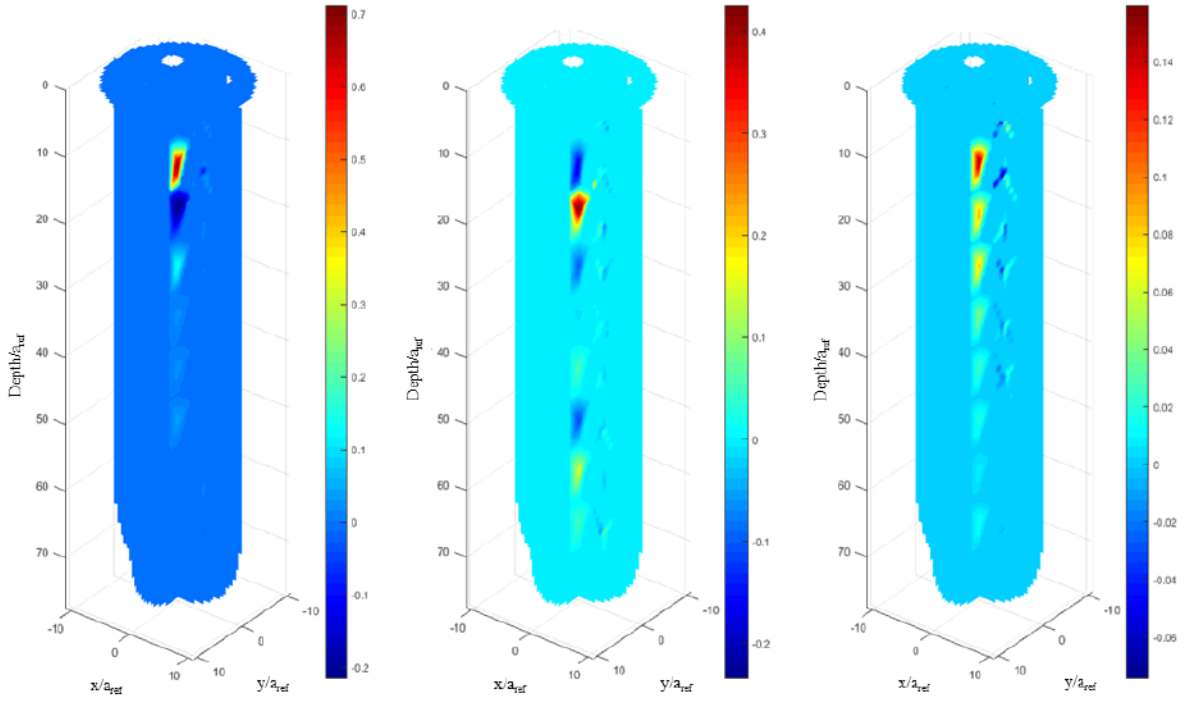

(a) u_x (b) u_y (c) u_z

Figure 3.48 *Relative error in real part of displacement field by derivation.*

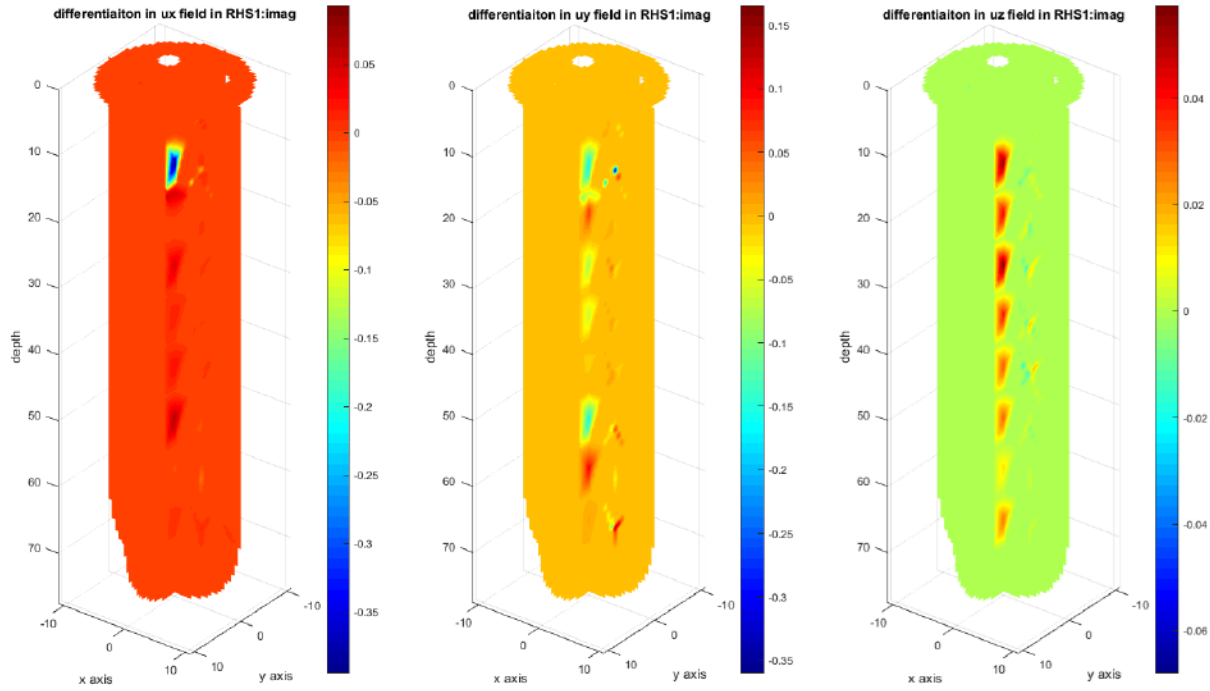

Figure 3.49 *Relative error in imaginary part of displacement field by derivation.*

errors can still be as high as 70% for real part, and 35% for imaginary part. Three potential factors are discussed below:1) grid resolution 2) interpolation method; and 3) number of internal points on z axis.

1) The default resolutions of the 3D gird in x-y and x-z planes are 40×40 and 40×(80+20), respectively. To see if a grid with higher resolutions would diminish or eliminate the high relative errors, the resolutions were then increased to 80×80 and 80×(160+40). However, the results suggest that the resolution has no impact on relative error.

2) The default interpolation method for displacement is 'linear', which guarantees C^0 continuous for the data on the grid. To investigate influence of interpolation method, the method was switched to 'natural', which is triangulation-based natural neighbor interpolation and guarantees C^1 continuity except at sample points. The results are presented in Figure 3.50 and Figure 3.51. The maximum relative error occurs in the hemispherical region with 0.3% for real part and 0.6% for imaginary part.

3) Since the relative errors are high only along the z axis, a possible explanation could be the insufficient internal points for interpolation along the z axis. To verify this assumption, 10 more points on z axis were added to the internal points. The updated relative error for real and imaginary parts of displacement field is shown in Figure 3.52 and Figure 3.53, respectively. The maximum relative errors drop from 70% and 35% to 40% and 30%. The regions having large relative errors were diminished significantly and now are mainly on y-z plane. Thus adding a set of internal points on z-axis proves to be helpful in diminishing relative error.

Once the "basic fields" become available, and the actual displacements at head of each pile are calculated from the substructuring formulation, actual displacement fields in soil can be derived by superposition.

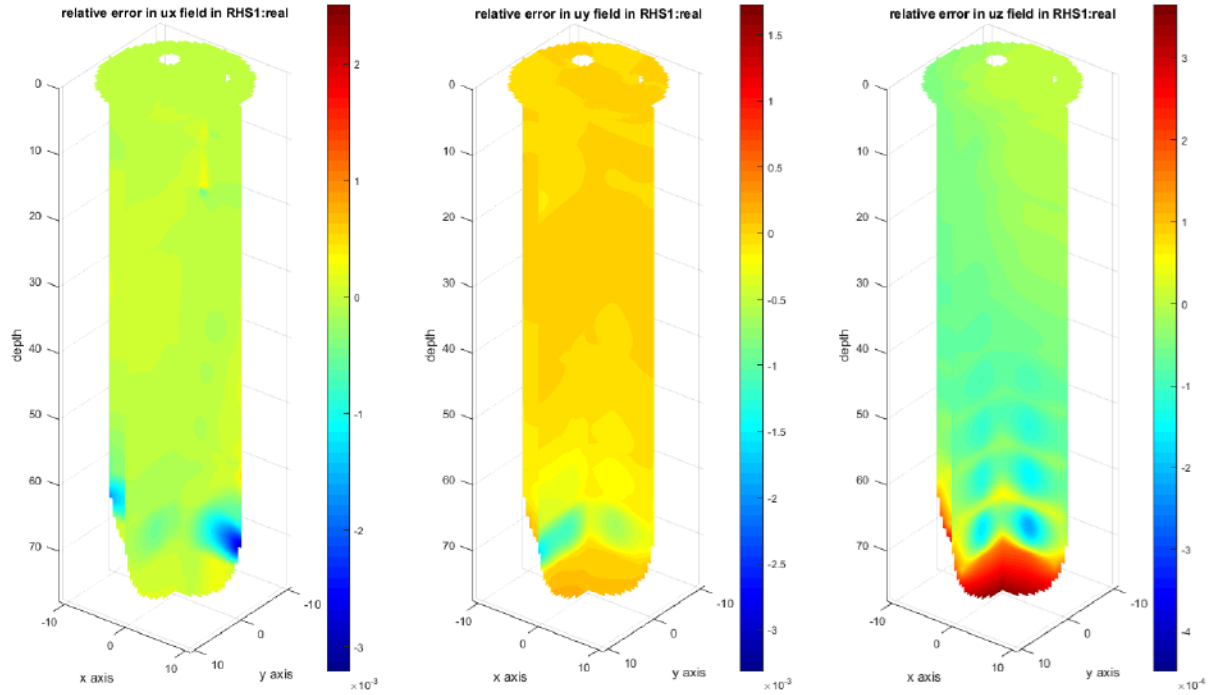

Figure 3.50 *Relative error in real part of displacement field by natural interpolation.*

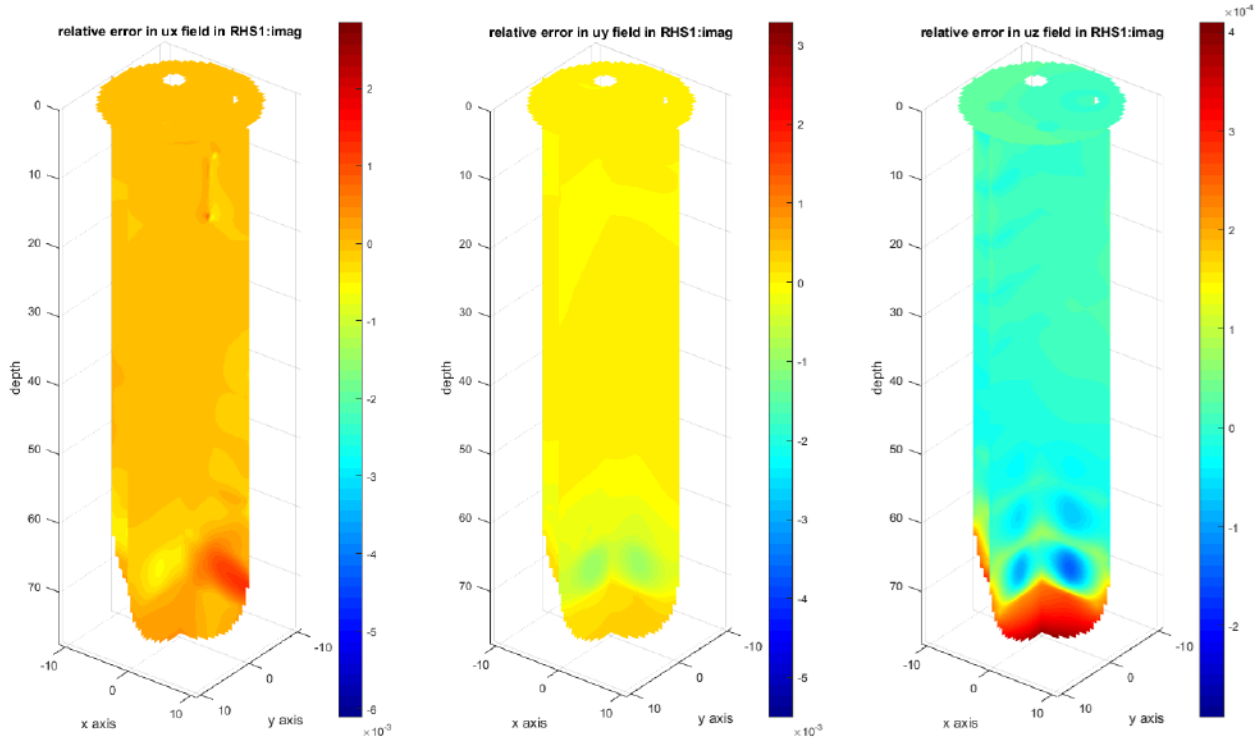

Figure 3.51 *Relative error in imaginary part of displacement field by natural interpolation.*

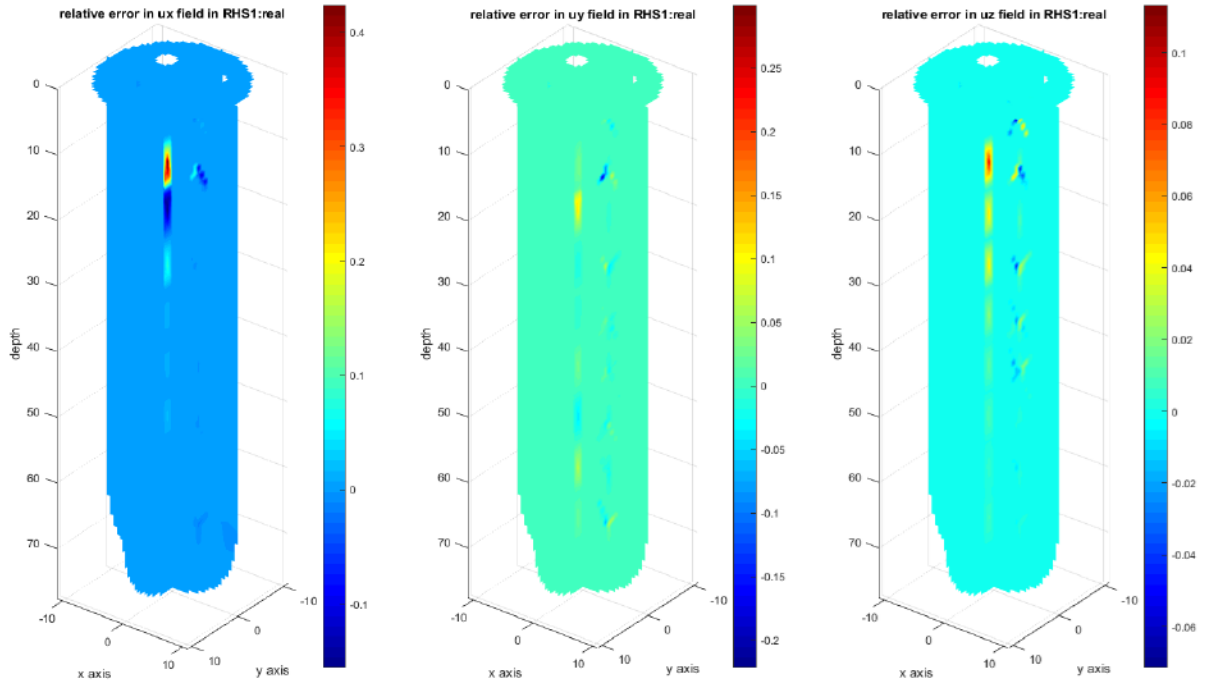

Figure 3.52 *Relative error in real part of displacement field with more internal points on z axis by linear interpolation.*

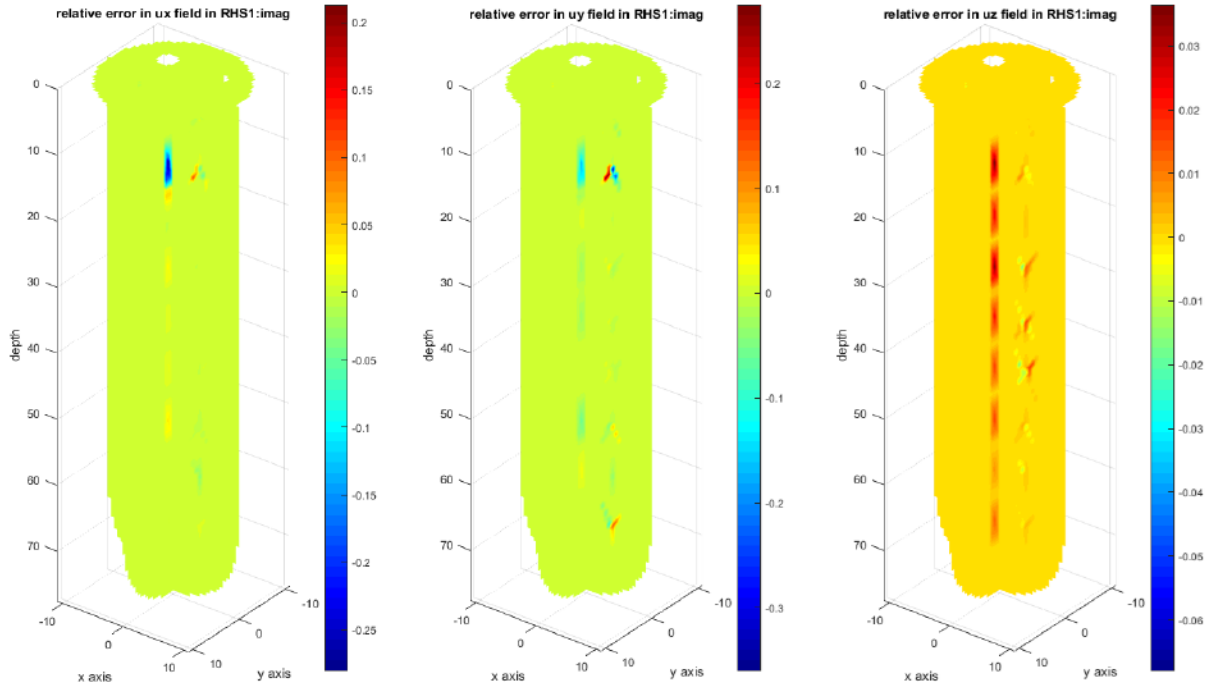

Figure 3.53 *Relative error in imaginary part of displacement field with more internal points on z axis by linear interpolation.*

2. Strain field in soil

The geometric equations that define axial and shear strains in terms of displacements are listed below:

$$\begin{cases} \varepsilon_x = \dfrac{\partial u}{\partial x}, & \gamma_{xy} = \dfrac{\partial u}{\partial y} + \dfrac{\partial v}{\partial x} \\ \varepsilon_y = \dfrac{\partial v}{\partial y}, & \gamma_{yz} = \dfrac{\partial v}{\partial z} + \dfrac{\partial w}{\partial y} \\ \varepsilon_z = \dfrac{\partial w}{\partial z}, & \gamma_{zx} = \dfrac{\partial w}{\partial x} + \dfrac{\partial u}{\partial z} \end{cases} \tag{3.103}$$

where u, v, w are displacement components in x, y, z directions.

Applying of these relations to the displacement fields provides numerical estimation of the strain tensor at each point on the grid. The established 3D grid in Cartesian coordinates also makes it very convenient to implement the estimation of strains at each point on the grid using finite difference formulae. For any point with all six adjacent points in the same domain, first-order partial derivative of directional displacement can be approximated by central finite difference formulae as Eqn (3.104). Subscript n denotes the point at which derivatives are estimated; subscripts $n+1$, $n-1$ denote adjacent points in either x, y, or z direction. Across the boundary between different domains, soil displacements are continuous due to the perfectly-bonded continuity condition, but shear moduli may vary sharply. This may result in drastic variations in soil strains, which is not C^0 continuous. Hence when apply the finite difference formulae, the adjacent point that locates within a different domain cannot be used in the interpolation. To handle the target points right next to boundaries, including the free surface and the disturbed zone boundaries, the central FDM formulae may be replaced by the backward or forward formulae as in Equations (3.105) and (3.106), depending on which side of the target point approaches the boundary.

$$
\begin{cases}
\left.\dfrac{\partial u}{\partial x}\right|_{(x_n,y_n,z_n)} = \dfrac{u_x(x_{n+1},y_n,z_n)-u_x(x_{n-1},y_n,z_n)}{x_{n+1}-x_{n-1}} \\
\left.\dfrac{\partial u}{\partial y}\right|_{(x_n,y_n,z_n)} = \dfrac{u_x(x_n,y_{n+1},z_n)-u_x(x_n,y_{n-1},z_n)}{y_{n+1}-y_{n-1}} \\
\left.\dfrac{\partial u}{\partial z}\right|_{(x_n,y_n,z_n)} = \dfrac{u_x(x_n,y_n,z_{n+1})-u_x(x_n,y_n,z_{n-1})}{z_{n+1}-z_{n-1}} \\
\left.\dfrac{\partial v}{\partial x}\right|_{(x_n,y_n,z_n)} = \dfrac{u_y(x_{n+1},y_n,z_n)-u_y(x_{n-1},y_n,z_n)}{x_{n+1}-x_{n-1}} \\
\left.\dfrac{\partial v}{\partial y}\right|_{(x_n,y_n,z_n)} = \dfrac{u_y(x_n,y_{n+1},z_n)-u_y(x_n,y_{n-1},z_n)}{y_{n+1}-y_{n-1}} \\
\left.\dfrac{\partial v}{\partial z}\right|_{(x_n,y_n,z_n)} = \dfrac{u_y(x_n,y_n,z_{n+1})-u_y(x_n,y_n,z_{n-1})}{z_{n+1}-z_{n-1}} \\
\left.\dfrac{\partial w}{\partial x}\right|_{(x_n,y_n,z_n)} = \dfrac{u_z(x_{n+1},y_n,z_n)-u_z(x_{n-1},y_n,z_n)}{x_{n+1}-x_{n-1}} \\
\left.\dfrac{\partial w}{\partial y}\right|_{(x_n,y_n,z_n)} = \dfrac{u_z(x_n,y_{n+1},z_n)-u_z(x_n,y_{n-1},z_n)}{y_{n+1}-y_{n-1}} \\
\left.\dfrac{\partial w}{\partial z}\right|_{(x_n,y_n,z_n)} = \dfrac{u_z(x_n,y_n,z_{n+1})-u_z(x_{n-1},y_n,z_{n-1})}{z_{n+1}-z_{n-1}}
\end{cases}
\tag{3.104}
$$

$$
\begin{cases}
\left.\dfrac{\partial u}{\partial x}\right|_{(x_n,y_n,z_n)} = \dfrac{u_x(x_{n+1},y_n,z_n)-u_x(x_n,y_n,z_n)}{x_{n+1}-x_n} \\
\left.\dfrac{\partial u}{\partial y}\right|_{(x_n,y_n,z_n)} = \dfrac{u_x(x_n,y_{n+1},z_n)-u_x(x_n,y_n,z_n)}{y_{n+1}-y_n} \\
\left.\dfrac{\partial u}{\partial z}\right|_{(x_n,y_n,z_n)} = \dfrac{u_x(x_n,y_n,z_{n+1})-u_x(x_n,y_n,z_n)}{z_{n+1}-z_n} \\
\left.\dfrac{\partial v}{\partial x}\right|_{(x_n,y_n,z_n)} = \dfrac{u_y(x_{n+1},y_n,z_n)-u_y(x_n,y_n,z_n)}{x_{n+1}-x_n} \\
\left.\dfrac{\partial v}{\partial y}\right|_{(x_n,y_n,z_n)} = \dfrac{u_y(x_n,y_{n+1},z_n)-u_y(x_n,y_n,z_n)}{y_{n+1}-y_n} \\
\left.\dfrac{\partial v}{\partial z}\right|_{(x_n,y_n,z_n)} = \dfrac{u_y(x_n,y_n,z_{n+1})-u_y(x_n,y_n,z_n)}{z_{n+1}-z_n} \\
\left.\dfrac{\partial w}{\partial x}\right|_{(x_n,y_n,z_n)} = \dfrac{u_z(x_{n+1},y_n,z_n)-u_z(x_n,y_n,z_n)}{x_{n+1}-x_n} \\
\left.\dfrac{\partial w}{\partial y}\right|_{(x_n,y_n,z_n)} = \dfrac{u_z(x_n,y_{n+1},z_n)-u_z(x_n,y_n,z_n)}{y_{n+1}-y_n} \\
\left.\dfrac{\partial w}{\partial z}\right|_{(x_n,y_n,z_n)} = \dfrac{u_z(x_n,y_n,z_{n+1})-u_z(x_n,y_n,z_n)}{z_{n+1}-z_n}
\end{cases}
\tag{3.105}
$$

$$\begin{cases} \left.\dfrac{\partial u}{\partial x}\right|_{(x_n,y_n,z_n)} = \dfrac{u_x(x_n,y_n,z_n)-u_x(x_{n-1},y_n,z_n)}{x_n-x_{n-1}} \\ \left.\dfrac{\partial u}{\partial y}\right|_{(x_n,y_n,z_n)} = \dfrac{u_x(x_n,y_n,z_n)-u_x(x_n,y_{n-1},z_n)}{y_n-y_{n-1}} \\ \left.\dfrac{\partial u}{\partial z}\right|_{(x_n,y_n,z_n)} = \dfrac{u_x(x_n,y_n,z_n)-u_x(x_n,y_n,z_{n-1})}{z_n-z_{n-1}} \\ \left.\dfrac{\partial v}{\partial x}\right|_{(x_n,y_n,z_n)} = \dfrac{u_y(x_n,y_n,z_n)-u_y(x_{n-1},y_n,z_n)}{x_n-x_{n-1}} \\ \left.\dfrac{\partial v}{\partial y}\right|_{(x_n,y_n,z_n)} = \dfrac{u_y(x_n,y_n,z_n)-u_y(x_n,y_{n-1},z_n)}{y_n-y_{n-1}} \\ \left.\dfrac{\partial v}{\partial z}\right|_{(x_n,y_n,z_n)} = \dfrac{u_y(x_n,y_n,z_n)-u_y(x_n,y_n,z_{n-1})}{z_n-z_{n-1}} \\ \left.\dfrac{\partial w}{\partial x}\right|_{(x_n,y_n,z_n)} = \dfrac{u_z(x_n,y_n,z_n)-u_z(x_{n-1},y_n,z_n)}{x_n-x_{n-1}} \\ \left.\dfrac{\partial w}{\partial y}\right|_{(x_n,y_n,z_n)} = \dfrac{u_z(x_n,y_n,z_n)-u_z(x_n,y_{n-1},z_n)}{y_n-y_{n-1}} \\ \left.\dfrac{\partial w}{\partial z}\right|_{(x_n,y_n,z_n)} = \dfrac{u_z(x_n,y_n,z_n)-u_z(x_n,y_n,z_{n-1})}{z_n-z_{n-1}} \end{cases} \tag{3.106}$$

3. Calculating stress field in soil

Since soil is modeled in BEASSI as linear viscoelastic medium, the stress-strain relation follows Hooke's Law:

$$\sigma_{ij} = 2\mu\varepsilon_{ij} + \lambda\varepsilon_{kk}\delta_{ij} \tag{3.107}$$

where μ and λ are Lamé constants, which are defined as:

$$\begin{cases} \mu = \dfrac{E}{2(1+\nu)} \\ \lambda = \dfrac{\nu E}{(1+\nu)(1-2\nu)} \end{cases} \tag{3.108}$$

The dynamic point-load Green's functions for multilayered viscoelastic half-space treats each soil layer as homogeneous medium with constant E and ν. For a point within a

certain layer, μ and λ can be determined from the soil profiles. For further analyses, the principal stresses and maximum shear stresses can be computed by obtaining eigenvalues and eigenvectors if necessary.

3.7.4 Bending Moment, Shear Force, and Axial Force Profiles

The bending moment and shear force profiles are commonly used due to their fundamental importance in pile design. They are often easily calculated by 1D analytical Winkler models, thus it is useful to explore how they can be calculated by the 3D BEASSI solutions which are in the form of displacements and tractions at the boundary surface nodes. For an Euler-Bernoulli beam, the bending moment M and shear force V of the piles can be calculated as (Novak 1974; Rollins et al. 1998):

$$M = -E_p I_p \frac{d^2 u_x}{dz^2} \text{ and } V = \frac{dM}{dz} \tag{3.109}$$

where E is Young's modulus, I is the second moment of area with respect to the neutral axis, u_x is the lateral displacement on the pile axis and z is the longitudinal coordinate along the pile. Based on the plane cross-section assumption, pile deformation does not stretch the cross-section of the pile and thus each node at the same depth should have the same u_x. Therefore, the 2D elements at the same depth were collapsed to 1D quadratic isoparametric elements for simplicity.

Then lateral displacement u_x and depth z at any point within an element can be interpolated by the shape functions of the reduced element as:

$$u_x = (\frac{1}{2}\eta^2 - \frac{1}{2}\eta)u_{x1} + (1-\eta^2)u_{x2} + (\frac{1}{2}\eta^2 + \frac{1}{2}\eta)u_{x3} \tag{3.110}$$

$$z = (\frac{1}{2}\eta^2 - \frac{1}{2}\eta)z_1 + (1-\eta^2)z_2 + (\frac{1}{2}\eta^2 + \frac{1}{2}\eta)z_3 \tag{3.111}$$

where u_{x1} and u_{x3} are displacements at the corner nodes of the collapsed 1D element, u_{x2} is displacement at the middle node, z_1 and z_3 are depths of the corner nodes, and z_2 is depth of the middle node.

Then the desired curvature can be obtained as

$$\frac{d^2u_x}{dz^2} = \frac{d(\frac{du_x}{dz})/d\eta}{dz/d\eta} = \frac{(u_{x1}-2u_{x2}+u_{x3})}{[(\eta-\frac{1}{2})z_1-(2\eta)z_2+(\eta+\frac{1}{2})z_3]^2} - \frac{(z_1-2z_2+z_3)[(\eta-\frac{1}{2})u_{x1}-(2\eta)u_{x2}+(\eta+\frac{1}{2})u_{x3}]}{[(\eta-\frac{1}{2})z_1-(2\eta)z_2+(\eta+\frac{1}{2})z_3]^3} \tag{3.112}$$

The BEM meshes in this study were generated such that a middle node is always exactly between two corners, i.e.,

$$z_1-2z_2+z_3=0 \tag{3.113}$$

Therefore the second term in the above equation is zero. The bending moment can thus be simplified to:

$$M_1=M_2=M_3=-4\frac{u_{x1}-2u_{x2}+u_{x3}}{(z_3-z_1)^2}E_pI_p \tag{3.114}$$

The 1D natural coordinate η has been eliminated, and the moment is constant within each element because of the quadratic displacement interpolation. Similarly, the third-order derivative is zero for quadratic elements, but the shear force can be approximated across elements in a finite difference sense. In this study, the shear force V at corner nodes of two adjacent elements is thus approximated as:

$$V_3^{(1)}=V_1^{(2)}=\frac{M^{(1)}-M^{(2)}}{z_2^{(2)}-z_2^{(1)}} \tag{3.115}$$

where superscripts (1) and (2) denote two different elements.

Likewise, for vertical vibration of piles, axial force of piles can be calculated as

$$N = E_p A_p \frac{du_z}{dz} \tag{3.116}$$

where A_p is cross-section area and u_z is the vertical displacement on the pile axis. u_z at any point within an element can be interpolated using shape functions as:

$$u_z = (\frac{1}{2}\eta^2 - \frac{1}{2}\eta)u_{z1} + (1-\eta^2)u_{z2} + (\frac{1}{2}\eta^2 + \frac{1}{2}\eta)u_{z3} \tag{3.117}$$

where u_{z1} and u_{z3} are displacements at the corner nodes of the collapsed 1D elements, u_{z2} is displacement at the middle node. Then desired axial pile strain can be obtained as

$$\frac{du_z}{dz} = \frac{du_z / d\eta}{dz / d\eta} = \frac{(\eta - \frac{1}{2})u_{z1} - 2\eta u_{z2} + (\eta + \frac{1}{2})u_{z3}}{(\eta - \frac{1}{2})z_1 - 2\eta z_2 + (\eta + \frac{1}{2})z_3} \tag{3.118}$$

Incorporating Equation (3.113) into Equation (3.118) provides

$$\frac{du_z}{dz} = \frac{(2\eta - 1)u_{z1} - 4\eta u_{z2} + (2\eta + 1)u_{z3}}{z_3 - z_1} \tag{3.119}$$

Two reference studies were conducted to validate the above derivations for bending moment, shear force, and axial force. The first reference study is about static and dynamic response of a cantilever beam, and the second one is for dynamic response of a floating pile embedded into homogeneous soil.

1. Reference study on cantilever beam

Static and dynamic response of a cantilever beam was studied due to the availability of analytical solutions. The dimensionless pile parameters for the reference study are listed in Table 3.13:

Table 3.13 *Dimensionless pile parameters of the cantilever beam.*

Parameter	**Value**
outer radius	1
inner radius	0.942
length	69.56
area	0.3538564
second moment of area	0.1669640
elastic modulus	(977.5, 0)
Poisson's ratio	0.26
density	4.05
excitation circular frequency	0.01, 1.00

The boundary conditions prescribed at pile head are unit translation in x and z directions, and unit rotation with respect to y axis, respectively. Pile toe was completely fixed. Natural boundary condition was prescribed on the lateral side of the pile. Structural Green's functions were applied for the pile domain. For the static case, the analytical solutions for axial force, shear force, and bending moment were obtained by mechanics of material. In Table 3.14, numerical results (3rd column) and analytical results (4th column) at pile head were compared.

Table 3.14 *Comparison of numerical and analytical results on cantilever beam for the static case.*

Loading case	Parameters	$E_{pile} = 977.5$		$E_{pile} = 97750$	
		Numerical results (BEASSI)	Analytical results	Numerical results (BEASSI)	Analytical results
axial loading	axial force	4.95200	4.97300	496.30000	497.30000
lateral loading	shear force	0.00154	0.00582	0.57600	0.58200
	bending moment	0.13534	0.20240	20.10000	20.24000
rotation	shear force	0.16436	0.20240	20.13000	20.24000
	bending moment	8.86472	9.38500	933.40000	938.50000

The results are consistent for the axial loading case, but diverge for the other two loading cases. A possible reason is that the dimensionless parameters may not be suitable for such analysis on a cantilever beam. Exclusion of the soil medium substantially reduces lateral resistance, and thus the force and moment required to displace the pile were greatly reduced. Numerical results became more susceptible to round-off errors and integration tolerance. To validate this assumption, the elastic modulus of pile was scaled up by 100 and the updated results are provided in 5th and 6th columns of Table 3.14. Good consistency is observed for all loading cases. It is suggested that the dimensionless parameters for BEASSI analyses should be sufficiently large to predominate influence of numerical errors. The following results are all based on the updated pile elastic modulus, i.e., 97750. Numerical and analytical lateral displacement, bending moment, shear force, and axial force profiles are presented in Figure 3.54 - Figure 3.56.

For dynamic case, the analytical solutions can be obtained by solving the general equations for cantilever beams subjected to free vibration (Equations (3.65)). Unknown coefficients $\mathbf{C} = [C_1, ..., C_6]^T$ can be determined using the following boundary conditions:

$$\text{lateral loading: } \begin{cases} u_x = 1 & (z = 0) \\ \Theta_y = 0 & (z = 0) \\ u_x = 0 & (z = 69.56) \\ \Theta_y = 0 & (z = 69.56) \end{cases}$$

$$\text{rocking loading: } \begin{cases} u_x = 0 & (z = 0) \\ \Theta_y = 1 & (z = 0) \\ u_x = 0 & (z = 69.56) \\ \Theta_y = 0 & (z = 69.56) \end{cases}$$

$$\text{axial loading: } \begin{cases} u_z = 1 & (z = 0) \\ u_z = 0 & (z = 69.56) \end{cases}$$

Numerical and analytical lateral displacement, bending moment, and shear force profiles are compared in Figure 3.57 - Figure 3.59. For the both static and dynamic cases, outcome numerical results by BEASSI conform to the analytical solutions fairly well at all depths. The only exceptions are the bending moment and shear force at depth of 1.45 when the cantilever is subjected to static lateral translation at pile head. After a closer examination, it is found out that when pile is laterally loaded with zero rotation at head, displacements at middle nodes for the upmost vertical pile elements are very close to those at pile head, i.e., the upper corner nodes. The derived bending moment for these pile elements becomes very sensitive to the numerical error for nodal displacements at the middle nodes. The inconsistent bending moment further leads to greater error in calculating shear force, which may have erroneous sign. In general, the reference study on the cantilever beam is satisfactory.

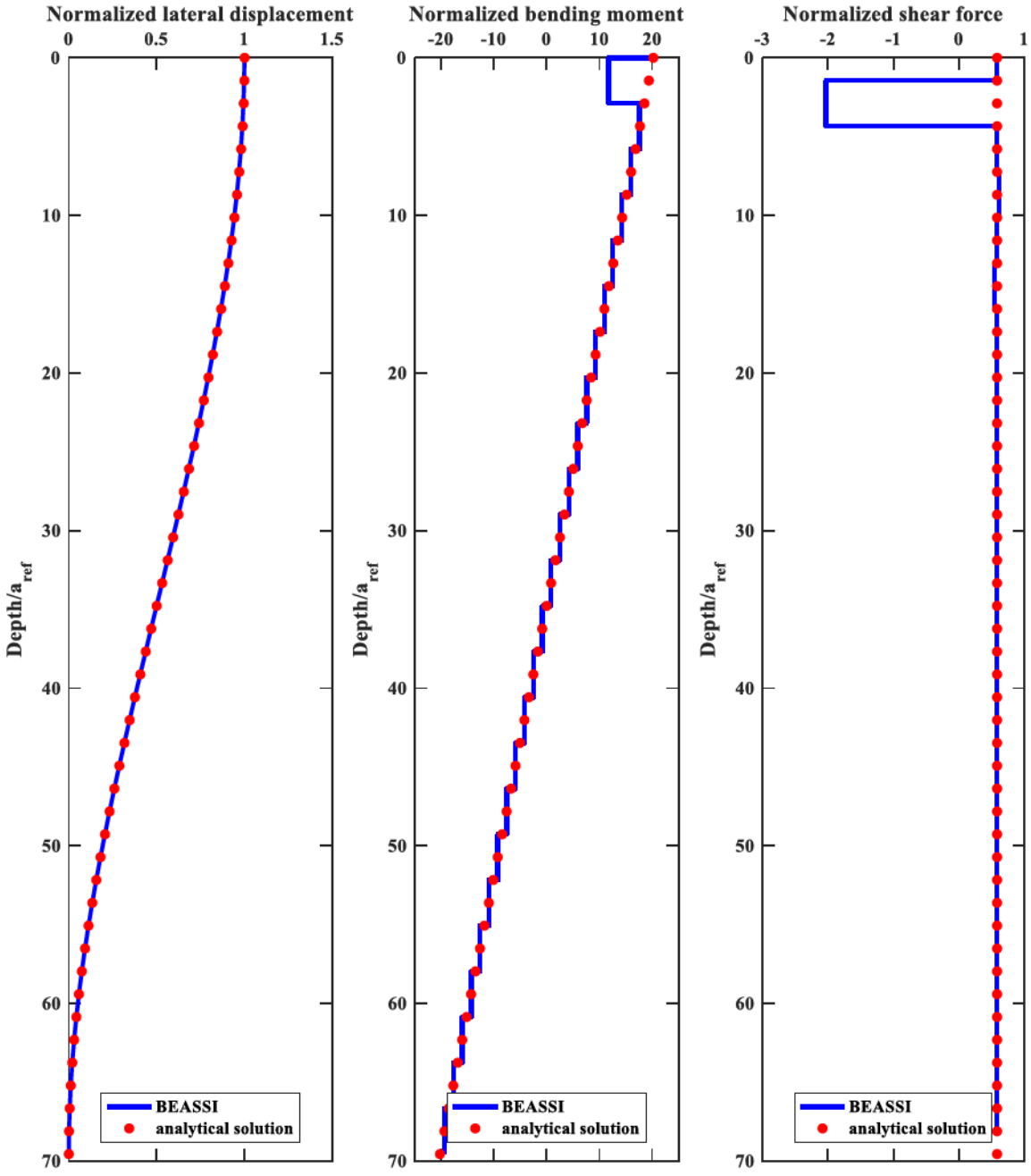

Figure 3.54 *Lateral displacement, bending moment, and shear force profiles of a cantilever beam subjected to static lateral load at head.*

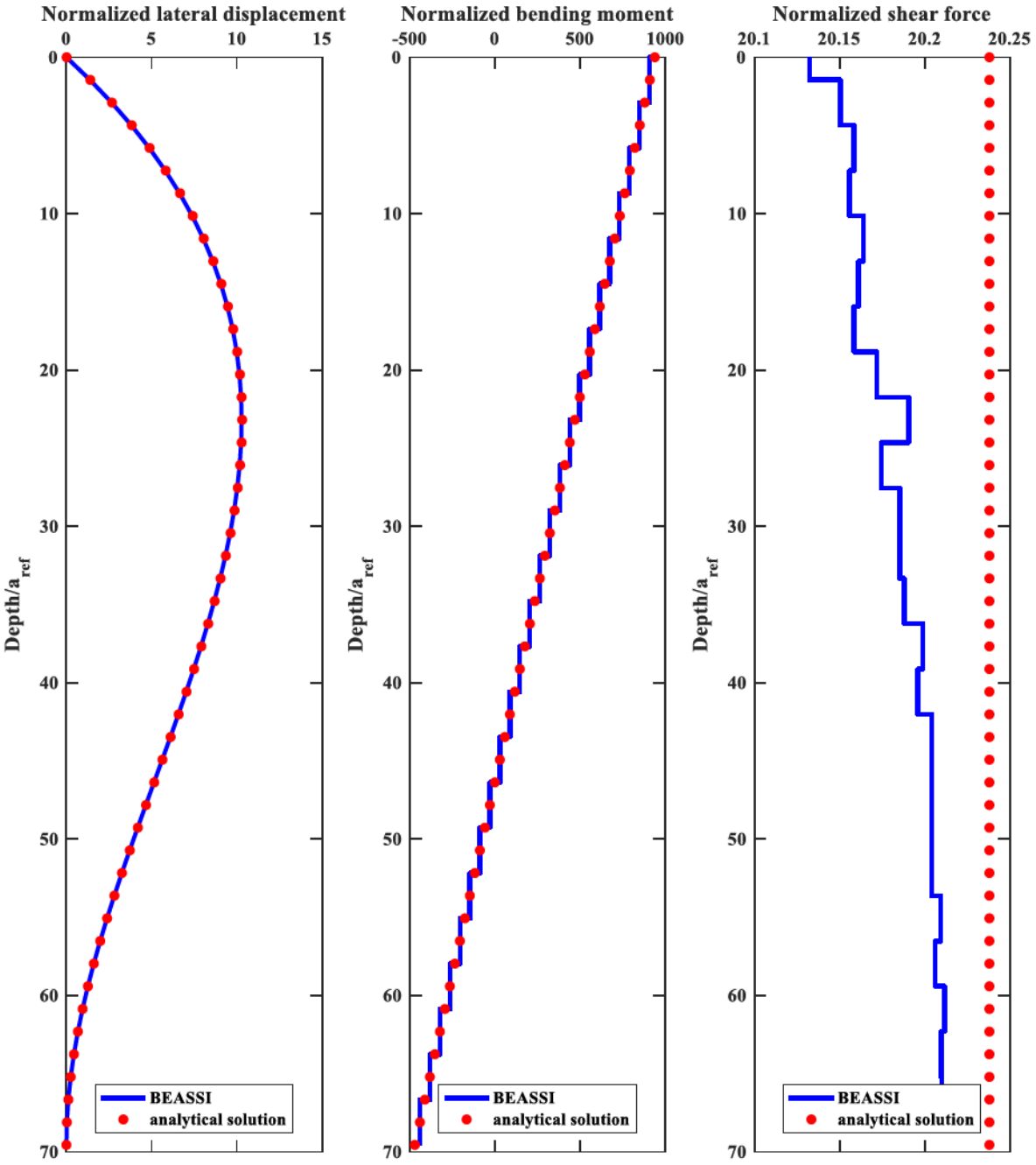

Figure 3.55 *Lateral displacement, bending moment, and shear force profiles of a cantilever beam subjected to static rocking load at head.*

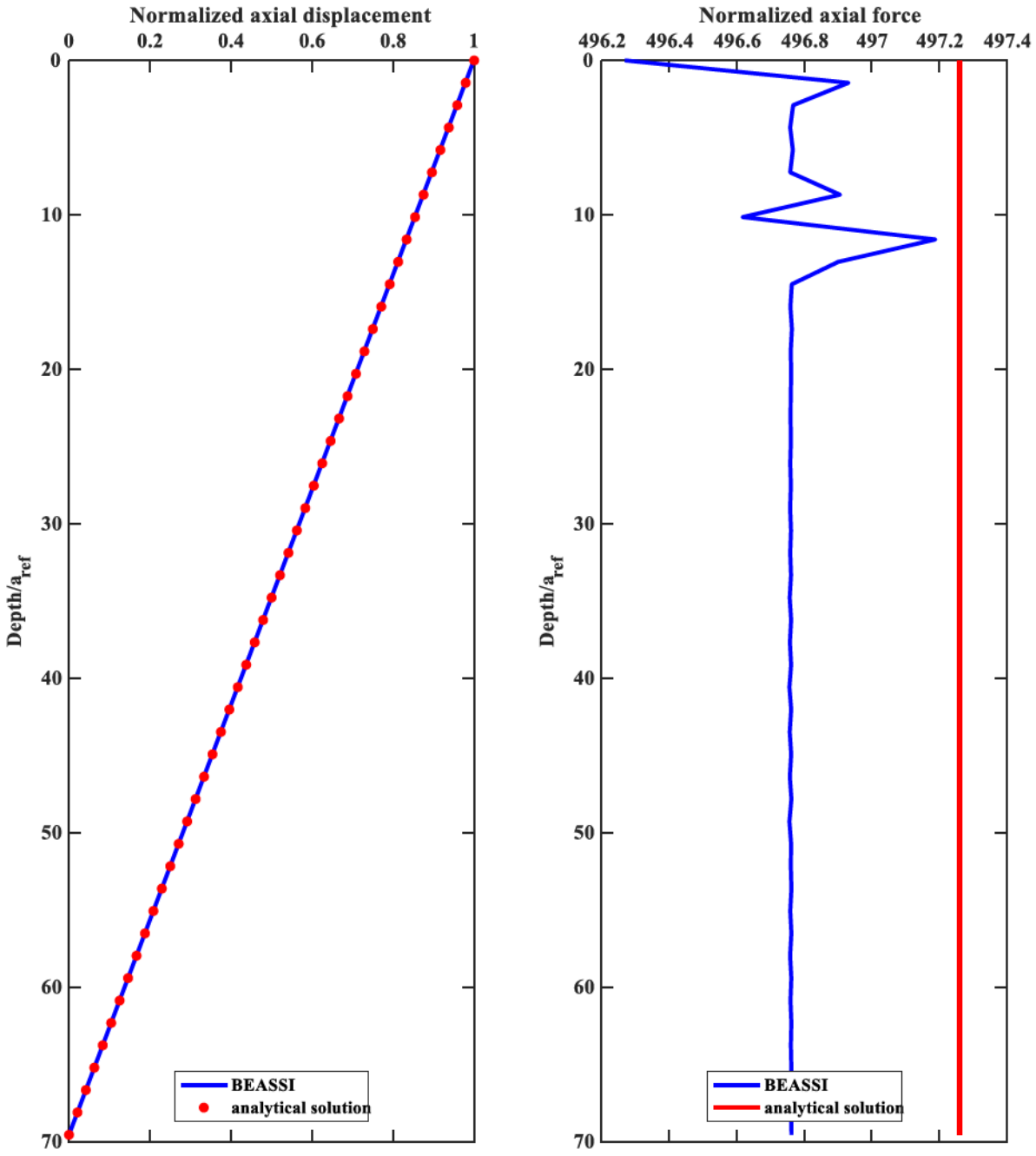

Figure 3.56 *Axial displacement and axial force profiles of a cantilever beam subjected to static axial load at head.*

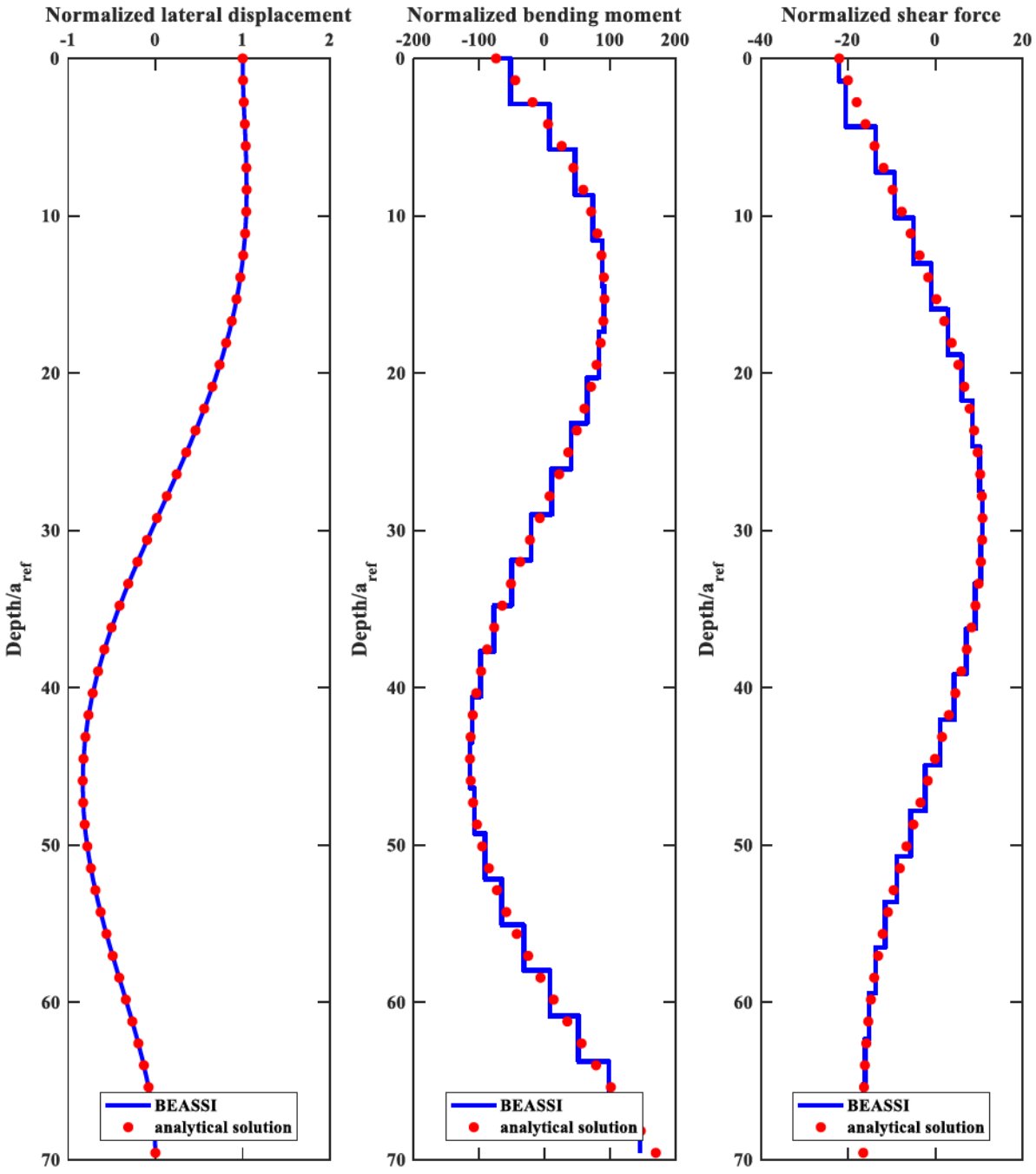

Figure 3.57 *Lateral displacement, bending moment, and shear force profiles of a cantilever beam subjected to dynamic ($\bar{\omega}=1.0$) lateral load at head.*

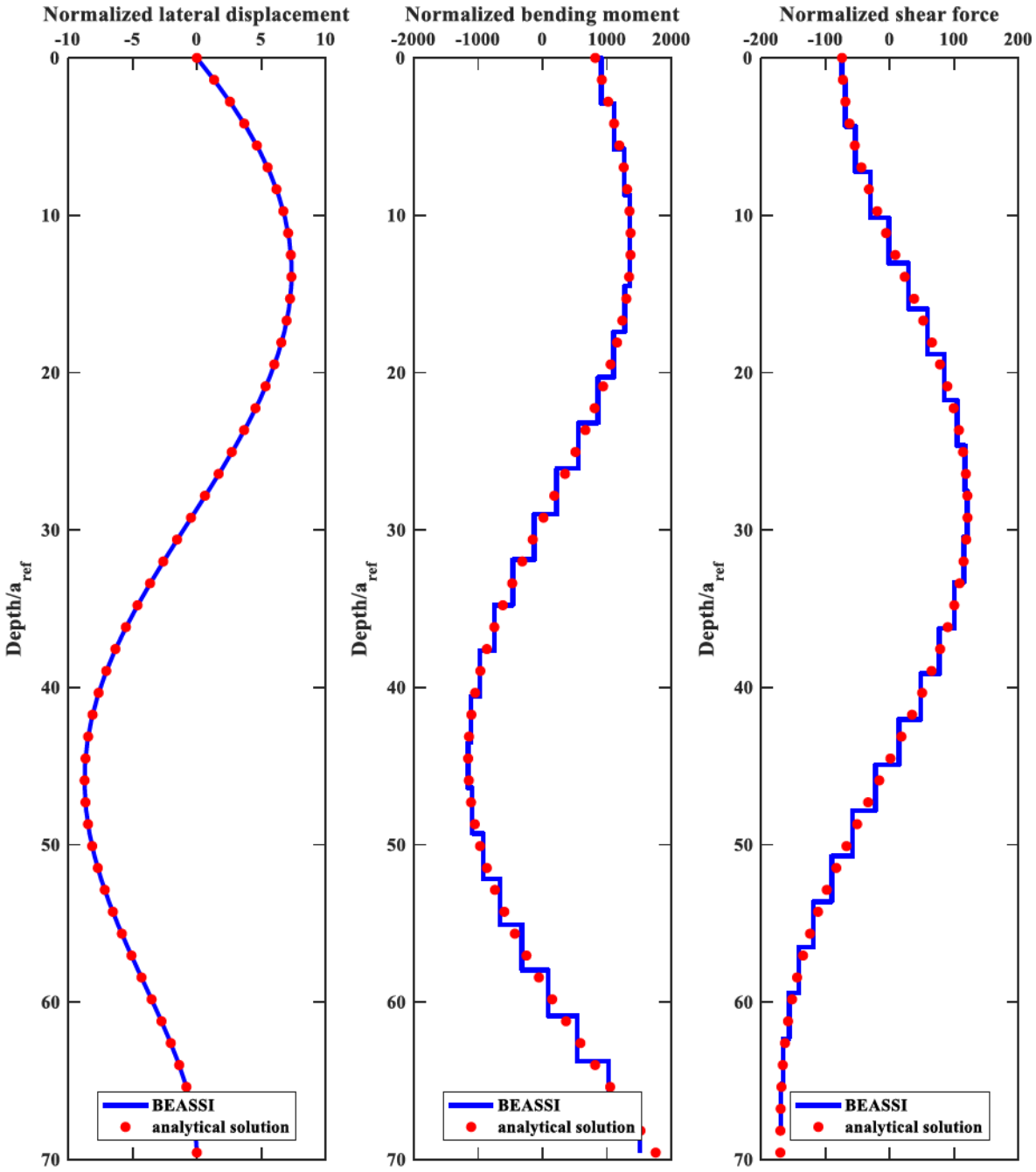

Figure 3.58 *Lateral displacement, bending moment, and shear force profiles of a cantilever beam subjected to dynamic ($\bar{\omega}=1.0$) rotation at head.*

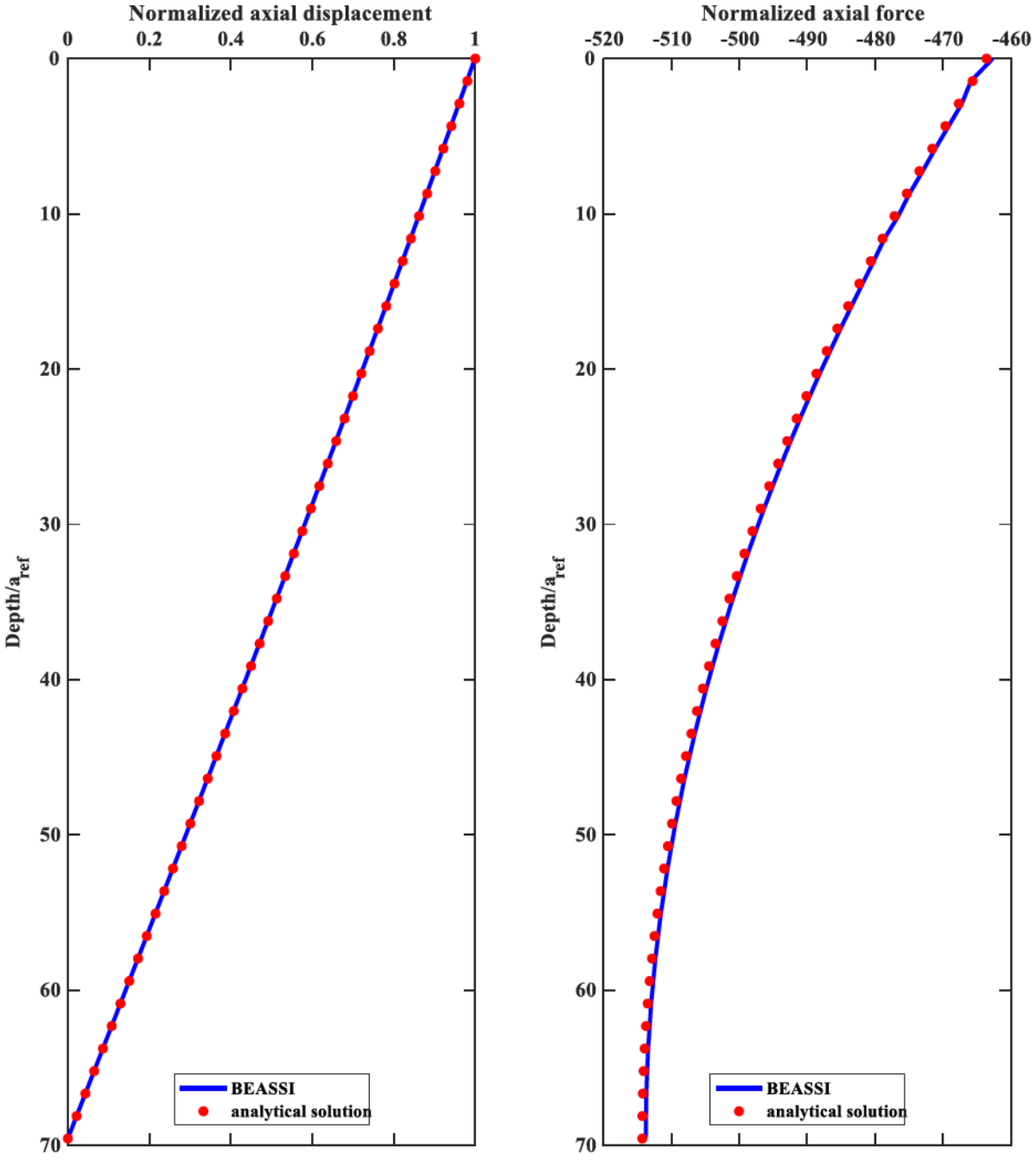

Figure 3.59 *Axial displacement and axial force profiles of a cantilever beam subjected to dynamic ($\overline{\omega}=1.0$) axial load at head.*

2. Reference study on a single floating pile embedded into homogeneous soil

Dynamic response of a floating pile embedded into homogeneous soil was studied and compared to Abedzadeh (1993). The dimensionless parameters are listed in Table 3.15

Table 3.15 *Dimensionless parameters for reference study on a floating pile.*

	Parameter	Value
Pile	Outer radius	1
	Inner radius	0.9
	Length	50
	Density	2
	Poisson's ratio	0.25
	Young's modulus	2500, 12500, 50000
	Shear modulus	1000, 5000, 20000
Soil	Density	1
	Poisson's ratio	0.25
	Young's modulus	1
	Shear modulus	0.4
	Dimensionless circular frequency	0.25
Boundary conditions	Lateral translation or rotation at pile head	1

The numerical results by BEASSI are compared to the reference solutions in Figure 3.60~Figure 3.65. Favorable overall agreement is observed in displacement, bending moment, shear force profiles for all modulus ratios. Abnormal bending moment, and shear force near the ground level are observed again for the lateral loading, especially with an increasing modulus ratio.

Bending moment is linearly proportional to the nodal displacement. When two types of deformations are superposed, the overall bending moment can be calculated through superposing the two bending moment profiles, or based on superposed displacement profile. A test was conducted on the same floating pile with $E_{pile} = 2500$ by superposing the two

boundary conditions – unit lateral translation and unit rocking. The comparison shown in Figure 3.66 validates the linearity in superposition.

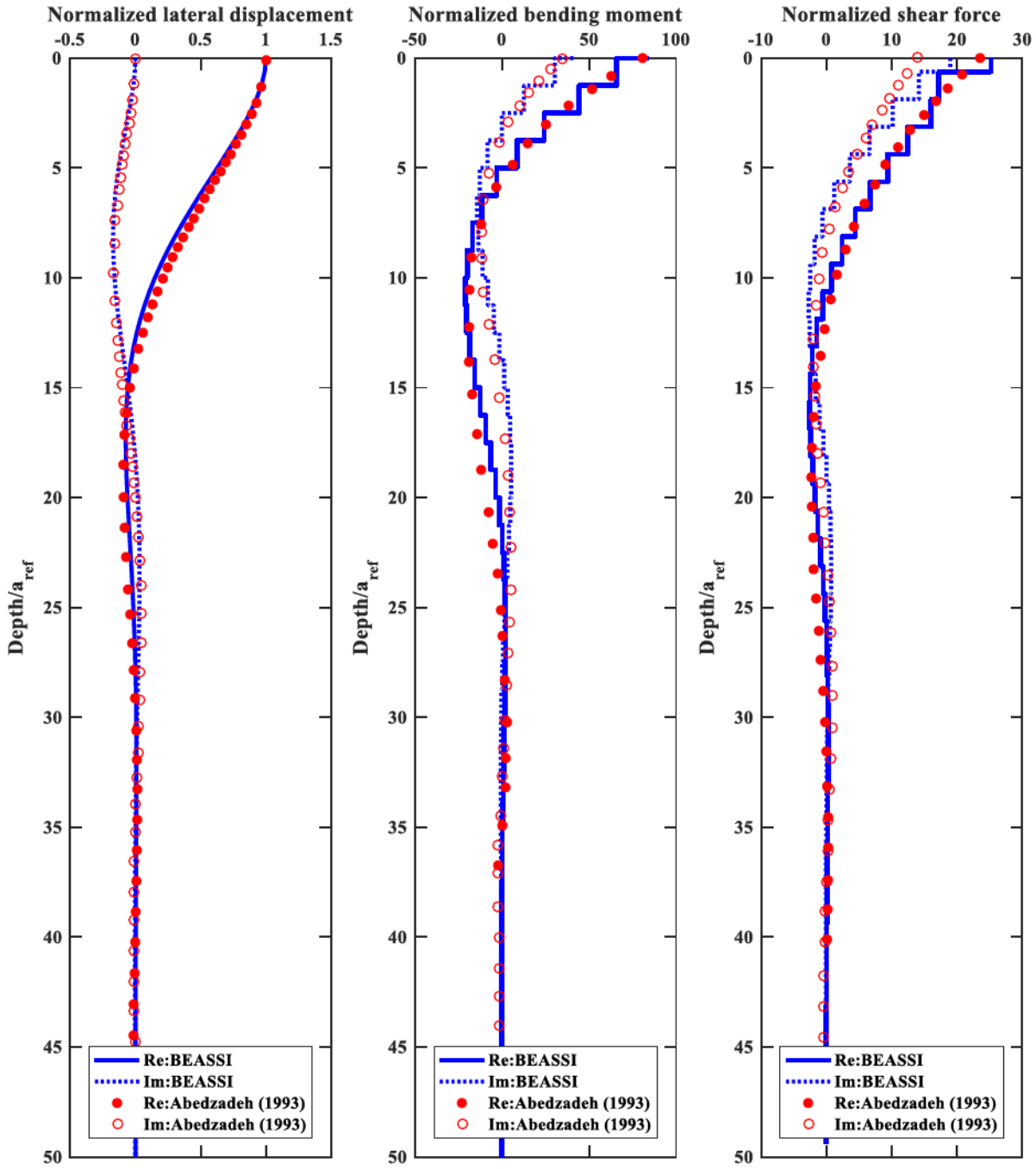

Figure 3.60 *Lateral displacement, bending moment, and shear force profiles of a floating pile subjected to dynamic lateral translation at pile head with* $E_{pile} = 2,500$.

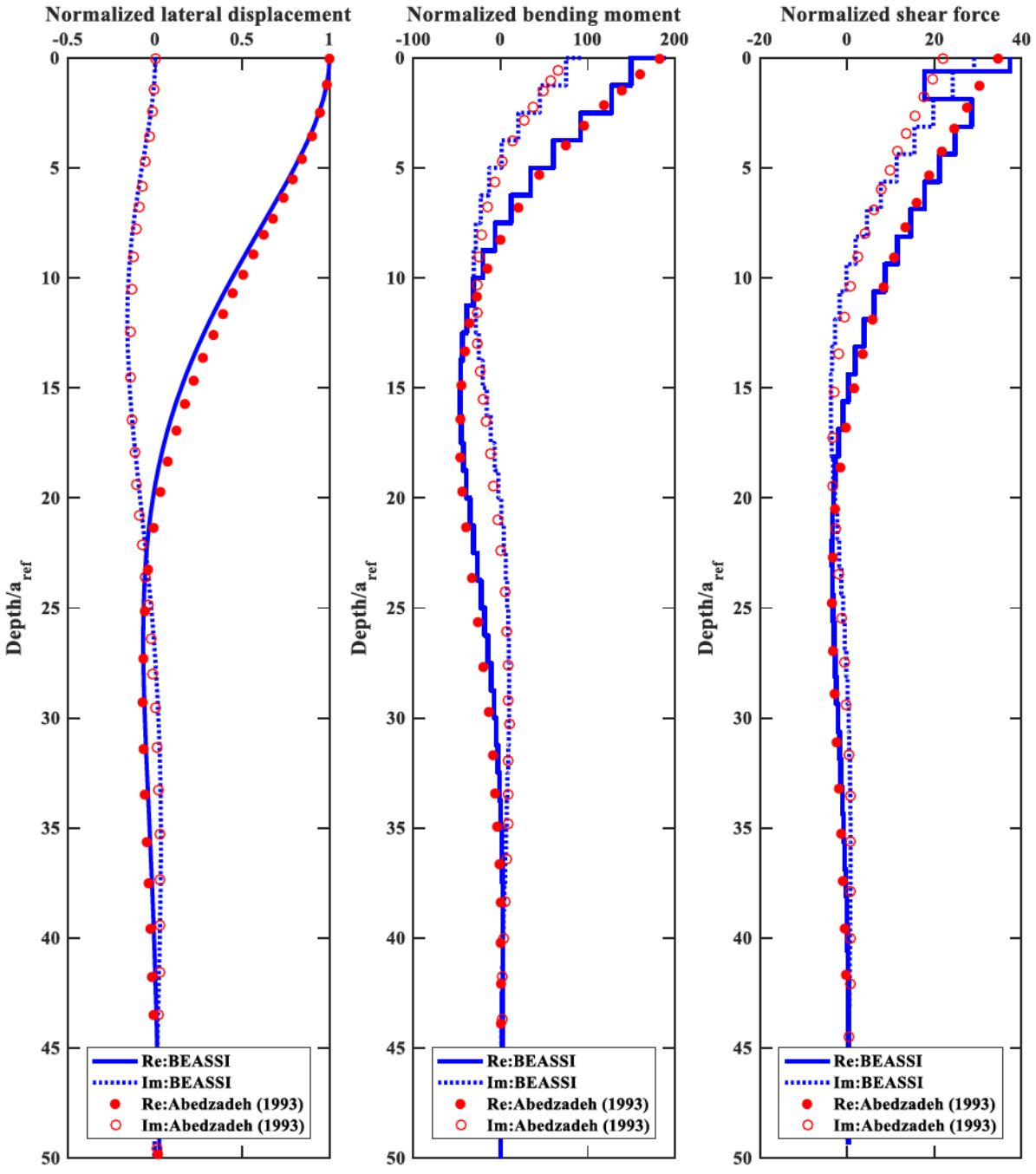

Figure 3.61 *Lateral displacement, bending moment, and shear force profiles of a floating pile subjected to dynamic lateral translation at pile head with* $E_{pile} = 12,500$.

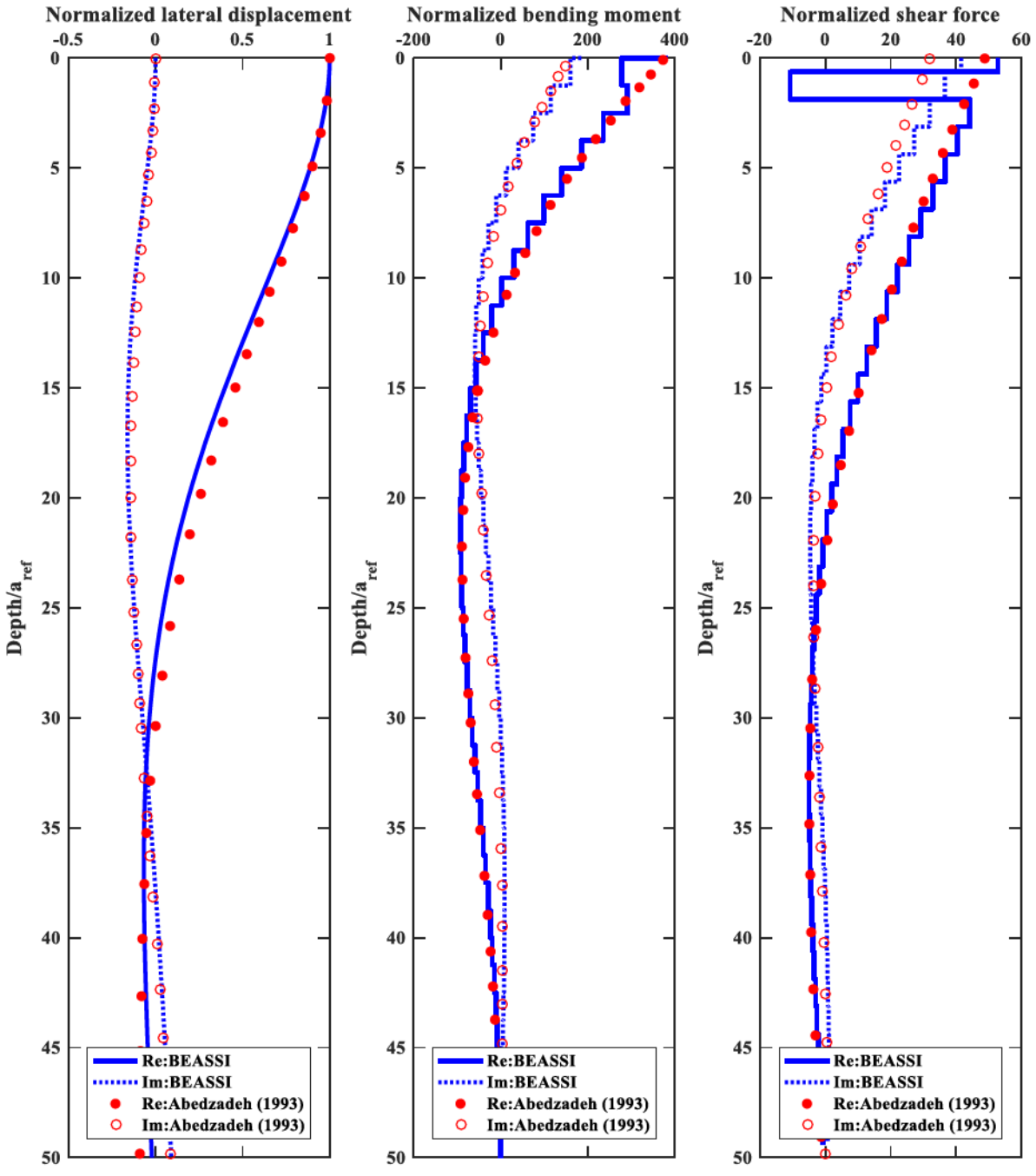

Figure 3.62 *Lateral displacement, bending moment, and shear force profiles of a floating pile subjected to dynamic lateral translation at pile head with* $E_{pile} = 50,000$.

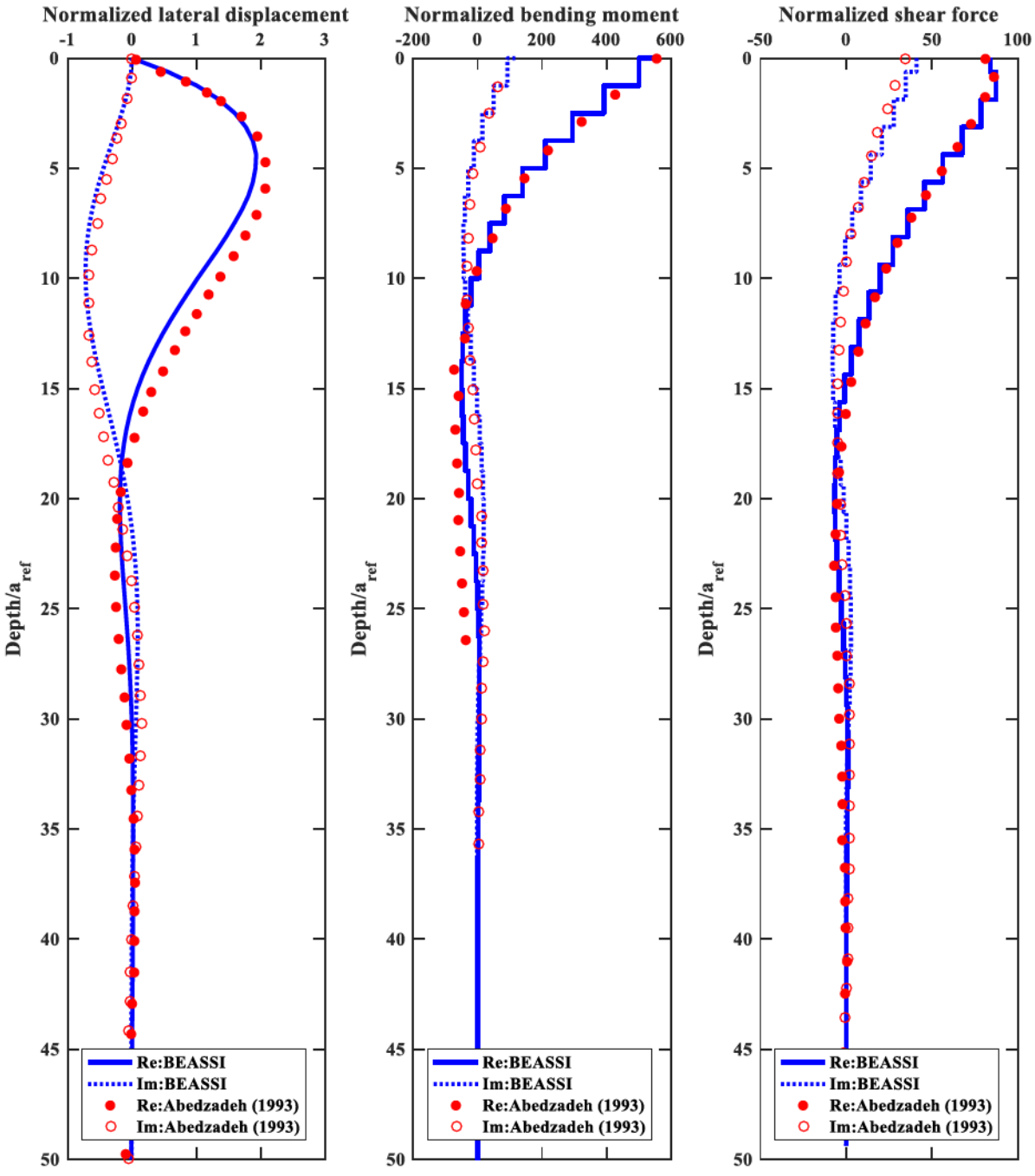

Figure 3.63 *Lateral displacement, bending moment, and shear force profiles of a floating pile subjected to dynamic rocking at pile head with* $E_{pile} = 2{,}500$.

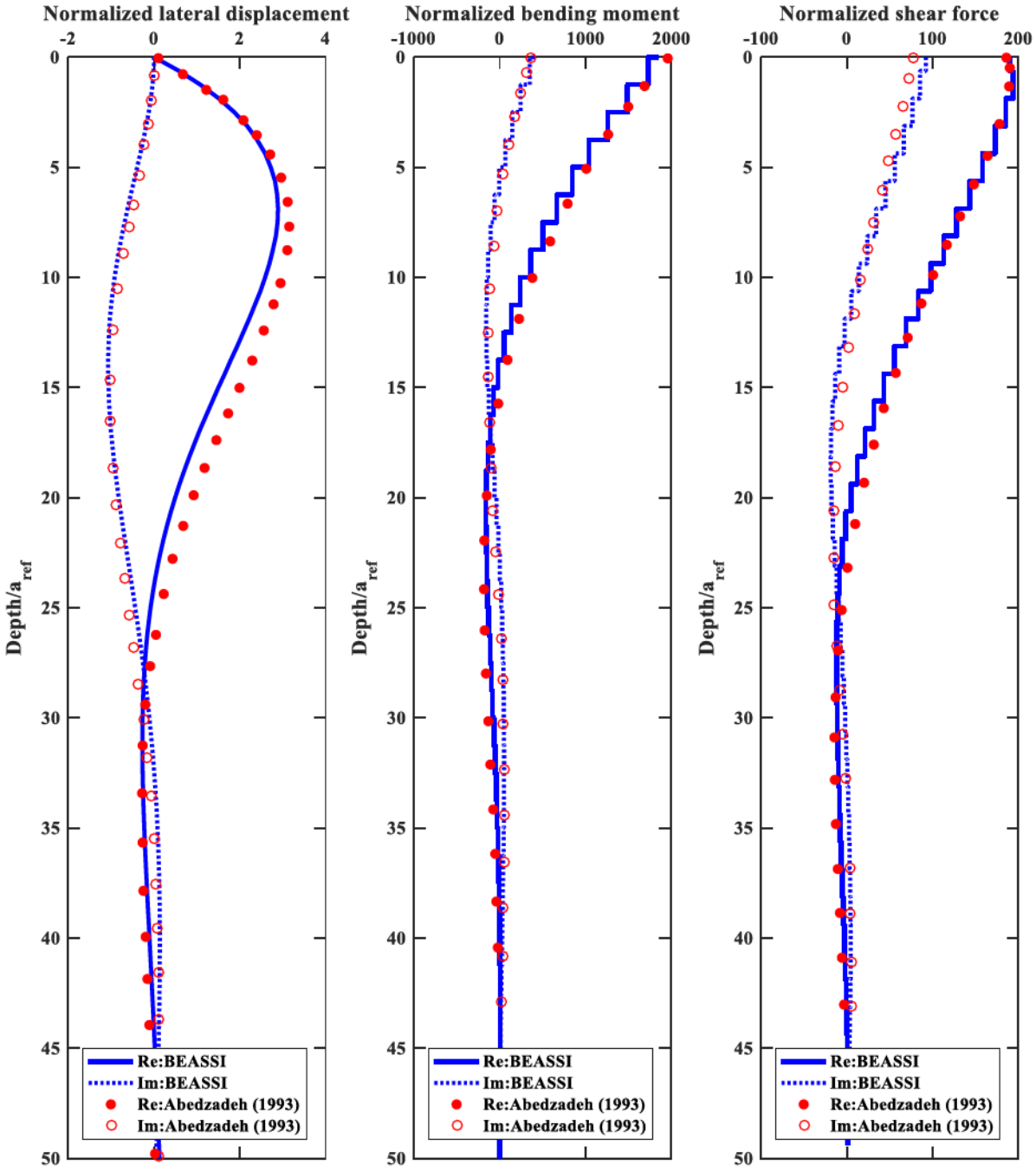

Figure 3.64 *Lateral displacement, bending moment, and shear force profiles of a floating pile subjected to dynamic rocking at pile head with* $E_{pile} = 12,500$.

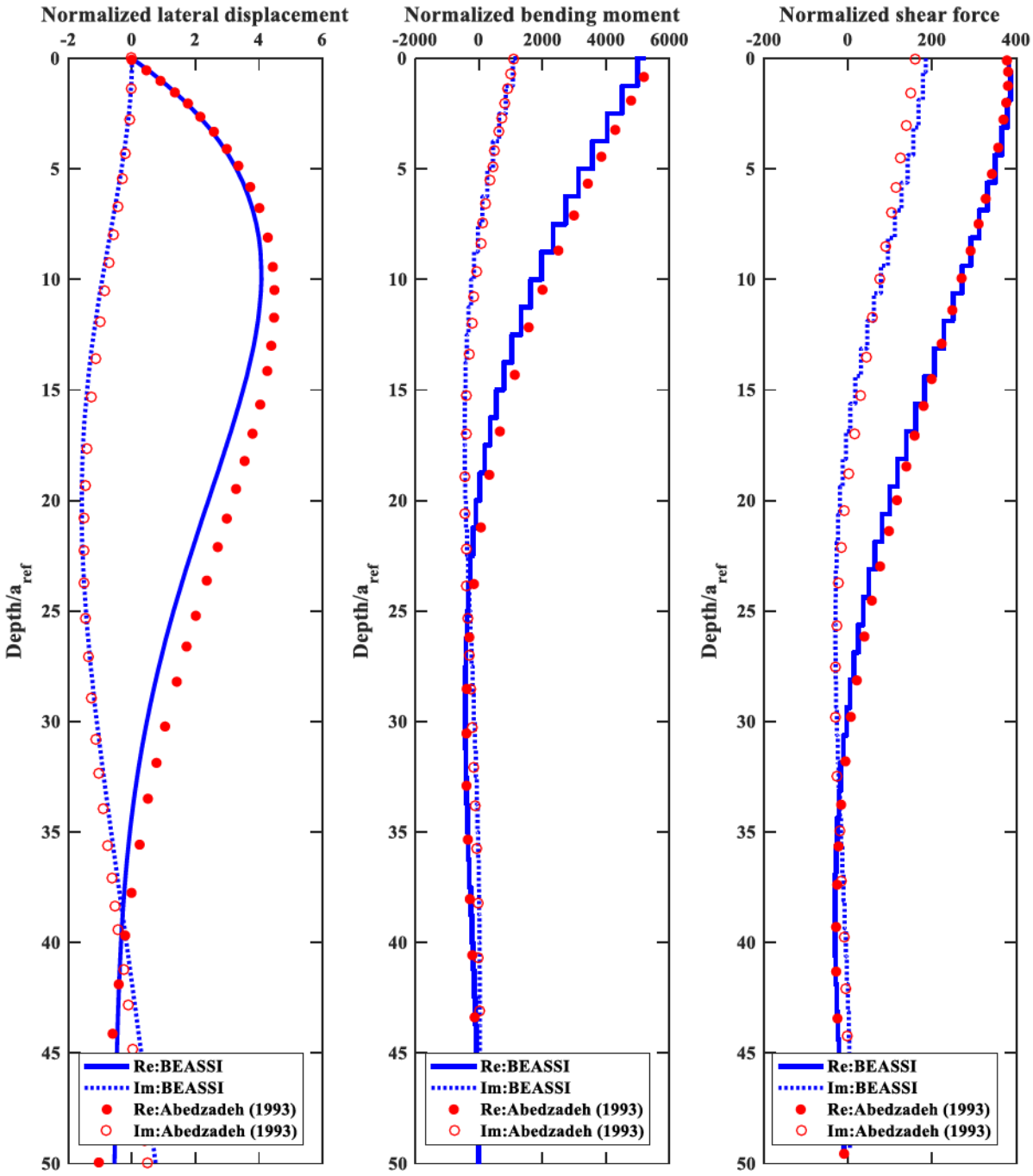

Figure 3.65 *Lateral displacement, bending moment, and shear force profiles of a floating pile subjected to dynamic rocking at pile head with* $E_{pile} = 50{,}000$.

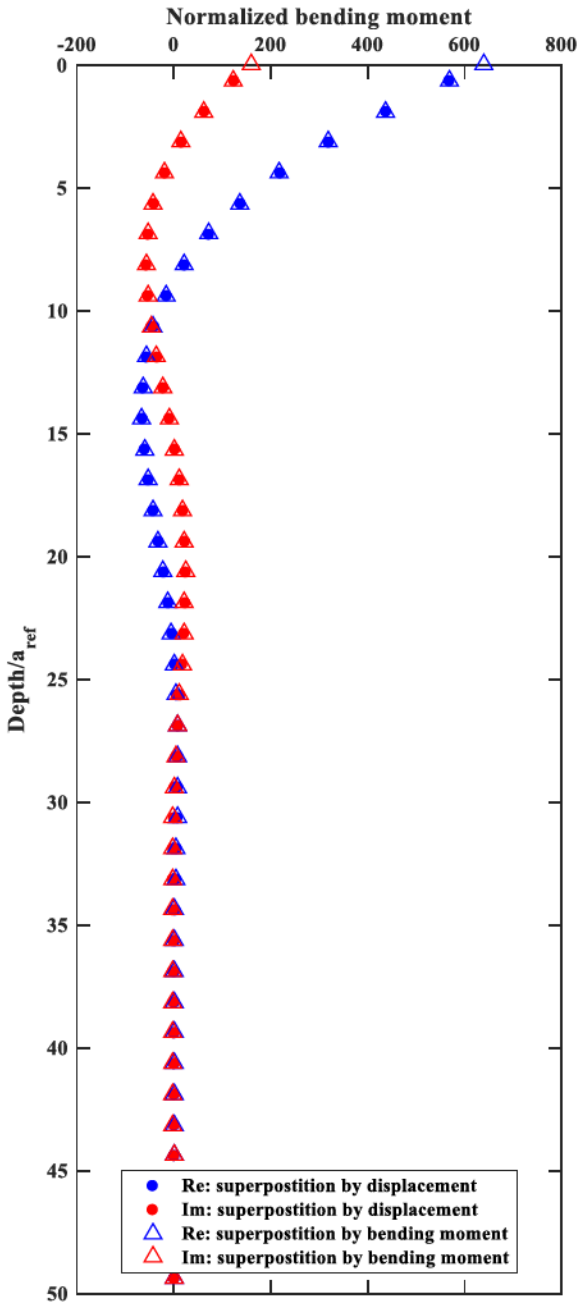

Figure 3.66 *Comparison of bending moment profiles by superposition of displacement and superposition of bending moment.*

3.8 Case Study

The best approach to validate the computational simulation proposed in this chapter is comparing numerical results to the experimental results reported in Chapter 2. For this purpose, Numerical analyses were performed on the single pile and the 2×2 pile group using BEM models with disturbed zones. The shear modulus and damping profiles for the half-space were based on SCPT tests. Soil profiles in the disturbed zone were established based on a calibration model developed in centrifuge tests on single pile in sands (Ashlock 2006) as a first approach.

$$\text{disturbed zone (inner):} \quad \begin{cases} G^I(z) = G_{ref}\left[\beta + \alpha\left(1 - \dfrac{1}{1+(\mathrm{z}/\,\mathrm{z}_d)^{\mathrm{n}}}\right)\left(\left(\dfrac{z}{a}\right)^{0.5} - \dfrac{\beta}{\alpha}\right)\right] \\ \xi^I(\mathrm{z}) = \xi_0 / [1+(\mathrm{z}/\,\mathrm{z}_d)^{\mathrm{n}}] + \xi^O(z) \end{cases} \tag{3.120}$$

$$\text{half-space (outer):} \quad \begin{cases} G^O(z) = \text{SCPT profile} \\ \xi^O(z) = \text{minimum material damping by SCPT profile} \end{cases}$$

where $\alpha = 1.1$, $\beta = 0.1$, $\mathrm{z}_d = 5$, $n = 3$, $\xi_0 = 0.3$, and a is the radius of pile.

The numerical results are presented in forms of theoretical accelerance functions – A_{yc}/VC, A_{xc}/HC, A_{yc} /VE, A_{xc} /VE, and A_{rc} /VE. All accelerances are calculated at centroid of pile cap.

3.8.1 Single Pile

1. Input parameters

The dimensionless parameters for the single pile are listed in Table 3.16. Dimensionless soil shear modulus profiles for the disturbed zone and the half-space are presented in Figure 3.67 and Figure 3.68, respectively. Soil dimensionless density is 1 and Poisson's ratio is 0.42. Reference number were $a_{ref} = 0.1095$ m, $\mathrm{G}_{ref} = 2.046\times10^8$ Pa, and $\rho_{ref} = 1936.8$ kg/m^3.

Table 3.16 *Dimensionless parameters of the single pile.*

Parameter	Value
Outer radius	1
Thickness	0.075
Length	69.56
Complex shear modulus	(387.9, 0)
Poisson's ratio	0.26
Density	4.05

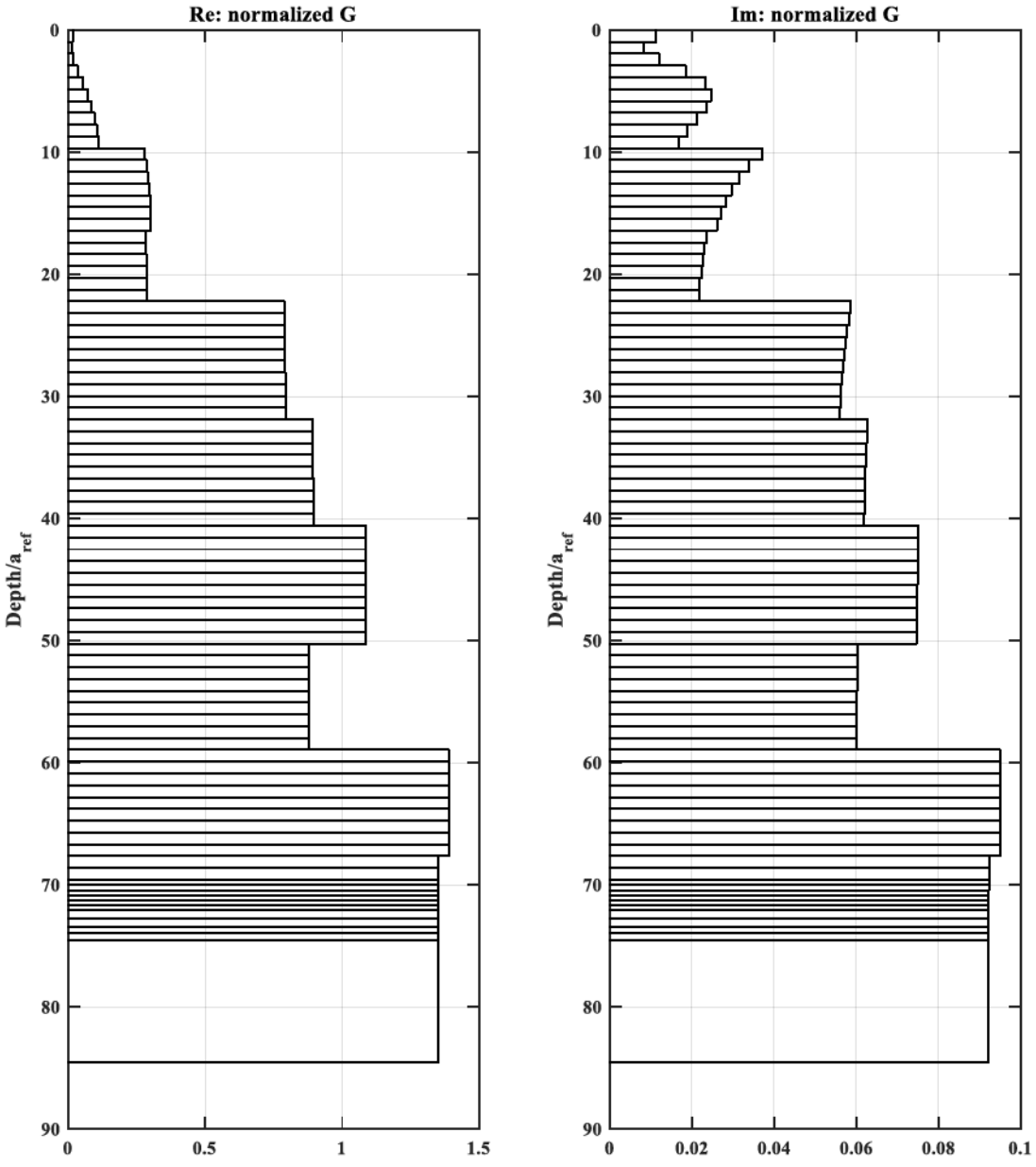

Figure 3.67 *Layered soil shear modulus and damping ratio profiles within disturbed zone for the single pile.*

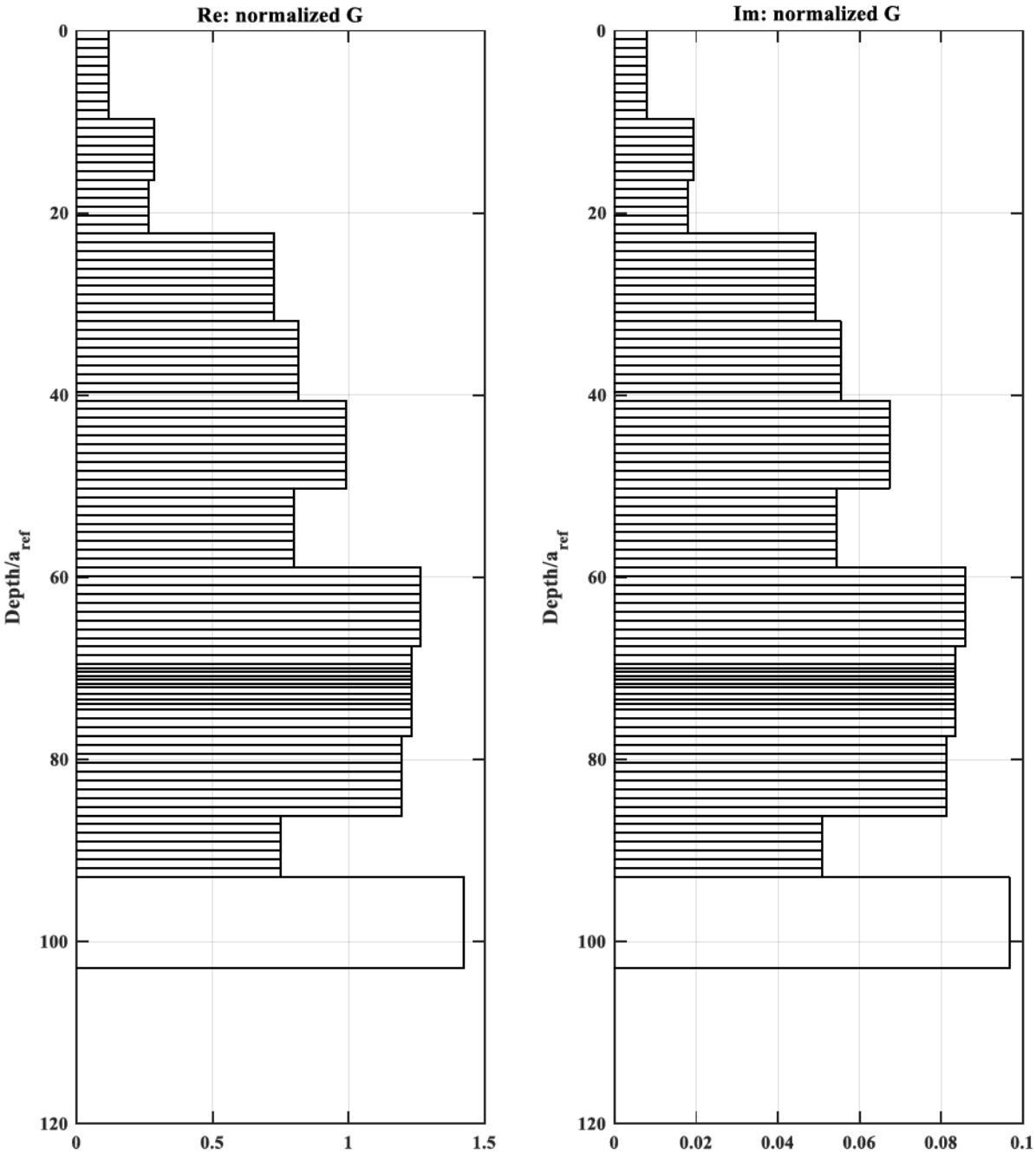

Figure 3.68 *Layered soil shear modulus and damping ratio profiles in the half-space for the single pile.*

2. Numerical results and comparison

The experimental accelerance functions for the single pile by R2 excitation in physical test are chosen as reference for comparison (Figure 3.69 - Figure 3.73). In general good consistency is found for all accelerances. For A_{yc}/VC, the theoretical accelerance has close resonant frequencies but slightly lower amplitudes for both real and imaginary parts. For A_{xc}/HC, the fundamental mode is well captured for the real part and slightly overestimated in amplitude for the imaginary part. The undesired mode at 15 Hz in the tests is not accounted for by the theoretical formulation. For A_{yc}/VE, the resonant frequencies are overestimated and amplitudes are underestimated. For A_{xc}/VE, both lateral mode and the coupled rocking-lateral mode are captured, but the resonant frequencies for the rocking mode are underestimated and amplitudes are noticeably overestimated. Similar trends can also be found for A_{rc}/VE.

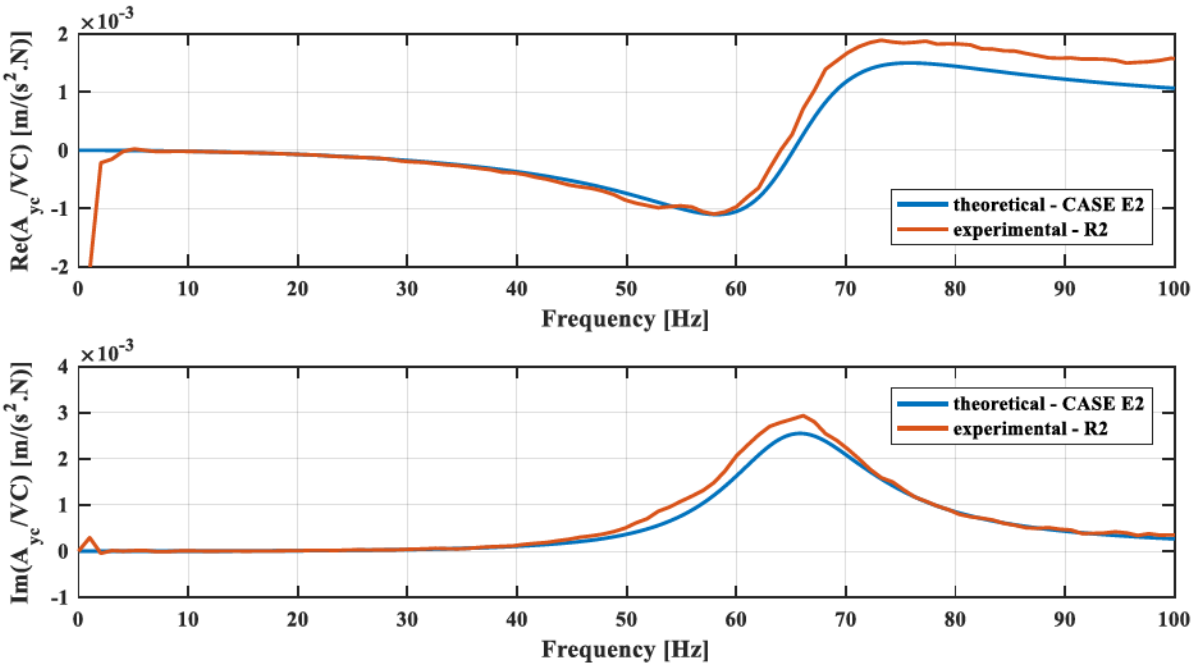

Figure 3.69 *Comparison of A_{yc}/VC accelerance for the single pile.*

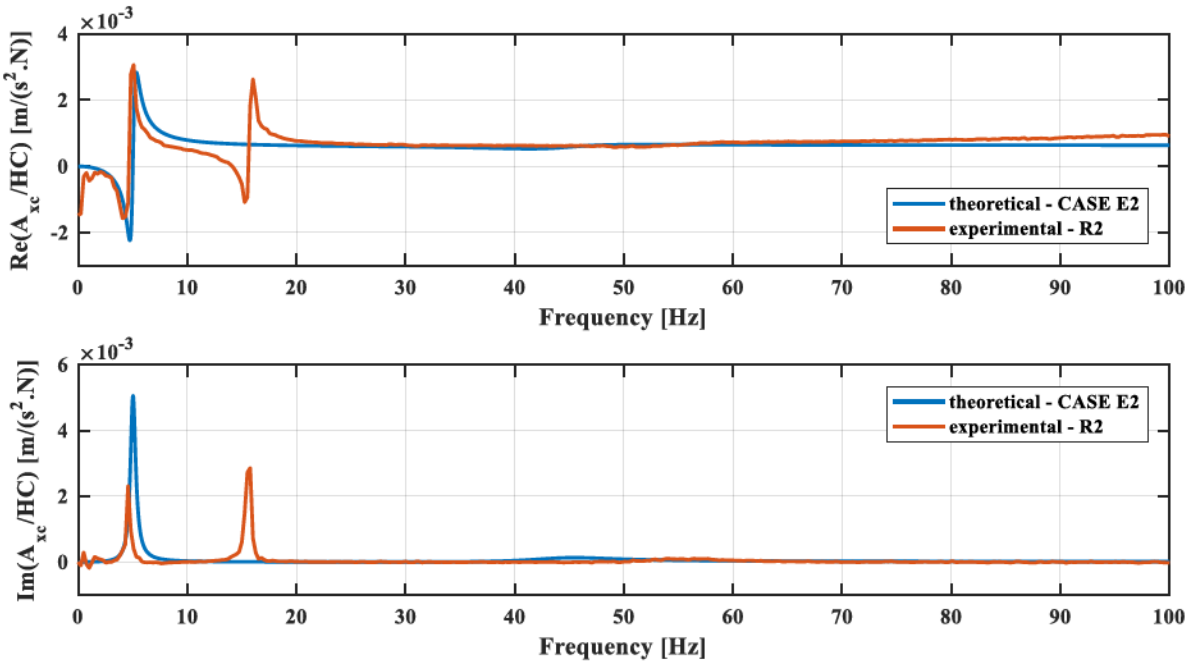

Figure 3.70 *Comparison of A_{xc}/*HC *accelerance for the single pile.*

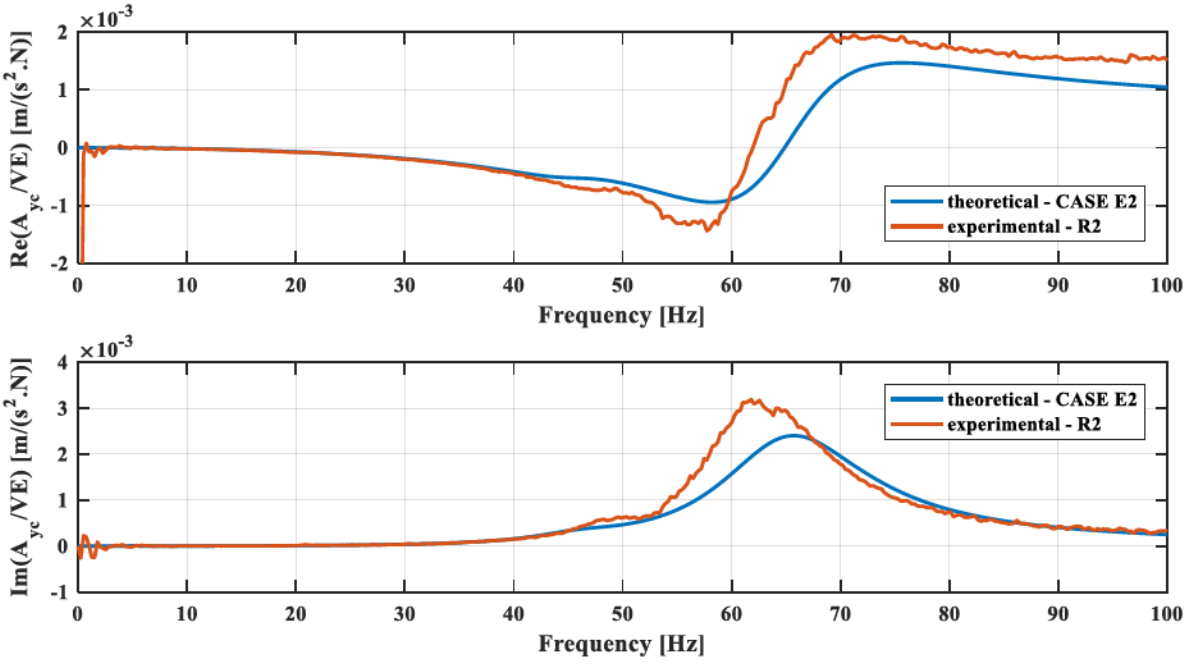

Figure 3.71 *Comparison of A_{yc}/*VE *accelerance for the single pile.*

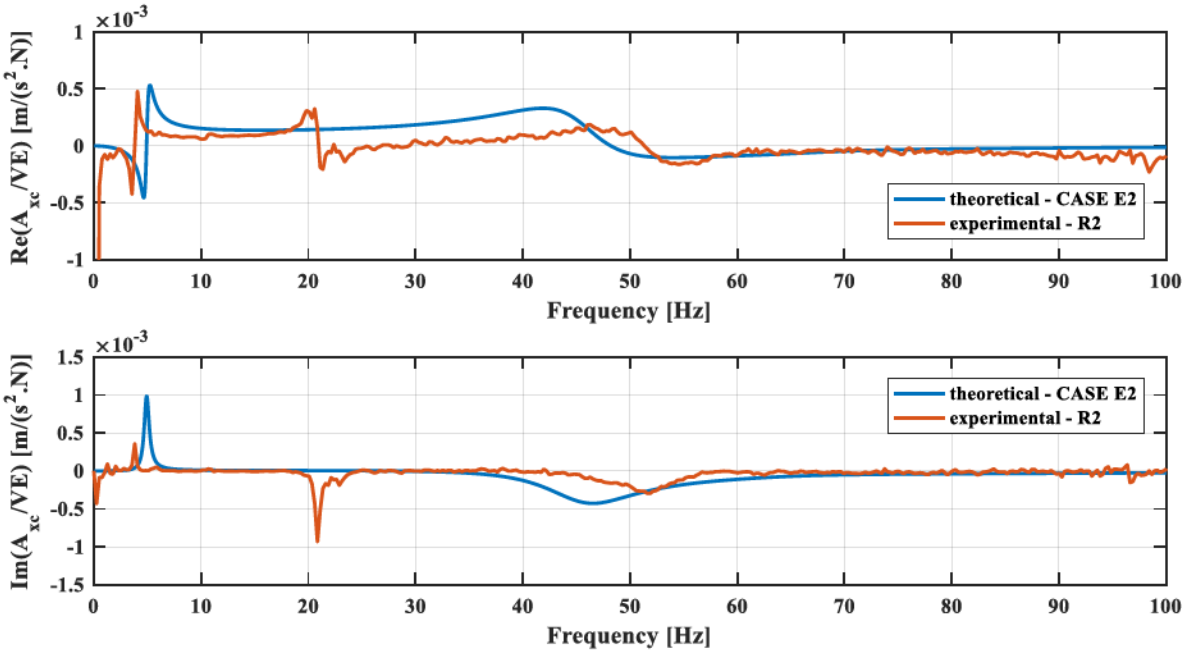

Figure 3.72 *Comparison of A_{xc}/*VE *accelerance for the single pile.*

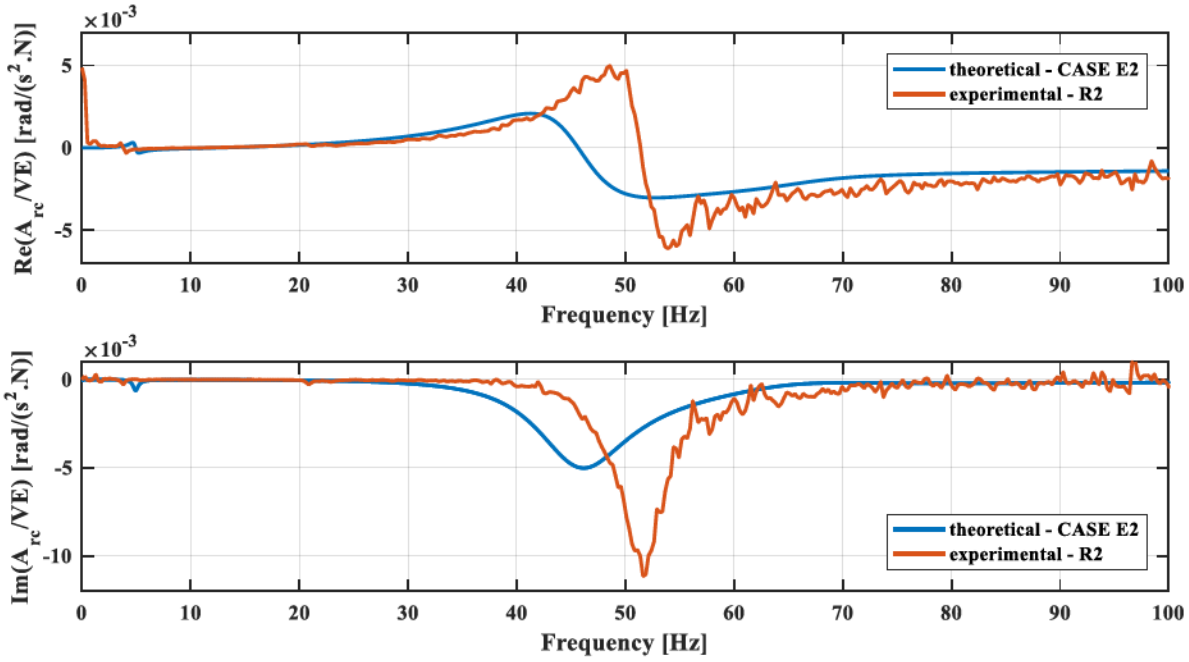

Figure 3.73 *Comparison of A_{rc}/*VE *accelerance for the single pile.*

3.8.2 2×2 Pile Group

1. Input parameters

The dimensionless pile parameters are identical to the single pile as in Table 3.16. Soil density and Poisson's ratio also remain constant. Dimensionless soil shear modulus profiles for the disturbed zone and the half-space are presented in Figure 3.74 and Figure 3.75.

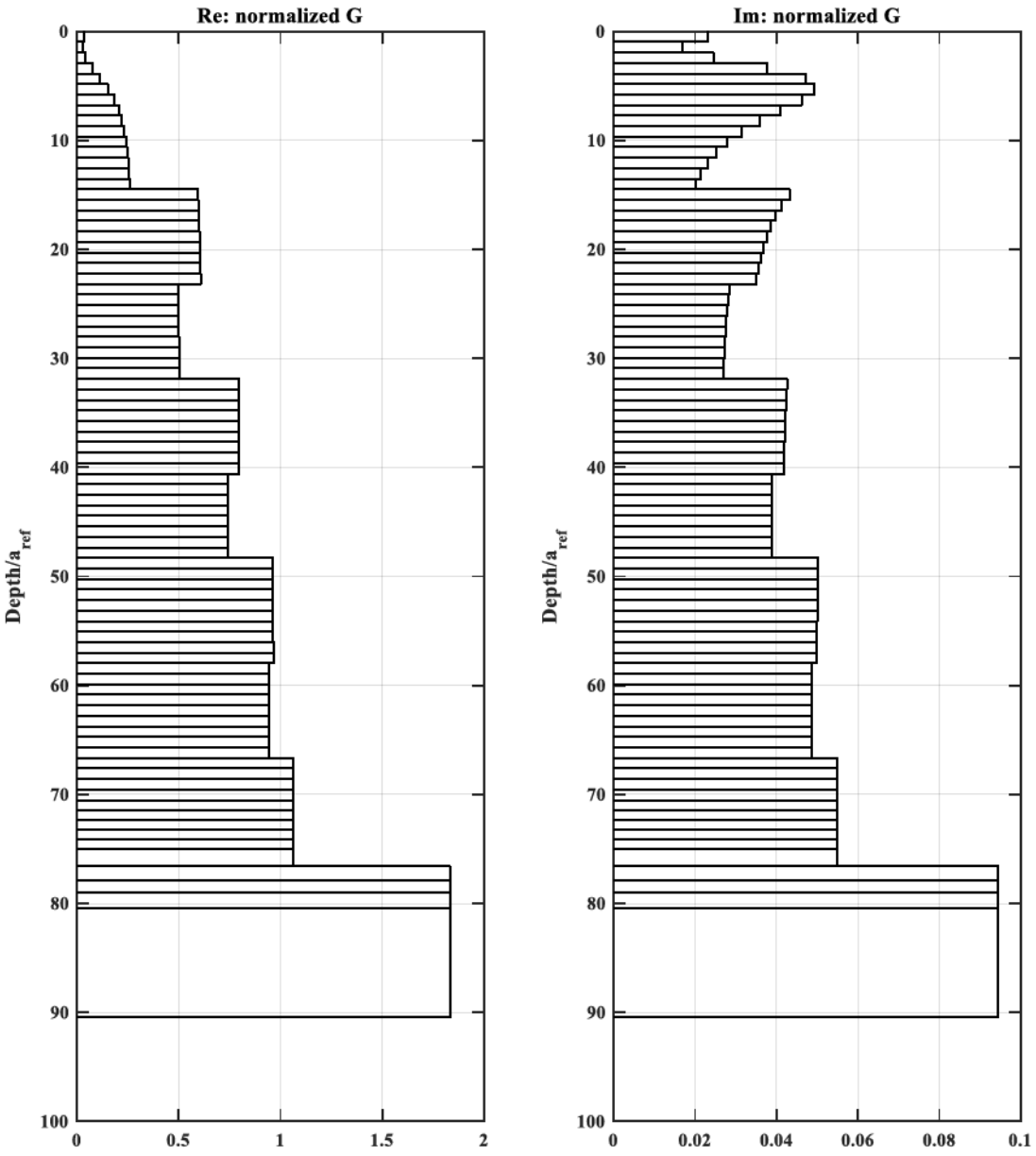

Figure 3.74 *Layered soil shear modulus and damping ratio profiles within the disturbed zone for pile group.*

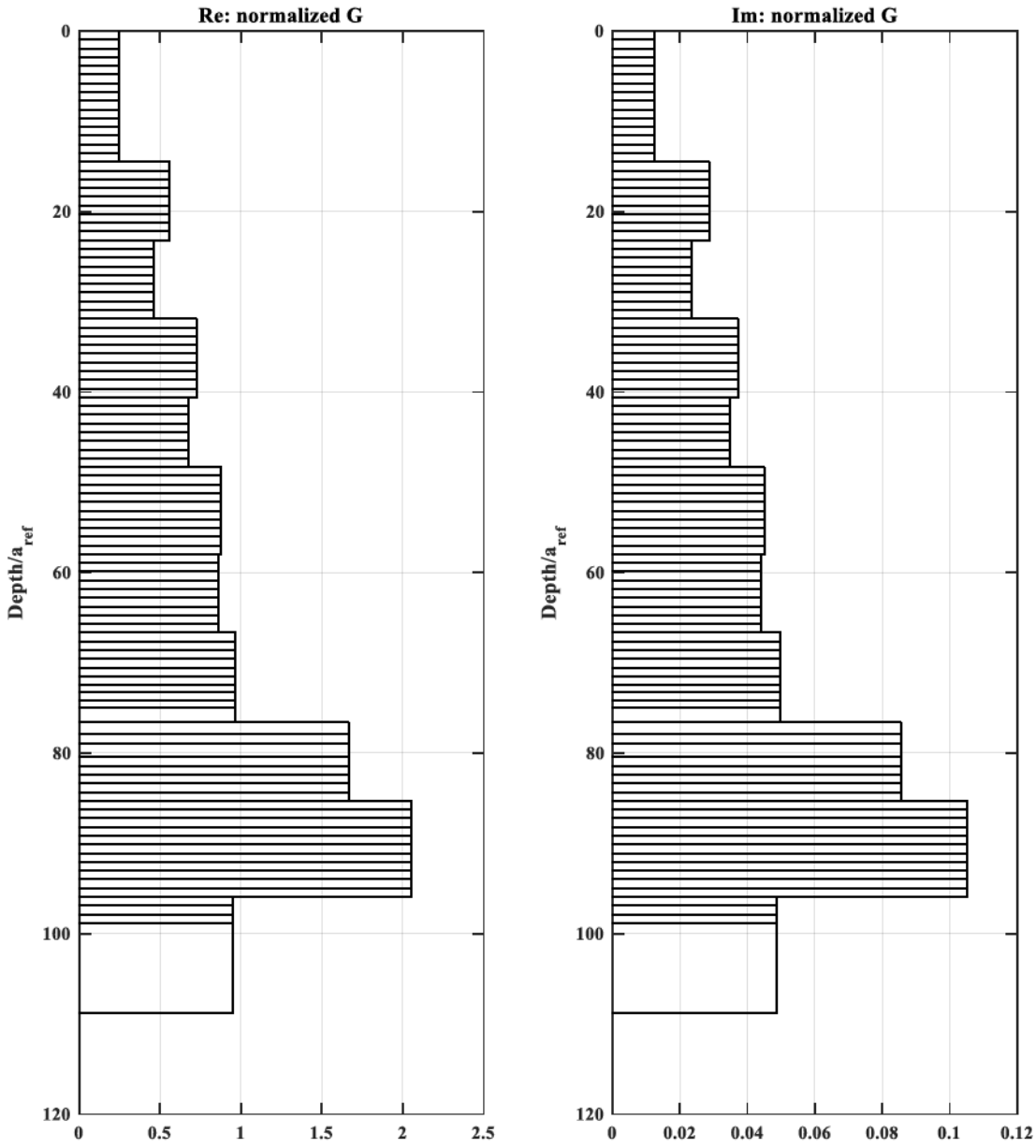

Figure 3.75 *Layered soil shear modulus and damping ratio profiles in the half-space for pile group.*

2. Numerical results and comparison

The comparison of theoretical and experimental accelerances for the 2×2 pile group is presented in Figure 3.76 - Figure 3.80. For A_{yc}/VC, the amplitudes of theoretical accelerance are only about half of the experimental ones. For A_{xc}/HC, the fundamental peak is captured

with a higher resonant frequency and lower amplitude. For A_{yc}/VE, the amplitude of the unique resonant peak is underestimated. For A_{xc} /VE, the fundamental mode at 14 Hz is well captured while the second mode is underestimated in amplitude. Similar situation is found for A_{yc} /VE.

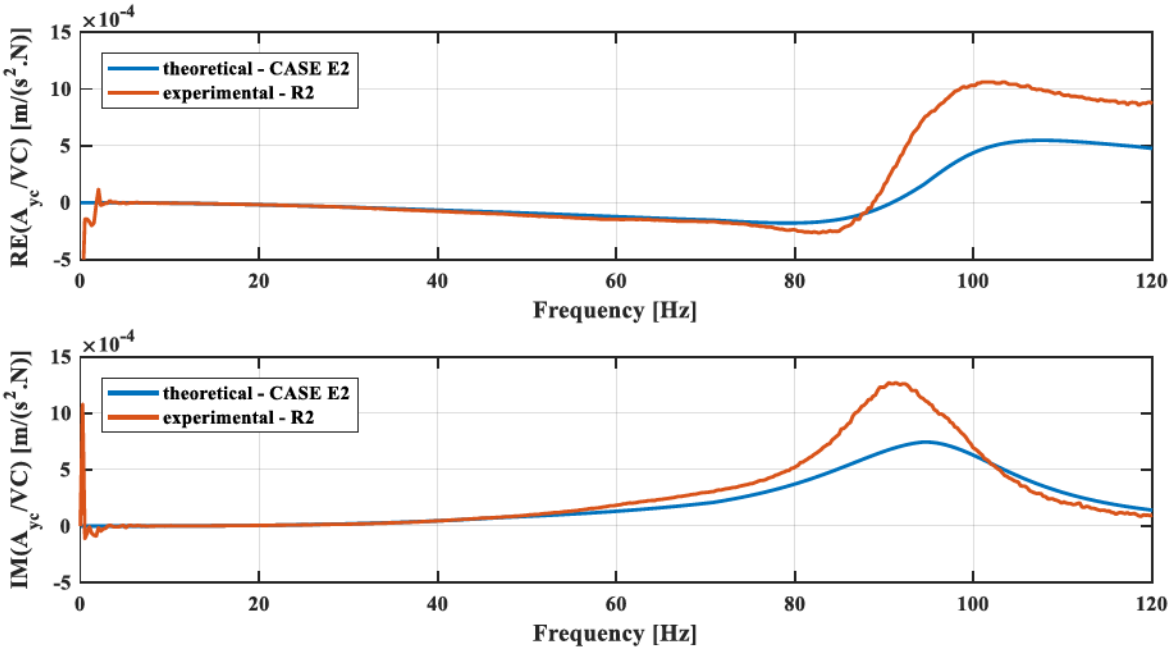

Figure 3.76 *Comparison of A_{yc}/VC accelerance for the pile group.*

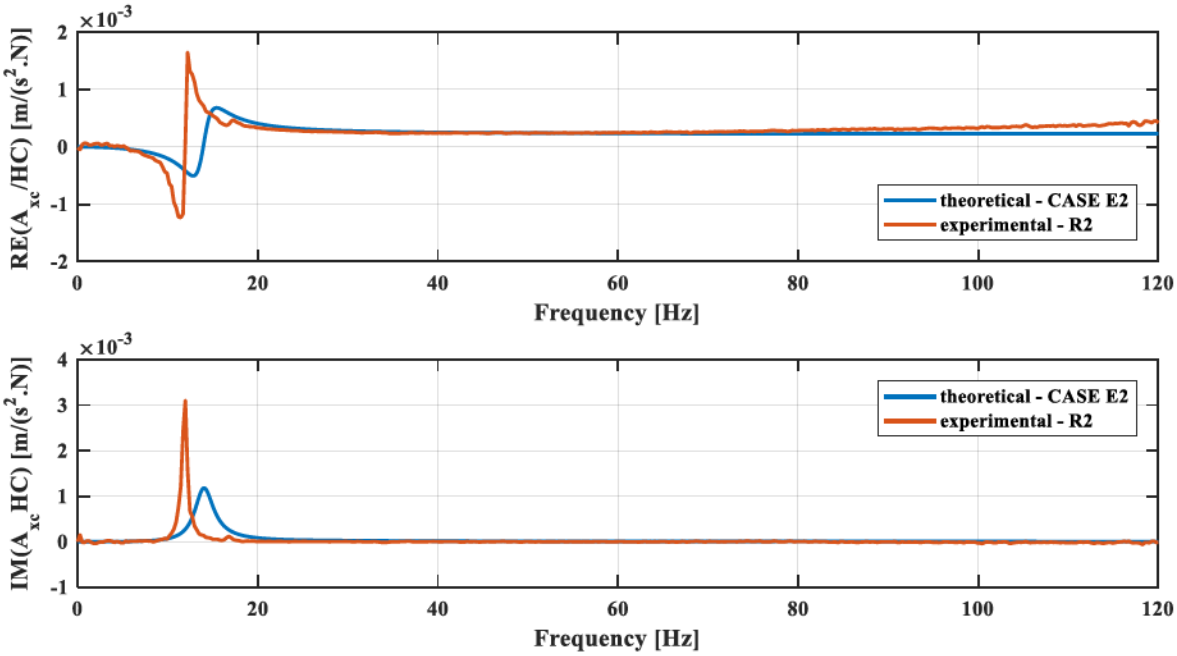

Figure 3.77 *Comparison of A_{xc}/HC accelerance for the pile group.*

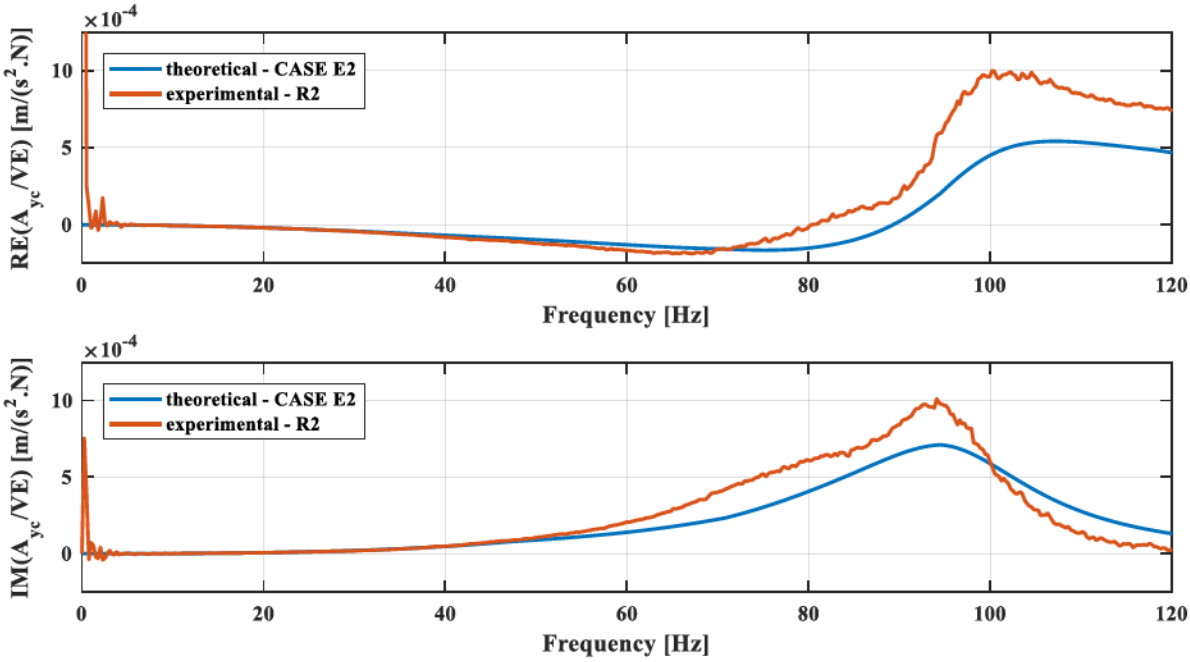

Figure 3.78 *Comparison of A_{yc}/VE accelerance for the pile group.*

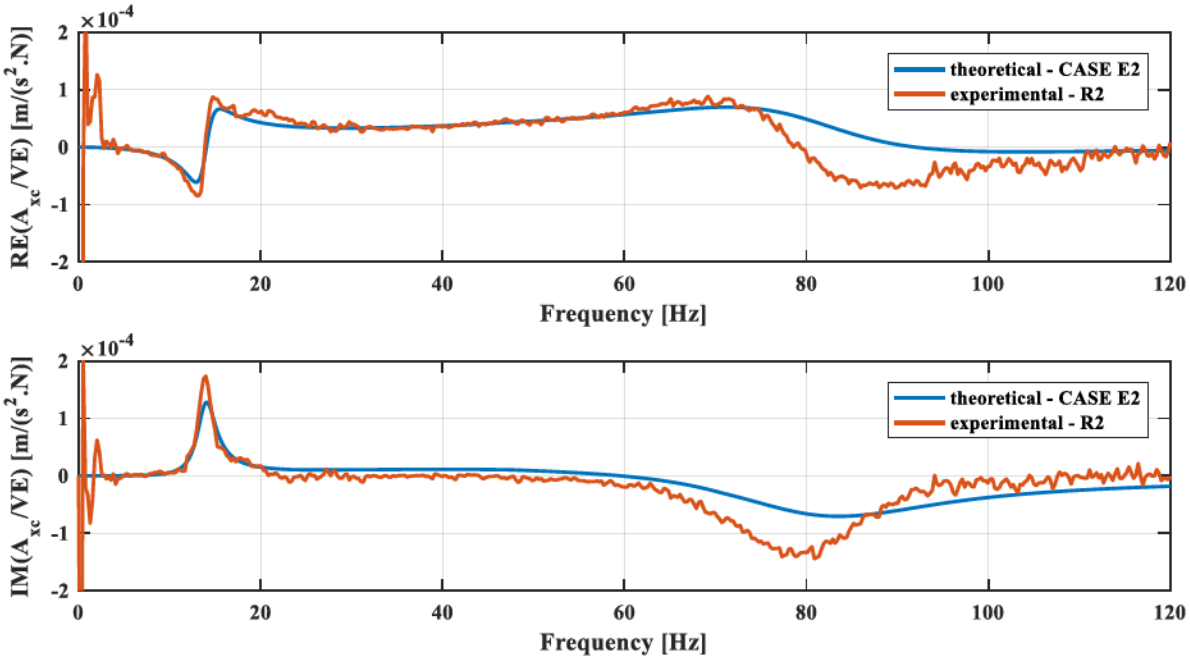

Figure 3.79 *Comparison of A_{xc}/VE accelerance for the pile group.*

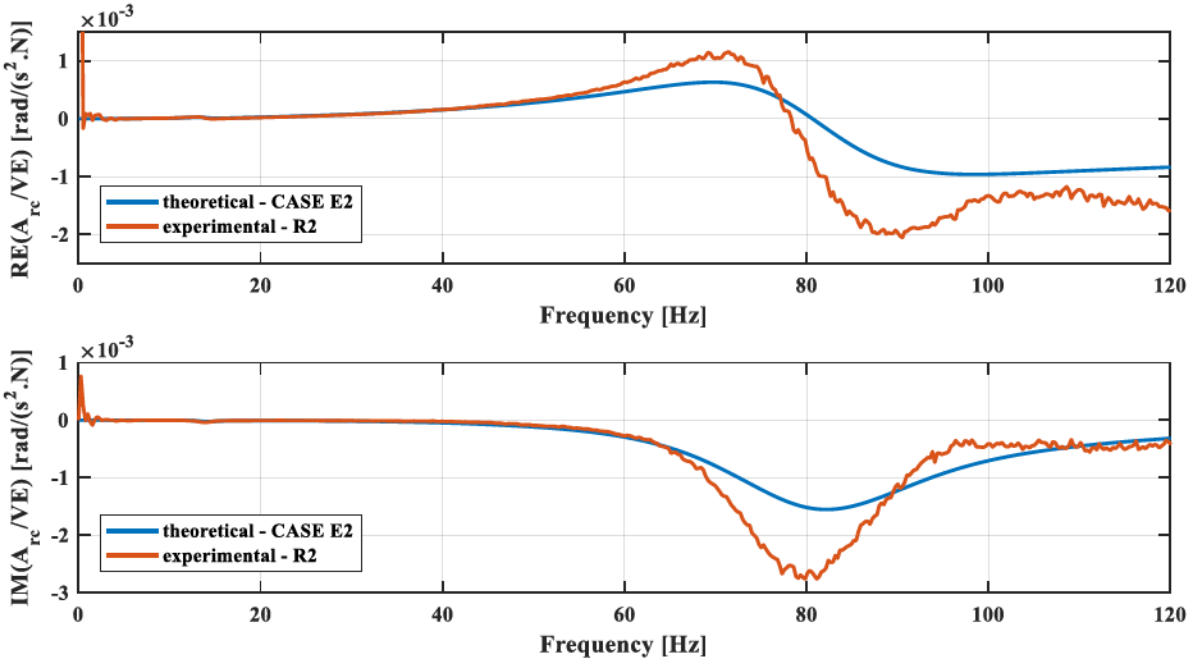

Figure 3.80 *Comparison of A_{rc}/VE accelerance for the pile group.*

3.9 Soil Profile Calibration

Past computational and experimental studies have revealed that the soil profiles in either theoretical or numerical models are typically calibrated to improve accuracy in predictions of pile-soil system responses (e.g., Blaney and O'Neil 1986). One reason is that assumptions applied in the models may not be realistic. Primary assumptions include axial symmetrically piecewise homogeneous soils, bonded pile-soil interface throughout vibration progress, and linearly viscoelastic behavior of soils. CPT and SCPT tests in this study have indicated variations in layered soil profiles for the three soundings. Gapping may also form near ground level for horizontal vibrations (e.g., Stewart et al. 2007). Another reason is the measurement error in site investigation and testing. The shear modulus and material damping ratio profiles obtained from the SCPT tests are a piecewise average of approximate every 1 m

depth, which cannot precisely capture the sharp variation in the soil shear modulus for thin layers, especially near ground level. In addition, soil bulk density has to be assumed since corresponding laboratory test is currently not available. Last but not the least, the disturbed-zone BEM models are still under study. Only homogeneous sands (e.g., Ashlock 2006) and in-situ soft clays (e.g., Fotouhi 2014) have been studied for the proposed disturbed-zone models. Disturbed-zone models for pile group in stiff clays have yet to be thoroughly investigated. Studies have demonstrated that by calibrating soil profile better consistency can be achieved between theoretical and experimental results (e.g., Crouse et al. 1990).

The soil profiles obtained from site investigation commonly need to be calibrated for the disturbed zone by trial-and-error until the best match is achieved (e.g., Vaziri and Han 1991; Manna and Baidya 2010; Elkasabgy and El Naggar 2013). This section presents several modified soil profiles that exhibit better match in accelerance functions.

3.9.1 Calibration for Single Pile

Although preliminary theoretical accelerances by CASE E2 soil profiles within the disturbed zone suggest generally good agreement with the experimental one, efforts are made for better match by calibrating soil profiles in both disturbed zone and half-space. For the CASE E2 soil profiles, the resonant frequencies for the vertical modes are slightly overestimated and the amplitudes are underestimated. Resonant frequencies for rocking modes in both A_{xc}/VE and A_{rc}/VE show lower resonant frequencies. Horizontal modes in A_{xc}/HC and A_{xc}/VE are well captured. As a general rule, both vertical stiffness and damping should be decreased for the single pile. Pile deformation suggests with rotation at pile head, second layer

of pile elements have largest horizontal deformation. To increase resonant frequencies for the rocking modes, soil shear modulus at this depth is to be increased and this change should also have minor effects on the horizontal modes. To this end, the soil profiles were calibrated by three steps. As an initiative, soil shear modulus for all depths within the disturbed zone was decreased by 30%. Based on the soil profiles in the Step 1, soil shear modulus within the disturbed zone was increased by four times at depth of the top layer pile elements and decreased by 50% for the second layer pile element. In Step three, material damping ratio within the disturbed zone was decreased to zero for all soils below Depth/a_{ref} of 5.80 and for all soils in the half-space. Layered soil profiles in the above three steps are termed as CASE E2 v1, CASE E2 v2, and CASE E2 v3 (Figure 3.81 - Figure 3.83). The resulting accelerances are compared with the reference experimental accelerances in Figure 3.84. The vertical modes in A_{yc}/VC and A_{yc}/VE now have better resonant frequencies and higher amplitudes. Horizontal modes in A_{xc}/VE have slightly higher, but still acceptable amplitudes. Resonant frequencies are not affected. The rocking modes, although show favorable improvement, still present obvious differentiation. The possible reason may be the error in polar moment of inertia of the pile cap. Further calibration was implemented with a focus on matching the rocking modes. However the soil profiles began to induce inconsistency in vertical and horizontal modes. Generally, the calibrated soil profiles progressively lead to better consistency with experimental data. For the time being CASE E2 v3 is regarded as suitable set of profiles for the single pile testing.

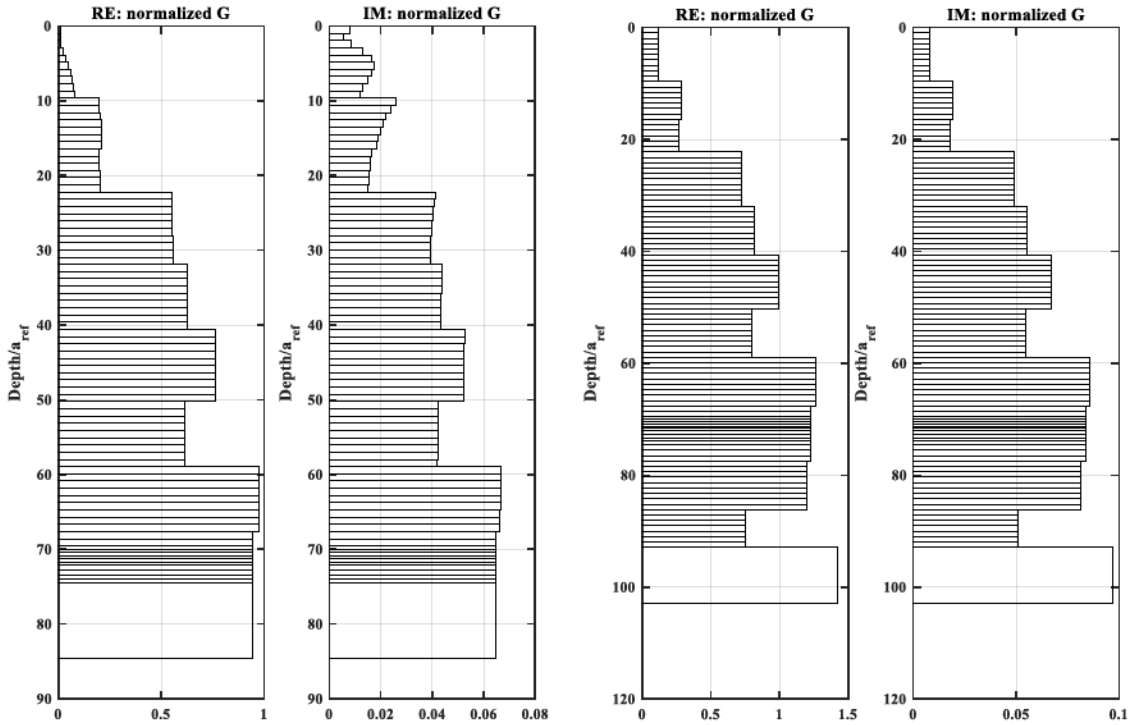

Figure 3.81 *Soil profile CASE E2 v1 (Step 1).*

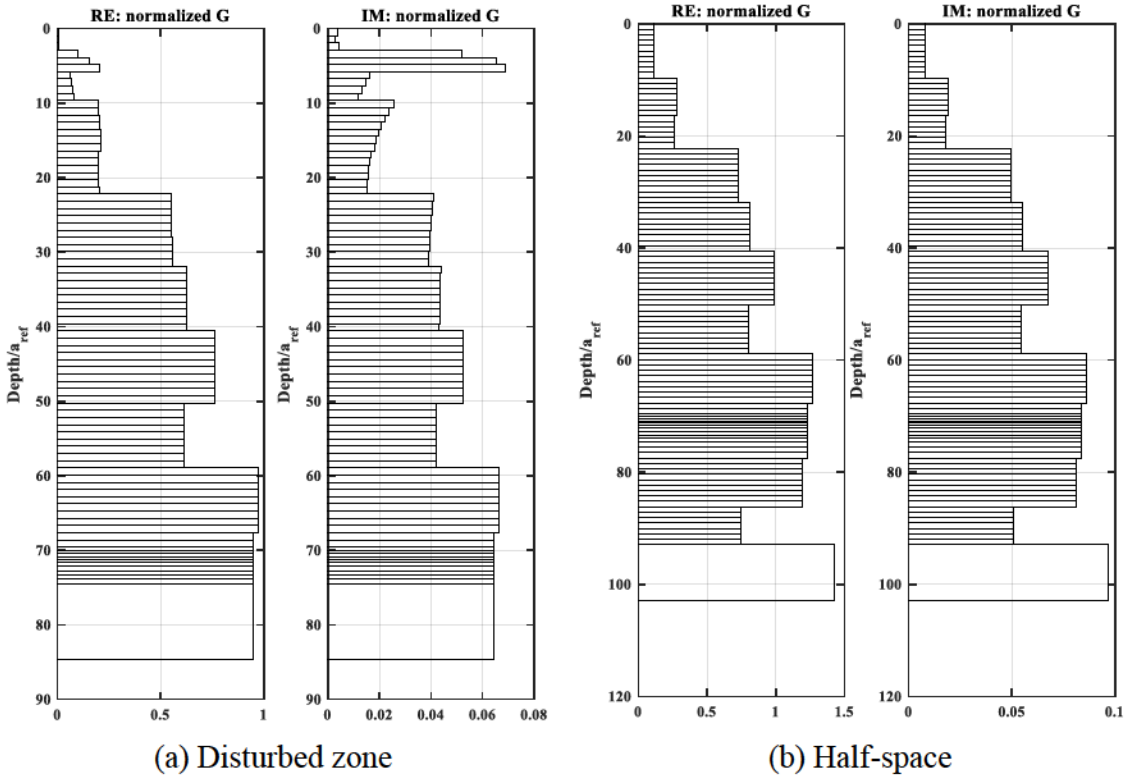

Figure 3.82 *Soil profile CASE E2 v2 (Step 2).*

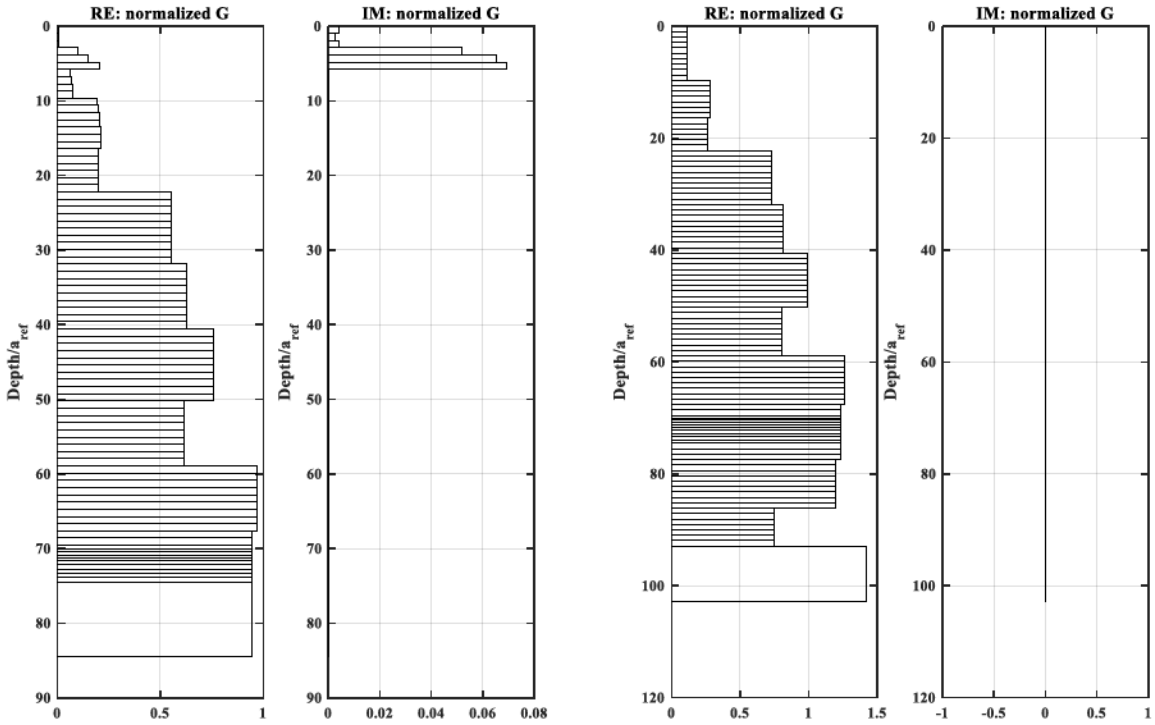

(a) Disturbed zone (b) Half-space

Figure 3.83 *Soil profile CASE E2 v3 (Step 3).*

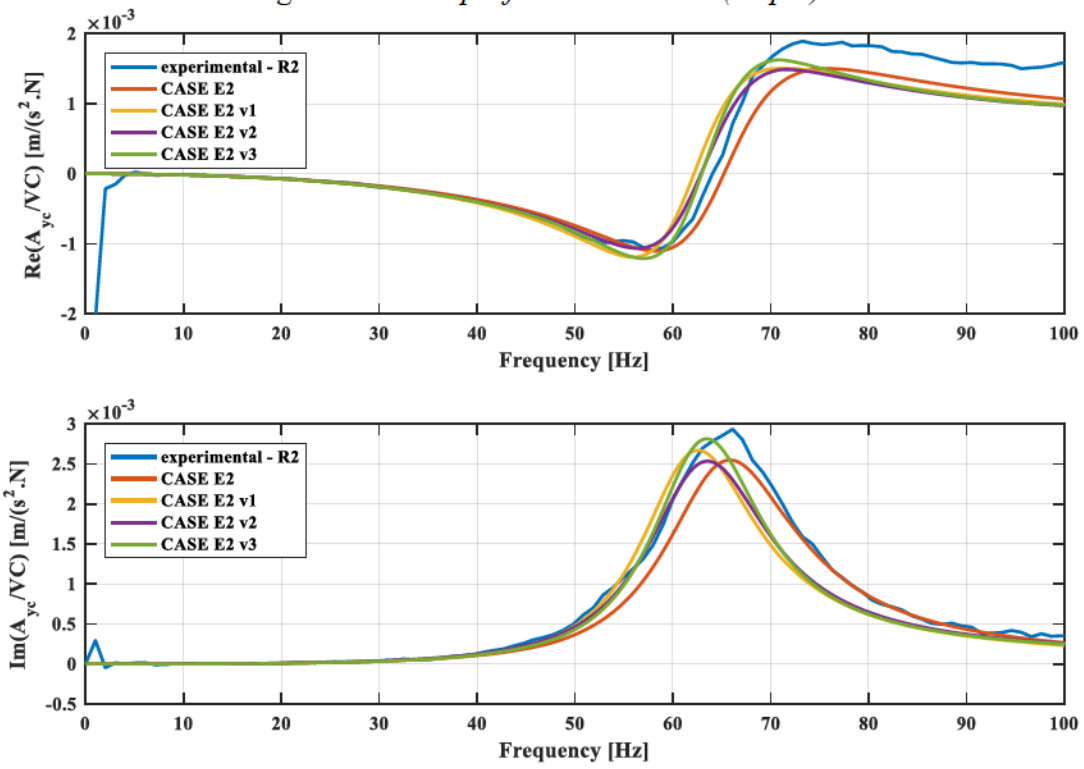

(a) A_{yc}/VC

Figure 3.84 *Accelerances by calibrated soil profiles for single pile tests.*

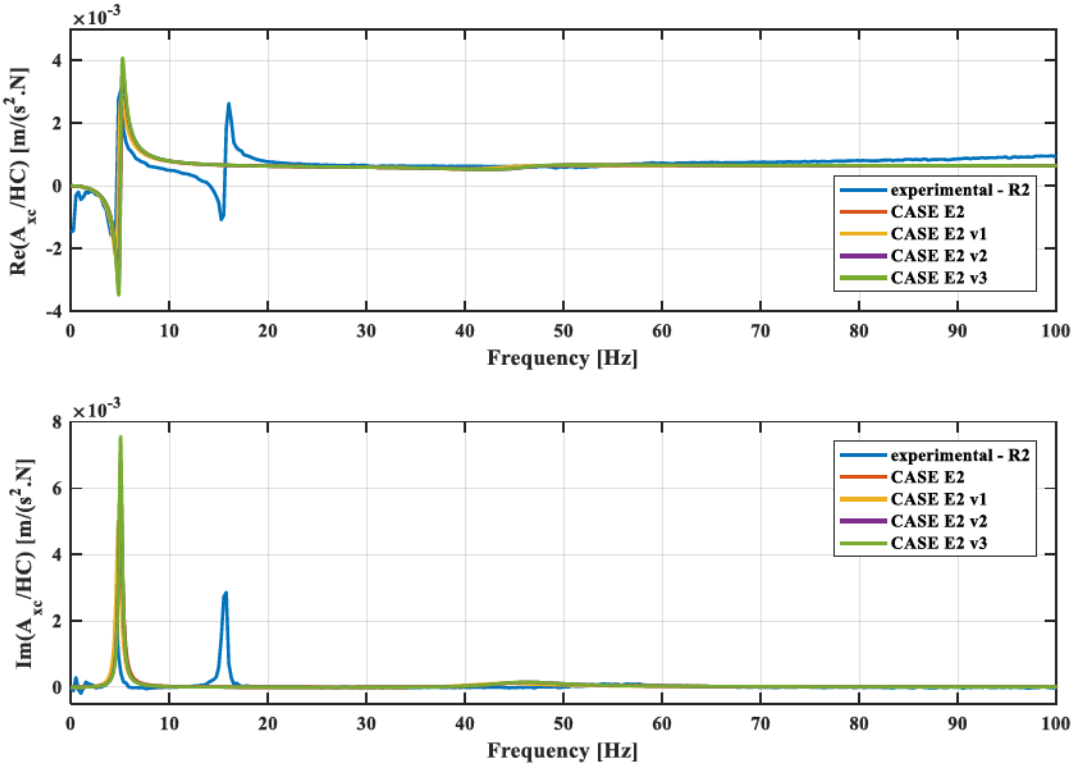

(b) A_{xc}/HC

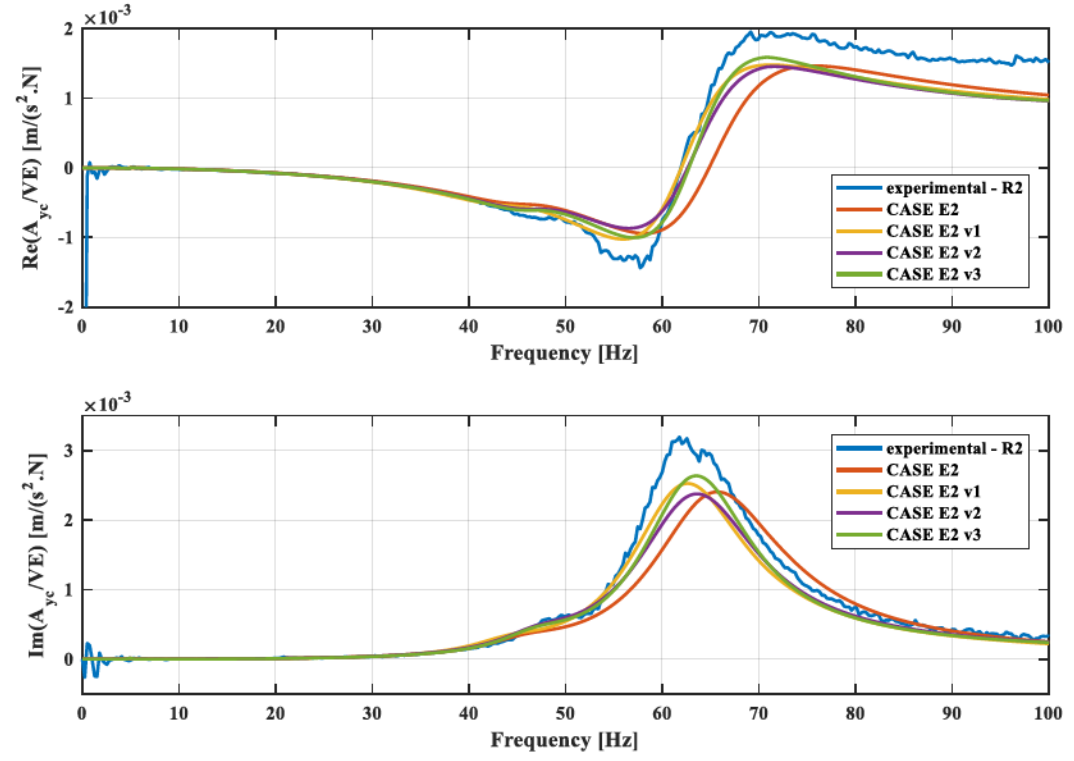

(c) A_{yc}/VE

Figure 3.84 *(continued)*

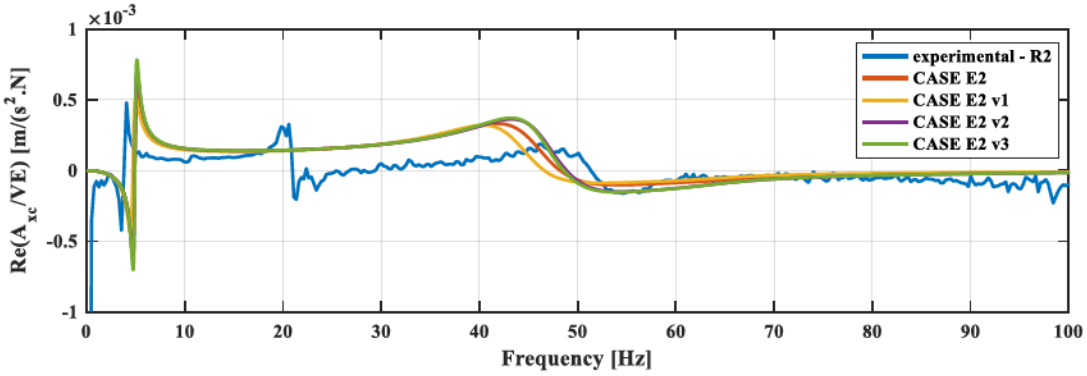

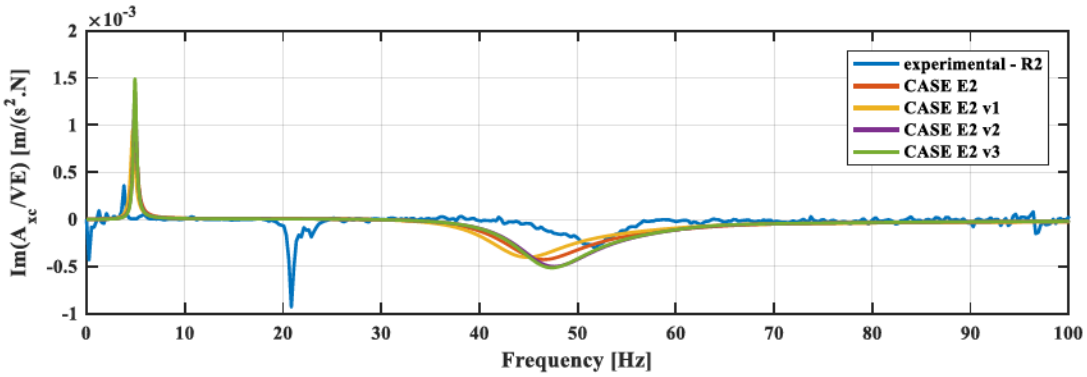

(d) A_{xc}/VE

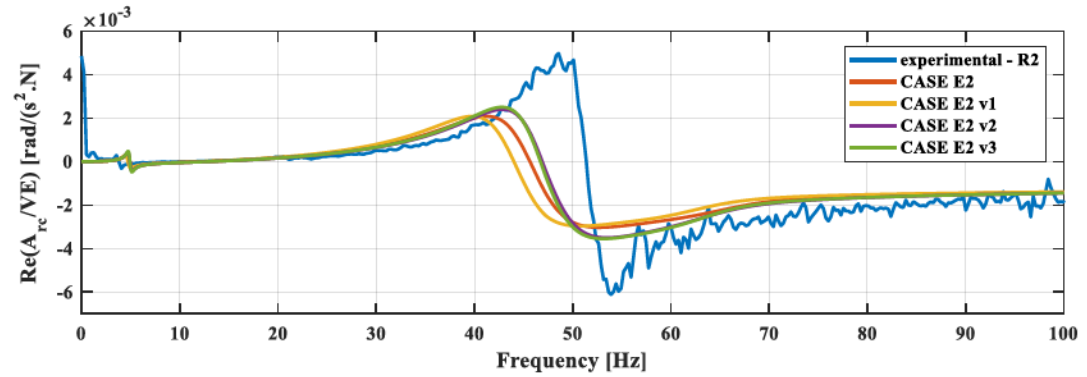

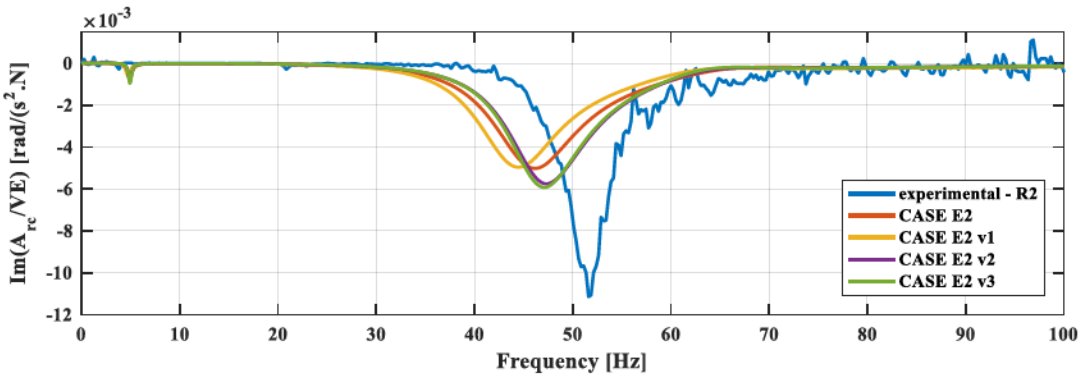

(e) A_{rc}/VE

Figure 3.84 *(continued)*.

3.9.2 Calibration for the Pile Group

Case study in Section 3.8.2 shows that the CASE E2 soil profiles for the pile group result in lower amplitudes for all vertical, horizontal, and rocking modes. In addition, the resonant frequencies for the horizontal mode in A_{xc}/HC are slightly overestimated. This suggests that the damping ratio is overestimated. To this end, the soil profiles were calibrated in two steps. In the first step, the damping ratio within the disturbed zone was decreased to minimum material damping ratio, i.e., 2.6%, for all depths. The soil profiles are termed as CASE E2 d1. In the second step, damping ratio within the disturbed zone was reduced to zero for depths greater than 15.457 and reduced to 0.87% for the depths above. Damping ratio in the half-space is also reduced to zero. The soil profiles for the second step are termed as CASE E2 d2. Additionally, 5-domain models were used to compute impedance functions. Shear modulus profiles were 100%, 80%, and 50% of the profile for half-space in Section 3.8.2 for all depths, and are termed as 5D d1, 5D d2, and 5D d3, respectively. The resulting impedance functions based on the above calibrated soil profiles are compared in Figure 3.85 . For A_{yc}/VC, CASE E2 d2 profiles elicit best match in resonant frequency but shows underestimation in amplitudes, especially for the real part. 5-domain models show sharp resonant peaks with higher amplitudes. Similar trends are also found for A_{yc}/VC. For A_{xc}/HC, all soil profiles result in overestimated resonant frequencies. CASE E2 d1 provides closest resonant amplitude. For A_{xc}/VE, CASE E2, 5D d1 and 5D d2 profiles all lead to well capture of the horizontal mode at around 14 Hz but none of them show good estimation for the rocking mode. Likewise, the amplitude of rocking mode in A_{rc}/VE is noticeably underestimated by all soil profiles, although 6-domain models show better consistency in terms of resonant frequency.

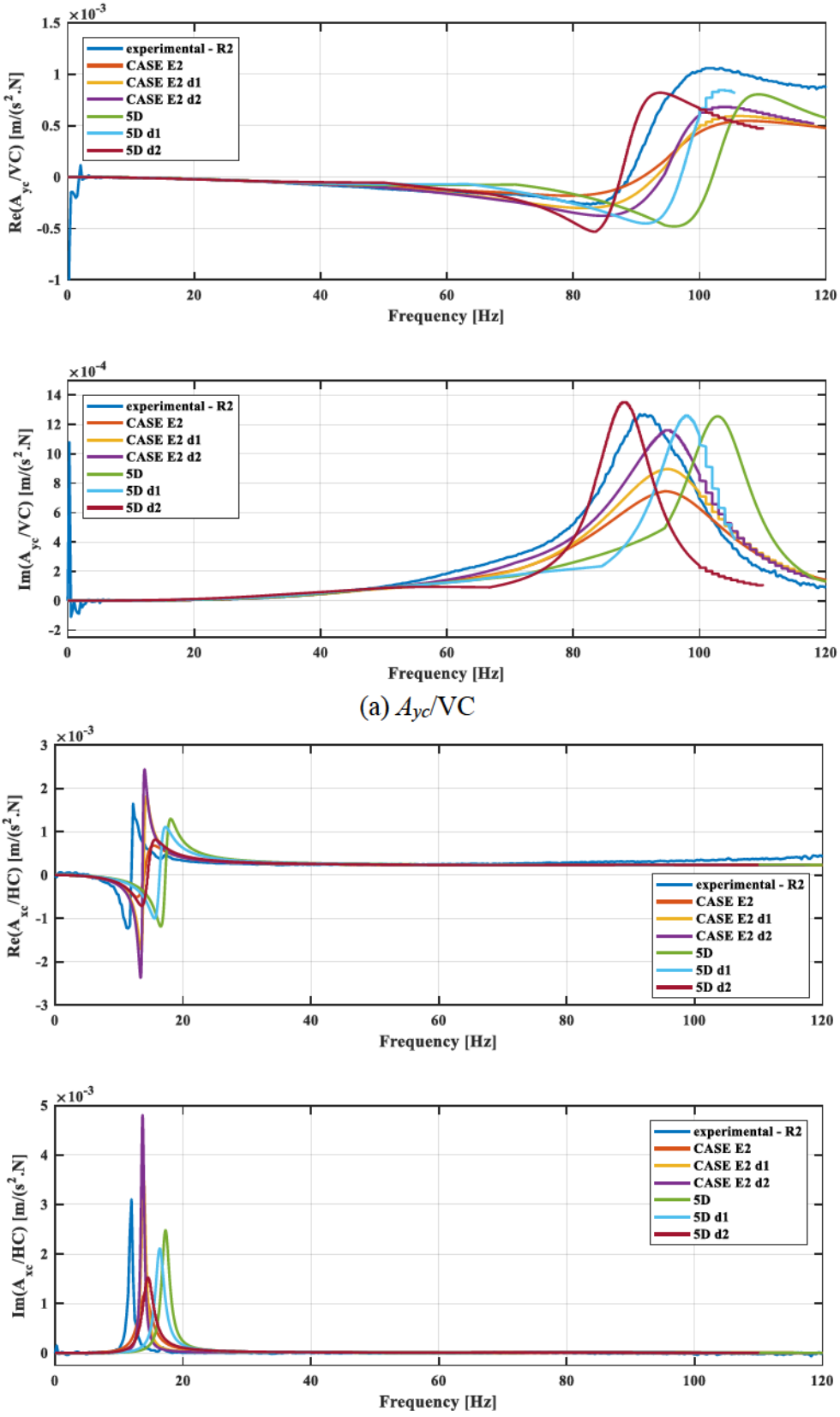

(a) A_{yc}/VC

(b) A_{xc}/HC

Figure 3.85 *Accelerances by calibrated soil profiles for pile group tests.*

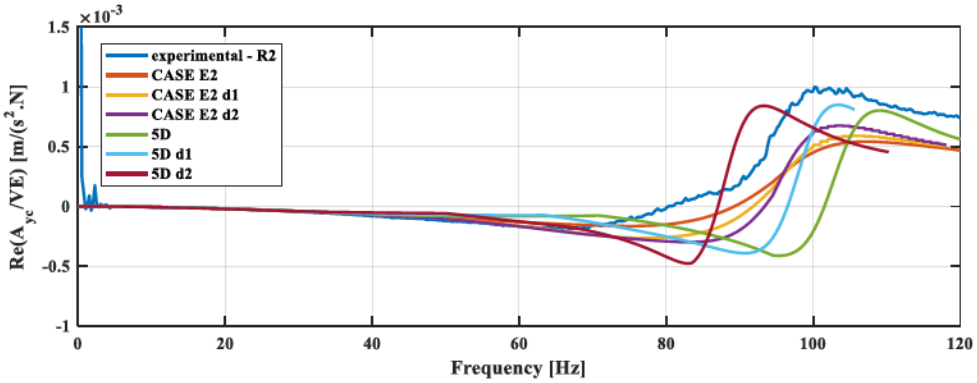

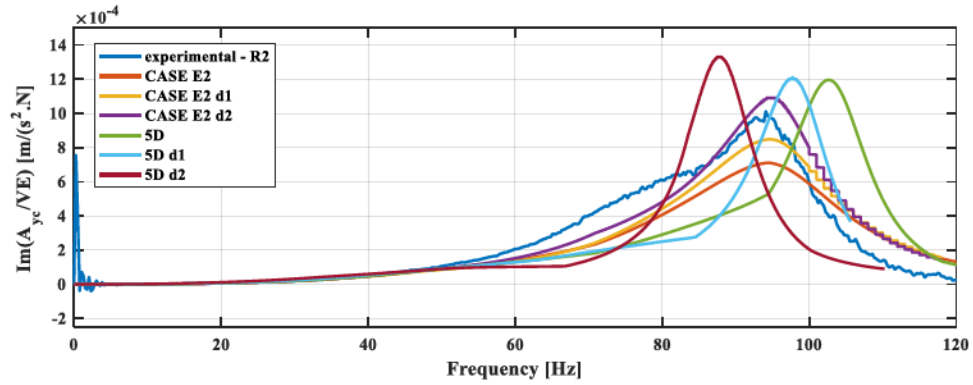

(c) A_{yc}/VE

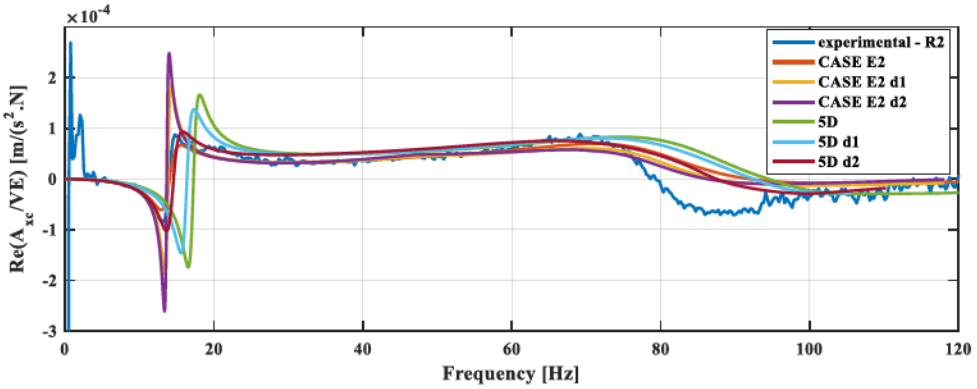

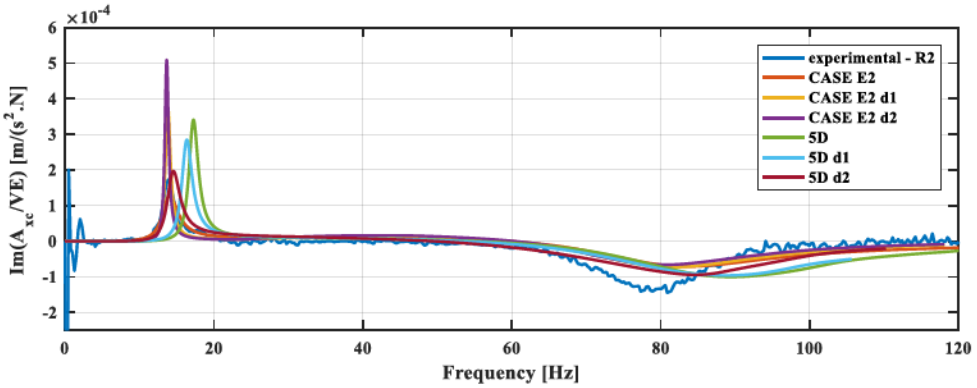

(d) A_{xc}/VE

Figure 3.85 *(continued)*

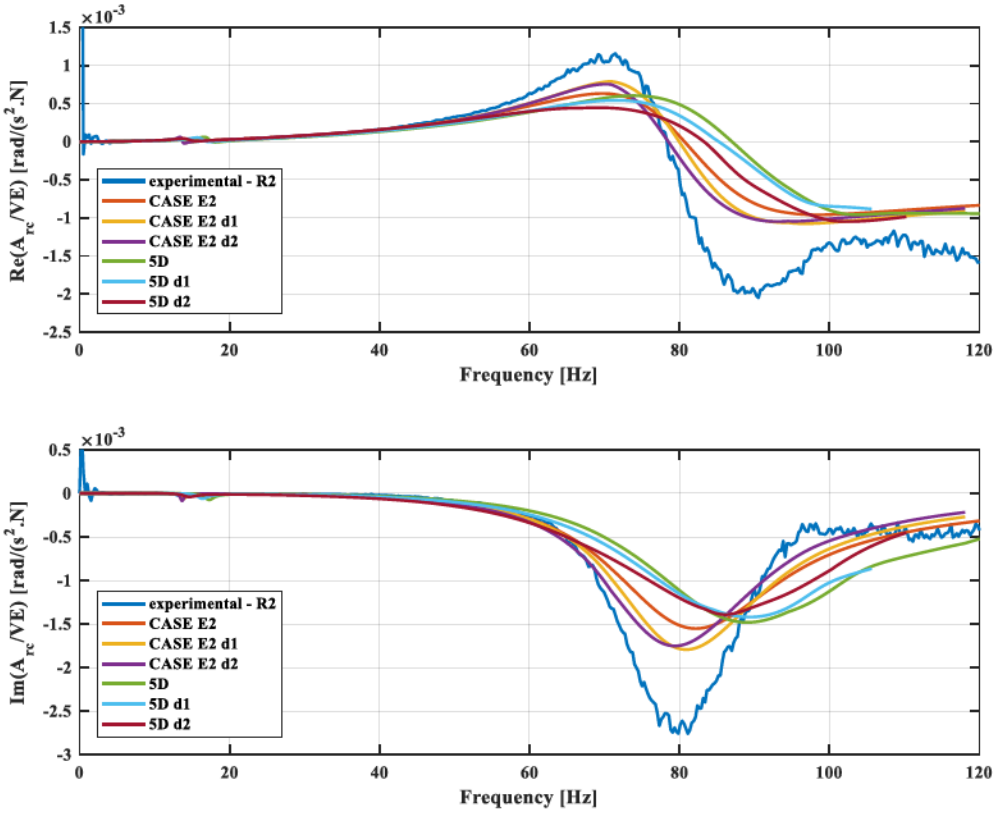

(e) A_{rc}/VE

Figure 3.85 *(continued)*

3.9.3 Summary

To be concluded, the theoretical accelerance functions have the same trends as the experimental results using the arbitrary CASE E2 soil profiles for the disturbed zone. More calibrated soil profiles lead to better match in accelerance functions. This validates the computations models established for single piles in previous studies and the models for pile groups in this study. Due to limitation of time, more effort will be put on soil profile calibration.

CHAPTER 4. PARAMETRIC STUDIES

Parametric studies were performed for a single pile case and a pile group focusing on shear modulus and damping ratio profiles within the disturbed zone and half-space. Influence of pile gapping, spacing, and size of disturbed zone were also investigated. For the superstructure, unembedded pile length, mass, and polar moment inertia that are incorporated in the substructuring formulation were examined.

Parametric studies in this chapter was completed shortly after the site investigation and ahead of pile installation and pile cap construction. The initially proposed pile properties in Table 4.1 were used. Note that they are generally consistent with the actual pile properties except for pile thickness. Actual properties of the pile caps in Section 2.3 were still adopted.

Table 4.1 *Initially proposed pile properties.*

Outer diameter	0.219 m
Thickness	0.635 cm
Embedded length in soil	7.62 m
Embedded length in pile cap	0.914 m
Young's modulus	200 GPa
Poisson's ratio	0.26
Density	7,850 kg/m^3
Spacing (x,y)	0.914 m

4.1 Sensitivity due to Soil Profiles within Disturbed Zone

Six soil profiles for disturbed zone were established based on the SCPT-1 profiles (Eqn.(4.1)). The general principle is linearly varying soil profiles such that shear modulus is reduced at shallow depths and decreased along lower portion of piles, respectively. The depth for transition point is controlled by z_o and the degree of variation is governed by k_o, which are listed in Table 4.2. The soil profiles are presented in Figure 4.1.

$$\text{disturbed zone (inner):} \quad \begin{cases} G^I(z) = G^O(z) \times [1 + k_o(\frac{z}{L} - z_o)] \\ \xi^I(z) = \xi_0 / [1 + (z/z_d)^n] + \xi^O(z) \end{cases} \tag{4.1}$$

$$\text{half-space (outer):} \quad \begin{cases} G^O(z) = \text{SCPT-1 profile} \\ \xi^O(z) = \text{minimum material damping by SCPT-1 profile} \end{cases}$$

where $z_d = 5, n = 3, \xi_0 = 0.3,$ and L is the pile length.

Table 4.2 *Parameters for linear variation of soil shear modulus within disturbed zone.*

Case	L1	L2	L3	L4	L5	L6
z_o	0.5	0.5	0.5	0.7	0.7	0.7
k_o	0.4	0.7	1.0	0.4	0.7	1.0

Due to computational intensity for pile group models, parametric studies on soil profile within disturbed zone were performed only for the single pile case. Output impedance functions are summarized in Figure 4.2 and compared to the case E2 profile. Case L6 that has the steepest slope in linear variation has the lowest stiffnesses (real parts) for almost all impedance functions. In general, Case L2 and CASE L6 result in the highest and the lowest stiffnesses. Case L2 and CASE E2 result in the highest and lowest damping (real parts), respectively. Excluding $\bar{k}_{zx}^{1-1}$ and $\bar{k}_{m_y z}^{1-1}$ that are negligibly small, all impedance functions follow the same trend such that the stiffnesses deviate from others with relatively constant offset with at all frequencies and dampings show increasing deviations at higher frequencies.

The resulting accelerance functions are presented in Figure 4.3 to Figure 4.7. The vertical modes in A_{yc}/VC and A_{yc}/VE show the lowest resonant frequencies for CASE L6, followed by CASE L4 and CASE L3, which is attributed to their relatively low vertical impedances. The remaining cases only show small variations in the vertical mode. The lateral modes in A_{xc}/HC and A_{xc}/VE exhibit negligible differences for all soil profiles, suggesting low sensitivities of the lateral modes to the horizontal impedance. For the rocking modes in A_{xc}/VE and A_{rc}/VE, CASE L6 leads to the lowest resonant frequencies and amplitudes.

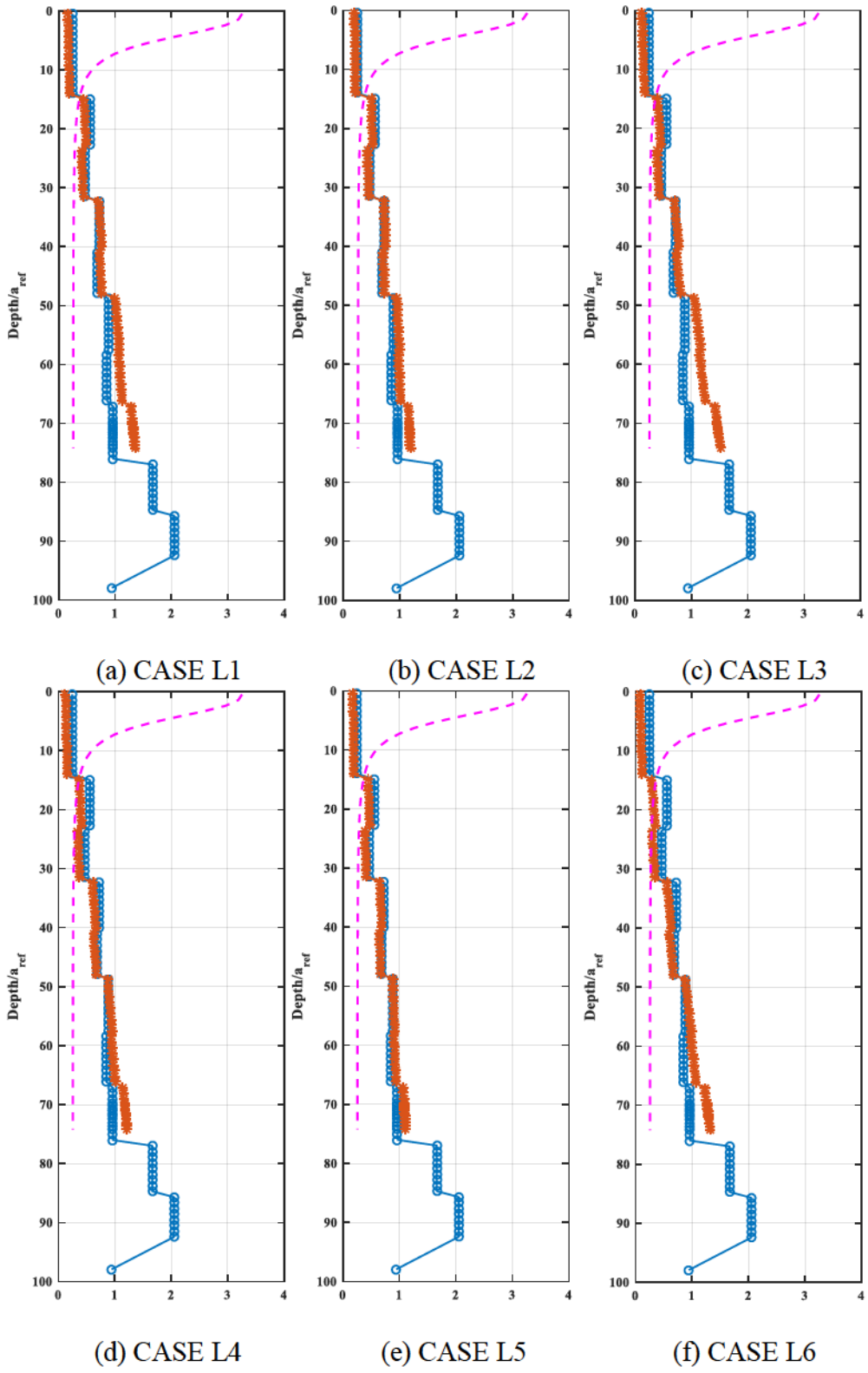

Figure 4.1 *Normalized soil profiles by linear variations for single pile case. (red: shear modulus within the disturbed zone; blue: shear modulus in the half-space; pink: 10 times damping ratio within the disturbed zone)*

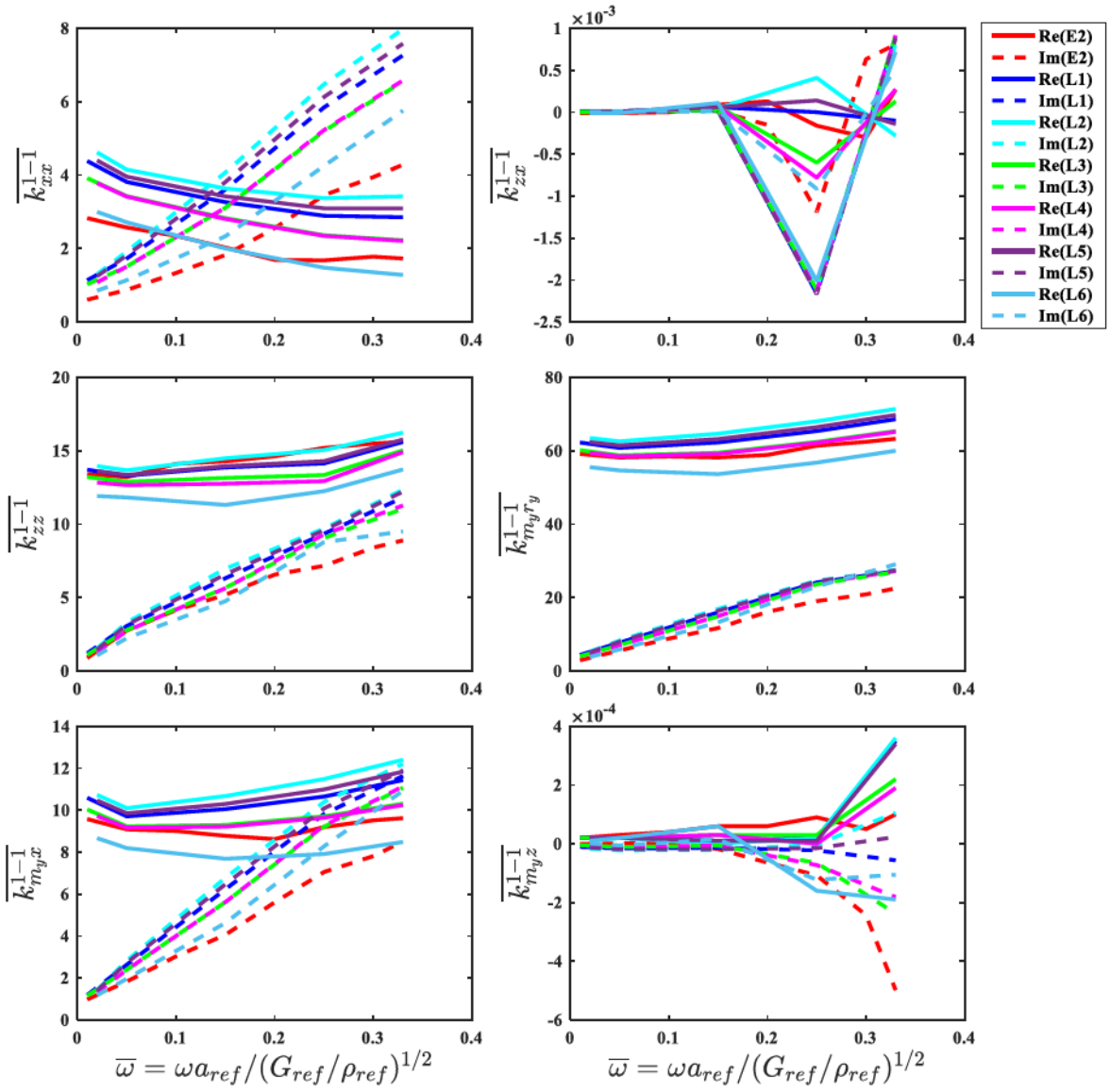

Figure 4.2 *Impedance functions for the single pile case by various soil profiles.*

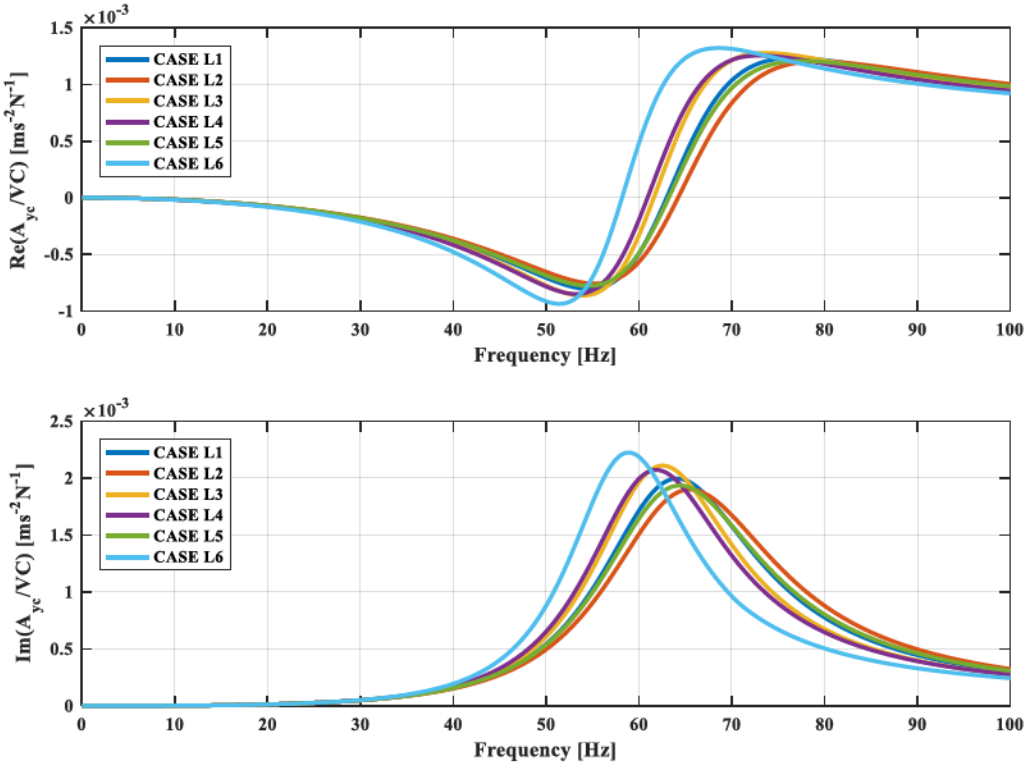

Figure 4.3 A_{yc}/VC *using CASE L1~L6 soil profiles for single pile.*

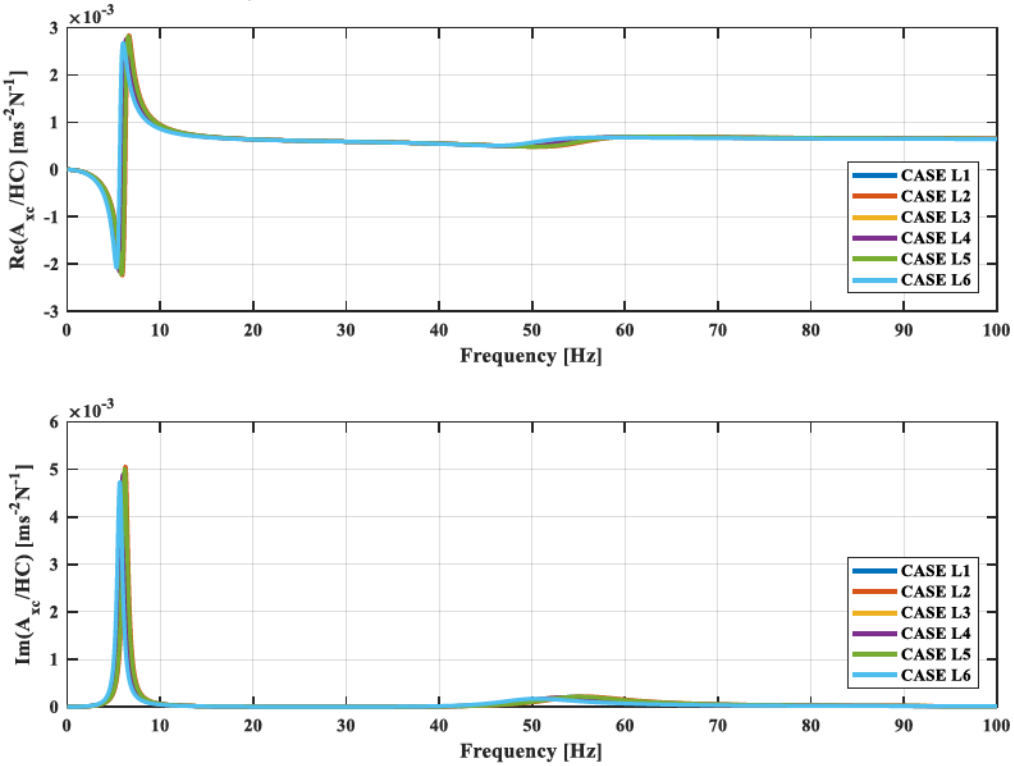

Figure 4.4 A_{xc}/HC *using CASE L1~L6 soil profiles for single pile.*

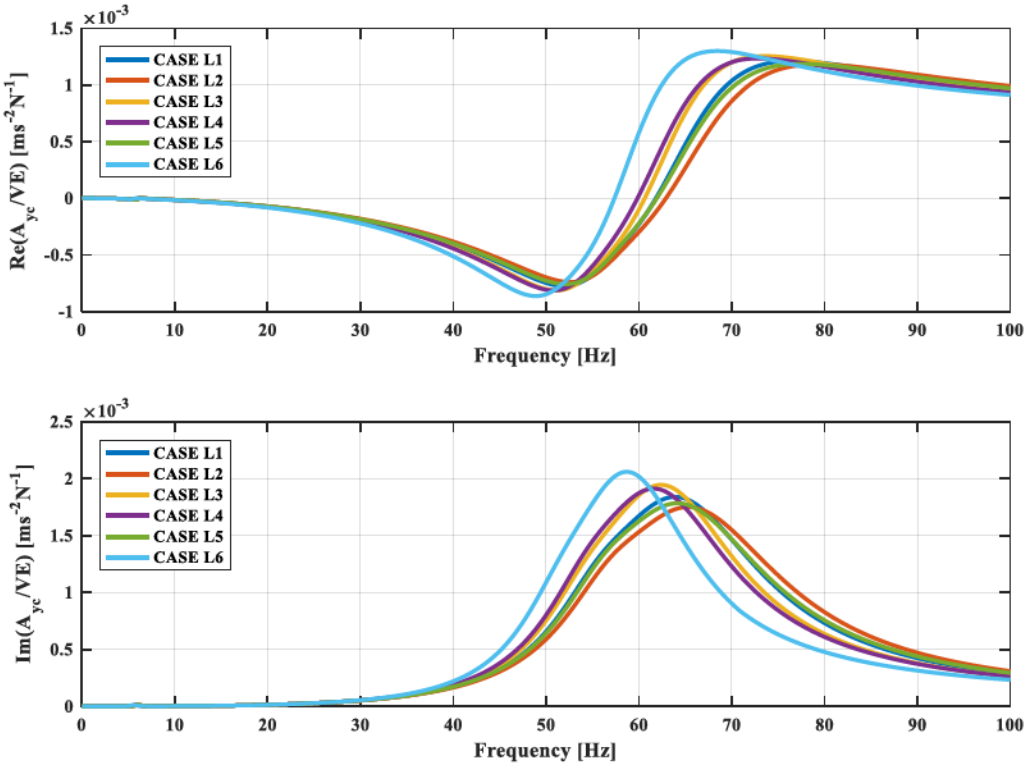

Figure 4.5 A_{yc}/VE *using CASE L1~L6 soil profiles for single pile.*

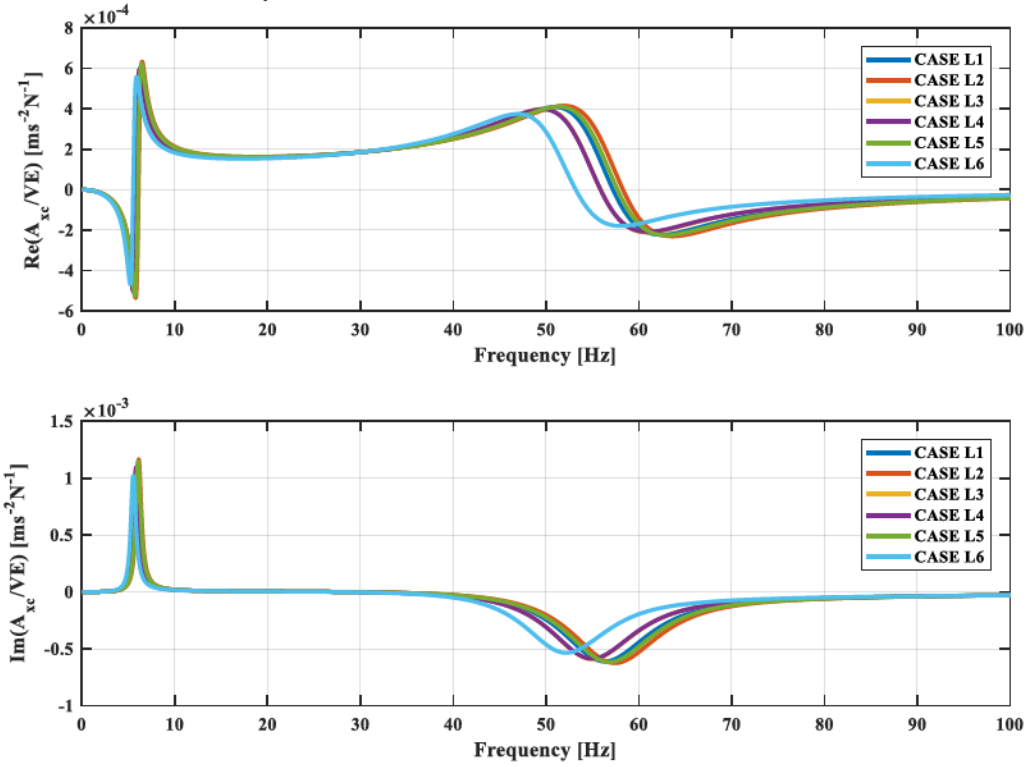

Figure 4.6 A_{xc}/VE *using CASE L1~L6 soil profiles for single pile.*

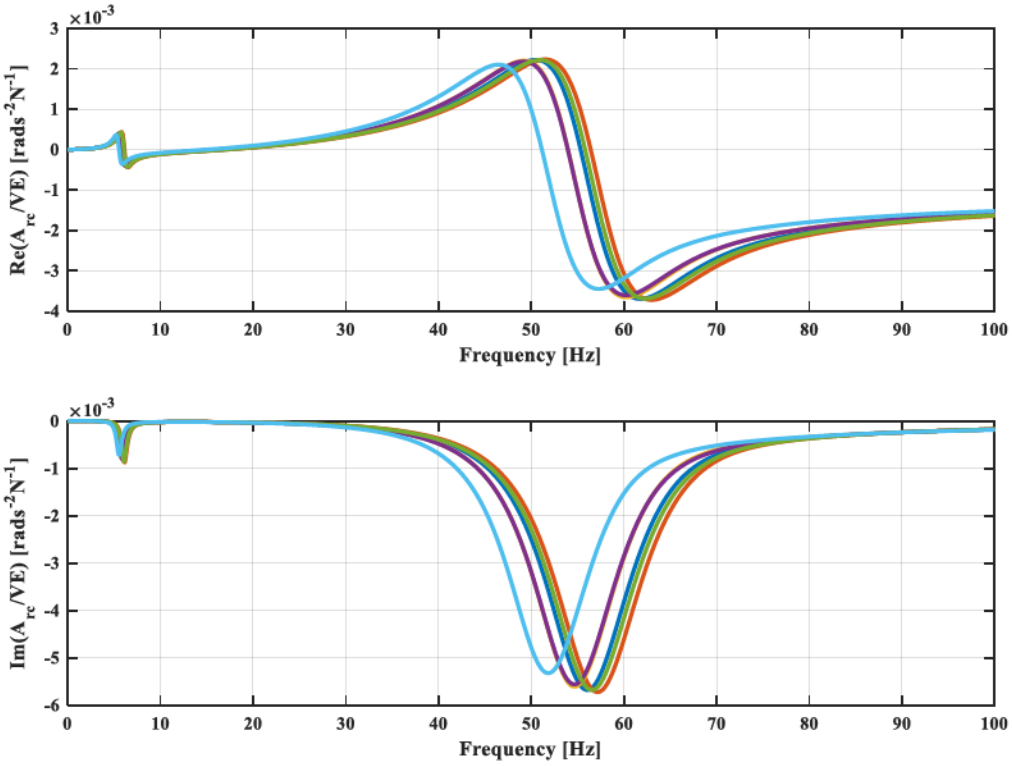

Figure 4.7 A_{rc}/VE *using CASE L1~L6 soil profiles for single pile.*

4.2 Sensitivity due to Soil Profiles in the Half-Space

In addition to soil profiles in the disturbed zone, it is also necessary to quantify the influence of soil profiles in the half-space. Two cases were examined – a single pile with disturbed zone and a 2×2 pile group with disturbed zone. Soil profiles for the half-space and the disturbed zone were modified based on profiles in Section 3.8.2. Specifically, shear modulus G was varied by ±20% for all depths and the material damping ratio $D_{\min}$ was then varied by 5 and 10 times for all depths.

4.2.1 Single Pile Case

Impedance functions due to the modified soil profiles are shown in Figure 4.8 and Figure 4.9. Compared to soil profiles within disturbed zone, influence of soil shear modulus and damping ratio in the half-space are drastically weak. Higher shear modulus G slightly

increases stiffnesses at low frequencies and subsequently reduces stiffness at frequencies higher than 0.2. The differences due to modified dampings are even less noticeable. The sharp variations in $\bar{k}_{zx}$ and $\bar{k}_{m_y z}$ can be ignored because of the small absolute values.

The sensitivity of accelerance functions to variations of soil shear modulus and material damping ratio in half-space are shown in Figure and Figure , respectively. Higher soil shear modulus in the half-space typically results in higher resonant amplitudes for the vertical and the rocking modes, but have no impact on the lateral modes. Higher soil material damping ratio in half-space leads to higher resonant amplitudes for the vertical modes but slightly lower amplitudes for the coupled lateral-rocking modes. The overall influence of soil profiles in the half-space for single pile is small.

4.2.2 2×2 Pile Group Case

As indicated in Figure 4.12 and Figure 4.13, the sensitivity of impedances due to soil profiles in the half-space for pile group is even less significant than for single pile. Varying soil shear modulus by ±20% or increasing soil material damping ratio up to 10 times only caused nuances for all impedance functions. Although some impedance functions such as $\bar{k}_{zz}$ and $\bar{k}_{m_y z}$ exhibit relatively large deviations, their small absolute values suggest very limited impact in dynamic pile analyses. In terms of accelerance transfer functions (Figure and Figure 4.16), lower soil shear modulus in the half-space suggests slightly higher resonant amplitudes for the vertical modes and no effects on the coupled lateral-rocking modes. The sensitivity of accelerance functions due to soil material damping ratio is also insignificant. To be concluded, parametric studies suggest that soil shear modulus and damping profiles in the half-space are minor factors for dynamic pile analyses and thus of less importance in calibration.

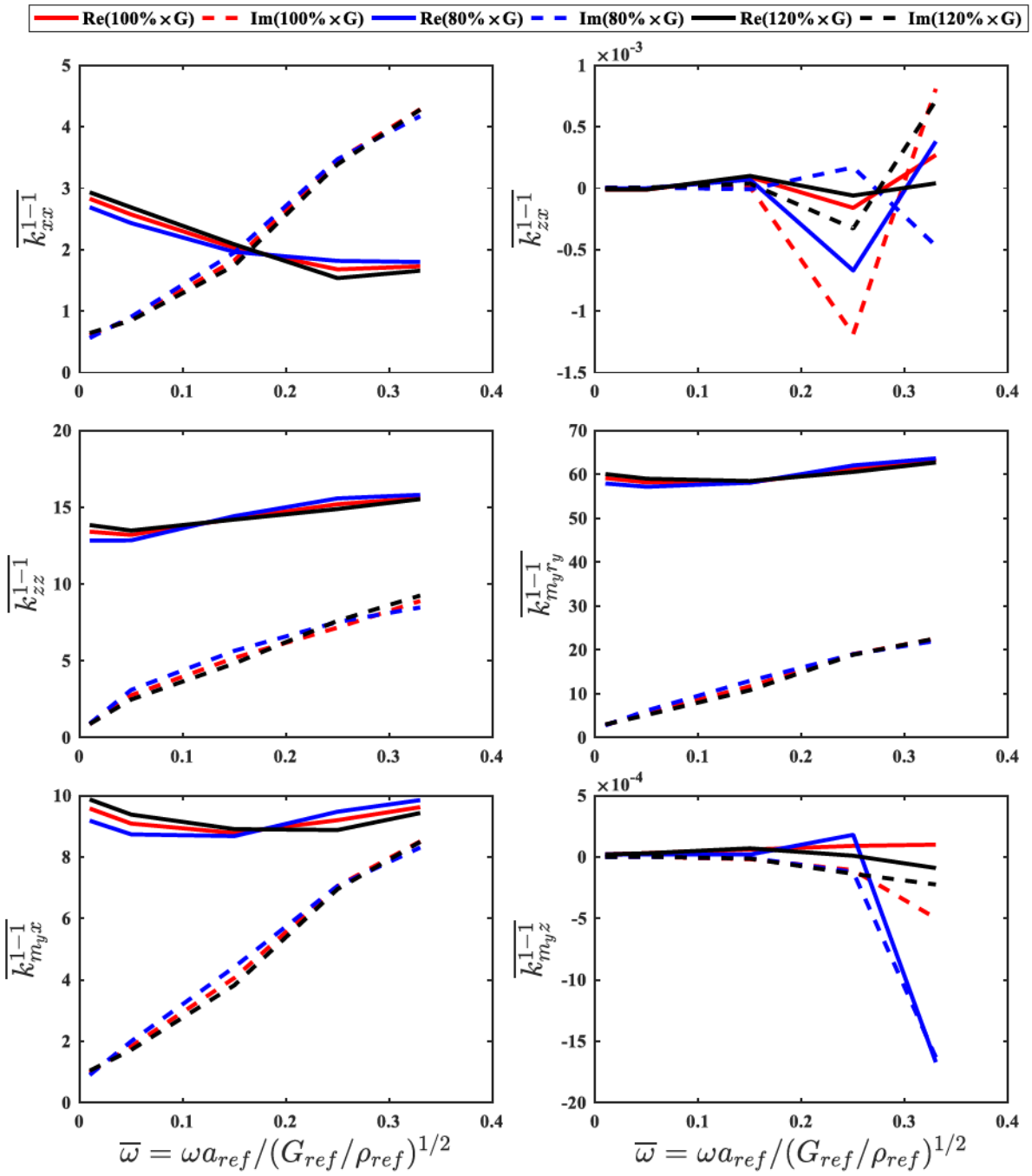

Figure 4.8 *Sensitivity of impedance functions for single pile to shear modulus in half-space.*

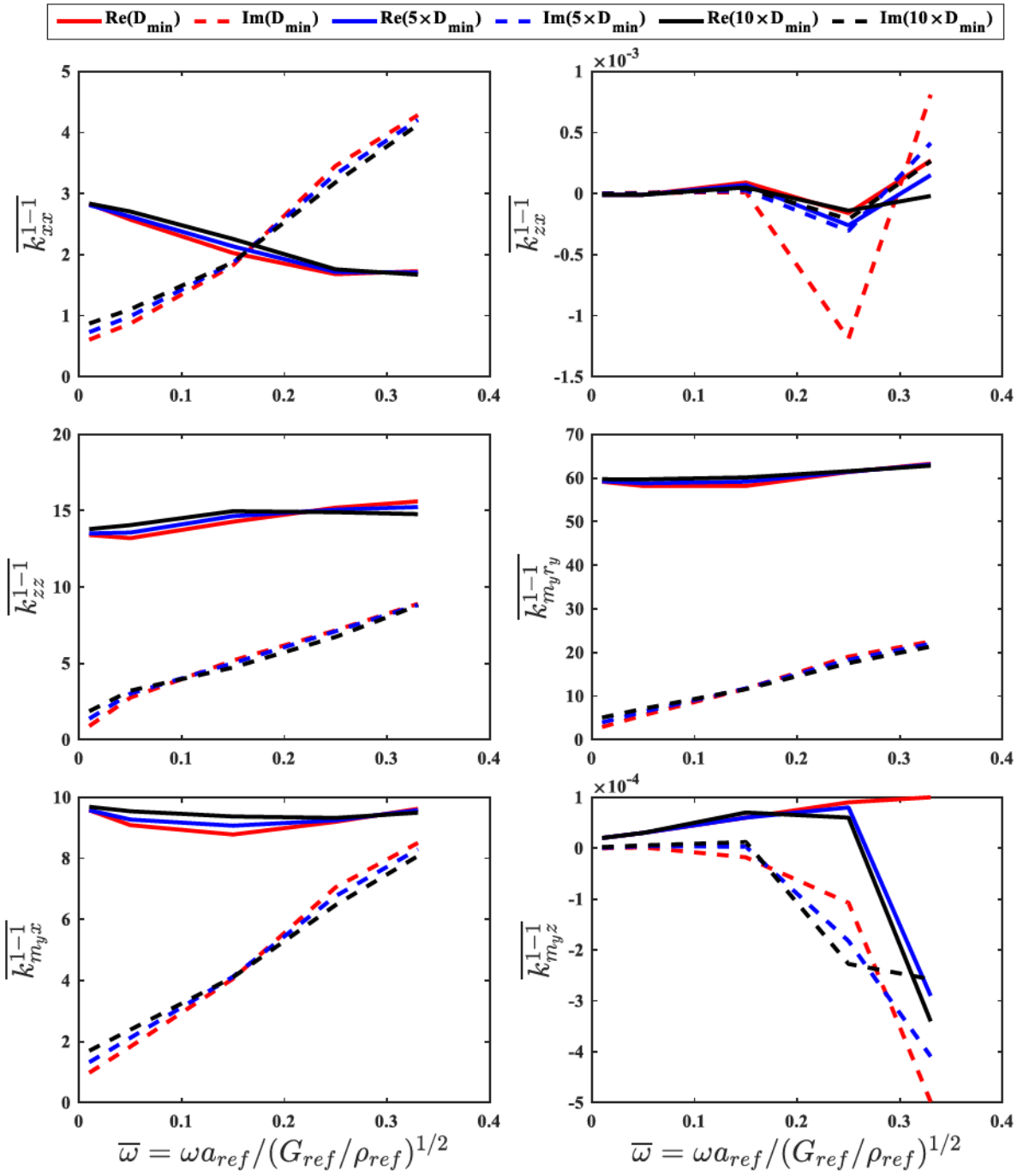

Figure 4.9 *Sensitivity of impedance functions for single pile to minimum soil material damping in half-space.*

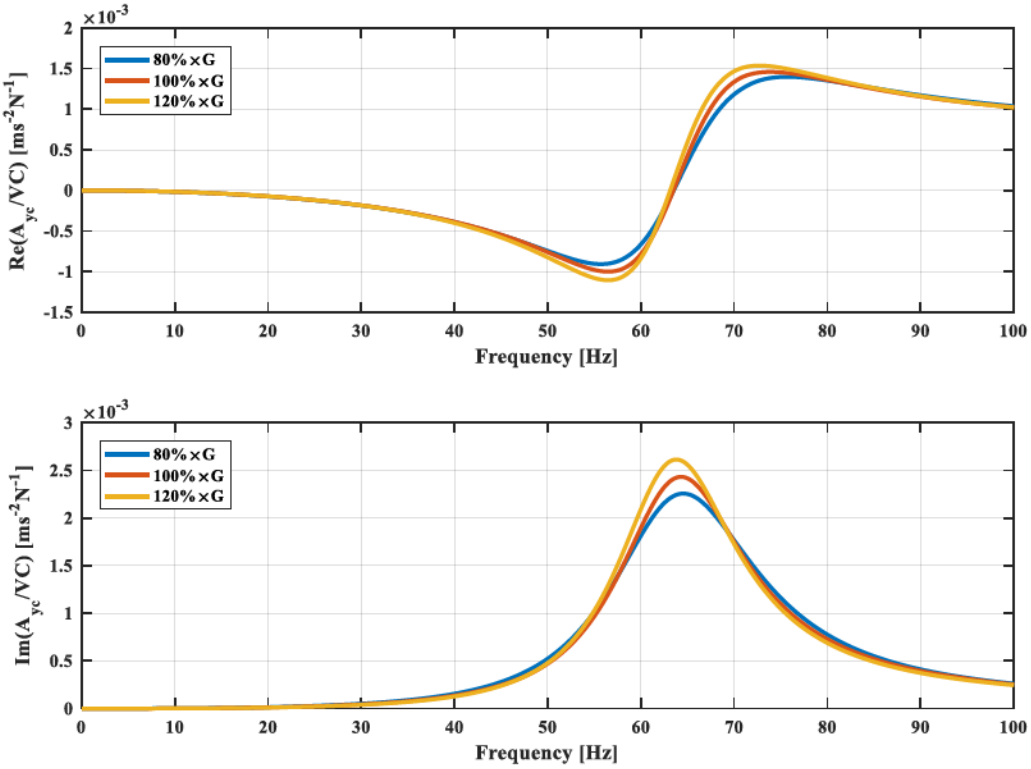

(a) Influence on A_{yc}/VC due to variation of soil shear modulus in half-space

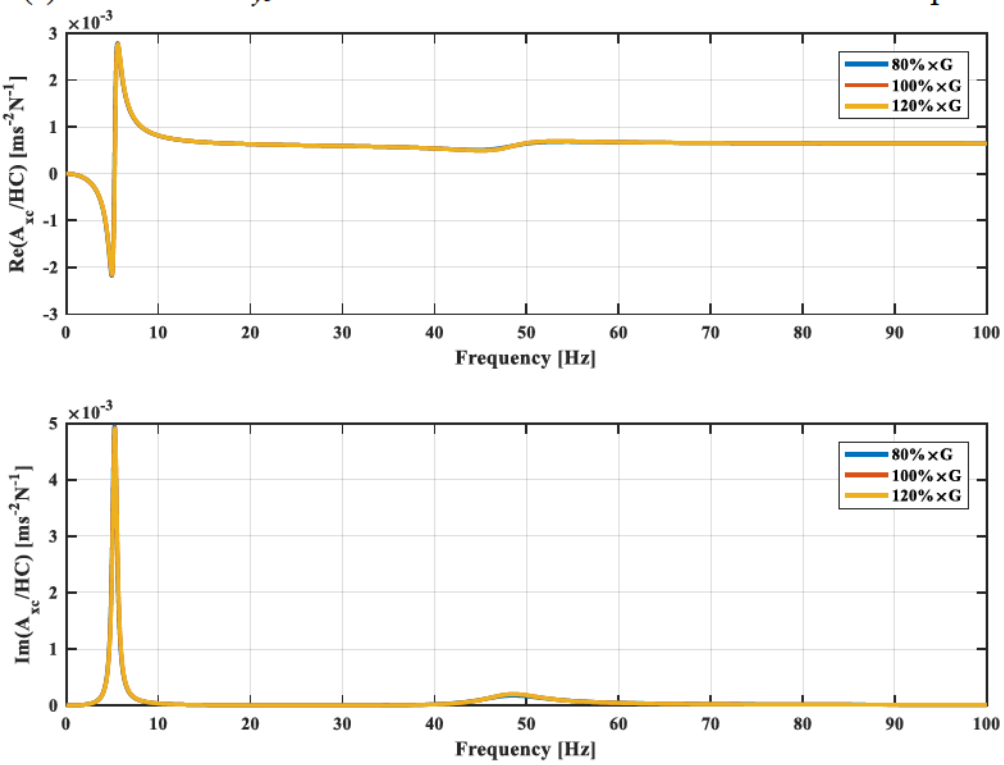

(b) Influence on A_{xc}/HC due to variation of soil shear modulus in half-space

Figure 4.10 *Sensitivity of accelerance functions to variations in soil shear modulus in half-space for single pile.*

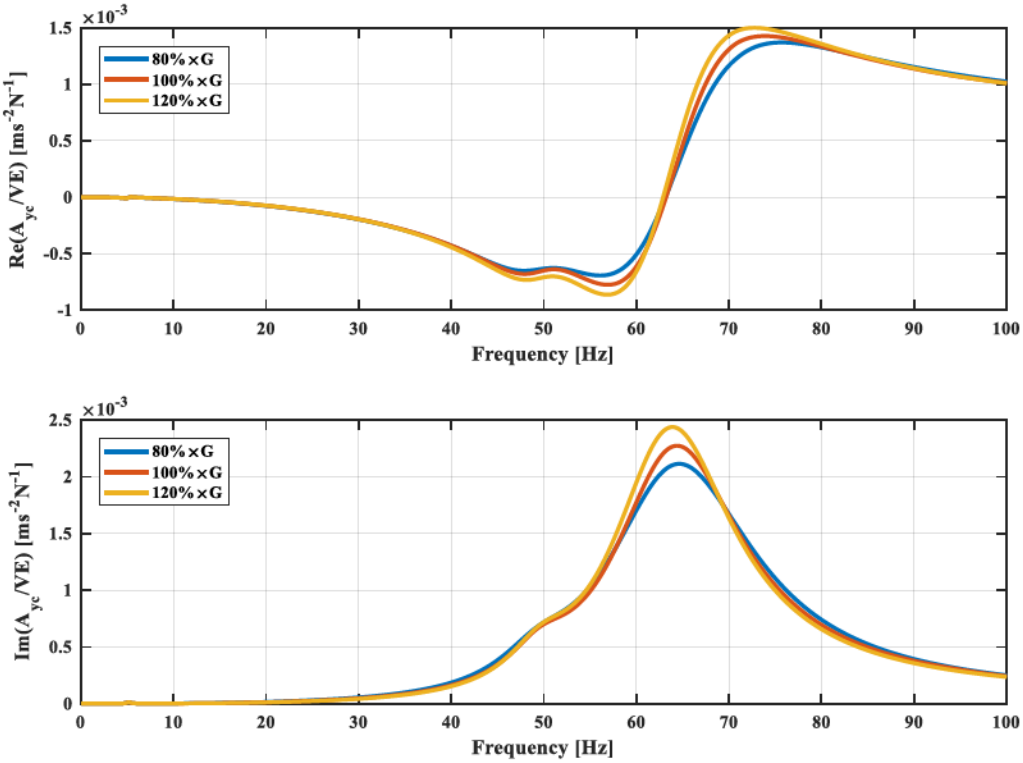

(c) Influence on A_{yc}/VE due to variation of soil shear modulus in half-space

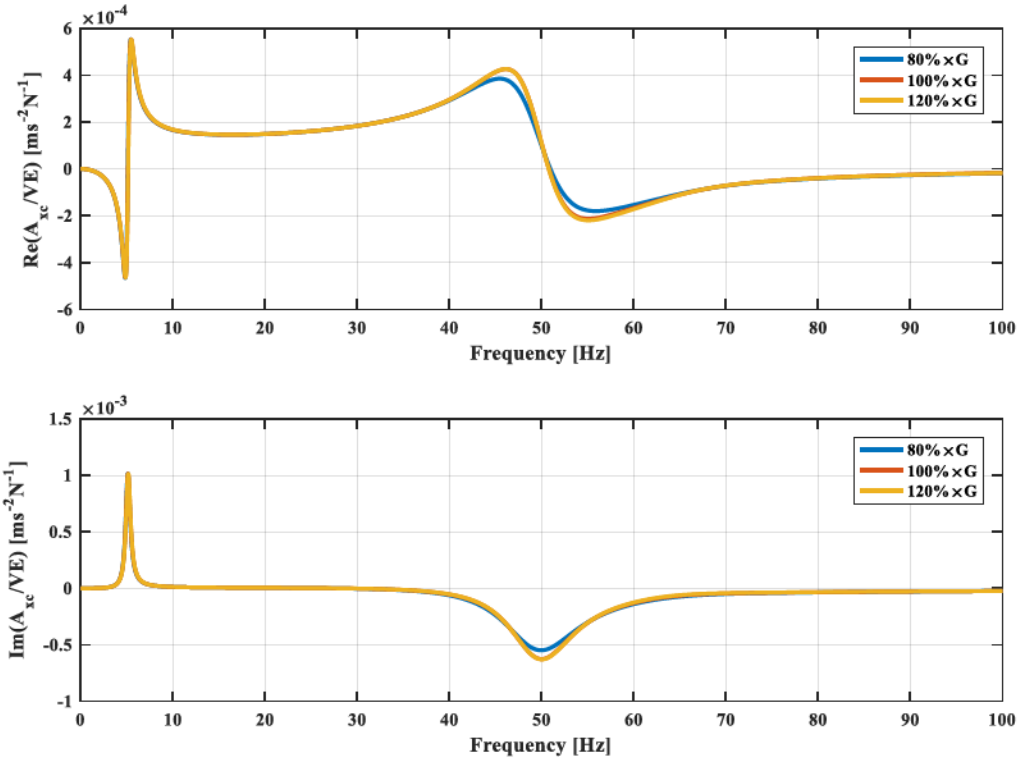

(d) Influence on A_{xc}/VE due to variation of soil shear modulus in half-space

Figure 4.10 *(continued)*

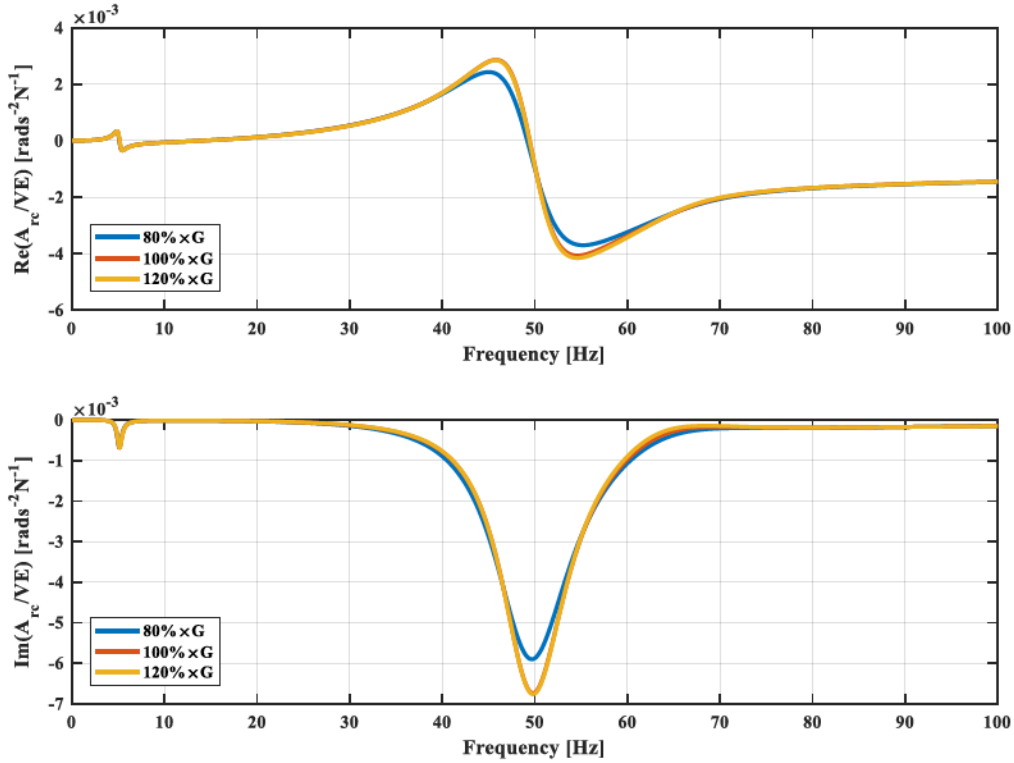

(e) Influence on A_{xc}/VE due to variation of soil shear modulus in half-space

Figure 4.10 *(continued)*

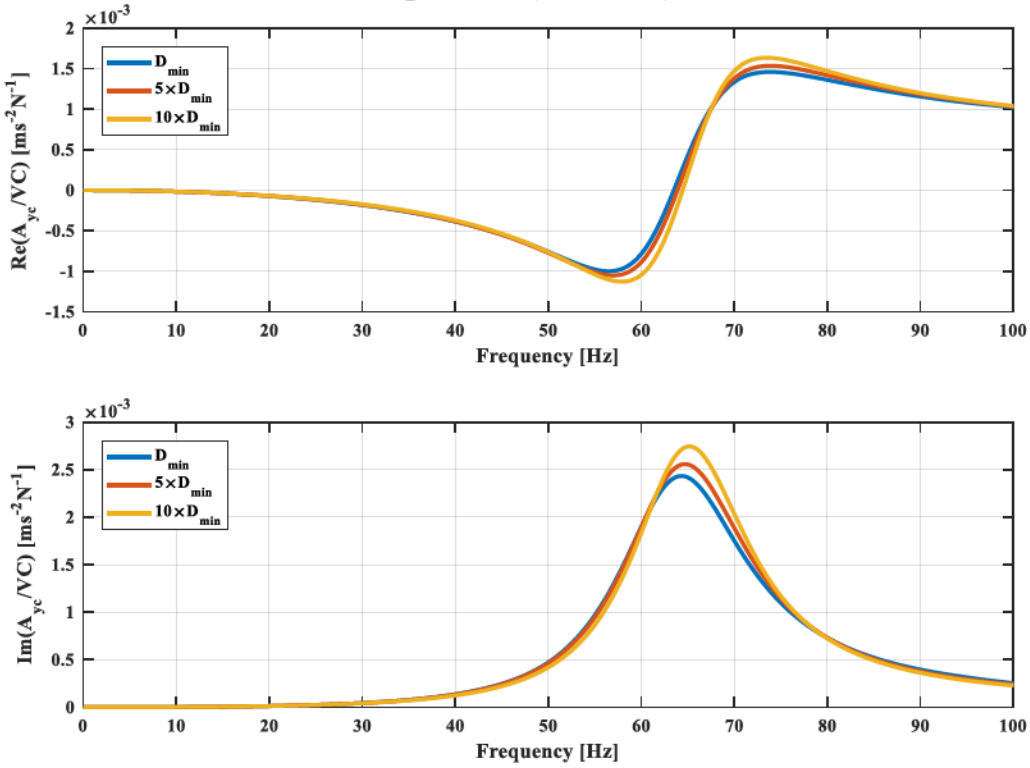

(a) Influence on A_{yc}/VC

Figure 4.11 *Sensitivity of accelerance functions to variations in soil minimum material damping ratio in half-space for single pile.*

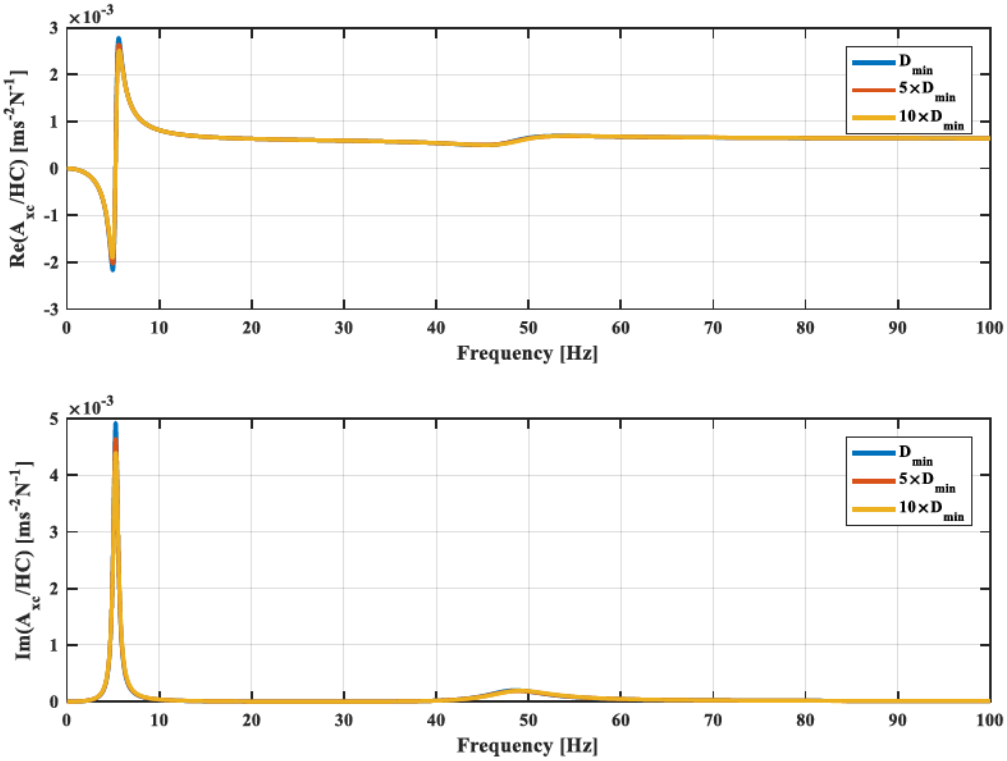

(b) Influence on A_{xc}/HC

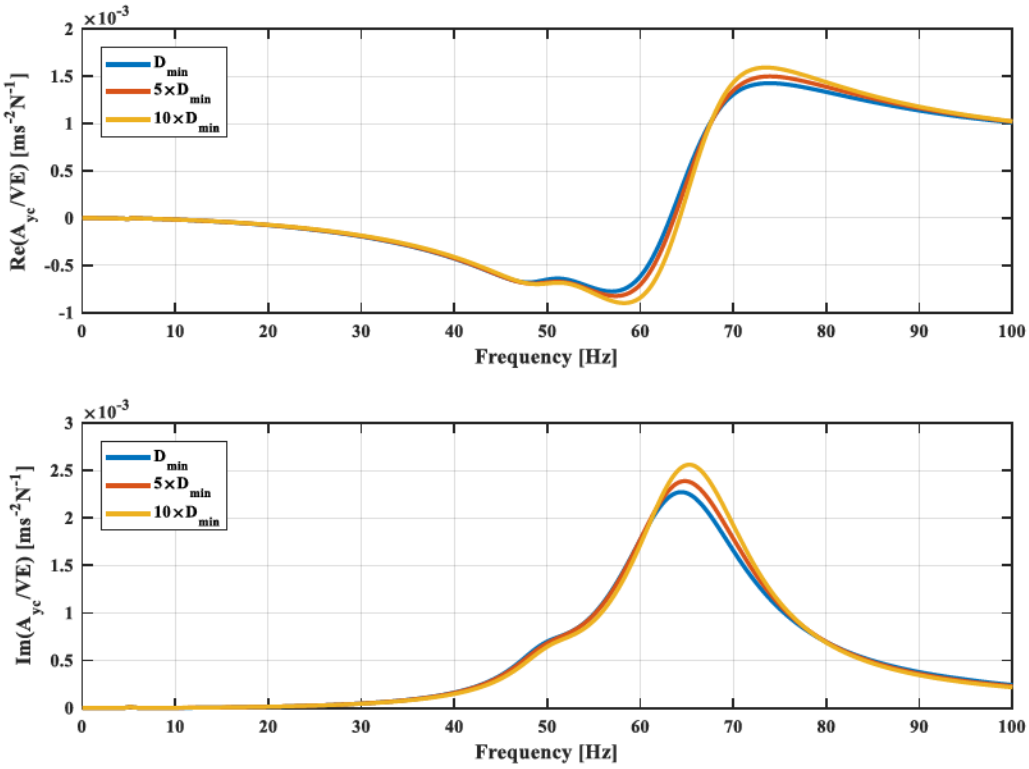

(c) Influence on A_{yc}/VE

Figure 4.11 *(continued)*

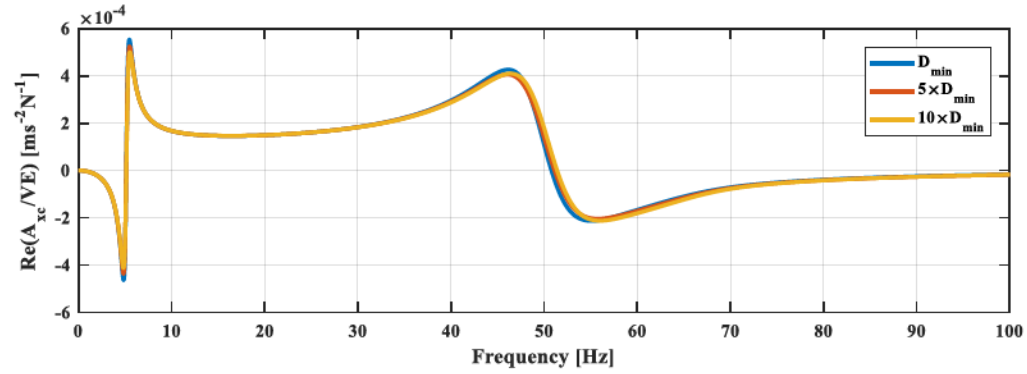

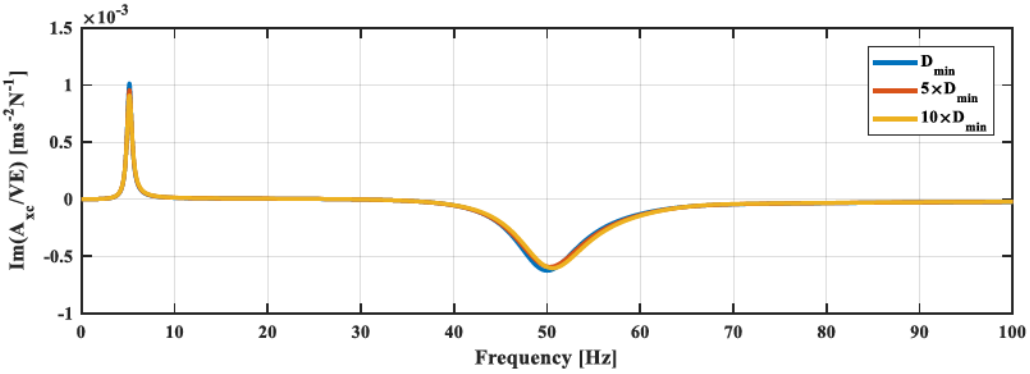

(d) Influence on A_{xc}/VE

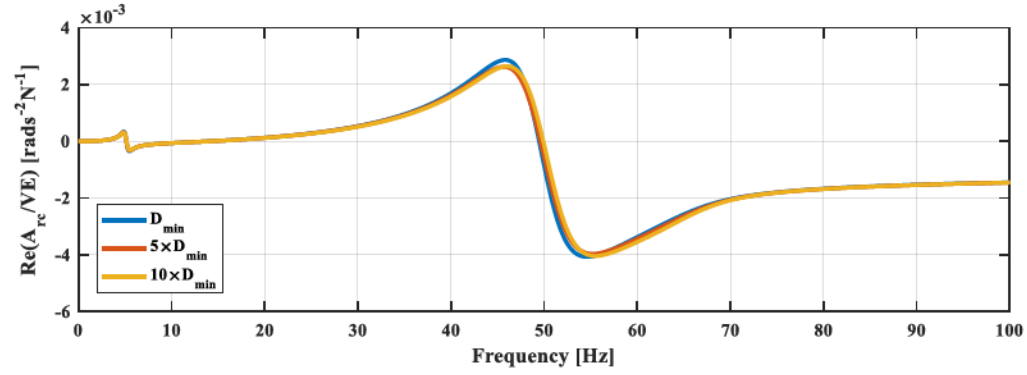

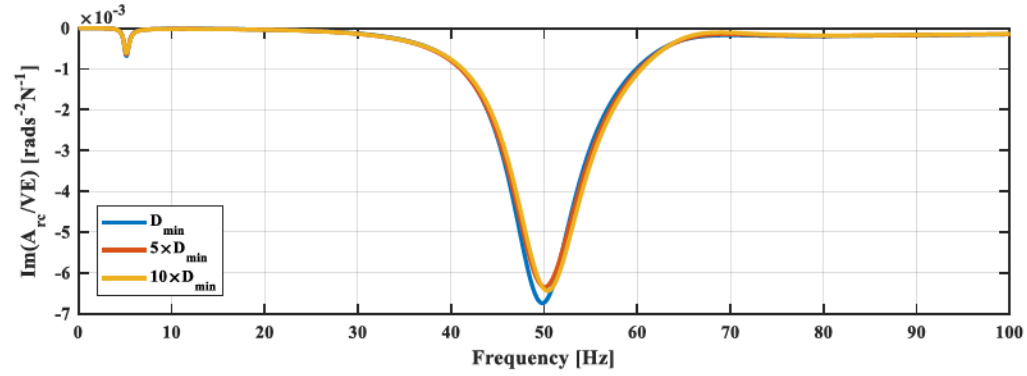

(e) Influence on A_{rc}/VE

Figure 4.11 *(continued)*

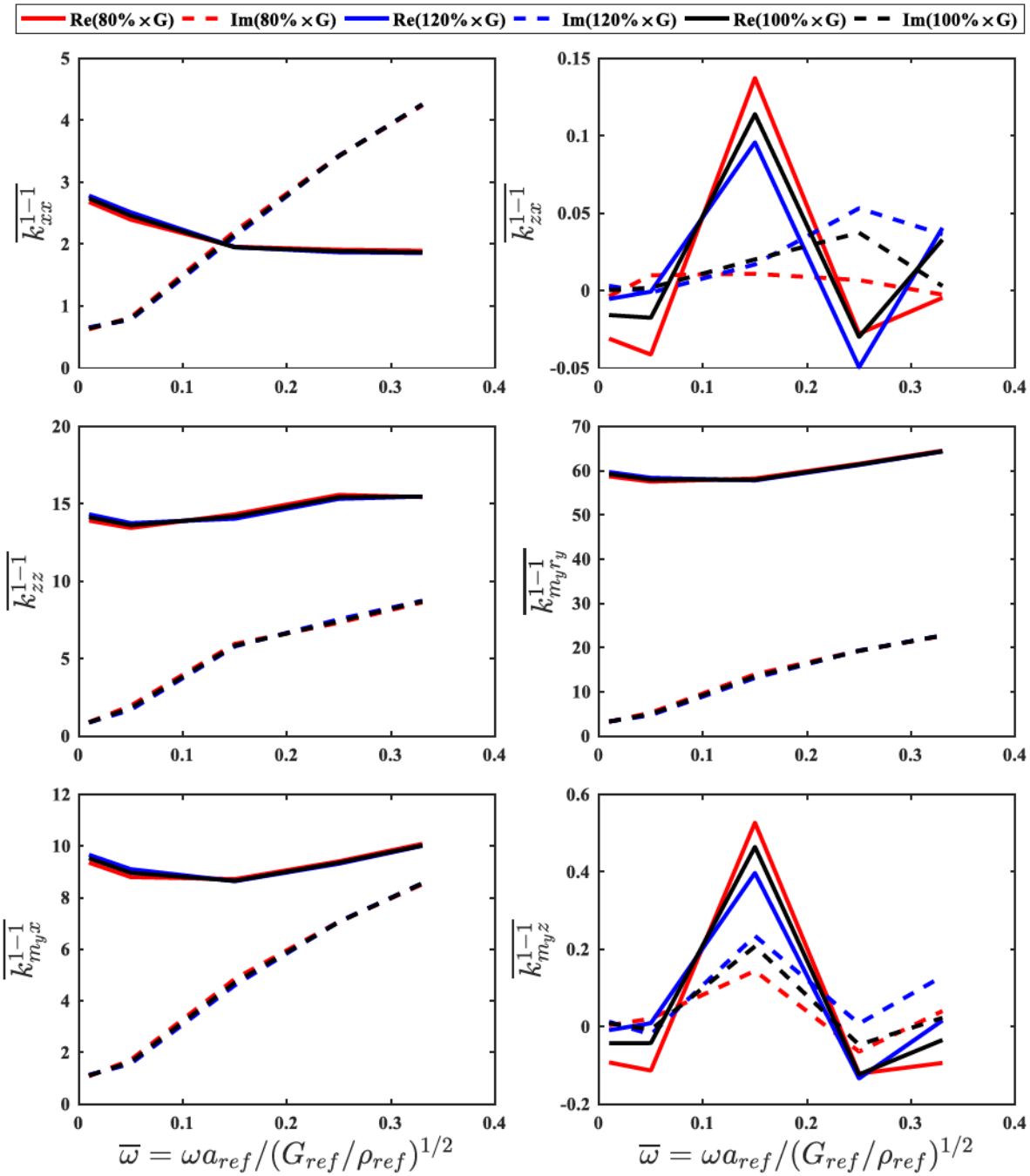

(a) Primary impedance functions in $\mathbf{K}^{1\text{-}1}$

Figure 4.12 *Sensitivity of impedance functions for ×2 pile group to shear modulus in half-space.*

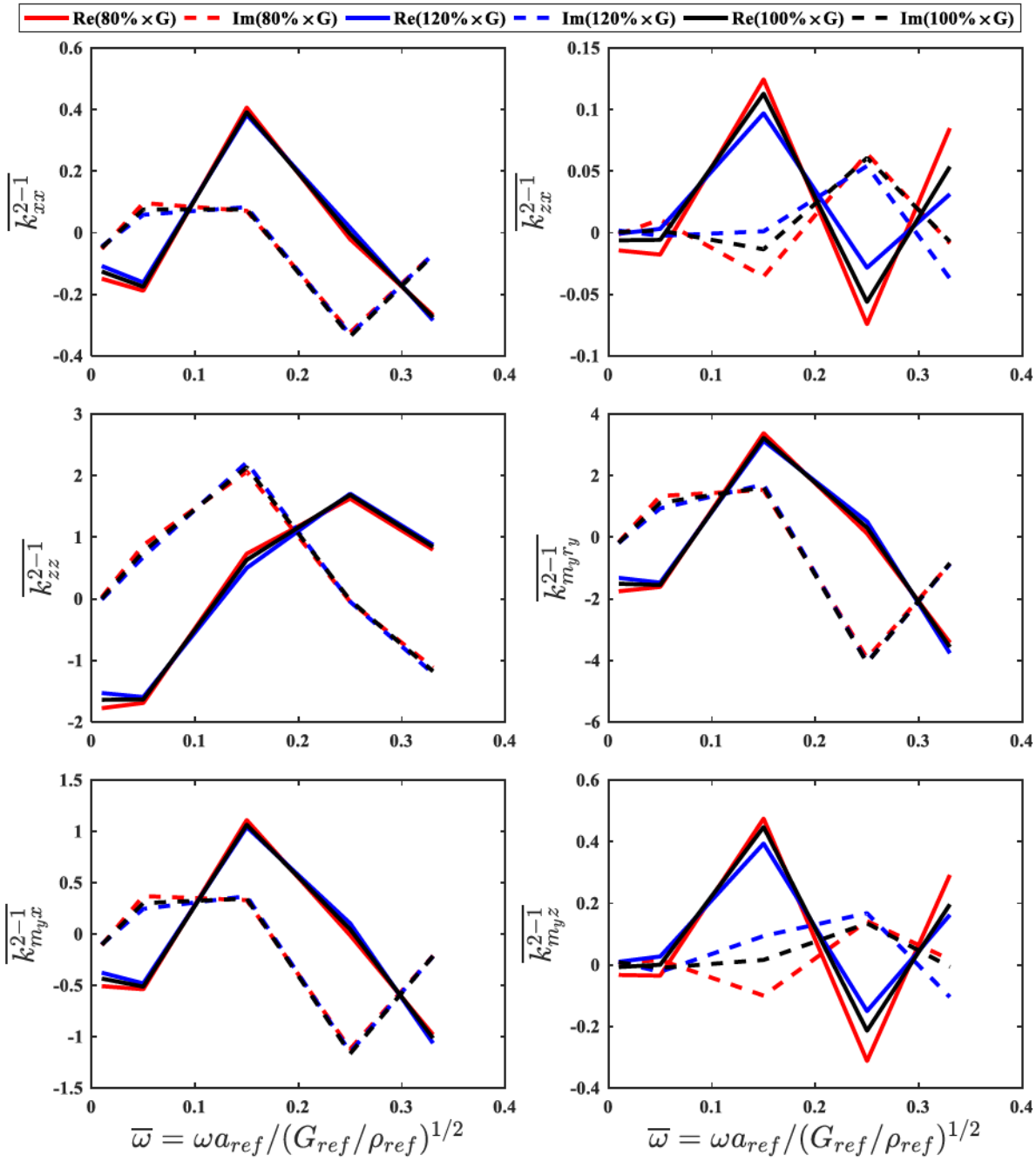

(b) Primary impedance functions in $\mathbf{K}^{2-1}$

Figure 4.12 *(continued)*

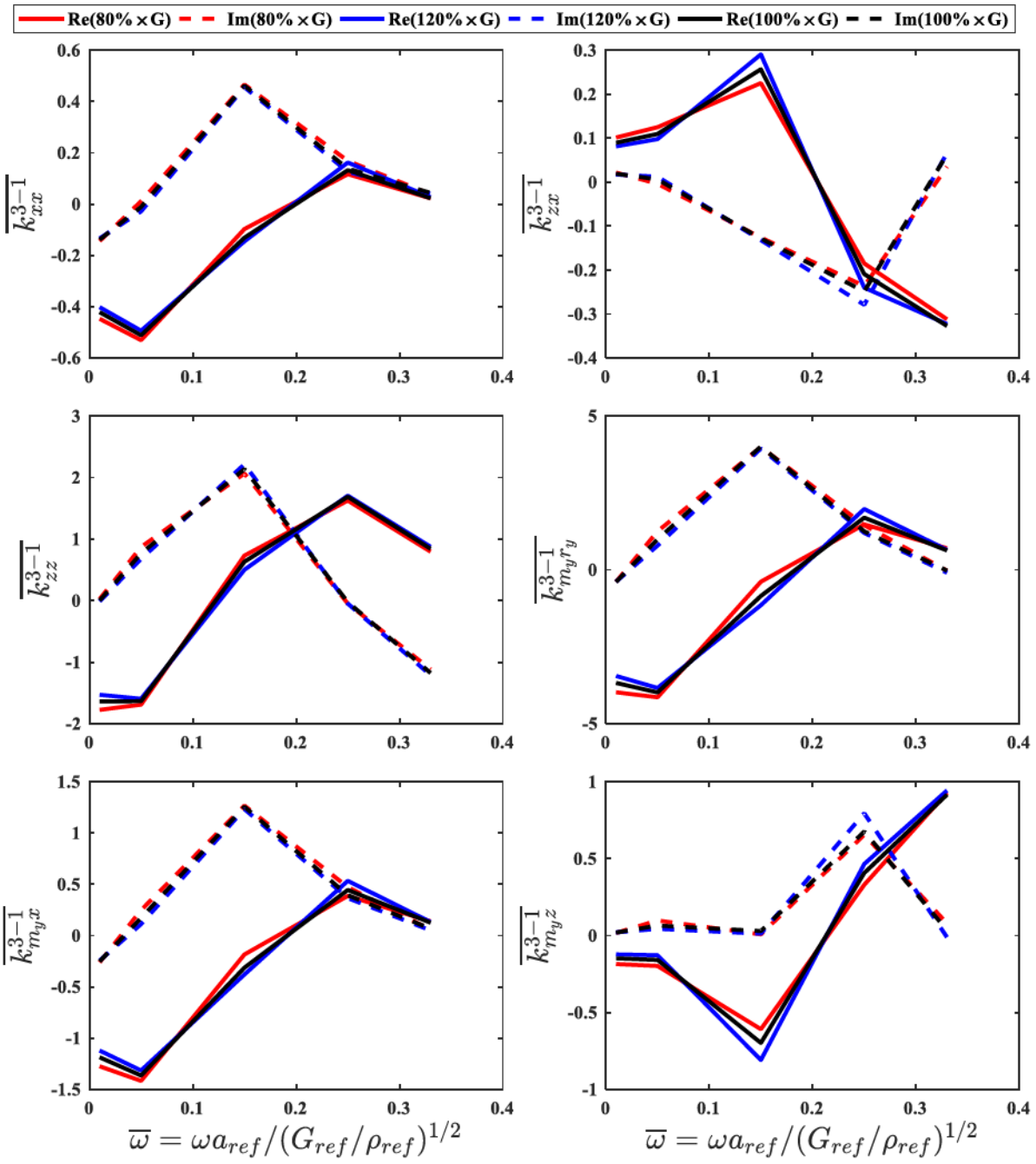

(c) Primary impedance functions in $\mathbf{K}^{3-1}$

Figure 4.12 *(continued)*

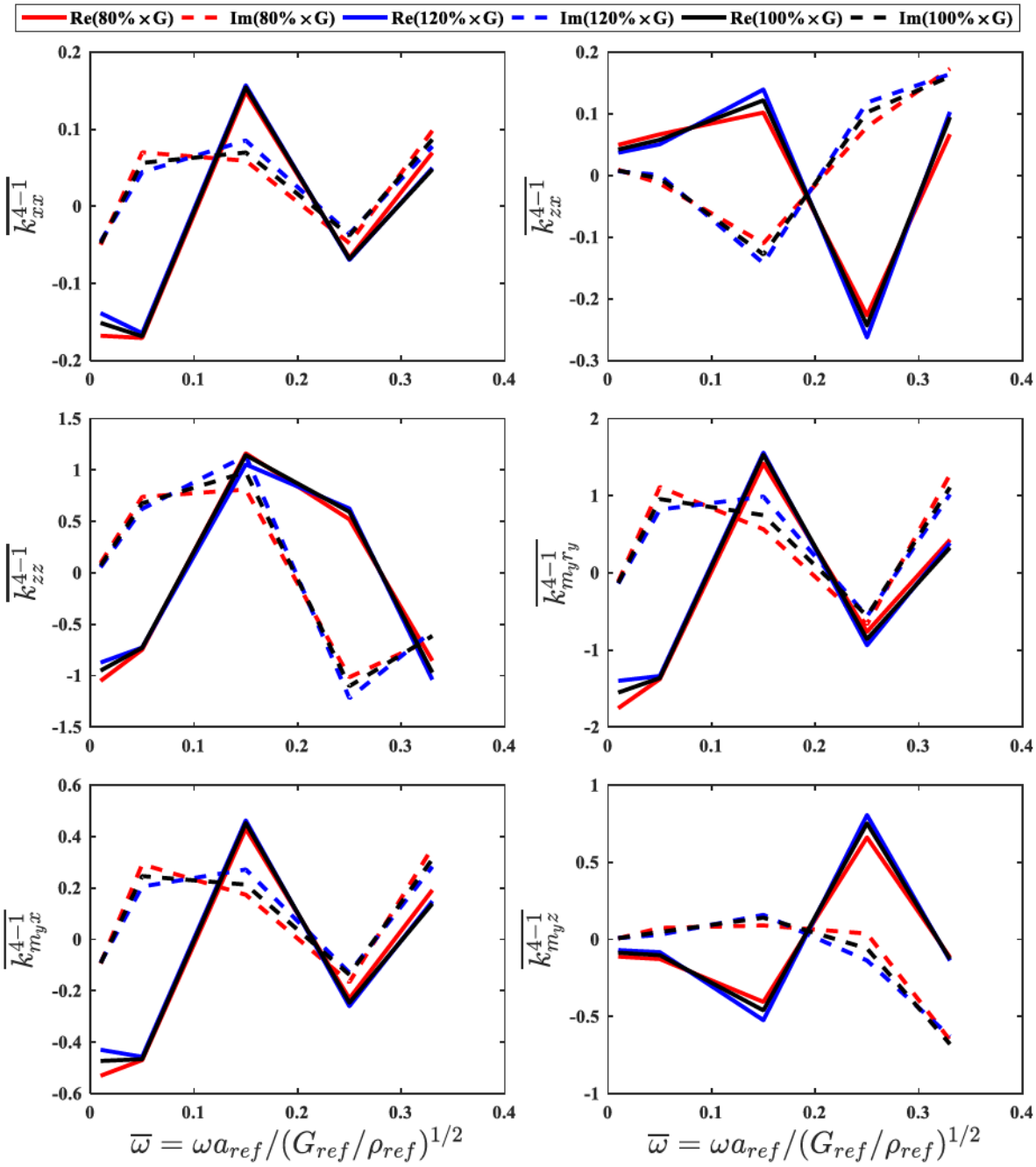

(d) Primary impedance functions in $\mathbf{K}^{4-1}$

Figure 4.12 *(continued)*

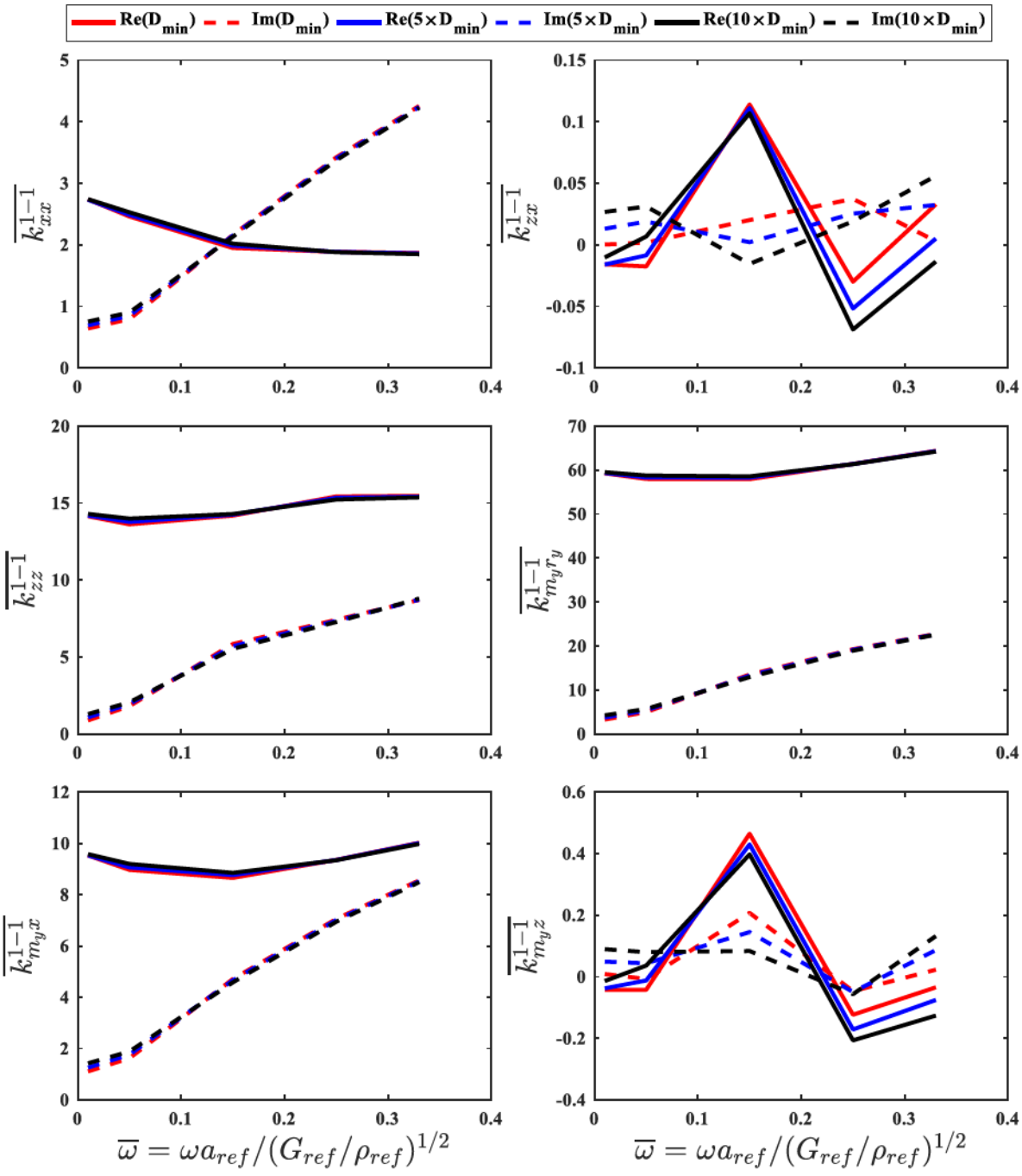

(a) Primary impedance functions in $\mathbf{K}^{1-1}$

Figure 4.13 *Sensitivity of impedance functions for 2×2 pile group to soil material damping in half-space.*

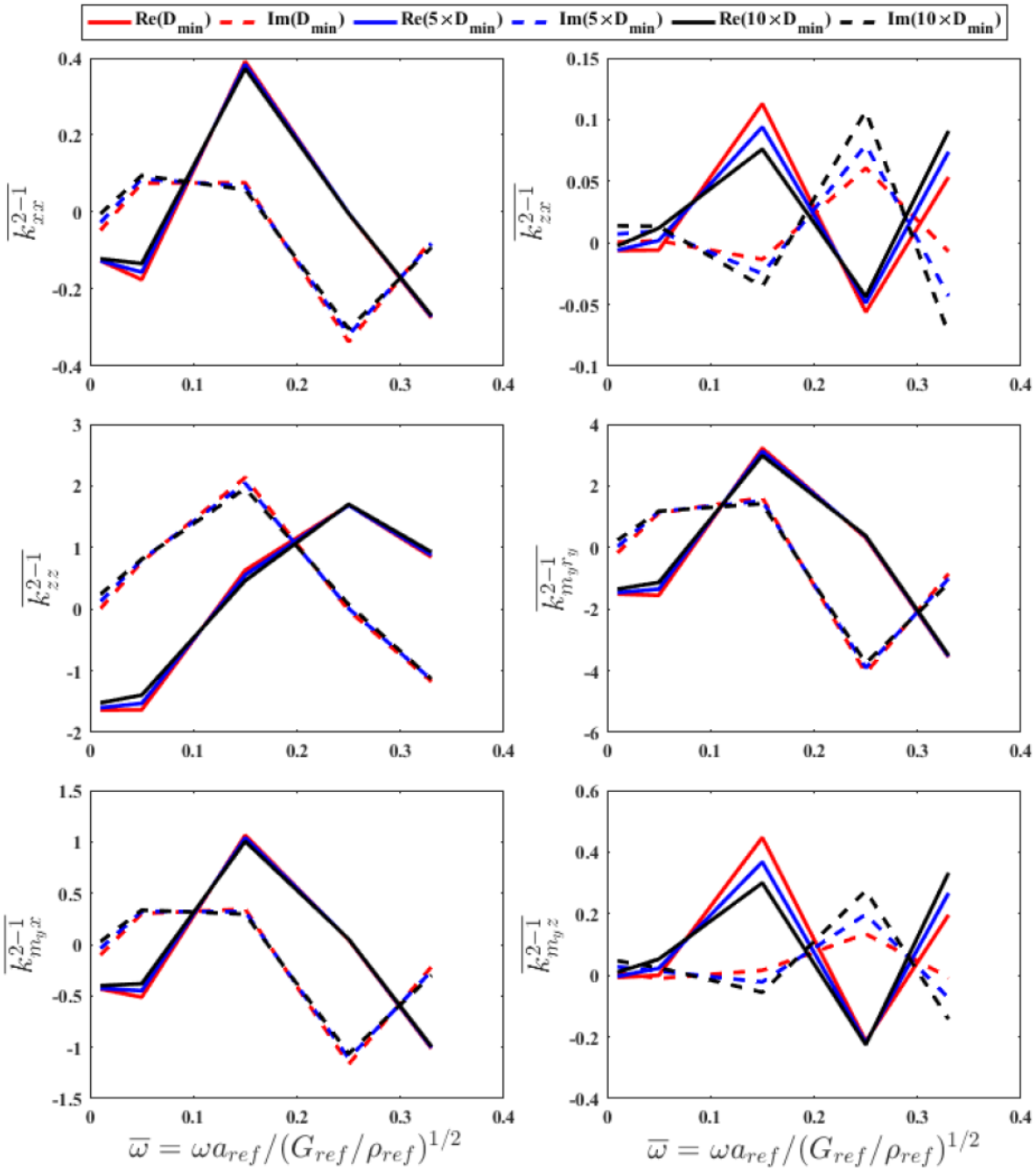

(b) Primary impedance functions in $\mathbf{K}^{2-1}$

Figure 4.13 *(continued)*

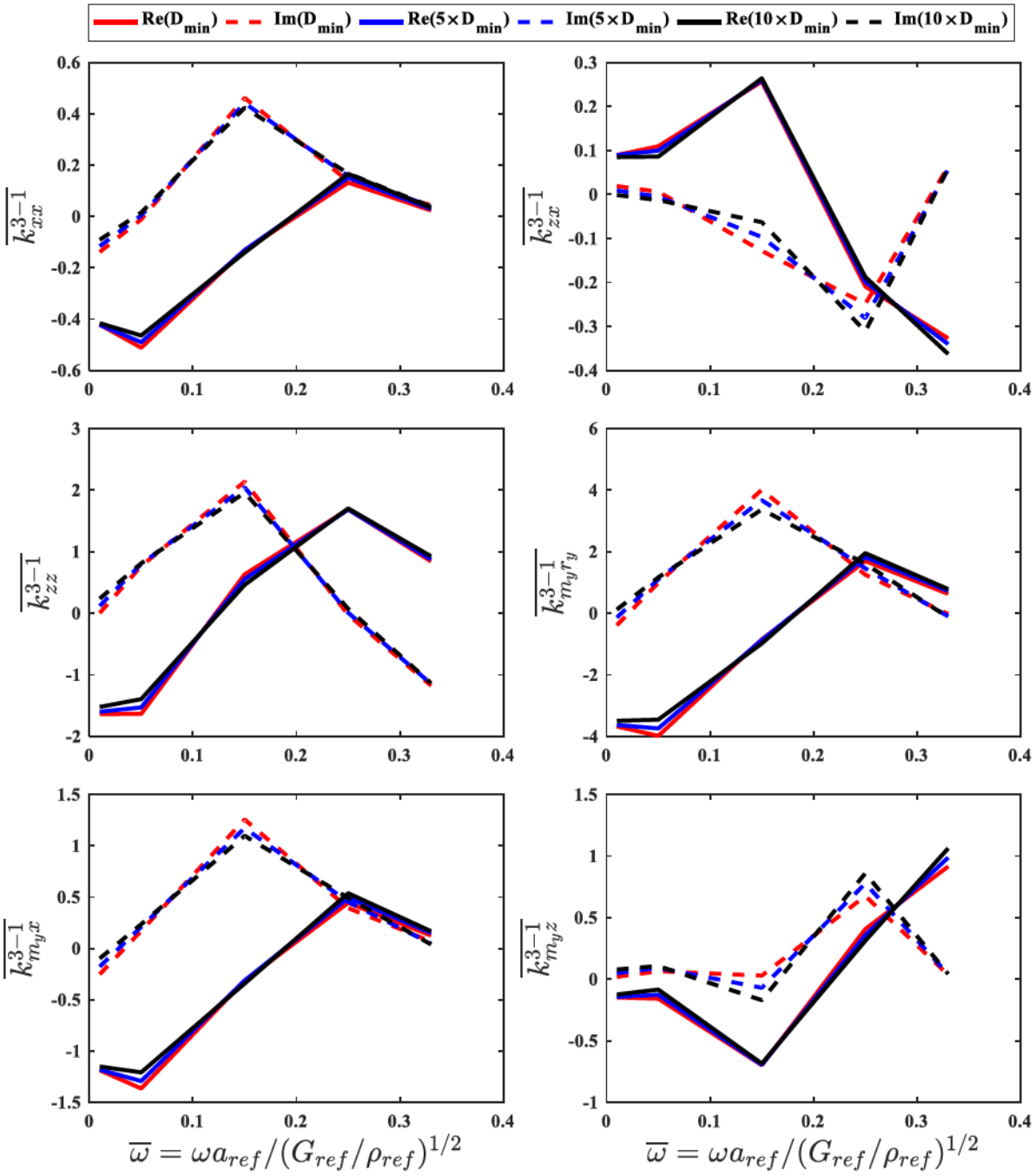

(c) Primary impedance functions in $\mathbf{K}^{3-1}$

Figure 4.13 *(continued)*

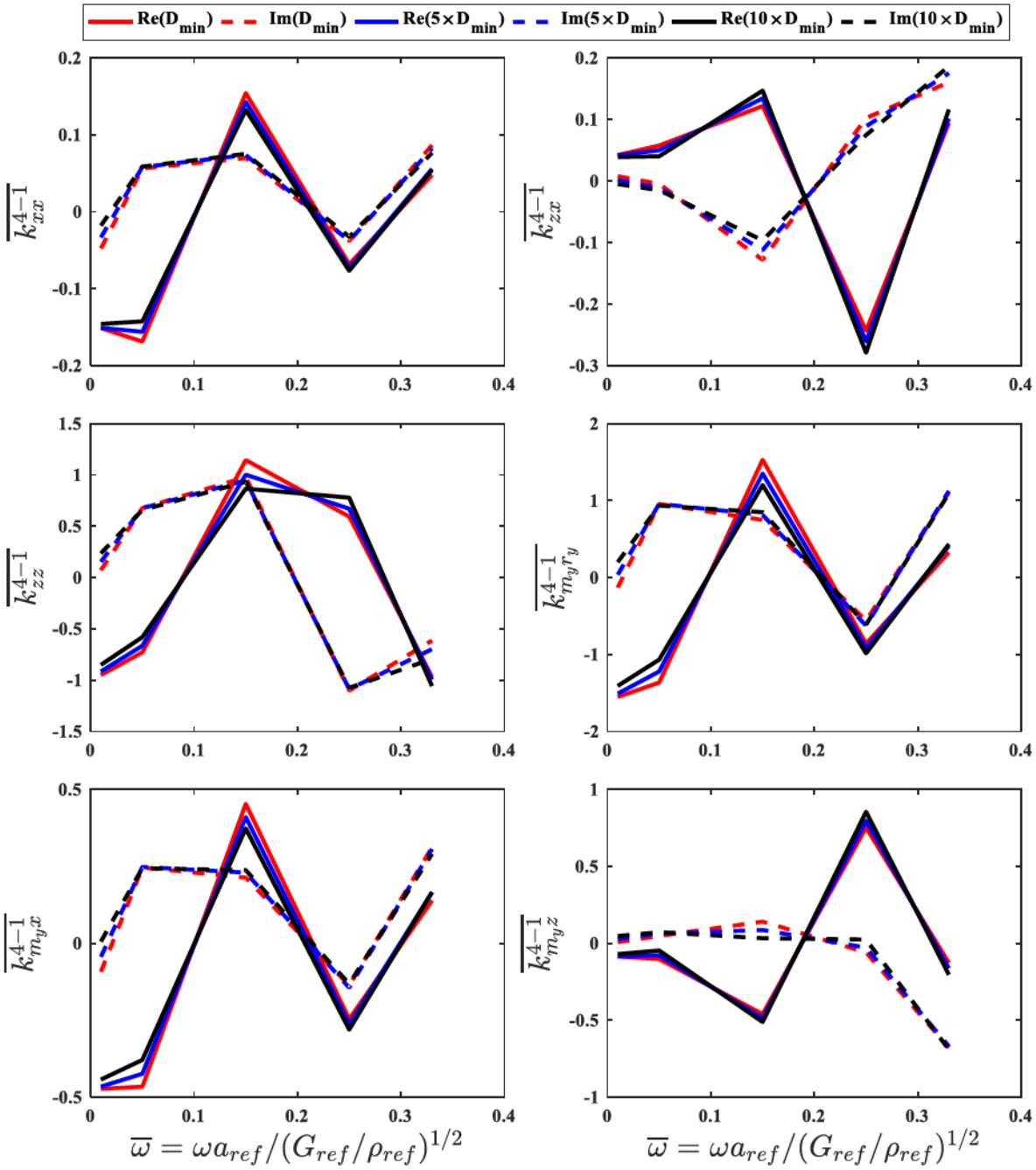

(d) Primary impedance functions in $\mathbf{K}^{4-1}$

Figure 4.13 *(continued)*

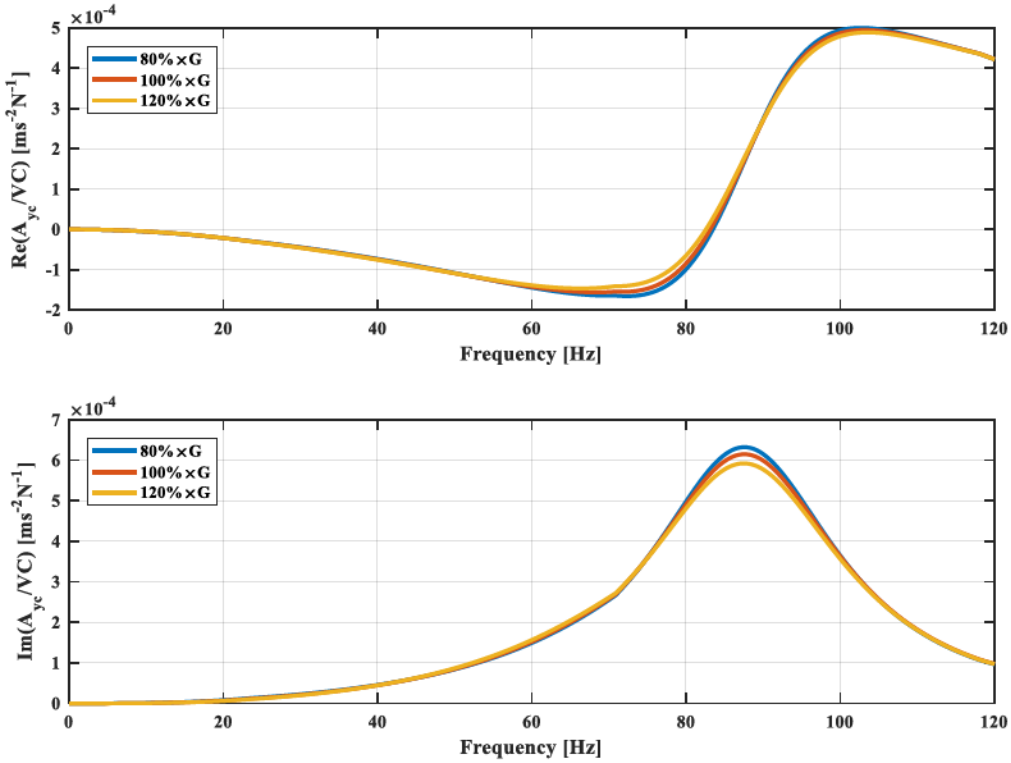

(a) Influence of varying shear modulus in half-space on A_{yc}/VC

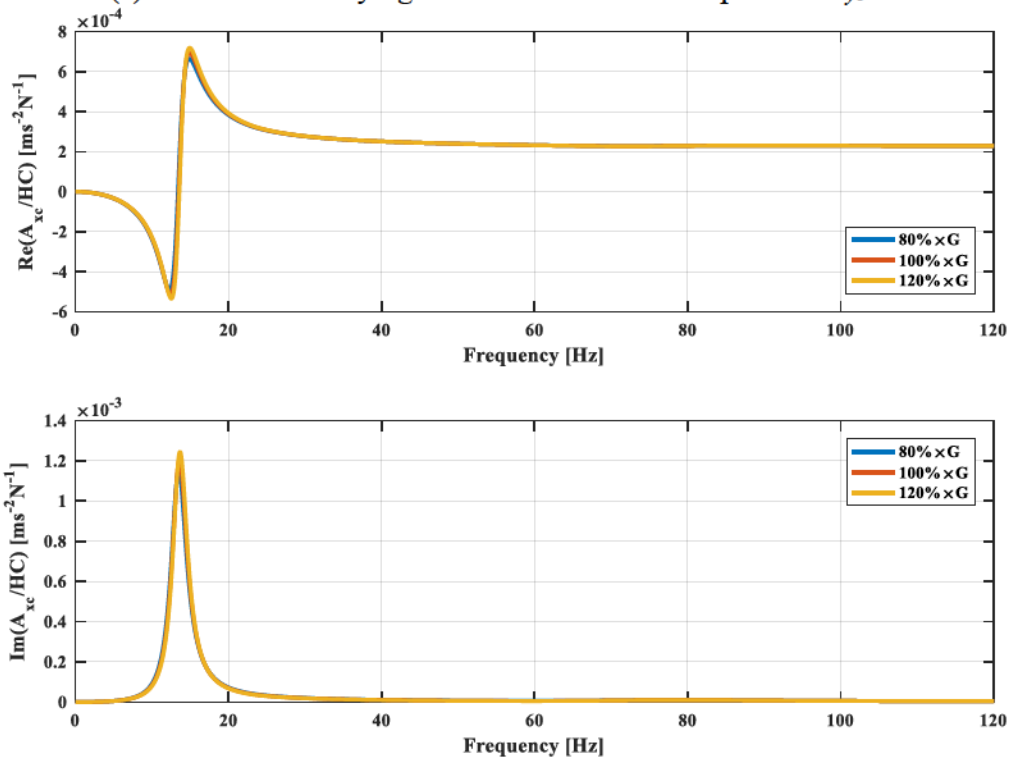

(b) Influence of varying shear modulus in half-space on A_{xc}/HC

Figure 4.14 *Sensitivity of accelerance functions to variations in soil shear modulus in half-space for pile group.*

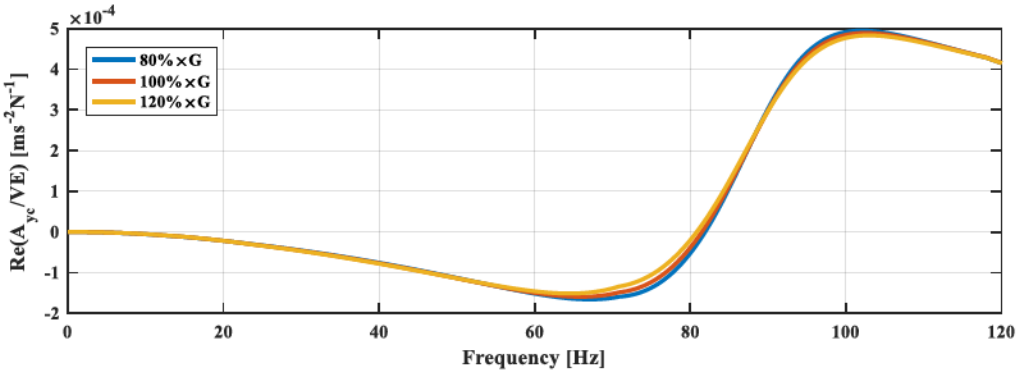

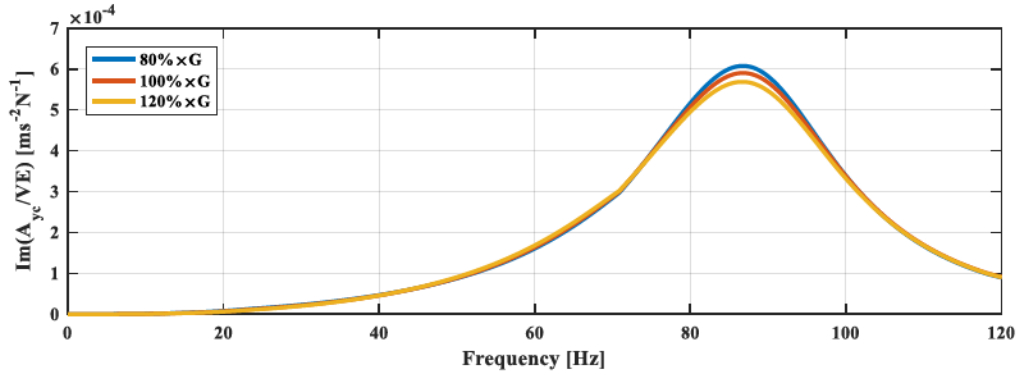

(c) Influence of varying shear modulus in half-space on A_{yc}/VE

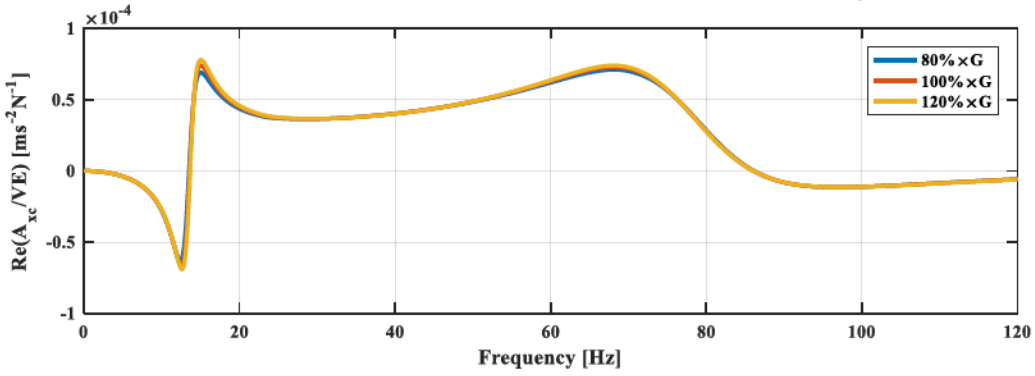

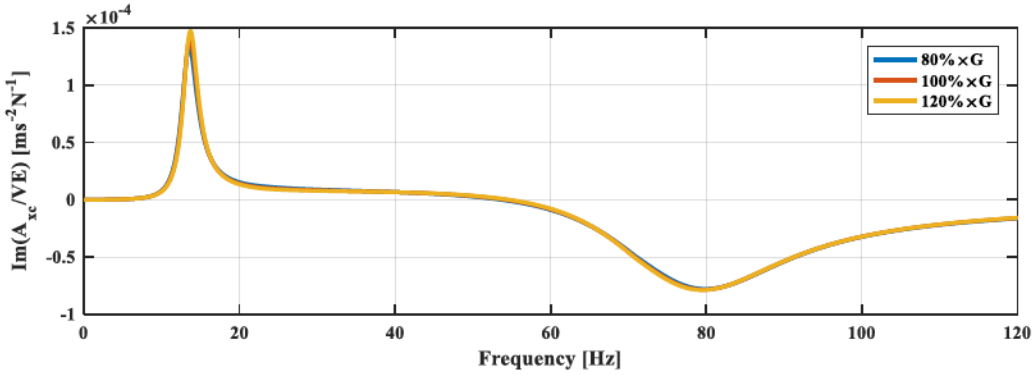

(d) Influence of varying shear modulus in half-space on A_{xc}/VE

Figure 4.14 *(continued)*.

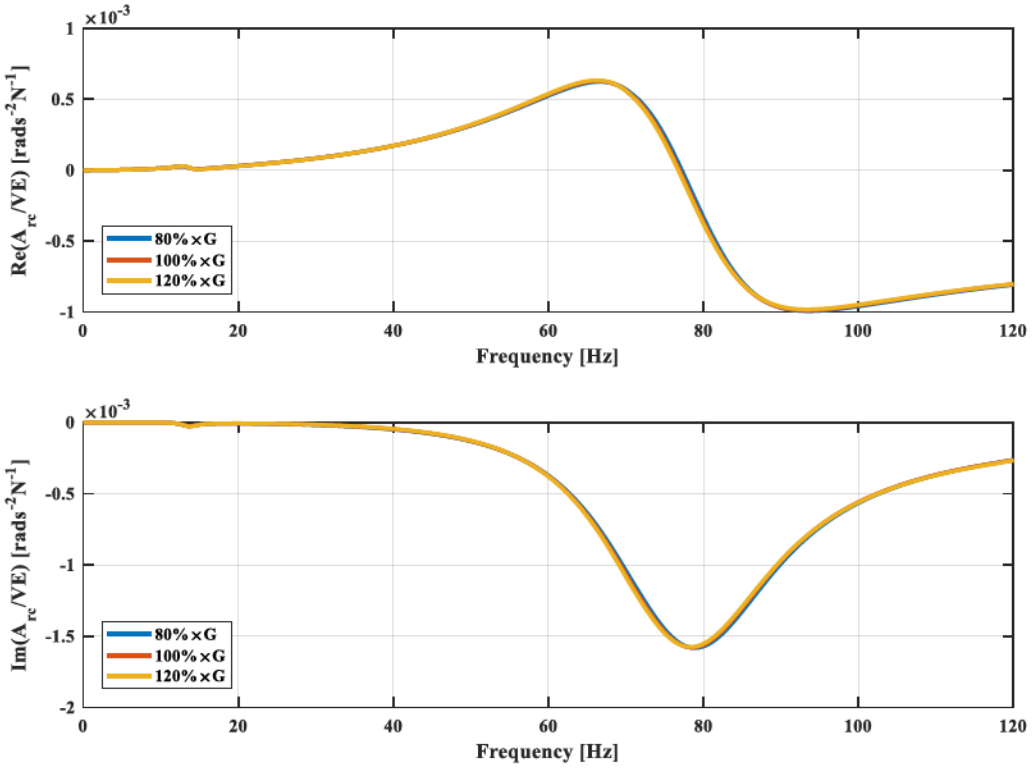

(e) Influence of varying shear modulus in half-space on A_{rc}/VE

Figure 4.14 *(continued)*

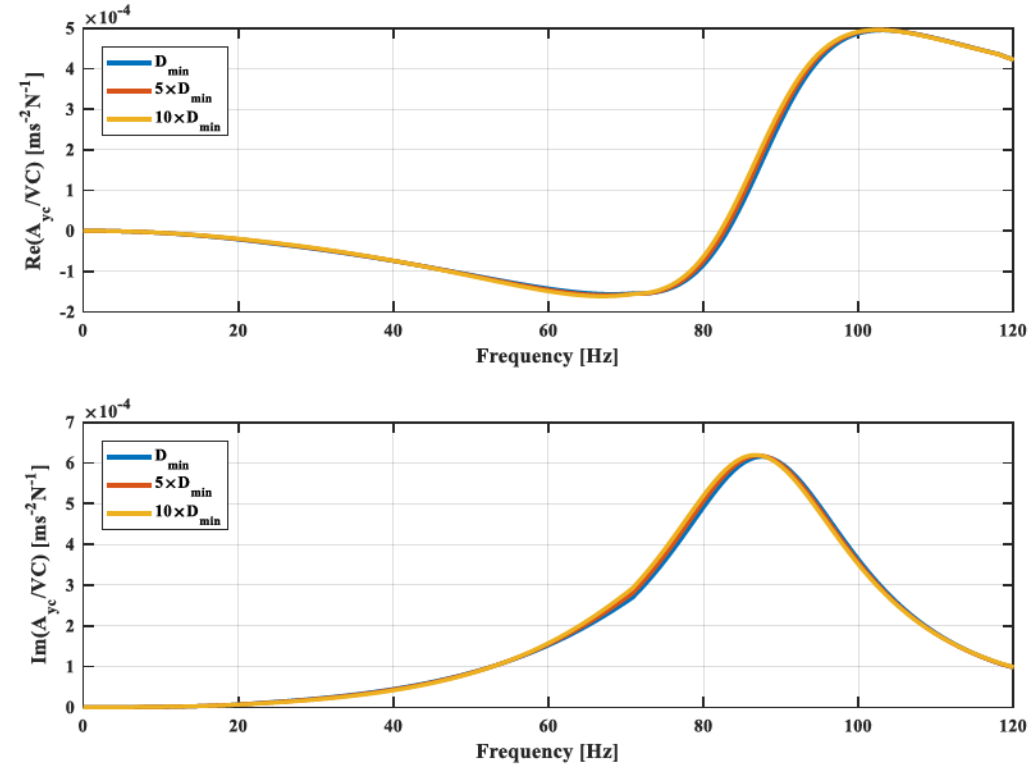

(a) Influence of varying damping ratio in half-space on A_{yc}/VC

Figure 4.15 *Sensitivity of accelerance functions to variations in soil minimum material damping ratio in half-space for pile group.*

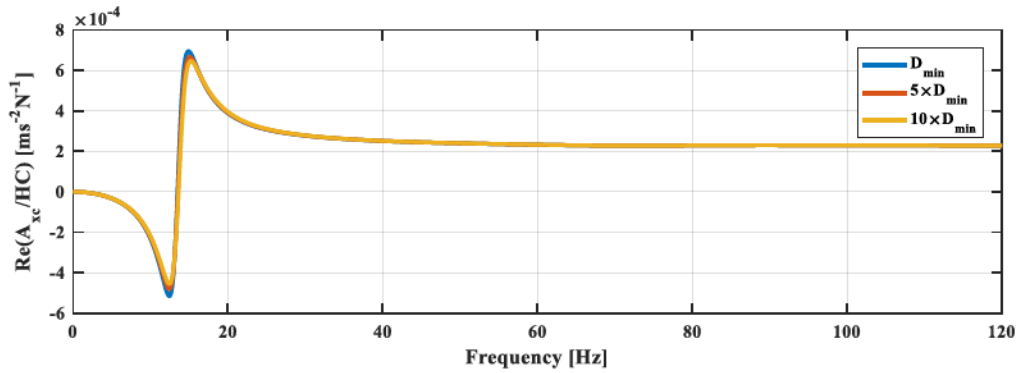

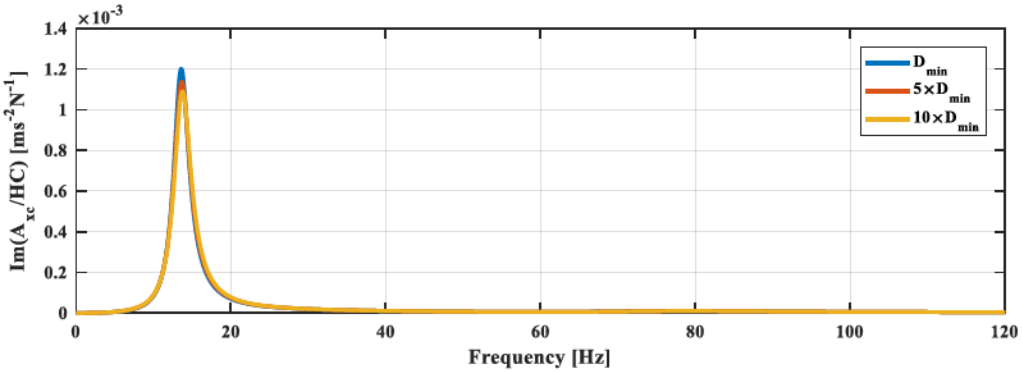

(b) Influence of varying damping ratio in half-space on A_{xc}/HC

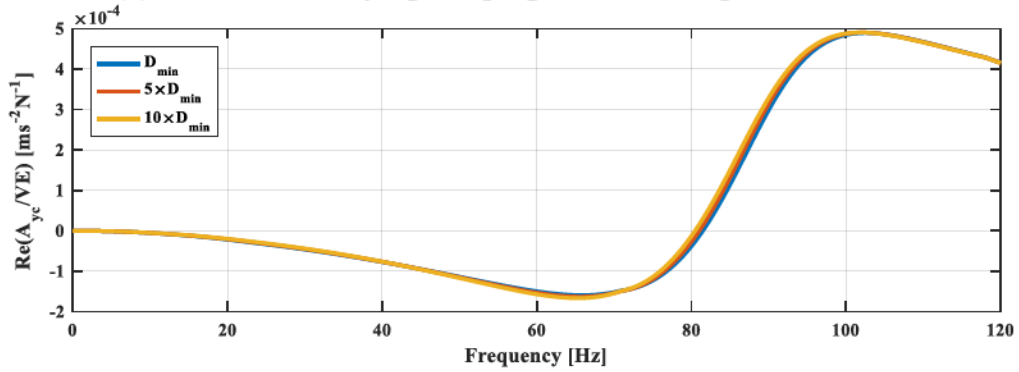

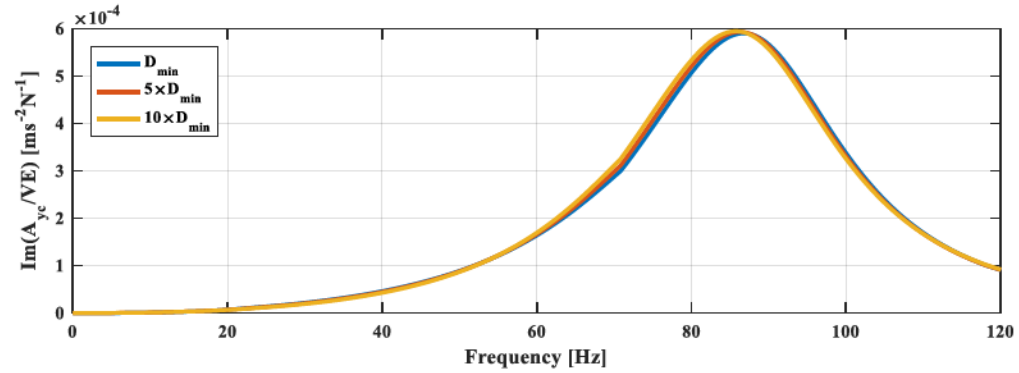

(c) Influence of varying damping ratio in half-space on A_{yc}/VE

Figure 4.15 *(continued)*

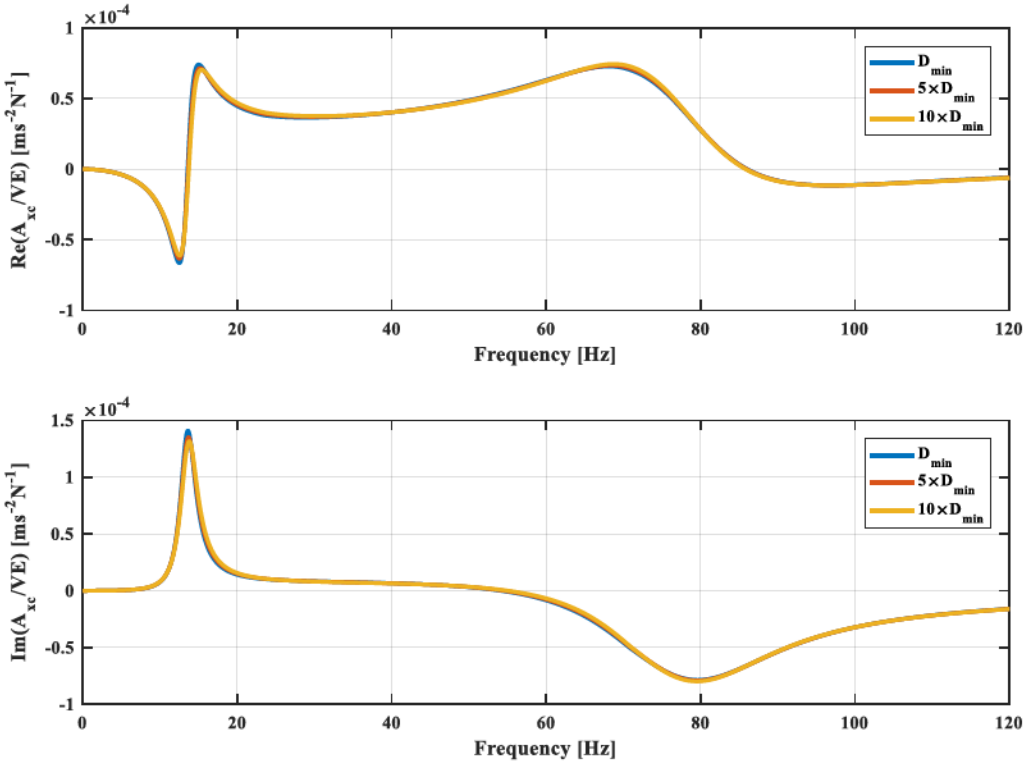

(d) Influence of varying damping ratio in half-space on A_{xc}/VE

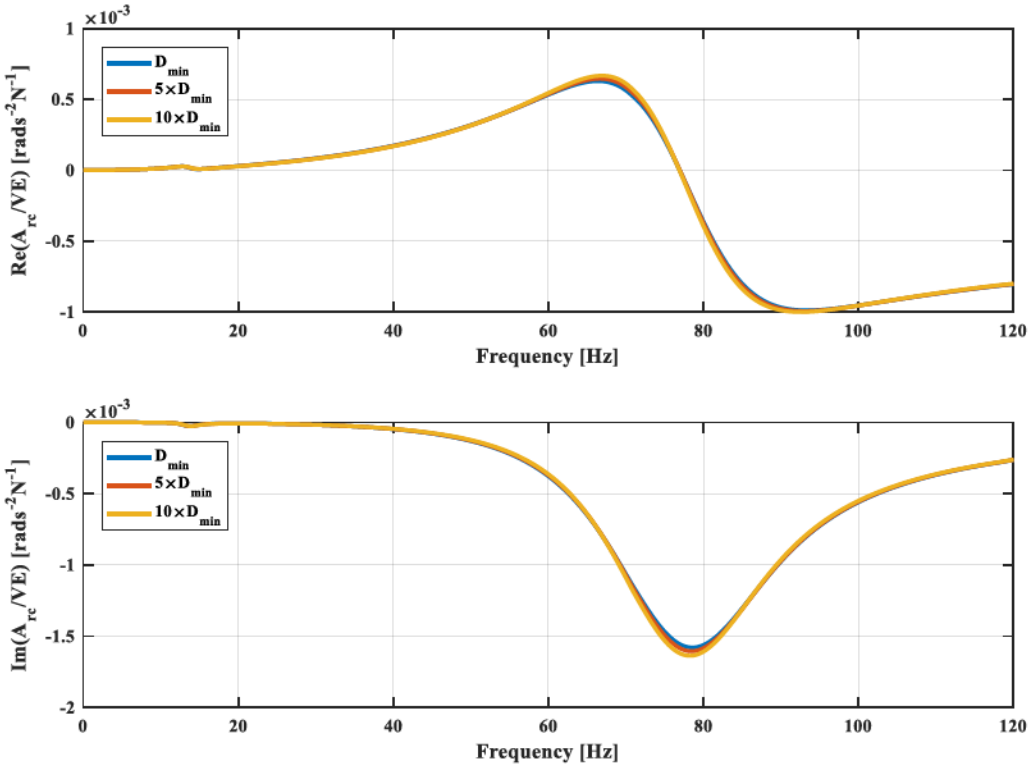

(e) Influence of varying damping ratio in half-space A_{rc}/VE

Figure 4.15 *(continued)*

4.3 Soil Layer Discretization

To apply layered Green's functions in BEASSI, continuous soil profiles obtained by CPT correlations or piecewise soil profiles obtained by SCPT need to be discretized. Similar to the boundary discretization discussed in Section 3.6.2, determining soil layer thickness brings a tradeoff between the accuracy of the impedance functions, and the computational time. To determine appropriate layering for the dynamics of soil-pile group problems, parametric studies were performed for two models:1) 2×2 pile group in the half-space with layered square-root soil profiles; and 2) 2×2 pile group with disturbed zone in layered soil profiles from the SCPT data.

4.3.1 2×2 Pile Group in Half-space with Layered Square-Root Soil Profile

For the 2×2 pile group in the half-space, the soil has zero material damping ratio, constant dimensionless density of unity, and Poisson's ratio of 0.42. The square-root shear modulus profile is determined using Eqn.(4.2):

$$G_o = G_{ref}\sqrt{\frac{z}{a_{ref}}} \tag{4.2}$$

where z is actual depth. Layering in the half-space was analyzed using pile Mesh B and all soil layers have uniform thicknesses. Number of layers per element (noted as L/E) was specified as 1, 2, 3, and 4 (Figure 4.16). The resulting primary impedance functions are compared in Figure 4.17.

When $\bar{\omega}$ is below 0.25, all four types of layer discretization show good agreement except for $\bar{k}_{xx}^{1-1}$ and $\bar{k}_{xx}^{3-1}$. This suggests that the horizontal impedances accounting for interaction between the loaded pile and the pile in line of the force are sensitive to layering even at low frequencies. When $\bar{\omega}$ goes beyond 0.50, most impedances exhibit diversion. The

variation in soil shear modulus near surface is magnified at higher frequencies. Only $\overline{k_{zz}^{1-1}}$ and $\overline{k_{m_y r_y}^{1-1}}$ that are determined by deeper soils are negligibly affected.

Overall, effects of soil layer discretization on impedance functions for the 5-domain model with square-root soil profile are noticeable at high frequencies. 3 L/E provides results close to the finer 4 L/E discretization for the frequency range of interest and thus deemed to give the optimal balance of accuracy and efficiency.

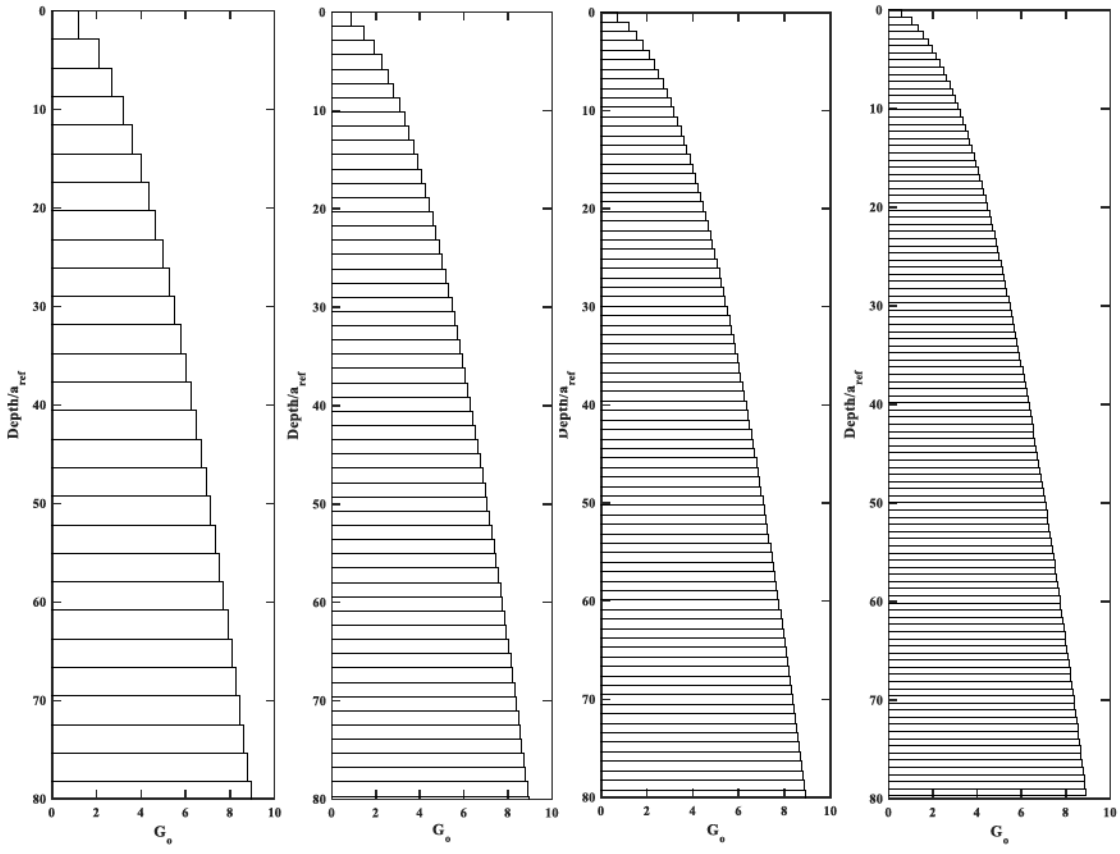

(a) 1 L/E (b) 2 L/E (c) 3 L/E (d) 4 L/E

Figure 4.16 *Layering for the 2×2 pile group in the half-space with the square-root soil profile.*

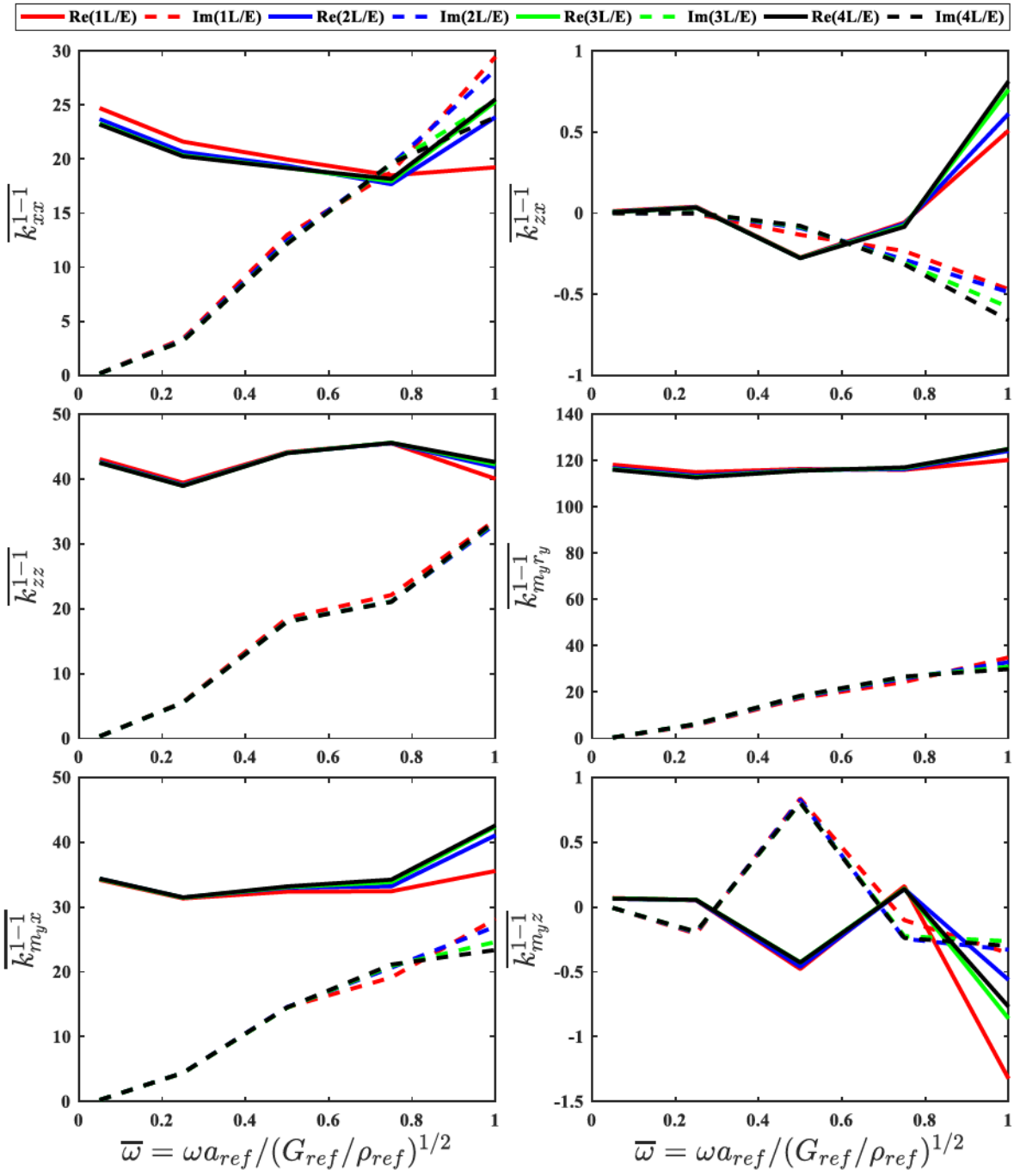

(a) Primary impedance functions in $\mathbf{K}^{1-1}$

Figure 4.17 *Impedance functions for 5-domain model by varying soil layer discretization in the half-space.*

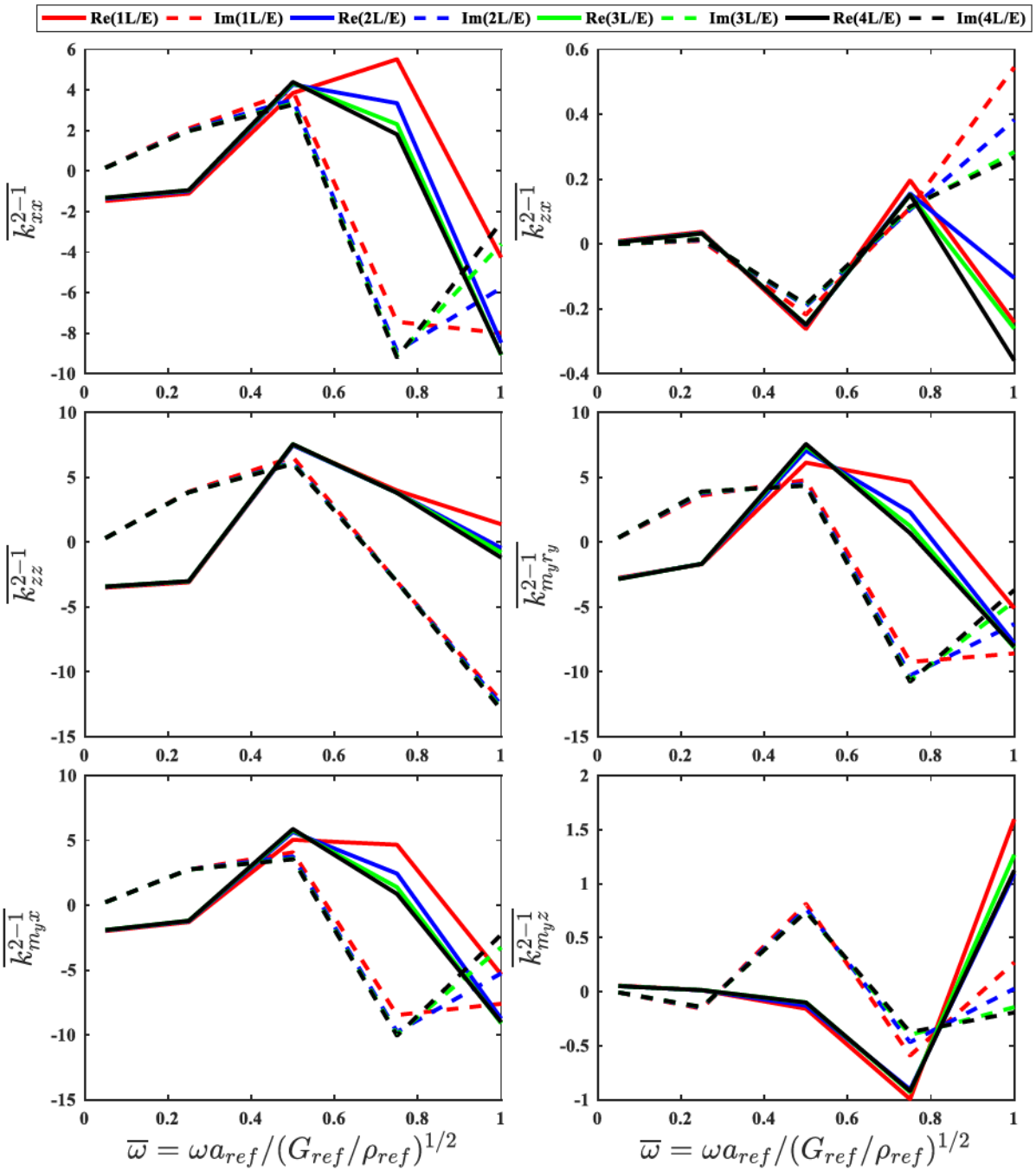

(b) Primary impedance functions in $\mathbf{K}^{2-1}$

Figure 4.17 *(continued)*

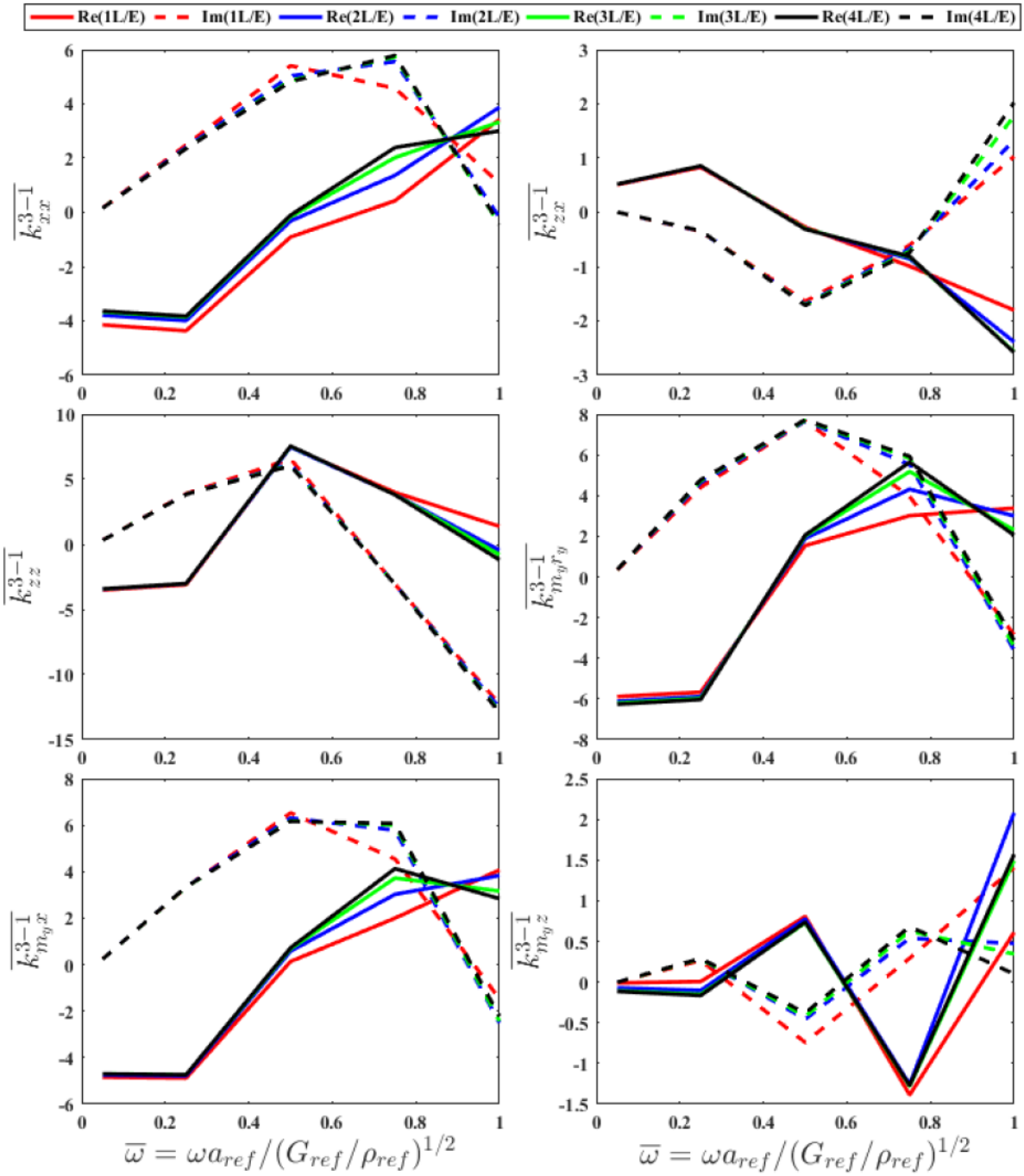

(c) Primary impedance functions in $\mathbf{K}^{3-1}$

Figure 4.17 *(continued)*

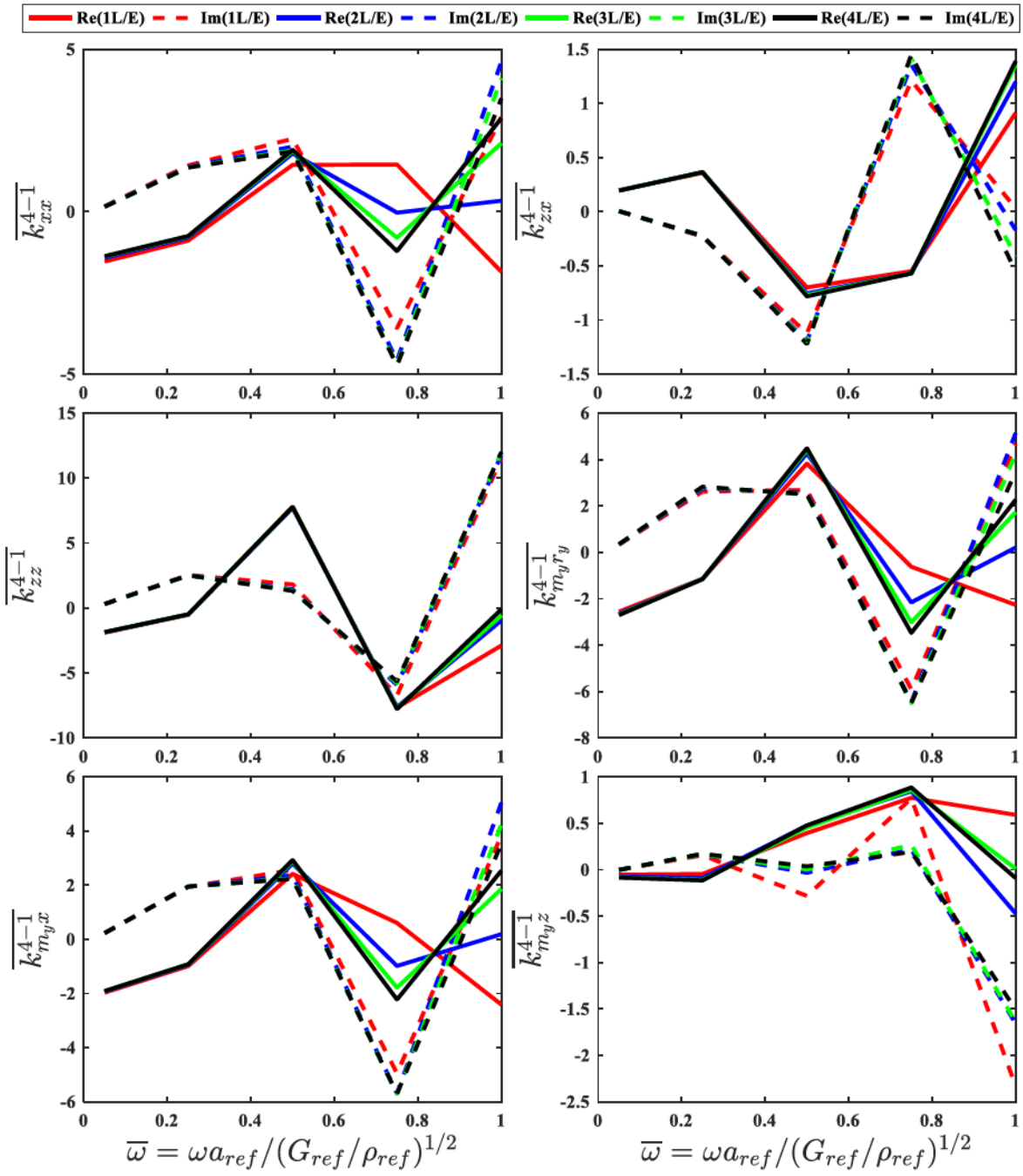

(d) Primary impedance functions in $\mathbf{K}^{4-1}$

Figure 4.17 *(continued)*

4.3.2 2×2 Pile Group Surrounded by Disturbed Zone and Half-space

To analyze layering effects for 6-domain models, two aspects need to be noted:

1) In BEASSI, number of layers per element for each vertical element is a constant value shared by two neighboring domains. When the actual layer thicknesses for an element in the two soil domains are different, resulting in different number of soil layers on each side, then number of layers per element specified for the element must be the least common multiple to avoid potential convergence problems when applying Gaussian quadrature. Otherwise, sub-regions per element may cross multiple soil layers with quadrature points in different soil layers. If there is a drastic variation in soil shear modulus. Green's functions evaluated at these quadrature points may have significant variations, ending up with using higher order Gaussian quadrature for numerical integration.

2) The actual number of layers per element indicated in *layercoordN.dat* can be smaller than the number specified for each element in *inp.dat*, so long as each sub-region does not cross two or more layers in either zone. If six layers per element is specified for an element, for example, the actual number of layers can also be 1, 2 or 3. Though no numerical difficulties are induced, redundant integrations are performed while they could be implemented over combined sub-regions without increasing Gaussian quadrature order.

An example of possible layer discretization within the disturbed zone and half-space are presented in Figure 4.18. Pile Mesh B (blue), inclusion Mesh F (green), and inclusion boundary at infinity (purple) are shown. Black solid lines denote discretization of soil layers. Number of layers was specified as 2, 3, and 4 for the disturbed zone, and 4, 3, 2 and 1 for the half-space. The least number of layer per inclusion element for each case, i.e., least common multiple, is listed in Table 4.3.

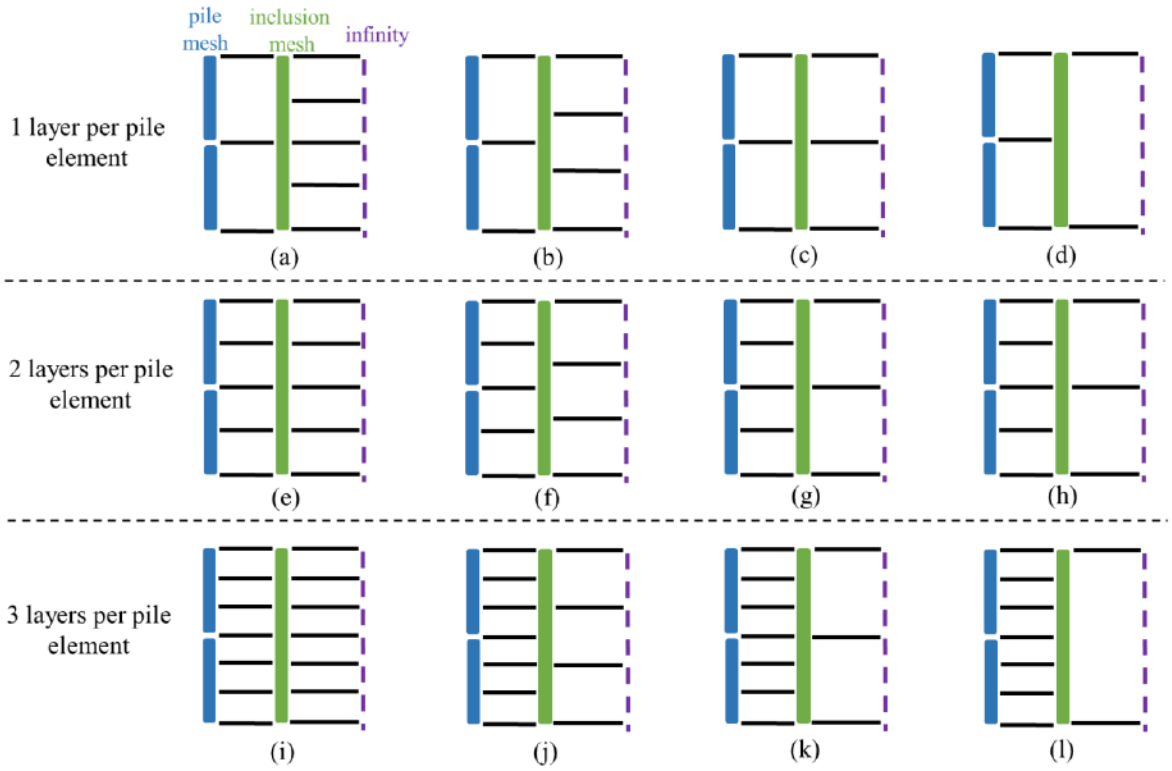

Figure 4.18 *Possible soil layer discretization for the disturbed zone and the half-space.*

Table 4.3 *Least number of layers per inclusion element for the example cases.*

Case	**(a)**	**(b)**	**(c)**	**(d)**	**(e)**	**(f)**
Least number of layers per inclusion element	4	6	2	2	4	12
case	**(g)**	**(h)**	**(i)**	**(j)**	**(k)**	**(l)**
Least number of layers per inclusion element	4	4	6	6	6	6

Cases (i), (k) and (l), which have the same layering in the disturbed zone but different layers in the half-space were analyzed first. Actual soil profiles are demonstrated in by case (i) in Figure 4.19 and the resulting impedance functions are presented in Figure 4.20. For $\mathbf{K}^{1-1}$ and $\mathbf{K}^{2-1}$, slight deviations are observed in $\bar{k}_{zx}$ and $\bar{k}_{m_y z}$ for the Case (l), and the impedance functions in $\mathbf{K}^{3-1}$ and $\mathbf{K}^{4-1}$ show good agreement. The primary reason is that the pile impedances are more sensitive to the soil shear modulus and damping values within the disturbed zone than those in the surrounding half-space, as discussed in Section 4.2.2. For the actual SCPT soil profiles obtained at the test site, the shear modulus does not change drastically at shallow depths. Two soil layers per inclusion element i.e., Case (k), was found to be sufficient for discretizing the outer half-space soil profile.

The soil layers within the disturbed zone need to be compatible with both the inclusion mesh and the pile mesh. For pile Mesh B and inclusion Mesh E, three scenarios using 1, 2, and 3 soil layers per vertical element of the pile were analyzed (Figure 4.21). A satisfactory agreement in each of the impedance functions can be seen, with the exception of $\bar{k}_{zx}^{1-1}$ and $\bar{k}_{xx}^{2-1}$ that deviate slightly at certain frequencies for the 1-layer case (Figure 4.22).

In conclusion, the two cases analyzed for the 2×2 pile group using the square-root and SCPT layered profiles show general convergence in impedance functions for the layer discretization studied herein. Consistency is observed at low frequencies while deviations normally occur with an increasing frequency. Discretization of soil profile near the ground level is accountable for the deviations. For soil profile with less variation such as in the half-space for the 6-domain model, fine discretization of soil layers does not necessarily lead to more accurate results.

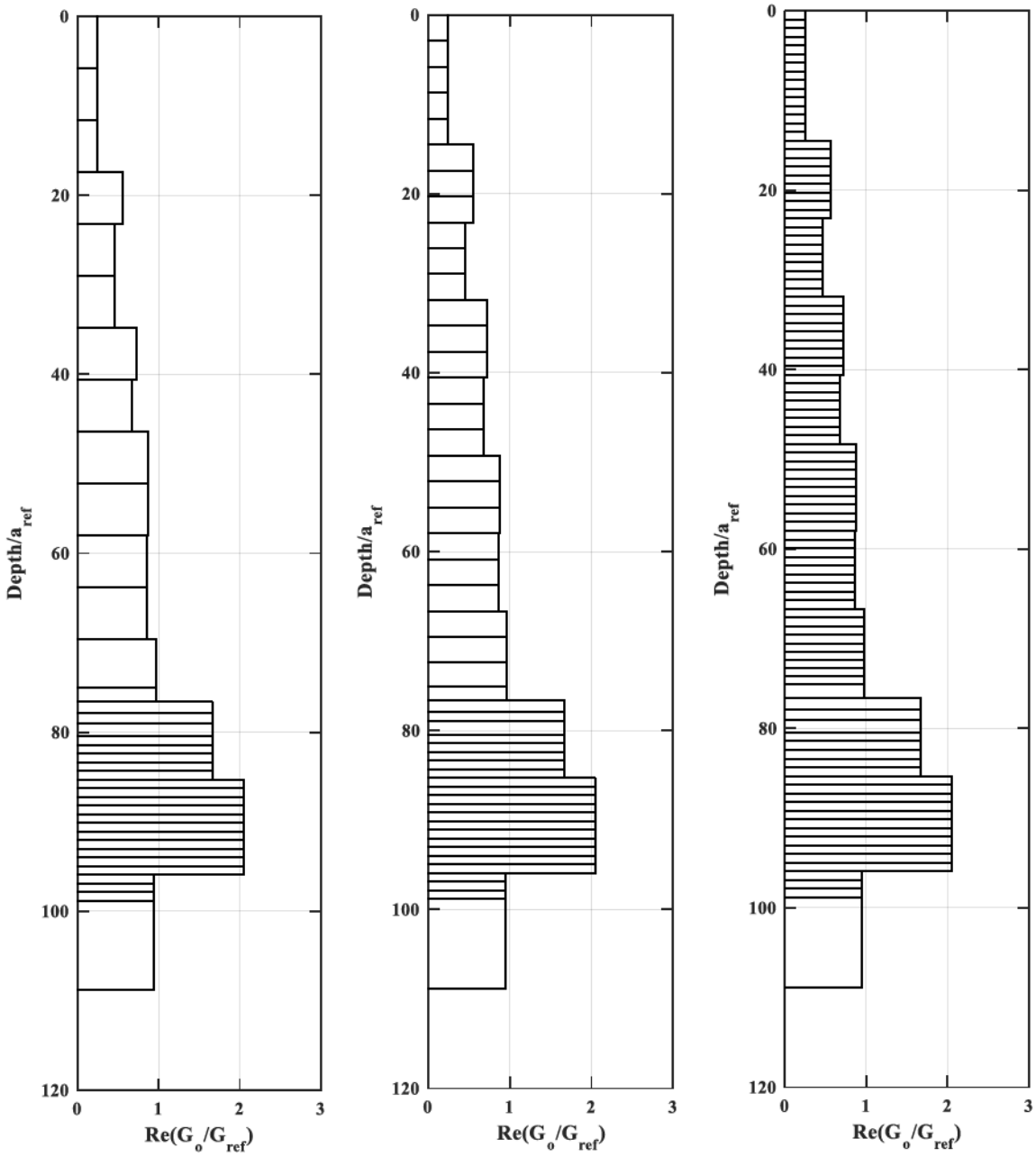

(a) Case (k) (b) Case (j) (c) Case (i)

Figure 4.19 *Soil layer discretization in the half-space for a 2×2 pile group.*

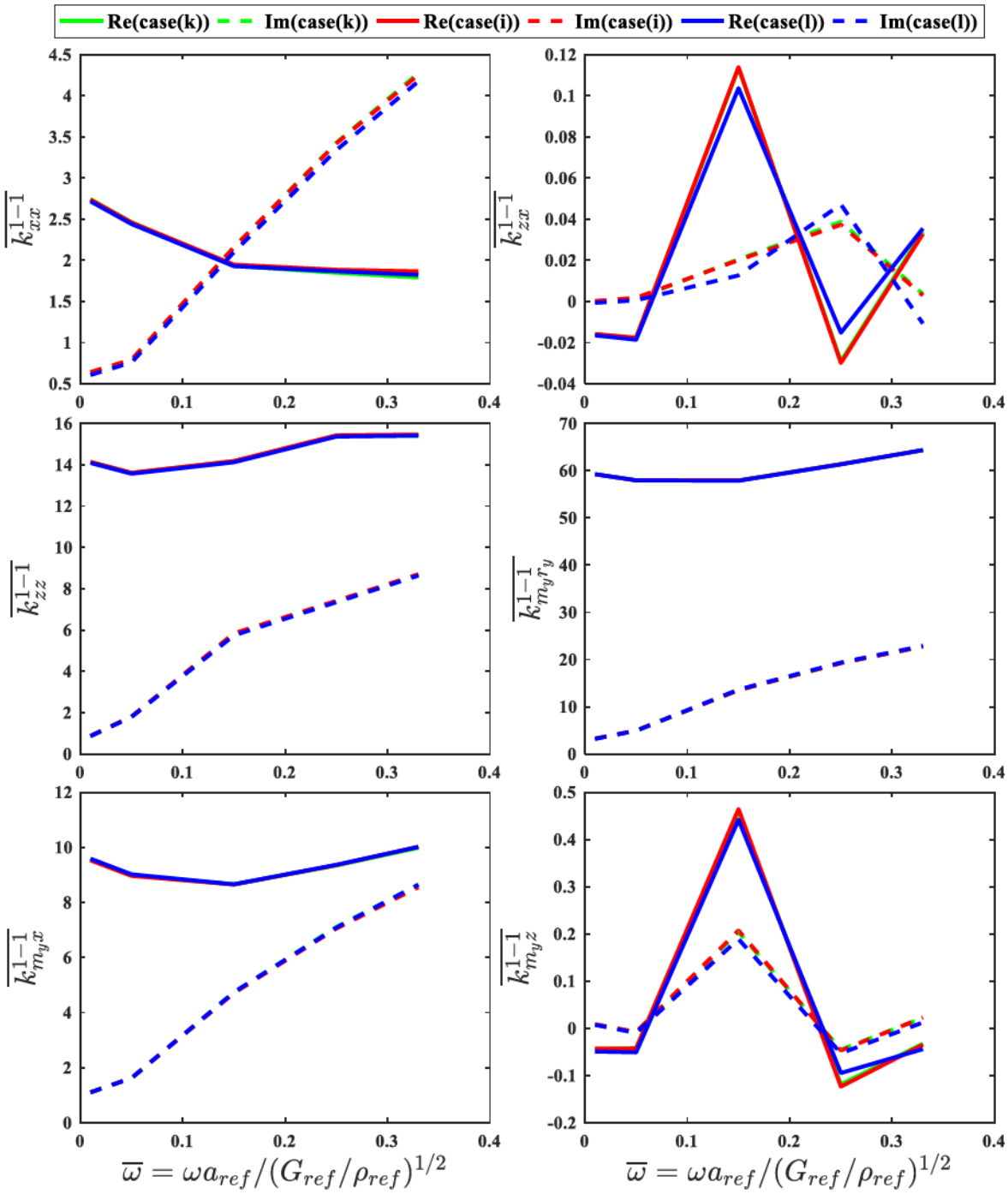

(a) Primary impedance functions in $\mathbf{K}^{1-1}$

Figure 4.20 *Comparison of impedance functions for discretizing square-root soil layer in the half-space for a 2×2 pile group with disturbed zone.*

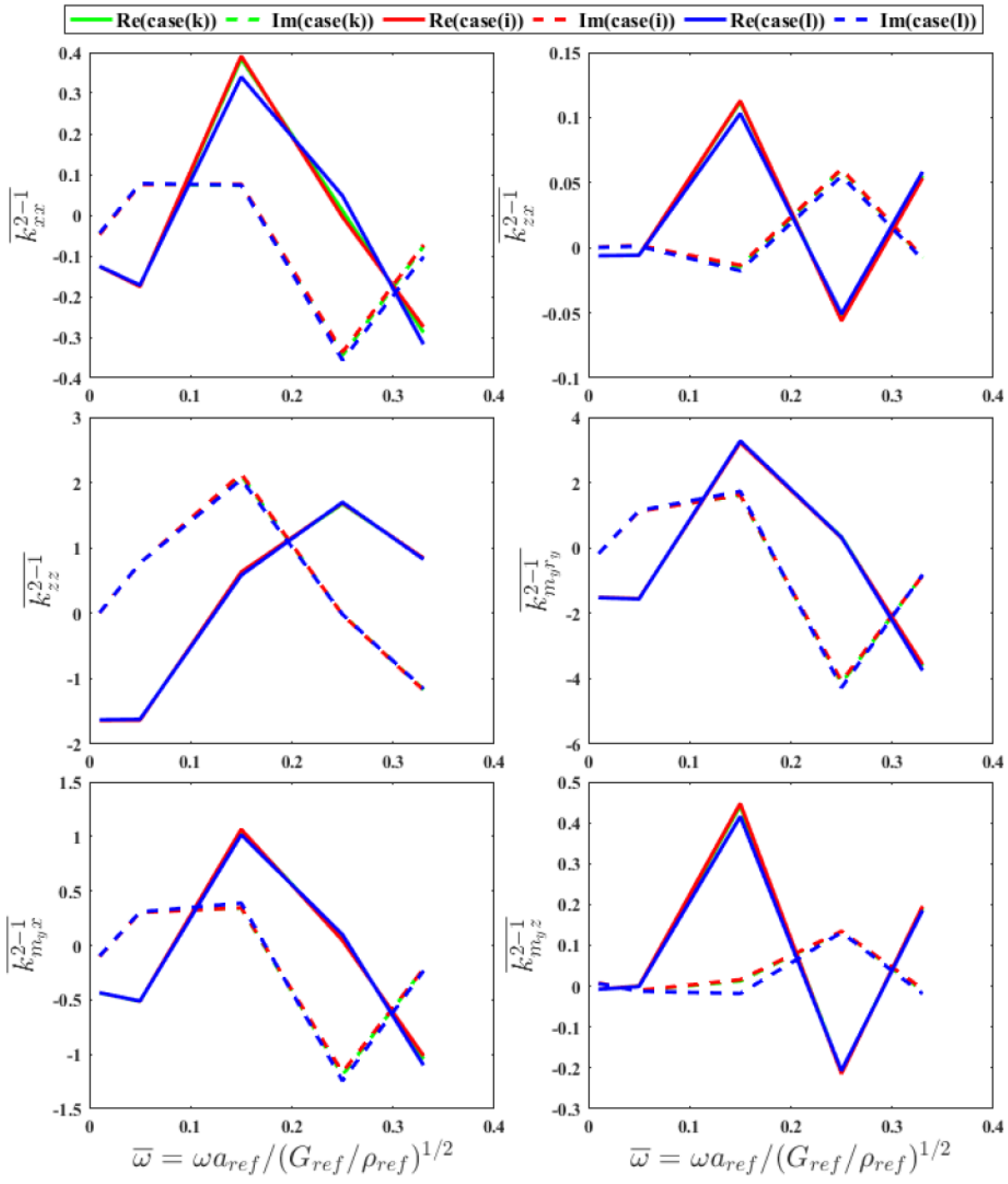

(b) Primary impedance functions in $\mathbf{K}^{2-1}$

Figure 4.20 *(continued)*

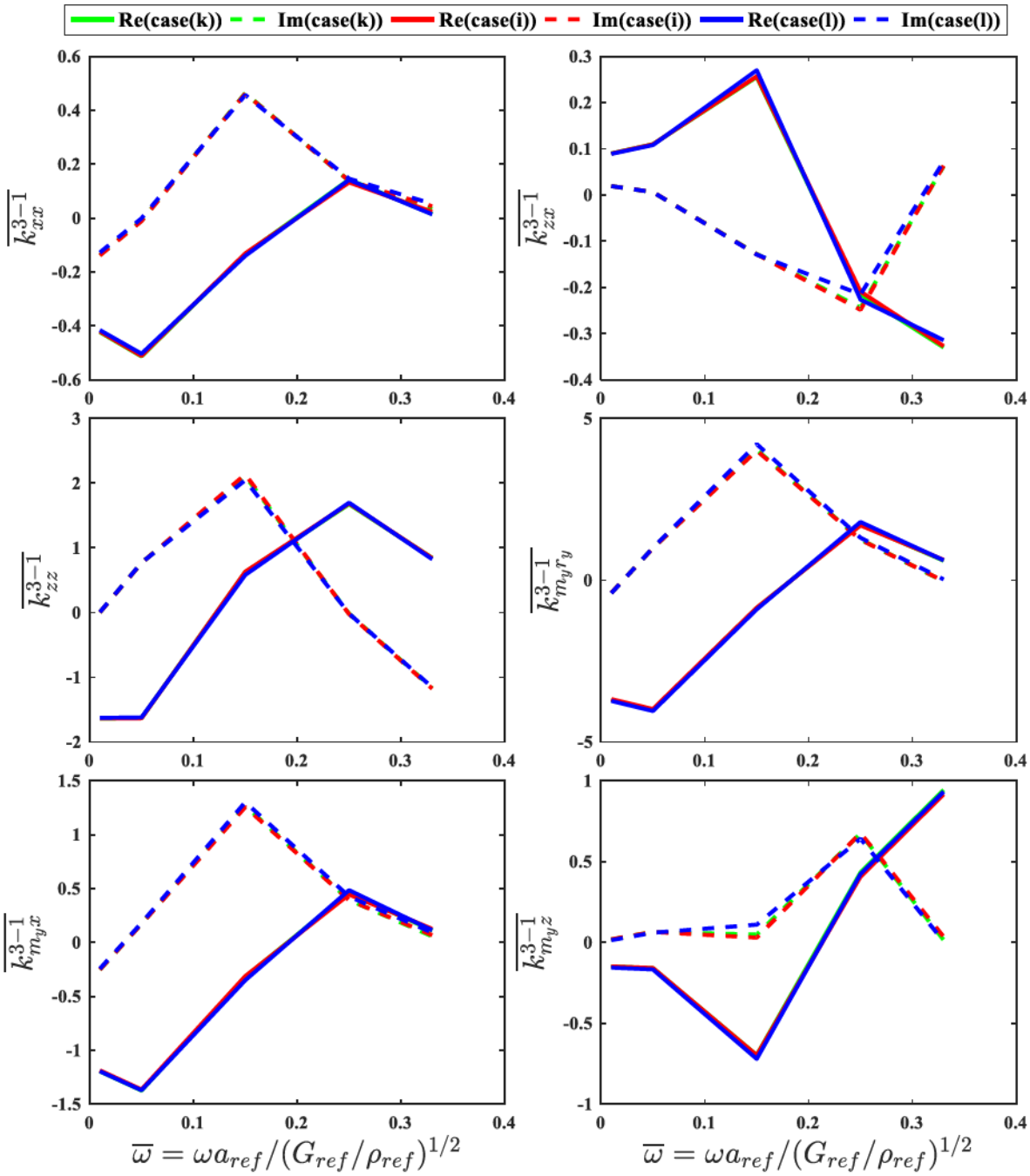

(c) Primary impedance functions in $\mathbf{K}^{3-1}$

Figure 4.20 *(continued)*

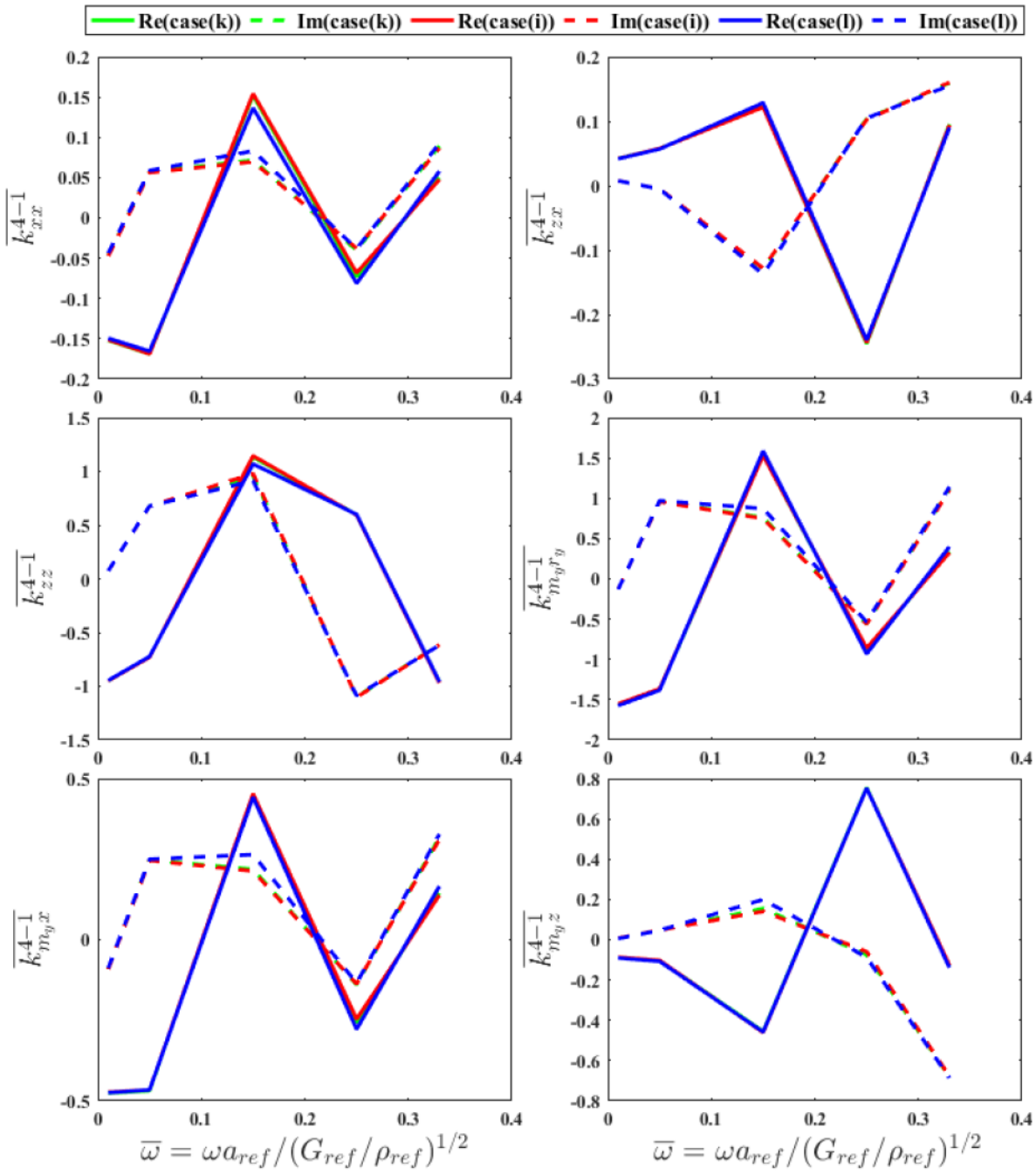

(d) Primary impedance functions in $\mathbf{K}^{4-1}$

Figure 4.20 *(continued)*

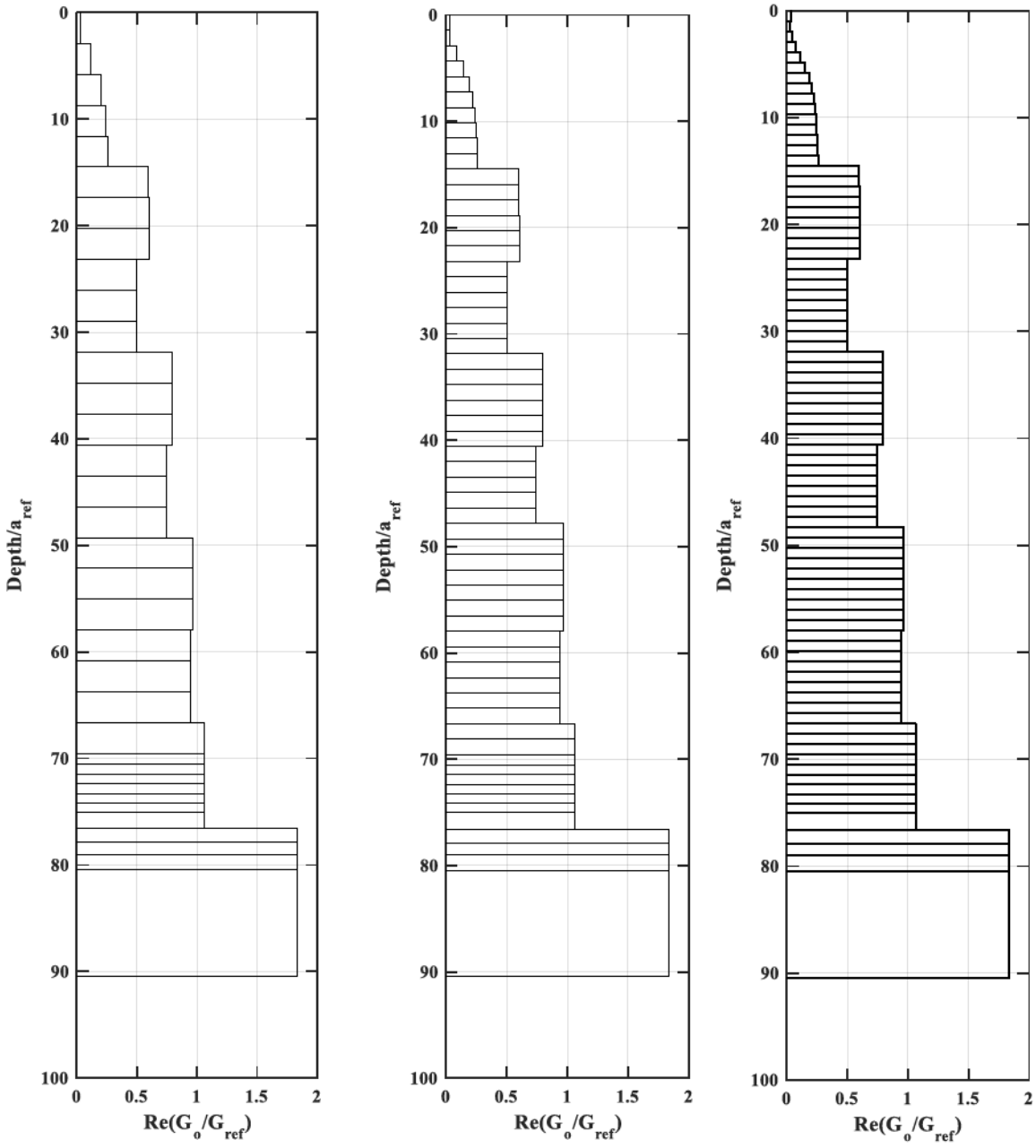

(a) Case (c) (b) Case (g) (c) Case (k)

Figure 4.21 *Soil layer discretization within the disturbed zone for a 2×2 pile group with disturbed zone.*

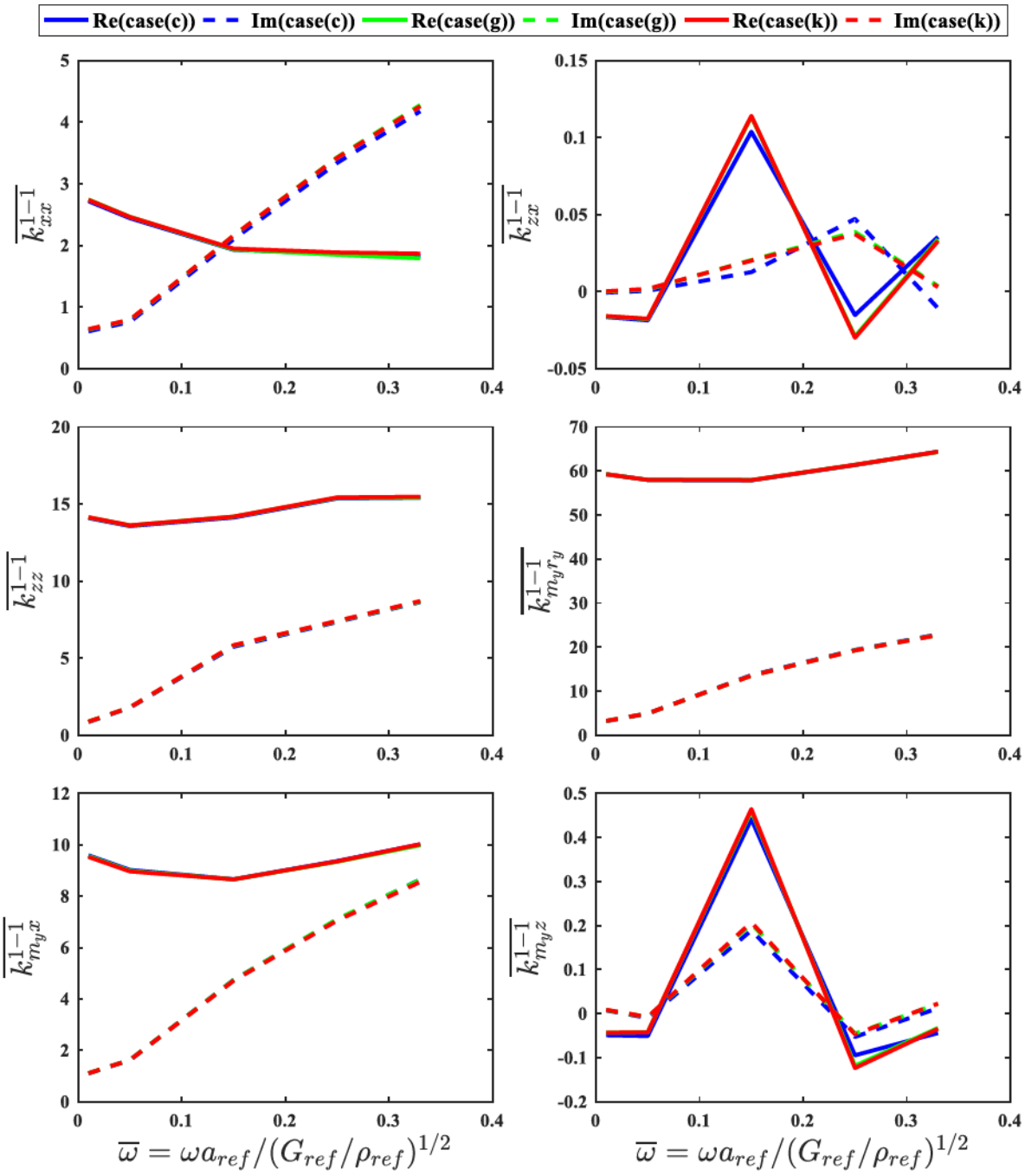

(a) Primary impedance functions in $\mathbf{K}^{1-1}$

Figure 4.22 *Impedance functions for various layer discretization in the disturbed zone for 2×2 pile group.*

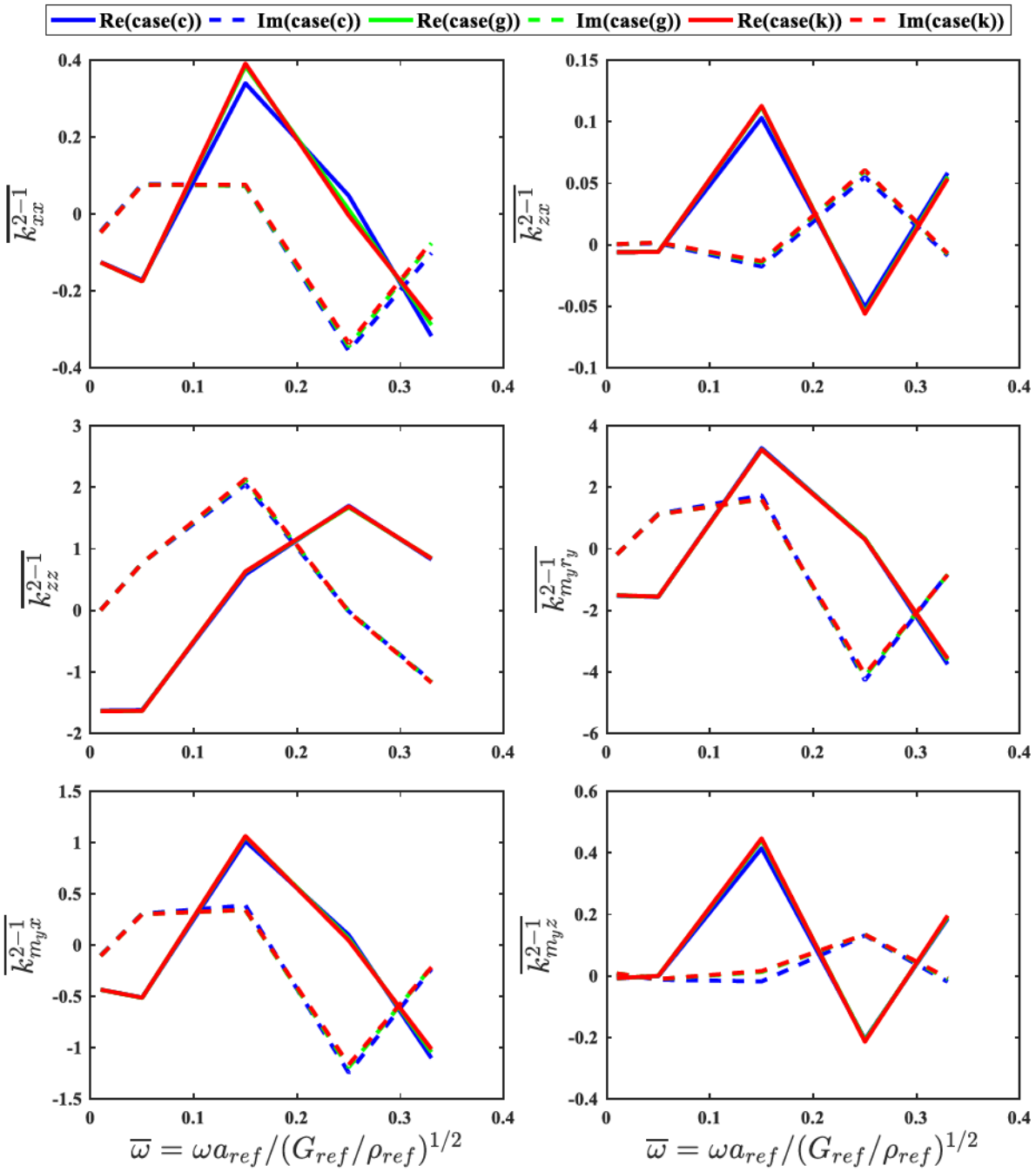

(b) Primary impedance functions in $\mathbf{K}^{2-1}$

Figure 4.22 *(continued)*

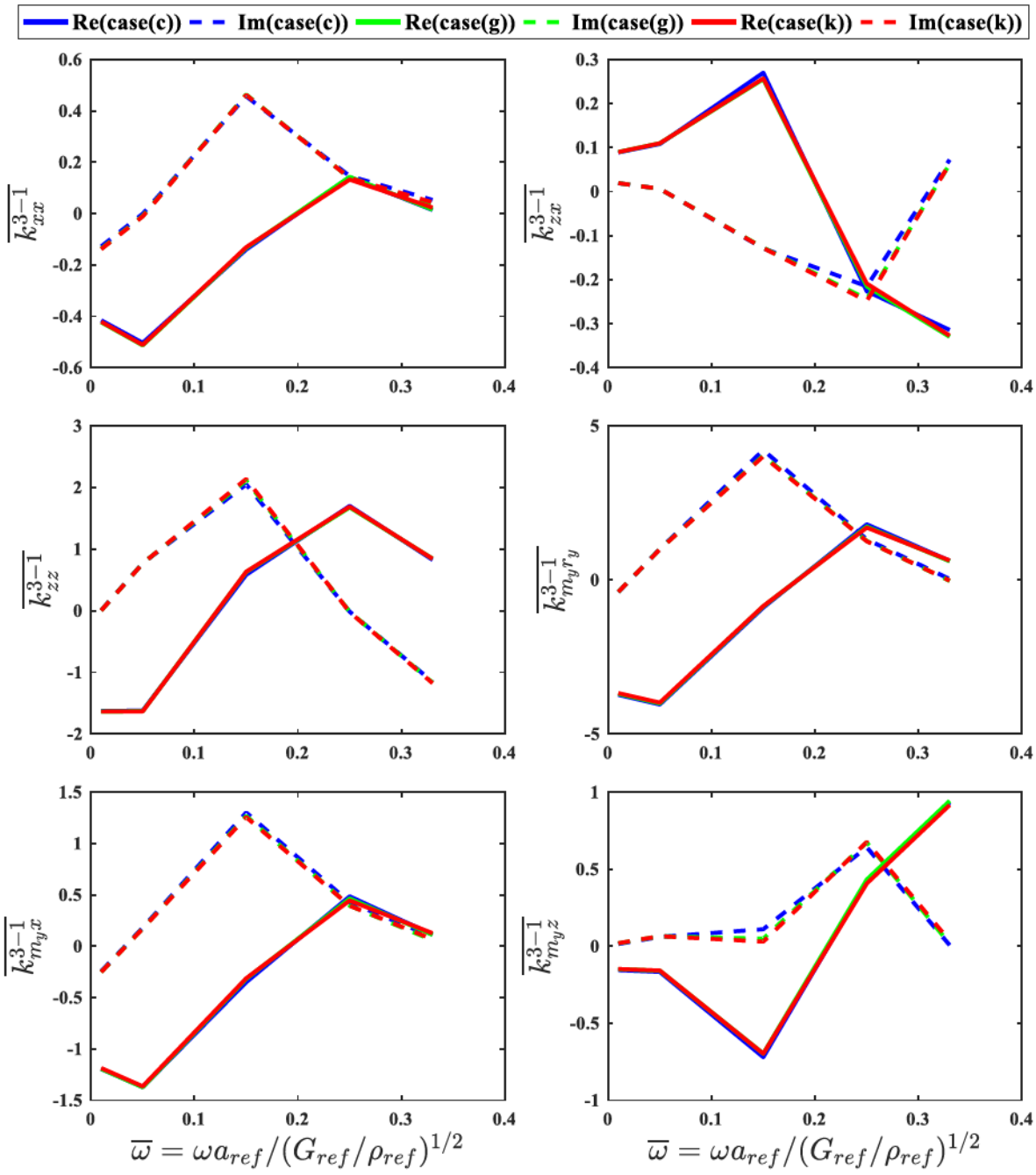

(c) Primary impedance functions in $\mathbf{K}^{3-1}$

Figure 4.22 *(continued)*

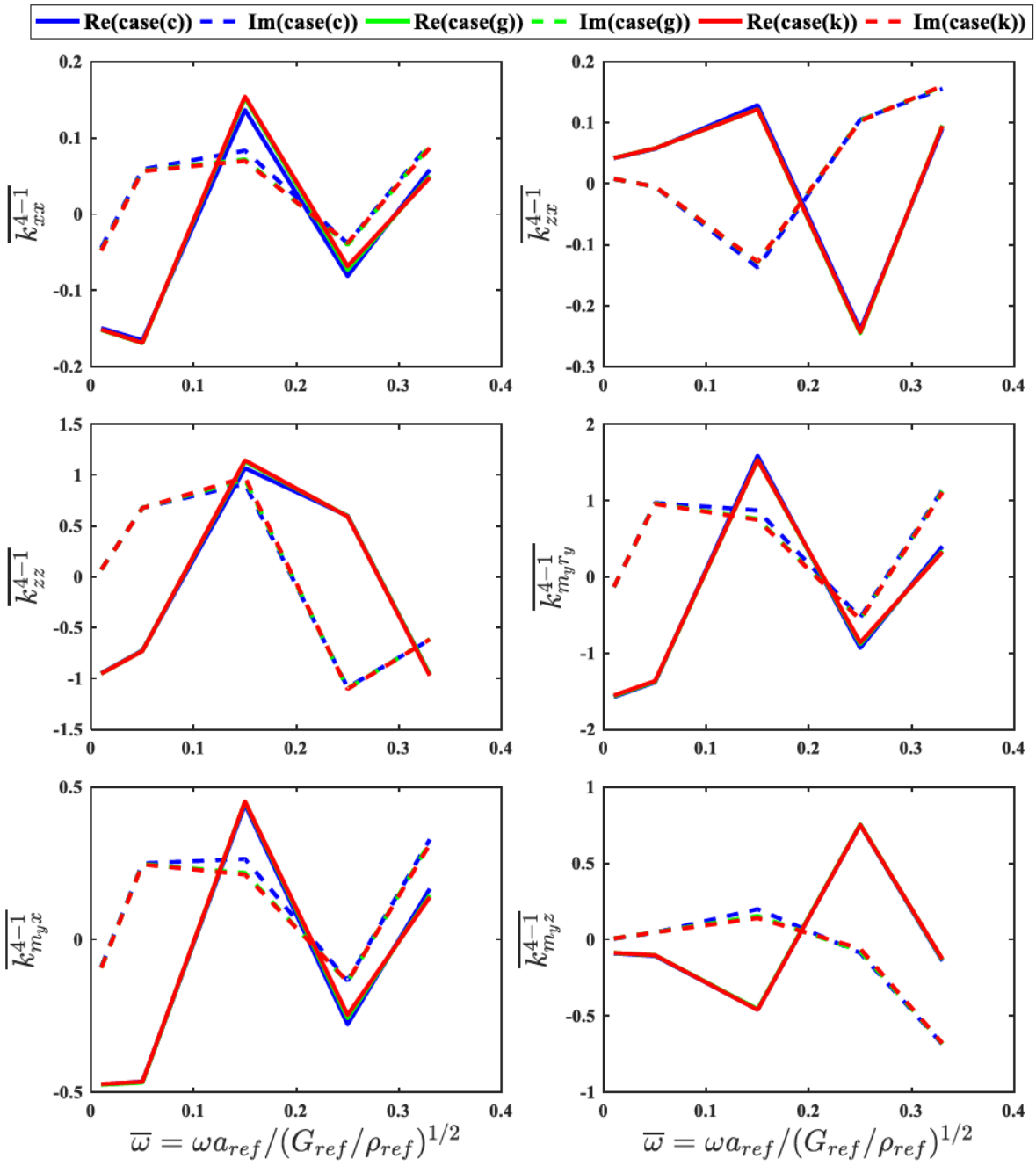

(d) Primary impedance functions in $\mathbf{K}^{4-1}$

Figure 4.22 *(continued)*

4.4 Pile Group Gapping

Gaps are commonly observed between piles and surrounding soil near the ground surface due to pile installation and lateral excitation (e.g., Rollins et al. 2003a; Stewart et al. 2007; Chandrasekaran et al. 2013). Formation of gaps normally accounts for the lower experimental impedances compared to the theoretical values (e.g., Manna and Baidya 2009), and incorporating gapping into theoretical or numerical models may lead to better consistency (e.g., Blaney and O'Neil 1986; El Naggar and Novak 1996; Ashlock and Fotouhi 2013). Thus it is essential to examine the influence of gapping on impedance functions for pile groups.

While the depth of gapping is difficult to be accurately measured or controlled in physical tests, it can be well determined or specified in numerical analyses. Two methods modeling gapping in BEM models were studied in previous studies. Ashlock (2006) modeled separation at pile-soil interface using double elements, at which zero tractions were prescribed. Half of the elements simulated the pile surface and the other half simulated the soil surface. Triple nodes were deployed on shared edges of soil, unembedded pile segment, and embedded pile segment for prescribing individual boundary and continuity conditions (Figure 4.23). The other approach adopted by Fotouhi (2014) was removing the top no-contact zone, shortening embedded pile length, and simultaneously increasing the unembedded pile length for compensation (Figure 4.24). Both approaches have their own limitations. The zero traction at pile and soil interfaces in the first approach may not be realistic since gap could temporarily enclose during steady-state vibration and hence transfer reaction between pile and soil. Even if a gap exists throughout vibration, the zero-traction boundary condition cannot prevent the pile elements and the soil elements from penetrating into each other in BEM simulation. Removing the entire top layer in the second approach not only eliminated the possible temporary contact between pile and soil, but also excluded the existence of the top soil layer

in the far region. This may affect distribution of soil self-weight and wave propagation, especially near ground surface. In a case of 2×2 pile group when a broader area is influenced than the single pile, drawback of the second approach might be more drastic. Therefore the first approach is applied in this study for pile group problems. Due to the high sensitivity of dynamic response of piles to the gapping, the lengths of gap studied herein are 1-element long (termed as short gap) and 2-element long (termed as long gap), corresponding to 0.317 m ($1.45d$) and 0.634 m ($2.9d$), respectively. To exclude effects of inclusion, a BEM model of 2×2 pile group in the half-space was reanalyzed with gapping. The BEM model for the long gap is shown in Figure 4.25 as an example.

The resulting impedance functions from BEASSI are plotted in Figure 4.26. The influence of gap on primary impedance functions in $\mathbf{K}^{1-1}$ is noticeable. $\bar{k}_{xx}^{1-1}$ is greatly reduced, which is consistent with the fact that the horizontal resistance on pile is mainly developed along the top portion. A longer gap results in a lower stiffness and damping. For $\bar{k}_{zz}^{1-1}$ and $\bar{k}_{m_y r_y}^{1-1}$, stiffnesses for the short gap are close to the case without gap at high frequencies but show deviation at low frequencies. Damping show the opposite trend. For the case of long gapping, both real and imaginary parts exhibit lower amplitudes at all frequencies. For $\bar{k}_{m_y x}^{1-1}$, short gapping does not significantly change the stiffnesses but decreases the damping. As for impedance functions in off-diagonal elementary matrices, it is difficult to describe the effect of gapping due to the strongly frequency-dependent pile-soil interaction. The general finding is that longer gap results in lower amplitude for impedance. The reduction is more significant for the horizontal impedance ($\bar{k}_{xx}$) and the coupled rotation- and vertical-horizontal impedances (e.g., $\bar{k}_{m_y x}, \bar{k}_{zx}$) than the vertical impedance ($\bar{k}_{zz}$). In the other words, gapping can

substantially decrease the degree of dynamic pile-soil-pile interaction, especially in horizontal direction.

The resulting accelerance functions are compared in Figure . The long gapping suggests lowest resonant frequencies and the short gapping results in highest resonant amplitudes for the vertical modes. As the length of gap increases, the lateral modes show lower resonant frequencies and higher amplitudes, and the rocking modes for A_{xc}/VE and A_{rc}/VE exhibit similar decreasing trends for the resonant frequencies.

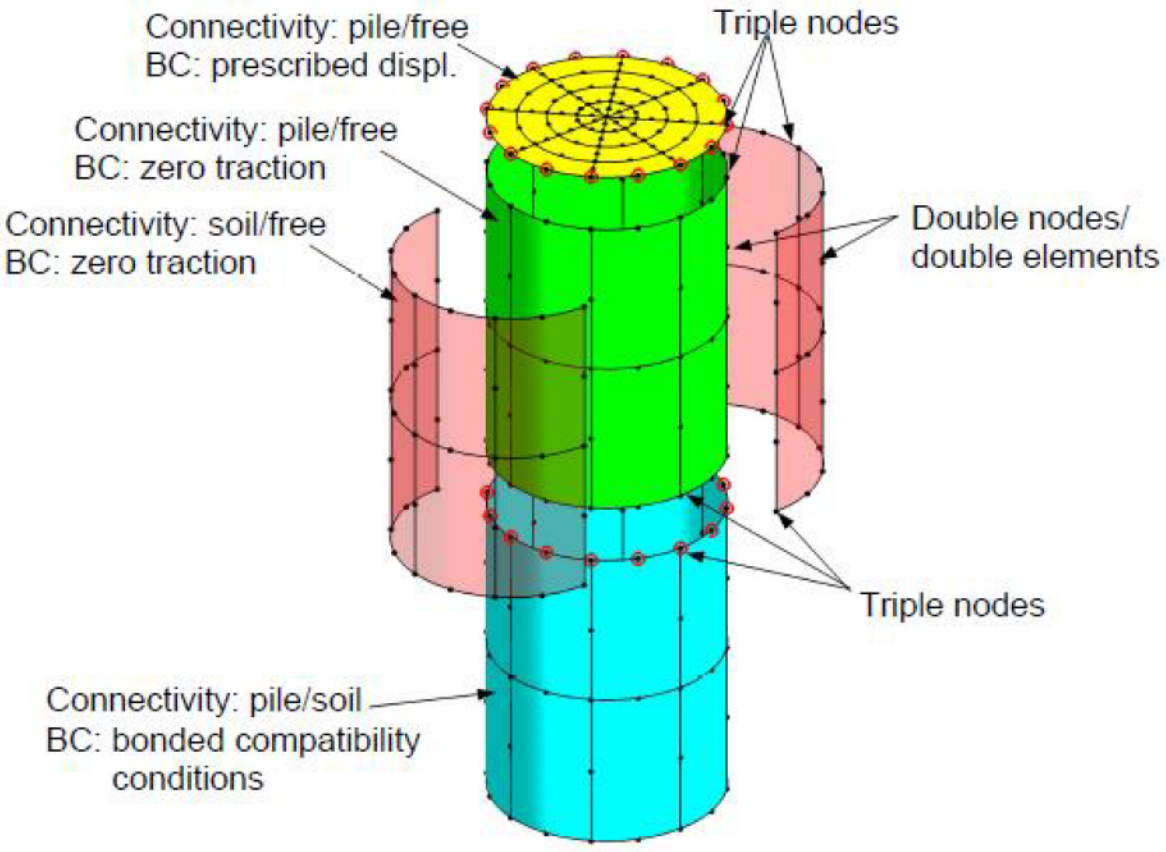

Figure 4.23 *Differentiating pile and soil using double elements (Ashlock 2006).*

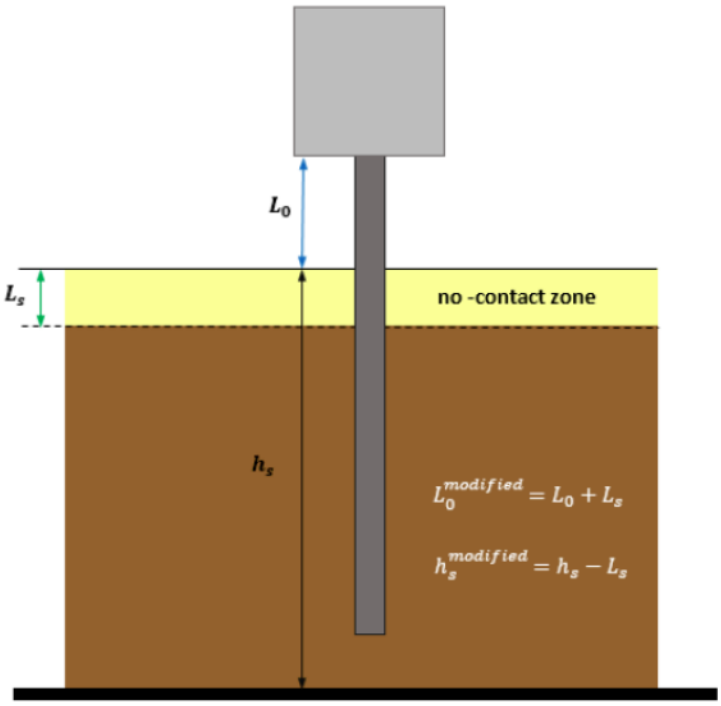

Figure 4.24 *Removing the entire top layer in BEA (Fotouhi 2014).*

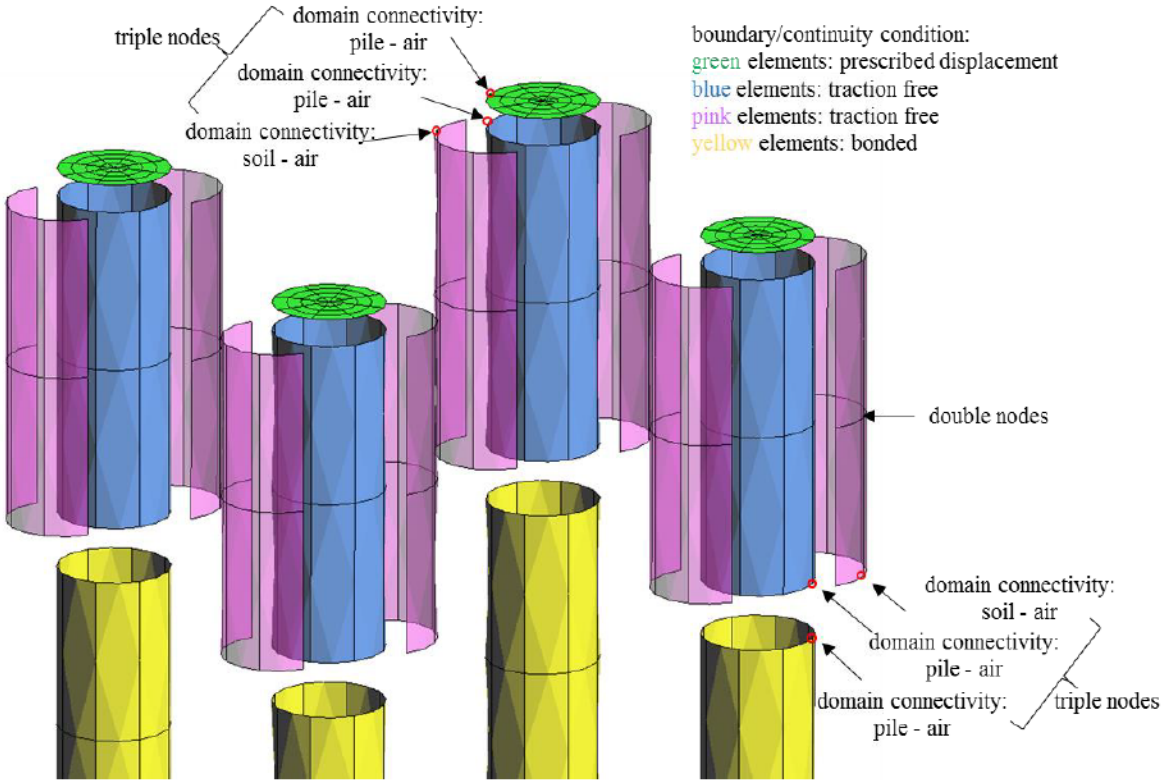

Figure 4.25 *Modeling 2-element-long gapping for 2×2 pile group.*

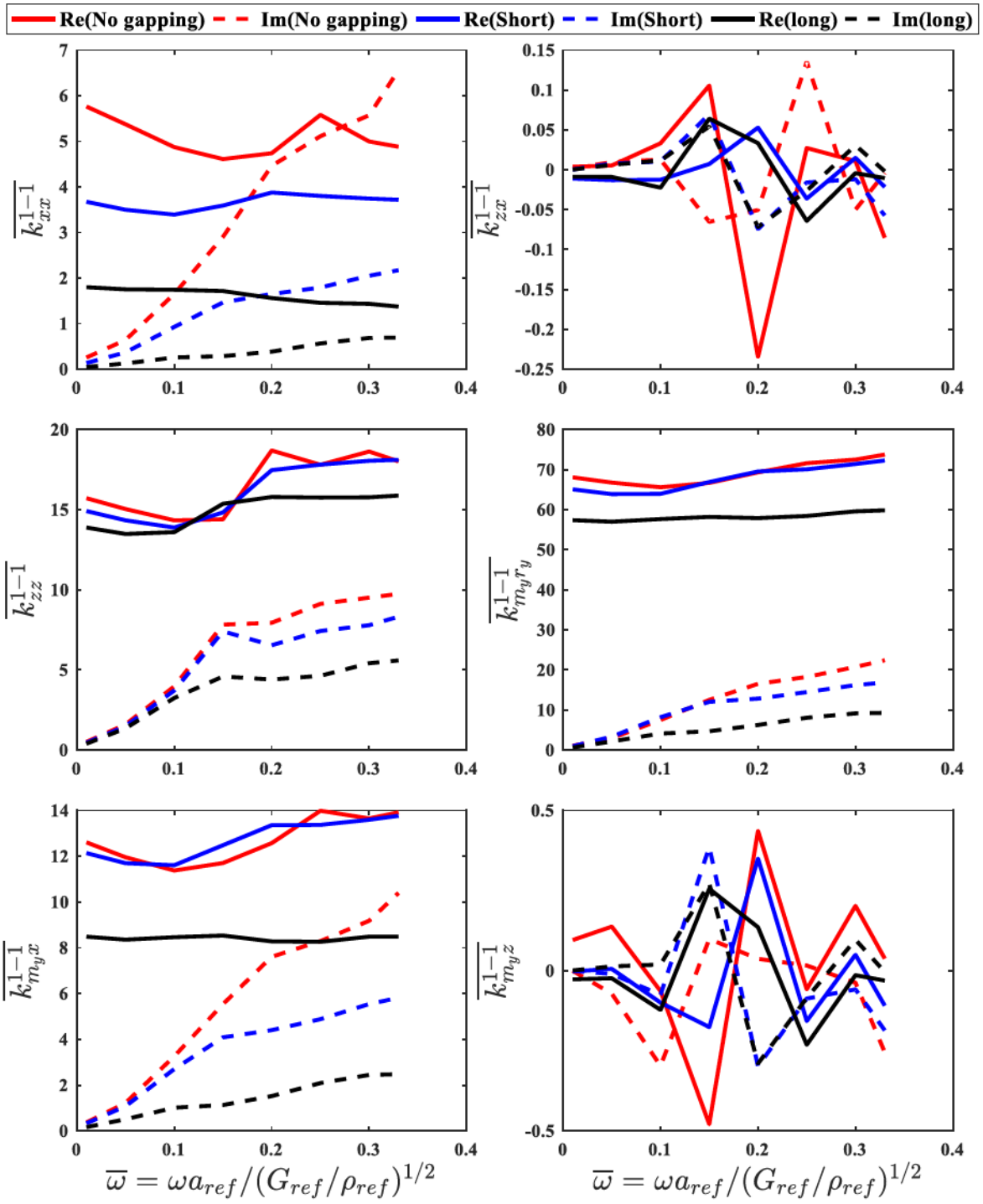

(a) Primary impedance functions in $\mathbf{K}^{1-1}$

Figure 4.26 *Influence of gapping on impedance functions of a 2×2 pile group.*

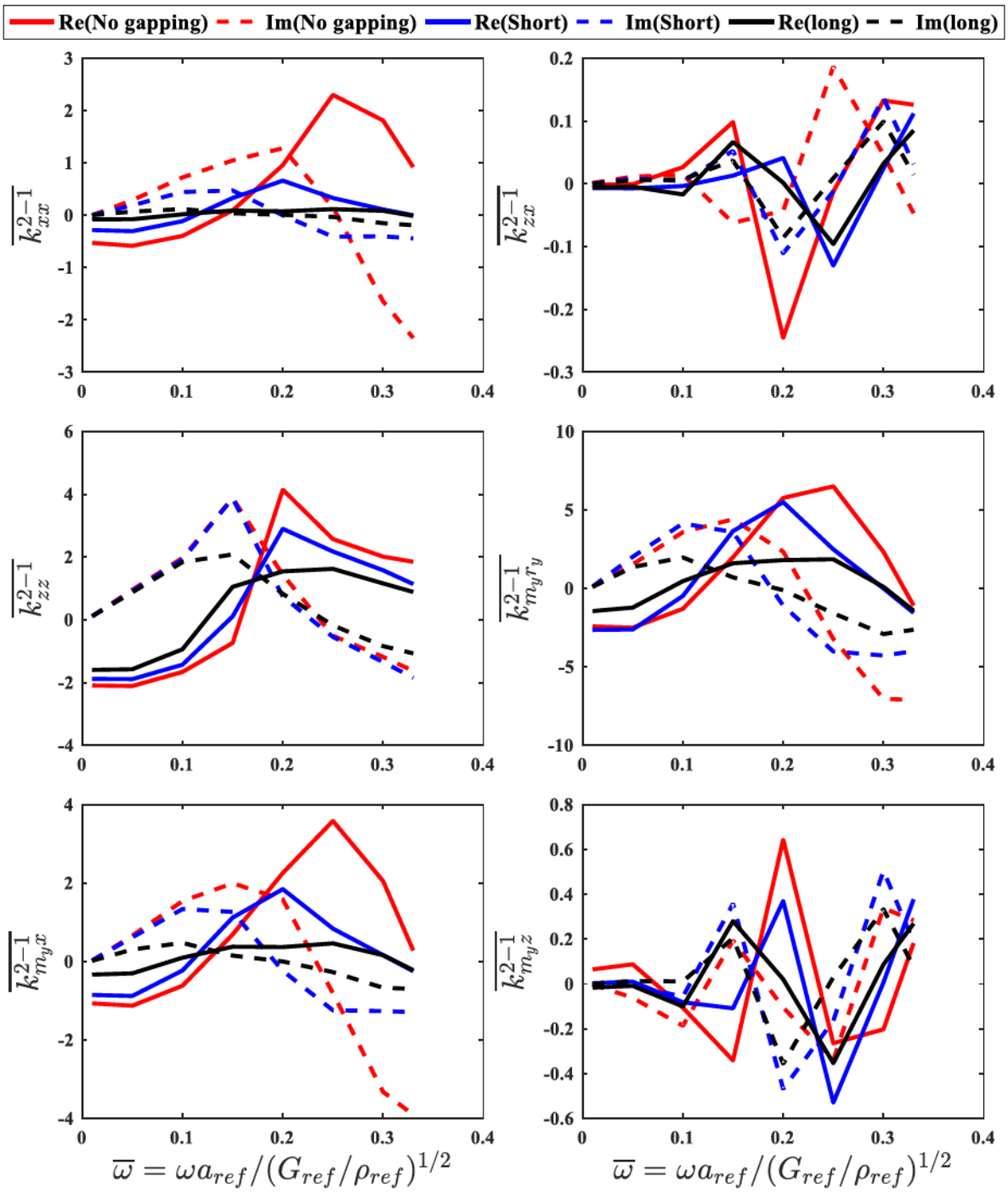

(b) Primary impedance functions in $\mathbf{K}^{2-1}$

Figure 4.26 *(continued)*

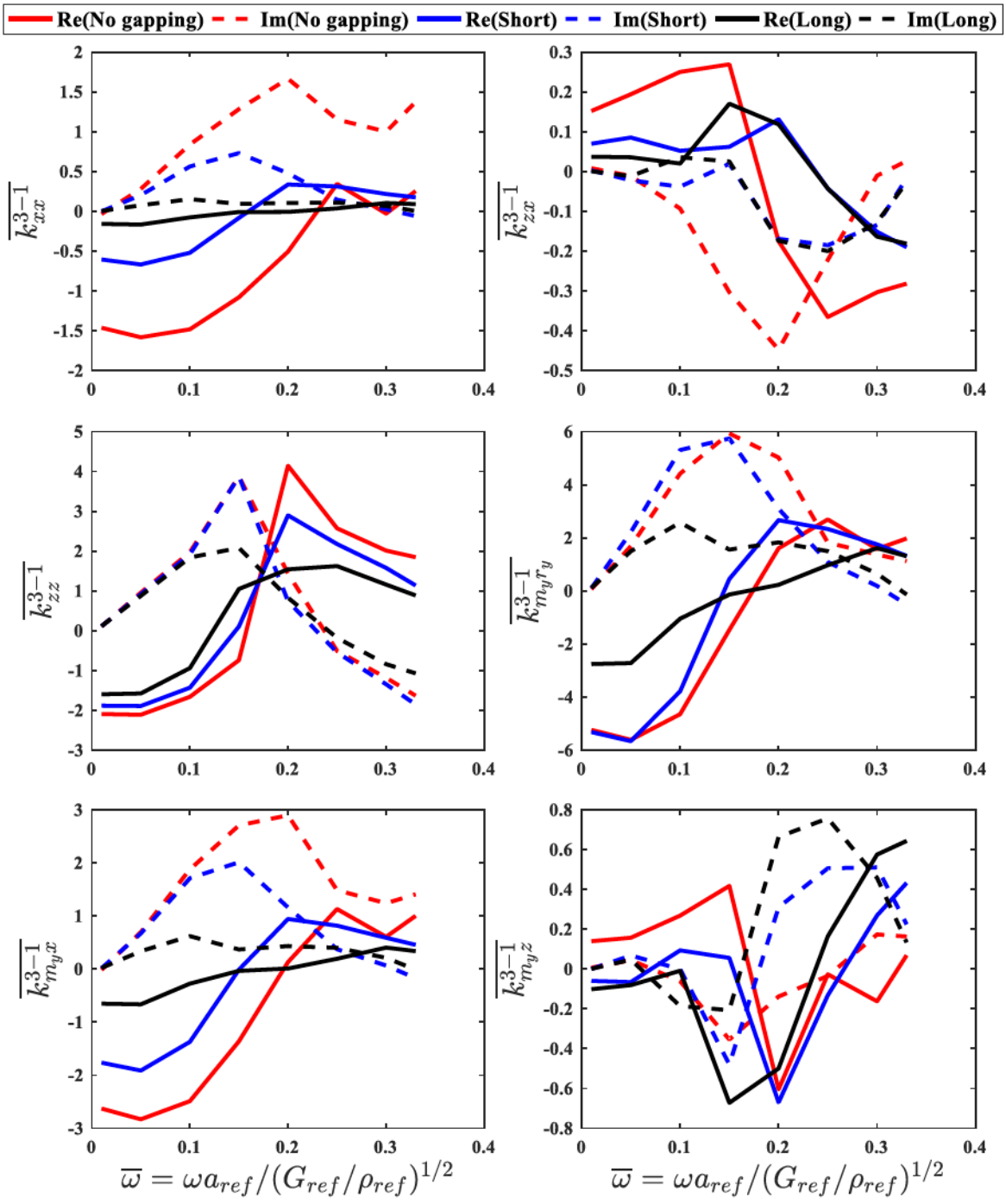

(c) Primary impedance functions in $\mathbf{K}^{3-1}$

Figure 4.26 *(continued)*

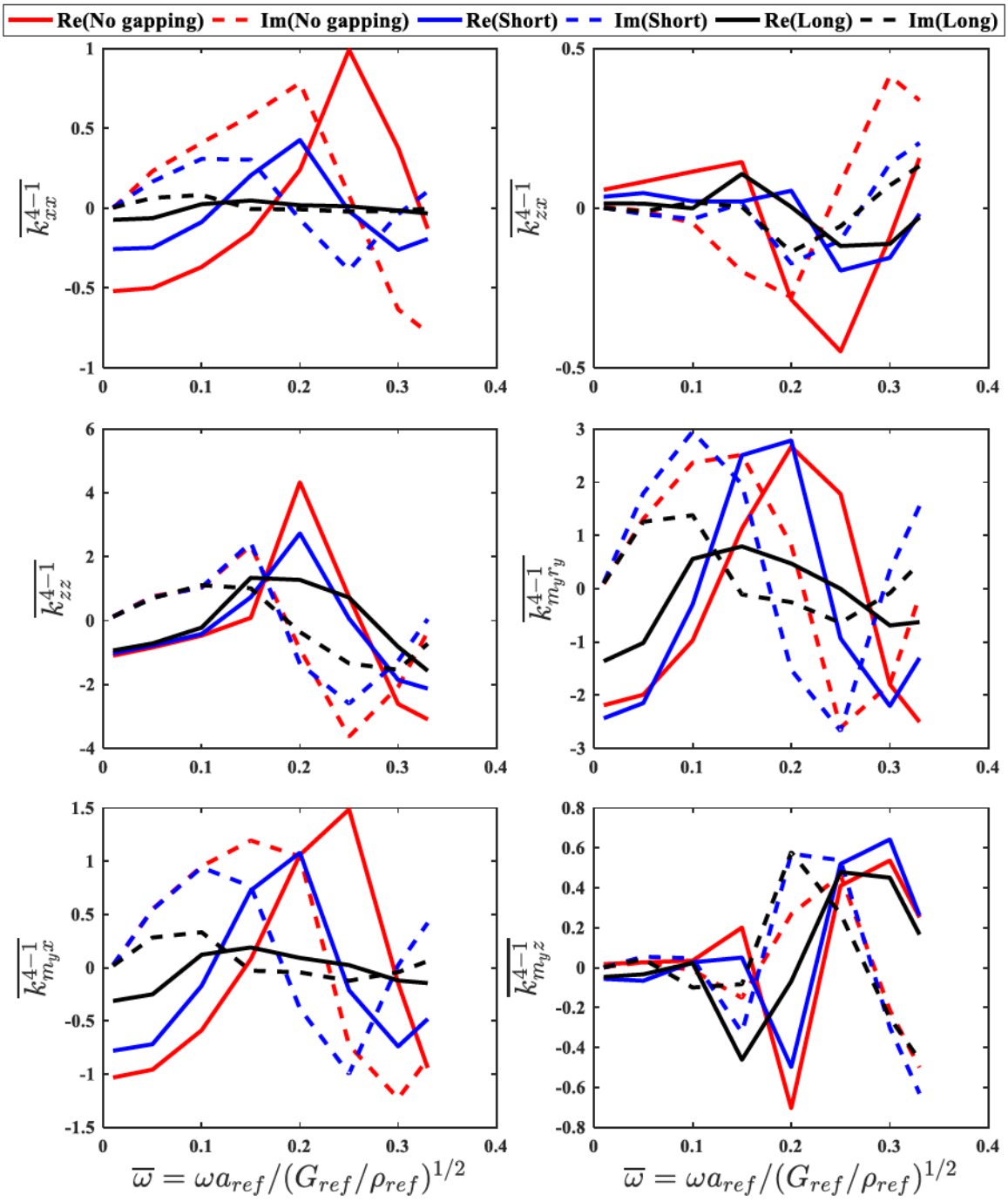

(d) Primary impedance functions in $\mathbf{K}^{4\text{-}1}$

Figure 4.26 *(continued)*

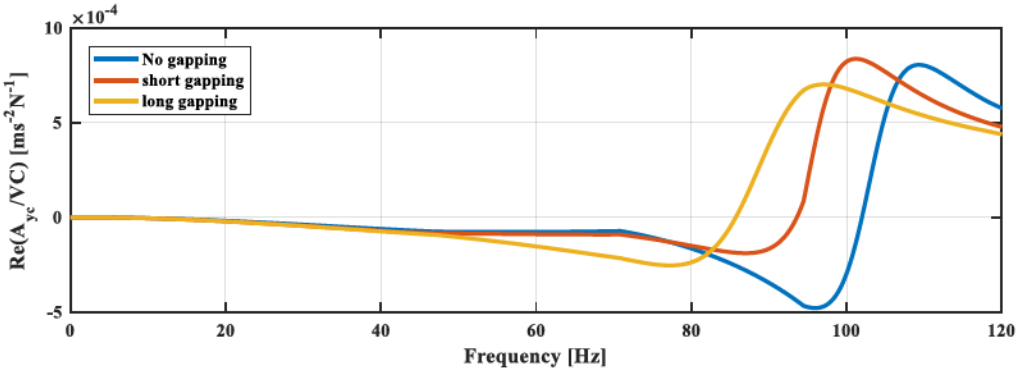

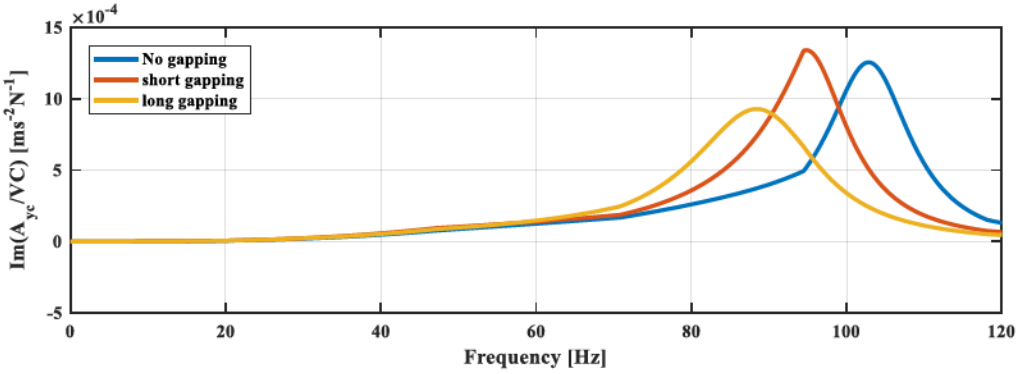

(a) Influence on A_{yc}/VC

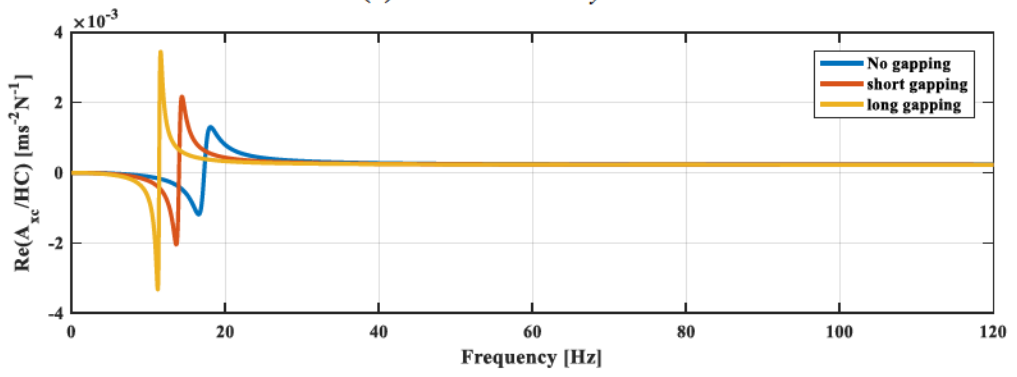

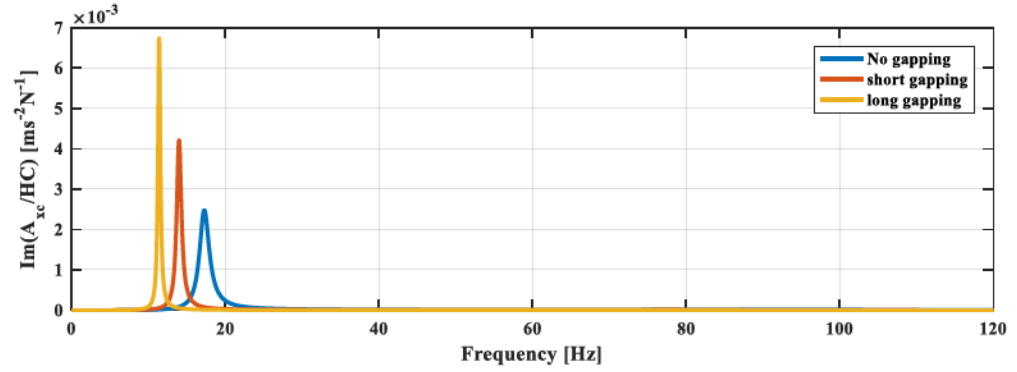

(b) Influence on A_{xc}/HC

Figure 4.27 *Sensitivity of accelerance functions to variations in soil minimum material damping ratio in half-space for pile group.*

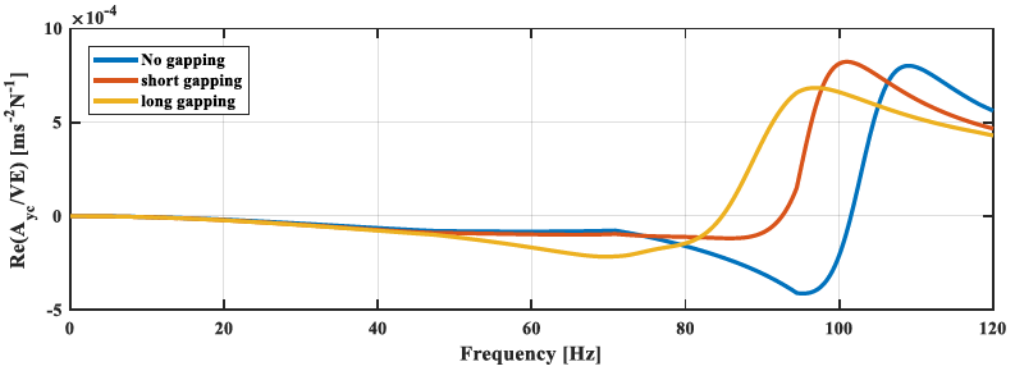

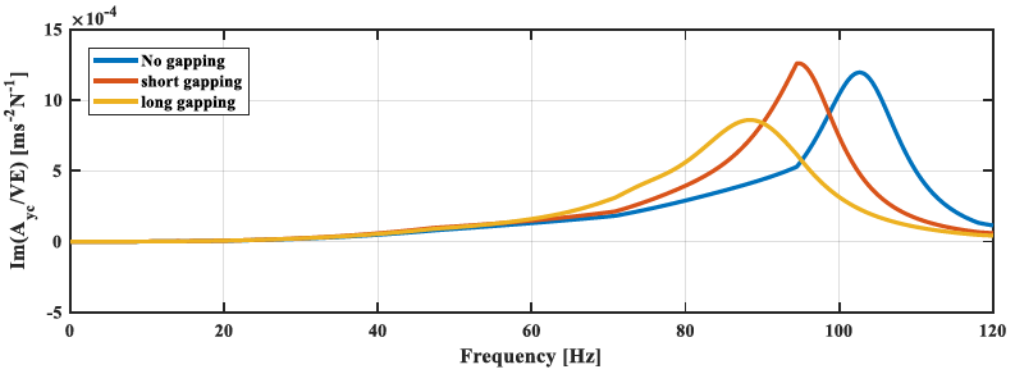

(c) Influence on A_{yc}/VE

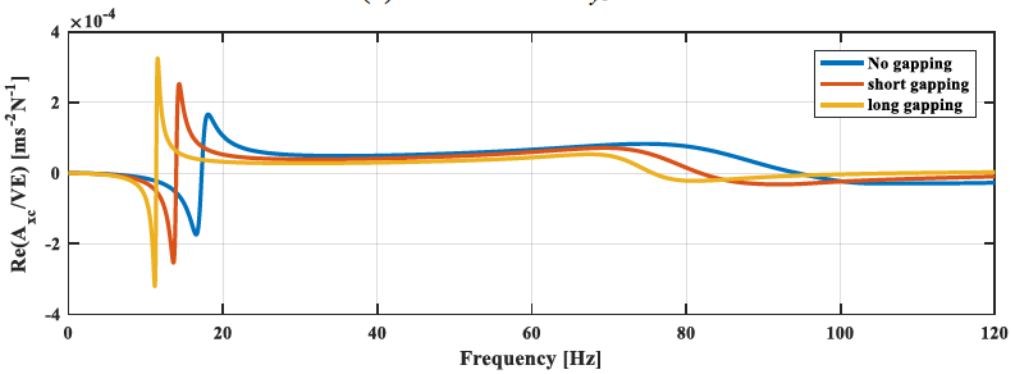

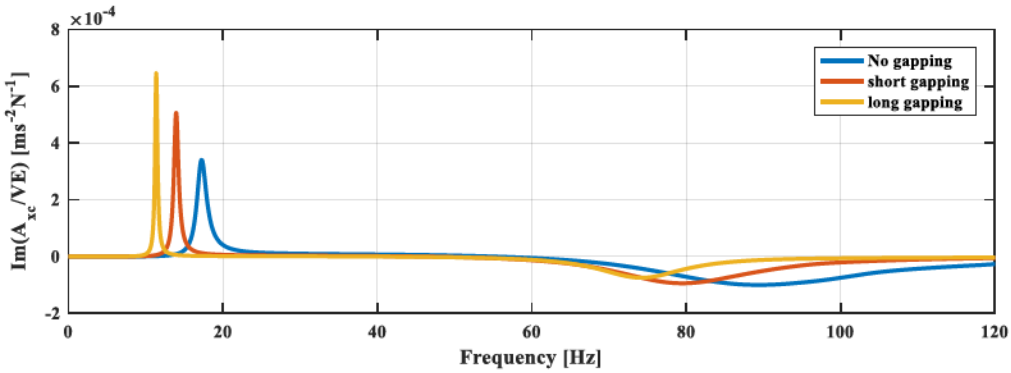

(d) Influence on A_{xc}/VE

Figure 4.27 *(continued)*

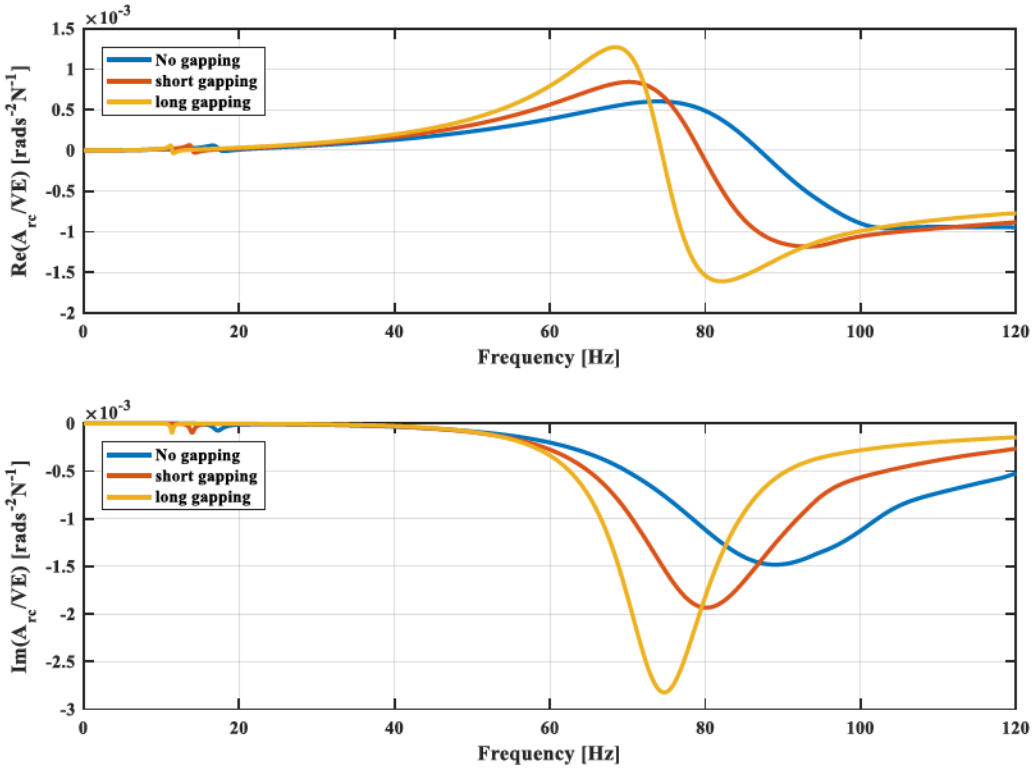

(e) Influence on A_{rc}/VE

Figure 4.27 *(continued)*

4.5 Pile Spacing

Pile spacing is an important factor in dynamics of pile group. Most previous experimental studies focused on close pile spacings with spacing-to-diameter ratios (S/*d*) below 10 and S/*d*=3 was most commonly studied (see Table 1.1). S/*d* ratios lower than 2 are not recommended in practice due to construction concern and a high S/d ratios make pile-soil-pile interaction less significant. Parametric studies on pile spacing by full-scale in-situ tests such as by Rollins et al. (2006), are time-consuming and costly. Demanding test conditions such as a large test field, complicated loading frames, and enormous load capacity are required. Small-scale laboratory tests (e.g., Goit et al. 2013), though economical using model piles and soils, may not be able to reveal true physical essence. On the other hand, it is pragmatic to analyze variable spacings using BEM models simply by translation of existing pile meshes

without increasing computational intensity. More importantly, all parameters other than spacing rigorously remain constant, which is arduous in physical tests.

In this study, four spacing-to-diameter ratios for a 2×2 pile group in layered soils are analyzed – 3, 4.174, 7, and 9. No disturbed zone is included to exclude influence of size and shape of the disturbed zone, as well as soil properties within the disturbed zone. Impedance functions are extremely shaky with frequency, exhibit various trends, and thus are not suitable for presenting the influence of pile spacing. Instead, presenting the response of the entire pile group is more helpful. Thus the results are presented in forms of directional group impedance (Figure 4.28), and group efficiency ratio (Figure 4.29).

Group impedances in the vertical and horizontal directions exhibit similar trends, such that with a larger spacing, the peaks occur at a lower frequency with a lower amplitude. At frequencies below $\bar{\omega} = 0.1$, larger spacings result in higher stiffnesses and dampings. As for group impedances in the rocking and torsional directions, peak frequencies still follow the same trends as in the vertical and horizontal directions. However, spacing becomes predominant in affecting peak amplitudes, which makes the frequency-dependent variation less significant within frequency range of interest.

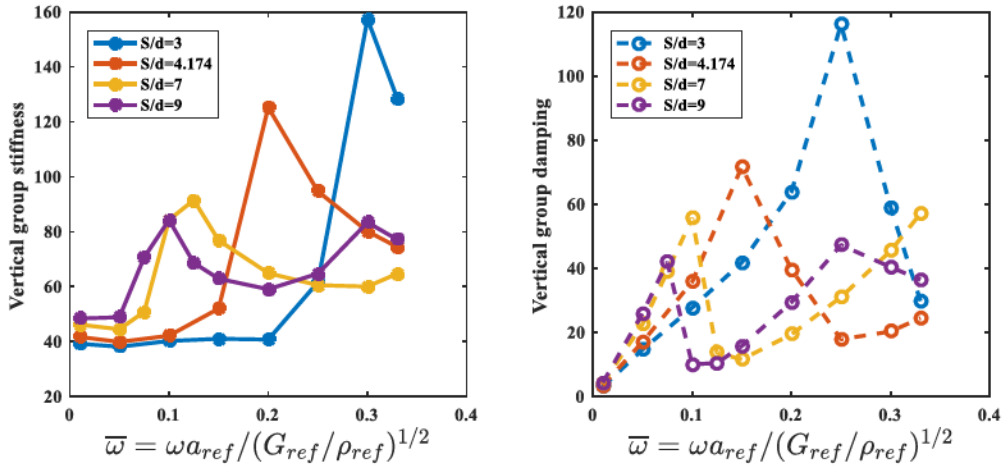

(a) Vertical group stiffness and damping

Figure 4.28 *Group impedance for a 2×2 pile group.*

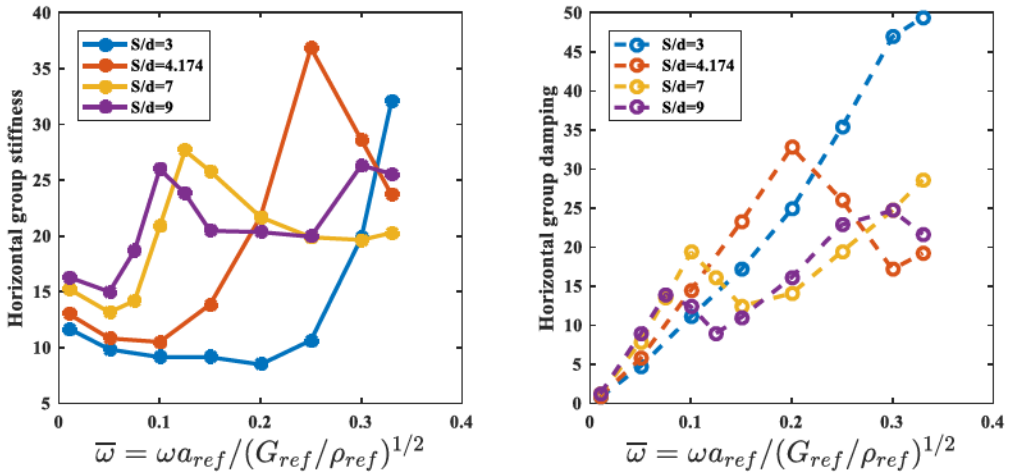

(b) Horizontal group stiffness and damping

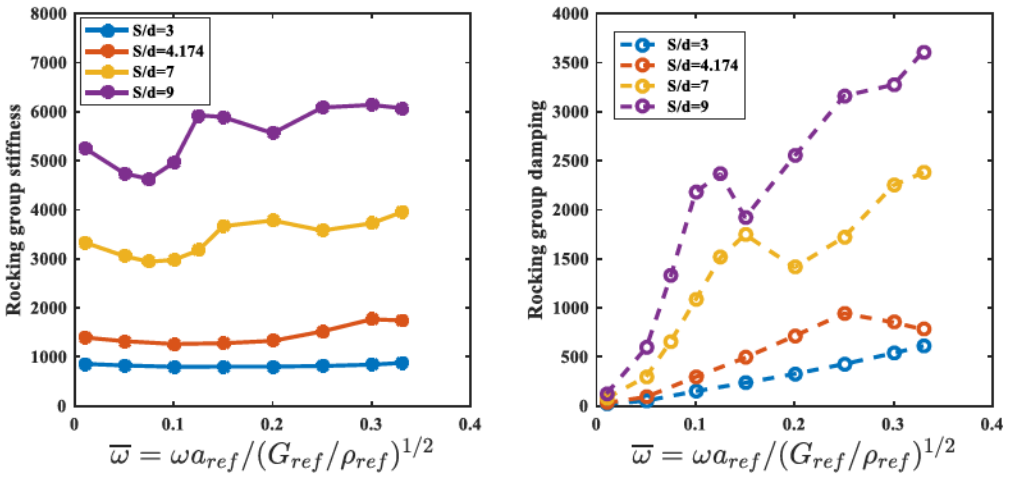

(c) Rotational group stiffness and damping

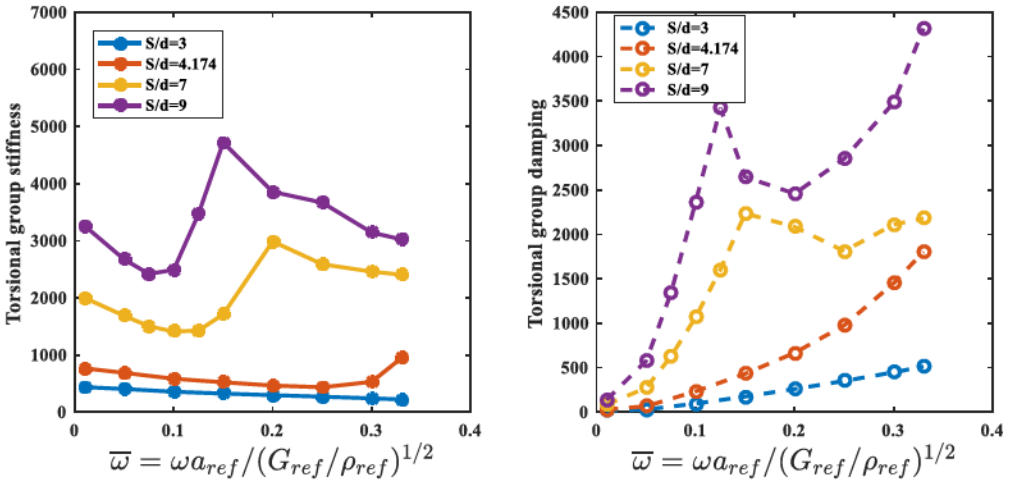

(d) Torsional group stiffness and damping

Figure 4.28 *(continued)*

GER was widely used to interpret dynamics of pile group in previous studies. However, the results were commonly reported for a limited frequency range. Novak and Mitwally (1990) calculated GER up to $\bar{\omega}$ of 0.25. Han and Vaziri (1992), and Manna and Baidya (2010) calculated GER up to 70 Hz and 50 Hz, respectively. Within the limited frequency range GERs appear to be monotonic, either increasing or decreasing. When frequency increases to $\bar{\omega}$ of 0.33 or f of 155 Hz in this study, however, GER shows fluctuation with frequency above and below unity, in both vertical and horizontal directions. The phenomena are observable for all S/*d* ratios. To be specific, for lower S/*d* ratios, the first GER peak has greater amplitude and occurs at higher frequency. As S/*d* increases, GER peak amplitudes and the corresponding frequencies decrease, except that the damping ratio in the horizontal direction remain approximately constant. The maximum and minimum GERs for vertical and horizontal vibrations for the examined case are summarized in Table 4.4. GER varies from 0.42 to 3.00 in the vertical direction and from 0.4 to 1.94 in the horizontal direction. The GER values provide insights in engineering design to achieve optimum ovreall performance of pile groups and highest safety factor for designated frequency range.

As a summary, pile spacing has substantial influence on the overall response of pile group, and the influence is strongly frequency-dependent. For vertical and horizontal group impedances, amplitude is mainly frequency-dependent. For rocking and torsional group impedances, the increase in spacing completely overshadow the effect of frequency. As a general trend, smaller spacing results in higher amplitude of peaks for group impedance and GER. For a given frequency range, the highest GER is achievable by specifying an optimum pile spacing.

Table 4.4 *Maximum and minimum GER values.*

Direction	Parameters	Maximum	Minimum
Vertical	stiffness	2.20	0.56
	damping	3.00	0.42
Horizontal	stiffness	1.70	0.40
	damping	1.94	0.70

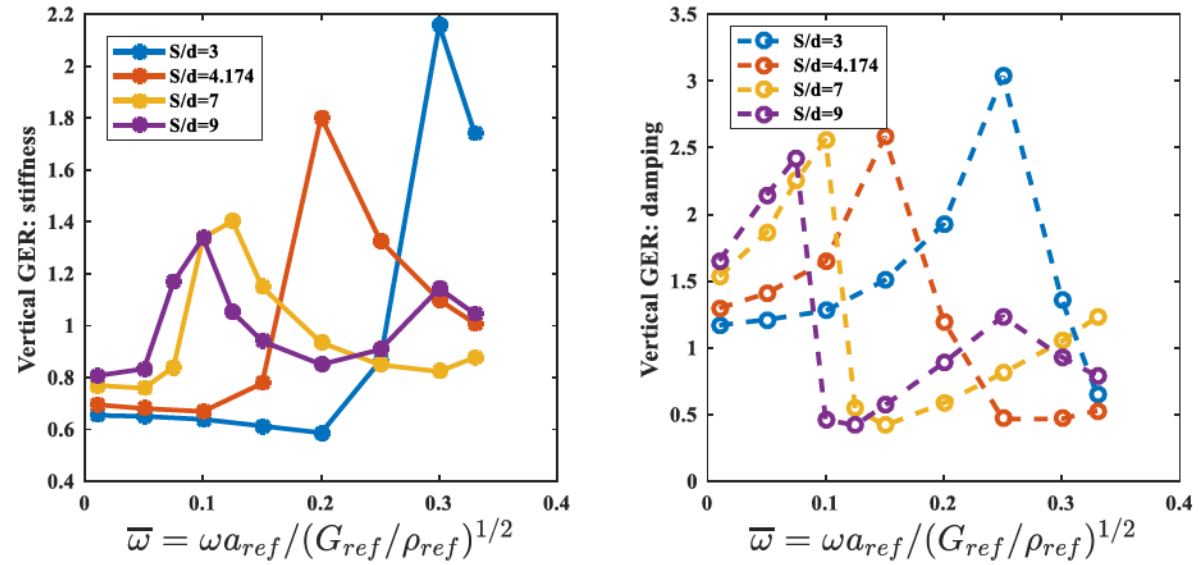

(a) Vertical GER

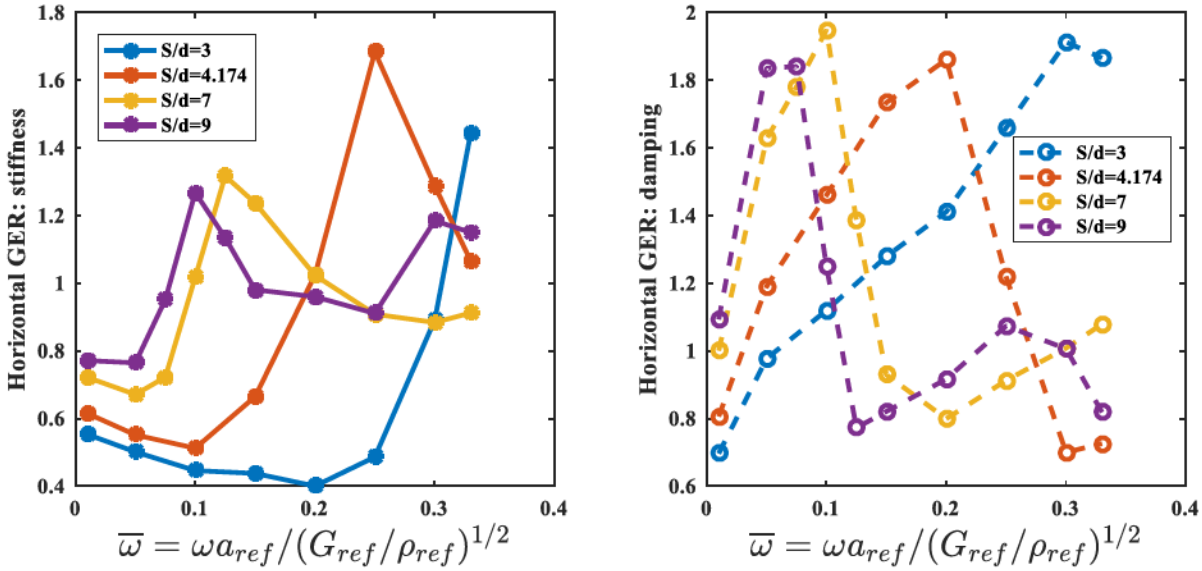

(b) Horizontal GER

Figure 4.29 *Group efficiency ratio for a 2×2 pile group in the vertical and horizontal directions.*

4.6 Size of Disturbed Zone

The size of the disturbed zone proposed in Section 3.6.1 is characterized by pile length and inclusion radius. The pile length must be conform to the actual pile length in tests or designs and thus is relatively affirmative. The disturbed-zone radius, however, is more subjective and flexible, especially for various pile group patterns and spacings. In this study, the disturbed-zone radius is an arbitrary value of $(\sqrt{2}/2)S+5r$. In this section parametric study is performed to justify the proposed disturbed-zone radius and quantify its influence on impedance functions.

The case study in Section 3.8.2 is reanalyzed with two additional inclusion radii of $(\sqrt{2}/2)S+3r$ and $(\sqrt{2}/2)S+7r$. The resulting impedances are compared in Figure 4.31. Negligible differences are found for $\bar{k}_{zz}^{1-1}$ and $\bar{k}_{m_y r_y}^{1-1}$. Impedances coupled with vertical motion such as $\bar{k}_{zx}^{1-1}$ and $\bar{k}_{m_y z}^{1-1}$ exhibit relatively greater deviations. But due to their small values, such deviations have minor effect on accelerance functions. Slight differences are found in $\bar{k}_{xx}^{1-1}$ and $\bar{k}_{m_y x}^{1-1}$ for inclusion radii of $(\sqrt{2}/2)S+5r$ and $(\sqrt{2}/2)S+7r$. General agreement is observed for all off-diagonal elementary matrices, except for only slight deviations at certain frequencies. In terms of accelerance functions (Figure 4.32), the differences for three cases are less significant. Inclusion radius of $(\sqrt{2}/2)S+3r$ induces slightly higher resonant amplitudes. To be concluded, the influence of inclusion radius is small and the proposed inclusion radius of $(\sqrt{2}/2)S+5r$ is considered as appropriate.

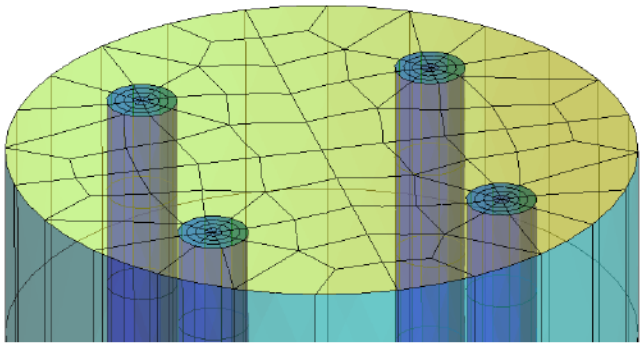

(a) Radius of the disturbed zone = $(\sqrt{2}/2)S + 3r$

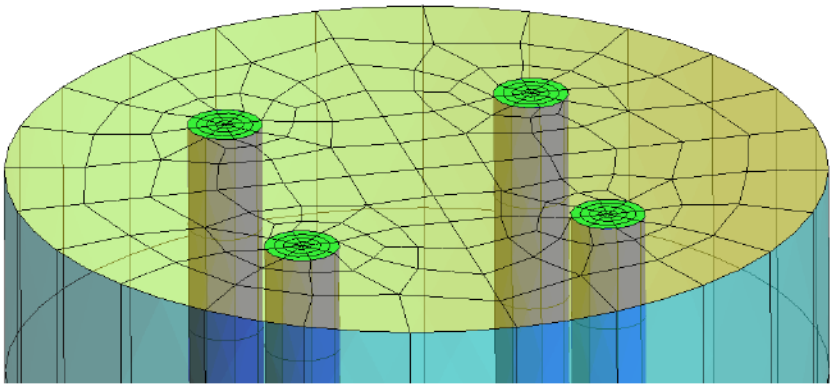

(b) Radius of the disturbed zone = $(\sqrt{2}/2)S + 5r$

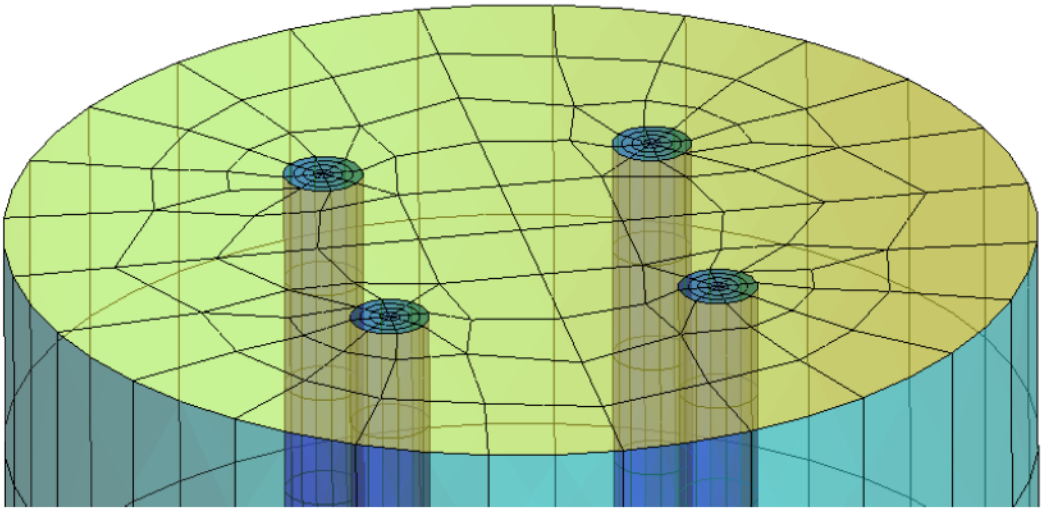

(c) Radius of the disturbed zone = $(\sqrt{2}/2)S + 7r$

Figure 4.30 *BEM models for parametric study on radius of the disturbed zone.*

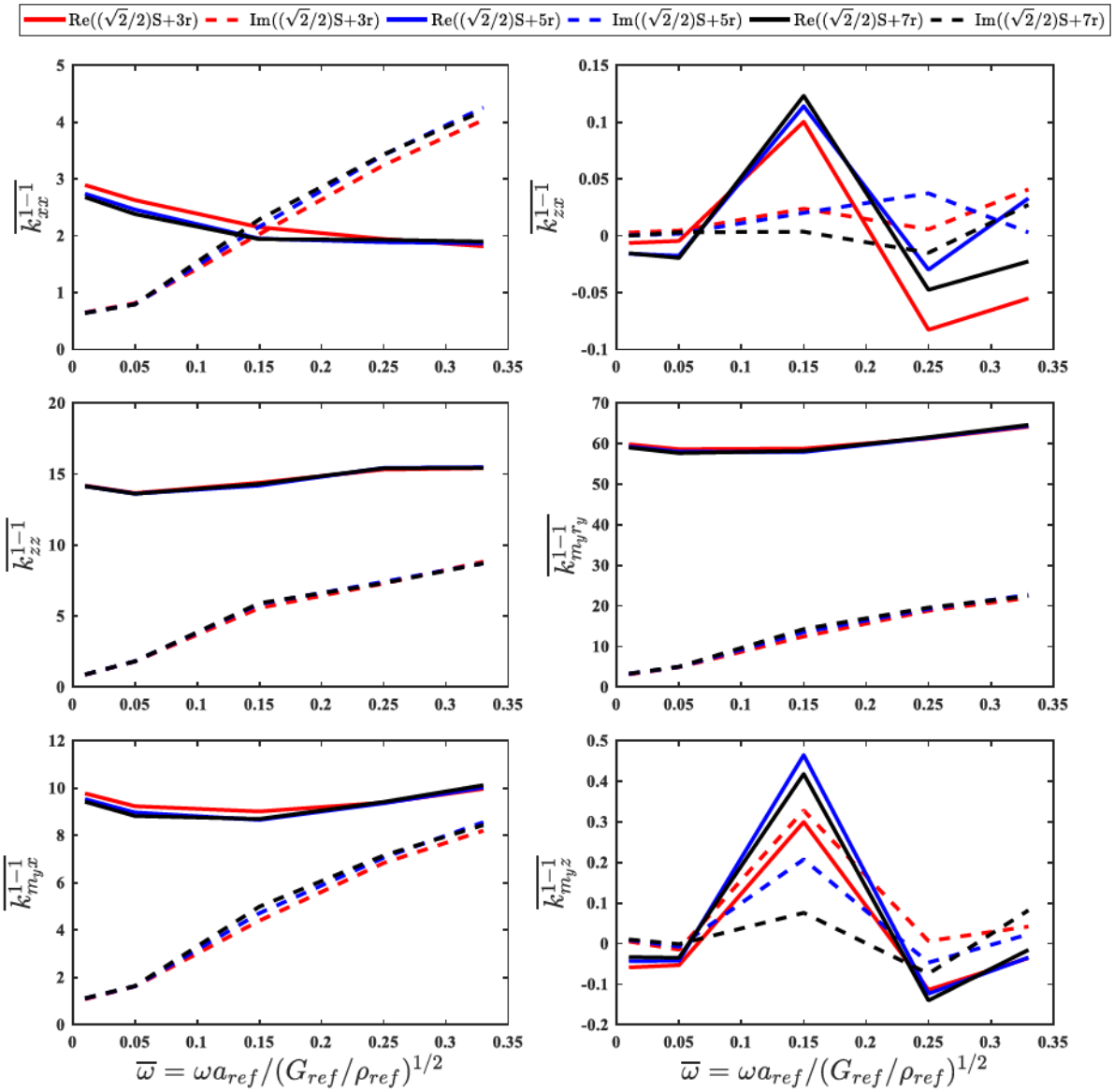

(a) Primary impedance functions in $\mathbf{K}^{1\text{-}1}$

Figure 4.31 *Comparison of impedance functions for various inclusion radii.*

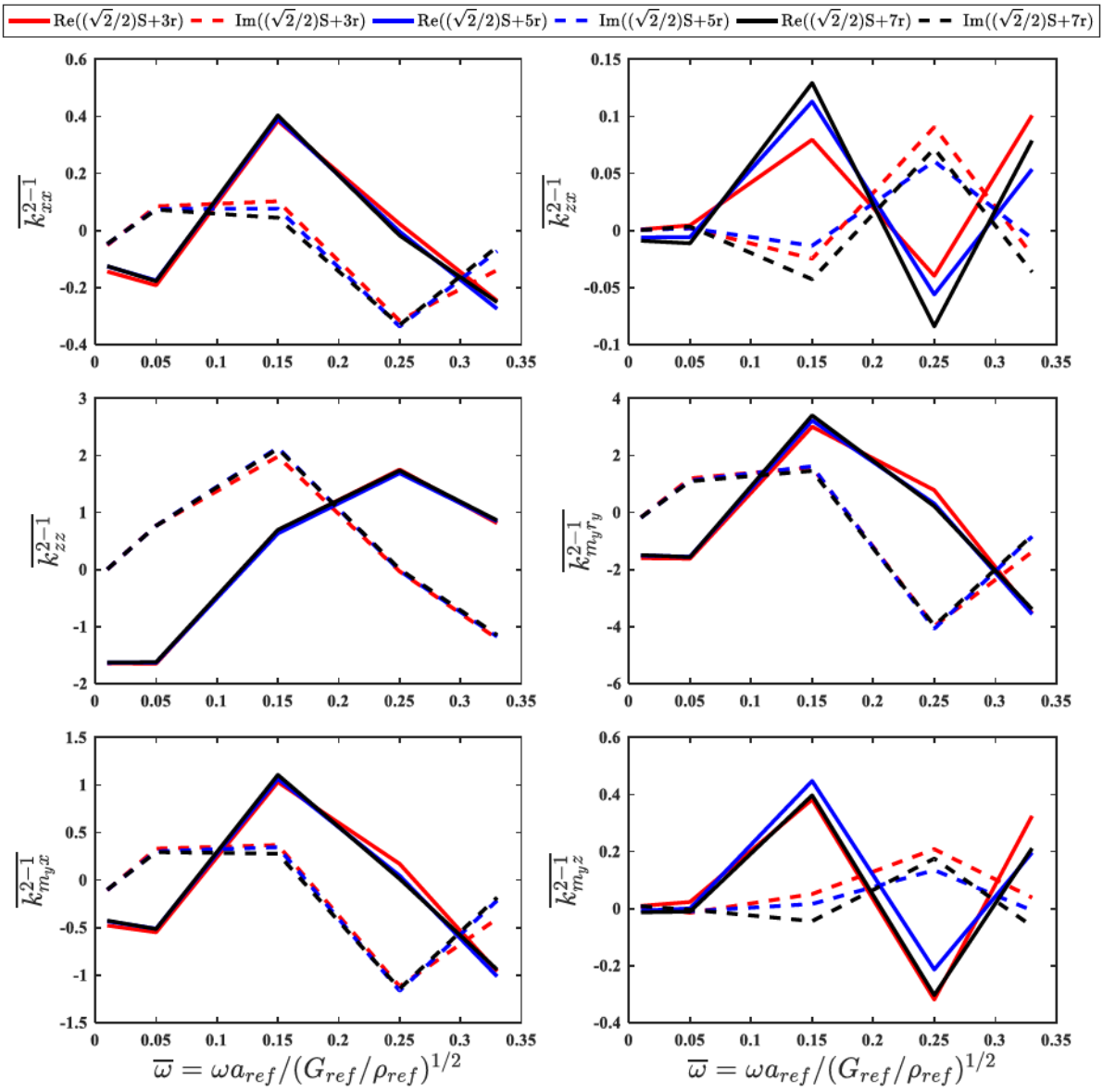

(b) Primary impedance functions in $\mathbf{K}^{2\text{-}1}$

Figure 4.31 *(continued)*

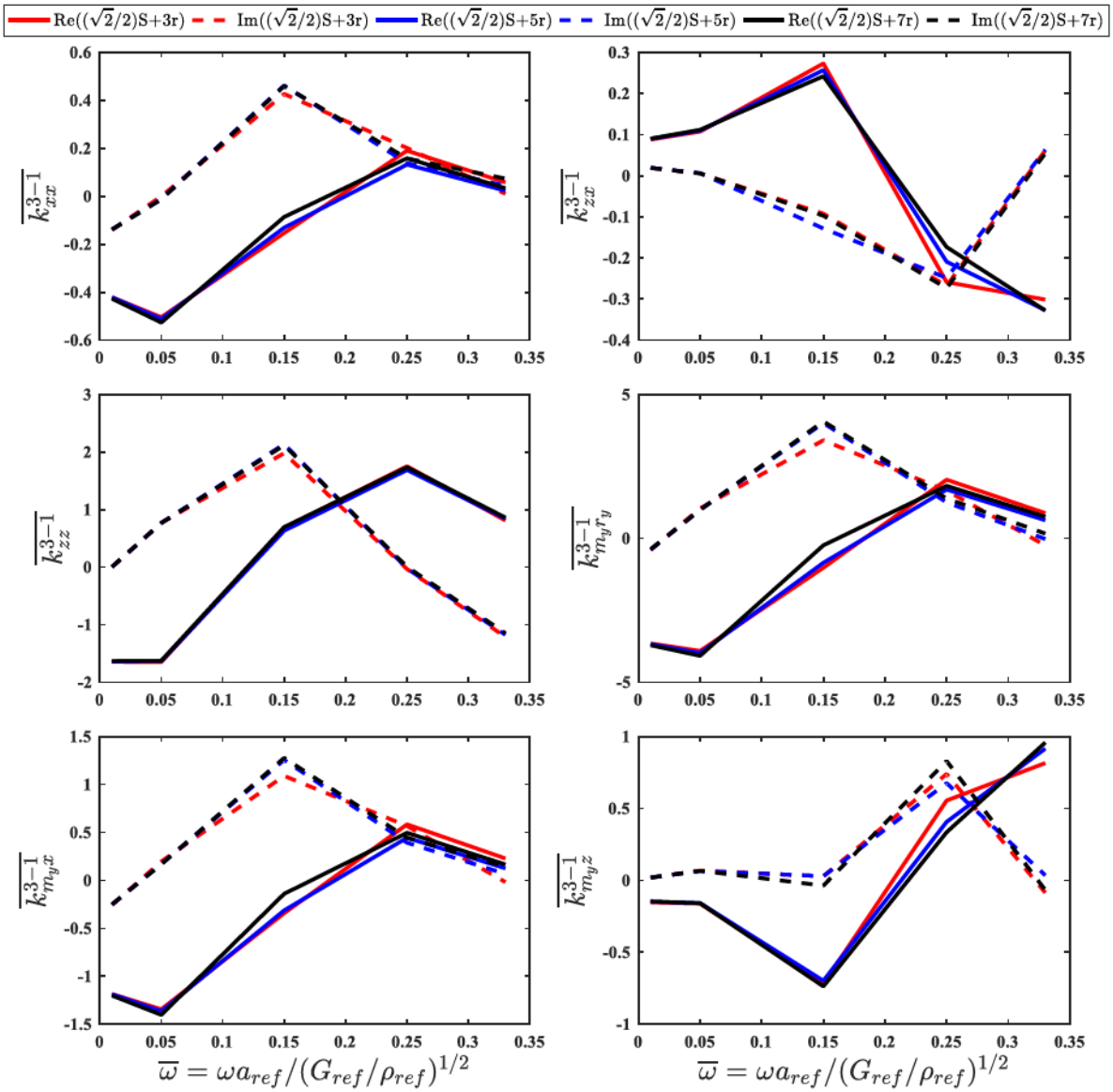

(c) Primary impedance functions in $\mathbf{K}^{3\text{-}1}$

Figure 4.31 *(continued)*

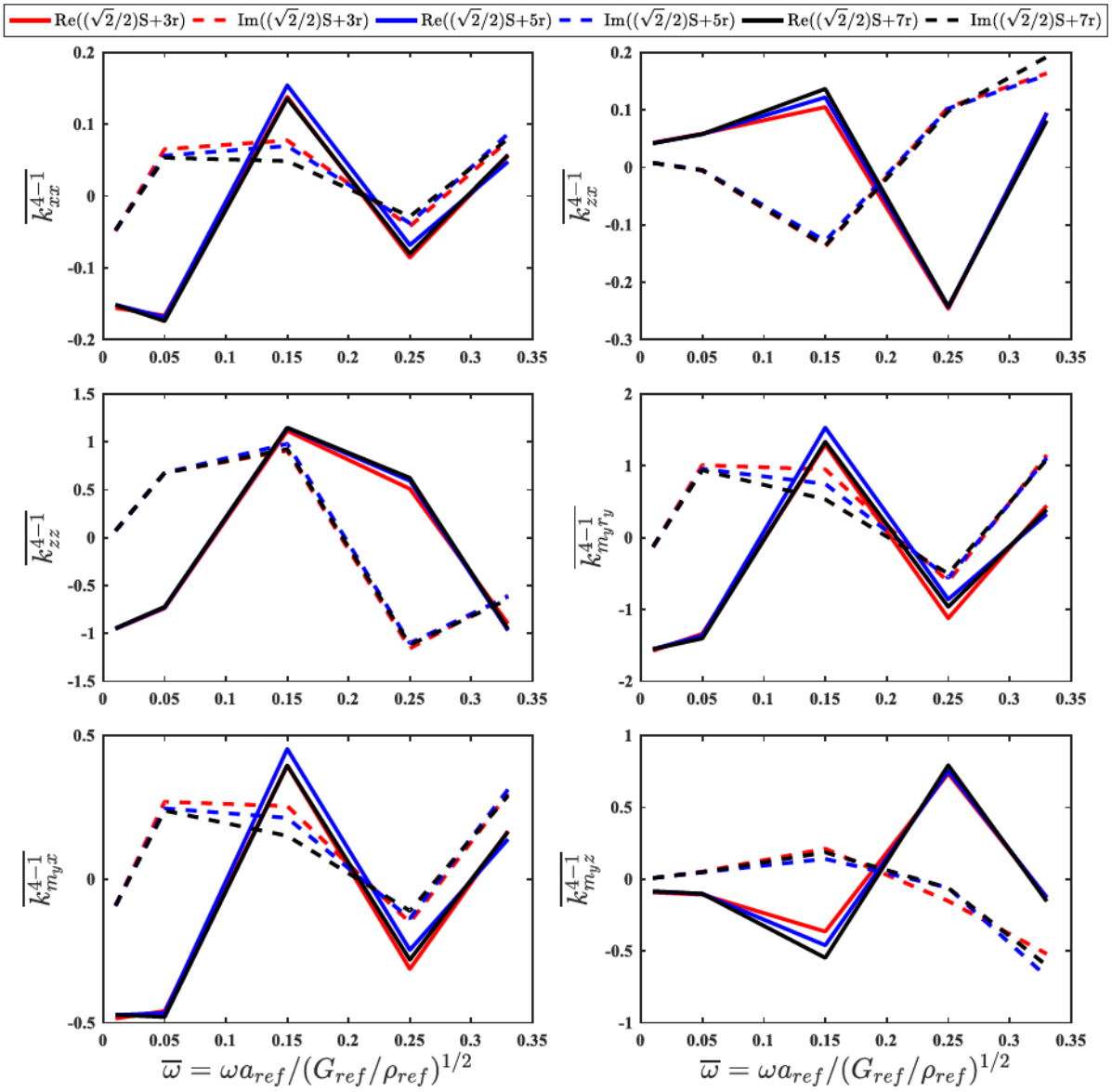

(d) Primary impedance functions in $\mathbf{K}^{4\text{-}1}$

Figure 4.31 *(continued)*

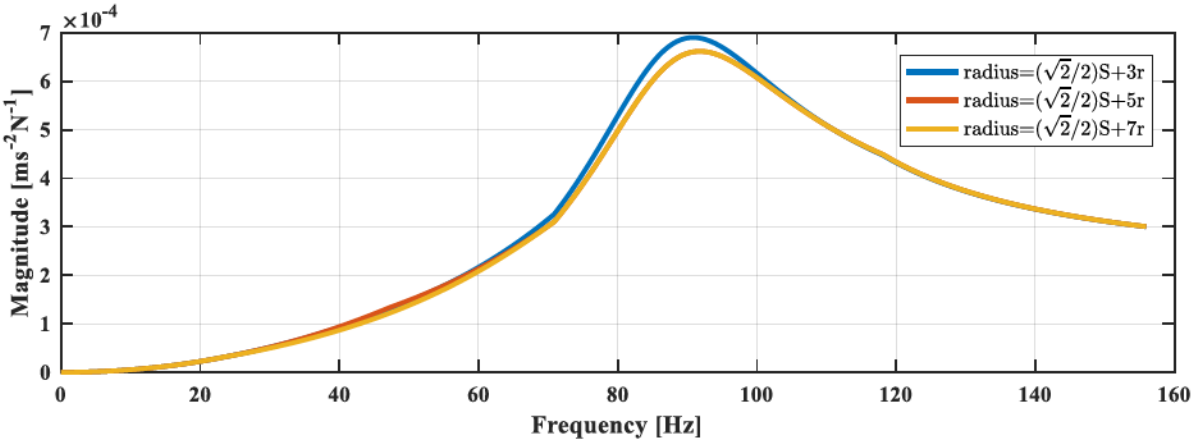

(a) A_{yc}/VC accelerance

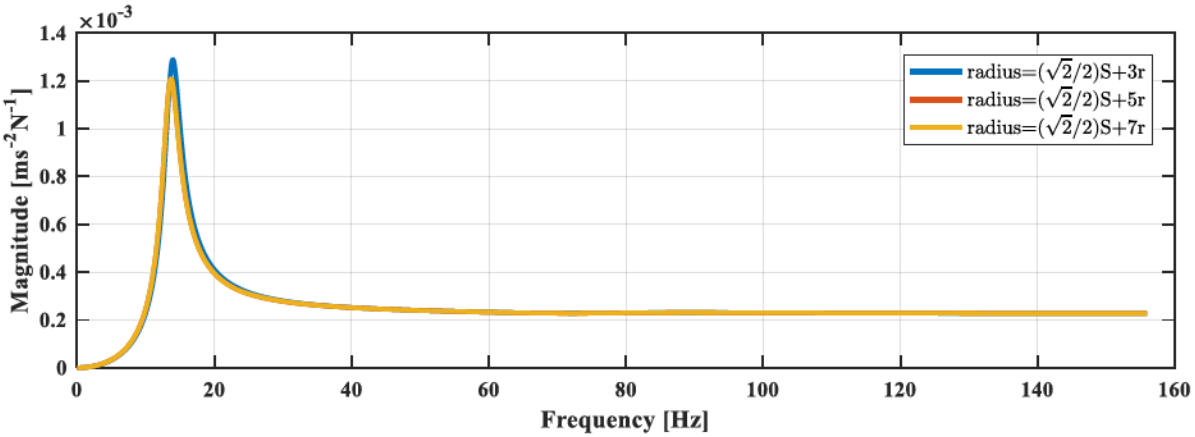

(b) A_{xc}/HC accelerance

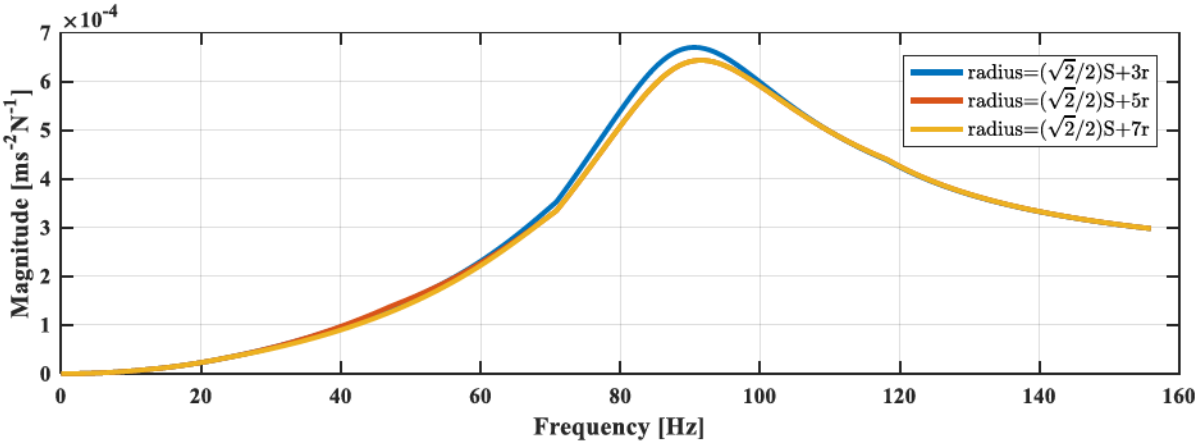

(c) A_{yc}/VE accelerance

Figure 4.32 *Comparison of impedance functions for various inclusion radii.*

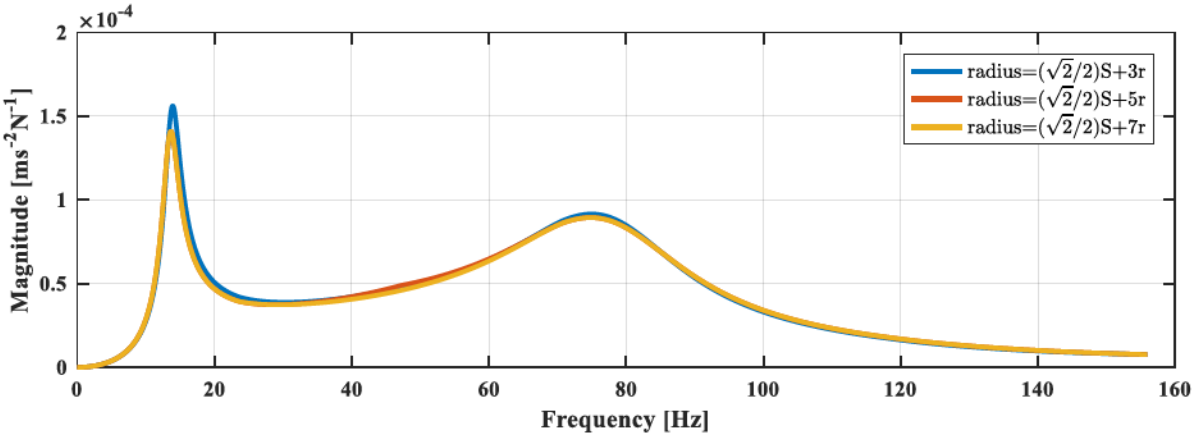

(d) A_{xc}/VE accelerance

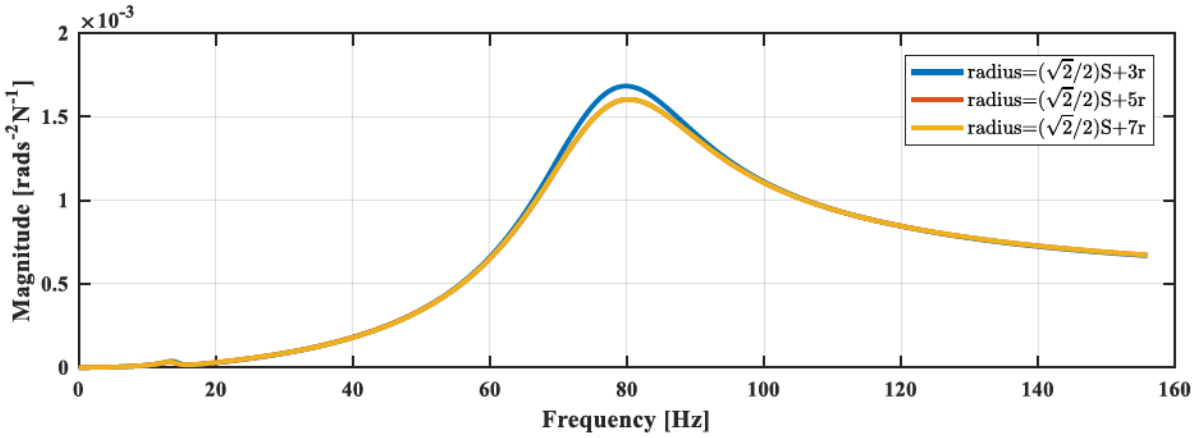

(e) A_{rc}/VE accelerance

Figure 4.32 *(continued)*

4.7 Superstructure

The general formulation established by method of sub-structuring suggests three parameters potentially having considerable influence on accelerance functions – unembedded length l_o, mass m, and polar mass moment of inertia J of pile cap. The parameters were analyzed herein using the impedance functions by the 3-domain model and the 6-domain model in Section 3.8. All parameters were varied by ±25% and ±10% of the original values. The results are interpreted as magnitude of five accelerance functions.

4.7.1 Single Pile

1. Unembedded length l_o

Figure 4.33 manifests that the rocking modes are most sensitive to l_o, followed by the vertical modes. For the rocking modes, long unembedded pile segments induce higher amplitudes and lower frequencies. A larger unembedded length also results in lower resonant frequencies and slightly higher resonant amplitudes for the vertical modes. Horizontal mode, however, is negligibly affected by l_o.

2. Mass of pile cap m

Figure 4.34 shows that mass of pile cap m is influential on all vibration modes, especially for the vertical modes. Take A_{yc}/VC for example, an increasing mass drastically decreases the resonant amplitude, as well as resonant frequency of the vertical mode. The same trend is also found for the horizontal modes, as suggested by the fundamental peaks in A_{xc}/HC and A_{xc} /VE. For the rocking modes, resonant amplitudes exhibit decreasing trends and resonant frequencies almost remain constant with an increasing m.

3. Polar moment of inertia J

Equation of motion indicates that primarily the rocking motion is associated with J. The vertical modes are not affected and the horizontal modes also show minor differences (Figure 4.38). The rocking modes, as expected, are susceptible to the variation of J. For the rocking mode in A_{xc}/VE, a larger J induces the peak shifting towards upper left. The rocking mode in A_{rc}/VE tends to shift towards lower left.

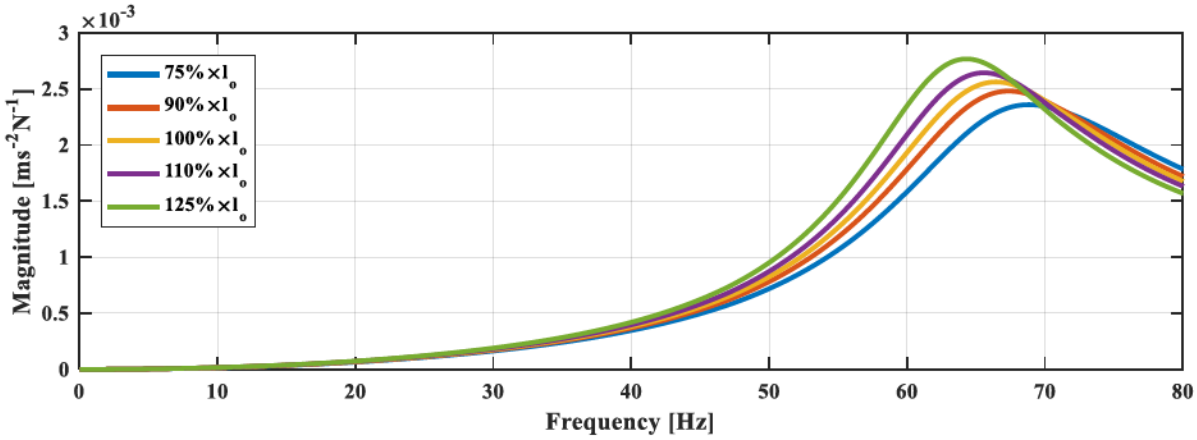

(a) A_{yc}/VC accelerance

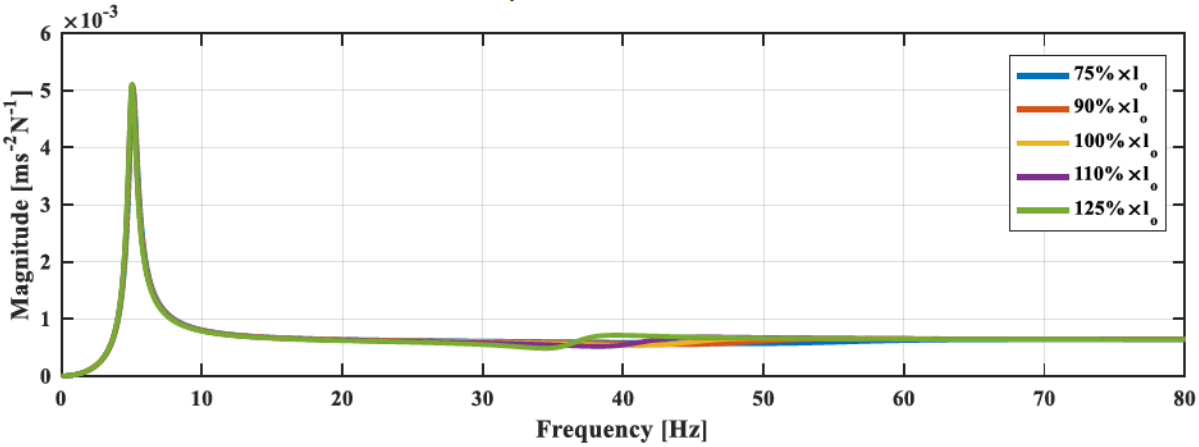

(b) A_{xc}/HC accelerance

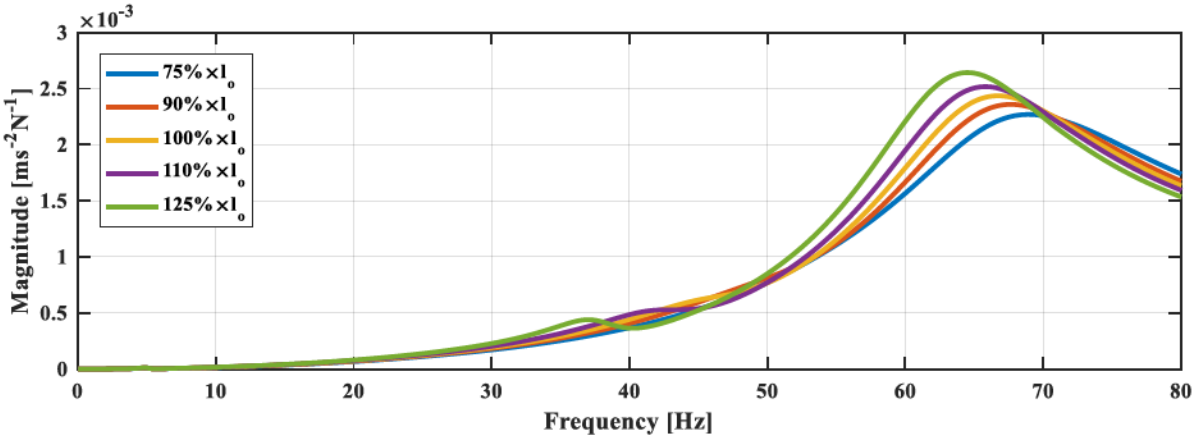

(c) A_{yc}/VE accelerance

Figure 4.33 *Sensitivity of accelerance functions for single pile to un-embedded length* l_o.

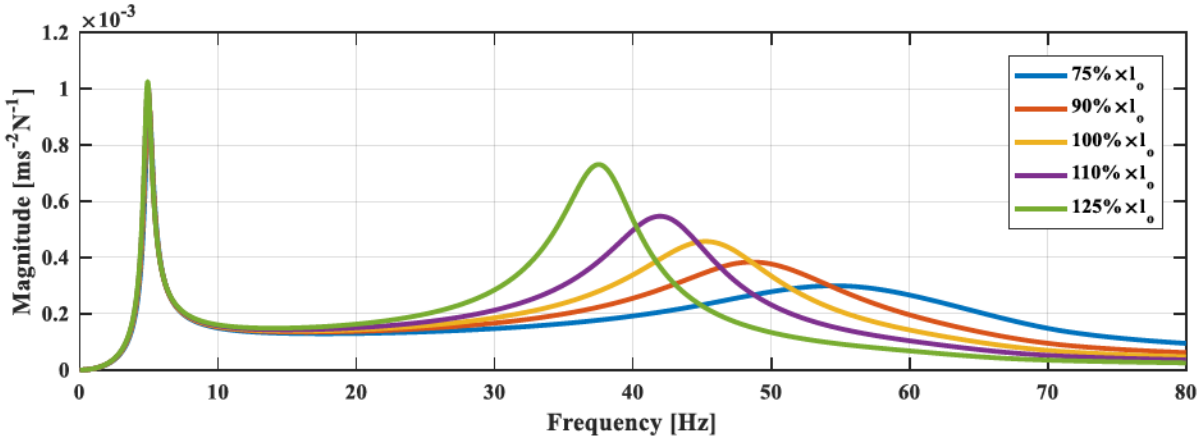

(d) A_{xc}/VE accelerance

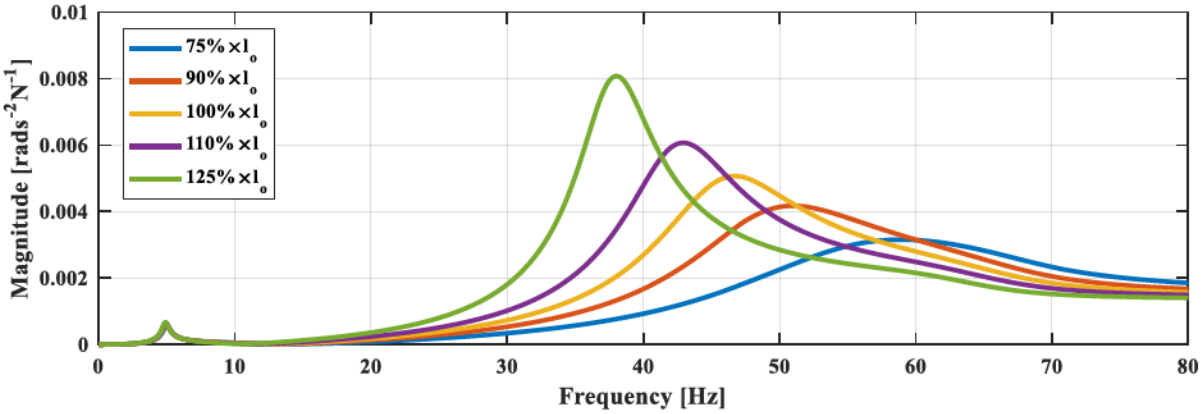

(e) A_{rc}/VE accelerance

Figure 4.33 *(continued)*

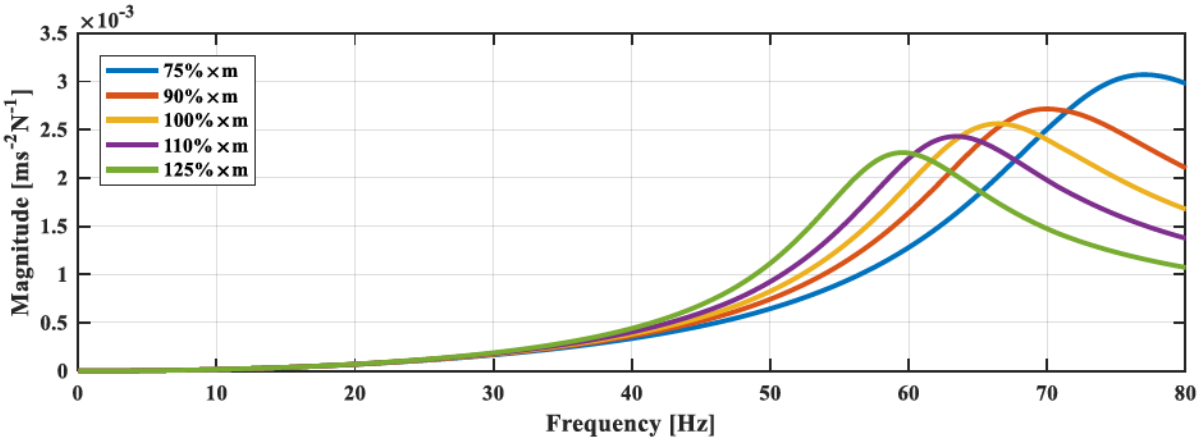

(a) A_{yc}/VC accelerance

Figure 4.34 Sensitivity of accelerance functions for single pile to m.

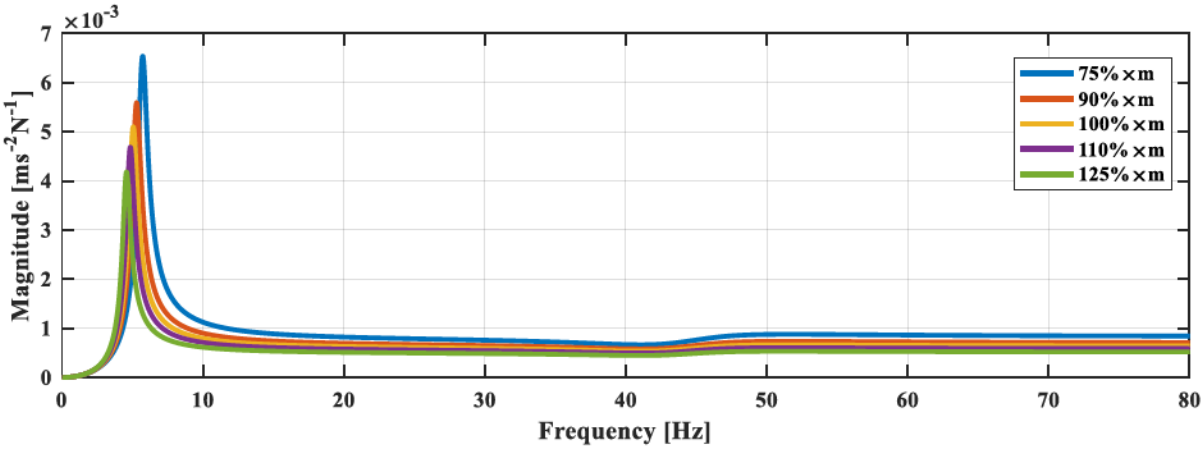

(b) A_{xc}/HC accelerance

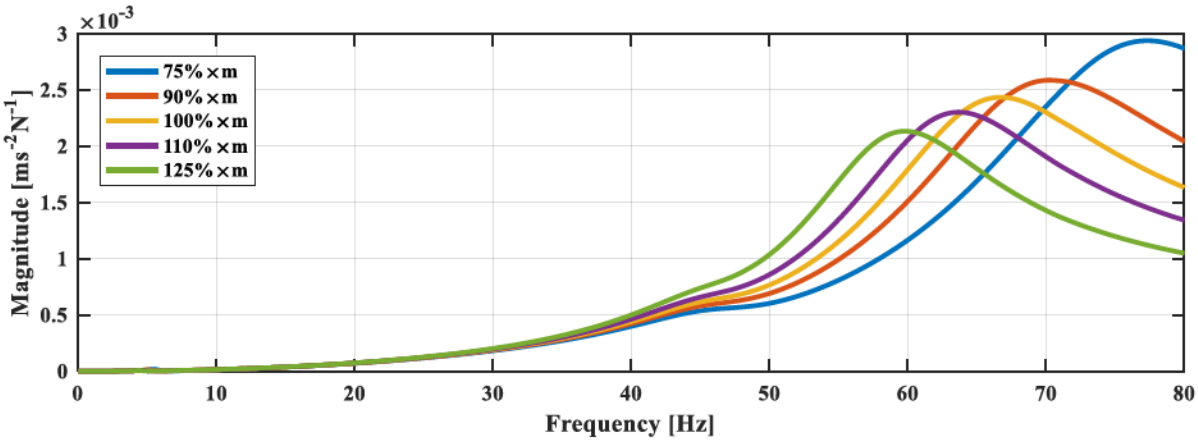

(c) A_{yc}/VE accelerance

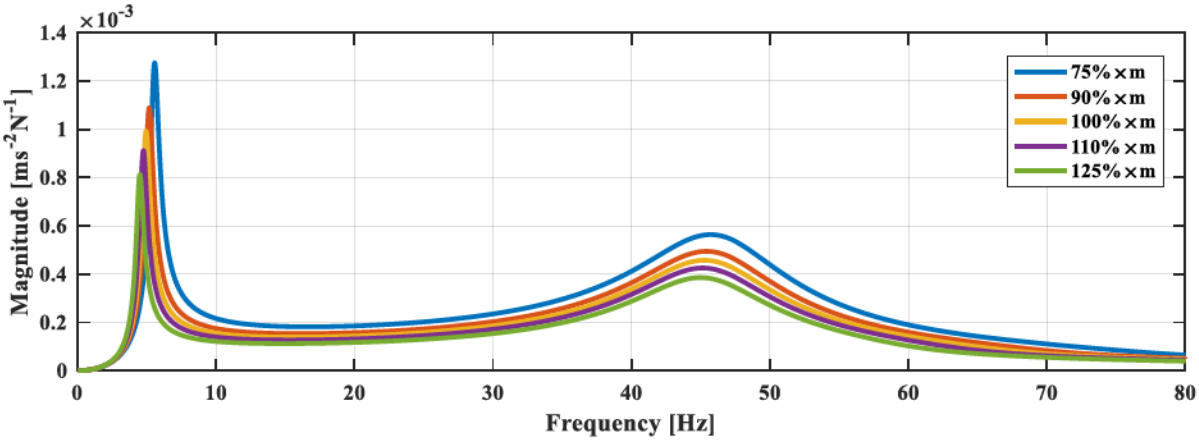

(d) A_{xc}/VE accelerance

Figure 4.34 *(continued)*

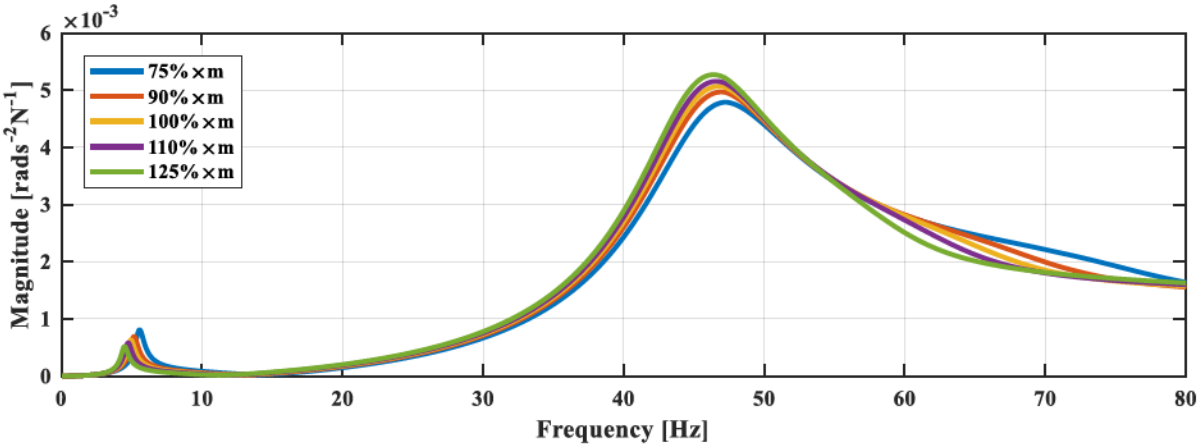

(e) A_{rc}/VE accelerance

Figure 4.34 *(continued)*

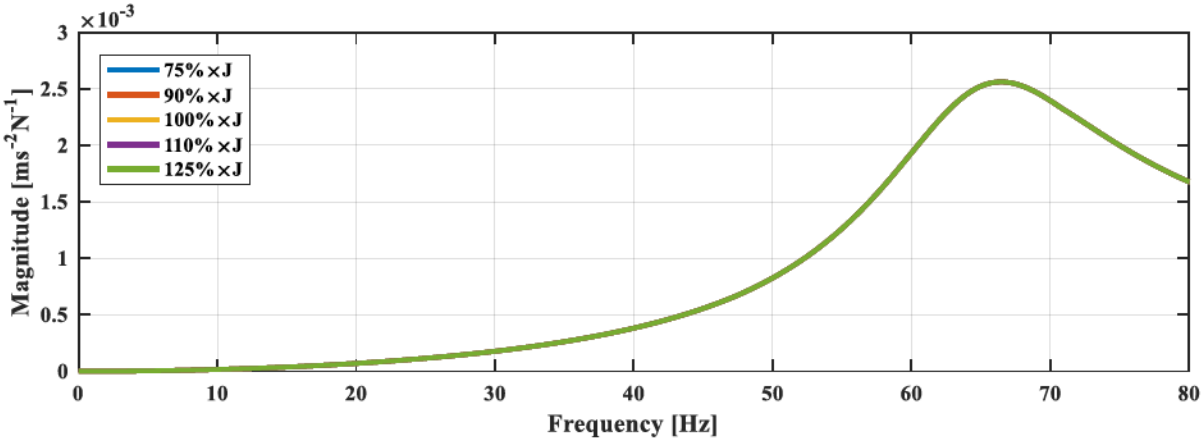

(a) A_{yc}/VC accelerance

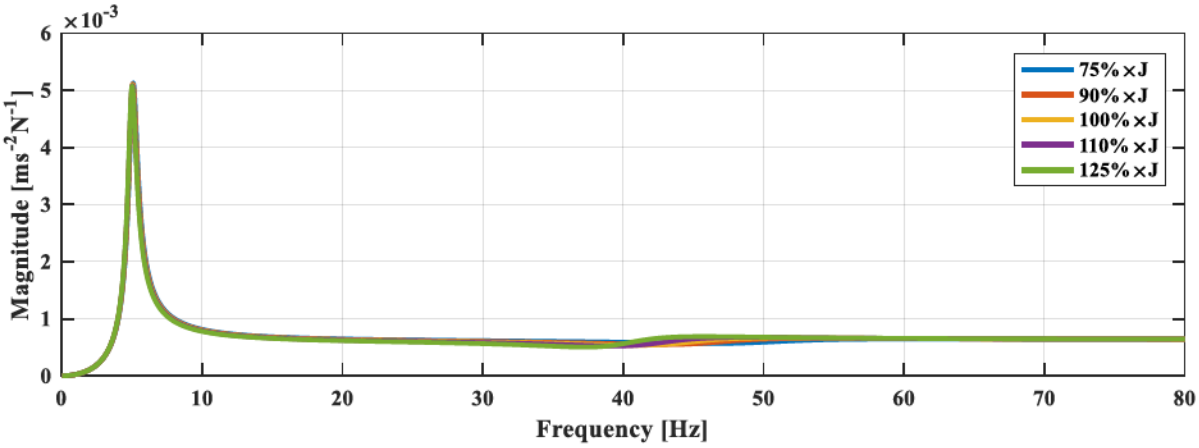

(b) A_{xc}/HC accelerance

Figure 4.35 *Sensitivity of accelerance functions for single pile to* J .

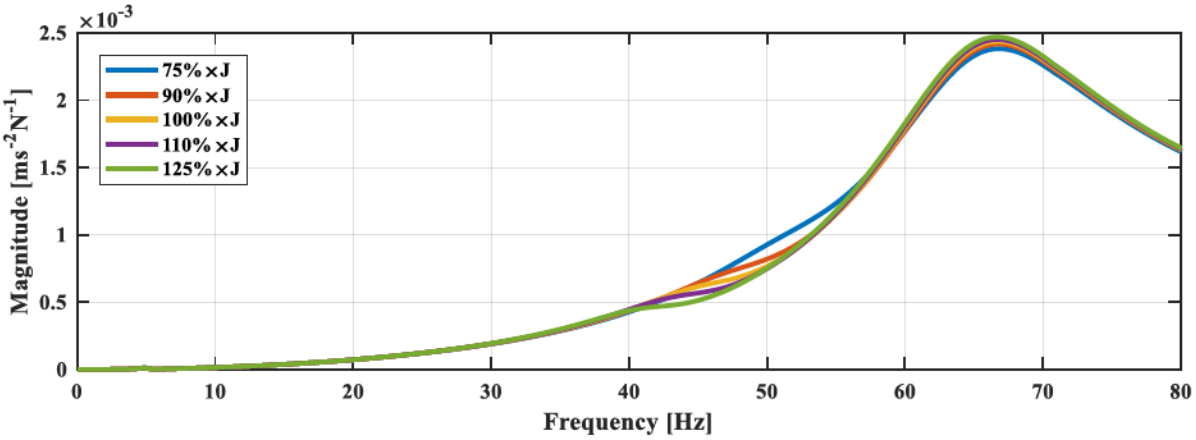

(c) A_{yc}/VE accelerance

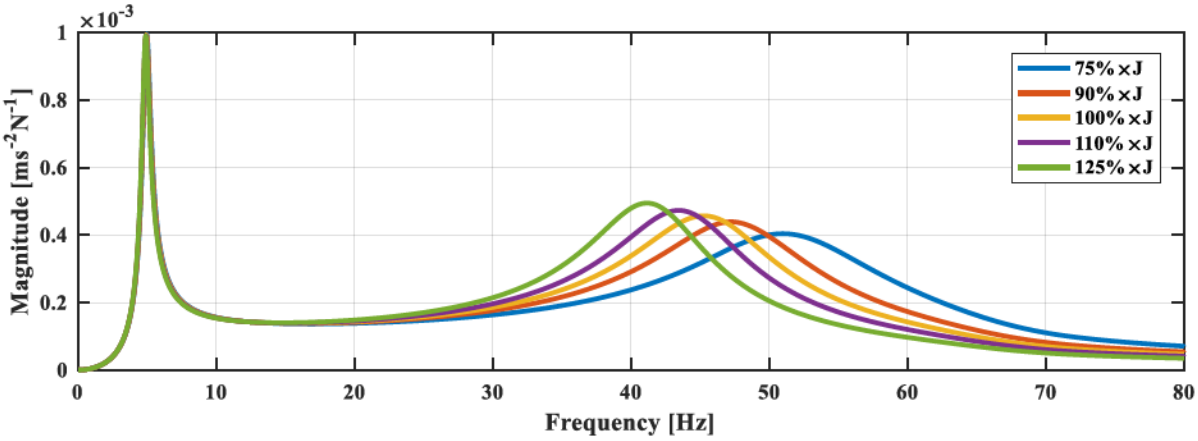

(d) A_{xc}/VE accelerance

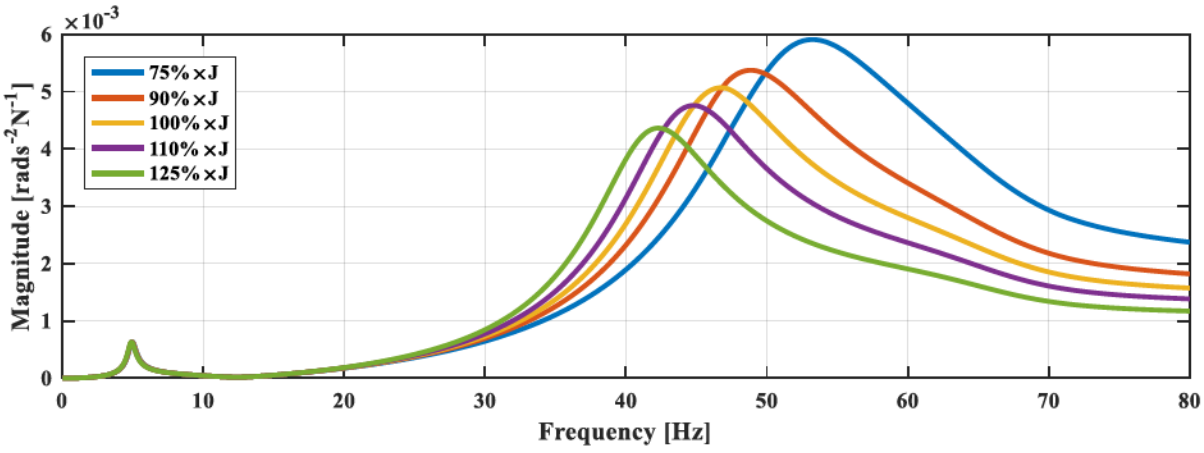

(e) A_{rc}/VE accelerance

Figure 4.35 *(continued)*

4.7.2 2×2 Pile Group

1. Unembedded length l_o

As suggested by Figure 4.36, all accelerance functions are sensitive to l_o. Specifically, longer unembedded pile segments result in lower resonant frequencies and slightly higher amplitudes for the vertical modes in A_{yc}/VC and A_{yc}/VE accelerances. Resonant frequencies of the horizontal modes in A_{xc}/HC and A_{xc}/VE decrease with l_o, while the amplitudes have opposite trends. This is different from the single pile case. Rocking mode is most sensitive to l_o, showing tremendous change in both resonant frequency and amplitude.

2. Mass of pile cap m

Mass of pile cap m also exhibits substantial influence on the vertical and horizontal modes (Figure 4.37). In general, an increasing mass leads to decreasing resonant frequencies and amplitudes of all vertical and horizontal modes. The rocking mode in A_{xc}/VE shows varying amplitude and resonant frequency. The rocking mode in A_{rc}/VE, however, is negligibly affected by m.

3. Polar moment of inertia J

As indicated in Eqns (3.55) and (3.56), the vertical and horizontal modes remain independent of J when no rocking mode is induced. This is verified by no variations for the resonant peaks in A_{yc}/VC and A_{xc}/HC (Figure 4.38). Although the resonant peak in A_{yc}/VE is primarily associated with the vertical mode, the rocking mode is also accounted for due to eccentricity of loading. That explains the slight differentiation observed. As expected, the rocking mode, either in A_{xc}/VE or A_{rc}/VE, exhibits significant change in both resonant frequency and amplitude.

The findings in parametric study on superstructure reveal intensive influence on accelerance functions due to variations of l_o, m, and J. Compared to the pile impedance functions at the ground level, these parameters have more substantial impact on dynamic responses of superstructure. Therefore, the accuracy of the parameters is of great importance in matching experimental accelerance functions. In physical tests, l_o should be from direct measurement. Mass and polar moment of inertia of the cap-shaker system, i.e., m and J, should be estimated both theoretically and numerically to ensure consistent results as demonstrated in Section 2.7.1. Finally, the parametric study on superstructure add some sights into planning of physical tests. By adjusting given parameters reasonably, it is possible to control the resonant frequencies and amplitudes for directional excitation. For example, longer unembedded pile segments l_o in full-scale pile group tests can increase magnitude of the rocking mode but simultaneously decreases the magnitude of the horizontal mode. A greater J, though making the amplitude for rocking mode in A_{yc}/VE higher, may lower the amplitude for the rocking mode in A_{rc}/VE. An appropriately designed superstructure should keep the resonant frequencies for directional vibration modes not beyond excitation capacity and measurement range, and simultaneous elicit relatively high resonant amplitudes to increase signal-to-noise ratio. For design of machine foundations, it is beneficial to choose appropriate mass and polar moment of inertia of the superstructure to keep structural resonant frequency away from the working frequency of the machine.

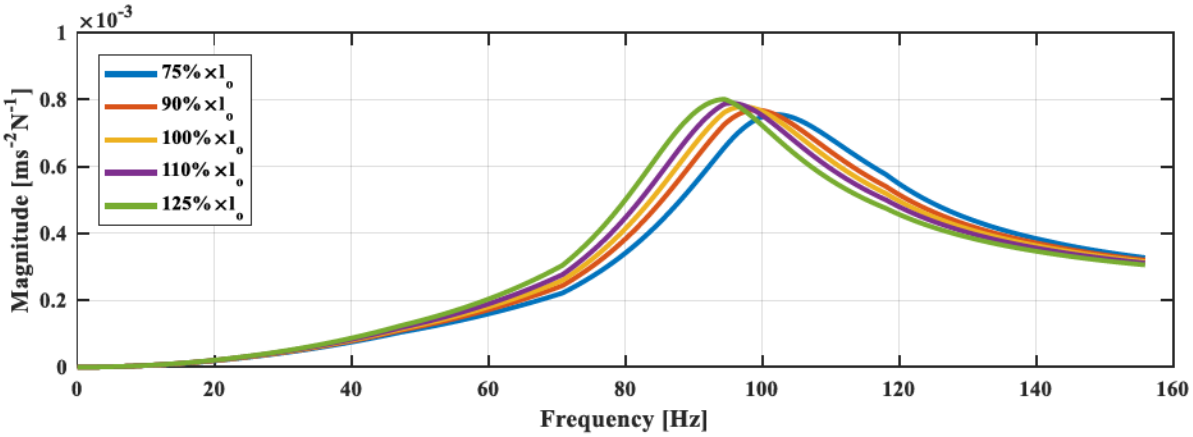

(a) A_{yc}/VC accelerance

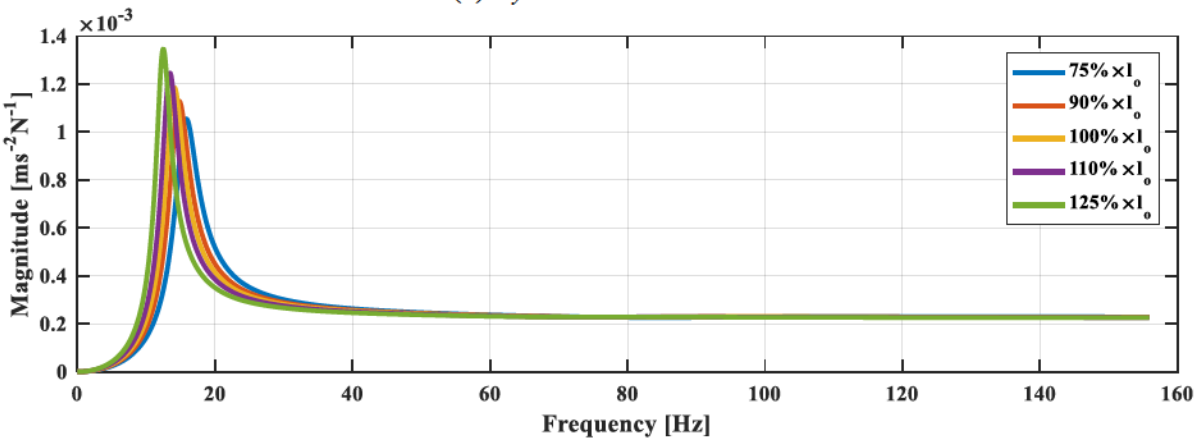

(b) A_{xc}/HC accelerance

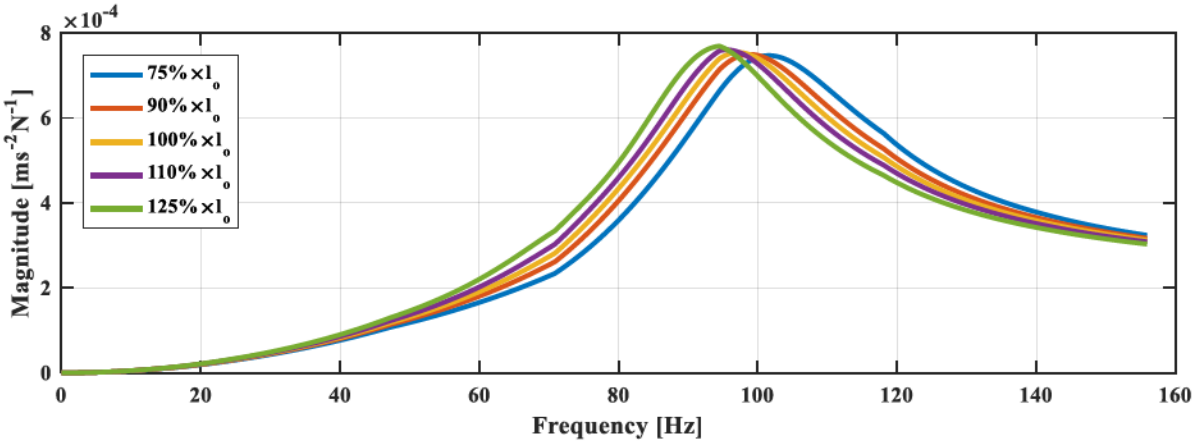

(c) A_{yc}/VE accelerance

Figure 4.36 *Sensitivity of accelerance functions for pile group to un-embedded length* l_o.

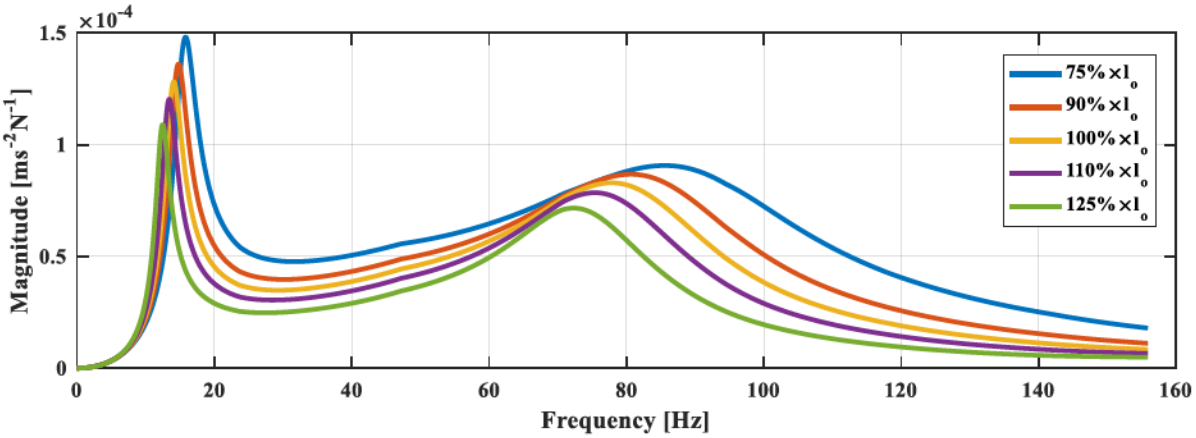

(d) A_{xc}/VE accelerance

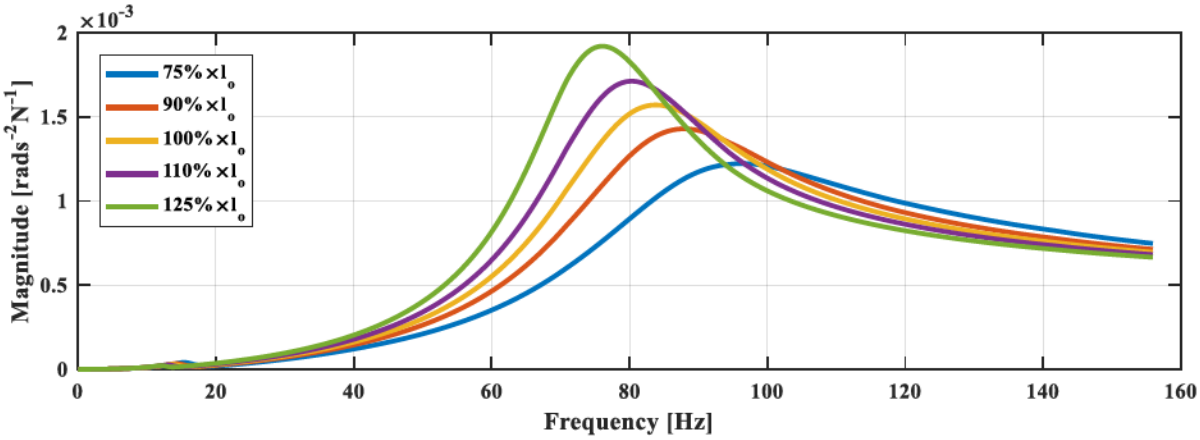

(e) A_{rc}/VE accelerance

Figure 4.36 *(continued)*

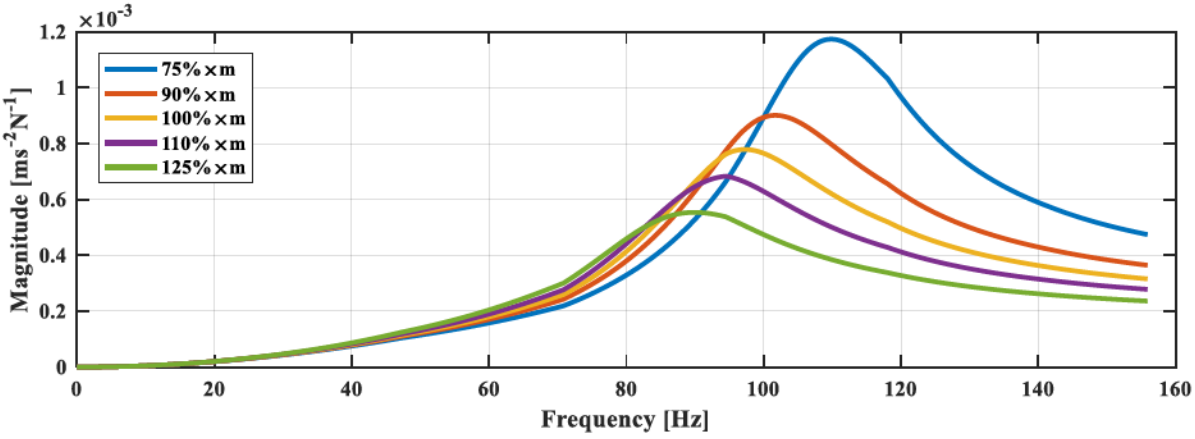

(a) A_{yc}/VC accelerance

Figure 4.37 *Accelerance functions for pile group due to varying mass of pile cap* m.

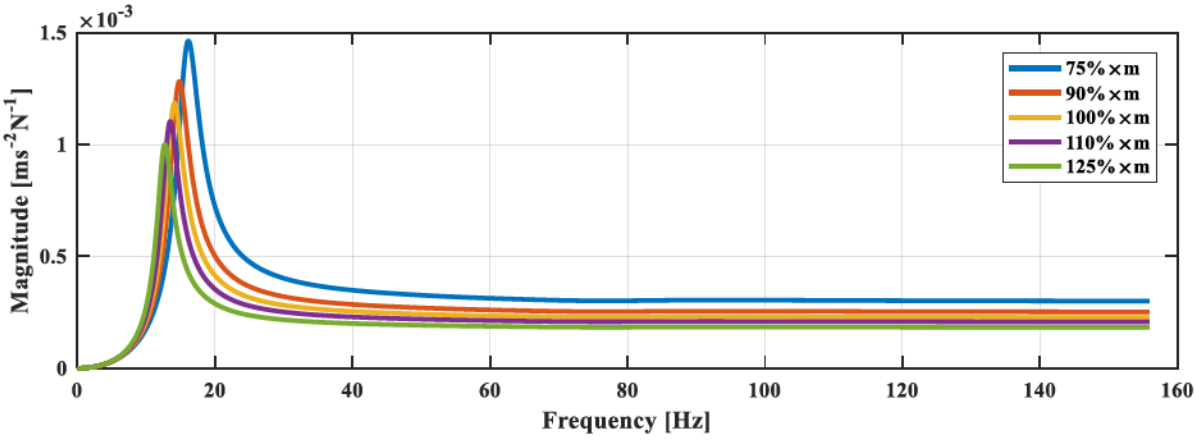

(b) A_{xc}/HC accelerance

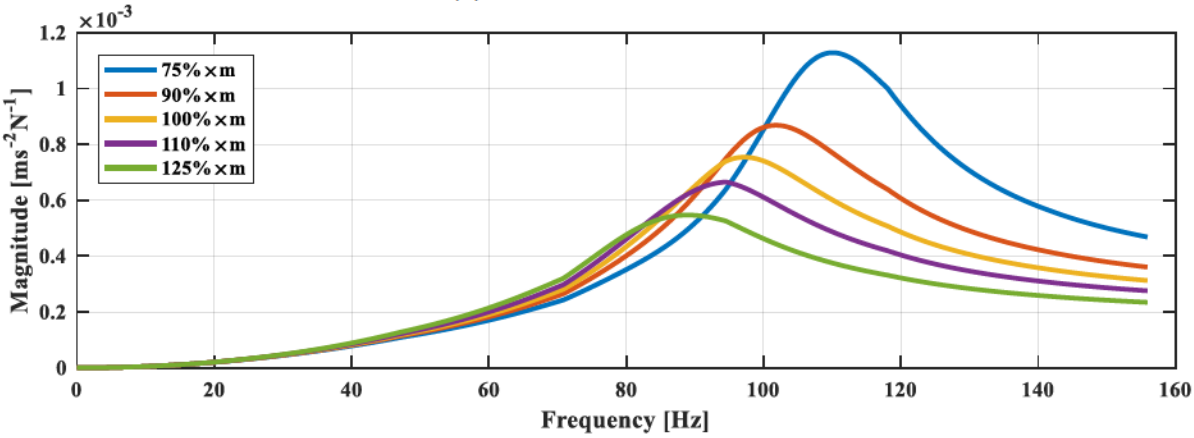

(c) A_{yc}/VE accelerance

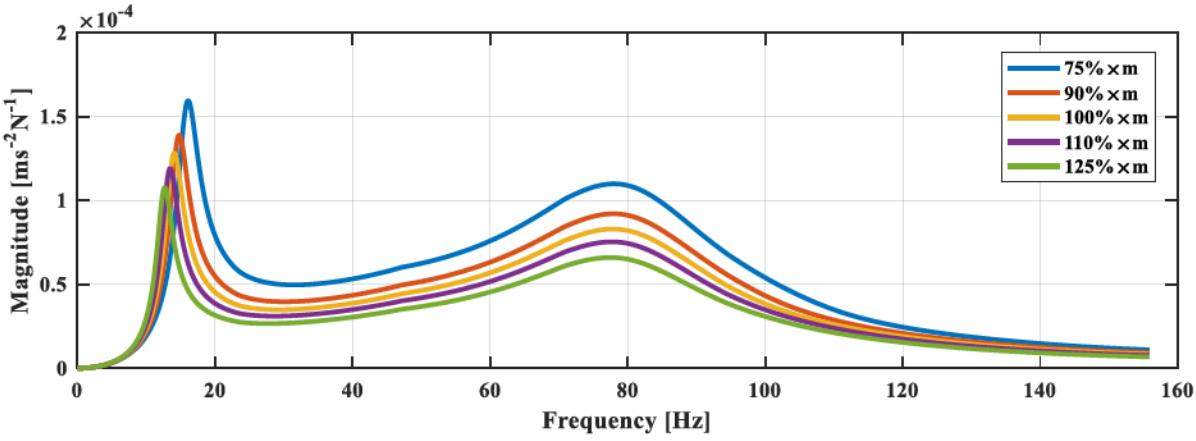

(d) A_{xc}/VE accelerance

Figure 4.37 (continued)

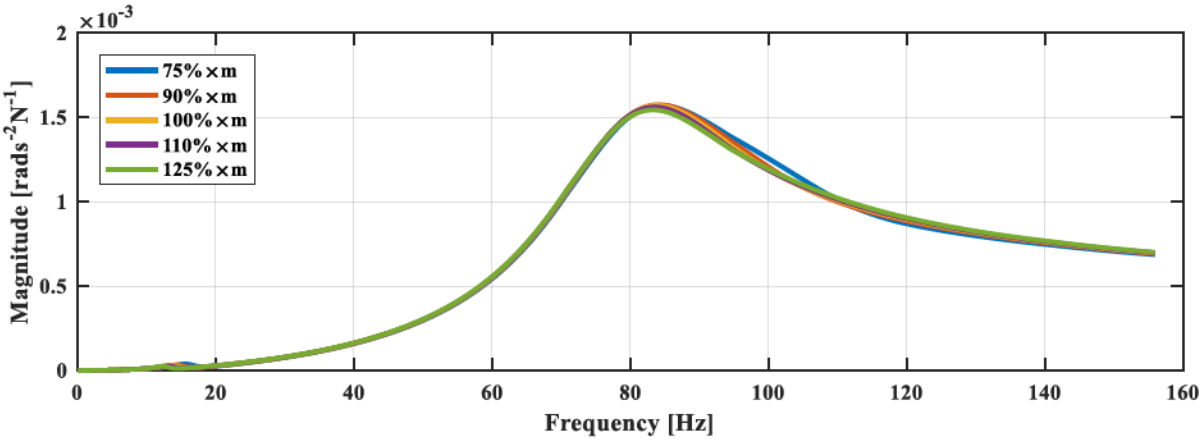

(e) A_{rc}/VE accelerance

Figure 4.37 *(continued)*

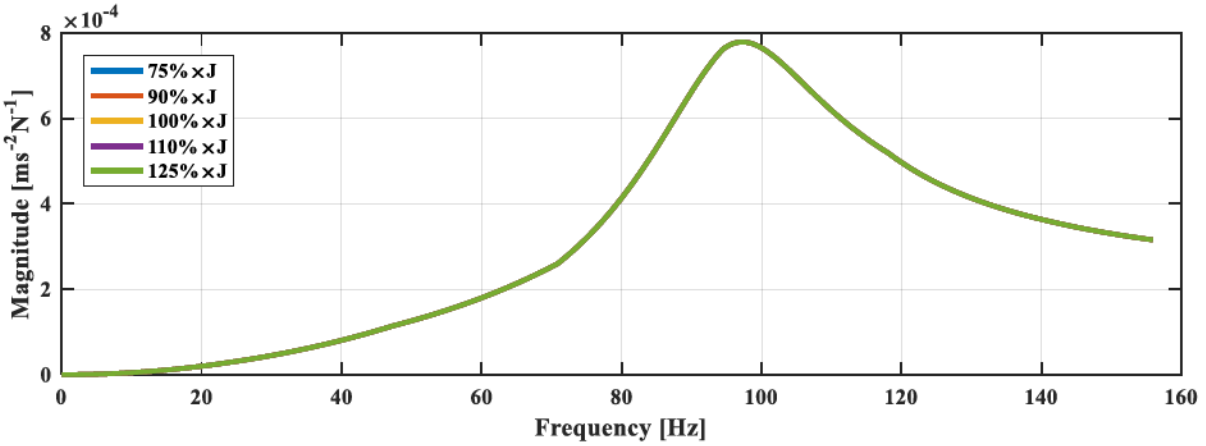

(a) A_{yc}/VC accelerance

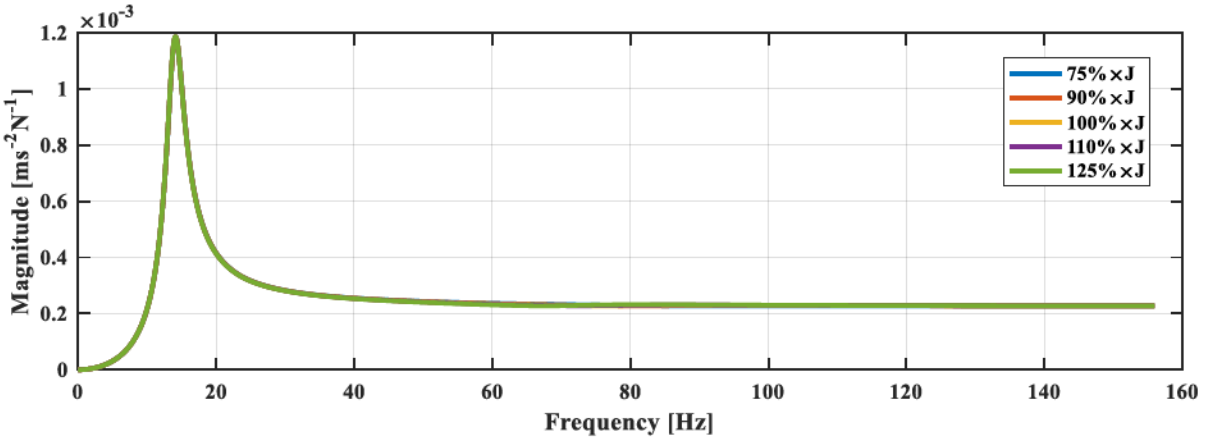

(b) A_{xc}/HC accelerance

Figure 4.38 *Sensitivity of accelerance functions for pile group to the polar moment of inertia of pile cap J .*

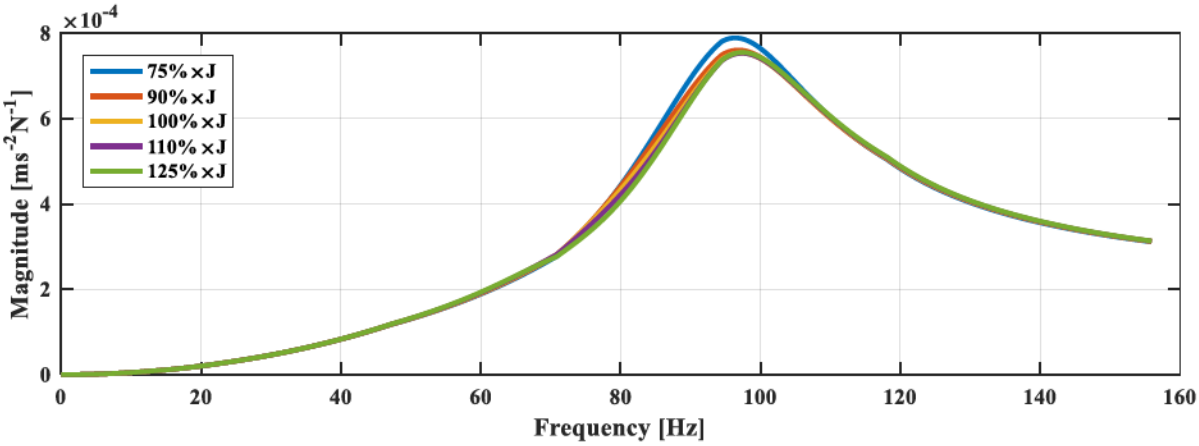

(c) A_{yc}/VE accelerance

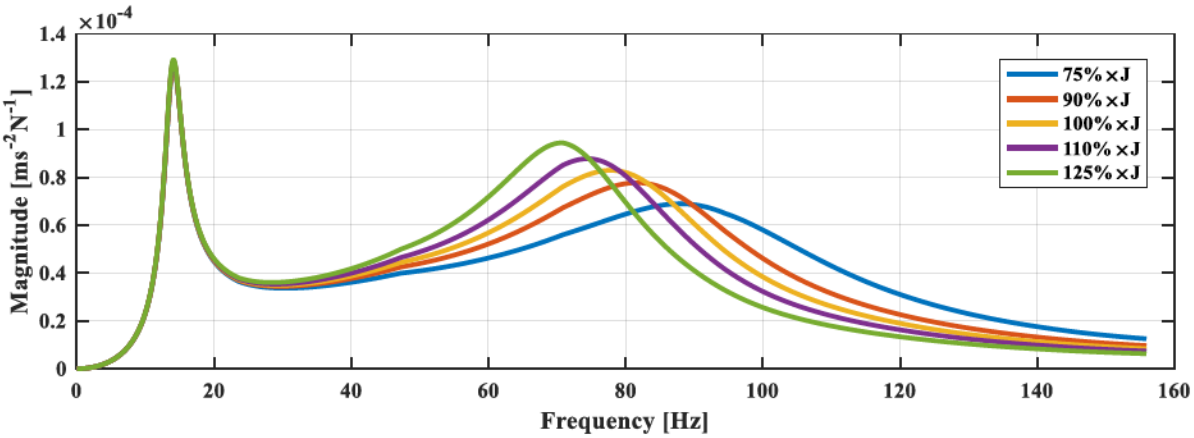

(d) A_{xc}/VE accelerance

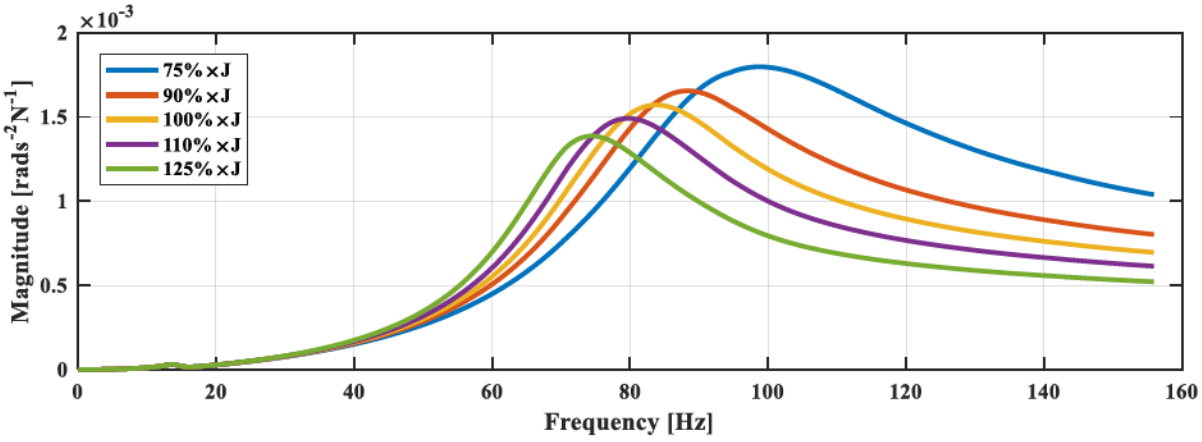

(e) A_{rc}/VE accelerance

Figure 4.38 *(continued)*

4.8 Incorporation of Nonlinearity in Soil Material

4.8.1 Derivation of Strain-compatible Soil Profiles in Layered Disturbed Zone

Kondner (1963a, 1963b) discovered relations between axial stress and deviator stress from the cyclic triaxial tests and established hyperbolic constitutive models for cyclically loaded soils. Since then a series of hyperbolic stress-strain models have been proposed (e.g., Seed and Idriss 1970; Kokusho et al. 1982; Vucetic and Dobry 1991; Stokoe et al. 1999). These models were mostly established based on laboratory tests such as the cyclic triaxial tests, cyclic simple shear tests, cyclic torsional tests, and resonant column tests. Among them, hyperbolic stress-strain relationship developed by Hardin and Drnevich (1972a 1972b) has been widely used (e.g., Schnabel et al. 1972; Vucetic and Dobry 1991). The original model is summarized by Equation (4.3):

$$\begin{cases} G = \dfrac{1}{1+\gamma_h} G_{\max} \\ D = \dfrac{\gamma_h}{1+\gamma_h} D_{\max} \end{cases} \tag{4.3}$$

where $\gamma_h = \dfrac{\gamma}{\gamma_r}\left[1 + ae^{-b(\gamma/\gamma_r)}\right]$ is hyperbolic shear strain and $\gamma_r = \dfrac{\tau_{\max}}{G_{\max}}$ is reference strain. Parameters a and b are soil constants depending on soil type. Small-strain shear modulus $G_{\max}$ primarily depends on effective mean principle stress, void ratio, and degree of saturation. Maximum damping ratio $D_{\max}$ is determined by effective mean principle stress, void ratio, and number of cycles.

This model was later modified to explicitly incorporate minimum material damping and simplify hyperbolic strain by Drnevich (2017):

$$\begin{cases} G = \dfrac{1}{1 + A\left(\dfrac{\gamma}{\gamma_r}\right)^n} G_{\max} \\ D - D_{\min} = \dfrac{A\left(\dfrac{\gamma}{\gamma_r}\right)^n}{1 + A\left(\dfrac{\gamma}{\gamma_r}\right)^n} (D_{\max} - D_{\min}) \end{cases} \tag{4.4}$$

where $A = 0.63$, $n = 1.338$ for sand, and $A = 0.68$, $n = 1.275$ for clayey and silty soils (private communication).

Within soil each layer, void ratio e, over consolidation ratio (OCR), value of K that depends on plasticity index, mean principal effective stress $\overline{\sigma_o}$, vibration frequency f, and number of cycles N are unlikely to change significantly. Then $G_{\max}$, $D_{\max}$, $D_{\min}$ can be seen as constants and $\frac{\gamma_{zx}}{\gamma_r}$ becomes the only variable in Equation (4.4). Multiple methods are available to calculate $G_{\max}$, $D_{\min}$ and $\tau_{\max}$. To be specific, $G_{\max}$ can be evaluated by empirical correlations, laboratory test such as resonant column tests and cyclic simple shear test, or in-situ tests like SCPT and cross-hole tests. $D_{\min}$ can be derived through the aforementioned laboratory tests or SCPT test as in Section 2.2.2, and $D_{\max}$ can be estimated by empirical correlations as in Equation (4.5). It should be noted that due to pile installation, the original soil profile may change from site investigation. Soil near pile toe is heavily displaced, resulting in a higher mean principal effective stress and a lower void ratio. Soils near ground surface, on the other hand, may be subjected to heaving, resulting reduced mean principal effective stress and increased void ratio. Thus, $G_{\max}$ is commonly reduced for top layers and increased for lower layers. In this section, only influence of shear strain level is studied.

$$\text{for saturated cohesive soil}: \begin{cases} G_{\max} = 1230 \dfrac{(2.973-e)^2}{(1+e)} (OCR)^K \overline{\sigma}_o^{1/2} \\ D_{\max} = 31 - (3+0.03f)\overline{\sigma}_o^{1/2} + 1.5 f^{1/2} - 1.5(\log N) \end{cases} \tag{4.5}$$

Recall that in the disturbed-zone BEM models, the half-space stands for undisturbed soils with negligible strain levels. Thus the strain-compatible soil shear modulus and damping models only need to be applied for the disturbed zone. To this end, three difficulties must be addressed for the application:

1. Soil stress state in aforementioned laboratory tests from which hyperbolic models were established is relatively simple such that minor principal stress σ_2 commonly equals σ_3. External shear stress τ is only applied on the same plane as σ_1 with the maximum value calculated by Equation (4.6). The stress state is suitable for site response analysis, such that major principal stress σ_1 simulates vertical soil pressure, σ_2 and σ_3 simulate lateral earth pressure, and τ refers to shear force between soil layers induced by earthquakes.

$$\tau_{\max} = \left\{ \left[\frac{(1+K_0)}{2} \overline{\sigma}_v \sin\overline{\phi} + \overline{c}\cos\overline{\phi} \right]^2 - \left[\frac{(1-K_0)}{2} \overline{\sigma}_v \right]^2 \right\}^{1/2} \tag{4.6}$$

However, for soil-pile interaction problems, soil stress states are far more complicated because of combination of piles' directional vibrations, and wave reflection and refraction at layers and pile interfaces. The in-situ soil stress state is unlikely to match the ideal case as in laboratory tests. Duncan and Chang (1970) suggests that for three–dimensional stress and strain states, it would be desirable to include failure criterion or effects of value of intermediate principal stress. Ni (1987) studied dynamic properties of dry sand under true triaxial loadings by resonant column and torsional shear tests. Low-amplitude shear modulus was found to be dependent on the principal stresses in the direction of wave propagation and particle motion,

and relatively irrelevant of stress in the out-of-plane direction. Due to limited studies on soil dynamic strain-stress behavior under true stress states, only torsional vibration of a single pile is considered to suitable for applying Hardin-Drnevich's hyperbolic model in this study. Torsion of a single pile induces most similar stress states to the laboratory tests such that major shear stresses are applied horizontally.

2. For harmonic vibrations, the strain level and corresponding shear modulus and damping ratio vary with time. For the equivalent linear analyses (Figure 4.39) performed in the frequency domain by BEASSI, shear strain γ should be a constant that corresponds to a unique shear strain level for each cycle.

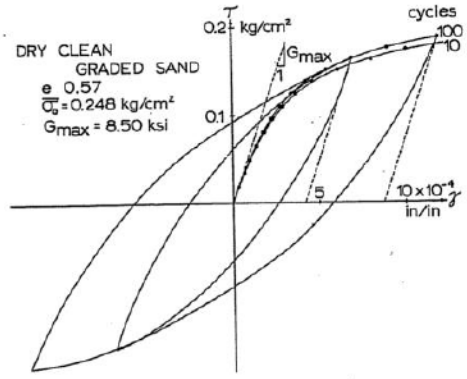

Figure 4.39 *Equivalent linear analysis (Hardin and Drnevich 1972b).*

3. In laboratory tests, soil samples has uniform shear strains at each cross section (i.e., depth). In in-situ tests, magnitude of shear strain varies from location to location even at each depth. In general, the soils near the vibrating pile(s) have higher strains than the soils in far region due to attenuation of wave energy (see accelerance functions for soil accelerometers in Section 2.6.4). The proposed BEM model treats soil in each layer as homogeneous medium with constant shear modulus and damping ratio. Thus a representative shear strain level should

be chosen for the soil layer at the same depth. In this study the representative value is defined as:

$$\overline{\gamma(\mathrm{z})} = average(\sqrt{\left|\gamma_{zx}(x,y,z)\right|^2 + \left|\gamma_{zy}(x,y,z)\right|^2}) \tag{4.7}$$

where (x,y,z) is located within the disturbed zone. For shear modulus at a certain depth of z within the disturbed zone,

$$G^I(\mathrm{z}) = \frac{1}{1 + A(\frac{\overline{\gamma(\mathrm{z})}}{\gamma_f})^n} G_{\max}(\mathrm{z}) \tag{4.8}$$

The measurement of shear modulus at small strains is more reliable than that of damping because of low signal-to-noise ratios, apparatus damping, and measurement method (Drnevich 2017). Thus it is suitable to calculate damping ratio in terms of shear modulus as:

$$D^I(\mathrm{z}) = D_{\min}(\mathrm{z}) + \left[D_{\max}(\mathrm{z}) - D_{\min}(\mathrm{z})\right](1 - \frac{G^I(\mathrm{z})}{G_{\max}(\mathrm{z})}) \tag{4.9}$$

As a common approach to apply equivalent linear method, an initial $\bar{\gamma}$ profile is assumed, based on which initial soil shear modulus and damping profiles are be calculated using Eqns (4.8) and (4.9). Performing BEM analysis with the initial modulus and damping profiles provides dynamic shear strain profiles (See Section 3.7.3). Using the updated representative shear strain profile, strain-compatible soil shear modulus and damping profiles are recalculated, which are then substituted into next round BEM analysis. Repeating the above steps until the representative shear strain profiles converges, which provides converged strain-compatible soil modulus and damping profiles.

4.8.2 Case Study on a Single Pile

To validate the proposed method, a simple case studied was performed for a single pile case. This is because proper characterization of displacement fields for a single pile requires

much less internal points than for a 2×2 pile group. Since accuracy of strain level is crucial in application of nonlinear constitutive models, a large amount of internal points are necessary to capture the displacement field. When Green's functions are not in closed form, analyzing a pile group case requires excessive time with the current computational power and thus becomes impractical. The dimensionless pile properties were assumed to the same as in Table 3.16. For simplicity, soil was assumed to be clay with $A = 0.68$, and $n = 1.275$. Dimensionless frequency was assumed as 0.1. Initial soil properties were assumed to be homogeneous: $G_{max} = 0.5$, $D_{max} = 30\%$, $D_{min} = 3\%$, $\tau_{max} = 0.0012$, $\nu = 0.42$, and $\rho = 1$. Then,

$$\gamma_f = \frac{\tau_{max}}{G_{max}} = \frac{0.0012}{0.5} = 0.0024 \tag{4.10}$$

For the first around calculation, the initial $\bar{\gamma}$ is assumed to be 0.1% at all depths. Then the initial strain-compatible soil shear modulus and damping ratios are calculated as:

$$G^I(z) = \frac{1}{1 + 0.68 \times (\frac{0.001}{0.0024})^{1.275}} \times 0.5 = 0.41 \tag{4.11}$$

$$D^I(z) = 0.03 + [0.30 - 0.03](1 - \frac{0.41}{0.5}) = 0.0786 \tag{4.12}$$

The results of $\overline{\gamma(z)}$, $G^I(z)$, and $D^I(z)$ profiles during the first three iterations are presented in Figure 4.40. The converged representative strain levels, differ from the initially assumed uniform G_{max}, and undulate sharply above depth of 20. The corresponding $G^I(z)$ and $D^I(z)$ profiles also exhibit similar trends. Beneath depth of 25, the dynamic strain levels become negligible. In addition, the iteration converges at a fast speed. Soil profiles calculated after 1st round iteration is very close to the profiles after 3rd round iteration. The case study suggests that the strain-compatible soil profiles are well captured and the convergence speed

is satisfactory. The dynamic strain level attenuates along depth of 25, 36% upper portion of the pile.

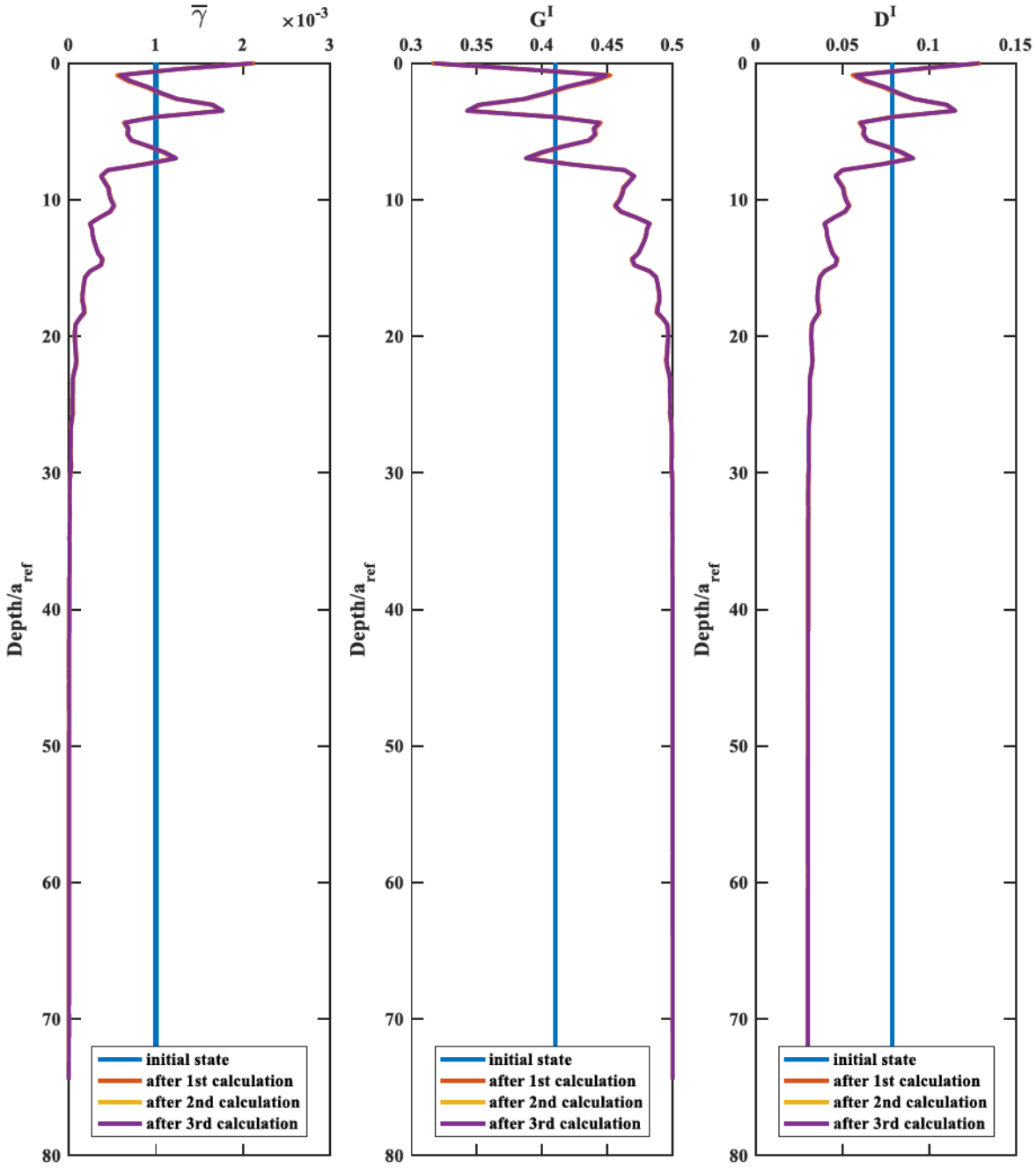

Figure 4.40 *Convergence of* $\overline{\gamma(z)}$, $G^I(z)$, *and* $D^I(z)$ *profiles within three rounds of iterations.*

CHAPTER 5. CONCLUSIONS AND RECOMMENDATIONS

5.1 Conclusions

Three dimensional dynamic soil-pile group interaction has been a subject of significant research interest in recent decades. Wide application of pile foundations subjected to a variety of dynamic excitations has led to increasing demands on seismic and machine foundation designs. The literature review in Chapter 1 summarizes numerous previous experimental and computational studies, in which discrepancies were commonly observed between computational and experimental results. To help advance fundamental knowledge on dynamic soil-pile interaction, improve the accuracy of current computational models, and contribute an additional experimental database, this study was aimed at performing computational and physical simulations on single piles and pile groups.

In Chapter 2, full-scale in-situ elastodynamic vibration tests on a 2×2 pile group and a single pile were studied. Subsurface conditions were evaluated by comprehensive site investigation, including standard penetration tests, cone penetration tests with pore pressure measurement, seismic cone penetration tests, soil classification, and other laboratory tests. Specifically, seismic data from the SCPT tests were analyzed to estimate the in situ profiles of small-strain shear modulus and damping, as well as Poisson's ratio. Empirical correlations to the SPT and CPT data were also examined to corroborate the SCPT results. Pile installation was monitored, with both blow counts and soil plugging recorded as a function of depth. The recorded blow counts were compared to pile driving analyses to ensure the integrity of piles after installation, and the soil plugging lengths indicated that the driven piles were categorized as small-displacement piles. The design and construction of the concrete pile caps were

detailed, and the corresponding geometric properties were rigorously calculated using CAD and simplified analytical models.

Multimodal forced vibration pile tests were conducted using random vibration techniques and a servo-hydraulic inertial shaker. Instrumentation included accelerometers on the pile caps and in the soil, strain gauges attached to the unembedded portions of the piles, and stringpots attached to the piles and caps. The test results were examined in the form of power spectra, coherence functions, accelerance functions, and transfer functions for strain gauges.

The computational simulation phase of the study was detailed in Chapter 3. The computational framework employed 3D BEM models of piles embedded in a disturbed zone and surrounded by a halfspace zone, with layered soil profiles in both zones. To lay a solid foundation for analyzing the dynamic pile-soil interaction problems, a series of validations and verifications were performed on a step-by-step basis. The CyEnce and CyStorm supercomputing clusters were used together with the new versions of the program and verified against benchmark problems previously analyzed on other clusters. The new capabilities of BEASSI for handing multi-domain problems were validated by comparing impedances for 6-domain models of the four piles and disturbed zone in a halfspace, and 5-domain models without the disturbed zone. Beam-column "structural" Green's functions for the piles were compared to use of 3D dynamic point-load Green's functions treating the pile as a viscoelastic solid. More rigorous reference studies were performed on static and dynamic cases of floating piles in homogeneous soils, showing general consistency between BEASSI and the reference studies. The disturbed-zone model for single piles was also validated against reference studies. For the purpose of deriving theoretical accelerance functions for the soil-pile system, a general

formulation was established using the method of sub-structuring. The dynamic response of the substructure was characterized by a global impedance matrix with account of pile-soil-pile interaction.

A new three-dimensional BEM disturbed-zone model for pile groups is proposed, with the boundary discretization validated by convergence studies. The numerical results were interpreted in the forms of theoretical centroidal accelerances, group efficiency ratios, displacements, strain and stress fields in the soil, and bending moment and shear force profiles in the piles. Case studies were performed corresponding to the soil and pile properties in the physical tests, and parametric studies were conducted to calibrate the computational models to the experimental results. By starting from a previously established model for single piles in sand for the disturbed zone, the simultaneous vertical and coupled lateral-rocking vibration modes were captured reasonably well in the theoretical accelerance functions. The soil profiles were then further calibrated to better capture the experimental results.

Parametric studies were conducted in Chapter 4 specific to the effects of soil profiles and layer discretization within the disturbed zone and in the half-space, as well as effects of gapping, pile spacing, size of the disturbed zone, and properties of the superstructure. The incorporation of nonlinearly strain-dependent soil profiles in equivalent linear-type analyses was also explored using the BEM models.

5.2 Recommendations for Future Work

To further build upon the insights generated in this study, several recommendations are listed below as possible directions for future work on dynamic soil-structure interaction.

1. Deepening understanding of soil calibration within the disturbed zone. For 3D BEM disturbed-zone models, the soil profiles within the disturbed zone were demonstrated to be crucial to the dynamic response of the superstructure, and require more thorough study. The

calibration of soil shear modulus and damping ratio is still based on approximate accounts of the most influential parameters, but the process is still too vague to efficiently guide the calibration, especially when computation is time-consuming as in pile group problems. A possible approach would be closer examination of all the factors contributing to the disturbed zone individually, and their measurement in physical tests. These factors include changes in the soil properties and behavior due to pile installation, the static foundation weight, dynamic strain levels, and pile-soil contact conditions, among others. Initial efforts have been made in this study to examine the influence of dynamic strain levels in the disturbed zone, and additional efforts of this kind are needed. Considering the issue of pile-installation for example, its horizontal influence in terms of both range and magnitude might be inferred from peak particle velocities meausured during pile driving (e.g., Lewis and Davie 1993; Massarsch and Fellenius 2008).

2. Enhancement of studies on the far-field soil domain. An advantage of 3D continuum models over Winkler type foundation models is that the former enable analyzing wave propagation and damping in the entire unbounded soil domain, while the latter only concentrate on reactions at the pile surfaces. Although the displacement, strain, and stress fields in dynamic problems are complicated, they can provide insights into the volume of influence, incorporation of soil nonlinearities, and representation of wave propagation as well as reflection and refraction at soil layer interfaces. In this study, the strain fields within the soil domain were approximated by finite difference formulae based on internal displacements from the BEM analyses. However, the resulting strain fields appear to be less stable than the displacement fields. A better solution would be solving for strains using the boundary integral

equation directly. The layered soil profile and horizontal inhomogeneities could be automatically accounted by Green's functions.

3. Improving computational performance. Nowadays numerical modeling is a common approach for handling complex geotechnical problems. As the dimensions of problems in research and practice drastically increase, computational capabilities become a limiting factor. For example, analysis of a 3–domain problem (single pile, disturbed zone, and halfspace) for a given frequency using the Texas Advanced Computing Center in 2014 took only 1.5 hours using 64 processors. Analysis of a 6-domain problem (four piles, disturbed zone, and halfspace) for a given frequency in 2018 took 10 hours using 96 processors and the optimized code, because of the greater number of mesh nodes required. As a point of reference, for the evolution of computational capability, single-threaded floating-point performance typically increases at a rate of 21% annually (Poley 2012), which corresponds to an improvement by a factor of 2.14 from 2014 to 2018. Even so, such improvement can hardly match the increase in computational power necessitated by the expansion from the single pile to the 2×2 pile group problem, unless there is a breakthrough in algorithms or more powerful hardware. Since closed-form Green's functions for a layered half-space due to a point source have been noted to not exist except in the simple case of a homogeneous half-space (Banerjee and Manoon 1990), more effort should focus on improving the existing numerically evaluated Green's functions, either by simplifying the algorithm or increasing convergence speed without compromising accuracy. In terms of parallelism, there is less than 25% room for improving CPU-based parallelization. Given the fast development of Graphical Processing Units (GPUs), it should be promising to explore heterogeneous computing such as GPU-based parallelization (e.g., Takahashi and Hamada 2009; Hamada 2011; Iuspa et al. 2015; Torky and Rashed 2017) in the long run.

4. Establishment of BEM and FEM hybrid models. It is typically difficult for BEM to handle nonlinearity, such as nonlinear soil constitutive models (see Lade 2005). This has also been demonstrated by the challenges in modeling pile group gapping and in applying the Hardin-Drnevich hyperbolic models to BEM analyses in this study. In contrast, FEM is more capable in modeling pile-soil contact conditions and handling soil nonlinearities, but in the time domain. The stress-strain relations can be easily customized using many commercial or open-source FEM codes available at the present time. Failure criteria could be incorporated into analyzing destructive tests for more complicated pile foundations, and coupling of BEM to handle the far-field wave propagation and FEM to handle nonlinearities in the disturbed zone could be applied to the pile group problems examined in this study. Such coupling might require first transforming the BEM formulation back to the time domain via the inverse Fourier transform.

5. Extensive experimental studies. Since the 1970s, researchers have been active in performing experimental studies on piles, ranging from full-scale to small-scale tests. A variety of tests were conducted for numerous pile configurations, loading and instrumentation configurations, and subsurface conditions. The discrepancies found between experiments and numerical predictions necessitate further experimental studies. Increasing the quality and number of pile test databases in the future would help reveal more fundamental phenomena of dynamic soil-structure interaction, provide a solid basis for establishment and calibration of computational models, and create more opportunities for innovating geotechnical testing techniques.

REFERENCES

Abedzadeh, F. (1993). Dynamic analysis of piles and pile groups: Theory and Application. Ph.D. dissertation, University of Colorado at Boulder.

Achenbach, J.D. (1973). *Wave Propagation in Elastic Solids*, North-Holland Publication Corporation, Amsterdam.

American Petroleum Institute (API) (1987). *Recommended Practice for Planning, Designing, and Constructing Fixed Offshore Platforms*. Washington, DC: American Petroleum Institute.

Andersen, L. (2006). *DCE lecture notes No.3: Linear elastodynamic analysis*. Department of Civil Engineering, Aalborg University.

Ashlock, J.C. (2006). Computational and experimental modeling of dynamic foundation interactions with sand. Ph.D. Thesis, University of Colorado at Boulder, Boulder, CO.

Ashlock, J.C., and Pak, R.Y.S. (2009). Experimental response of piles in sand under compound motion. *J. Geotech. Geoenviron. Eng.*, 135(6), 799–808.

Ashlock J.C. and Phipps, J.N. (2011). Experimental multi-modal foundation vibrations and comparison with benchmark half-space solutions. *Proc., GeoFrontiers 2011*, Dallas, TX, 3118-3127.

Ashlock, J.C., and Jiang, Z. (2017). Three-dimensional soil-pile group interaction in layered soil with disturbed zone by boundary element analysis. *Geotechnical Special Publication No. 279,* ASCE, Reston: VA, 334–344.

Banerjee, P.K. (1978). Analysis of axially and laterally loaded pile groups. *Developments in Soil Mechanics,* 317–346.

Banerjee, P.K., and Manoon, S.M. (1990). A fundamental solution due to a periodic point force in the interior of an elastic half-space. *Earth Eng. Struct. Dyn.*, 19(1), 91–105.

Baranov, V.A. (1967). On the calculation of excited vibrations of an embedded foundation. (in Russian). Voprosy Dynamiki Prochnocti, No.14, Polytech. Inst. Riga, 195-209.

Becker, D.E., and Moore, I.D. (2006). *Canadian Foundation Engineering Manual* (4th edition). Canadian Geotechnical Society.

Bendat, J.S. and Piersol, A.G. (1986). *Random Data*. Wiley-Interscience Publications, New York.

Bharathi, M., Dubey, R.N., and Shukla, S.K. (2019). Experimental investigation of vertical and batter pile groups subjected to dynamic loads. *Soil Dyn. Earthquake Eng.*, 116(2019), 107–119.

Biswas, S., Choudhary, S.S., Manna, B., and Baidya, D.K. (2013). Field test on group piles under machine induced coupled vibration. *International Journal of Geoengineering Case Histories*, 3(1), 10–23.

Blaney, G.W., and O'Neill, M.W. (1986). Measured lateral response of mass on single pile in clay. *J. Geotech. Engrg.*, 112(4), 443–457.

Blaney, G.W., Muster, G.L., and O'Neill, M.W. (1987). Vertical vibration test of a full-scale pile group. *Geotechnical Special Publication No.11*, ASCE, Reston: VA, 149–65.

Blaney, G.W., and O'Neill, M.W. (1989). Dynamic lateral response of a pile group in clay. *Geotech. Test. J.*, 12(1), 22–29.

Borden, R.H., Shao, L., and Gupta, A. (1996). Dynamic properties of piedmont residual soils. *J. Geotech. Engrg.*, 122(10), 813–821.

Brebbia, C.A., Telles, J.C.F., and Wrobel, L.C. (1984). *Boundary Element Techniques:Theory and Applications in Engineering*. Springer-Verlag.

Brebbia, C.A., and Domínguez, J. (1989). *Boundary Elements: An Introductory Course*. Computational Mechanics Publications.

Broms, B.B. (1964). Lateral resistance of piles in cohesive soils. *J. Soil Mech. Found. Div.*, 90(SM2), 27-63.

Brown, D.A. O'Neil, M.W., Hoit, M., McVay, M., EL Naggar, M.H., and Chakraborty, S. (2001). *NCHRP Report 461: Static and dynamic lateral loading of pile groups*. Transportation Research Board – National Research Council.

Brown, D.A., Turner, J.P., and Castelli, R.J. (2010). Drilled shafts: construction procedures and LRFD design methods. FHWA-NHI-10-016, Washington, D.C.

Burr, J.P., Pender, M.J., and Larkin, T.J. (1997). Dynamic response of laterally excited pile groups. *J. Geotech. Geoenviron. Eng.*, 123(1), 1–8.

Bycroft, G.N. (1956). Forced vibrations of a rigid circular plate on a semi-infinite elastic space and on an elastic stratum. *Phil. Trans. Roy. Soc.*, 248(1956), 327–368.

Campanella, R.G., and Stewart, W.P. (1992). Seismic cone analysis using digital signal processing for dynamic site characterization. *Can. Geotech. J.*, 29(3), 477–486.

Canadian Foundation Engineering Manual (2006). Canadian Geotechnical Society, Canada.

Carfagni, M., Lenzi, E., and Pierini, M. (1998). The loss factor as a measure of mechanical damping. *Proc., 6th International Modal Analysis Conference*, Kissimmee, FL, 580-584.

CEN (European Committee for Standardization). (2004). "Design of structures for earthquake resistance Part 5: Foundations, retaining structures and geotechnical aspects". *Eurocode 8*, Brussels.

Chandrasekaran, S.S., Boominathan, A., and Dodagoudar, G.R. (2010a). Experimental investigations on the behavior of pile groups in clay under lateral cyclic loading. *Geotech. Geol. Eng.*, 28(5), 603–617.

Chandrasekaran, S.S., Boominathan, A., and Dodagoudar, G.R. (2010b). Group interaction effects on laterally loaded piles in clay. *J. Geotech. Geoenviron. Eng.*, 136(4), 573–582.

Chandrasekaran, S.S., Boominathan, A., and Dodagoudar, G.R. (2013). Dynamic response of laterally loaded pile groups in clay. *J. Earthquake Eng.* 17(1), 33–53.

Chapman, S. J. (2003). *FORTRAN 90/95 for Scientists and Engineers* (2nd Ed.). McGraw-Hill College.

Choi, Y.S., Lee, J., Prezzi, M., and Salgado, R. (2017). Response of pile groups driven in sand subjected to combined loads. *Geotech. Geol. Eng.*, 35(4), 1587–1604.

Chow, Y. K. (1991). Pile-soil-pile interaction considering weakened zone of soil around PILES. *Computers and Geotechnics*, 12(2), 163–174.

Christensen, R.M. (1971). *Theory of Viscoelasticity*, Academic Press, New York.

Clough, R.W., and Penzien, J. (1995). Dynamics of Structures (3rd edition). Berkeley, CA: Computers and Structures, Inc.

Crouse, C.B., and Cheang, L. (1987). Dynamic testing and analysis of pile-group foundations. *Geotechnical Special Publication, No. 11*, ASCE, Reston: VA, 79-98.

Crouse, C.B., Hushmand, B., Luco, J.E., and Wong, H.L. (1990). Foundation impedance functions: Theory versus experiment. *Journal of Geotechnical Engineering*, 116(3), 432–449.

Dai, G., Salgado, R., Gong, W., and Zhang, Y. (2012). Load tests on full-scale bored pile groups. *Can. Geotech. J.*, 49(11), 1293–1308.

Das, B.M. (2014). *Principles of foundation engineering (8th edition)*, Chapter 3, Cengage Learning, Stanford, CT, U.S.,

Dobry, R., and Gazetas, G. (1988). Simple method for dynamic stiffness and damping of floating pile groups. *Géotechnique*, 38(4), 557–574.

Domínguez J. (1978a). Dynamics Stiffness of Rectangular Foundations. *Research Report R78-20*, Department of Civil Engineering, Massachusetts Institute of Technology, Cambridge, MA 02139.

Domínguez J. (1978b). Response of Embedded Foundations to Traveling Waves. *Research Report R78-24*, Department of Civil Engineering, Massachusetts Institute Technology, Cambridge, MA 02139.

Domínguez, J., and Abascal, R. (1984). On fundamental solutions for the boundary integral equations method in static and dynamic elasticity. *Engineering Analysis*, 1(3), 128–134.

Drnevich, V.P. (2017). A relationship between modulus and damping provides for simple, unified modeling of both. *Geotechnical Special Publication, No.281*, ASCE, Reston: VA, 48-60.

Duncan, J.M., and Chang, C.-Y. (1970). Nonlinear Analysis of Stress and Strain in Soils. *J. Soil. Mech. Found. Div.*, 96(SM5), 1629–1653.

Elkasabgy, M., and El Naggar, M.H. (2011). Field and theoretical dynamic response of vertically loaded helical and driven steel piles. *Proc., 2011 Pan-Am CGS Geotechnical Conference*, 521–535.

Elkasabgy, M., and El Naggar, M.H. (2013). Dynamic response of vertically loaded helical and driven steel piles. *Can. Geotech. J.,* 50(5), 521–35.

El-Marsafawi, H., Kaynia, A.M., and Novak, M. (1992). The superposition approach to pile group dynamics. *Geotechnical Special Publication, No.34,* ASCE, Reston: VA, 114-136.

El Naggar, M.H., and Novak, M. (1994). Non-linear model for dynamic axial pile response. *J. Geotech. Engrg*, 120(2), 308–329.

Naggar, M. H. E., and Novak, M. (1996). Nonlinear analysis for dynamic lateral pile response. *Soil Dyn. Earthquake Eng.*, 15, 233–244.

El Sharnouby, B., and Novak, M. (1984). Dynamic experiments with group of piles. *J. Geotech. Engrg.*, 110(6), 719–737.

EI Sharnouby, B. and Novak, M. (1986). Flexibility coefficients and interaction factors for pile group analysis. *Can. Geotech. J.*, 23, 441–450.

EI Sharnouby, B., and Novak, M. (1990). Stiffness constants and interaction factors for vertical response of pile groups. *Can. Geotech. J.*, 27, 812–822.

Finn, W.D.L., and Gohl, W.B. (1987). Centrifuge model studies of piles under simulated earthquake lateral loading. *Geotechnical Special Publication, No. 11,* ASCE, Reston: VA, 21-38.

Finn, W.D.L., and Gohl, W.B. (1992). Response of model pile groups to strong shaking. *Geotechnical Special Publication, No. 34*, ASCE, Reston: VA, 27–55.

Fotouhi, M.K., and Ashlock, J.C. (2012). Analysis of experimental dynamic soil-pile interaction by approximate numerical solutions. *Proc., 15th World Conference on Earthquake Engineering*, Lisbon, Portugal.

Fotouhi, M.K. (2014). Dynamic soil-pile interaction by random vibration methods. Ph.D. dissertation, Iowa State University, Ames, IA.

Gazetas, G. (1983). Analysis of machine foundation vibrations: state of the art. *Soil Dyn. Earthquake Eng.*, 2(1), 2–42.

Gazetas, G., and Makris, N. (1991). Dynamic pile-soil-pile interaction. Part I: analysis of axial vibration. *Earthquake Eng. and Struct. Dyn.*, 28(4), 115–132.

Gazetas, B.G., Fan, K., Kaynia, A., and Kausel, E. (1991). Dynamic interaction factors for floating pile groups. *J. Geotech. Engrg*, 117(10), 1531–1548.

Gazetas, G., Fan, K., and Kaynia, A. (1993). Dynamic response of pile groups with different configurations. *Soil Dyn. Earthquake Eng.*, 12(4), 239–257.

Ghasemzadeh, H. and Alibeikloo, M. (2011). Pile-soil-pile interaction in pile groups with batter piles under dynamic loads. *Soil Dyn. Earthquake Eng,* 31(8), 1159–70.

Goit, C.S., Saitoh, M., Mylonakis, G., Kawakami, H., and Oikawa, H. (2013). Model tests on horizontal pile-to-pile interaction incorporating local non-linearity and resonance effects. *Soil. Dyn. Earthquake Eng.*, 48, 175–192.

Guzina, B.B. (1996). Seismic response of foundation and structures in multilayered media. Ph.D. dissertation, University of Colorado at Boulder, Boulder, CO.

Hamada, S. (2011). GPU-accelerated indirect boundary element method for voxel model analyses with fast multipole method. *Comput. Phys. Commun.*, 182(5), 1162–1168.

Han, Y.C., and Vaziri, H. (1992). Dynamic response of pile groups under lateral loading. *Soil. Dyn. Earthquake Eng.,* 11(2), 87–99.

Han, Y.C., and Sabin, G.C. (1995). Impedances for radially inhomogeneous viscoelastic soil media. *J. Eng. Mech.*, 121(9), 939–947.

Han, Y.C. (1997). Dynamic vertical response of piles in nonlinear soil. *J. Geotech. Geoenviron. Eng.*, 123(8), 710–716.

Hannigan, P.J., Goble, G.G., and Likins, G.E. (2006). Design and construction of driven pile foundations, FHWA-NHI-05-042, Washington, D.C.

Hardin, B.O., and Drnevich, V.P. (1972a). Shear modulus and damping in soils: measurement and parameter effects. *J. Soil Mech. Found. Div.*, 98(SM6), 603–624.

Hardin, B.O., and Drnevich, V.P. (1972b). Shear modulus and damping in soils: design equations and curves. *J. Soil Mech. Found. Div.*, 98(SM7), 667–692.

Hassini, S., and Woods, R.D. (1989). Dynamic experiments with model pile foundations. *Proc., 12th international conference on soil mechanics and foundation engineering*, Rio de Janeiro, Brazil, 1135–1138.

Hegazy, Y.A., and Mayne, P.W. (1995). Statistical correlations between vs and cone penetration data for different soil types. *Proc., International Symposium on Cone Penetration Testing*, Linköping, Sweden, 173–178.

Iuspa, L., Fusco, P., and Ruocco, E. (2015). An improved GPU-oriented algorithm for elastostatic analysis with boundary element method. *Compu. Struct.*, 146, 105–116.

Jiang, Z., and Ashlock, J.C. (2018). Prediction of three-dimensional dynamic soil-pile group interaction in layered soil by boundary element analysis and seismic cone penetration tests. *Proc.,* Geotechnical Earthquake Engineering and Soil Dynamics V. *Geotechnical Special Publication No. 292*, ASCE, Reston: VA, 237–247.

Kagawa, T., and Kraft, L.M. (1981a). Dynamic characteristics of lateral load-deflection relationships of flexible piles. *Earthquake Eng. Struct. Dyn.*, 9, 53–68.

Kagawa, T., and Kraft, L. M. (1981b). Lateral pile response during earthquakes. *J. Geotech. Engr.*, 107(12), 1713–1731.

Kagawa, T. (1983). Dynamic lateral pile-group effects. *J. Geotech. Engrg.*, 109(10), 1267–1285.

Karl, L., Haegeman, W., and Degrande, G. (2006). Determination of the material damping ratio and the shear wave velocity with the seismic cone penetration test. *Soil. Dyn. Earthquake Eng.*, 26(12), 1111–1126.

Kausel, E. (2006). *Fundamental Solutions in Elastodynamics - A Compendium*. New York: Cambridge University Press.

Kausel, E. (2010). Early history of soil-structure interaction. *Soil Dyn. Earthquake Eng.*, 30(9), 822–832.

Kaynia, A.M. (1982). Dynamic stiffness and seismic response of pile groups. Ph.D. dissertation. Massachusetts Institute of Technology.

Kaynia, A.M., and Kausel, E. (1982). Dynamic behavior of pile groups. *Proc., 2nd International Conference on Numerical Methods in Offshore Pilling*, Austin, Texas, 509–532.

Kaynia, A.M. (1988). Characteristics of the dynamic response of pile groups in homogeneous and nonhomogeneous media. *Proc., 9th World Conf. on Earth. Eng.,* Tokyo-Kyoto, Japan, 575–580.

Kaynia, A.M., and Kausel, E. (1991). Dynamics of piles and pile groups in layered soil media. *Soil Dyn. Earthquake Eng.*, 10(8), 386–401.

Kaynia, A.M. and Mahzooni, S. (1994). Forces in pile foundations under seismic loading. *J. Eng. Mech.*, 122(1), 46–53.

Kong, L.G., Chen, R.P., Wang, S.H., and Chen, Y.M. (2015). Response of 3×3 pile groups in silt subjected to eccentric lateral loading. *J. Geotech. Geoenviron. Eng.*, 141(7), 1–10.

Kim, Y.-S., Roesset, J.M., and Stokoe, K.H. (1987). Interpretation of vertical vibration tests on small scale piles. *Geotechnical Special Publication, No. 11*, ASCE, Reston: VA, 110-126.

Klar, A. and Frydman, S. (2002). Three-dimensional analysis of lateral pile response using two-dimensional explicit numerical scheme. *J. Geotech. Geoenviron. Eng.* 128(9), 775–84.

Kokusho, T., Yoshida, Y., and Esashi, Y. (1982). Dynamic properties of soft clay for wide strain range. *Soils and Foundations*, 22(4), 1–18.

Kondner, R.L. (1963a). Hyperbolic stress strain response: cohesive soils. *J. Soil. Mech. and Found. Div.*, 89, 115–143.

Kondner, R.L., and Zelasko, J.S. (1963b). A hyperbolic stress-strain formulation for sands. *Proc., 2nd Pan-American Conference on Soil Mechanics and Foundations Engineering*, 289–324.

Kramer, S.L. (1996). *Geotechnical Earthquake Engineering*. Upper Saddle River, New Jersey: Prentice Hall.

Lade, P. V. (2005). Overview of constitutive models for soils. *Geotechnical Special Publication No.139*, ASCE, Reston: VA, 1–34.

Lewis, M.R., and Davie, J.R. (1993). Vibrations due to pile driving. *Proc., 3rd International Conference on Case Histories in Geotechnical Engineering*, St. Louis, MI, 649-655.

Luco, J.E. (1974). Impedance functions for a rigid foundation on a layered medium. *Nucl. Eng. Des.*, 31, 204–217.

Makris, N., and Gazetas, G. (1992). Dynamic pile-soil-pile interaction. Part II: lateral and seismic response. *Earthquake Eng. Struct. Dyn.*, 21(2), 145–162.

Manna, B., and Baidya, D.K. (2009). Vertical vibration of full-scale pile — Analytical and experimental study. *J. Geotech. Geoenviron. Eng.,* 135(10), 1452–1461.

Manna, B., and Baidya, D.K. (2010). Dynamic nonlinear response of pile foundations under vertical vibration-Theory versus experiment. *Soil Dyn. Earthquake Eng.*, 30(6), 456–469.

Manna, B., Baidya, D.K., and Prusty, S.S.K. (2013). Prediction of boundary zone parameters and soil–pile separation under horizontal and rocking vibrations. *Int. J. of Geotech. Eng.*, 7(1), 45–54.

Massarsch, K.R., and Fellenius, B.H. (2008). Ground vibrations induced by impact pile driving. *Proc., 6th International Conference on Case Histories in Geotechnical Engineering,* Arlington, VA, 1-38.

Matlock, H. (1970). Correlations for design of laterally loaded piles in soft clay. *Proc., 2nd Annual Offshore Technology Conference,* Vol. 1, 577–594.

Mayne, P.W., and Rix, G. (1995). Correlations between shear wave velocity and cone tip resistance in natural clays. *Soils and Foundations*, 35(2), 107–110.

McVay, M., Bloomquist, D., Vanderlinde, D., and Clausen, J. (1994). Centrifuge modeling of laterally loaded battered pile groups in sand. *Geotech. Test. J.,* 17(2), 129–37.

McVay, M., Casper, R., and Shang, T.-I. (1995). Lateral response of three-row groups in loose to dense sands at 3d and 5d pile spacing. *J. Geotech. Engrg.*, 121(5), 436–441.

MPI: A Message-Passing Interface Standard Version 2.2. http://mpi-forum.org/docs/mpi-2.2/mpi22-report.pdf

Mylonakis, G., and Gazetas, G. (2000). Seismic soil-structure interaction: beneficial or detrimental? *J. Earthquake Eng.*, 4(3), 277–301.

Ni, S.-H. (1987). Dynamic properties of sand under true triaxial stress states from resonant/column torsional shear tests. Ph.D. dissertation, University of Texas at Austin.

Nogami, T., and Novak, M. (1976). Soil-pile interaction in vertical vibration. *Earthquake Eng. Struct. Dyn.*, 4(3), 277–293.

Nogami, T. (1983). Dynamic group effect in axial response of grouped piles. *J. Geotech. Engrg*, 109(2), 228–243.

Nogami, T., and Chen, H. (1984). Simplified approach for axial pile group response analysis. *J. Geotech. Engrg.*, 110(9), 1239–1255.

Novak, M. and Beredugo, Y.O. (1972). Vertical vibration of embedded footings. *J. Soil Mech. Found. Div.*, 1291-1310.

Novak, M. (1974). Dynamic stiffness and damping of piles. *Can. Geotech. J.*, 11(4), 574–598.

Novak, M., and Grigg, R.F. (1976). Dynamic experiments with small pile foundations. *Can. Geotech. J.,* 13(4), 372-385.

Novak, M., and Aboul-Ella, F. (1978a). Impedances functions of piles in layered media. *J. Eng. Mech. Div.*, 104(EM6), 643–661.

Novak, M., and Aboul-Ella, F. (1978b). Stiffness and damping of piles in layered media. *Proc., ASCE Geotechnical Engineering Division Specialty Conference,* Pasadena, CA, 1, 704.

Novak, M., and Sheta, M. (1980). Approximate approach to contact effects of piles. *Special Technical Publication on Dynamic Response of Pile Foundations: Analytical Aspects*, O'Neill and Dobry, eds., 53–79.

Novak, M., and El Sharnouby, B. (1984). Evaluation of dynamic experiments on pile group. *J. Geotech. Engrg.*, 110(6), 738–756.

Novak, M., and Mitwally, H. (1990). Random response of offshore towers with pile-soil-pile interaction. *J. Offshore Mech. Arct. Eng.*, 112, 35–41.

Novak, M. (1991). Piles under dynamic loads. *Proc., 2nd International Conference on Recent Advances in Geotechnical Earthquake Engineering and Soil Dynamics,* St. Louis, MI, 2433–2456.

Ntotsios, E., Hamad, W.I., Thompson, D.J., Hussein, M., Hunt, H., and Talbot, J.P. (2015). Predictions of the dynamic response of piled foundations in a multi-layered half-space due to inertial and railway induced loadings. *Proc., 5th ECCOMAS Thematic Conference on Computational Methods in Structural Dynamics and Earthquake Engineering*, Crete Island, Greece.

O'Neill, M.W., Hawkins, R.A., and Mahar, L.J. (1982). Load transfer mechanisms in piles and pile groups. *J. Geotech. Eng. Div.*, 108(GT12), 1605–1623.

Pak, R.Y.S., and Guzina, B.B. (1999). Seismic soil-structure interaction analysis by direct boundary element methods. *Int. J. Solids Struct.*, 36(31-32), 4743–4766.

Pak, R.Y.S., and Guzina, B.B. (2002). Three-dimensional green's functions for a multilayered half-space in displacement potentials. *J. Eng. Mech.*, 128(4), 449–461.

Pak, R.Y.S., and Ashlock, J.C. (2007). Method of adaptive-gradient elements for computational mechanics. *J. Eng. Mech.*, 133(1), 87–97.

Pak. R.Y.S., and Ashlock, J.C. (2011). A fundamental dual-zone continuum theory for dynamic soil-structure interaction. *Earthquake Eng. Struct. Dyn.*, 40(9), 1011-1025.

Pender, M.J., Hogan, L.S., and Wotherspoon, L.M. (2018). Comparison of experimental and computational snap-back responses of driven steel tube piles in stiff clay. *Geotechnical Special Publication, No.292*, ASCE, Reston: VA, 330–339.

Poley, H. (2012). A look back at single-threaded CPU performance. http://preshing.com/20120208/a-look-back-at-single-threaded-cpu-performance/(accessed June 2018)

Poulos, H.G. (1968). Analysis of the settlement of pile groups. *Géotechnique*, 18, 449-471.

Poulos, H.G., and Davis, E. H. (1980). *Pile Foundation Analysis and Design*. John Wiley and Sons.

Rice, A.H. (1984). The seismic cone penetrometer. Master of applied science thesis. University of British Columbia.

Richart, F.E. Jr., Hall, J.R. Jr., and Woods, R.D. (1970). *Vibrations of Soils and Foundations*. Prentice-Hall Inc., Englewood Cliffs, New Jersey. 1970.

Robertson, P.K., Campanella, R.G., Gillespie, D., and Rice, A. (1986). Seismic CPT to measure in situ shear wave velocity. *J. Geotech. Engrg.*, 112(8), 791–802.

Rollins, K.M., Peterson, K.T., and Weaver, T.J. (1998). Lateral load behavior of full-scale pile group in clay. *J. Geotech. Geoenviron. Eng.*, 124(6), 468–478.

Rollins, K.M., Johnson, S.R., Petersen, K.T., and Weaver, T.J. (2003a). Static and dynamic lateral load behavior of pile groups based on full-scale testing. *Proc., Thirteenth International Offshore and Polar Engineering Conference*, Honolulu, Hawaii, 506–513.

Rollins, K., Olsen, R., Egbert, J., Olsen, K., Jensen, D., and Brian, G. (2003b). *Response, Analysis, and Design of Pile Groups Subjected to Static and Dynamic Lateral Loads*. Utah Department of Transportation Research Division.

Rollins, K.M., Olsen, R.J., Egbert, J.J., Jensen, D.H., Olsen, K.G., and Garrett, B.H. (2006). Pile spacing effects on lateral pile group behavior: Load tests. *J. Geotech. Geoenviron. Eng.*, 132(10), 1262–1271.

Salgado, R., Tehrani, F.S., and Prezzi, M. (2014). Analysis of laterally loaded pile groups in multilayered elastic soil. *Comput. Geotech.*, 62, 136–153.

ScaLAPACK: Scalable Linear Algebra PACKage. http://www.netlib.org/scalapack/explore-html/d5/dd7/pzgesv_8f_source.html (accessed June 2017)

Schnabel, P.B., Lysmer, J., and Seed, H.B. (1972). *SHAKE: A computer program for earthquake response analysis of horizontally layered sites*. University of California, Berkeley.

Scott, R.F., Tsai, C.-F., Steussy, D., and Ting, J.M. (1982). Full-scale dynamic lateral pile tests. *Proc., 14th Annual Offshore Technology Conference*, Houston, TX, 435-450.

Seed, H.B., and Idriss, I.M. (1970). *Soil Moduli and Damping Factors for Dynamic Response Analyses*. Earthquake Engineering Research Center.

Shelman, A., Levings, J., and Sritharan, S. (2010). Seismic design of deep bridge pier foundations in seasonally frozen ground. *Reports and White Papers,* Paper 13, Iowa State University.

Standard Test Method for Standard Penetration Test (SPT) and Split-Barrel Sampling of Soils, ASTM D1568-11, American Society for Testing and Materials, West Conshohocken, PA., 2011.

Stewart, W.P. (1992). *Insitu measurement of dynamics Soil properties with emphasis on damping*. Ph.D. dissertation, Department of Civil Engineering, University of British Columbia.

Stewart, J.P., Taciroglu, E., and Wallace, J.W. (2007). *Full scale cyclic large deflection testing of foundation support systems for highway bridges. Part I: Drilled shaft foundations*. Department of Civil and Environmental Engineering, University of California, Los Angeles.

Stokoe, K.H., Darendeli, M.B., Andrus, R.D., and Brown, L.T. (1999). Dynamic soil properties: laboratory, field and correlation studies. *Proc., Second International Conference on Earthquake Geotechnical Engineering*, Lisbon, Portugal, Vol. 3.

Sy, A., and Siu, D. (1992). Forced vibration testing of an expanded base concrete pile. *Geotechnical Special Publication, No.34*, ASCE, Reston: VA, 170–186.

Taghavi, A., Muraleetharan, K.K., Miller, G.A., and Cerato, A.B. (2016). Centrifuge modeling of laterally loaded battered pile groups in improved soft clay. *J. Geotech. Geoenviron. Eng.*, 142(4).

Takahashi, T., and Hamada, T. (2009). GPU-accelerated boundary element method for Helmholtz' equation in three dimensions. *Int. J. Numer. Methods Eng.*, 80, 1885–1891.

Tomlinson, M.J. (1994). Pile Design and Construction Practices (4th Ed.). Taylor & Francis.

Tomlinson, M.J, and Woodward, J. (2008). *Pile design and construction practice* (5th Ed.). Taylor & Francis.

Torky, A.A., and Rashed, Y.F. (2017). GPU acceleration of the boundary element method for shear-deformable bending of plates. *Engineering Analysis with Boundary Elements*, 74, 34–48.

Vaziri, H., and Han, Y. (1991). Full-scale field studies of the dynamic response of piles embedded in partially frozen soils. *Can. Geotech. J.*, 28(5), 708–718.

Veletsos, A.S., and Verbic, B. (1973). Vibration of viscoelastic foundations. *Earthquake Eng. Struct. Dyn.*, 2(1), 87–102.

Veletsos, A.S., and Dotson, K. (1986). Impedances of soil layer with disturbed boundary zone. *J. Geotech. Engrg.*, 112(3), 363–368.

Veletsos, A.S., and Dotson, K. (1988). Vertical and torsional vibration of foundations in inhomogeneous media. *J. Geotech. Engrg.*, 114(9), 1002–1021.

Vucetic, M., and Dobry, R. (1991). Effect of soil plasticity on cyclic response. *J. Geotech. Engrg.*, 117(1), 89–107.

Wair, B.R., Dejong, J.T., and Shantz, T. (2012). *Guidelines for estimation of shear wave velocity profiles*. Pacific Earthquake Engineering Research Center.

Wilson, D.W., Boulanger, R.W., and Kutter, B.L. (1997). *Soil-pile-superstructure interaction at soft or liquefiable soils sites - centrifuge data report for CSP1*. Department of Civil and Environmental Engineering, University of California at Davis.

Wu, W., Jiang, G., Dou, B., and Leo, C.J. (2013). Vertical dynamic impedance of tapered pile considering compacting effect. *Mathematical Problems in Engineering*, 2013.

Yang, D. Y., Wang, K. H., Zhang, Z. Q., and Leo, C. J. (2009). Vertical dynamic response of pile in a radially heterogeneous soil layer. *Int. J. Numer. Anal. Methods Geomech.*, 33, 1039–1054.

Yao, S., and Kobayashi, K. (1992). Soil-pile-superstructure system in liquefaction. *Geotechnical Special Publication No.34*, ASCE, Reston: VA, 241–255.

Zhu, X.M., Niu, H.P., and Zhang, S.X. (1992). Dynamic parameters analysis of piles. *Geotechnical Special Publication No.34*, ASCE, Reston: VA, 224–240.